Ram P. Bajpai
U. Chandrasekhar *Editors*

Innovative Design and Development Practices in Aerospace and Automotive Engineering

I-DAD, February 22–24, 2016

Springer

Lecture Notes in Mechanical Engineering

About this Series

Lecture Notes in Mechanical Engineering (LNME) publishes the latest developments in Mechanical Engineering—quickly, informally and with high quality. Original research reported in proceedings and post-proceedings represents the core of LNME. Also considered for publication are monographs, contributed volumes and lecture notes of exceptionally high quality and interest. Volumes published in LNME embrace all aspects, subfields and new challenges of mechanical engineering. Topics in the series include:

- Engineering Design
- Machinery and Machine Elements
- Mechanical Structures and Stress Analysis
- Automotive Engineering
- Engine Technology
- Aerospace Technology and Astronautics
- Nanotechnology and Microengineering
- Control, Robotics, Mechatronics
- MEMS
- Theoretical and Applied Mechanics
- Dynamical Systems, Control
- Fluid Mechanics
- Engineering Thermodynamics, Heat and Mass Transfer
- Manufacturing
- Precision Engineering, Instrumentation, Measurement
- Materials Engineering
- Tribology and Surface Technology

More information about this series at http://www.springer.com/series/11236

Ram P. Bajpai · U. Chandrasekhar
Editors

Innovative Design and Development Practices in Aerospace and Automotive Engineering

I-DAD, February 22–24, 2016

Editors
Ram P. Bajpai
Vel Tech Rangarajan Dr. Sagunthala R&D
    Institute of Science and Technology
Chennai, Tamil Nadu
India

U. Chandrasekhar
Vel Tech Rangarajan Dr. Sagunthala R&D
    Institute of Science and Technology
Chennai, Tamil Nadu
India

Preface

Designs and developments are the aspirations of tomorrow's technologies for aero and auto industries to be alive in the competitive world, where cost-effective solutions, improvements in greenhouse environment, longevity/life cycle, eco-friendly materials and manufacturing, certification and government legislation demands are becoming stringent. Whether aerospace or automotive, the pulse and echo are similar in meeting the expected performances in air or on road, respectively. Both the industries have come to symbolize the essence of a modern industrial society. Perhaps more than any other single icon, it is associated with a desire for independence and freedom of movement; an expression of economic status. For the next decades they are marching towards new concept designs, analysis and manufacturing technologies, where more swing is for improved performance through specific and/or multifunctional linguistic design aspect to downsize the system, improve the weight-to-strength ratio, fuel efficiency, make better the operational capability at room and elevated temperatures, reduce wear and tear, NVH aspects while balancing the challenges of beyond Euro IV emission norms, greenhouse effects, and recyclable materials.

The conference covered the areas such as additive manufacturing, aerodynamics, CAD and rapid prototyping, CFD, design engineering, environment, finite element method, fuels and energy source, integration of analysis and expected results, life cycle engineering, manufacturing, materials, MDO techniques, modeling of materials, optimization technologies, propulsion systems, quality, reliability and durability, sensors and health monitoring, simulations, 3D scanning and re-engineering, and 3D printing.

The conference aimed at addressing these issues of tomorrow where academia—industry—R&D partnerships and collaborative programs can be shared and implemented.

The organizers of the 2nd International Conference on Innovative Design, Analysis and Development Practices in Aerospace and Automotive Engineering (IDAD 2016) wish to provide a platform for deliberations on design engineering, numerical methods, analysis/optimization techniques, life cycle engineering, system

engineering, configuration managements, advanced materials, novel manufacturing/
prototyping, vibration and health monitoring, propulsion system and quality and
reliability in the aerospace and automotive field. The response to the conference
was overwhelming on both national and international fronts.

Chennai, India   Ram P. Bajpai
                                                                                        U. Chandrasekhar

Logos of Organizers

Organizer

Knowledge Partners

Organizing Committee

Col. Prof. Dr. Vel. R. Rangarajan, Chief Patron
Founder—President, Vel Tech Dr. RR and Dr. SR Technical University, India
Dr. U. Chandra Sekhar, Organizing Chair
Pro. Vice-Chancellor, Vel Tech Dr. RR and Dr. SR Technical University, India
Dr. Sarasu P., Convenor
Director—R&D, Vel Tech Dr. RR and Dr. SR Technical University, India
Mr. Sivaperumal S., Organizing Secretary
Vel Tech Dr. RR & Dr. SR Technical University, India

International Advisory and Technical Committee

Dr. Amala Justus, Professor, Vel Tech Dr. RR & Dr. SR Technical University, India
Dr. Arvind Chandrasekaran, Research Scientist and Engineering Manager, Center for Engineering in Medicine: Harvard Medical School, USA
Prof. Avinash Arankalle, Visiting Professor, Vel Tech Dr. RR & Dr. SR Technical University, India
Dr. Balasubramanian E., Associate Professor, Vel Tech Dr. RR & Dr. SR Technical University, India
Dr. R.P. Bajpai, Chancellor, Vel Tech Dr. RR & Dr. SR Technical University, India
Prof. Beela Satyanarayana, Vice-Chancellor, Vel Tech Dr. RR & Dr. SR Technical University, India
Dr. Bhujanga Rao V., Former Distinguished Scientist & Director General (NS&M), Defence Research and Development Organisation (DRDO), India
Dr. Chun-Yi Su, Professor, CONCORDIA University, Canada
Dr.-Ing. Christoph Herrmann, Head of Institute, Technische Universität Braunschweig, Germany
Shri. Datar AM, Former Distinguished Scientist & Director General (ACE), Defence Research and Development Organisation (DRDO), India
Dr. Deepak Srivastava, Lead, CANEUS, USA

Dr. Dheepa Srinivasan, Principal Engineer—GE, Power and Water, GE India Technology Centre, India

Prof. Dr.-Ing. Dieter Scholz, Hamburg University of Applied Sciences, Germany

Dr. Dhananjay Kumar, Professor, North Carolina A&T State University, USA

Prof. Eckhardt Schneider, Professor, Saarland University, Germany

Mr. François Falempin, Head of Advanced Powered Airframe, Chief Engineer Hypersonic Programs, Executive Technical Expert, MBDA, France

Dr. Gopalakrishnan S., Professor, Indian Institute of Science, Bangalore

Dr. Gowrishankar N., Whole Time Director, IP Rings Ltd, India

Dr. Gowthaman S., Associate Professor, Vel Tech Dr. RR & Dr. SR Technical University, India

Dr. Gregory Odegard, Associate Professor, Michigan Technological University, Michigan, USA

Dr. Indira Narayanaswamy, Technology Director (ARD&P), ADA, India

Dr. Jagannathan Sankar, Director—(CAMSS), North Carolina A&T State University, USA

Dr. S. Jaichandar, Professor, Vel Tech Dr. RR & Dr. SR Technical University, India

Dr. Jaiswal, Professor, Vel Tech Dr. RR & Dr. SR Technical University, India

Dr. Jayaraman K., Researcher, ICARE-CRNS, Olreans, France

Dr. Khaled Chetehouna, Head of Industrial Risk Engineering Department, INSA Centre Val de Loire, France

Shri. Krishna Prasad Balike, Senior Analyst Materials/Structures, Pratt & Whitney, Canada

Dr. Kunigal Shivakumar, Professor & Director, North Carolina A&T State University, USA

Dr. Mannan S.L., Advisor, Vel Tech Dr. RR & Dr. SR Technical University, India

Dr. Mariappan R., Associate Professor, Vel Tech Dr. RR & Dr. SR Technical University, India

Mr. Murugan N., Assistant Professor, Vel Tech Dr. RR & Dr. SR Technical University, India

Dr. Muthukumaran Packirisamy, Professor and Concordia Research Chair on Optical Bio MEMS, Optical-Bio Microsystems Laboratory, Concordia University

Mr. Prabhakar R., Advisor, Vel Tech Dr. RR & Dr. SR Technical University, India

Dr. Rama Bhat, Professor, Concordia University, Canada

Mr. Ravi Bollina, Visiting Professor, Mahindra Ecole, India & POSTECH, Korea

Dr. Senthilkumar S., Associate Professor, Vel Tech Dr. RR & Dr. SR Technical University, India

Prof. Sivakumar C.S., Professor, Vel Tech Dr. RR & Dr. SR Technical University, India

Mr. Subramanian S., Assistant Professor, Vel Tech Dr. RR & Dr. SR Technical University, India

Dr. Suwas Nikumb, Scientist, Laser Materials Processing NRC, London, Canada
Dr. Vinayak Kabadi, Professor, North Carolina A&T State University, USA
Dr. Vora K.C., Sr. Dy. Director and Head, ARAI Academy, the Automotive Research Association of India, India
Prof. Xian- Cheng Zhang, Professor, East China University of Science & Technology, China

Contents

About the Editors

Dr. Ram P. Bajpai, Ph.D. (IIT Delhi), D.Sc. (Hokkaido University, Japan) is presently the Chancellor of Vel Tech Dr. RR & Dr. SR Technical University, Chennai. He has also been the Director General of MM Group of Institution, MM University, Mullana and Vice-Chancellor of MM University, Solan till November 30, 2011. At the time, he was also holding charge of three universities as Vice-Chancellor, namely (1) Kurukshetra University, Kurukshetra; (2) Guru Jambheshwar University of Science and Technology, Hisar and (3) Deen Bandhu Chhotu Ram University of Science and Technology, Murthal simultaneously. Before joining GJU, Hisar, Dr. Bajpai was Director/Distinguished Scientist/ Scientist at Central Scientific Instrument Organization, Chandigarh, one of the pioneering research laboratories under CSIR, Government of India, New Delhi. He has excellent knowledge of Japanese and German languages, having a large number of publications in national and international journals of repute and a good number of patents. Dr. Bajpai has supervised several Ph.D. and M.S./M.Tech/B.Tech students in various areas of electronics/microelectronics, materials science, nano-electronics, optoelectronics, etc. Dr. Bajpai was UNDP Project Co-ordinator/ Director for the Microelectronics Instrumentation Development program started in 1984 at CSIO, Chandigarh. He has filed and registered a large number of patents. Dr. Ram P. Bajpai has been Scientist/Visiting Professor at several universities in Japan, Germany, Switzerland, France, and USA.

Dr. U. Chandrasekhar is the Pro Vice-Chancellor of Vel Tech Dr. RR & Dr. SR Technical University, Chennai. Previously, he was Director of Engineering Staff College of India (ESCI), an autonomous organ of the Institution of Engineers (India). Before taking charge as Director, ESCI, he was Additional Director at a Ministry of Defence R&D organization called Gas Turbine Research Establishment. For the past 26 years, he has been involved in design, analysis, prototyping, rapid manufacturing, and testing of aero gas turbine engines. He set up the first-ever rapid prototyping laboratory in the country. For his research efforts, he received commendation medal from the Scientific Advisor to the Defence Minister. He received a B.E. in Mechanical Engineering from NIT, Suratkal, M.Tech

in Design Stream from IIT, Madras and Ph.D. from VTU. For his academic excellence at IIT Madras, he received an award from the former President of India, Dr. A.P.J. Abdul Kalam. He was trained in Germany, UK, and Belgium in RP and sensor technologies. He is currently leading a critical technology development project of high-temperature thin film sensors in collaboration with NRC, Canada. He currently serves in the council of the Institution of Engineers and National Design and Research Forum. He was also chosen to represent India in the Young Leaders Convention of World Federation of Engineering Organisations at Geneva. He has been invited by several national and international professional bodies as the keynote speaker on advanced prototyping and sensor technologies.

Promising Configurations for Future Passenger Aircraft

Dieter Scholz

Abstract Passenger aircraft carries passenger with their baggage and often additional cargo over a certain distance or range. Passenger, baggage, and cargo are called payload because they generate revenue for the airline operating the aircraft for profit. An aircraft consists of major components. For a conventional aircraft these components are one fuselage, one wing, a horizontal tail, and a vertical tail. Horizontal tail and vertical tail are together called empennage and are located aft. An unconventional configuration deviates in one or more aspects from the definition of the conventional configuration.

Aircraft burns fuel to CO_2 and dumps CO_2 and other pollutants into the atmosphere. Fossil energy resources are final and the atmosphere has limits to the amount of pollutants it can take. Hence a reduction in fuel consumption is paramount to the life cycle balance of aircraft. All aeronautical disciplines (aerodynamics, structures, propulsion, etc) have their share in researching ways to reduce fuel consumption of aircraft. Aircraft design is responsible for the aircraft configuration and for integrating fuel saving technologies from other aeronautical disciplines into the aircraft.

A promising configuration for future passenger aircraft is a conventional or unconventional combination of major aircraft components also integrating the effects of new technologies from other aeronautical disciplines such that operating costs are reduced by also reducing fuel burn considerably. Today the dominant configuration for passenger aircraft is the conventional configuration with a low wing and engines in nacelles mounted with pylons to the lower side of the wing. This configuration has evolved during decades of aircraft design, production, and operation with the objective to reduce operating cost.

D. Scholz (✉)
Hamburg University of Applied Sciences, Hamburg, Germany
e-mail: info@profscholz.de

There is not just one promising aircraft configuration for future passenger aircraft with reduced fuel consumption. Depending on payload and range requirements, different configurations can be proposed.

For very large aircraft with more than 1000 passengers, the wing becomes the dominating major component and the Blended Wing Body (BWB) configuration should be chosen. The Blended Wing Body consists of a wide lift generating fuselage blending into conventional outer wings. Similar to a flying wing the BWB has no horizontal tail. One or two vertical tails should be included. The BWB has a low wetted area compared to its wing area. It has a higher L/D compared to conventional aircraft due to lower zero lift drag. Problem for the BWB is its structural layout as a passenger aircraft needs a pressure cabin. Not solved is the integration of supercritical airfoils and the requirement for static longitudinal stability for civil certification. Difficulties come from evacuation after ditching and from landing gear integration.

For the typical short to medium range aircraft with up to 200 passengers (in mixed class cabin layout with one aisle) a turboprop aircraft with large propeller diameter should be chosen. Innovative is here the choice of a propeller for bigger aircraft which is so far only available as jets. The propeller has a higher propulsive efficiency than a jet. In contrast to the unducted fan, the path to certification of a propeller aircraft is known. Cabin noise should be kept low with additional sound insulating material. Starting from a reduced fuel mass, aircraft mass goes down further from snow ball effects including increased aspect ratio within the span limited wing to 36 m of ICAO class C. The concept can benefit further from a strut-braced wing with natural laminar flow. This configuration is further detailed in the conference proceedings.

Most important for an efficient aircraft design is a high aspect ratio. For a given span (at the airport), the effective aspect ratio can be increased with winglets, folding wings, or with a box wing. The Box Wing Aircraft (BWA) consists of two wings of half chord (compared to the conventional reference aircraft) in a biplane layout with winglets connecting the wingtips. All these solutions have disadvantages and it is proposed to offer instead the option of (horizontal) wing tip extensions to standard layouts (conforming to ICAO span limits) just violating the span limit and as such accepting the next larger ICAO category for the aircraft.

With the ideas above, we have assumed that fossil fuel will still be available in the future. If this is not the case, fuel has to come from some regenerative process. Biofuel production is not a regenerative process (as has been shown by other authors). Regenerative electrical energy (e.g., from wind, water, or sun) needs to be used instead. If this energy is stored in batteries on board of the aircraft, range is limited to only about 700 km due to the weight of the batteries. When electrical energy is converted to hydrogen (electrolysis), it can be used in gas turbine engines (turbofan, turboprop), and medium range flight is easily possible. However, the aircraft configuration needs to be adapted due to the larger volume of the liquid hydrogen (LH2) with its low density compared to jet fuel. It is recommended to

stretch the fuselage and to install the hydrogen tanks in front and aft of the cabin. Research is on the way to directly convert energy to hydrocarbons. Fuel which can be used as a full substitute or in a mixture with today's jet fuel is called drop-in fuel. Synthetic fuel is a drop-in fuel. It could be used even in older aircraft without the need for any modification of the aircraft.

Ultrasonic Material Characterization and Testing of Anisotropic Components

Eckhardt Schneider and Christian Boller

Abstract All components are more or less anisotropic. In many cases, the anisotropy is beneficial and reduces the quality costs of the deep drawing process of automotive parts. In other cases the anisotropic behavior is tried to be reduced in order to minimize the deflection of rolled parts during machining. During the ultrasonic testing of anisotropic components the anisotropy causes a beam skewing and hence difficulties to precisely localization detected defects. The characterization of anisotropy is an issue and ultrasonic techniques offer appropriate possibilities applicable on automotive and aeronautical components. The anisotropic structure of the metallic single crystal causes a more or less significant direction dependency of material properties. Most of the automotive and aeronautical components are of Al- and Fe-alloys exhibiting a texture, means a preferred grain orientation. Among others, texture causes direction dependent elastic, plastic, and electromagnetic properties. The evaluation of X-ray pole figures is a widely used method to describe texture quantitatively, a variety of mechanical and magnetic techniques are in use for the quantitative texture analysis. The mentioned state-of-art techniques request samples of the component. Ultrasonic technique allows a nondestructive characterization of the anisotropic material behavior and the testing of components exhibiting anisotropy. The contribution presents in its first part the potential of ultrasonic techniques to evaluate texture of components and to characterize texture. The elastic anisotropy of fcc and bcc single crystals is described in terms of the ultrasonic velocities and the change of the times-of-flight of different ultrasonic wave modes are used to determine the texture symmetry axis and to evaluate the strength of the texture. Correlations of ultrasonic time-of-flight data are used to characterize the drawability parameters of rolled products which will be cold or hot pressed into automotive body parts. Among others texture also influences the stiffness and strength values of Al- and Fe-alloys. Ultrasonic techniques enable the evaluation of the mentioned quality measures and hence support the appropriate heat treatment of the parts. Stress states also cause a direction dependent elastic

E. Schneider (✉) · C. Boller
Saarland University Chair for Nondestructive Testing and Quality Assurance,
Saarbrücken, Germany
e-mail: eckhardt.schneider@uni-saarland.de

5

behavior and inhomogeneous distributed residual stress states cause spring back reaction of sheets and plates during the cutting and shaping process of the part. The ultrasonic stress analysis supports the needed heat treatment and the optimization of the machining sequence. The second part deals with the ultrasonic testing of anisotropic structures as welds of austenitic steel on one side and particle and fiber reinforced components on the other. The orientation of the dendritic structure of an austenitic weld causes beam skewing resulting in significant errors of the localization of welding defects. Using basic results of experimental investigations performed on samples cut from a real austenitic weld, a technique is developed to iteratively evaluate the appropriate material elastic constants, and hence to calculate the skewing angle and to correctly localize the welding defect. In particle reinforced metallic (MMC) or ceramic (CMC) components the transversal isotropy of particular planes are a quality measure. The application of linear polarized ultrasonic shear waves allows the check of that measure. The determination of the glass or carbon fiber orientation in reinforced components using the direction dependent change of ultrasonic times-of-flight is limited to thin sheets and plates because of the high ultrasonic attenuation of that material.

Measurement of Some Special Parameters of Engines

P.A. Lakshminarayanan

Abstract The subject of reciprocating engines revolves around efficient combustion with emissions lower than legal limits and transferring the power safely to the shaft. Engineers work with various models for combustion and power train. However, we understand only about 80 % of what happens inside the engine even when advanced simulation techniques based on multi-physics is carried out. To verify or improve combustion in the engine, various parameters are to be measured either at steady or at transient states. In this lecture, we are presenting measurement of some important parameters namely airflow, egr flow, combustion performance, and ammonia.

Keywords Engine parameters · Reciprocating engine · Combustion performance and ammonia · Simulation technique · Airflow · Egr flow etc.

P.A. Lakshminarayanan (✉)
Simpson & Co. Ltd, Chennai, India
e-mail: pal@simpson.co.in

The Wind Tunnel Test and Unsteady CFD of an Ornithopter Formation

Lung-Jieh Yang, Hsi-Chun Lee, Ai-Lien Feng, Chien-Wei Chen, Jenmu Wang, Yuan-Lung Lo and Chia-Kuo Wang

Abstract According to Lissaman and Shollenberger's article published in *Science* in 1970, birds fly in formation to reduce the overall energy expenditure for flight. Thus, this work adopted the same principle of flight formation to ornithopters to save energy. Two experiments and one numerical simulation try are described herein. In the first experiment, a rigid frame housing three ornithopters was made and a tethered flight of it around a fixed suspension point was performed to evaluate the cruise performance of the ornithopter formation and check for energy saving by monitoring the endurance against a known reference value. In the second experiment, a jig housing three ornithopters was subject to a wind tunnel test at the Wind Engineering Center of Tamkang University. The aerodynamic force evaluation of the formation was done. From the preliminary examination, it is found that 3 m/s, 10° angle of attack was the best case for ornithopter formation subject to 14 Hz flapping to generate largest lift and thrust. In the unsteady numerical simulation using COMSOL-Multiphysics, the simple case of two-flapping wings dogging streamwisely was demonstrated. The upstream condition of 1 m/s and 20° angle of attack was formulated and the output instantaneous resultant force on the flapping wings reveal the obvious difference from the single-flapping case. When compared to the real birds flying in a formation, the energy saving of ornithopters may be further improved by replicating the dynamic adjustments of frequency, phase

L.-J. Yang (✉) · H.-C. Lee · A.-L. Feng · Y.-L. Lo · C.-K. Wang
Department of Mechanical and Electromechanical Engineering,
Tamkang University, New Taipei City, Taiwan
e-mail: ljyang@mail.tku.edu.tw

H.-C. Lee
e-mail: zionarmylee@gmail.com

Y.-L. Lo
e-mail: yllo@mail.tku.edu.tw

C.-K. Wang
e-mail: yllo@mail.tku.edu.tw

C.-W. Chen · J. Wang
Department of Civil Engineering, Tamkang University, New Taipei City, Taiwan
e-mail: wang@mail.ce.tku.edu.tw

change, and separation among neighboring ornithopters, to obtain best energy-saving results in the future.

Keywords Wind tunnel · Formation flight · Ornithopter · Comsol-Multiphysics

1 Introduction

Observed from the development of flapping micro air vehicles (MAVs) or ornithopters in the past decade, the flight endurance of ornithopters is still limited much less than 1 h [1, 2]. The short flight time of mini ornithopters like the example in Fig. 1a confined the degree of freedom of their real applications very much. People need to prolong the flight endurance to a great extent in the next generation of ornithopters. Referred to long-distance migration of natural birds, Lissaman and Shollenberger found that these flyers adopted the formation flight to save their flight power during cruising [3]. This previous article also addressed that the Vee-formation is the best rank for birds. Therefore, the prior art from natural birds inspire us to apply the formation flight concept to the mini ornithopters assembled like Fig. 1b.

There are two parts of experiments and one numerical try initiatively done in this work.

2 Tethered Flight Test

During cruising, the power consumption is due to overcoming the air drag on the aircraft body. It is also true for ornithopter formation. Without the real remote flight control for ornithopter formation, we first did the tethered flight test as Fig. 2. In other words, the formation flight and the mono-ornithopter flight are both done via a
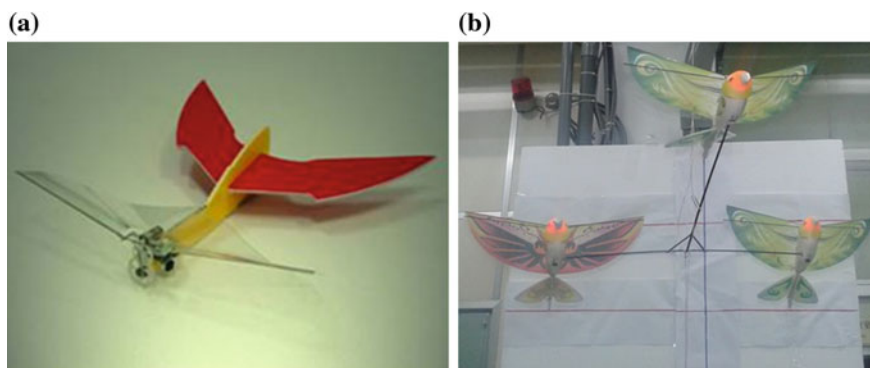
Fig. 1 Mini ornithopters. **a** Tamkang's "Golden Snitch". **b** formation of ornithopters
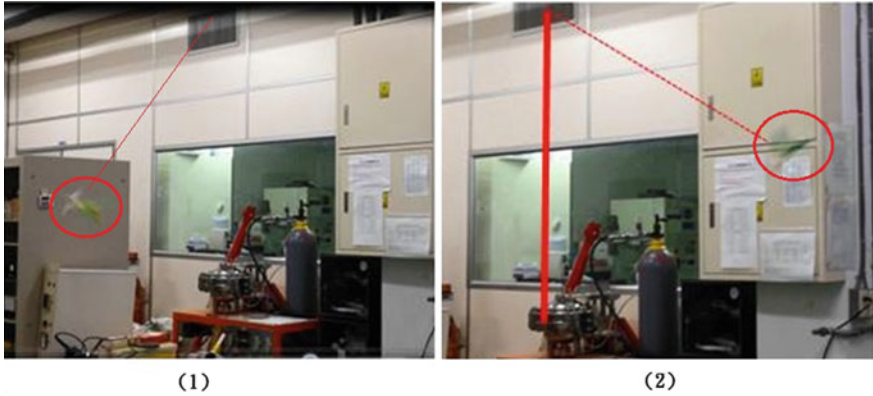
Fig. 2 Tethered flight of an ornithopter **1** to the *left*; **2** to the *right*

level-turning with keeping a constant-flight altitude and cruising velocity by their manual remote controller. After running out all electricity in a Lithium battery on board, we record the total flight time and summarize the test result in Table 1.

From Table 1, the power consumption of a tri-flapper formation is found to be larger than the mono-ornithopter case and contradict the conclusion of Lissaman and Shollenberger's work [3]. Due to the intrinsic instabilities of the MAVs, lack of data consistency about power saving in formation flight concludes less promising results from this first experiment. The reason may be also due to the improper manipulation of the tri-flapper formation flight. The testing field in Fig. 2 is also too small to provide an ideal air domain for formation cruising. Without making sure the perfect flight gesture for all the ornithopters in a formation all the time, the measured flight time is not a reliable evidence to verify the global flight performance about the formation flight.

Table 1 Flight endurance of an ornithopter subject to Fig. 2 (Lithium battery: 75 mAH, cruising speed = 2.22 m/s)

Item	Mono-flapper	Tri-flapper (formation)
The 1st (s)	814	474
The 2nd (s)	792	490
The 3rd (s)	856	485
The 4th (s)	826	473
The 5th (s)	808	492
Averaged endurance (s)	819 ± 6.7 %	482 ± 7.8 %
Driving current (A)	0.33 ± 6.7 %	0.56 ± 7.8 %
Driving voltage (V)	1.9–3.7 (2.5 V in average)	
Power per ornithopter (W)	0.8 ± 6.7 %	1.4 ± 7.8 %

3   Wind Tunnel Test

The second experiment is the aerodynamic force measurement of the ornithopter
formation installed in a wind tunnel located at the Wind Engineering Center of
Tamkang University. This suction type wind tunnel has a test section of 22 m long,
and the cross section is 2.2 m wide, and 1.8 m high. The wind speed ranged from 1
to 28 m/s. The extraction ratio of the entrance is 3.92:1. Honeycomb tube array and
damping networking were mounted at the entrance to make sure the turbulence
strength as small as 0.5–1 %. A 6-axis force gauge (Bertech, OH, USA) is accessed
to take the aerodynamic forces. The measure range of lift/thrust forces are 200 and
100 gf, respectively. The error due to nonlinearity and hysteresis is 0.2 % FSO.
Figure 3 shows the schematic of the wind tunnel, the tailor-made truss for holding
the ornithopter formation, tri-flapping setup (three-flapping), and bi-flapper setup
(two-flapping).

The authors changed several testing parameters including wind speed (1–4 m),
angle of attack (AOA = 10°–30°), distance between ornithopters (1–5 cm). The
flapping frequency is fixed as 13–14 Hz so far. Figure 4 show the best case
(U = 3 m/s; AOA = 10°) of these testing subject to the 20 cm-span ornithopter.
Due to the mechanical vibrations from the jig itself and the wind tunnel structure,
interpretation of the complicated lift/thrust data was processed by the help of fast
Fourier transform (FFT).
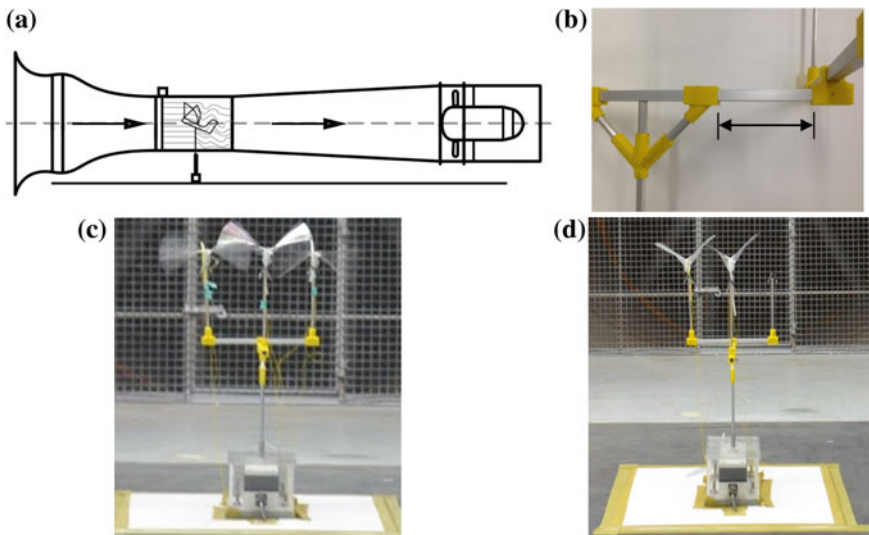
Fig. 3 Setup of the wind tunnel test; **a** schematic; **b** definition of distance between ornithopters;
c tri-flapper case; **d** bi-flapper case
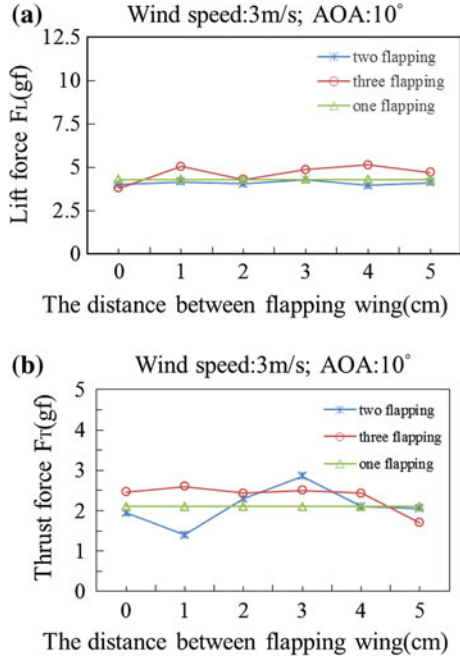
The lift force measurement in Fig. 4 demonstrated that the tri-flapper is the best one compared to mono-flapper and bi-flapper. The net thrust force also has the best performance unless the high speed (5 m/s) point.

4 Unsteady CFD (Computational Fluid Dynamics) for Two-Ornithopter Formation

Regarding the numerical simulation or CFD on the flapping wings, the authors novelly adopted COMSOL-Multiphysics to solve this moving-boundary, solid-fluidic interaction problem. Figure 5 shows the configuration of a flapping wing and the computation domain. Only half wing has been investigated and the centerline of the wing is assigned as the symmetric plane. The whole flapping flow field is conducted by setting the wing leading ledge with a sinusoidal up-and-down motion. The frequency is set as 14 Hz, and the flapping stroke angle is 90°. The upstream velocity is arranged during 0–3 m/s. The angle of attack or the inclination angle of the wing frame is 20°.

The authors qualitatively compare the flow fields of CFD and smoke track in Fig. 6. The 2D slicing plane is along the aerodynamic chord about 24 % span from the centerline. In the upstroke case of Fig. 6a, the vortex area is actually below the wing even though it is not very clear. In the downstroke case of Fig. 6b, the leading
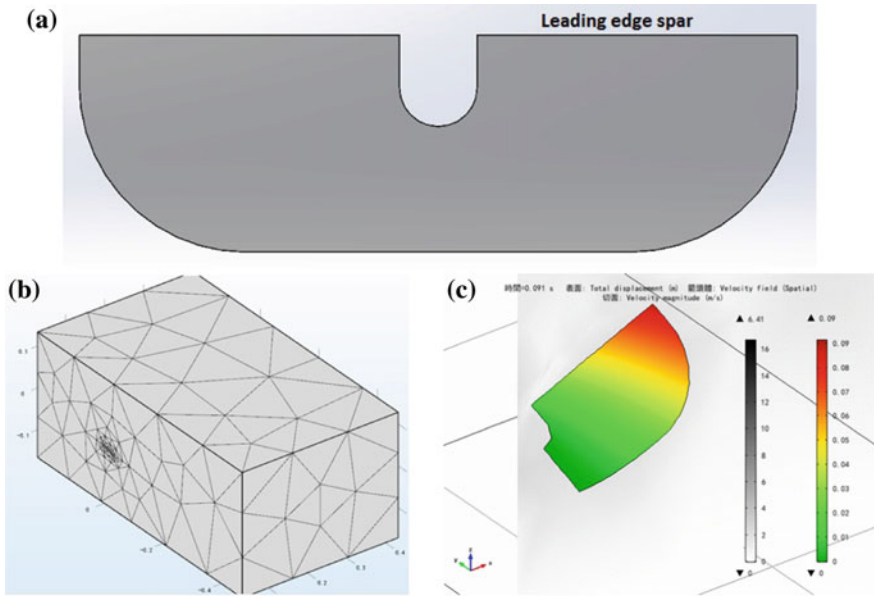
Fig. 5 Numerical 3D simulation of a flapping wing **a** geometry of a wing; **b** meshing of the computation domain; **c** output of a single-flapping flow field
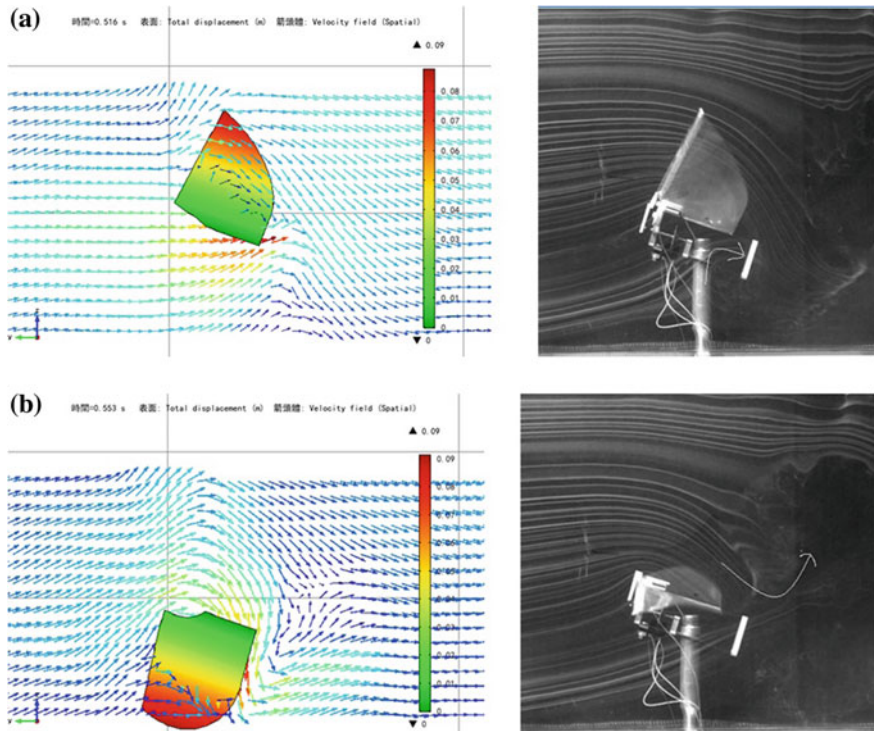
Fig. 6 CFD results versus smoke track; **a** upstroke; **b** downstroke
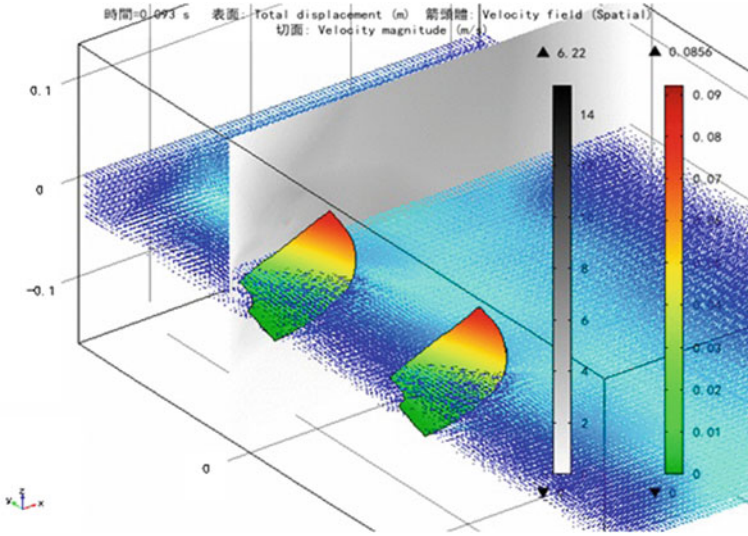
Fig. 7 COMSOL simulation of two-flapping wings

Table 2 Lift forces of two-flapping wings in formation

Cycle	Wing in front (gf)	Wing behind (gf)
1st	10.28	10.38
2nd	4.94	5.24
3rd	6.79	7.34

edge vortex, the main source of flapping lift, both shows clearly in CFD results and the smoke track pictures.

After verifying the feasibility using COMSOL in a single-flapping wing, the next step the authors would like to try si to extend it to the two-flapping case as shown in Fig. 7.

These two-flapping wings beat in phase. The other operation parameters are the same as the single wing case. The authors summarized the lift force data of the first wing-beating cycle in Table 2.

Due to the divergence inaccuracy of CFD simulation, the lift forces of the first and the second cycles may be not reliable. Comparing the data of the third cycle, the lift of the wing behind is obvious. lt better than the wing in front by about 8 %!

5   Conclusions

The aerodynamic force measurement of the ornithopter formation was novelly done in this work. It is found that at 3 m/s and 10° angle of attack was the best case to generate largest lift and thrust. An unsteady CFD using COMSOL-Multiphyscis is

also done on two-flapping wings dogging streamwisely. The energy saving of ornithopter formation may be further improved by replicating the dynamic adjustments of frequency, phase change, and separation among neighboring orni-thopters in the future [4].

References

1. Yang, L.-J., Hsu, C.-K., Han, H.-C. and Miao, J.-M. (2009), "Light Flapping Micro-aerial-vehicles Using Electrical Discharge Wire Cutting Technique," Journal of Aircraft, 46(6), 1866–1874.
2. Keennon, M., Klingebiel, K., Won, H. and Andriukov, A. (2012) "Development of the Nano Hummingbird: a Tailless Flapping Wing Micro Air Vehicle," AIAA Paper, 2012–0588.
3. Lissaman, P.B.S. and Shollenberger, C.A. (1970) "Formation Flight of Birds," Science, 168, 1003–1005.
4. Portugal, S.J., Hubel, T.Y. and Fritz, J. (2014) "Upwash Exploitation and Downwash Avoidance by Flap Phasing in Ibis Formation Flight," Nature, 505, 399–402.

Strategies for Better Fuel Economy, Light Weighting, and Friction Reduction in Cylinder Components of IC Engines

R. Mahadevan

Abstract Automotive OEMs have been working on various technologies for reducing CO_2 emissions and improving fuel economy in their vehicles. Among the strategies that are being employed relating to the IC Engine, light weighting, and friction reduction are the two areas that have received special attention. As the Piston assembly has a direct influence on the friction power of the engine, attempts have been made to reduce the reciprocating mass and improve friction through innovation in design materials and manufacturing processes. Improvements in design and manufacture of pistons and new surface coatings for Pistons & Rings have been able to significantly reduce friction and improve fuel economy. Some of these developments are discussed in this paper.

Keywords CO_2 emission · Cylinder components · Surface coating · Engine friction · Manufacturing process

R. Mahadevan (✉)
India Pistons Limited, Chennai, India
e-mail: rm@indiapistons.com

Fatigue and Fracture Reliability of Additively Manufactured Al-4047 and Ti-6Al-4V Alloys for Automotive and Aerospace Applications

Shafaqat Siddique and Frank Walther

Abstract Metal additive manufacturing is at a stage that it can now be used not only for rapid prototyping but for rapid manufacturing of functional components as well. However, for the reliable employment of parts, their mechanical performance is an important parameter not only in terms of their quasistatic strength but their fatigue performance for dynamic applications. Their fatigue performance should be at par with that of conventionally manufactured alloys. There can still be reliability issues for the additively manufactured parts, as the specific issues—remnant porosity, surface finish, residual stresses, and fatigue scatter—are influenced by the selected process parameters. This paper presents the state-of-the-art of fatigue performance for additively manufactured Al-4047 and Ti-6Al-4V and ways to improve and manipulate the part properties. The results show that their mechanical performance is comparable, even better in some cases, to that of conventionally manufactured materials if appropriate processing parameters and post-processing techniques are employed.

Keywords Additive manufacturing (AM) · Selective laser melting (SLM) · Al-4047 · Ti-6Al-4V · Fatigue behavior

1 Introduction

Selective laser melting (SLM) is a powder-based additive manufacturing process. The process is especially suitable for customized or complex geometries which are difficult or expensive to be manufactured by conventional processes. It overcomes the constraints of conventional processes, such as tooling and physical access to

S. Siddique (✉) · F. Walther
Department of Materials Test Engineering (WPT), TU Dortmund University,
Baroper Str. 303, 44227 Dortmund, Germany
e-mail: shafaqat.siddique@tu-dortmund.de

F. Walther
e-mail: frank.walther@tu-dortmund.de
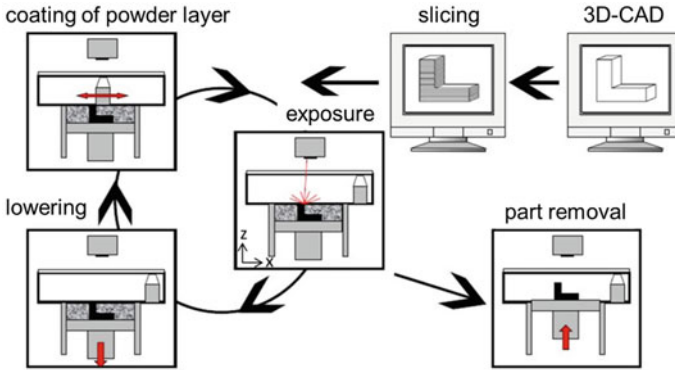
Fig. 1 Schematic representation of SLM process [2]

surfaces for machining. These constraints previously restricted the freedom of design. Most of the applications of SLM are in light-weight parts for aerospace and automotive components or individual and complex parts for medical applications. Using this technique, parts can be produced virtually of any design. Figure 1 shows the typical layout of the SLM process. Data is provided to the SLM system in the form of a CAD model in STL (standard tesselation language) format. The CAD model is sliced into small layers according to the defined layer thickness. The scanner scans the corresponding cross-section of the model. The corresponding powder material is fused by thermal energy resulting from the absorption of the laser beam. The part is produced on a building plate based on a movable platform. After melting one layer, the base plate moves down one layer thickness in z-direction and the process is repeated for the next layer. The process continues till the entire part is manufactured [1, 2].

Some studies are already available investigating the fatigue performance of SLM parts [3–11]. These studies vary in their investigations in terms of surface conditions. As-built condition, which is usually rough after the SLM process, gives a fatigue strength significantly reduced [3, 11] as compared to wrought materials which are tested in polished condition. The achieved fatigue strength is only 30–40 % that of wrought material under as-built condition irrespective of the build orientation. The fatigue strength is usually improved sufficiently when tested after polishing the samples [3, 10, 11]. After improving the surface finish, the achieved strength is usually comparable or even better than that of wrought alloy. Rough surfaces act as micro-notches and are preferred sites for crack initiation which reduces the time to crack initiation drastically. Though the fatigue performance is improved after polishing, there is a high amount of scatter in the fatigue strength [10, 11]. The remnant porosity is responsible for this scatter. Similarly, there is an effect of residual stresses induced during the process on the fatigue performance [8], which needs to be controlled. Microstructure also plays a very important role in fatigue behavior, however, its effect is diminished and remnant porosity remains the

dominating factor, and microstructure comes into play only after micro-level porosity is eliminated [6, 8].

2   Experimental Methodology

Samples from Al-4047 were manufactured using SLM 250 HL, developed by SLM Solutions, and the samples from Ti-6Al-4V were manufactured using EOS M 270 machine developed by Electro Optical Systems. Samples were manufactured with parameters obtained after process optimization with the best achievable relative density. To eliminate the residual stresses induced in the samples due to the high cooling rates, a stress relieving heat treatment was employed for both the alloys. The set of processing parameters for the two alloys are listed in Table 1.

The samples for high cycle fatigue (HCF) tests were machined to the final geometries as shown in Fig. 2.

Tests were carried out for two different configurations for Al-4047 and three different configurations for Ti-6Al-4V. The investigated batches for the two materials are listed in Table 2. HCF tests for Al-4047 were carried out on an Instron 8872 servohydraulic testing system with a load cell of 10 kN, and the

Table 1 Processing parameters for the as-built samples

Parameter	Laser power (W)	Scan speed (mm/s)	Scan spacing (mm)	Layer thickness (μm)	Stress relief
Al-4047	350	930	0.19	50	240 °C, 2 h
Ti-6Al-4V	170	1,250	100	30	650 °C, 3 h

Fig. 2 High cycle fatigue geometry for Al-4047 (**a**), and Ti-6Al-4V (**b**)
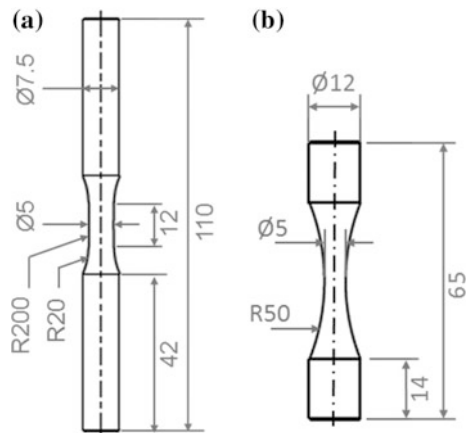
Table 2 Specifications of the investigated Al and Ti batches

Batch	Specifications
Al-I	Al-4047, As-built without base plate heating
Al-II	Al-4047, As-built with base plate heating at 200 °C
Ti-I	Ti-6Al-4V, As-built
Ti-II	Ti-6Al-4V, Polished
Ti-III	Ti-6Al-4V, Shot-peened

corresponding tests for Ti-6Al-4V on an MTS 318.10 equipped with a load cell of 100 kN. Fracture analysis was carried out using a scanning electron microscope Tescan Mira XMU (EOS).

3   Results and Discussions

Stress levels of 120 and 140 MPa were selected for constant amplitude tests for comparison of fatigue strength of Al-4047. These amplitudes were selected after performing a load increase test [12, 13] for both of these batches. Load increase test serves as a useful tool for selection of stress amplitude for constant amplitude tests. The details regarding selection of these stress amplitudes can be found in [8, 14]. The results of the constant amplitude tests at the selected stress levels are shown in Fig. 3a. At stress amplitude of 140 MPa, samples without base plate heating out-perform the samples manufactured with base plate heating, whereas this effect is almost eliminated at lower stress amplitude of 120 MPa where the samples with base plate heating have a fatigue strength slightly lower than the other samples. This behavior exhibits the interaction of microstructural influences on the fatigue strength at different stresses as well as the role of process-induced defects.

Finer microstructures offer more resistance to crack initiation. Samples without base plate heating have more fine microstructure [8]. Therefore, high life for batch Al-I is according to the expectation. Second, samples without base plate heating have slightly higher fraction of gas porosity and may generate multiple crack initiation. At low stresses, these small gas pores are not activated and there is a higher proportion of life which is dominated by crack propagation resistance. Batch Al-II is more resistant to crack propagation due to coarser microstructure. Therefore, the influence of base plate heating depends upon the applied stress amplitude. Batch Al-II was selected for testing for a complete Woehler curve due to its relevance in the high cycle fatigue (HCF) region, and is presented in Fig. 3b with a survival probability of 50 % with a resulting standard deviation, $s(\sigma_a)$ of the Basquin line to be 9.63 MPa.

Figure 4 shows the Woehler curves for the investigated batches of Ti-6Al-4V. As-built samples have a low fatigue strength which is due to the high surface roughness of the specimens obtained from the process. Their fatigue strength at 10^7 cycles was found to be 210 MPa. Average roughness (R_a) of these samples is about 13 μm. These rough surfaces act as micro-notches and offer favorable spots of

Fig. 3 Comparison of fatigue
strength of Al-4047 at 120
and 140 MPa (a); complete
Woehler curve (b)
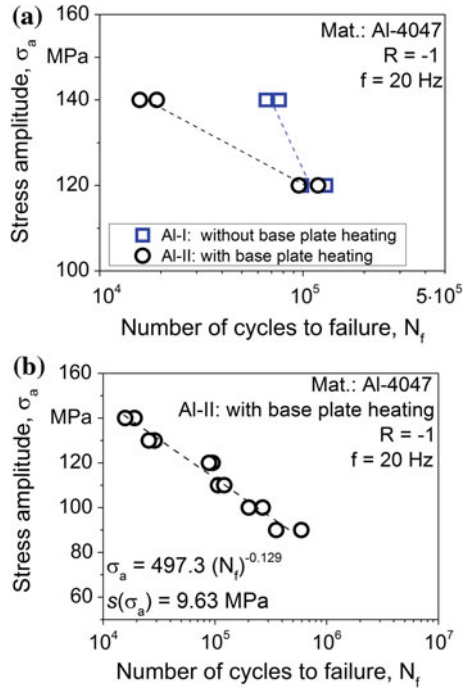
Fig. 4 Woehler curve for
different configurations of
Ti-6Al-4V [10]
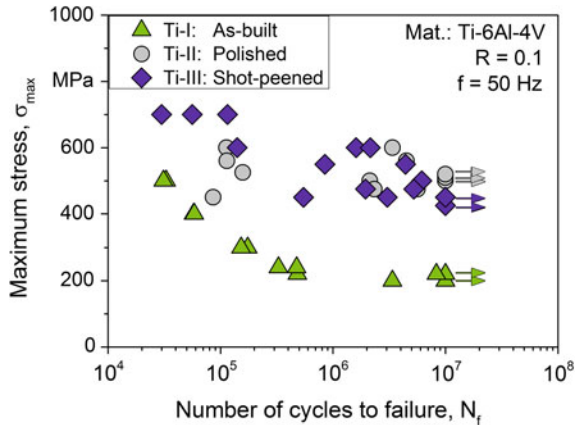
crack initiation which reduce their fatigue strength. Surface was improved by
polishing for batch Ti-II and by shot peening for batch Ti-III. Polished samples
resulted in R_a of 0.5 µm and shot-peened sample in R_a of 2.9 µm. The corre-
sponding fatigue strength at 10^7 cycles was 510 and 435 MPa, respectively.
Though the fatigue strength is increased after polishing and shot peening, it caused
a higher fatigue scatter. Fracture analysis was carried out to investigate the cause of
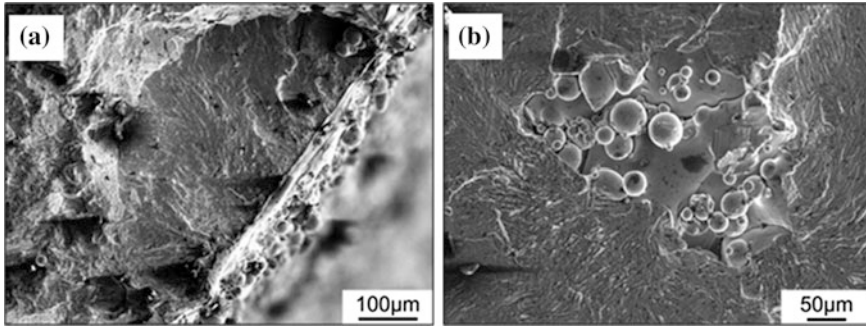
Fig. 5 Fatigue crack initiation: from surface (**a**); from internal material defect (**b**) [10]

scatter and it turned out that in the case of as-built samples, crack initiation occurred from the rough surface resulting in reduced but reliable fatigue life; however, after post-processing, mixed crack initiation was observed with internal crack initiation occurring from unmelted pores. Examples of surface and internal crack initiation are shown in Fig. 5.

4 Conclusions and Outlook

Fatigue strength of Al-4047 was determined with and without base plate heating. It was found that the influence of base plate heating varies depending on the applied stress amplitude. At high stress amplitudes, it reduces the fatigue strength; however, the effect is reversed with reduction of the applied stress amplitude. Fatigue strength of as-built Ti-6Al-4V is drastically less due to rough surfaces; however, it is improved after appropriate post-processing.

Even after achieving the relative density more than 99.5 % from the SLM process, there still exist some powder particles which remain unmelted. These particles are not uniformly distributed but have a random existence. This randomness causes scatter in the fatigue strength. For reliable results, the small remnant porosity needs to be controlled. Base plate heating helps to reduce it by causing degassing, thereby reducing gas porosity. Other techniques like remelting need to be explored for controlling the porosity keeping in view the associated increase in cost. Additionally, in-process monitoring of the melting process needs to be carried out with an integrated feedback system to ensure quality of SLM parts.

References

1. A. Gebhardt, Understanding Additive Manufacturing: Rapid Prototyping—Rapid Tooling—Rapid Manufacturing, HANSER, 2012.
2. E. Wycisk, J. Kranz, C. Emmelmann, Proceedings of Direct Digital Manufacturing Conference (2012), March 14–15 Berlin.
3. P. Edwards, M. Ramulu, Materials Science and Engineering A 598 (2014) 327–337.
4. K.S. Chan, M. Koike, R. Mason, T. Okabe, Metallurgical and Materials Transactions A 44 (2013) 1010–1022.
5. S. Leuders, M. Thöne, A. Riemer, T. Niendorf, T. Tröster, H.A. Richard, H.J. Maier, International Journal of Fatigue 48 (2013) 300–307.
6. E. Brandl, U. Heckenberger, V. Holzinger, D. Buchbinder, Materials & Design 34 (2012) 159–169.
7. E. Brandl, Microstructural and mechanical properties of additive manufactured titanium (Ti-6Al-4V) using wire, SHAKER, Germany, 2010.
8. S. Siddique, M. Imran, E. Wycisk, C. Emmelmann, F. Walther, Journal of Materials Processing Technology 221 (2015) 205–213.
9. G. Kasperovich, J. Hausmann, Journal of Materials Processing Technology 220 (2015) 202–214.
10. E. Wycisk, C. Emmelmann, S. Siddique, F. Walther, Advanced Material Research 816–817 (2013) 134–139.
11. E. Wycisk, A. Solbach, S. Siddique, D. Herzog, F. Walther, C. Emmelmann, Physics Procedia 56 (2014) 371–378.
12. F. Walther, D. Eifler, International Journal of Fatigue 29 (2007) 1885–1892.
13. F. Walther, Mater. Test. 56 (2014) 519–527.
14. S. Siddique, M. Imran, M. Rauer, M. Kaloudis, E. Wycisk, C. Emmelmann, F. Walther, Materials and Design 83 (2015) 661–669.

Recent Advances in High Temperature Structural Integrity

Shan-Tung Tu

Abstract In the last decade, there has been an increasing need of structural integrity technology due to the construction of high temperature installations (e.g., aeroengine, ultra-supercritical power plant, ethylene cracking plant and advanced nuclear power station) in China. To ensure the safe design and long-term reliable operation of the high temperature components, some fundamental issues concerning the deterioration and failure of the materials and structures should be investigated. The lecture summarizes the progresses in recent years in the development of high temperature constraint, fracture theory, and failure assessment techniques. It comprises three major parts:

Part I: Determination of creep properties. Testing principles are proposed to determine creep properties by use of nontraditional specimens.
Part II: High temperature constraint fracture theory. The influences of in-plane and out-of-plane constraints on high temperature fracture are studied. A unified constraint parameter is proposed to modify the current creep crack growth law.
Part III: Damage mechanics-based failure assessment. A new multiaxial creep-damage model considering the cavity growth and microcrack interaction. Special emphasis is put on developing and validating the multiaxial creep ductility factor.

Keywords High temperature · Structural integrity · Constraint fracture · Damage model · Nontraditional specimen

S.-T. Tu (✉)
East China University of Science and Technology, Shanghai, China
e-mail: sttu@ecust.edu.cn

Future Technology Scenarios
for Urban Mobility in India

Shankar Venugopal

Abstract Our ability to ensure clean and convenient mobility in our cities is a key to the sustainable growth of our economy. Volatile fuel prices, rising levels of emissions (and associated problems like smog), and traffic congestions are the key challenges that we face in most Indian cities today. We need the best of our young minds to look at emerging technologies, like smart and connected vehicles, to overcome these challenges. I expect that urban mobility, both personal and commercial, will be shaped by disruptive technologies such as: the move to on-demand mobility, the impact of autonomous vehicles, and the growth of electric vehicles. I will present future technology scenarios and describe technology innovations that could help us to respond to these future scenarios.

Keywords Future automotive technologies · Autonomous vehicles · Hybrid electric vehicles · Battery technologies

S. Venugopal (✉)
Director—Technology Planning and Innovation, Cummins, Chennai, India
e-mail: shankar.venugopal@cummins.com

Wiring the Tin–Silver–Copper Alloy by Fused Deposition Modeling

Yuh-Chung Hu, Yi-Ta Wang and Hsiu-Hsien Wu

Abstract   This paper aims at investigating the feasibility of extrusion and molding a low-melting point metal, Sn–Ag–Cu alloy, on a substrate by fused deposition modeling (FDM). Two Sn–Ag–Cu alloys, one is eutectic Sn–3.0Ag–0.5Cu (SAC305) and another non-eutectic Sn–0.3Ag–0.7Cu (SAC307), are studied for their molding resolutions, material compositions, tensile strength, tear strength, and sheet resistivities after FDM process. The FDM system is assembled by the authors. The molding resolutions are measured by caliper and micrometer. The material compositions are analyzed by energy dispersive spectrometer (EDS). The tensile strengths and tear strengths are measured by Lloyd-LS1 tensile tester. The sheet resistivities are measured by four-point probe station. Some conclusions are drawn according to the experiments. For better resolution, the extrusion temperature is a little higher than the melting point of the material. The FDM process significantly reduces the tensile strength of the materials. For the tear strength, SAC305 is better than SAC0307. The higher the extrusion temperature is, the higher the sheet resistivity is.

Keywords   Fused deposition modeling · Metal wiring · 3D printing

1   Introduction

3D printing, also known as additive manufacturing refers to various processes used to form a three-dimensional structure by successive layers of material directly from computer-aided design to prototype or part. It does not need mold and casting. Nowadays 3D printing can make many of the complex parts, such as thin shells, complex curvatures, and high aspect ratio structures. The common additive manufacturing processes include: selective laser sintering (SLS), stereo lithography (SLA), laminated object modeling (LOM), and fused deposition modeling (FDM) [1–3]. Table 1 makes a comparison of the materials and resolutions for the

Y.-C. Hu (✉) · Y.-T. Wang · H.-H. Wu
Department of Mechanical and Electromechanical Engineering,
National ILan University, 1, Sec. 1, Shennong Road, Yilan 26041, Taiwan
e-mail: ychu@niu.edu.tw

Table 1 Comparison of the additive manufacturing processes [5, 6]

Process	Binding method	Material	Layer thickness (mm)
SLS	Laser	PA/GF, metal, ceramic	0.076
SLA	UV	Photosensitive resin	0.02
LOM	Adhesive sheet material	Roll paper, Aluminum	0.05
FDM	Thermoplastic	ABS/PLA	0.178

aforesaid additive manufacturing processes [4, 5]. SLS uses a laser as the power source to sinter metal or ceramic powders, aiming the laser at points in space defined by a 3D model, binding the material together to create a solid structure. SLA works by focusing an ultraviolet laser on to the photopolymer resin which is solidified and forms a single layer of the desired 3D structure. LOM is a rapid prototyping system which forms 3D structure by successively gluing layers of adhesive-coated paper, plastic, or metal laminates together and cutting to shape with a knife or laser cutter. FDM uses a thermoplastic filament, which is heated to its melting point and then extruded, layer by layer, to create a 3D structure.

For FDM, recent researches focus on the development of new material to improve the mechanical properties of polymers, such as polymethylmethacrylate (PMMA) [6], polypropylene (PP) [7], Polycaprolactone (PCL) [8], and ULTEM*9085 [9]. Some composite material mixing metals and polymers were also proposed [10]. The FDM process is mainly divided into five steps: model establishment by computer-aided design, STL file transform, model layer analysis, fused deposition modeling, and post-FDM process. The dimension errors mainly attribute to the thermal expansion of material. Many researchers focused on the optimization of the foregoing steps [11–14]. According to the aforesaid literature survey, most materials for FDM are polymers. However, metal materials were seldom mentioned for FDM process because of their high-melting point though they have better properties of mechanical, electrical, and thermal conductivity than polymers. This paper tries to form the Sn–Ag–Cu alloy of low-melting point by FDM process. Two Sn–Ag–Cu alloys, one is eutectic Sn–3.0Ag–0.5Cu (SAC305) and another non-eutectic Sn–0.3Ag–0.7Cu (SAC0307), are studied for their molding resolutions, material compositions, tensile strength, tear strength, and sheet resistivities after FDM process. The FDM system is assembled by the authors.

Sn–Ag alloy system has good thermal resistivity and mechanical properties [15]. By adding the third element, say copper, its melting point can be reduced from 221 to 217 °C [16]. Sn–Ag–Cu alloy system is commonly used by industries because of its lower melting point, better mechanical properties, and wettability on substrate. An intermetallic compound (IMC) layer will be induced at the boundary between Sn–Ag–Cu layer and Cu-substrate by the atomic diffusion at that boundary, which refers to interfacial reaction. The morphology of IMC layer depends on the composition of Sn–Ag–Cu alloy as well as on the substrate [17–19]. The IMC with high-concentration Ag and Cu may cause coarseness of structural defects, not only reduce the mechanical strength of alloy but also change to brittle fracture damage.

Therefore, low-concentration Ag and Cu is recommended for Sn–Ag–Cu alloy in FDM. In recent years, FDM has been used to directly deposit low-melting point conductive metal material on the circuit board or embedded electronical/mechanical devices to form the so-called structural electronics, such as 3D metal wires and connectors [20–23]. FDM can directly form 3D metal wires and connectors on the curved surfaces of parts and thus save the volume of circuit board. Therefore, it is applied to the antenna of cell phone, vehicle electronics, and aerospace engineering.

2 Methodology

Low-melting point metals are suitable for FDM because of their wettability, weldability, and low creep rate. However, after the thermal cycles of FDM process, the microstructure coarsening and changing to be brittle of the material may cause the block of extrusion nozzle and structure crack, respectively. Therefore, the authors select SAC305 and SAC0307 (Table 2), which can preferably against thermal fatigue. Print the alloys on copper substrate. The control parameters FDM include: nozzle aperture, nozzle temperature, printing speed, and single layer thickness. The printed 3D structures are studied for their molding resolutions, material compositions, tensile strength, tear strength, and sheet resistivities.

The FDM system is assembled by the authors (Fig. 1), which consists of an X-Y table to control the horizontal motion of substrate and a Z-axis to control the vertical

Table 2 Material properties of SAC305 and SAC0307

Material	Solidifying behavior	Solidus/liquidus temperature (°C)	Surface tension (MPa)	Elongation (%)	Young's modulus (GPa)
SAC305	Eutectic	217/219	53.3	46	41.6
SAC0307	Non-eutectic	217/227	37.1	50	37.5

Fig. 1 The FDM system
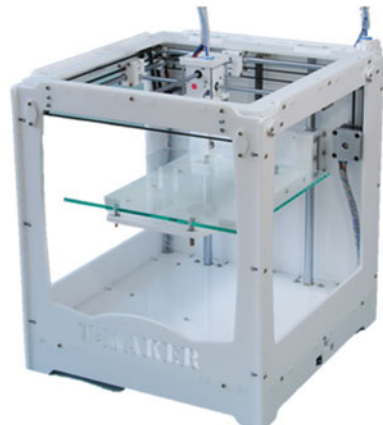
Fig. 2 The nozzle and throat module
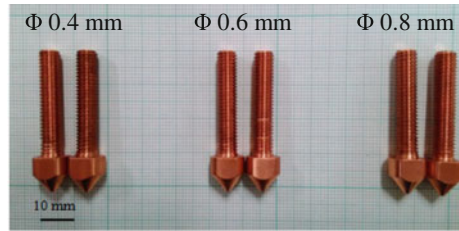
Fig. 3 The test wiring pattern design
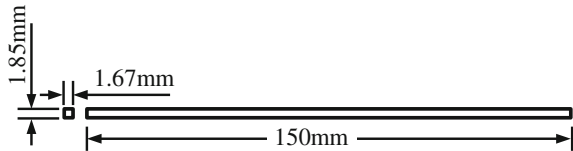
motion of nozzle, and its firmware and hardware can be tuned according to the material properties. The homemade of the nozzle and throat module, whose length is 40 mm and three apertures Φ: 0.4, 0.6, and 0.8 mm (Fig. 2). The Sn–Ag–Cu wire materials are supplied by a step motor and a pressure roller into a heating aluminum to melt and then extruded by the nozzle. The user interface software is developed by Ultimaker Co. Ltd., which provides the functions of model layering and printer control. The authors design a test wiring pattern for FDM process tuning (Fig. 3).

Prior to the FDM process, the real melting points of the wire materials must be verified, Fig. 4 shows the measured cooling curves of the two Sn–Ag–Cu alloys. The copper substrate must be polished by water sandpaper to remove the oxide layer and then washed by 75 % ethanol to remove oil. According to the cooling curves of the alloys, the authors test three different FDM process recipes and nozzle apertures for each test alloys (Table 3). Compare the molding resolutions, material compositions, tensile strength, tear strength, and sheet resistivities.

Fig. 4 The cooling curves of the alloys
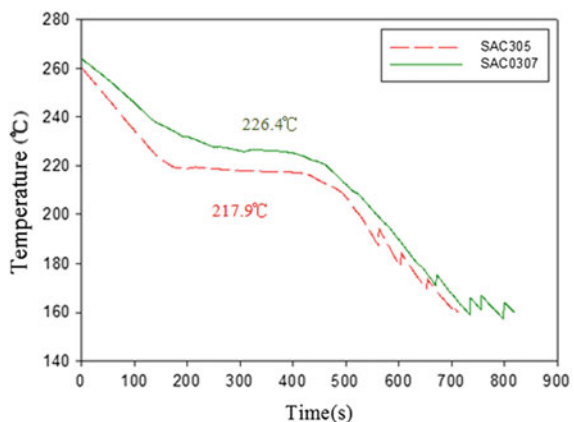
Table 3 The FDM process recipes for SAC305 and SAC0307

Recipe No.	Printing speed (mm/s)	Nozzle temperature (°C)	Layer thickness (mm)
SAC305			
Recipe 1	30	230	0.2
Recipe 2	35	235	0.3
Recipe 3	40	240	0.4
SAC0307			
Recipe 1	30	240	0.2
Recipe 2	35	245	0.3
Recipe 3	40	250	0.4

3   Results and Discussion

Table 4 shows that, both of the SAC305 and SAC0307, the recipe 3 using Φ0.8 mm nozzle aperture can obtain consistent 3D structure and have the best extrusion ability. The extrusion ability of SAC305 is better than that of SAC0307 while the resolution of the latter one is better than that of the former. Figure 5 shows the printed NIU-words pattern. Figure 6 shows that the average dimension errors of SAC0307 are better than that of SAC305. Furthermore, the length error is much better than those of thickness and width. The results of EDS (Figs. 7 and 8) show that the alloy composition has not significant change by FDM. The results of extension test (Fig. 9) show that FDM changes the alloys from ductile to brittle and significantly reduces the tensile strength. Figure 10 shows that the tear strength of SAC305 is better than that of SAC0307. Figure 11 shows that increasing the extrusion temperature may increase the sheet resistivities.

Table 4 Comparison of the extrusion results of the recipes

Alloy	Recipe No.	Spray nozzle aperture		
		Φ0.4 mm	Φ0.6 mm	Φ0.8 mm
SAC305	Recipe 1	△	O	△
	Recipe 2	△	O	O
	Recipe 3	O	O	O
SAC0307	Recipe 1	△	O	O
	Recipe 2	△	△	O
	Recipe 3	x	x	O

O Consistent deposit; △ Inconsistent deposition; x Non-extrusion
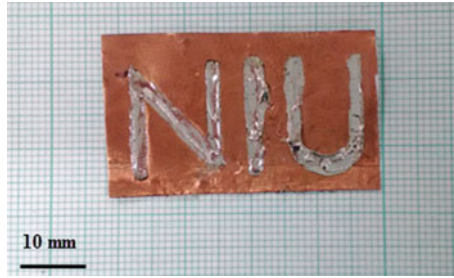
Fig. 5 3D printed NIU pattern, SAC0307, Φ0.8 mm, speed 40 mm/s, temp. 250 °C
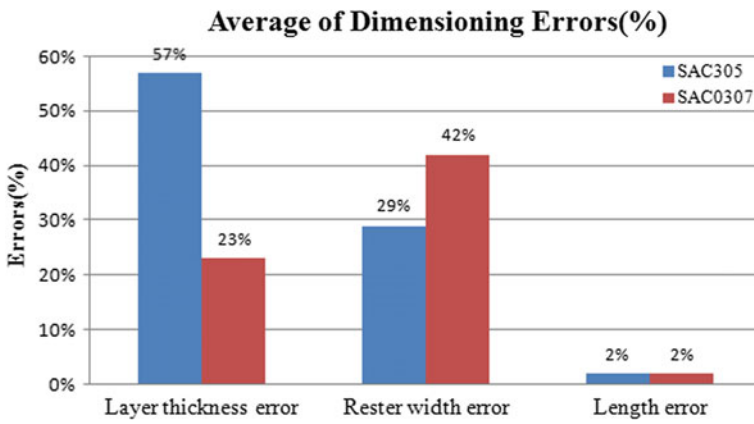
Fig. 6 Average dimension errors of SAC305 and SAC0307
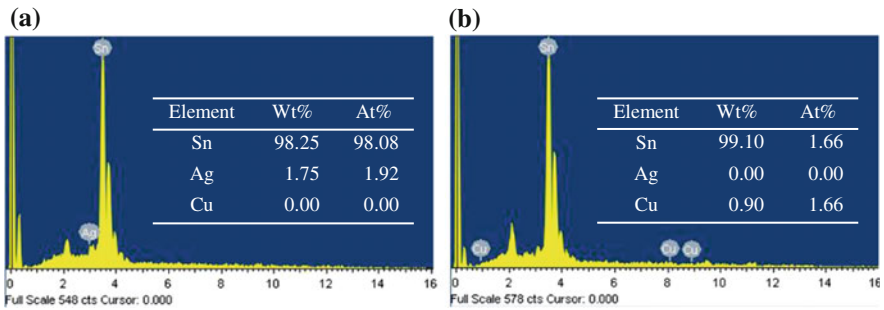
Fig. 7 EDS prior to FDM: **a** SAC305, **b** SAC0307

Element	Wt%	At%
Sn	36.34	23.72
Ag	2.63	1.89
Cu	61.03	74.39

Element	Wt%	At%
Sn	3.72	2.03
Ag	0.00	0.00
Cu	96.28	97.97
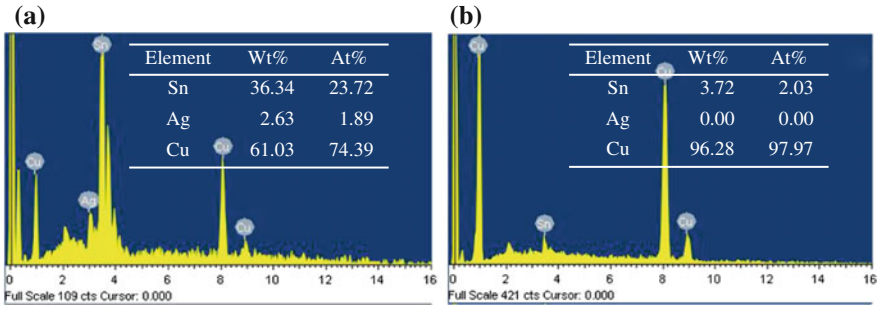
Fig. 8 EDS post-FDM: **a** SAC305, **b** SAC0307
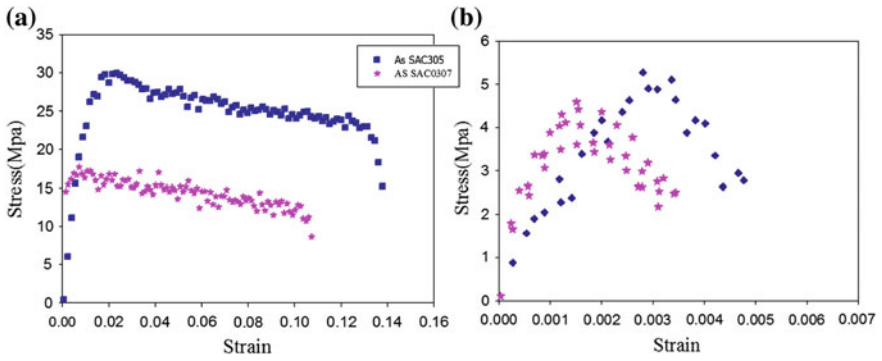
Fig. 9 Tensile test prior and post-FDM

Fig. 10 Tear test
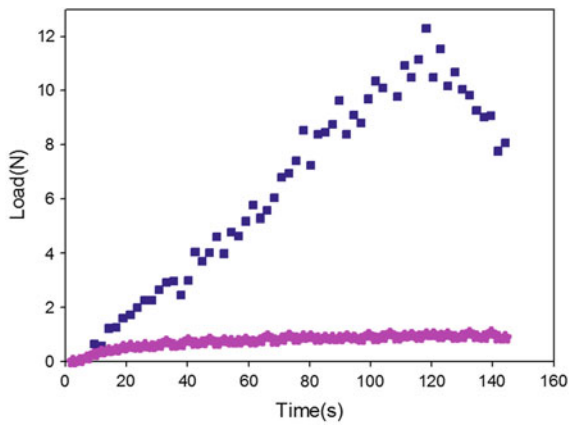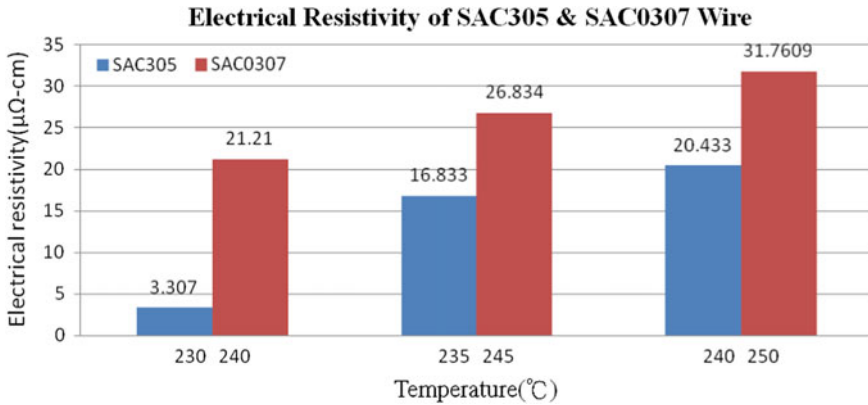
Fig. 11 Sheet resistivities measurement

4   Conclusions

Some conclusions are drawn according to the experiments. For better resolution, the extrusion temperature is a little higher than the melting point of the material. The FDM process significantly reduces the tensile strength of the materials. For the tear strength, SAC305 is better than SAC0307. The higher the extrusion temperature is, the higher the sheet resistivity is.

References

1. Tang Y, Loh H, Wong Y, Fuh J, Lu L, Wang X (2003) Direct laser sintering of a copper-based alloy for creating three-dimensional metal parts. Journal of Materials Processing Technology, 140: 368–372
2. Arnold CB, Serra P, Piqué A (2007) Laser direct-write techniques for printing of complex materials. MRS Bulletin, 32: 23–31
3. Jones J B, Wimpenny D I, Chudasama R, Gibbons G J (2011) Printed circuit boards by selective deposition and processing. In: Proceedings of 22nd Solid Freeform Fabrication Symposium, Aug. 8–10, Austin, TX, USA, 639–656
4. Shellabear M, Danzig A, Heugel M, Kotila J, Nyrhilä O (2001) The Breakthrough to 20 Micron Layers-Increasing Precision and Efficiency in Direct Metal Laser Sintering. In: Proceedings of Rapid 2001 International User's Conf, 245–252
5. Kim G, Oh Y (2008) A benchmark study on rapid prototyping processes and machines: quantitative comparisons of mechanical properties, accuracy, roughness, speed, and material cost. Journal of Engineering Manufacture, 222: 201–215

6. Bourell D, Stucker B, Espalin D, Arcaute K, Rodriguez D, Medina F (2010) Fused deposition modeling of patient-specific polymethylmethacrylate implants. Rapid Prototyping Journal, 16: 164–173

7. Kalita S J, Bose S, Hosick H L, Bandyopadhyay A (2003) Development of controlled porosity polymer-ceramic composite scaffolds via fused deposition modeling. Materials Science and Engineering C, 23: 611–620

8. Cao T, Ho K-H, Teoh S-H (2003) Scaffold design and in vitro study of osteochondral coculture in a three-dimensional porous polycaprolactone scaffold fabricated by fused deposition modeling. Tissue engineering, 9: 103–112

9. Fischer M, Schöppner V (2013) Some investigations regarding the surface treatment of Ultem*9085 parts manufactured with fused deposition modeling. In: Proceedings of 24th Annual International Solid Freeform Fabrication Symposium, Austin, Aug. 12–14, 805–815

10. Masood S, Song W (2004) Development of new metal/polymer materials for rapid tooling using fused deposition modelling. Materials & Design, 25: 587–594

11. Lee B, Abdullah J, Khan Z (2005) Optimization of rapid prototyping parameters for production of flexible ABS object. Journal of Materials Processing Technology, 169: 54–61

12. Thrimurthulu K, Pandey P M, Reddy N V (2004) Optimum part deposition orientation in fused deposition modeling. International Journal of Machine Tools and Manufacture, 44: 585–594

13. Anitha R, Arunachalam S, Radhakrishnan P (2001) Critical parameters influencing the quality of prototypes in fused deposition modelling. Journal of Materials Processing Technology, 118: 385–388

14. Sood A K, Ohdar R, Mahapatra S (2009) Improving dimensional accuracy of Fused Deposition Modelling processed part using grey Taguchi method. Materials & Design, 30: 4243–4252

15. Choi S, Lee J, Guo F, Bieler T, Subramanian K, Lucas J (2001) Creep properties of Sn-Ag solder joints containing intermetallic particles. Journal of Minerals, Metals and Materials Society, 53: 22–26

16. Moon K-W, Boettinger W, Kattner U, Biancaniello F, Handwerker C (2000) Experimental and thermodynamic assessment of Sn-Ag-Cu solder alloys. Journal of Electronic Materials, 29: 1122–1136

17. Kim H, Liou H, Tu K (1995) Three-dimensional morphology of a very rough interface formed in the soldering reaction between eutectic SnPb and Cu. Applied Physics Letters, 66: 2337–2339

18. Kim K, Huh S, Suganuma K (2003) Effects of intermetallic compounds on properties of Sn-Ag-Cu lead-free soldered joints. Journal of Alloys and Compounds, 352: 226–236

19. Lu H Y, Balkan H, Ng K S (2006) Microstructure evolution of the Sn-Ag-y% Cu interconnect. Microelectronics Reliability, 46: 1058–1070

20. Perez K B, Williams C B (2013) Combining additive manufacturing and direct write for integrated electronics-a review. In: Proceedings of 24th International Solid Freeform Fabrication Symposium-An Additive Manufacturing Conference, SFF, 962–979

21. MacDonald E, Salas R, Espalin D, Perez M, Aguilera E, Muse D (2014) 3D printing for the rapid prototyping of structural electronics. Access IEEE, 2: 234–242

22. Espalin D, Muse D W, MacDonald E, Wicker R B (2014) 3D Printing multifunctionality: structures with electronics. The International Journal of Advanced Manufacturing Technology, 72: 963–978

23. Kief C J, Zufelt B K, Christensen J H, Mee J K (2011) Trailblazer: proof of concept CubeSat Mission for SPA-1. AIAA Infotech, 1–7

Design and Study of Aerodynamics of Wind-Solar Hybrid System for Domestic Application by Using Balsa Wood

Nikhil V. Nayak, P.P. Revankar and M.B. Gorawar

Abstract Increasing levels of modernization in different countries worldwide have lead to an exponential growth in national energy demand. India with its huge population base had a total grid connected electric power close to 285 GW during 2015 with annual generation of 1106 TWh accounting to a per-capita energy consumption of 746 kWh. The Government of India under its ambitious plan "Power for all" envisages 24×7 power supply for the entire domestic and Industrial loads by the year 2022. This power sector initiative also promises the generation through green path by targeting reduction in carbon footprint. The plan has sanctioned funds for production of 190 GW power based on go green initiative of United Nations Organization and a step forward to create a better environment for future generations. The proposed work aims at design of wind-solar hybrid system for light load decentralized applications. The computational tools were used to model and analyze wind turbine (WT) blade structure for low power applications to suit decentralized power generation based on renewable energy. The comparative studies of test aerofoil with standard NACA 0018 aerofoil indicated conformance of the test aerofoil as a profile for WT blades. The test aerofoil has the feature of easier manufacturability as against standard NACA 0018 profile adopted in commercial WT blades. The studies conformed suitability of test profile at specified angle of attack with WT blade structure and hub construction using balsa wood. The choice of balsa wood was based on properties of lighter weight and adequate strength that was supported on the designed tower of tripod type. The designed WT system was for a rated power output of 75 W while operating at an average wind speed of 4.5 m/s. The system developed will be a feasible option for powering households in rural India.

Keywords Aerofoil blades · Balsa wood · Hybrid renewable energy system · Wind history

N.V. Nayak (✉) · P.P. Revankar · M.B. Gorawar
Mechanical Engineering, B.V. Bhoomaraddi College, Hubli, India
e-mail: nikhilnayak17@gmail.com

1 Introduction

The exploitation of alternative energy sources as a substitute to the fossil fuels is gaining popularity worldwide owing to the onus placed on environmental protection. The lot of interest in particular to harness wind and solar energy as future source of energy has been reported by several researchers [1]. The study focuses on design and simulation of wind-solar hybrid standalone system that can be used for rural electrification [2]. The proposed work focuses on use of green and renewable energy to provide electricity to areas that do not have access to grid supply. The main objective is to generate power through wind-photovoltaic hybrid power system with battery storage for light loads, to integrate the hybrid system to save on high fuel costs and minimizes noise [3].

2 Literature Survey

The extensive research survey on the reported work has been summarized in this section.

Narayanswamy et al. [4], have reported on the use and availability pattern of wind energy at selected locations based on the data collected by wind monitoring department [4]. The data of wind speed at the location is a useful parameter for design of wind-based power generation systems in India.

Vikram Singh et al. [5], have focused primarily on designing the blade for tapping power in the regions of low wind power density by using a VAWT. This can be achieved by using wood [5] as the blade material, which has good strength to weight ratio and has sufficient stiffness to the loads applied.

Kianoosh Yousef et al. [6] have studied the effects of varying angle of attack on blade and suction flow control which were evaluated for an airfoil [7]. The study suggests that for a particular angle of attack the designed foil can behave similar to a standard NACA aerofoil and can be used in place of such aerofoil when needed for an application where the high cost and manufacturing complexity are not required (Table 1).

3 Wind System Design

Average wind speed (U_m)

$$U_m = \frac{1}{n-1} * \Sigma(U_i) \quad (\text{from } 1 \text{ to } n-1) \tag{1}$$

Table 1 Wind data for Hubli city

Monthly wind speed (for: 2014)	For a height of 5 m (m/s)	For a height of 10 m (m/s)
January	2.32	2.78
February	2.27	2.72
March	2.37	2.84
April	2.11	2.33
May	3.36	4.02
June	5.24	6.38
July	4.99	5.98
August	4.39	5.27
September	4.46	5.14
October	1.92	3.32
November	2.79	3.45
December	2.63	3.16

$$U_m = \frac{1}{12 - 1} * (37.34)$$
$$U_m = 3.43 \, \text{m/s}$$

Standard deviation (σ)

$$\sigma^2 = \frac{1}{n - 1} * \Sigma (U_i - U_m) \tag{2}$$

$$\sigma = \sqrt{\left[\frac{1}{12 - 1} * (15.71) \right]}$$
$$\sigma = 1.19$$

Shape parameter

(a)

$$k = \sqrt{[d_1 * (U_m)]}, \tag{3}$$

where d_1 is site parameter = 0.94 (average)

$$k = 0.94 * (3.43)^{1/2}$$
$$k = 1.48$$

(b)

$$k = \left(\frac{\sigma}{U_m}\right)^{-1.086} \tag{4}$$

$$k = \left(\frac{1.19}{3.43}\right)^{-1.086}$$

$$k = 2.24$$

Scale parameter

$$c = \frac{U_m}{\Gamma\left\{\left(1 + \left(\frac{1}{k}\right)\right)\right\}} \tag{5}$$

$$c = \frac{3.43}{\Gamma\left\{\left(1 + \left(\frac{1}{2.24}\right)\right)\right\}}$$

$$c = 1.4306$$

Weibull density function

$$f(u) = \frac{k}{c} * \left(\frac{u}{c}\right)^{k-1} * \exp\left[-\left(\frac{u}{c}\right)^{k}\right] \tag{6}$$

$$f(u) = \frac{2.24}{1.43} * \left(\frac{4.11}{1.43}\right)^{2.24-1} * \exp\left[-\left(\frac{4.11}{1.43}\right)^{2.24}\right]$$

$$f(u) = 0.32$$

Power density factor in terms of Weibull

$$\text{Power Density} = \frac{\text{Pavail}}{A} = \frac{1}{2} * \rho * c^3 * \left(1 + \frac{3}{k}\right) \tag{7}$$

$$\text{Power Density} = \frac{\text{Pavail}}{A} = \frac{1}{2} * 1.22 * 4.56^3 * \left(1 + \frac{3}{2.24}\right)$$

$$\text{Power density} = 55.59 \, \text{W/m}^2$$

Energy density

$$\text{Energy Density} = \frac{1}{2} * \rho * c^3 * \left(1 + \frac{3}{k}\right) * \text{time}, \tag{8}$$

Where time is in seconds

$$\text{Energy Density} = \frac{1}{2} * 1.22 * 4.56^3 * \left(1 + \frac{3}{2.24}\right) * 8760$$

$$\text{Energy Density} = 486.968 \, \text{kWh/m}^2$$

Wind speed corresponding to maximum energy (U_{me})

$$U_{me} = c * \left[\frac{k+2}{k}\right]^{\frac{1}{k}} \tag{9}$$

$$U_{me} = 4.56 * \left[\frac{2.24+2}{2.24}\right]^{\frac{1}{2.24}}$$

$$U_{me} = 5.24 \, \text{m/s}$$

Maximum energy available from turbine

$$W = \frac{1}{2} * A * U_{me}^3 * f(U_{me}) * \text{time} \tag{10}$$

$$W = \frac{1}{2} * 1.22 * 5.24^3 * 0.206 * 8760$$

$$W = 156 \, \text{kWh/m}^2$$

The above equations suggest that for an average wind speed of 3.43 m/s for a pole height of 10 m the maximum available energy is 156 kWh/m^2 which is sufficient for domestic lighting application. The wind speed corresponds to maximum energy is 5.24 m/s (Fig. 1).

Power Output from Turbine

$$\text{Power Output} = a + (b * 7.5^{2.24}), \tag{11}$$

where a and b are constants (Figs. 2 and 3 and Tables 2 and 3).

$$a = 100 * \frac{2.24^{2.24}}{3^{2.24} - 9^{2.24}}$$

$$b = \frac{100}{9^{2.24} - 3^{2.24}}$$

$$\text{Power Output} = -2.44 + (0.066 * 7.5^{2.24})$$

$$\text{Power Output} = 62.79 \, \text{W}$$
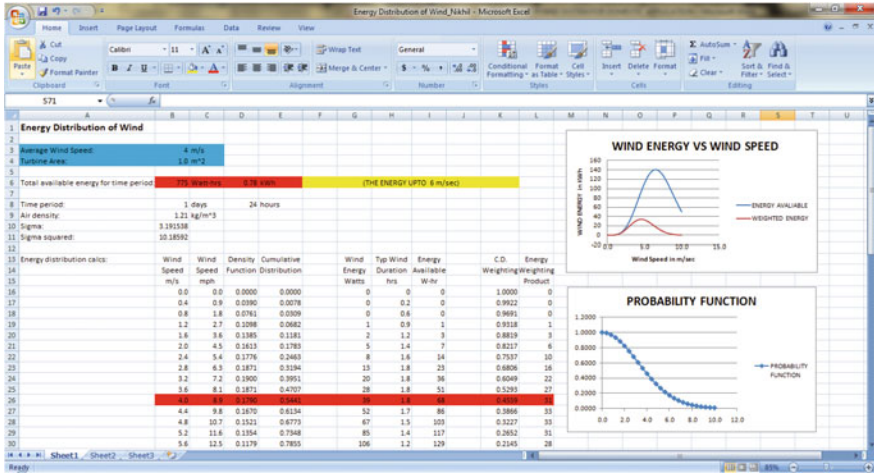
Fig. 1 Excel sheet for calculation of wind energy available for wind speed of 4 m/s
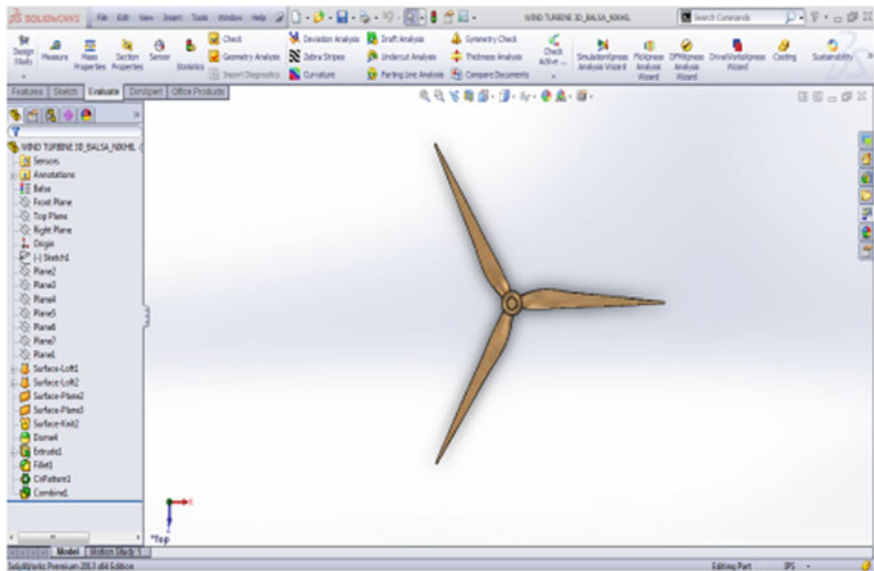
Fig. 2 Front view of CAD model
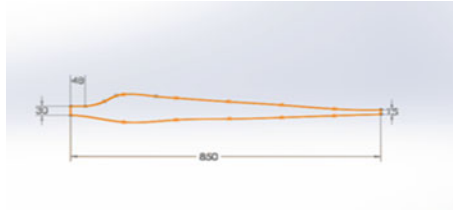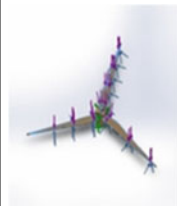
Fig. 3 Dimensions of blade

Table 2 Properties of Balsa wood [12]

Name	Balsa
Model type	Linear elastic isotropic
Shear modulus	0.23 GPa
Yield strength	25 MPa
Elastic Modulus	3 GPa
Density	0.13 g/cm^3

Table 3 Boundary conditions

Load name	Load image	Load details	
Force		Entities Type Value	3 face(s) Apply normal force 115 N (X Component) 130 N (Y Component)
Pressure		Entities Type Value Units	3 face(s) Normal to face 1.0 Atm

4 Design of the System

The Solidwork's analysis is performed to determine a feasible material for the particular application (Figs. 4, 5, 6, 7, 8, and 9 and Table 4).

The Solidworks analysis suggests that Al 6061 [8] is safe and rigid because maximum stress is lower than stress developed but is not easy to manufacture.
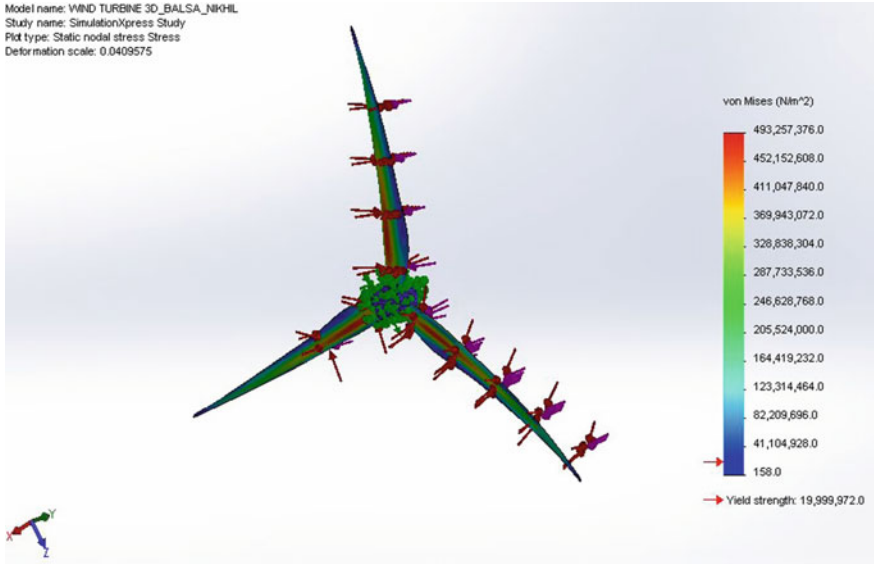
Fig. 4 von-Mises equivalent stress for balsa
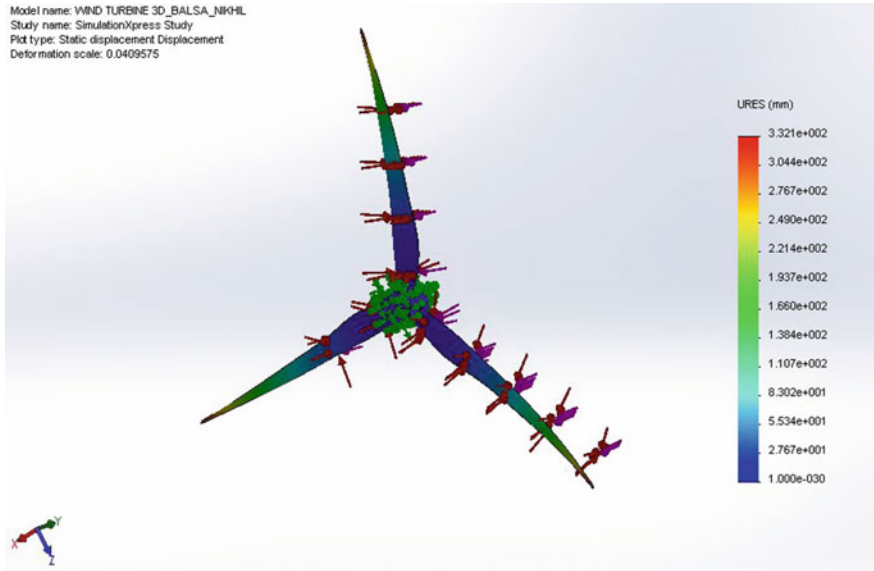
Fig. 5 Static displacement for balsa
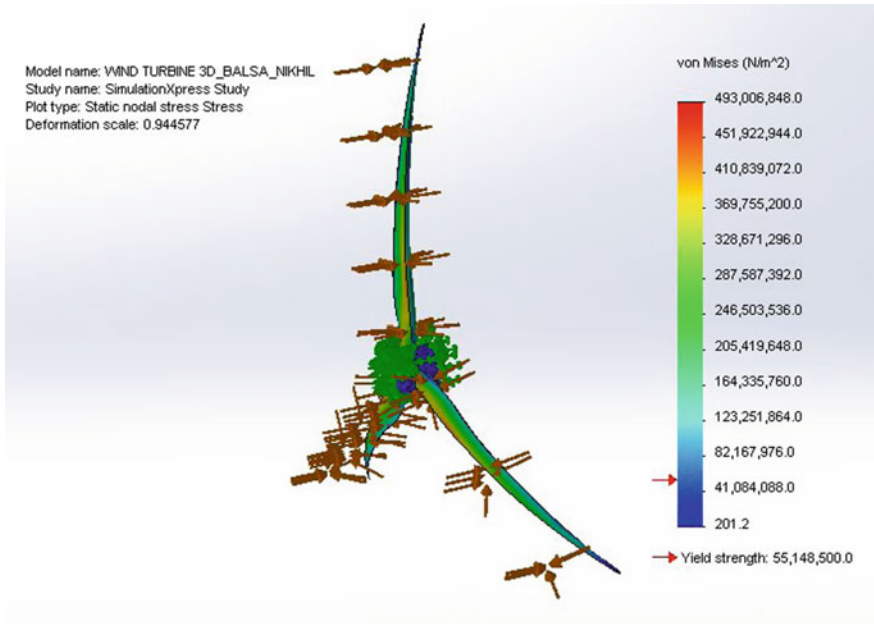
Fig. 6 von-Mises equivalent stress for Al 6061
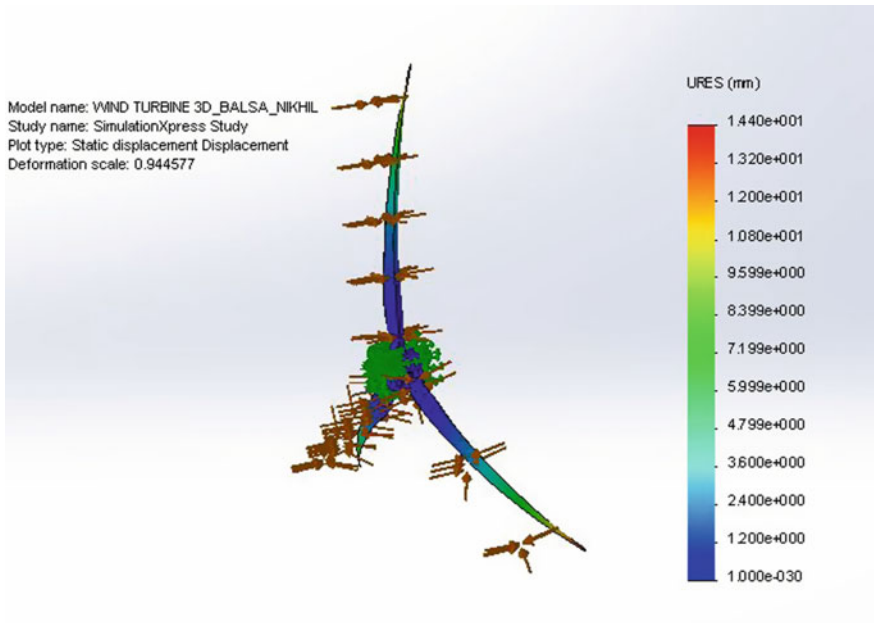
Fig. 7 Static displacement for Al 6061
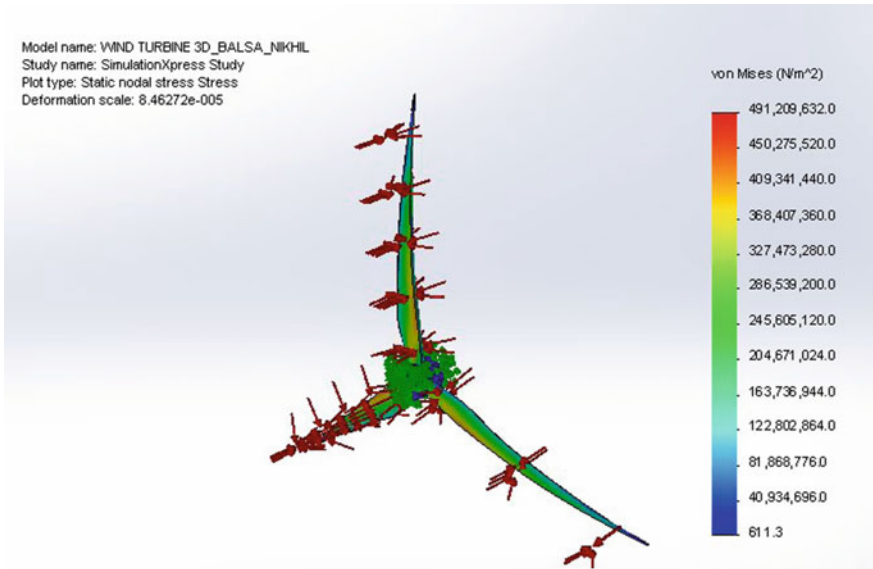
Fig. 8 von-Mises equivalent stress for PVC
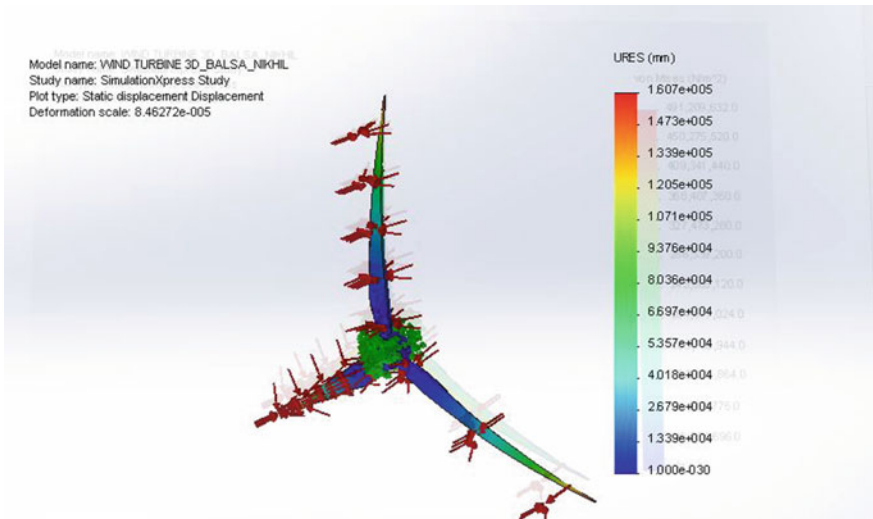
Fig. 9 Static displacement for PVC

Table 4 Comparison of different materials

Material	Balsa wood	AI 6061	PVC
Number of elements	7763	7782	7592
Yield strength (MPa)	25	55.15	12.8
Max normal stress (MPa)	45.4	49.1	45.0
Static displacement (m)	0.0016	0.0014	0.0032

Fig. 10 Balsa wood manufactured by Kaveri wood works Bangalore [6]
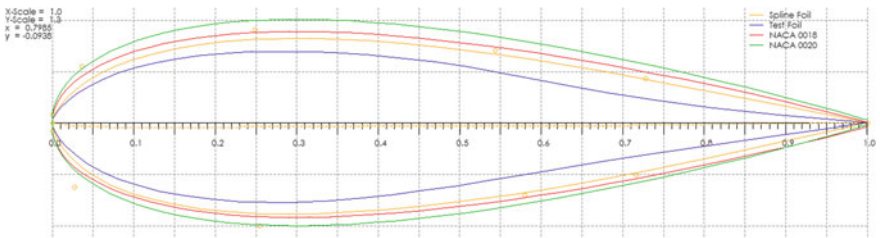
Fig. 11 Foils generated for chord length of 100 mm, maximum thickness of 18 mm at 50 mm from the leading edge

While PVC is easily, available but is not as rigid as the other two and the static displacement, the von-Mises equivalent stress is not too high, and that the balsa wood material [9] selected for the blade can withstand the loads and pressure and can perform effectively (Fig. 10).

The Qblade simulation carried out was to compare the different aerofoil profiles for the blade and to find the performance under dynamic conditions. The study of effect by varying different parameters like wind speed, rotor speed, etc., done was to find their impact on the performance of the system (Figs. 11 and 12).

From Figs. 13 and 14 the test foil and the NACA 0018, profiles have similar nature of graph for coefficient of performance but the pressure distribution is better in case of NACA 0018 profile.

Keeping cost of manufacturing and application [10] of the wind turbine in mind, the test foil can be preferred. The comparison shows the pressure distribution along
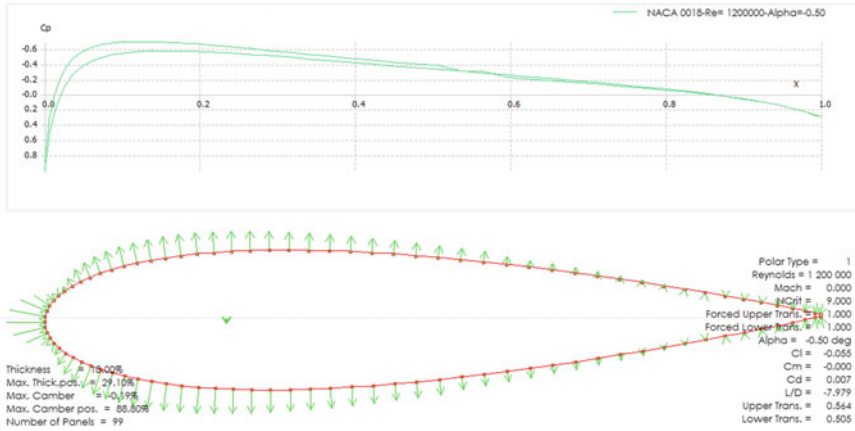
Fig. 12 Pressure distribution and the graph of coefficient of performance against position for NACA0018
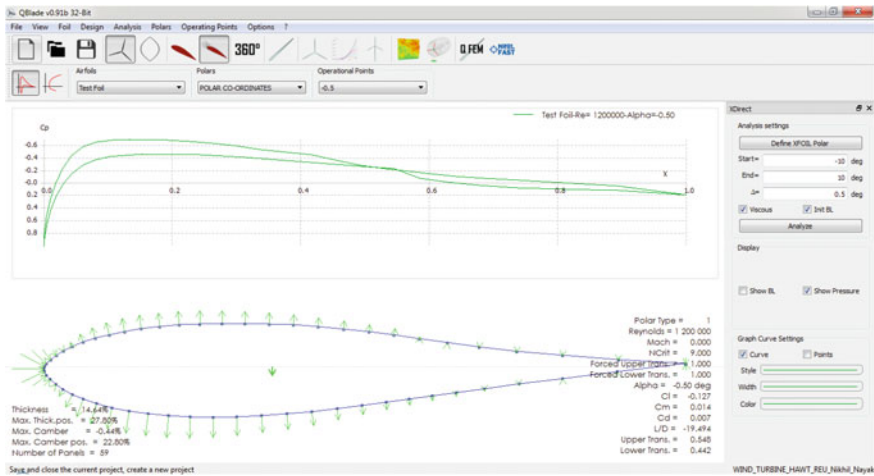
Fig. 13 Pressure distribution and the graph of coefficient of performance against position for Test Foil

the test foil along with a plot of C_p (Coefficient of performance) against the position. The angle of attack is −0.5 which also shows the maximum camber.

This figure shows four graphs that were obtained for different rotor speeds. The green colored line represents 100 rpm, red colored line represents 200 rpm, and the dark blue colored line represents the 300 rpm rotor speed.

The graphs plotted against the pitch angle suggest that the power is highest if the pitch angle is on the lower side and power reduces with increase in pitch angle.
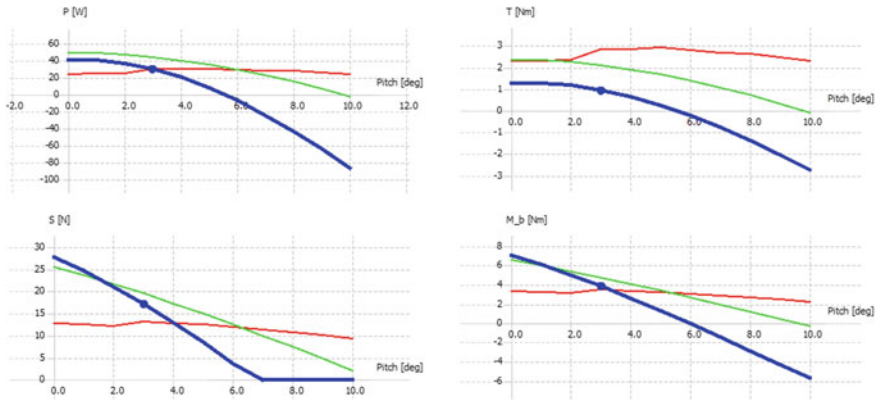
Fig. 14 Impact on pitch angle for different rotor speeds

A similar trend seen in other graphs as well for thrust force (*S*), bending moment (*M*$_b$), and Torque (*T*). Rotor speed of 200 rpm and pitch angle ranging 2°–4° seems appropriate for the application.

Figure 15 shows four graphs that were obtained for different rotor speeds. The convention for rotor speeds remains the same as Figure 14.

The graphs are plotted against T.S.R. (tip speed ratio) which suggest that the power is high at low T.S.R. and reduces with increase in T.S.R. and becomes constant.

A similar trend is seen in other graphs as well for thrust force (*S*), bending moment (*M*$_b$), and Torque (*T*). Rotor speed of 300 rpm and T.S.R. on the lower side is appropriate for the application.

Figure 16 shows four graphs that were obtained for different rotor speeds. The convention for rotor speeds remains the same as previous figure.
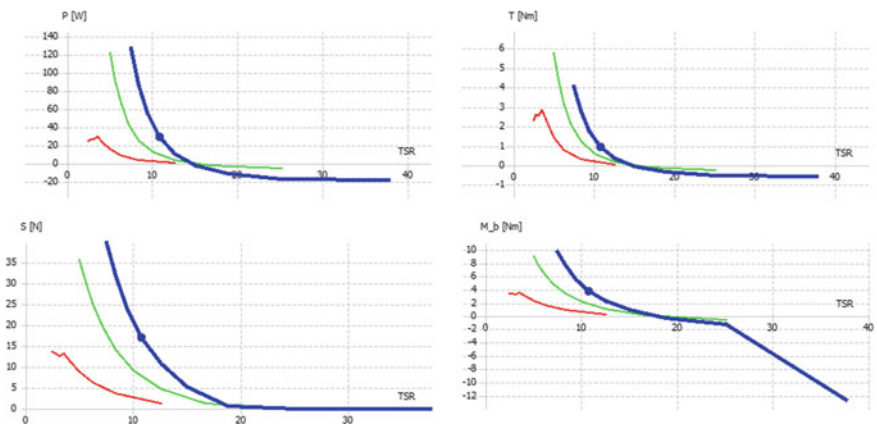
Fig. 15 Impact on tip speed ratio for different rotor speeds
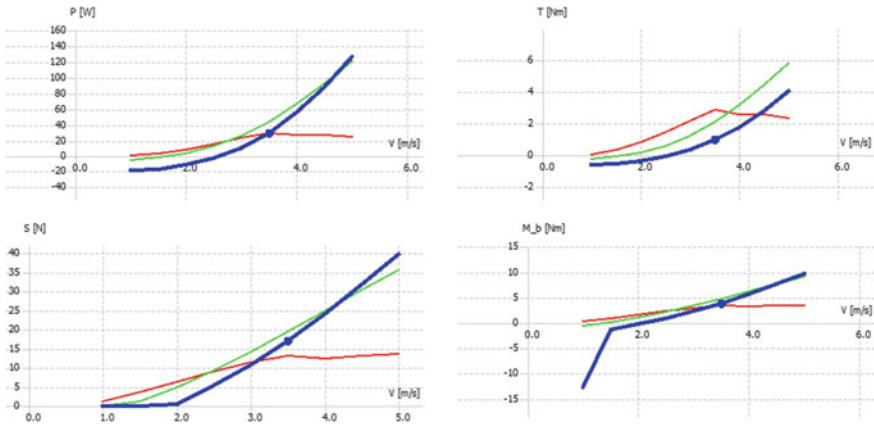
Fig. 16 Impact on wind speed for different rotor speeds
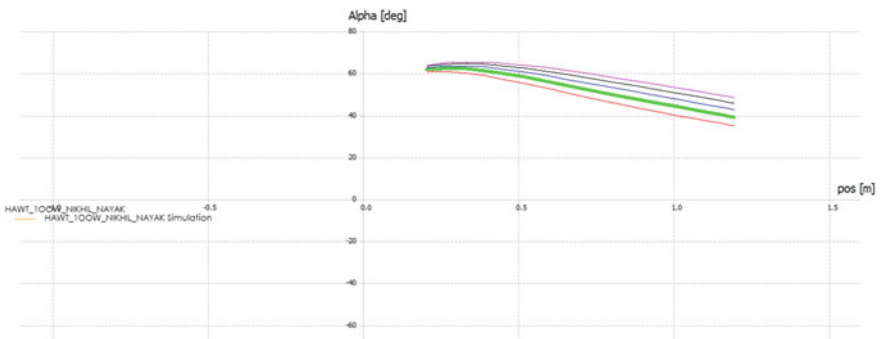
Fig. 17 Angle of attack against position for different wind speeds

The graphs plotted against different wind speeds suggest that the power increases with increase in the wind speeds. Rotor speed of 300 rpm and the wind speed calculated for the given area 4 m/s suggests that a power output of 60 W for rotor speed of 300 rpm.

Figure 17 used to study the effect of different wind speeds on the angle of attack and its variation with the position. The graph suggests that the angle of attack for the designed wind speed of 4 m/s dips drastically as the position increases and is marked in green color (Fig. 18).

Figure 19 shows the model that was prepared using the Qblade software for the purpose of simulation. After subjecting to a simulation of time step of 360 we can observe that the power that are obtained is 43.5 W for a wind speed of 4 m/s and a height of 10 m from the ground for the given area in Hubli.

From the above graph it is clear that the horizontal axis wind turbine is a "lift based" turbine and that the behavior of the test foil is comparable to standard
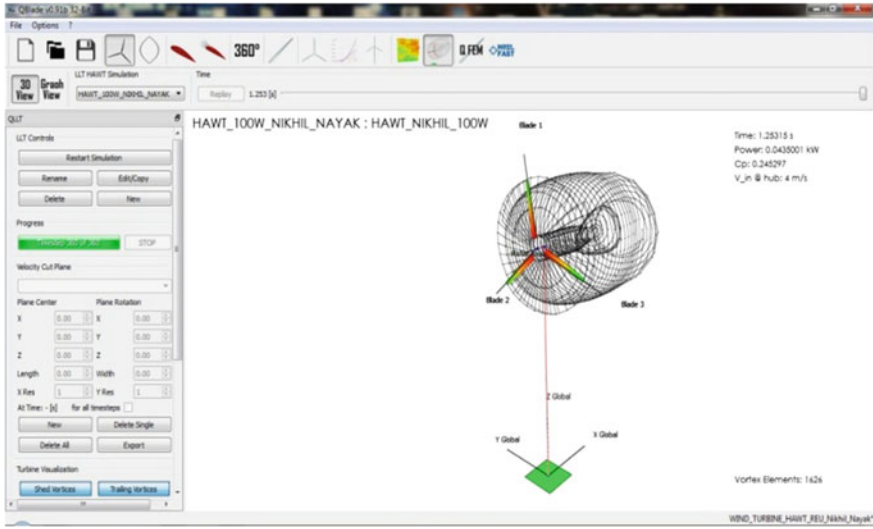
Fig. 18 Dynamic simulation results
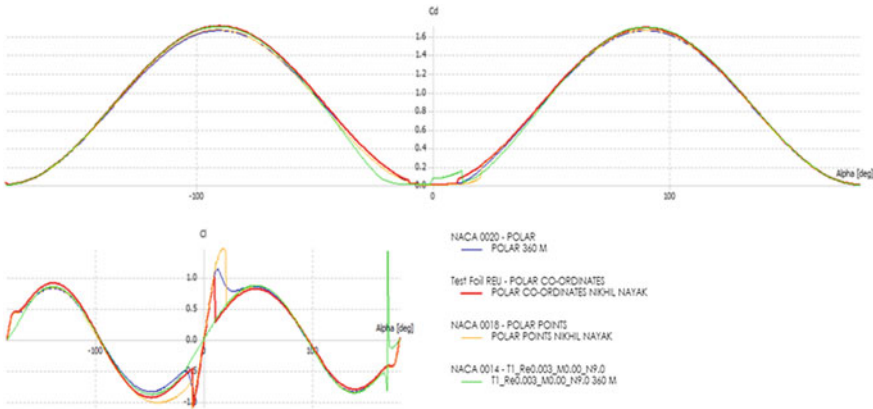
Fig. 19 360° polar comparison between test foil and NACA 0018

NACA 0018, hence the test foil which can be adopted for the blade because it can be easily manufactured [4] (Fig. 20).

The solar system calculations is as follows (Table 5):

Total load = 100 W
Period of operation = 12 h

Then, Total Watt-Hour = 100 × 12 = 1200 W h
The period of the solar panel exposed to the sun = 8 h.

Fig. 20 Dimensions of
designed wind turbine in mm
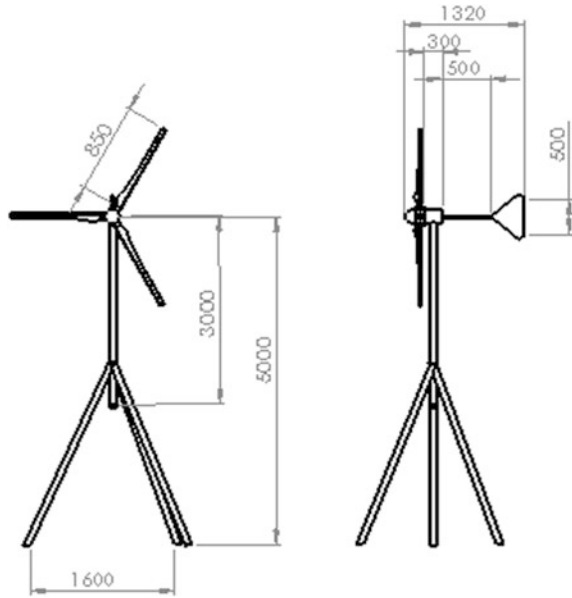
Table 5 Condition of battery
under different situations

Battery voltage	Load status
Less than 12.5 V	Not connected to battery
Equal to 12.5 V	Connected
More than 12.5 V	Not connected to battery

(Between 9 am and 3 pm)

If solar panel of 15 W is to be used, the number of panels to arrange in parallel to achieve 150 W will be:

Number of panels required = 150 W/15 W = 10

$P = IV$,

where

I = Expected charging current

V = Voltage of the battery and = 12 V

P = Power supply rating = 100 W

I = 83 A

Lighting load calculation is

The annual energy consumed by an average rural household is as follows:

Table 6 Comparison of literature and test foil

Reference/test foil	Airfoil	Rotor diameter (m)	Wind speed (m/s)	Rotor speed (rpm)	Pitch angle (°)	Max C_p
Kianoosh Yousef et al.	MG4250	2.1	Up to 13	50–600	15	0.2
Vikram Singh et al.	FX 63–137	2.2	1–11	0–1200	18	0.4
Hansena	ABM	1.26	7	500	20	0.255
Bai et al.	–	0.394	<4	100	2	0.28
Chen and Liou	NACA 4415	4	4–20	0–3000	18	0.45
Test foil Nikhil	–	1	Up to 5	100–300	2–4	0.36

Maximum demand = 30 W

$$\text{Average load} = \frac{\text{Area under daily lighting load}}{24}$$
$$= \frac{187}{24}$$
$$= 7.79 \, \text{W}$$

$$\text{Load factor} = \frac{\text{Average load}}{\text{Maximum demand}}$$
$$= \frac{7.79}{30}$$
$$= 0.259$$

The peak load at any instant is assumed to be 30 W [11] for lighting. The theoretical value of power generated by this wind-solar hybrid estimated to be 62.79 W, which can meet this demand (Table 6).

5 Conclusion

The analysis from tools like Qblade and Solidworks support the calculations made and show that the material used for the blade balsa wood and the tower a tripod can withstand the loads acting on them and expected to produce a power output 100 W for an average wind speed 4 m/s. This may not be a significant amount of power but it can be employed to ensure that remote areas can benefit from the solution proposed. The test foil behavior is similar to the compared aerofoil profile and hence can be used as it is less complex and can be easily manufactured.

References

1. Y.Sudhakar, Experimental study of airfoil performance with vortex generators. Bragg, M.B., Gregorek, G.M., 19876. Aerodynamics of Wind Turbines, China Power Press, Beijing (2009).
2. E. Akcayoz and I. H. Tunce, Numerical investigation of flow control over an airfoil using synthetic jets and its optimization. International Aerospace Conference, Turkey (2009).
3. Waleed, Numerical investigation of leading edge blowing and optimization of the slot geometry for a circulation control airfoil, Notes on Numerical Fluid Mechanics and Multidisciplinary Design. 112 (2010) 183–190. C.
4. C.N. Narayanswamy [2006], Study of Availability of wind energy and its characteristics International Conference on Design pages 472–478.
5. Vikram Singh [2014], Timber wood as the blade material for horizontal axis wind turbine National Conference on Mechanical Engineering pages 293–302.
6. Kianoosh Yousef, Numerical Investigation of Flow Control Over an airfoil Using Synthetic Jets and its Optimization, International Aerospace Conference, Turkey, 2009.
7. U Anand, Drag minimization using active and passive flow control techniques. Aerospace Science and Technology, 17 (1) (2012) 21–31.
8. Jang-Oh Mo and Young-Ho Lee "Design and Finite Element Analysis of an OceanCurrent Turbine Blade", Vol. 38, pp. 1–6.
9. Hansena, Investigation of flow control over aerofoil by suction effect on aerodynamic characteristics, Canadian Journal on Mechanical Sciences and Engineering pages 102–109.
10. Hansena M O L, Sorensen J N, Voutsinas S, Sorensen N and Aa Madsen H (2006), "The State of the Art in Wind Turbine Aerodynamics and Aero Elasticity", Progress in Aerospace Science, Vol. 42, pp. 285–330.
11. Herbert Sutherl and John, Investigation of Boundary layer Suction on a Wind Turbine aerofoil using CFD, Master Thesis, Technical University of Denmark, Denmark, 2010.
12. Bai C J, Hsiao F B, Li M H, Huang G Y and Chen Y J (2013), "Design of 1 KW Horizontal-Axis Wind Turbine (HAWT) Blade and Aerodynamic Investigation Using Numerical Simulation", Vol. 67, pp. 279–287.

An Automated System for Motioning the Cargo for Ground and Air Operations

Utsav Bhardwaj

Abstract There are instances encountered very often when some cargo items are to be loaded to or unloaded from some motored vehicles operating on ground, or some commercial cargo aircrafts. This is one of the key requirements in case of scenarios like occurrence of some natural disasters like floods, earthquakes, cloudbursts, cyclones, etc. post-war situation, etc. Food packets, drinking water, communication devices, etc., constitute a major fraction of cargo in such cases. Pace and quickness of delivery of aid material becomes one of the major concerns then, since generally a huge number of people are affected by these disastrous events. We need quick loading and unloading of cargo then. To ensure fast loading of cargo on to the trucks and more especially cargo aircrafts, quick unloading at the desired site, as well as quick airdrop, an automated system has been designed for the same at CFI, IIT Madras. This paper explains the conceptual design of that automated system. The dynamics of the system have been discussed and some force analysis of the cargo motioning process has been carried out.

Nomenclature

m	Mass of one loaded cargo box
g'	Effective acceleration due to gravity in the situation under consideration
W	Effective weight of one loaded cargo box
k_s	A dimensionless and unitless constant
f_s	Static frictional force between one cargo box and the base plate rollers
n	Number of cargo boxes dragged in one go
F_d	Maximum dragging force for "n" cargo boxes
F	Maximum force exerted by one drag plate

U. Bhardwaj (✉)
Department of Mechanical Engineering, Indian Institute of Technology Madras,
Chennai 600036, India
e-mail: u.bhardwaj88@yahoo.in

1   Introduction

Unfortunately, we keep on suffering from the natural disasters like massive floods, cyclonic winds and heavy rains, cloudbursts, earthquakes, etc. at a considerable frequency [1]. Wars have also become somewhat common in some of the regions of the world [2], either between the countries, or involving terrorism. In such cases, massive destruction happens, leading to a huge loss of life and property. Huge residential areas are devastated like anything. Several times, people have to spend time without shelter for several days, along with a big scarcity of food and other basic stuff. There are several other problems too faced after a disaster [3].

Disaster relief camps are then established by the government, assisted by various NGOs too. In all such situations, humanitarian aid material, like food, drinking water, clothes, etc., is to be supplied to the affected people in an optimized manner if possible [4], in both the cases, either they are under open sky without shelter or they are staying in a relief camp. Number of affected people depends upon the extent of the disaster and nature of the affected area. In certain cases, like earthquakes and massive floods, number of affected people is generally huge, may be in lacs. This puts a huge pressure on the government agencies to ensure the delivery and reach of the aid material to the affected people as soon as possible, that too in bulk. It is very less likely that road transport will be fine near an affected area. If there is road transport available, we can use large trucks to transport the aid material to a location nearest possible to the affected area or relief camp. If it is not so, then cargo aircrafts are used. Cargo aircraft can deliver the aid material either using roll on/roll of mechanism after landing at an airbase nearest possible to the affected area or relief camp, or can opt for airdrop, if it is suitable. Suitability of airdrop depends upon the nature of cargo, nature of the region being served, as well as the local ground terrains.

In any of these above-mentioned cases, cargo is to be first loaded on to the trucks or aircraft base, then transported and finally unloaded at the desired location. In case of airdrop, it is to be suitably brought to the cargo door of the cargo aircraft during the flight. The process of loading is generally done fully mechanically, using so called "loaders." The process of loading like this is laborious, cumbersome, and time consuming. It needs considerable man power too. Similarly, the process of unloading too is done mechanically, even manually several times, due to unavailability of the loaders/machines to unload the cargo at the landing site, which is several times not a permanent and well settled airbase. Again, that process of unloading is highly laborious and time consuming. A lot of people are again required to accomplish the task. This leads to a long standby time duration for the aircraft, during which it could make some more back-and-forth trips for aid delivery if it would have been unloaded quickly. Thus, it leads to highly inefficient time management and big delays in the delivery of aid materials. Affected people keep on waiting, and when delivery is done, that becomes too stressful for the authorities after a long waiting duration, leading to an uneven distribution [5].

So, what the author felt is that there should be an automated system with suitable controls, which can first load the cargo on to cargo floor of the trucks or cargo aircrafts very quickly and intelligently, and then the same system should be there to unload the cargo from the cargo floor to the ground quickly. For airdrop too, the same system should be capable of suitably bringing the cargo to the cargo door and subsequently pushing it out of the cargo aircraft ultimately. Keeping in mind some of the realistic problems faced during loading, unloading, and airdrop processes, an automated cargo motioning system has been designed at Centre for Innovation (CFI), IIT Madras. This paper discusses in details, the conceptual design of the proposed system as well as its operational aspects. Some force analysis has also been carried out.

2 Conceptual Design of the Automated System

Whatever be the cargo stuff to be transported that is to be first packed in the standard cargo boxes, designed as per the dimensions of the loading area of the cargo floor of aircraft/ground vehicle. One such cargo, box has been shown in Fig. 1. A cargo box is such that at one of its vertical faces, two U-clamps are to be attached facing opposite to each other.

The cargo boxes will be made with required strength so as to hold the cargo safely in worst possible scenarios, like free fall over the ground from the airdrop height in case of failure of parachute system. The boxes should be highly rugged and impact resistant. The joints of U-clamps are also to be capable of withstanding large stresses experienced during loading and unloading processes, as discussed later on.

The whole conceptual design of the automated system for carrying out the operations of loading, unloading, and airdropping has been shown in Fig. 2. The cargo boxes have also been shown lying on the cargo floor.

There is a horizontal base plate, on which rollers will be provided for smooth and easy motion of the cargo boxes over it. Lower half of each roller will be present in the slot made in the base plate while upper half will be protruding out of the

Fig. 1 Conceptual design of the cargo box
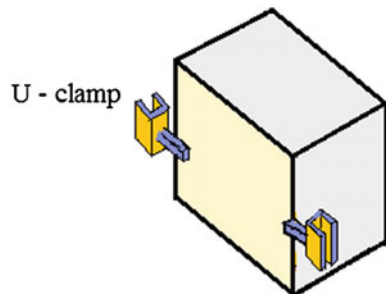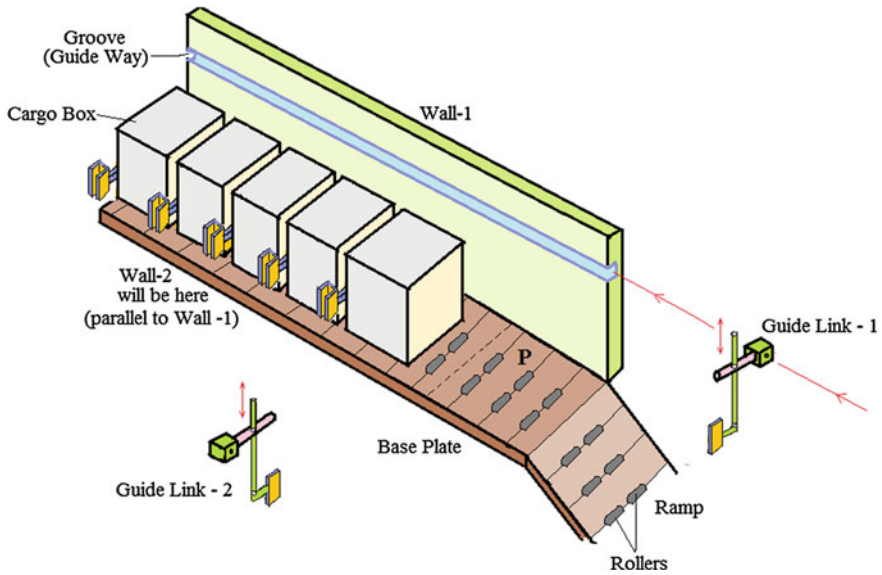
Fig. 2 Conceptual design of the system for automated loading, unloading, and air drop

surface of the base plate. The distance between the consecutive rows of the rollers is also to be decided very wisely, depending upon the weight and size of loaded cargo boxes. This base plate can be taken separately and laid parallel to the cargo floor, or the cargo floor of ground vehicle or a cargo aircraft itself can be constructed just like the base plate considered here. The width of the base plate is somewhat more than that of the cargo boxes, so that when boxes are lying on the base plate symmetrically, there is some space on either side of the row of boxes. At the outer end of the base plate or cargo floor, there is an inclined plane, hereby referred to as "ramp," which is also provided with rollers. The inclination angle of the ramp is generally adjustable, and the ramp serves as a closing door too for the cargo area, when it is just rotated up about the joint of ramp and the horizontal cargo floor.

On each lateral side of the base plate, there is one vertical wall, hereby referred to as Wall-1 and Wall-2, which are parallel to each other and have some gap between them equal to the width of the base plate. In each of the walls, one groove or guide way is there, at some vertical height above the base plate more than the height of the boxes. Now, in each of the guide ways, a link termed as "guide link" is put, which can slide along the length of the guide way, the motion of the link along the guide way being guided with the help of a suitable computer program. The guide link has been shown in Fig. 3. The guide link consists of a block, which stays inside the groove and is moved linearly along the groove. From mechanical aspect, this motion can be accomplished by putting a threaded rod inside and along the groove, passing through the block with inner threading in the hole made in it. Then, only the rotation of the threaded rod is to be controlled, including the control over

Fig. 3 Conceptual design of
the guide link
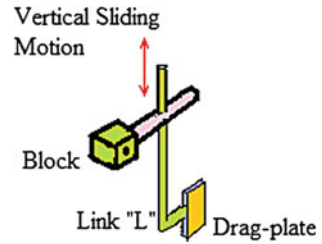
direction of rotation, whether clockwise or counter clockwise, as well as the angle
of rotation, to slide the block as per the requirement.

All such aspects are to be incorporated in the computer code. Across a rod
attached to the block, another link "L" is passed. It is a bent link (with bend angle as
90°). At its lower end, a plate has been attached, termed as the "Drag-plate," since,
it drags the boxes during the processes of loading, unloading, and airdrop. As and
when desired during its operation, the link "L" can be lowered down or raised up by
some mechanism (not discussed here). All about how much to lower down or lift
up, when to lower down or lift up, is incorporated in the computer program pre-
pared for its operation. Also, accordingly, hardware, i.e., different controls and
buttons are to be designed to run that code as per the requirements.

Moreover, there may be two or multiple rows of the cargo boxes on the cargo
floor. For each row, same set of components is to be there. There may be inde-
pendent control system for each of the rows.

3 Operation of the Automated Cargo Motioning System

The operation of this automated system is very simple in nature. It has been
explained below specifically for the cases of loading and unloading or airdropping.

(1) Operation for Automated Loading
Loading is to be done from the outer or back side of the base plate. There is some
portion of the base plate at its outer end, shown as platform "P" in Fig. 2, which is
mainly utilized for loading purpose. The ground loader will bring the loaded cargo
boxes and will place them over the platform "P," in a manner such that the face of
each box, on which U-clamps have been attached, will be facing the front or inner
side of the base plate.

Then, the operator will instruct the system to start the loading process, which
will activate the guide link. This initiation leads to sliding of both the blocks
through their respective grooves together and finally placing them over the U-clamp
of the box which is nearest to the ramp, i.e., which has been loaded by ground
loader lastly. Then, the link "L" will be lowered simultaneously on both sides till
the drag plates come within the U-clamps of the box. Then, the blocks, along with
the Link "L" and drag plate, will slide simultaneously along their respective

grooves into the ground vehicle or cargo aircraft toward the front end of the base plate, thereby, dragging all the placed boxes together into the vehicle or aircraft, over the rollers of the base plate. In a similar manner, loader will keep on placing the boxes, and this process of dragging them will be repeated over and again, till the requirements are fulfilled.

Every motion of block, link "L," etc. is to be controlled by a computer program already loaded into the system. Every time, a known and fixed number of boxes will be placed by the loader over "P," and the block would already know that how much it is to slide every time, to the last box nearest to ramp, and then, back into the vehicle. The backward displacement will go on decreasing with continued loading, every time decreasing by the total length of all the boxes loaded in one go added to the suitable gaps between them. The length of each box and number of boxes would be certainly known, hence, the rate at which this back-displacement is to be reduced will be known. All that will be incorporated into the program and system will accordingly work and load the boxes. The system should be such that it can be operated by manual instructions too, overriding the automatic settings, if required.

One thing to be ensured is that the system should load the boxes keeping a certain and well known gap between the consecutive boxes, so that the automation works properly.

(2) Operation for Automated Unloading and Airdrop

Now, at very beginning, the operator will instruct the system about how many boxes are to be unloaded or air-dropped first time. The blocks will slide in their respective grooves to a position above the U-clamps of the box, which is farthest from the ramp, but is among the boxes to be dropped or unloaded. The distance to be traversed along the groove will be again told by the loaded program, depending upon the number of boxes to be taken out and the gap between the consecutive boxes. Then, the links "L" at the two sides will be lowered till the drag plates reach within their corresponding U-clamps of the box. Then, the blocks will slide toward the outer end of base plate, i.e., toward the Platform "P" or ramp, thereby, dragging all the boxes (present ahead them as seen from the back side) together toward the "P," over the rollers of the base plate. Finally, as can be seen from Fig. 2, the blocks will move up to the outer end of the respective vertical walls, thus pushing all the dragged boxes on to the ramp and making them slide down the ramp over its rollers smoothly. All those boxes are thus finally unloaded to the ground, if the ground vehicle is being used, or if the aircraft has landed, while all those boxes are thus air-dropped off the cargo aircraft if this operation is being carried out during the flight.

Now, whatever number of boxes were dropped/unloaded in the first go, that number will be stored in the system memory. As soon as the operator specifies the number of boxes to be dropped/unloaded in the second go, that number will be added to the number of boxes dropped/unloaded in the first go and the resulting summation will give the direct indication of the distance from the outer end of the base plate, at which the U-clamps of the box which is now farthest from the ramp, but is among the newest boxes to be dropped, lie. Hence, as soon as the system will be activated, the blocks will slide to that position and the rest of the

unloading/airdropping process will proceed as earlier. This process goes on as per the requirements.

4 Force Analysis of the Automated System

In this section, brief analysis of the forces involved in the operation of the proposed system has been carried out. The effective weight of each loaded cargo box (weight being assumed to be same for different loaded cargo boxes for simplicity in analysis) is given by Eq. (1).

$$W = mg'$$ (1)

Here, we used the term effective weight, because if it is a case of airdrop, the effective weight is different from the actual. "W" is infact, the normal reaction to the cargo box from the rollers.

The static frictional force between one cargo box and the rollers will be higher than the corresponding kinetic friction, hence should be used for designing the components. The static frictional force will be proportional to the effective weight of the loaded cargo box, as given by

$$f_s = k_s W,$$ (2)

where "k_s" is a dimensionless and unitless constant accounting for all the factors like coefficient of friction between the roller surface and the base of cargo box; forces at the roller axle, i.e., the forces present in the roller mounting, etc. Assuming the process of dragging of cargo boxes being executed at a constant velocity, the maximum force to be applied by the drag plates on U-clamps of the terminal cargo box to drag all the "n" boxes together is given by,

$$F_d = n k_s W$$ (3)

This force is assumed to be equally divided among the two U-clamps of the terminal cargo box. Thus, the maximum force, which one drag plate exerts is given by Eq. (4).

$$F = \frac{F_d}{2}$$ (4)

Thus ultimately, all the components of the dragging system, like U-clamps attached to the cargo boxes along with their joints with the boxes, drag plates, links "L," blocks, threaded rods and grooves, all the joints, etc., are to be designed to safely bear this force "F" or the force acting on them locally, with a considerable factor of safety. Effect of stress concentration should also be considered, since there are contours involved in the system design which lead to stress concentration [6].

5   Conclusions and Suggestions for Improvement

An automated system for loading, unloading, and airdropping the cargo has been designed, which can be used either with a ground operated vehicle or with a cargo aircraft. The designed system can operate for all the practises under consideration very smoothly, quickly, and with very little manpower. Mainly, just one trained operator is enough. The operation is not laborious and cumbersome at all. Repeatability of the motions involved in the task of loading and unloading justifies the worthy application of automated system to accomplish the task. The system will ensure quick operations, thus will save considerable stand-by time of the ground vehicles or cargo aircrafts. Saving that time, multiple to-and-fro trips are possible leading to transport of the desired cargo volume in a shorter span of time. Thus, quick and highly frequent delivery of the aid material to the affected people at some disaster/war affected area or a relief/refugee camp can be ensured. Operational aspects of the system for each of the cases of loading, unloading, and airdropping have been properly emphasized. Also, force analysis carried out near the end may be a general guideline for finalizing the dimensions of the various components of the system. Still, some improvements in the basic design can probably be incorporated. For example, if cargo floor consists of multiple rows of the cargo boxes, some automated mechanism for transverse movement of the cargo boxes from one row to another can be installed, since this kind of movement may also be needed sometimes.

References

1. D. Guha-Sapir, R. Below, Ph. Hoyois—EM-DAT: International Disaster Database—www. emdat.be—Université Catholique de Louvain—Brussels—Belgium.
2. Mark Harrison, Nikolaus Wolf, "The Frequency of Wars", March 10, 2011.
3. José Holguín-Veras, Eiichi Taniguchi, Miguel Jaller, Felipe Aros-Vera, Frederico Ferreira, Russell G. Thompson, "The Tohoku disasters: Chief lessons concerning the post disaster humanitarian logistics response and policy implications", *Transportation Research Part A: Policy and Practice, Elsevier*, Volume 69, November 2014, pp. 86–104.
4. José-Fernando Camacho-Vallejo, Edna González-Rodríguez, F.-Javier Almaguer, Rosa G. González-Ramírez, "A bi-level optimization model for aid distribution after the occurrence of a disaster", *Journal of Cleaner Production, Elsevier*, Volume 105, October 2015, pp. 134–145.

5. Vasudha Chhotray, "Disaster relief and the Indian state: Lessons for just citizenship", *Geoforum, Elsevier*, Volume 54, July 2014, pp. 217–225.
6. V.B. Bhandari, "Chapter 5: Design against Fluctuating Load", *Design of Machine Elements, Tata McGraw-Hill Education*, 2010, pp. 141–183.

Analytical Studies on TIG Welding of TI–6AL–4V Alloy Plates Using CAE

T.V.B. Babu, V. Ajay and N. Nagendran

Abstract Welding is a permanent metal joining process in which molten metal is applied in the joint with or without applying pressure and heat. Filler material is chosen in such a manner that it is exactly as the parent metal when solidified after welding. A weld can be qualified as good weld as it should not have any surface or internal defects and its weld strength should be close to the parent metal. One such attempt is made in this project. Through study of basics of welding. TIG welding, Ti alloy and welding simulation in ANSYS, based on the study initial trials were carried to simulate welding in CAE. Results like thermal distribution and structural distortion were obtained for various parameter combinations and suggested for welding. Welding was carried out based on the parameters suggested and resulted in a good weld.

Keywords Permanent metal joining process · TIG welding · ANSYS simulation · Parameter combination

1 Introduction

Aerospace segments can be planned as a solitary and basic one to have the most extreme proficiency. Basically this is impractical as there exists a solid restriction on material, fabricating techniques, and geometry of the material. Material chose for the parts is the first element chose in view of the usefulness of the segment.

T.V.B. Babu (✉) · N. Nagendran
Department of Mechanical Engineering, Vel Tech High Tech Dr. Rangarajan Dr. Sakunthala
Engineering College, Chennai, India
e-mail: t.v.b.babu@velhightech.com

N. Nagendran
e-mail: nagendran@velhightech.com

V. Ajay
Tata Consultancy Services, Chennai, India
e-mail: ajay_vlydham@rediffmail.com

Geometry, likewise, relies on the usefulness of the part. Configuration of the segment relies on the accessibility of material to the specific measurement.

In spite of the fact that the diverse procedures have their own favorable circumstances and constraints, and are required for unique and particular applications, manual metal curve welding keeps on getting a charge out of the overwhelming position as far as aggregate weld metal stored. The TIG procedure delivers the finest quality weld on every single weldable metal and composites. The curve temperature may be up to 20,000 K. In spite of the fact that TIG welding creates the most noteworthy quality welds, it is a moderate and costly process.

Aviation segments must show the properties like of high quality at hoisted temperatures, high solidness for burden conveying and anticorrosion to environment. Not very many materials are the possibility for such applications like Inconel, Titanium, High quality steels, Aluminium, and so on.

Computer aided design/CAM space has sufficiently developed today to investigate and see the conduct of manufacture procedures on hard to machine materials as clarified prior. Late basic examinations programming has been enlarged with numerous propelled highlights for this recreation and the force of those product lies in its yields which is a promptly usable info to begin the movement. One such work is done in this task in which basic investigation programming is utilized to recreate the TIG welding procedure in Titanium combination.

Ti–6Al–4V

An amalgam is a halfway or complete strong arrangement of one or more components in a metallic lattice. Complete strong arrangement amalgams give single strong stage microstructure, while incomplete arrangements give two or more stages that may be homogeneous in circulation relying upon warm (warmth treatment) history. Amalgams more often than not have diverse properties from those of the part components (Table 1).

TIG welding parameters

Materials	Current (A)	Diameter of W-electrode (mm)	Diameter of filler rod (mm)	Flow rate of argon (lpm)
1. Mild, low alloy, and stainless steel	250–350 (DCSP)	3.0	3–4	7
2. Gray cast iron	160 (AC/DCSP)	3.0	5.0	8
3. Aluminium	250–375 (DCSP)	4.5	3–5	9
4. Copper	200–375 (DCSP)	3.0	3.0	7
5. Magnesium	100–150 (AC)	2.5	4.0	10
6. Silicon bronze	150–200 (DCSP)	2.5	3–4	9

Table 1 TIG welding parameters for different materials

Plate thickness	6 mm
Type of joint	Butt
Welding position	Flat

2 RLV-TD-Elevon Assembly

RLV-TD:

ISRO ventures into reusable dispatch vehicle innovation and sufficiently developed to dispatch a mechanical demonstrator in not so distant future. Two Stage to Orbit (TSTO) is a definitive launcher went for which the innovation demonstrator will be an initial step. For this reason a Winged Reusable Launch Vehicle Technology Demonstrator (RLV-TD) has been arranged. The RLV-TD will go about as a flying proving ground to assess different innovations, namely hypersonic flight, self-ruling landing, fueled voyage flight, and hypersonic flight utilizing air breathing impetus. In the first place in the arrangement of exhibit trials is the hypersonic flight investigation (HEX), which is an endorsed venture in ISRO.

Configuration of RLV-TD:

RLV-TD is a winged airframe structure associated with a strong sponsor at back by method for an inter stage. The promoter is associated with a base cover and balance get together at its tail bit for move control (Fig. 1).

The overall length of the vehicle m. The cross section is of D shape to a size of m. The major sub assemblies of the RLV-TD are

- Nose cap
- Fuselage Nose Body (FNB)
- Fuselage Straight Body (FSB)
- Hood assembly

Fig. 1 Configuration of RLV-TD
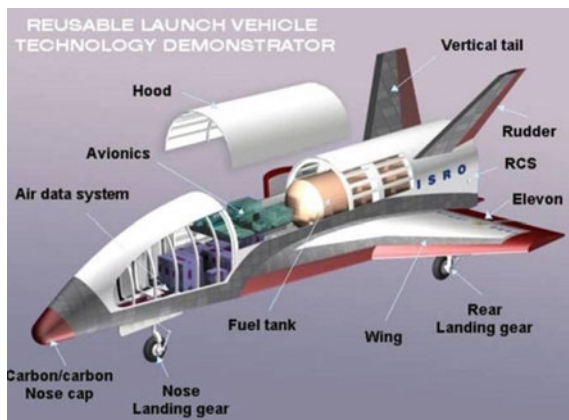
- Vertical tails (P+ and P−)
- Wings (P+ and P−)
- Leading edges (P+ and P−)
- Inter stage
- Sold booster
- Base shroud and fin assembly
- Control elements

The major portion of realization of RLV-TD is taken by manufacturing/fabrication of components for the above mentioned sub assemblies and assembly of them.

3 Elevon Assembly and Its Realization

The business airplane comprises more than one elevon structure which relies on upon the length of the wing and load experienced in the vehicle. RLV-TD is intended to have one and only elevon for one side thus that there are two elevons altogether (for P+ and P−).

Elevon is a case structure made of torsion box as the primary basic component wrapped by skins. These elevons are activated by water driven actuators which are controlled by the vehicle direction programming. Torsion box of the elevon is the fundamental basic component comprises of front fight and back fight associated by ribs. Torsion box is verging on like a skeleton for the elevon gathering. Model of an elevon is appeared beneath for better comprehension (Fig. 2).

The weld joint is of 'Butt sort' joint for front fight—ribs and back fight—ribs. There is a projection of 3 mm thickness is given along the edges confronting ribs in front and back fights. Welding for this condition is not created at VSSC and there is no weld procedure sheet (WPS) accessible. Ti–6Al–4V is the material utilized for these segments as they are having higher quality, higher firmness, great durability and lower thicken.
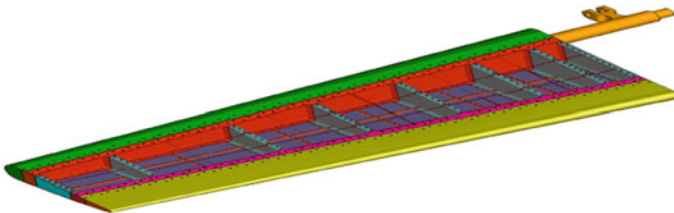
Fig. 2 Configuration of Elevon Assembly

4 Scope of the Project

Welding of Ti–6Al–4V alloy is new work at VSSC for which WPS document is to be made as a basic document. WPS document is the mother document any welding technology in which the complete details about the parameters, setting of the job and process of welding are given. Any production work in welding is being carried out based on this document. Several welding trials are to be done to form the welding process from which the document shall be made. As welding Ti–6Al–4V alloy is a new work, to know about the thermal behavior of the welding, a simulation can be done.

ANSYS Multi physics is the analysis software which is having a feature for moving heat source simulation for welding and corresponding outputs like welding distortion, stress induced and thermal distribution. ASTM–A370 standards are used as the reference for making any test specimens in VSSC.

The jobs done for space activities call for tight control over the standards and specifications. Welding activities for flight components are qualified based on the acceptance limit given in the ASTM 1025 SE standard. Hence before making the WPS document CAD simulation was carried for TIG welding of Ti–6Al–4V alloy plates and the result is considered for making the actual welding. Following are the activities carried out in this project.

(a) Study of basics of Welding, TIG welding, welding acceptance standards
(b) Study of Ti–6Al–4V for flight applications
(c) Study of ANSYS for welding simulation and its post processing
(d) Simulation of TIG welding on Ti alloy
(e) Post processing and acceptance of parameters
(f) Preparation of weld specimens and parent metal specimens as per the standards
(g) TIG welding of Ti–6Al–4V specimens as per the accepted parameters Inspection of weld specimen

TIG Welding of TI–6AL–4V Plate
Inputs for Welding from Digital Simulation
Outputs of the digital simulation were given as the inputs for the welding section. Thermal distribution for various heat fluxes, structural distortion for various heat fluxes were taken as outputs from the digital simulation and given to welding section. These results were analyzed by the welding experts and they have selected the following parameters as the input for the actual welding (Table 2).

Preparation, Welding and Testing of Specimens
Weld specimens:
Ti–6Al–4V plate for 3 mm thickness is not readily available for welding. So, a 10 mm plate is taken and thickness is reduced to 3 mm by milling

Table 2 Welding parameter used in VSSC

S. no.	Input parameters	Value
1	Voltage	14 V
2	Current	75 A
3	Electrode	Tungsten 3 mm
4	Shielding gas	Argon
5	Power supply	DC EN

Table 3 UTM testing result

S. no.	Specimens	Identification no.	UTS (MPa)	0.2 % PS (MPa)	% EL	Hardness (HRC)	Remarks
Weld specimens							
1	110–0265	1	943	838	10.6	28/29	Material is in annealed condition
2	110–0265	2	940	827	9.2		
3	110–0265	3	937	834	8.8		
Parent metal							
1	110–0266	1	985	880	11.8	29/30	Material is in annealed condition
2	110–0266	2	983	882	10.3		
3	110–0266	3	983	881	10.1		

Evaluation of Weld Joint
Qualitative Checks of Weld:

Nondestructive testing
Radiographic test (X-Ray)
Dye Penetrant test (DP)

Quantitative Checks:

UTM testing

Weld joints can be evaluated quantitatively by methods like UTM testing, Impact testing, etc. Quantitative checks are mostly of destructive types. Any weld joint showing the values more than 90 % of its parent metal is called as good welds. Weld specimens and Parent metal specimens are tested and the results were presented below. The specimens are made as per the ASTM standard A370 (Table 3).

5 Results and Discussion

ANSYS simulation results have benefitted in a better way for preceding the welding process on Ti alloy plates. The results of the simulation are
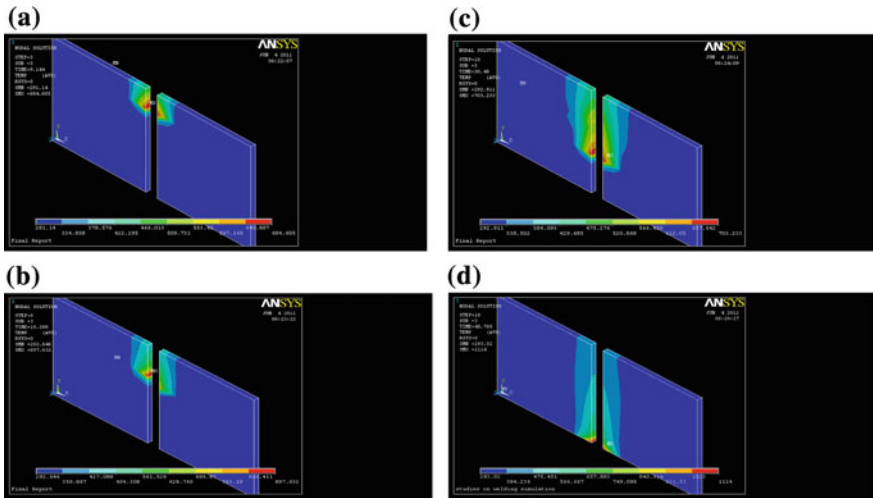
Fig. 3 **a** Image of temperature distribution @9.144 s, **b** image of temperature distribution @ 18.288 s, **c** image of temperature distribution @ 30.48 s, **d** image of temperature distribution @ 48.72 s

1. Thermal distribution at various time intervals:

Welding is a process a molten metal is supplied to join the metals to join together with or without pressure. The heat is flowing in the material and it varies according to the material. Heat distribution alters the metallurgical characteristics which results in the change in behavior of the material. Heat distribution at various time intervals are shown below (Fig. 3).

HAZ of weld joint.

2. Graphical Representation of Temperature with Time:

With the suggested results welding was carried out. NDT checks and X-ray inspection were done to inspect the quality of the weld. DP check resulted in no defects hence there is so surface defects on the weld. X-ray inspection shows some isolated porosities of 0.3 mm dia and it is acceptable as it is less than 10 % of the thickness of the material (as per ASTM 1025 SE standard). Porosity is seen at only one location. Hence this location is omitted for taking specimens. These NDT results shows that the weld carried out is a sound weld as there are very minimal defects and almost negligible (Fig. 4).

Tensile specimens were made on the weld plate and weld strength is evaluated by testing the specimens in UTM. In the same way parent metal specimens were made and tested (Table 4). Following are the results

Comparison:

(i) Welded Metal UTS/Parent metal UTS = 943/985 = 0.957*100 = 95.7 %

(ii) Welded Metal 0.2 % PS/Parent metal 0.2 % PS = 838/880 = 0.952272*100 = 95.22 %.
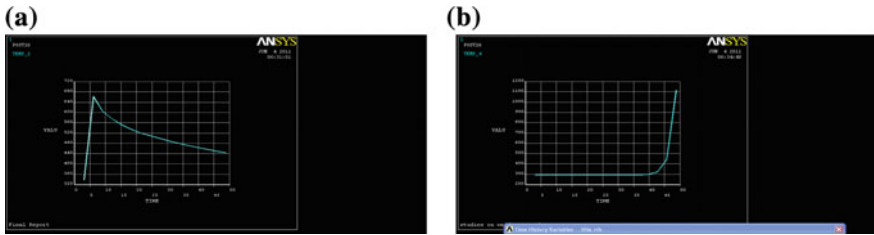
Fig. 4 **a** Temp versus time (at node 123), **b** Temp versus time (at final node 502)

Table 4 Comparison of weld efficiency

S. no.	Specimens	Identification no.	UTS (MPa)	0.2 % PS (MPa)	% EL	Hardness (HRC)	Remarks
Weld specimens							
1	110–0265	1	943	838	10.6	28/29	Material is in annealed condition
2	110–0265	2	940	827	9.2		
3	110–0265	3	937	834	8.8		
Parent metal							
1	110–0266	1	985	880	11.8	29/30	Material is in annealed condition
2	110–0266	2	983	882	10.3		
3	110–0266	3	983	881	10.1		

6 Conclusion

Welding is a developing area in VSSC where still developments are raised. Such a development was given as project. Thorough literature survey was done to study the welding, TIG welding, Ti alloy material, digital simulation, etc. With the available outputs initial trial for digital simulation were carried out and improved with the suggestions of the experts. Finally, a fully fledged simulation of welding is carried out for the welding and the results were given as input for starting the welding. With the parameters suggested, the welding is carried out successfully. Post weld inspection shows that quality of weld is good and tensile specimen testing shows the weld strength has obtained in the range of 9X%. Hence CAE simulation is used for carrying out a welding process with almost no defects and better results.

References

1. Rong-Hua, Shih-Pin Liaw, Hong-Bin Yu,."Thermal Analysis of Welding on Aluminum plates" Journal of Marine Science and Technology Vol. 11, No. 4, pp. 213–220 (2003).
2. Scott Funderburk. R "Key Concepts in Welding Engineering" Welding Innovation Vol. XV, No. 2, (1998).
3. Dragi Stamenkovi Ivana Vasovi Finite Element Analysis of Residual Stresses in Butt Welding Two Similar Plates Scientific Technical Review, Vol. LIX, No. 1,(2009).
4. Li Yajiang, Wang Juan, Chen Maoai, Shen Xiaoqin "Finite Element Analysis of Residual Stress in the Welded Zone of a high Strength Steel". Journal of Bulletin of Materials Science Volume 27, No 2, pp 127–132 (2004).
5. Andrea Capriccioli, Paolofrosi "Multipurpose ANSYS FE procedure for Welding process Simulation," Journal of Fusion Engineering and Design, Vol. 84, Issues 2–6, Pg 546–553 (2009)
6. P.N. Rao "The Text book of Manufacturing Technology".
7. A. C. Davies "The text book of Science and Practice of Welding", Cambridge University. Volume 2 10th Edition, (1993).
8. S.A. Rizvi, Katson "The text book of Advanced Welding Technology", Publisher: Excel Books, (2010).
9. Sacks and Bonhart. "Welding Principles and Practices" (Third Edition).

Shape Parameterization of Airfoil Shapes Using Bezier Curves

A. Shikhar Jaiswal

Abstract Shape parameterization plays an important role in aerodynamic shape optimization process. The parameterization method used for optimization must be able to accurately model the aerodynamic body and also it should be flexible enough to take all the possible shapes in the design space. In this paper, we have studied Bezier curve approximation of airfoil using fourth-order, sixth-order and eighth-order Bezier curves. We observe that sixth-order Bezier can accurately model the airfoil shape. In order to represent an airfoil using Bezier curves we have to find control points vector P and vector t of nodes, where each node corresponds to one data point. An iterative process with an initial guess of vector t was used to find the best possible control points vector P and vector t. Two different airfoil geometries were modeled using Bezier curves in this paper. The results for both the airfoil problems show that sixth-order Bezier curves can model airfoil shapes accurately. Also new shapes can be produced easily from Bezier curves just by moving the control points, hence Bezier curves can be used to parameterize aerodynamic shapes for shape optimization problems.

Keywords Bezier curve · Airfoil · Parameterization method · Optimization · Aerodynamics

1 Introduction

In the design and development of modern aircrafts, several design configurations are tested and analyzed using computational simulations. Wind tunnel tests are then used to confirm the performance results obtained using computer simulations. The best possible design is then selected for further development. The use of computational simulations to analyze different design configurations has been proved to be extremely valuable in practice, but it suffers from the limitation that it does not

A. Shikhar Jaiswal (✉)
National Aerospace Laboratories, Bangalore, India
e-mail: jaiswal.shikhar@gmail.com

assure the best possible design. In order to ensure that the true best design is used, the final aim of the computational simulations should not be the analysis of the given shapes, but to find the true optimum shape automatically for the intended use.

The aim of aerodynamic shape optimization problem is to find an optimal shape which minimizes certain cost function while satisfying given constraints. In order to optimize any shape, it is necessary to express it with a finite number of variables, preferably as few as possible to minimize computation cost during optimization. This process is called shape parameterization. By parameterizing a shape, it becomes easy to generate points on the surface which it represents. Also, geometric transformations also become easier to implement. There are many methods by which we can parameterize an aerodynamic shape. The method used should be able to model the aerodynamic surface accurately and it should be able to easily adapt to changes in the shape. Also, it should be able to model all the shapes in the design space. Airfoils can be represented as coordinate points. But it would be very difficult to use coordinate-based method within an optimization process, because it would involve enormous number of parameters and the associated high computation cost in exploring the design space. Other ways of parameterizing a given aerodynamic shape are using Bezier curves, B-Spline curves, Hicks-Henne shape functions, PARSEC, CST, etc. In the paper [2], the airfoil geometry is represented by B-spline curves of various degrees. In the paper [3], the airfoil shape is parametrized using Bezier curves. Airfoil shapes are represented by NURBS in the paper [4].

The main objective of this study is to parameterize the surface of an airfoil using Bezier curves. The advantage of using Bezier curves is that the airfoil can be modeled using very few number of control points and also new shapes can be generated without much effort. In optimization problems, it is good to have less number of control variables because as the number of control variables increase, searching for an optimal shape in design space would become more expensive. Also, the interaction between the parameters may lead to unrealistic airfoils being produced.

2   Bezier Curves

Bezier curves are parametric curves which are used to represent a set of data points. The mathematical form of a Bezier curve of degree n is given by

$$[b_0^n(t)]^T = \sum_{i=0}^{n} B_i^n(t)[b_i]^T \tag{1}$$

where $b_0^n(t) = [x \quad y]$ and it is a point on the curve for a particular $t \in [0 \quad 1]$. The points b_i where $i = 1, \ldots, n$ are called control points. The term B_i^n is a Bernstein polynomial which is given by

$$B_i^n = n_{c_i}(t)^i (1-t)^{n-i} \qquad (2)$$

We can see that the Bezier curve is a weighted sum of control points, where the weights are Bernstein polynomials evaluated at a particular value of t. We refer to a point along a Bezier curve determined by a particular node t_i as the point τ_i. So we have

$$[\tau_i] = [b_0^n(t_i)] \qquad (3)$$

One important property of Bezier curves is that they are affine invariant. An example of affine transformation is rotation, scaling, and reflection. For example we want to rotate a given Bezier curve; we can either transform the relatively few control points or transform all the points of the curve. In general, transforming the control points and replotting the curve costs much less.

2.1 Matrix Representation of Bezier Curves

The representation of Bezier curve in matrix form is

$$\left[b_0^n(t)\right]^T = \left[B_0^n(t)\dots B_n^n(t)\right]\left[b_o^T\dots b_n^T\right]^T = B(t)P \qquad (4)$$

Here we refer $B(t)$ as a Bernstein matrix and P is a vector of control points. The Bernstein matrix for a vector $t = [t_1\dots t_m]^T$, $t_i \in [0 \quad 1]$ is given by

$$[B(t)] = \begin{bmatrix} B_0^n(t_1) & \cdots & B_n^n(t_1) \\ \vdots & \vdots & \vdots \\ B_0^n(t_m) & \cdots & B_n^n(t_m) \end{bmatrix} \qquad (5)$$

2.2 Bezier Curve Representation of Airfoil Surface

An airfoil surface is defined by a set of m data points d_i, $i = 1, 2, \dots, m$. In order to define a Bezier curve which best represents the airfoil surface, we have to find a set of control points b_i, $i = 0, 1, \dots, n$, where n is the degree of the Bezier curve and a vector t of nodes, $0 \le t_1 \le t_2 \le \cdots \le t_m \le m$ which minimize

$$\|B(t)P - D\|_F \qquad (6)$$

where the matrix D contains the data points. The matrix P and vector t which minimize the Eq. (6) are not unique and the final value of P and t is determined by the stopping criteria of the algorithm.

Equation (6) has two unknowns, the matrix P and vector t, so in order to solve we have to make an initial guess of either one of them. Suppose we make an initial guess of vector t, then we can solve for matrix P which is a linear least squares problem. When we know the matrix P and we want to solve for vector t it becomes non-linear least squares problem. If we observe the non-linear least squares problem, it is nothing but the nearest point problem, where each element in t which corresponds to a particular data point in matrix D, must be nearest to its corresponding data point to minimize Eq. (6).

In order to solve the linear least squares problem for matrix P, we need an initial set of nodes t. Since the elements of t must be between $\begin{bmatrix} 0 & 1 \end{bmatrix}$, we can use chord length method where each t_i depends on the length of segment given by

$$t_i = t_{i-1} + \frac{\|d_i - d_{i-1}\|_2}{\sum_{i=2}^{m} \|d_i - d_{i-1}\|_2}, \quad i = 2, 3, \ldots, m \tag{7}$$

The chord length method is not invariant under all affine transformations. An affine invariant chord length method is described in reference [1] which also considers bending of data.

3   Algorithm

The algorithm to find (P^*, t^*) which minimizes the Eq. (6) is as follows:

1. Determine the initial set of nodes.
2. Solve the linear least squares parametric functional problem for P.
3. Solve the non-linear least squares problem for the nearest points.
4. Repeat steps 2 and 3 until the algorithm reaches the stopping criteria.

The basic idea behind the algorithm is given an ordered set of data points and an initial guess t_1, we solve the linear least squares problem for P_1. So we have

$$\|B(t_1)P_1 - D\|_F = \sigma_1 \tag{8}$$

The initial guess of points τ will most likely not be the nearest points, so some improvement to t_1 is possible. Solving the nearest point problem for t_2 gives

$$\|B(t_2)P_1 - D\|_F = \sigma_2 < \sigma_1 \tag{9}$$

Now we have improved set of nodes but we have not improved the initial Bezier curve as described by P_1. If there is a better fitting Bezier curve using the vector of nodes t_2 then solving the least squares problem for P_2 will result in

$$\|B(t_2)P_2 - D\|_F = \sigma_3 < \sigma_2 \qquad (10)$$

In this manner we approach (P^*, t^*).

In the step 1 of the algorithm, we use affine invariant angle method to find an initial guess of vector t. In step 2 we find the matrix P for a given initial vector t from step using Moore–Penrose pseudoinverse of matrix B. The matrix P thus obtained is least squares solution of Eq. (6). In step 3 for a given matrix P, Guass Newton method is used to find the non-linear least squares solution for the nearest points.

4 Results

Two airfoil surfaces were modeled using the Bezier curves in this study namely, NACA 0012 and RAE 2822. The surface of each airfoil was defined using 130 data points. A Bezier curve of sixth degree was used to model airfoil surface initially. The results for RAE 2822 airfoil using sixth-degree Bezier curve is shown in Fig. 1. The figure shows the initial guess solution obtained using the vector t from affine invariant angle method and the final solution obtained by solving the iterative process which minimizes Eq. (6), near the leading edge of airfoil. Further analysis was done using fourth- and eighth-degree Bezier curve to model each airfoil surface. Figure 2 shows comparison of fourth-, sixth-, and eighth-degree Bezier curve approximation of RAE 2822 airfoil. For the sake of visualization zoomed sections of airfoils for different x/c intervals are shown in the remaining of the paper. Figure 3 shows zoomed view of Figs. 3 and 4 for specific x/c intervals. Figure 4 shows results for NACA 0012 airfoil. From these figures we observe that the fourth-degree Bezier curve is unable to model airfoil surface accurately. The sixth-degree and eighth-degree Bezier curves give almost similar results and were able to model airfoil surface with sufficient accuracy. From the above results we can
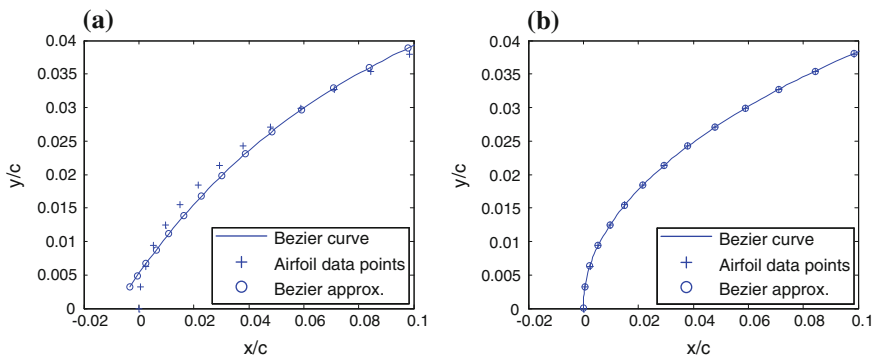
Fig. 1 Bezier curve representation of upper surface of RAE 2822 airfoil
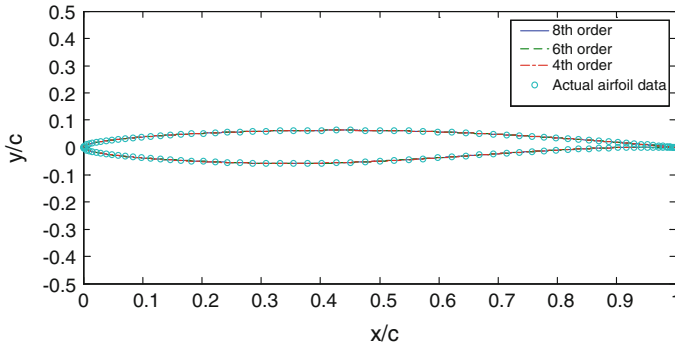
Fig. 2 Comparison of fourth-, sixth-, and eighth-order Bezier curves for RAE 2822 airfoil
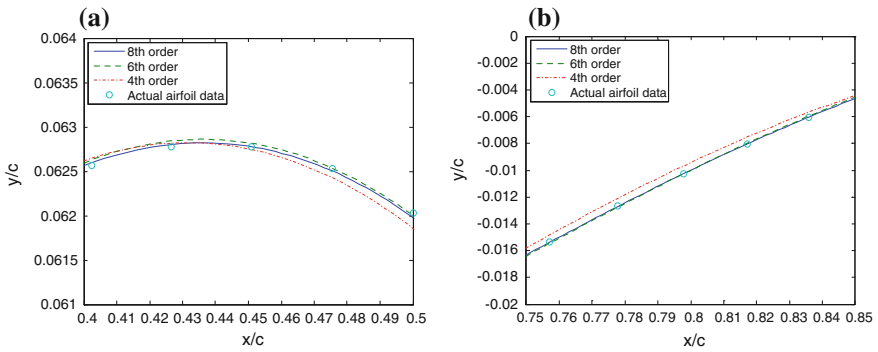
Fig. 3 Comparison of fourth-, sixth-, and eighth-order Bezier curves for RAE 2822 airfoil
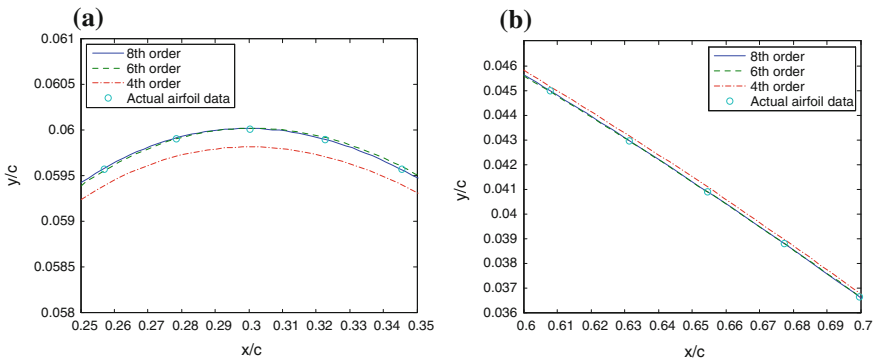
Fig. 4 Comparison of fourth-, sixth-, and eighth-order Bezier curves for NACA 0012 Airfoil

observe that Bezier curves can model both NACA 0012 and RAE 2822 airfoil with good accuracy. The value of residue used for the stopping criteria in all the cases was e^{-8}.

5 Conclusion

Two different airfoil geometries namely NACA 0012 and RAE 2822 were modeled using Bezier curves. Bezier curves of fourth-, sixth-, and eighth-degree were used to model each upper surface and lower surface of airfoils. From the results, it can be concluded that sixth-degree Bezier curves are enough to model these two airfoil surfaces with sufficient accuracy. Hence, we can conclude that Bezier curves can model aerodynamic shapes accurately with few number of control points. New airfoil shapes can be easily obtained by moving control points. So Bezier curves can be used to parameterize aerodynamic shapes for aerodynamic shape optimization problems.

References

1. Jamshid A Samareh, A Survey of Shape Parameterization Techniques, NASA Langley Research Centre, NASA/CP-1999-209136, pp. 333-343, 1999.
2. Vicini, A., and Quagliarella, Q., 1998, "Airfoil and Wing Design Through. Hybrid Optimization Strategies," AIAA Paper No. 98-2729.
3. Hacioglu, A., 2007, "Fast Evolutionary Algorithm for Airfoil Design via Neural Network," AIAA J., 45_9_, pp. 2196–2203.
4. Painchaud-Ouellet, S., Tribes, C., Trépanier, J.-Y., and Pelletier, D., 2006, "Airfoil Shape Optimization Using a Nonuniform Rational B-Splines Parametrization Under Thickness Constraint," AIAA J., 44_10_, pp. 2170–2178.

Flow Configuration Influence on Darcian and Forchheimer Permeabilities Determination

Hussain Najmi, Eddy E.L. Tabach, Khaled Chetehouna, Nicolas Gascoin, Safaa Akridiss and François Falempin

Abstract Within the framework of fuel cells, porous materials are used for the filtration purpose. Determining physical properties like porosity and permeability are of utmost importance to predict and manage filtration efficiency of these materials. Permeability of material is often determined experimentally in laboratory with disc samples (the fluid is flowing through the porous material) that are not exactly similar to the tubes of realistic operating conditions (fluid is mainly flowing tangentially to the surface and only a small part is flowing through the material). Thus, the effect of a secondary outlet on the Darcian's permeability characterization should be studied. In the current paper, we present a new test bench to determine experimentally the Darcy's and Forchheimer's permeabilities for a porous media by taking into account two outlets. The pressure, mass flow rate, and temperature are registered for three different setups: with secondary outlet (S.O) (a) 0 %, (b) 50 %, and (c) 100 % open. Then Darcy's and Forchheimer's permeabilities for these three cases are calculated and discussed in detail. It has been found that the S.O opening does not affect the Darcian's permeability, but have substantial influence on the Forchheimer's one.

Keywords Sintered porous stainless steel · Darcy's and Forchheimer's permeabilities · Filtration · Fuel cell application

H. Najmi (✉) · K. Chetehouna · N. Gascoin · S. Akridiss
INSA-CVL, University of Orléans, PRISME EA 4229, 18022 Bourges, France
e-mail: hussain.najmi@insa-cvl.fr

E.E.L. Tabach
IUT Bourges, University of Orléans, PRISME EA 4229, 18000 Bourges, France

F. Falempin
MBDA-France, 8 Rue Le Brix, 18000 Bourges, France

1   Introduction

The three main technologies for hydrogen separations are pressure swing adsorption, cryogenic distillation, and selective permeation through a membrane. For fuel cell applications, H_2 separation by selective permeation through membrane has several advantages compared to the first two methods. Several literature works mention that this filtration technique is a simple operation, which is characterized by a low cost and a less energy consumption as well as a high purity of hydrogen [1–5]. This filtration process related to fuel cell can be found in other fields of application such as geology [6, 7], petrochemical [8, 9], combustion [10, 11], or aeronautics. There have been large numbers of literature regarding transpiration cooling [12–14]. Performance parameters required for the membrane are high flux rate, stability at various temperature ranges, pressure, and high selectivity even in the presence of other gases and contaminants (e.g., CO_2, CH_4, and H_2S etc.). Temperature and pressure are the external parameters which can be controlled outside the porous media, but selectivity depends upon the permeability of the material [15, 16]. It has been recognized in the past decade that the separation factor for gas pairs varies inversely with the permeability of the more permeable gas of the specific pair. An analysis of literature data for binary gas mixtures from the list of He, H_2, O_2, N_2, CH_4, and CO_2 reveals the above relationship for these mixtures [17, 18]. Hence the determination of the permeability and studying the affecting factor is of prime importance. Despite numerous studies on porous media, there is still a lack of data regarding the flow evaluation through porous media. Permeability of the material is mostly determined using disc sample in laboratory. The outflow through the porous media is measured to determine the permeability of the material. But it is not exactly similar to a real condition where fluid flows through a tube. In such cases, a perpendicular flow, to the main tangential flow, occurs through the porous media (cf. Fig. 1). Thus, it is necessary to study the effect of second outlet on the determination of K_D and K_F. The secondary flow occurring from the S.O is nothing but the tangential flow.

The primary goal of this article is to improve previously used experimental setup in order to measure accurate values of permeabilities (Darcian's and Forchheimer's) in a more realistic configuration. The effect of a second outlet on the K_D and K_F is

Fig. 1 A realistic flow configuration through porous material
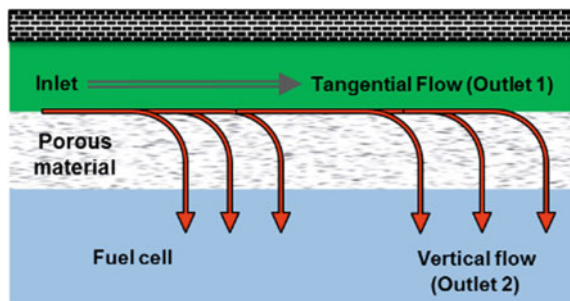
investigated. The following section of this paper is devoted to the description of the adapted test bench where different opening of second outlet is studied. The K_D and K_F of porous stainless steel materials of class 3 (SS3) and class 20 (SS20) are measured and the obtained results are presented and analysed in the last section of this paper.

2 Materials and Methods

2.1 Test Methodology for Permeation

The test bench composes of a cylindrical cell with provisions for gas injection. Porous samples are placed inside the permeation cell which has two main parts (High Pressure Chamber and Low Pressure Chamber). One inlet and two outlets (outlet-1 and outlet-2) enable to measure the pressure and mass flow rate at upstream and downstream of the samples. The outlet-2 is considered as a Primary Outlet (P.O) and the outlet-1 is considered as S.O. Fluids are injected into the inlet using high pressure injection systems (100 bars, 5 g s^{-1}). For the present study, N$_2$ was used. Various sensors connected to a data acquisition system are used to monitor mass flow rate, pressure and temperature. A mass flowmeter (0–3 g/s) is connected at the P.O. Range of the inlet pressure sensor is 0–60 bar and ΔP is 0–635 m bar. Flow from the S.O is controlled at percentage values of 0, 50, and 100. Permeability measurements are performed on two different classes of stainless steel samples (SS3 and SS20). Characteristics of both porous materials can be found elsewhere [12]. Apart from the fact that the outlet of permeation cell should be at atmospheric pressure during the experiments, the norm ISO 4022 for permeability determination is followed. All tests are performed at room temperature and repeatability was checked with 3 more tests.

2.2 Method for Determining Darcian's and Forchheimer's Permeabilities

Navier–Stokes equations gives the transient behavior of the fluid in porous media, Brinkman's equation (1) describes the macroscopic fluid flow in large flow regimes (Fig. 2):

$$\frac{\Delta P}{L} = \mu \frac{V}{K_D} + \rho \frac{V^2}{K_F} \tag{1}$$

where $\Delta P = P_{\text{inlet}} - P_{\text{outlet}}$ is the pressure drop across the sample, L is the thickness, μ is the fluid viscosity, V is the fluid velocity inside porous material, ρ is the inlet
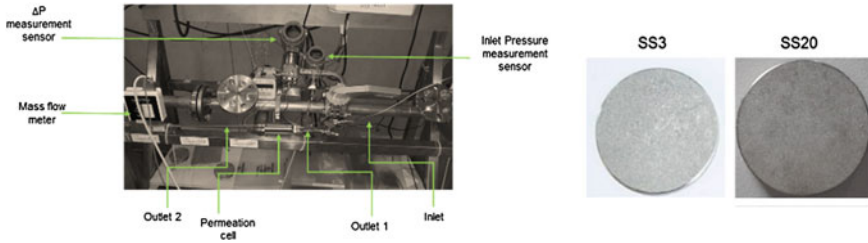
Fig. 2 Picture of experimental setup and stainless steel porous material

density, K_D and K_F are the Darcy's and Forchheimer's term, respectively. The right hand side of Eq. (1) is composed of two terms, first term relates to Darcy's law for low velocity regime and the second term relates to Stokes's law (non-Darcian flows) which takes into account the inertial effects with respect to the flow resistance. In order to compute K_D and K_F from the measured parameters, a modified form of the above equation is used:

$$\frac{\Delta p}{L \mu V} = \frac{1}{K_D} + \frac{1}{K_F} \frac{\rho V}{\mu} \tag{2}$$

$\Delta P/L\mu V$ is plotted as a function of $\rho V/\mu$. The origin of the plot is linked to the Darcian's term while the slope of the plot is related to the Forchheimer's term. Due to the effects of density and dynamic viscosity in the pressure drop in the Eq. (2), their estimation is important. The density is computed on the basis of measured pressure and temperature, thanks to the modified perfect gas law with the compressibility factor Z which depends notably on the critical coordinates and on the Pitzer acentric factor [12]. The dynamic viscosity is computed by Chung's method [19].

3 Results and Discussion

As described in previous sections, the K_D and K_F of two kinds of stainless steel porous materials are determined and the influence of different levels of opening of S.O is investigated. Some preliminary experiments were performed on SS3 in order to verify that the connection of mass flowmeter at P.O instead of inlet, as per ISO 4022 norm, does not affect the permeabilities estimation. Results of Darcian's permeability in the two cases show clearly that the relative gap do not exceed 8 %, whereas that of Forchheimer's permeability is inferior to 13 %. These relative gaps confirm that the connection of mass flowmeter at P.O do not affect the determination procedure. When Brinkman's equation is considered (for turbulent flow), the K_D for carbon cooled porous structure is found to range from 10^{-13} to 10^{-12} m^2 and the K_F ranges from 10^{-8} to 10^{-7} m [20]. The K_D and K_F are determined with the
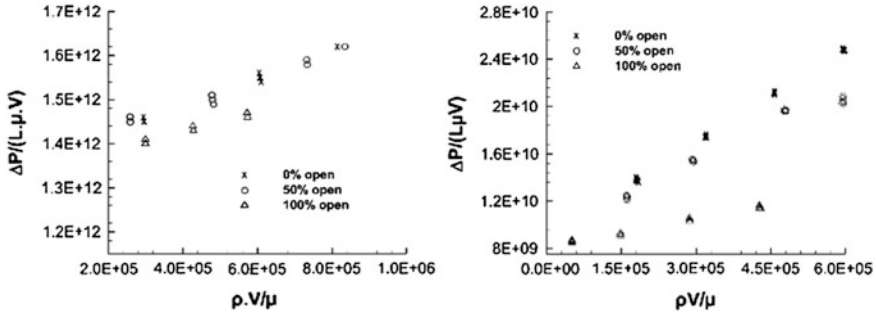
Fig. 3 Determination of Darcian's and Forchheimer's permeabilities for different openings of secondary outlet. *Left* SS3 and *Right* SS20

plots of the term $\Delta P/L\mu V$ a function of $\rho V/\mu$ for the both stainless steel porous media which are illustrated in Fig. 4 for different opening of S.O (0, 50 and 100 %).

Using the results plotted in Fig. 3, interception of the different lines with Y axis will give the K_D and their slopes give K_F. The obtained results of K_D and K_F are given in Table 1 for different openings of S.O. It can be seen clearly from Table 1 that in case of both the porous materials the determination of K_D is not affected by the opening of the S.O. For SS3, a discrepancy of 1.21 and 0.1 % are found, respectively, for 50 and 100 % open cases. Similarly in case of SS20, relative difference of 5.4 and 10.8 % are, respectively, obtained for 50 and 100 % openings of S.O. But, for K_F, the opening of S.O seems to have a very good effect, relative changes of 11 and 71 % are found in case of SS3, whereas values of 34 and 237 % are obtained for SS20 for 50 and 100 % open cases respectively. K_F is varying a lot for the cases of 100 % opening, it is due to the fact that the flow through the porous media is very low that results in decrease of pressure drop which is linearly proportional to square of velocity at higher flow rates (Non-Darcian Flow). Since K_F coefficient is associated to the turbulent flow inside the porous media [3, 21, 22], the velocity of fluid in the material is too low and the flow is either not turbulent or less turbulent making the determination less accurate. This is the reason why the value for the K_F is quite far from the "real" values. In order to give more detailed explanation to the above statement and study the influence of Darcian's and Forchheimer's contribution on pressure losses, Fig. 4 presents the evolutions of these contribution as well as their ratio as functions of pore Reynolds number (R_e).

Table 1 K_D and K_F values for three different S.O opening for SS3 and SS20

Material	Permeability	Secondary outlet opening percentage		
		0 % Open	50 % Open	100 % Open
SS3	K_D (m²)	7.38×10^{-13}	7.29×10^{-13}	7.37×10^{-13}
	K_F (m)	3.08×10^{-06}	3.43×10^{-06}	5.28×10^{-06}
SS20	K_D (m²)	1.11×10^{-10}	1.05×10^{-10}	1.23×10^{-10}
	K_F (m)	3.79×10^{-05}	5.11×10^{-05}	1.28×10^{-04}
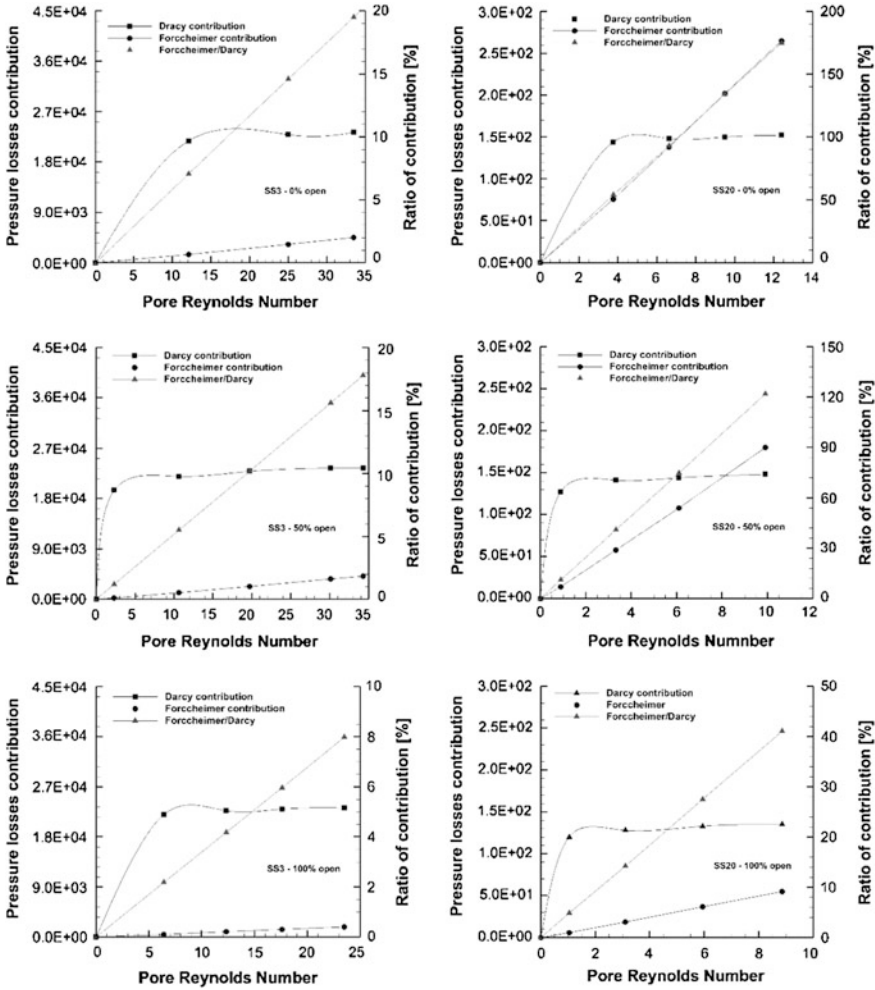
Fig. 4 Permeation contributions plotted as a function of the estimated pore Reynolds number for class 3 and class 20 for different openings of secondary outlet

For metallic samples, the pore Reynolds number has been computed using the relation $R_e = \rho V \, d_p/\mu$, where $d_p = 4\varepsilon/(a_g(1 - \varepsilon))$ is the pore diameter, ε is the porosity of material, $a_g = 6/d_g$ is the grain area, and d_g is grain diameter.

The grain diameter of the SS3 sample measured in a previous work [12] $d_g = 14.1$ μm, whereas the one for the SS20 $d_g = 55.2$ μm is computed from a correlation between class and grain diameter deduced from the literature data. From the set of plotted data, it is observed that in case of SS3 Darcian's term is always higher than the Forchheimer's term for all the three different opening of S.O (0, 50, and 100 %), which shows that the flow is always in the laminar regime. There is no

influence of S.O opening on Darcian's term and its contribution remains constant for all the three cases but Forchheimer's contribution decreases as the S.O opening increases. A similar trend is observed in case of SS20 except in case of 0 and 50 % opening of S.O, where the Forchheimer's contribution overcomes the Darcian's contribution as the pore Reynolds number exceeds a critical value of R_{ec} 6–8. It is also observed that the decrease in Forchheimer's term for SS3 is less evident compared to the Forchheimer's decrease in case of SS20.

4 Conclusion

In fuel cell applications, porous materials are used for filtration. Determining physical properties like porosity and permeability are of utmost importance to predict filtration efficiency of these materials. An experimental test bench was developed to determine both K_D and K_F. Later it was found that using the experimental values of these permeabilities on complete integrated fuel reforming systems led to discrepancies of higher magnitude. Hypothesis posed was that the geometrical configuration might have an impact on the results. In other words, having one inlet and one outlet or one inlet and two outlets may lead to different permeabilities. Thus, the effect of S.O on permeability determination has been investigated. It was found that there is no change in K_D when the mass flowmeter is placed at P.O instead of the inlet as per the norms of ISO 4022 for determining permeability. When K_D is determined for SS3 and SS20 with different opening of S.O, negligible changes in values were observed, hence it shows that this term is not affected by change in flow configuration for the case of stainless steel material. But S.O opening has significant effect on the determination of K_F for both kinds of porous materials. Its determination criterion is highly governed by turbulent flow regime. This flow regime is found in just two cases out of six cases and that is only when the pore Reynolds number exceeds its critical value. In future works, K_D and K_F will be studied in a tube configuration using different composite. Mathematical background will be developed in order to correlate these permeabilities to the selectivity of the porous materials. Further, selectivity of several binary mixtures of gases will be investigated on different porous media using an adapted experimental setup.

References

1. Spillman R. *Chemical Engineering Journal*, 1989, Vol 85.
2. Lu G. and Zhao X. ISBN-13: 978-1860942112, London, 2004.
3. Phair J. and Badwal S. Science and Technology of Advanced Materials, 2006, Vol 7.
4. Chen W. and Chi I. International Journal of Hydrogen Energy, 2009, Vol 34.
5. Chi Y., Yen P., Jeng M., Ko S. and Lee T. Int. Jour. of Hydrogen Energy, 2010, Vol 35.
6. Luquot L., Abdoulghafour H. & Gouze P. Int. Jour. of Greenhouse Gas Control, 2013, Vol 16.

7. Abdulgader H., Kochkodan V. & Hilal N. Separation & Purification Technology, 2013, Vol 116.
8. Tanakaa D., Tancoa M., Niwaa S., Wakuia Y., Mizukamia F. Jour. of Membrane Science, 2005.
9. Shamsabadia A., Kargarib A., Babaheidaria M. Jour. of Ind. & Eng. Chem., 2013, Vol 19 (2).
10. Franza J., Schiebahnb S., Zhaob L. Int. Jour. of Greenhouse Gas Control, 2013, Vol 13.
11. Barreiro M., Maroño M. and Sánchez J. Int. Jour. of Hydrogen Energy, 2014, Vol 39 (9).
12. Gascoin, N. Int. Jour. of Multiphase Flow, 2011, vol. 37.
13. Wang, J., Zhao, L., Wang, X., Ma, J. Int. Jour. of Heat and Mass Transfer, 2014, vol. 75.
14. Zhao, L., Wang, J., Ma, J., Lin, J., Peng, J., Qu, D. Int. Jour. of Thermal Sciences, 2014, vol. 84.
15. Thomasa S., Pinnaua I., Dub N. and Guiver M. Jour. of Mem. Science, 2009, Vol 333 (1–2).
16. Baker W., Wijmans G. and Huang Y. Journal of Membrane Science, 2010, Vol 348.
17. Robeson L. Journal of Membrane Science, 1991, Vol 62.
18. Chenara M., Soltanieha M., Matsuurab T. Sepa. & Purification Technology, 2006, Vol 51.
19. Poling B., Prausnitz J. & O'Connell S. ISBN-13: 063-9785322160, McGraw-Hill Prof, 2001.
20. Langener T., von Wolfersdorf J. In: 44th AIAA/ASME/SAE/ASEE JPC & Exhibit 2008.
21. Firoozabadi A. and Katz D. Jour. of Petroleum Tech., 1979.
22. Lemos M. Springer-Verlag Berlin and Heidelberg & Co. K, ISBN-13: 978-3642282751, 2012.

An Experimental Study on Flow of Micronized Silicon Carbide Particles Through Sintered Porous Materials

Aswin Chinnaraj, Eddy E.L. Tabach, Khaled Chetehouna and Nicolas Gascoin

Abstract Transport of suspended particles in porous media occurs in numerous processes of civil engineering and aerospace engineering. Literature survey indicating the mechanism of movement of suspended particles through porous media and the subsequent damage in engineering environment are not sufficiently known. This paper deals with a new concept of a laboratory test bench which permits to better understand the mechanism of particle intrusion into porous media. The results of the laboratory studies on the flow of suspended particles (silicon carbide) through sintered porous material (stainless steel) are discussed. The effects of flow rate and particle concentrations on the amount of damage (i.e. permeability impairment) and depth of penetration (from inlet towards outlet) are emphasized particularly.

Keywords Suspended particles · Transport · Sintered porous medium · Micro-particles

1 Introduction

The transport of suspended particles in porous media occurs in a variety of natural and industrial process such as propagation of coke, formed by fuel pyrolysis at high temperatures, through porous materials used in the combustion chamber of hypersonic vehicles [1–3]. Many attempts were made by different investigators to explain the mechanism of particles flow through porous media. Still the problem is far from being solved, there are some points of agreement among various investigators regarding the importance of various factors such as flow rate, particle size,

A. Chinnaraj (✉) · K. Chetehouna · N. Gascoin
INSA Centre Val de Loire, PRISME Laboratory, University of Orleans,
88 Boulevard Lahitolle, 18000, Bourges, France
e-mail: aswin.chinnaraj@insa-cvl.fr

E.E.L. Tabach
PRISME Laboratory, University of Orleans, 63 avenue de Lattre de Tassigny,
18020 Bourges, France

etc. on these mechanisms. We can find many studies in the literature related to damage caused by particles suspended in fluid flows. Most of the literature on this subject is on natural porous material [4] or artificially created porous material [5, 6].

Donaldson et al. [7] made significant contribution to the mechanism of the flow of particles through porous media using laboratory experiments and a statistical interpretation of the results. They conducted some experiments by passing suspended silica particles through three types of core plugs. The specific core plugs used in their experiments were taken from Berea, Noxie and Cleveland sandstone. Additional studies on the flow of suspended particles through porous media were performed by Davidson [8]. Davidson used alundum cores with a mean pore diameter of 90 μm, a permeability of Darcies and a porosity of 35 %. The suspended particle is made with silica powder having a particle size distribution characterized by a median size of 3 μm with a 12 μm upper bound. Gruesbeck and Collins [9] attempted to explain the abnormal decline in productivity of producing wells in terms of the movement of naturally occurring fine particles in porous media. They made a rather questionable hypothesis on the interrelationship of the flow velocity and the rate of entrainment. Muecke [10] presented an interesting qualitative analysis of fine particles movement through unconsolidated sand. The results are based essentially on a visual observation using a microscope. The work of Jordan et al. [11] dealt with an offshore sea water injection project where the brine was filtered through 0.45 μm filters prior to injection.

According to the clean-bed filtration theory, the flow of suspended micro-particles through porous material can be characterized by two important phenomena, the transport and the attachment. The transport is defined as the movement of the particles to the grain surface (porous material or the solid matrix) and is quantified by the single collector efficiency factor η_0. The deposition of the micro-particles on the porous material is defined as the attachment phenomenon. The attachment of the particles to the grain surface is quantified by the collision efficiency α, which is either favourable ($\alpha = 1$) or unfavourable ($\alpha < 1$). In favourable conditions, the suspended micro-particles and the grain surface are differently charged and vice versa in unfavourable conditions. Both favourable and unfavourable conditions are the results of the collision of the dispersed particles with the grain surface. Under favourable conditions every collision results in an attachment. The amount of the particles collected in the porous material can be calculated or verified by the collector efficiency factor. In this condition, the transport step plays an important role in the deposition of the particles on the grain surface; the smaller the particles are, larger the amount of transported particles due to enhanced diffusion of the particles in the fluid flow. Hence, in this condition, the size of the particles also plays an important role in the deposition. But the effects of particle size in the unfavourable conditions are difficult to understand, due to the various factors associated with them [6].

Apart from the above two phenomena, aggregation is another important process which occurs when the suspended particles clump together forming clusters. This may result in increase of size of the suspended particles, which, when encountered by the grain surface can block the fluid flow completely. These aggregates loss their kinetic independence while they retain the individual properties and are more likely

to deposit on the solid matrix during the flow through porous material. The instability of the suspended particles results in the aggregation and it depends on the type of system (fluid and the suspended particles) involved. Further details can be found in [12, 13]. Brownian motion of the micro-particles plays an important role in all the above phenomenon.

The literature survey indicates that the mechanism of particle intrusion into sintered porous materials is not known in sufficient way. In this paper, we present an experimental test bench in order to better understand the mechanism of particles intrusion into sintered porous materials. The obtained results, using this test bench, by studying the flow of silicon carbide micro powder into sintered porous material (stainless steel) are discussed.

2   Experimental Setup

The developed experimental setup consists of an autoclave which is used to mix the water and the micronized powder. The autoclave consists of a motor and this is used to stir the mixture of water and the powder. This ensures the transport of the particles to the cell and also prevents the settling of the powder in the bottom of the autoclave. Nitrogen is used to pressurize the autoclave at a constant pressure (P_{in}) and push the mixture of powder and water into the experimental cell. Due to safety reasons, we used micronized silicon carbide (SiC) for our experiments. The mass flow rate is measured from the Coriolis mass flowmeter (Brooks). The inlet pressure of the experimental cell is measured using a pressure transducer (Rosemont 3051S). The pressure difference between the inlet and outlet of the test cell is measured using a differential pressure transducer (Rosemont 3051S). Both the pressure transducers and the mass flowmeter are connected to the data acquisition card. This data acquisition card is connected to the Keithley multimeter and Excel is used to control the data acquisition through the Keithley multimeter. The acquired data are stored in the Excel for future exploitation. The data obtained can be used to calculate the change in permeability of the porous material with respect to time during the experiment. The porous material used here is fabricated by STEMM located in France. The overall porosity of this porous material is of about 30 %. The active diameter of the porous material is 16 mm. The SiC powder used for this set of experiment has an average particle size of 35 μm. The micronized powder used in this study is relatively smaller than the pore diameter of the porous material.

The porous material used in these experiments is made up of stainless steel with individual spherical particles. This material has a thickness of 3 mm with a density of 7850 kg m^{-3}. The maximum pore diameter of the porous material used is 88 μm and the average grain size of the material is 200 μm. The porous material was weighed before and after the experiment. The porous material is then dried in an oven for 30 min and again weighed. Several trails were conducted before choosing

the duration of time for the drying process and it is found that there is no significant difference on the material weight above 15 min of drying. The difference in the weights of the porous material gives the amount of particles deposited on the porous material (Fig. 1).

3   Results and Discussion

The experiments were conducted using the above experimental setup on the sintered porous material (stainless steel). After each experiment, the surface porous samples are needed to be wiped due to the deposition of the SiC particles on the surface which do not interest us to study it. Fig. 2 gives a brief idea about the unwiped and the wiped surface of the porous samples after the test. Usually the deposition on the surface is wiped after drying the porous sample in oven for 30 min at 100 °C. It is found that, if the surface is wiped before the oven drying process, there are possibilities of few SiC particles resting on the porous surface due to wetness.

1. Nitrogen Gas Bottle
2. Autoclave
3. Controller for Motor
4. Experiment Cell
5. Pressure Sensor (P_{in})
6. Mass Flow meter

8. Differential pressure Sensor (ΔP)
9. Beaker to collect water
10. Acquisition Card
11. Computer to acquire data

13. Tightening seal
14. Porous material
15. Carbon Seal
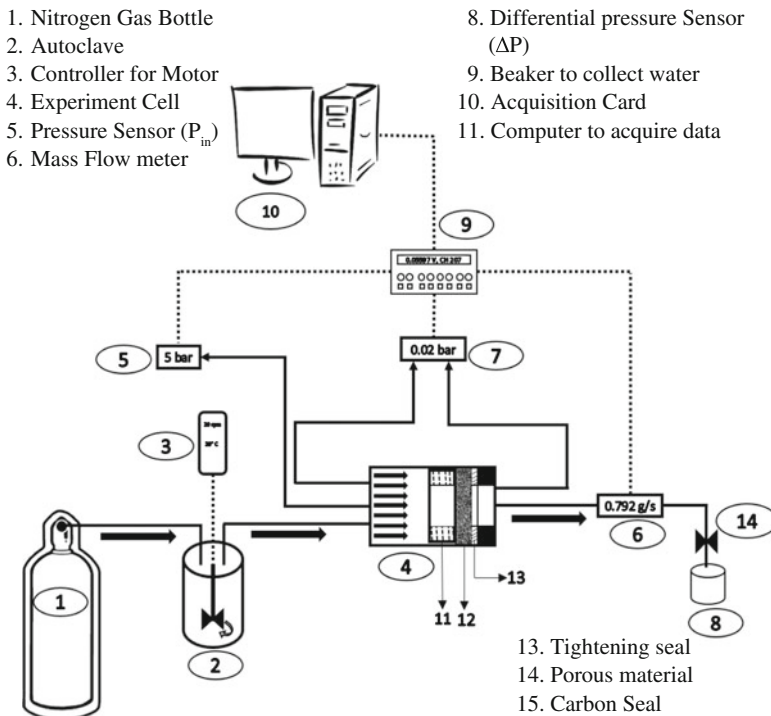
Fig. 1 Experimental setup

Fig. 2 Porous sample before and after surface cleaning

Figure 3 gives the cumulated weight rise (W_c) in the porous material after each interval of the tests, while Fig. 4 gives the results of weight increase (W) in the porous material (after cleaning the powder on the porous material surface) after each test for different P_{in} values. It can be noted that W_c in the 5 bar tests is higher than that of 2 and 10 bar. This is explained by the fact that the pressure (P_{in}) of 2 bar is not sufficient for pushing enough particles inside the porous material. While, with a value of 5 bar for P_{in} the particles enter the porous material. On the other hand, increasing P_{in} to 10 bar, certain amount of the particles flow through the porous material due to high pressure. The total weight increase in the porous sample for different values of P_{in} tests of 2, 5 and 10 bar of the pressure are 0.182, 0.1876 and 0.1697 g, respectively.

It is important to note that for tests of 5 and 10 min there was no flow after certain period of time due to the total blockage of the porous sample inside the experimental cell. Hence for flow duration more than 2 min, the permeability of the porous sample becomes zero.

Fig. 3 Cumulated increase in weight of the porous material after 3 durations
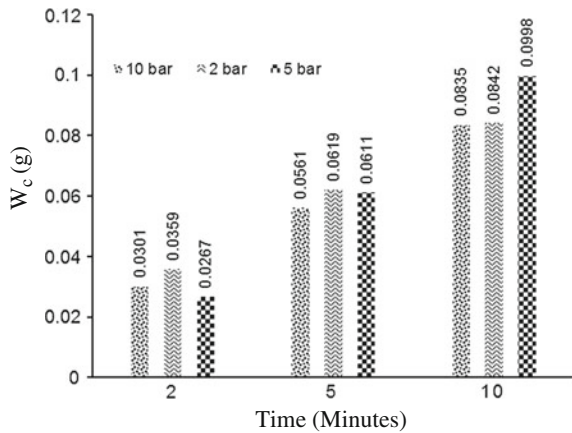
Fig. 4 Weight increase data after each experiment
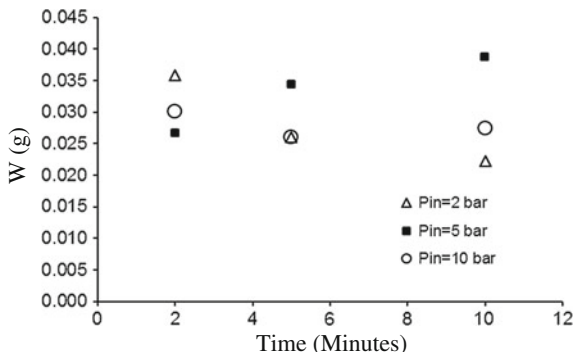
4   Conclusion

In this paper, the experimental test bench for studying the effects of infiltration of the micronized SiC particles was discussed and the results of the first few experiments were published. The increase in weight of the porous samples due to the deposition and infiltration of the SiC particles was studied and important results were found. It is found that the SiC particles with sizes thrice smaller than the average pore diameters of the porous materials block completely the porous samples for the tests of durations higher than 2 min. During the future experiments, the investigation of the other SiC particles with higher particle sizes is to be accomplished and a numerical model is to be developed based on these results.

References

1. Gascoin, N., Fau, G., Bioud, J., Gillard, P., Permeation of inert and supercritical reactive fluids through metallic and composite material, 40th AIAA/ASME/SAE/ASEE Joint Propulsion Conference & Exhibit, 2010.
2. Fau, G., Gascoin, N., Gillard, P., Bouchez, M., Steelent, J., Fuel pyrolysis through Porous Material: Coke Formation and Coupled effect on Permeability, J. Analytical and Applied Pyrolysis, 2010.
3. Gascoin, N., High temperature and pressure reactive flow through porous material, International Journal of Multiphase flow 37 (2011), pp. 24–35.
4. Tahar, I., Ahmed, B., Mohamed, K., Nasre-Dine, A., Particle transport within water saturated porous material: Effect of pore size on retention kinetics and size selection, C.R. Geoscience 345 (2013), pp. 392–400.
5. Amir, Z., Brij, M., Flow of dispersed particles through porous material – Deep bed filtration, Journal of Petroleum Science and Engineering 69 (2009), pp. 71–88.
6. Ryan, M., Yusong, L., The effect of particle size on the deposition of fluorescent nanoparticles in porous material: Direct observation using laser scanning cytometry, Colloids and Surfaces A: Physicochem, Eng. Aspects 418 (2013), pp. 84–91.
7. Donaldson, E.C., Baker, B.A., Carroll, H.B., Particle transport in sandstones, SPE 6905, presented at the 52nd Annual Fall Meeting of the SPE, October 9–12 (1977), Denver, Colorado.

8. Davidson, D.H., Invasion and impairment of formations by particulates, SPE 8210, presented at the 54th Annual Fall Meeting of the SPE, September 23–26 (1979), Las Vegas, Neveda.

9. Gruesbeck, C. and Collins, R.E., Entrainment and deposition of fine particles in porous media, SPE 8430, presented at the 54th Annual Fall Meeting of the SPE, September 23–26 (1979), Las Vegas, Neveda.

10. Muecke, T.W., Formation fines and factors controlling their movement in porous media, Journal of petroleum technology, 1979, pp. 144–150.

11. Jordan, C.A., The bay marchand pressure maintenance project-unique challenges of an offshore sea water injection system, Journal of petroleum technology, 1969, pp. 389–396.

12. Elimelech, M., Gregory, J., Jia, X., Williams, R.A. (1998). Particle deposition and aggregation: measurement, modelling, and simulation. Colloid and Surface Engineering Series, Butterworth-Heinemann, Oxford.

13. Hiemenz, P.C., Rajagopalan, R., (1997). Principles of Colloid and Surface Chemistry. Marcel Dekker Publishing Co. New York.

Design and Fabrication of a Quick Dismantlable Remotely Controlled Semirigid Finless Airship

Sohrab R. Mistr and Rajkumar S. Pant

Abstract Remotely controlled airships are very much suitable for aerial photography, product promotion, and surveillance. This paper describes a methodology for sizing and design of a small semirigid airship that can be quickly assembled or dismantled. The airship is meant for flight demonstrations and as an aerial platform for indoor surveillance. The propulsion system is a novel design where the differential thrust and swiveling motors control the entire flight regime, with no fins or control surfaces. Topics such as all-up weight estimation based on payload weight, envelope sizing calculations, design and fabrication of a quick dismantlable semirigid structure design are covered.

Keywords Lighter-than-air systems · Semirigid airships

1 Introduction

Airships were once at the forefront of aeronautical technology; when the Wright brothers were struggling to make their first airplane fly, Count Ferdinand von Zeppelin was contemplating an airline for transatlantic passenger operations using giant airships. However, airships developed a connotation of being unsafe as a mode of air transportation after a string of disasters and accidents, viz., the loss of RH-101 in 1930 in the UK, the USS *Akron* in 1933 in USA, followed by the infamous *Hindenberg* in 1937 in USA.

S.R. Mistr (✉) · R.S. Pant
Aerospace Engineering Department, IIT Bombay, 400076 Powai, Mumbai, India
e-mail: sohrabmistri@hotmail.com

S.R. Mistr
Mechanical Engineering Department, Sardar Patel College of Engineering, Mumbai, India

R.S. Pant
School of Mechanical & Aerospace Engineering, Nanyang Technological University, Singapore, Singapore

Interest in airships was rekindled in mid-1990s when a request for proposal for a Battle Surveillance Airship System (BSAS) was floated by the US Navy in mid 1980s, which resulted in the creation of Sentinel-1000 airship, a scaled model of the proposed solution. Though the project was discontinued by the US Navy in 1989 due to financial cuts, airship technology was effectively revived.

Airships are extremely efficient aerial platforms for long endurance applications; they can stay much longer in the air as compared to fixed wing or rotary wing aircraft. Thus, they are platforms for choice for niche applications such as product promotion, and aerial surveillance or photography.

From the point of view of their structural configuration, Airships are of three main types, viz., rigid, nonrigid, and semirigid. Rigid airships consist of a solid shell framework, inside which gas bags are installed. Such a configuration is now considered obsolete, and is inefficient only for very large-sized airships (of lengths greater than 100 m).

Most remotely controlled airships are of nonrigid configuration, in which there is no internal structure, and the shape is maintained solely by the envelope over-pressure. A Gondola is mounted below the envelope, and all subsystems and payload (which include engines, avionics and sensors) are mounted on this Gondola using load-bearing patches, which distribute these loads to the envelope. The key advantage of nonrigid configuration is low self-weight, and ease in transportation, since the envelope can be folded and packed.

However, the constraint of not being able to mount the subsystems and payload at any other location except the Gondola results in severe limitations in performance, operational safety, and center of gravity management of the airship. Further, the envelope has to fulfill two roles; to hold the lighter-than-air gas with least possible leakage, as well as to carry all the loads acting on the system. Poor design of the load-bearing patches can result in severe stress concentration at the mounting locations, which can lead to tears and leakages in the envelope. One could use a double chambered envelope in which the inner bladder contains the gas, and the outer fabric takes care of the load-bearing requirement. But this usually results in a heavier envelope, and hence lower payload capacity for a given envelope size (i.e., volume).

Semirigid airships have a stiff keel or truss structure mounted inside or outside the envelope, which relieves the envelope from carrying concentrated loads. This structural configuration also results in much greater flexibility in mounting various items on the airship; for instance, the engines can be mounted on the side of the envelope (on the keel or truss framework), rather than below the envelope (on the Gondola), which greatly increases maneuverability and control response. Further, one can mount the other load-bearing components (for e.g., the empennage, onboard equipment, and payload) rigidly on the framework, at the desired location. This flexibility, however, comes at the cost of poor transportability, and increase in self-weight.

2 Aim of Present Study

The aim was to design, fabricate, and test-fly a remotely controlled semirigid airship suitable for indoor demonstrations. The key design requirement was that it should be possible to quickly assemble (and dismantle) this airship, so that it can be easily transported to (and fro) the venue of demonstration. The sizing was carried out with the constraint that it should have a payload capacity of ~ 400 g when operated at ISA + 15° conditions. Another important requirement was that the airship should look somewhat like how actual airships are, since the key aim of this airship is for demonstration and educational purposes, apart from a platform for aerial surveillance.

Further, some constraints were imposed on the size of the airship, and operating requirements were decided, keeping in mind the likely area of operation, viz., Overall Length ≤ 4 m, Envelope Volume ≤ 6 m^3, and Max. Operating Speed ≥ 3 m/s, and Endurance (on one battery charge) ≥ 2 h.

3 Initial Sizing of the Airship

A methodology for sizing of indoor remotely controlled airships was developed by Bansal et al. [1] in 2013, and by Dusane et al. [2] recently. This methodology was applicable to only nonrigid airships, and the approach used to design the semirigid airship was broadly on the same lines. In this approach, the shape of the envelope to be used for the airship is decided, and an iterative procedure is used to estimate the size of this envelope to generate sufficient buoyant lift to overcome the self-weight and payload. This approach is quite involved, and needs estimation of the drag acting on the airship while in flight, for proper estimation of the weight of the propulsion system.

The first-cut estimate for the size of the airship was obtained by creating an empirical relationship between payload capacity and all-up weight. Let us define Lift Ratio (LR) as

$$LR = \frac{All - Up\,Weight}{Payload\,Weight} \tag{1}$$

Data related to LR and Payload capacity of 25 unmanned airships (Ref. Table 1) powered by electrical motors built in the past was plotted (Ref. Fig. 1) and a correlation was developed as

$$LR = 9.4 - 0.9843\,W_{payload} \tag{2}$$

Based on this co-relation, the expected all-up weight of the airship for a payload weight of 400 g comes out be ~ 3.6 kg.

Table 1 Lifting Ratio for 23 past airships

Sr.	Airship Company and airship	Payload (g)	Net lift (kg)	LR
1	Airship solutions E13	900	4.482	4.98
2	Airship solutions-Stadium size	1000	8.964	8.964
3	Airship solutions AS7	1340	14.567	10.871
4	Aerodrum limited indoor 2 m blimp	200	1.680	8.404
5	Aerodrum Ltd. Indoor 3.5 m blimp	500	3.922	7.844
6	Aerodrum Ltd. Indoor 4.5 m blimp	750	6.163	8.217
7	Aerodrum Ltd indoor 7 m Blimp	2500	15.687	6.275
8	Aerodrum outdoor 5 m blimp	1200	8.964	7.470
9	Aerodrum outdoor 7 m blimp	2000	15.687	7.844
10	Aerodrum outdoor 10 m blimp	5000	26.892	5.378
11	Aerodrum outdoor 12 m blimp	5000	31.374	6.275
12	Microflight inc.-e300B300	100	1.793	17.928
13	Microflight inc.-e300B350 v	200	2.353	11.765
14	Microflight inc.-e300B400	400	2.689	6.723
15	Microflight inc.-e700B400	400	4.202	10.505
16	Microflight inc.-e700B450	800	4.706	5.883
17	Microflight inc.-e700B500	1200	5.266	4.389
18	Microflight inc.-e1000B450	750	7.619	10.159
19	Microflight inc.-e1000B500	1500	8.964	5.976
20	Microflight inc.-e1000B600	2100	11.093	5.282
21	Airshop for snow scientists	3000	29.850	9.950
22	Mini PADD airship(IIT Bombay)	3000	9.636	3.212
23	PADD micro airship(IIT Bombay)	1000	7.619	7.619
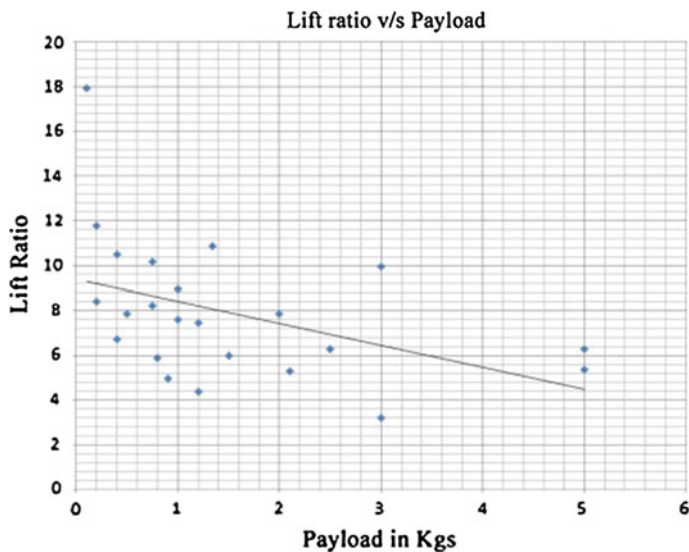
Fig. 1 Co-relation between Payload and Lift Ratio

4 Envelope Sizing and Fabrication

4.1 Profile Selection

The envelope profile should result in large volume but low surface area, since the lift producing capacity of an airship envelope is directly proportional to its volume, and its weight is proportional to the surface area. It should also have good stability and permit good stability.

The ratio of length to diameter (L/D) of the envelope (also called slenderness ratio) affects the longitudinal stress, hoop stress, and the stress induced due to aerodynamic and hydrostatic loading [3]. Airships that were used in the pre-World War-II period had a very high L/D, of the order of 10–11, which was subsequently reduced to 6–7 [4]. However, CFD analyses [5, 6], and an analytical study [7] have indicated that envelopes suitable for airships have an L/D between 4 and 6, with the optimum value being around 5.5. One standard profile for airship envelopes is the double ellipsoid NPL shape [8], which has an L/D of 4, but this shape has a very large envelope surface area to volume ratio, which is undesirable.

The modified GNVR shape [7] with a cylindrical portion of 1 ft (0.305 m) added in the middle of the standard GNVR profile was chosen, as suggested by Joshi et al. [9]. The profile of this shape and the rendered 3-D view is shown in Fig. 2. Table 2 lists the key geometrical parameters of the envelope.

4.2 Gore Design

There are three methods available for approximating the shape of the envelope using flat patterns, viz., Gore, Zone and Compound Method, as explained by Thiele [10], and Gawale et al. [11].

A gore design approach was chosen, as it is the simplest in construction, and quite suitable for small envelopes. Six gores (also called petals) were selected to create the development of the 3-D shape of the envelope in 2-D. We divide the profile into each of its geometrical components, for e.g., the modified GNVR profile is divided into four main components (viz., elliptical, cylindrical, circular, parabolic, as shown in Fig. 2). The coordinates of the petal can then be obtained by simple geometrical constructs. For example, consider the elliptical part of the modified GNVR profile. Let the coordinates of the ellipse be x and y and its corresponding gore profile be X and Y, as shown in Fig. 3.
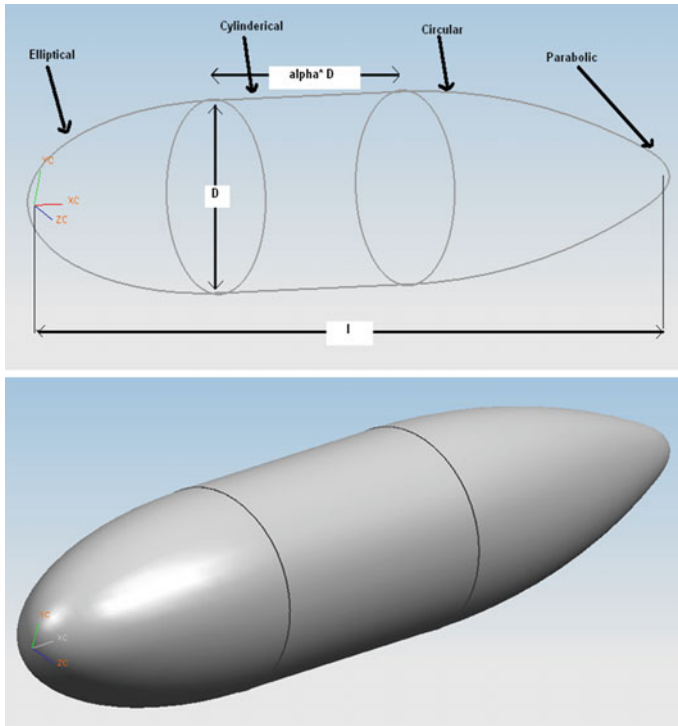
Fig. 2 Modified GNVR shape [9]

Table 2 Key geometric parameters of the envelope

Parameter	Value
Envelope length	4.305 m
Maximum diameter	1.311 m
Length of extension	0.305 m
Volume	3.753 m^3
Surface area	14.08 m^2

Now X will be the circumference at any point divided by number of gores, hence

$$X = \int_a^b \left[\sqrt{1 + \left(\frac{dy}{dx}\right)^2} \right] dx, \quad \text{and } Y = \pm\frac{\pi y}{n} \tag{3}$$

The petal coordinates for the other parts of the envelope can be obtained on the same lines, by replacing Eq. (3) with the relevant ones.
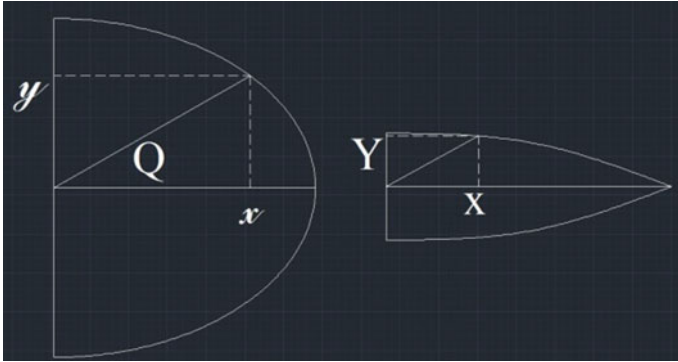
Fig. 3 Procedure for generating petal geometry
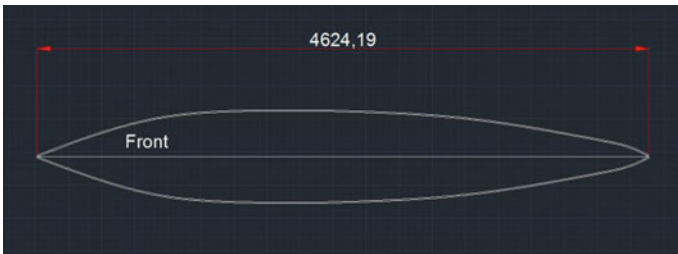
Fig. 4 Petal geometry generated using *SolidWorks™*

The other technique that we have used for petal geometry construction is through the use of *SolidWorks*.[1] The sheet metal feature of this software was used to create the Gore of the envelope, and then the flatten tool was used to generate the petal profile, as shown in Fig. 4.

5　Review of Previous Semirigid Airships

Kshirsagar et al. [12] have carried out conceptual design and sizing of a semirigid airship. Loharkar et al. [13] fabricated and tested a semirigid airship based on a slightly modified design, as shown in Fig. 5.

However, this airship, though 4 m in length, had a payload capacity of only 100 gm. Second, more than 2 man-hours were needed to assemble/disassemble this

---

[1]A proprietary CAD/CAE software program produced by DassaultSystèmes, France, which runs on Microsoft *Windows*™.

Fig. 5 Semirigid airship fabricated by Loharkar et al. [13]

airship, which is far too much. Further, this airship had limited performance capability, since the motors mounted on it were fixed, and could not be swiveled.

A critical review of this design revealed that the structure was quite heavy, since it covered the entire envelope. The front and rear portions of this structure were of limited use, since most of the load acts on the middle section.

An attempt has been made to overcome some of these limitations, as described in the next section.

6   Details of the Semirigid Structure

6.1   Structural Layout

The structure is mounted below the airship envelope to evenly distribute the weight that it carries, as can be seen in Fig. 6.

The middle ring takes the load of the motors and all the three rings take the load of the gondola, through a horizontal link. Two ribbons are attached on the front and rear rings, which allow the loads to be transferred to the upper part of the envelope.

6.2   Ensuring Ease of Assembly and Disassembly

One of the prime requirements for this airship was the need to quickly assemble/dismantlable it. With this in mind, the structure was divided into 15 major components, which can be press-fit into each other, as shown in Fig. 7.

A dowel pin is used to lock them together, and a rubber band holds the dowel pin in place, hence the structure can be assembled or dismantled in less than 5 min. Figure 8 illustrates the dowel pin-based locking mechanism.

Fig. 6 CAD model of the assembled airship
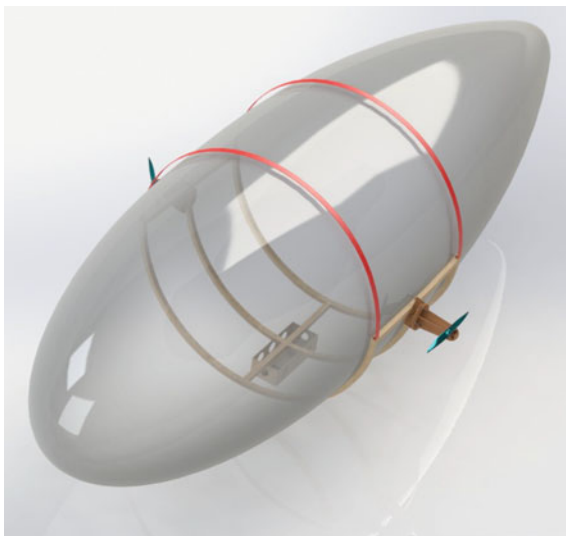
Fig. 7 Breakup of the Semirigid framework
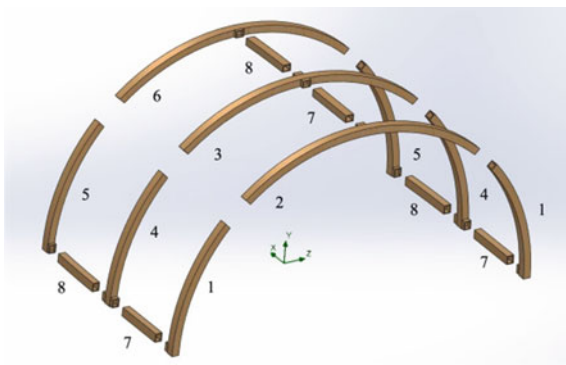
Fig. 8 Illustration of dowel pins for locking
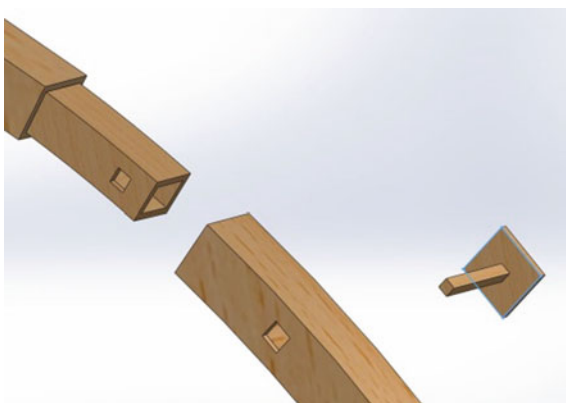
Fig. 9 Components that make the semirigid structure

6.3 Construction Technique

The semirigid assembly is made from balsa wood, and each component is broken up into four sides. The components are designed in such a way that they interlock and only fit in one way.

For the curved parts, hot water had to be applied onto the balsa wood sheets, which were then held together in bent position while they were being glued together. All the parts were cut from 3 mm sheets of balsa or plywood, using high-precision laser cutting techniques. The various components are shown in Fig. 9.

6.4 Gondola Structure

The gondola was made out of a light-weight box-type Balsa structure, and it was attached to the two outer semicircular rings. It houses the receiver and battery pack, and the payload too, if needed, as shown in Fig. 10.

6.5 Propulsion System

Selection of suitable power plant for the airship needs estimation of the drag force acting on it at the maximum operating speed. The volumetric drag coefficient (C_{DVe}) of an envelope can be estimated using the semiempirical equation suggested by Cheeseman in [8] as

$$C_{DVe} = \frac{0.172\left(\sqrt[3]{\left(\frac{l}{D}\right)_e}\right) + \left(\frac{0.252}{(l/D)_e^{1.2}}\right) + \left(\frac{1.032}{(l/D)_e^{2.7}}\right)}{Re^{1/6}} \tag{4}$$

The Reynolds Number (Re) for ISA + 15° C sea-level condition and forward speed of 3 m/s is estimated as 0.7977 million. For envelope having L/D of 3.2836, and this Re value, C_{DVe} was estimated using Eq. (4) as 0.0372. Assuming that the drag of envelope is a fixed part of the total drag, the drag coefficient of the entire airship (C_{DV}) can be computed using Eq. 5 as

$$C_{DV} = \frac{C_{DVe}}{k_d} \tag{5}$$

Looking up the values of past airships, the value of k_d is found to be 0.5243, and hence, using Eq. 5, C_{DV} = 0.0709.

The maximum drag acting on the airship (D_{max}) can be estimated using Eq. 6 as

$$D_{max} = \frac{1}{2}\rho_{air}V_{max}^2 V_{env}^{2/3} C_{DV} \tag{6}$$

For the expected operating conditions, D_{max} was estimated to be 0.8972 N. This drag could easily be overcome by using two Emax PM1306 motors [14], each of which can generate 110 g (1.08 N) thrust, and weigh only 12 g. However, it was decided to use two EmaxGT 2815/07 motors [14]; each of which can generate 800 g (7.86 N) thrust, which is far more than needed, and are also quite heavy (at 120 g each). One justification for using such oversized motors was to ensure that enough excess thrust is available to overcome loss of buoyancy due to leakages from the envelope or change in ambient atmospheric conditions. Another reason was to cut down the costs, since they were already available in the laboratory.

Fig. 11 Swiveling
mechanism using high-torque
Servo
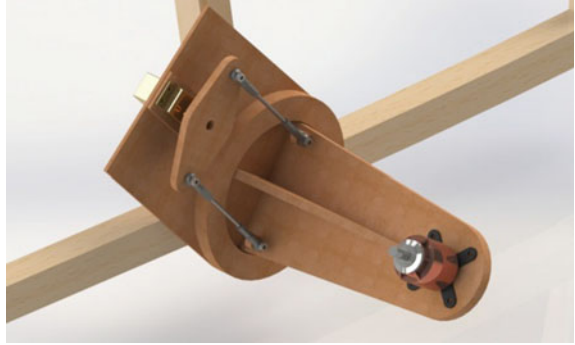
For the swiveling mechanism (Ref. Fig. 11), the engine firewall was directly mounted on a circular insert in the base plate, which is rotated with the help of a high-torque servo (110 oz-in, or 0.777 Nm).

7 Flight Control System

The three standard parameters that are to be controlled by a pilot are Velocity-V, Altitude-A, and Yaw-Y. The receiver sends signals to control four parameters, viz., RPM of port and starboard motor (S_L and S_R), and the angle of port and starboard motor with the horizontal (θ_L and θ_R).

Using basic trigonometric geometry one can map the output signals in terms of input signals, as shown in Eqs. 7 and 8.

$$S = \sqrt{((C_1 \times V) \pm (C_2 \times Y))^2 + (C_3 \times A)^2} \tag{7}$$

$$\theta = \tan^{-1}\left(\frac{C_3 \times A}{(C_1 \times V) \pm (C_2 \times Y)}\right) \tag{8}$$

The net buoyant Lift (L_B) can be calculated using Eq. 9 as

$$L_b = (\rho_a - \rho_{he})V_{env}g \tag{9}$$

L_B was estimated to be 3695 N, or 3768 g, under ISA + 15° C conditions.

Table 3 lists the weight breakdown of the airship assembly. It can be seen that the requirement of payload capacity of 400 g is met, with a margin of $\sim$68 g. As per Eq. 2, the weight of a nonrigid airship meeting the same requirements was estimated to be $\sim$3.6 kg; this semirigid airship was found to be lighter by around 300 g.

The fully assembled airship can be seen in Fig. 12. It was test flown successfully in a closed environment to test the agility of the control system.

Table 3 Weight breakdown of the semirigid airship

Parameter	Weight (g)
Envelope	1300
Semirigid structure	850
Motor mount and swiveling assembly	466
Gondola	67
Receiver (Futaba 12 channel)	22
Battery pack	150
Propulsion system ($2 \times$ GT 2815/07 E_{max} motors + 50 amp ESC + Propellers)	360
Handling ropes, ties, cables, and other items	85
Empty weight	3300
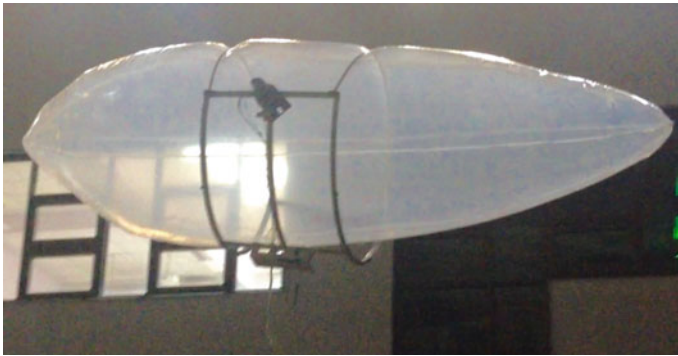
Fig. 12 The final assembled semirigid airship

The airship was found to be very responsive to the pilot inputs and could be easily flown even in tight spaces. It was found that the airship had higher than expected inertial resistance in yaw, due to the absence of fins. However the airship was completely controllable. The oversized motors generated enough direct upward force to overcome gravity, which helped when the airship lost some buoyancy due to weather changes, or leakages. A short video of the flight test is available at https://youtu.be/xGiqqbFHzo8.

8 Conclusions

It can be concluded that the semirigid airship developed has met all the key requirements that were specified, especially the ability to mount payload and/or systems away from the gondola, and also ensuring quick assembly and disassembly. Contrary to expectations, the semirigid airship was found to be ~ 8.33 % lighter than the corresponding nonrigid type This is mainly because the semirigid

structure allows the use of thinner (and hence lighter) material for the envelope, since it carries most of the structural loading. The semirigid airship was also found to be more robust in handling, and demonstrated higher maneuverability.

References

1. Bansal, G., Bhardwaj, U., Jain, N., Mulay S., Sawardekar, S., and Pant, R. S., **Design Fabrication and Flight testing of a Non-rigid Indoor Airship**, AIAA-2013-1297, Proceedings of 20th AIAA LTA Systems Technology Conference, 25–27 March 2013, Daytona Beach, FL, USA.
2. Dusane, C. R., Wani, A., and Pant, R. S., **Design and Fabrication of an Indoor Remotely Controlled Airship for Autonomous Control**, Proceedings of 29th National Convention of Aerospace Engineers, November 27 and 28, 2015, Chennai, India.
3. Burgess, C. P., "**Bending Moment, Envelope & cable stresses in non-rigid airships**." NACA-TR-115, Bureau of Aeronautics (Navy); Washington, DC, United States, 1923.
4. Kirilin, A. N., Ivchenko, B.A., "**Basic Design Parameters of Non-Rigid Airships**", Technical Report, Russian Dirigible Society, Moscow, 2000.
5. Narayana C.L., and Srilatha, K. R., "**Analysis of aerostat configurations by panel methods**", NAL PD CF 0010, Technical Report, National Aerospace Laboratories, Bangalore, India, July 2000.
6. Lutz, T., Schweyher, H., Wagner S., "**Shape Optimization of Axi-symmetric Bodies inIncompressible Flow**", Journal of Aircraft, Vol. 20, Feb. 1985, pp. 520–526.
7. Rao, G. N. V., "**Note on Optimization of the body of tethered aerostat airship**", Unpublished paper, Indian Institute of Science Bangalore, 2006.
8. Cheeseman, I., "**Chapter 3: Aerodynamics**," Airship Technology, Vol. 2, Khoury G. A., ed., Cambridge Aerospace Series 10, ISBN978-1-107-01970-6, Cambridge University Press, New York, 2012, pp. 25–58.
9. Joshi, R, Raina, A. A, and Pant, R.S., **Conceptual Design of an Airship using Knowledge Based Engineering**, AIAA-2009-2861, Proceedings of 18th AIAA Lighter-Than-Air Systems Technology Conference, Seattle, Washington, USA, 4th–7th May 2009.
10. Thiele, J.R. "**Patterning Techniques for Inflatable LTA Vehicle**", AIAA, proceedings of 16th Fluid and Plasma Dynamics Conference, Danvers, MA, USA, July 12–14, 1983.
11. Gawale, A. C., Raina, A. A., Pant, R. S., and Jahagirdar, Y. P., "*Design, Fabrication and Operation of Remotely Controlled Airships in India*" AIAA-2008-8853, Proceedings of 26th Congress of ICAS and 8th AIAA ATIO, Anchorage, Alaska, Sep. 14–19, 2008.
12. Kshirsagar, A., and Sharma V., and Pant, R. S., **Design and Development of a Semi Rigid Remotely Controlled Airship**, Proceedings of the 10th International Convention of Airship Association, 17–19 April 2015, Friedrichshafen, Germany.
13. Loharkar, S. A., Kshirsagar, A., and Pant, R. S., **Design and Fabrication of a Portable Semi-Rigid Airship**, Proceedings of 29th National Convention of Aerospace Engineers, November 27 and 28, 2015, Chennai, India.
14. Website of YINYAN Model Tech MFT, online store for purchase of Brand EMAX Motors, http://www.emaxmotors.com, last accessed on 13th January 2015.

Experimental and Simulation Study of Modified Acoustic Horn Design for Sonic Soot Cleaning

Deshmukh N. Nilaj and Arti Vishwanath

Abstract Ash deposits and dust particles are formed inside process equipments like boilers and electrostatic precipitators; and in material handling equipments like hoppers and silos during its operation. These deposits hinder the working of the equipment, gradually reducing its efficiency. So, removal of these deposits at regular intervals is necessary for smooth operation of the equipments. Sonic soot cleaning is a method which uses sound waves to dislodge the deposits. It employs an acoustic horn which is the source to produce sound and is designed such that it produces a frequency of sound that matches with the natural frequency of the particles to be cleaned. In this study, modified geometries of an acoustic horn are designed and fabricated so that the desired sound pressure level (SPL) and frequencies are obtained for effective cleaning. The frequency can be reduced by increasing the horn length. The increase in length however causes installation problems, due to space constraint. To overcome this problem, numbers of bends are introduced to increase the overall length of the horn. Using these modified designs, frequency and sound pressure level are obtained experimentally as well as by conducting simulations for all cases, and results obtained from both are compared. It is seen that for the case where horn is attached to 6, 8, and 10 number of bends; frequency obtained fell in the range of desired frequency. The percentage of error obtained after comparison is found to be within acceptable limits.

Keywords Sonic soot cleaning · Acoustic horn · Frequency · Sound pressure level

D.N. Nilaj
Mechanical Engineering Department, Fr. C. Rodrigues Institute of Technology,
Vashi, Navi Mumbai, India

A. Vishwanath (✉)
Mechanical Engineering Department, Datta Meghe College of Engineering,
Airoli, Navi Mumbai, India
e-mail: arti.2905@gmail.com

1   Introduction

Industrial process equipments are delivered clean with no soot, slag, and/or scale. Based on different mechanisms of formation of ash deposits [1] on the heat transfer surface, two general types of ash deposition have been defined namely slagging and fouling. If the deposits are soft, loose, and slimy it is called as slag or sludge. If the deposits are hard and adhering to the inner walls of surface it is called as fouling or scale. After a while, ash deposits in the form of scales are formed on the inner surfaces of the equipment during its operation. If at regular intervals, these deposits are not cleaned, it will eventually decrease the efficiency of the equipment. Many techniques exist and are used to clean the surface of process equipments [2], viz., internal cleaning, acid cleaning, mechanical cleaning, and steam soot blowing. However, these methods had their own limitations mostly of shutting down of the equipment resulting in increased system downtime during cleaning and corrosion problems which led to the invention of sonic soot cleaning. Sonic soot cleaning is a method applied to remove the ash and/or fossil deposits by the use of sound waves and its energy.

2   Sonic Soot Cleaning

Sonic soot cleaning is a technique which employs compressed air operated blowers. The blowers are designed in such a way that it will produce sound waves at a frequency that matches with the natural frequency of the particles to be cleaned and when the sound waves strike the particles, due to resonance, it vibrates and falls off the surface. Buhl [3] concluded that the most correct physical explanation of how acoustic waves dislodge the dust was that gas movement influences the particles due to friction at the surface and thus removes them.

2.1   Advantages and Applications of Sonic Cleaning

Sonic soot cleaning has many benefits [4], i.e., improved efficiency of equipments [5], less energy dissipation, reaches everywhere of the surface due to reflection and diffraction of sound waves. Also, as air is used no surface corrosion problem arises. It is better from economic point of view as it requires less maintenance and operational cost. Sonic soot cleaning finds many proven applications, i.e., in boilers, boiler tubes, heat exchanger surfaces, bag house fabric filters, electrostatic precipitators [6], hoppers, silos, evaporative gas cooling systems, and spray dryers.

Fig. 1 Acoustic horn

2.2 Construction and Operation of Acoustic Horn

An acoustic cleaner consists of two main components, a compression driver and a horn as seen in Fig. 1 [7]. The horn is a component with its gradual change in cross-sectional area from throat to mouth that increases the efficiency of sound radiation by matching the acoustic load driven at the horn throat. The narrow part of the horn next to the driver is called as the throat. The larger part at the other end is called as the mouth. Horn flares are used to control the spatial distribution of sound radiating from the horn mouth. An approximate equation can be used to estimate the performance characteristics of horns, provided the function that governs the change in cross-sectional area is simple.

From the pressurized air input, compressed air enters the horn and sets the metallic diaphragm into mechanical motion. The movement of the diaphragm produces vibrations resulting in pressure fluctuations. As these pressure fluctuations travel through the horn, sound waves are generated.

3 Design of Modified Horn Geometry

Seiffert [8] studied samples of dust collected from different power plants and boilers. He found that the dust samples collected showed similar characteristics. The size of deposits [3] on an average was found to be 50 microns across their largest dimension. Our basic aim is to obtain desired SPL at a lesser frequency for effective cleaning. From literature survey, it is concluded that the natural frequency of the dust particles lies in the range of 50–450 Hz. The desired SPL required [9] for efficient cleaning is 140–150 dB. In order to obtain such less frequency, it is necessary that the length of acoustic cleaner should be increased. It is also seen that

the overall length [10] of acoustic cleaner lies in the range of 0.4–2 m. To avoid space restrictions within process equipments, the overall length of horn can be distributed in form of bends [11]. For this study, six cases are considered for carrying out simulation and experimentation, that is, plain horn and horn attached to 2, 4, 6, 8, and 10 numbers of bends.

Figure 2a–e shows horn attached to 2, 4, 6, 8, and 10 numbers of bends. The plain horn is of length 150 mm to which bends are attached. The mouth diameter of the horn is 50 mm and the throat diameter is 10 mm. The bends that are attached
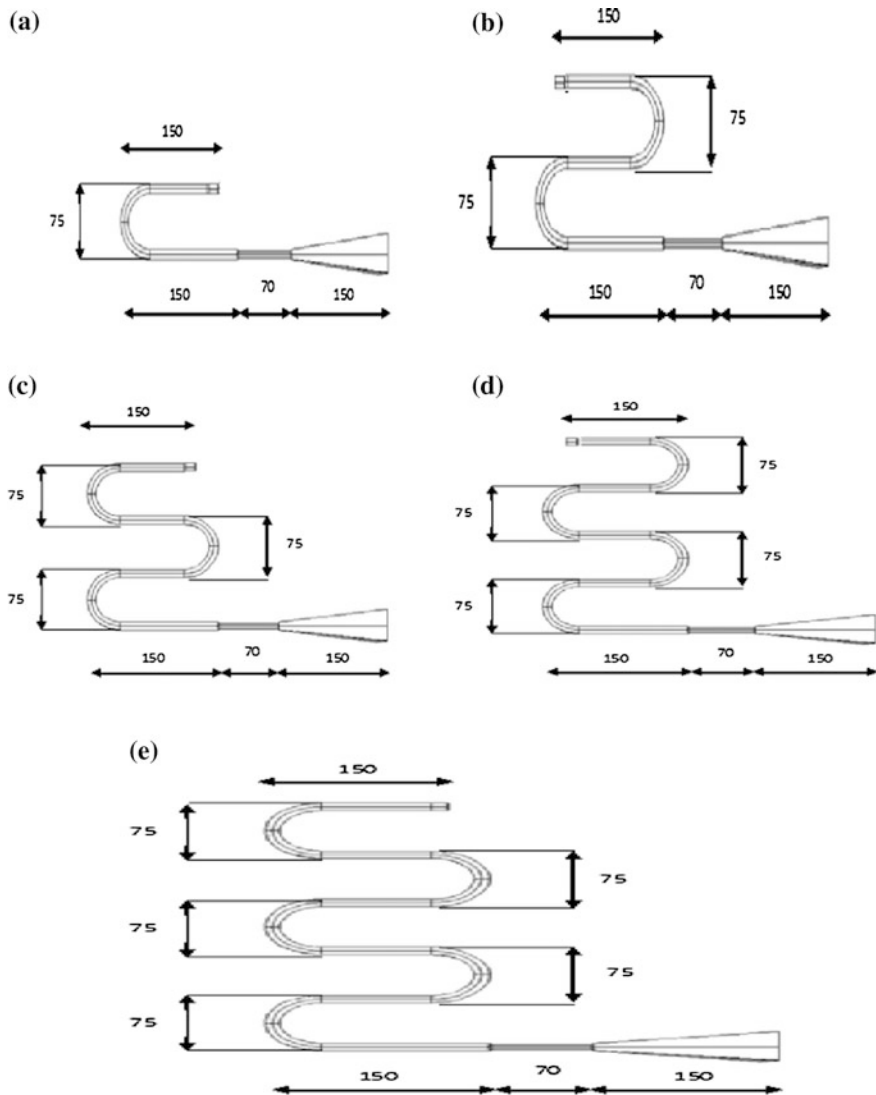
Fig. 2 Dimensions of horn attached to **a** 2 **b** 4 **c** 6 **d** 8, and **e** 10 bends

Table 1 Overall length of different geometries of acoustic horn

No. of bends	Overall length of horn (mm)
0	150
2	595
4	820
6	1045
8	1270
10	1495

are of the same diameter as that of the throat diameter of the horn. When compressed air passes through the horn; at bends, air gets further compressed [12] resulting in greater SPL. However due to greater length of travel, SPL gets reduced. So, just before entering the flaring part of the horn the throat diameter is reduced to 7 mm. This results in further compression of air resulting in higher SPL at the outlet of the horn. Table 1 shows the overall length of the modified horn geometry considered for all the cases.

4 Simulation Study

Simulation study of acoustic horn [13] is used to find out the amount of sound pressure level generated at a particular distance from the source of sound wave generation. Also frequency spectra are obtained for all cases. Simulation is carried out using COMSOL Multiphysics software version 4.3. Simulation was carried out for plain horn and for horn attached to 2, 4, 6, 8, and 10 numbers of bends.

Simulation of an acoustic horn requires the completion of following steps:

1. Modeling horn geometry
2. Meshing the geometry
3. Assigning boundary conditions
4. Studying results

4.1 Modeling Horn Geometry

Horn geometry in 3D is created for all cases exactly according to the dimensions. Sound generated from a point source propagates in a spherical wave pattern. Also, acoustic soot blowers are generally installed at a distance of 1 m from the target area. Hence, a spherical domain of 1 m is created in front of the outlet of horn. An additional perfectly matched layer of 0.01 m is created as an extended part of the spherical domain. It is an artificial absorbing layer for wave equations commonly used to truncate computational regions in numerical methods to simulate problems with open boundaries.
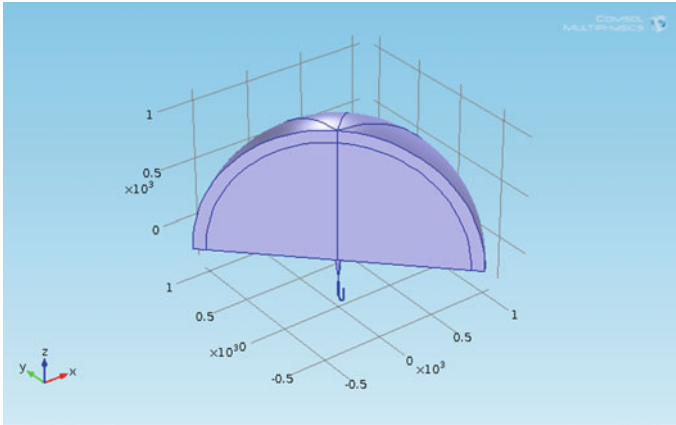
Fig. 3 Model of horn attached to 2 bends

Figure 3 shows 3D model of the horn attached to 2 bends.

4.2 Meshing

Meshing is a very important step while performing simulation. In order to analyze fluid flows, flow domains are split into smaller sub-domains made up of geometric primitives like hexahedral and tetrahedral in 3D and quadrilaterals and triangles in 2D. The governing equations are then discretized and solved inside each of these sub-domains. The element selected for this simulation is free tetrahedral element. From COMSOL's mesh tool, extra fine mesh is selected.

4.3 Assigning Boundary Conditions

At the diaphragm of the horn, spherical wave radiation is assigned. When compressed air is sent through the pressurized air input of the horn, it sets the diaphragm present inside to vibration [14]. The vibration of the diaphragm results in generation of sound waves. In COMSOL, we need to give the inward acceleration of the air particles due to the deflection of the diaphragm as an input.

Acceleration of the diaphragm is calculated as,

$$a = f_n^2 \times y_0 \tag{1}$$

where,
f_n Natural frequency of the diaphragm in Hz.
y_0 Deflection of diaphragm in m.

Table 2 Inward acceleration values of air particles at different pressures	Input air pressure (bar)	Inward acceleration (m/s^2)
	1	4605
	1.5	6909
	2	9210

Natural frequency of the diaphragm is calculated as,

$$f_n = \left(\frac{1}{2\pi}\right) \times \sqrt{\left(\frac{k}{m}\right)} \tag{2}$$

where, k = Stiffness of the diaphragm in N/m.
  m = mass of the diaphragm in kg.
  Stiffness of the diaphragm is calculated as,

$$k = P \times \pi \times R^2 / y_0 \tag{3}$$

where, P = Input air pressure in N/m^2.
  R = Radius of the diaphragm in m.
  Mass of the diaphragm is calculated as,

$$m = \rho \times \pi \times R^2 \times t \tag{4}$$

where, ρ = Density of the diaphragm in kg/m^3.
  t = thickness of the diaphragm in m.
  Deflection of the diaphragm is calculated as,

$$y_0 = \left(\frac{3}{16}\right) \times \frac{P(1 - \vartheta^2)}{E \times t^3} \times R^4 \tag{5}$$

where, E = Young's Modulus of diaphragm in N/m^2
  ϑ = Poisson's Ratio of the diaphragm
  The values of ϑ, E, ρ, t, and R for the diaphragm are given by the manufacturer of horn. Table 2 shows the value of inward acceleration of air particles at different compressed air pressures considered.

4.4 Studying Results

- Simulation results of horn attached to 2 bends at 1 bar

Figure 4 shows the distribution of sound pressure level over the entire domain for horn attached to 2 bends and compressed air pressure is 1 bar.
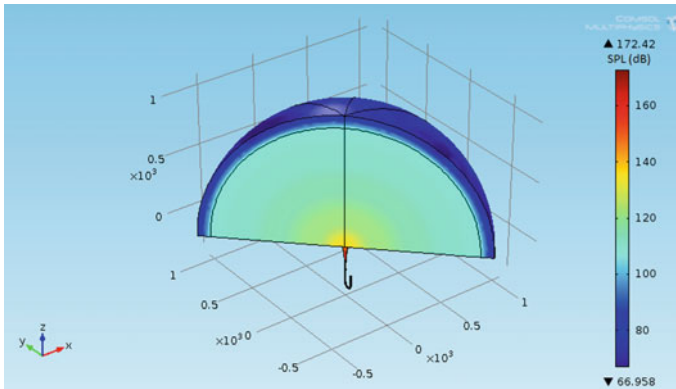
Fig. 4 Distribution of SPL over the domain for horn attached to 2 bends
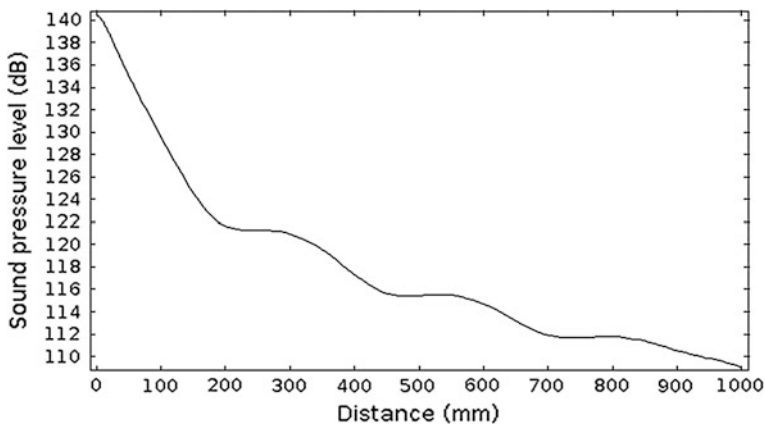
Fig. 5 SPL versus variation of SPL with distance for horn attached to 2 bends

Figure 5 shows that at a distance of 1 m from mouth of the horn, SPL obtained is 108.76 dB.

Figure 6 shows frequency spectra for horn attached to 2 bends and at 1 bar. The first peak indicates the fundamental frequency resulting from the horn. The frequency obtained is 729.17 Hz.

Similarly results are obtained for plain horn and horn attached to 4, 6, 8, and 10 numbers of bends. It is seen that as the length increases, frequency and sound pressure level gradually reduces.
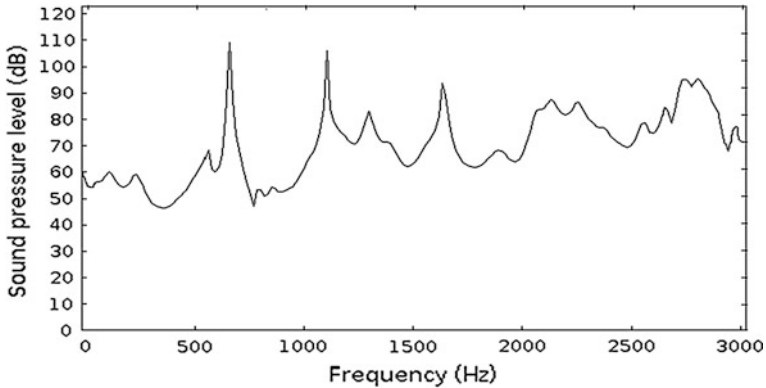
Fig. 6 Frequency spectra for horn attached to 2 bends

5   Experimental Study

Experiments are to be carried out to find the SPL versus frequency of modified design of acoustic horn. SPL is obtained at a distance of 1 m from the outlet of the horn, as, acoustic soot blowers are generally mounted at the mentioned distance from the target area which is to be cleaned. Experiments are carried out in open environment.

5.1   Experimental Setup

Experimental setup consists of following parts:

1. Single-stage reciprocating air compressor.
2. A bourdon pressure gauge.
3. Acoustic horn of desired geometries.
4. A transducer–Microphone.
5. FFT analyzer.

Figure 7 shows the line diagram of the experimental setup. The compressor used is a single-stage air-cooled reciprocating compressor. Bourdon-type pressure gauge is used. Six cases of horn geometry are considered, i.e., plain horn and horn attached to 2, 4 6, 8, and 10 numbers of bend. Microphone [15] acts as a transducer which converts sound waves into an analog signal. Microphone used is of Bruel–Kjaer make having frequency range of 20 Hz–20 kHz and a dynamic range of 16.5–134 dB. Acoustical signal like sound waves are continuous, i.e., they have a defined value for every possible instant of time. The sound pressure to be analyzed requires converting the signal into a stream of digital samples, with each sample representing a numeric value, i.e., proportional to the measured signal at a

Fig. 7 Line diagram of experimental setup
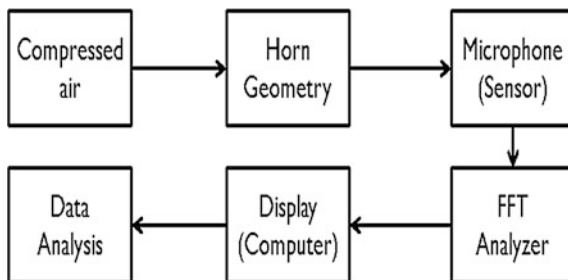
specific instant of time. This process of converting an analog signal into a digital signal is called as sampling which is done using FFT analyzer [27]. The FFT (Fast Fourier Transform) is an algorithm which resolves a time waveform into its sinusoidal components. The FFT takes a block of time-domain data and returns the frequency spectrum of the data. Thus, the FFT does not yield a continuous spectrum, but returns a discrete spectrum in which frequency content of waveform is resolved into a finite number of frequency lines. The sampled time waveform input to FFT determines the computed spectrum. If a signal is sampled at a rate equal to 'f_s' over an acquisition time 'T', 'N' number of samples are acquired.

FFT spectrum computed from the sampled signal has a frequency resolution dF, which is given by,

$$\mathrm{d}F = f_s/N \tag{5}$$

For carrying out experiments, value of fs chosen is 6400 Hz and N considered is 400. Hence, dF = 16.

Figure 8a shows horn which is mounted on a stand. Outlet of the horn is seen, through which sound waves are emitted. Figure 8b, c shows horn attached to 2 and 4 numbers of bends, respectively. Figure 8d shows microphone mounted on a stand.

5.2 Experimental Procedure

Figure 9 shows the photograph of the experimental setup to obtain SPL and frequency for horn attached to 2 bends. Compressed air is sent through inlet of the horn at 1, 1.5, and 2 bar. Microphone is placed at a distance of 1 m from the outlet of the horn. Microphone is connected to the dynamic signal analyzer, at channel a1, which in turn is connected to the laptop consisting of RT photon plus software. Measurement settings are made in the software which constitutes of setting all units as per SI system, setting of dF value, choosing channel a1, selecting time capture, FFT, power spectra, octave spectra, and RMS. Frequency spectra is obtained for all cases.
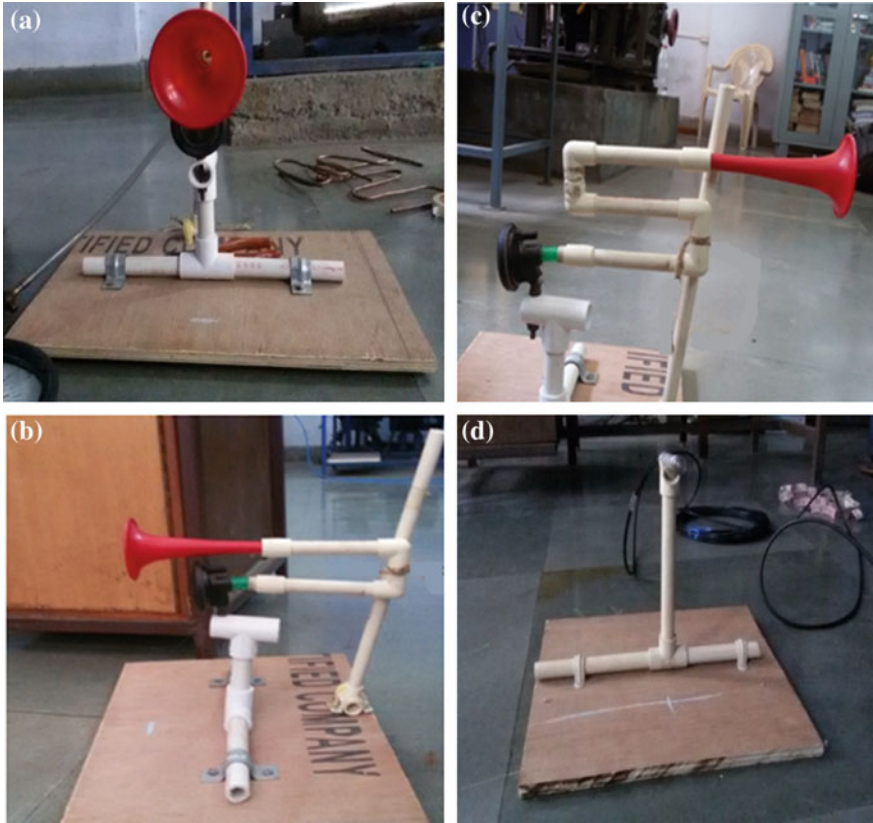
Fig. 8 **a** Horn mounted on a stand. **b** Horn attached to 2 bends. **c** Horn attached to 4 bends. **d** Microphone mounted on a stand

Fig. 9 Experimental setup

5.3   Experimental Results

Figure 10a shows a plot of frequency spectra obtained for plain horn at 1, 1.5, and 2 bar. At 1, 1.5, and 2 bar, peak SPL obtained is 111.48, 114.87, and 117.42 dB, respectively. Frequency obtained is 720 Hz at all pressures.

Figure 10b shows a plot of frequency spectra for horn attached to 2 bends at 1, 1.5, and 2 bar. At 1, 1.5, and 2 bar, peak SPL obtained is 110.17, 112.80, and 115.85 dB, respectively. Frequency obtained is 688 Hz at all pressures.

Figure 10c shows a plot of frequency spectra for horn attached to 4 bends at 1, 1.5, and 2 bar. At 1, 1.5, and 2 bar, peak SPL obtained is 107.34, 109.68, and 112.38 dB, respectively. Frequency obtained is 592 Hz at all pressures.

Figure 10d shows a plot of frequency spectra for horn attached to 6 bends at 1, 1.5, and 2 bar. At 1, 1.5, and 2 bar, peak SPL obtained is 105.68, 107.89, and 110.39 dB, respectively. Frequency obtained is 480 Hz at all pressures.

Figure 10e shows a plot of frequency spectra for horn attached to 8 bends at 1, 1.5, and 2 bar. At 1, 1.5, and 2 bar, peak SPL obtained is 103.46, 106.12, and 108.27 dB, respectively. Frequency obtained is 320 Hz at all pressures.
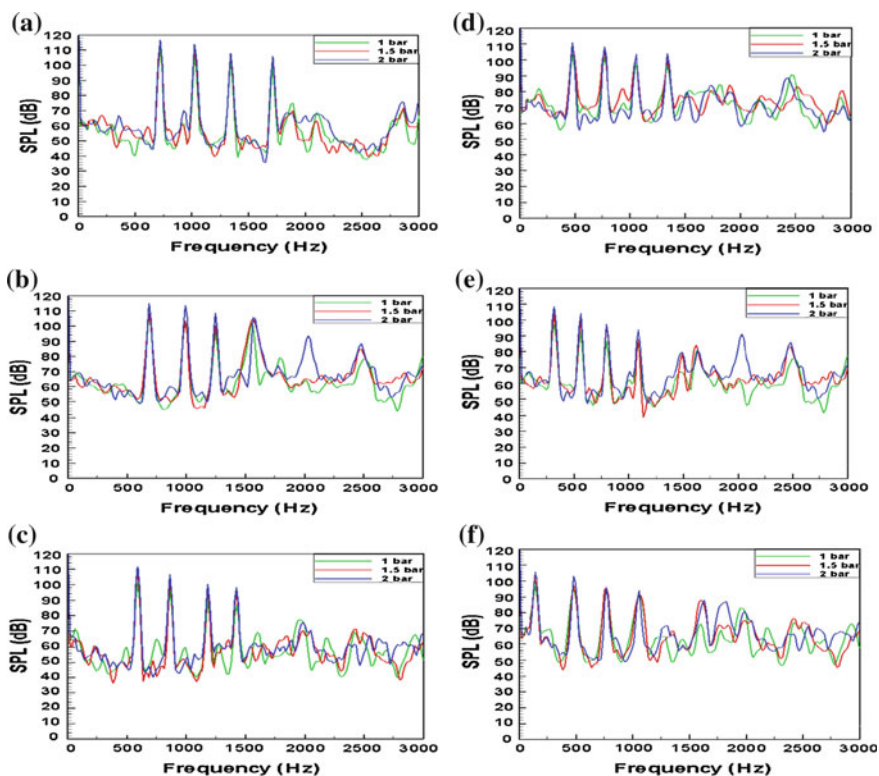
Fig. 10   Frequency spectra for horn attached to **a** 0 **b** 2 **c** 4 **d** 6 **e** 8 **f** 10 bends at different pressures

Figure 10f shows a plot of frequency spectra for horn attached to 10 bends at 1, 1.5, and 2 bar. At 1, 1.5, and 2 bar, peak SPL obtained is 100.33, 103.69 and 105.60 dB, respectively. Frequency obtained is 144 Hz at all pressures.

6 Comparison of Simulation and Experimental Results

Simulation and experimental results are obtained. The values of peak SPL and frequency obtained from simulation and experimental study are compared. Also, percentage reduction in frequency obtained from both simulation and experimentation is calculated.

6.1 Comparison of SPL Obtained From Simulation and Experimentation

Figure 11 shows SPL obtained at different pressures for horn attached to 0, 2, 4, 6, 8, and 10 number of bends obtained from simulation and experimentation. It shows variation of SPL with input compressed air pressure for all cases of horn geometry. It is seen that with increase in pressure, SPL increases. Also, percentage error in SPL is obtained by comparing simulation and experimental results. SPL obtained in experimentation is slightly more as compared to that obtained from simulation. The probable reason could be that while performing experiments background noise may add up to the actual SPL. Percentage error obtained is within acceptable limits.

6.2 Comparison of Frequency Obtained From Simulation and Experimentation

Figure 12 shows frequency at different lengths obtained from simulation and experimental results. It is seen that, frequency reduces as overall length of acoustic horn increases (Table 3).
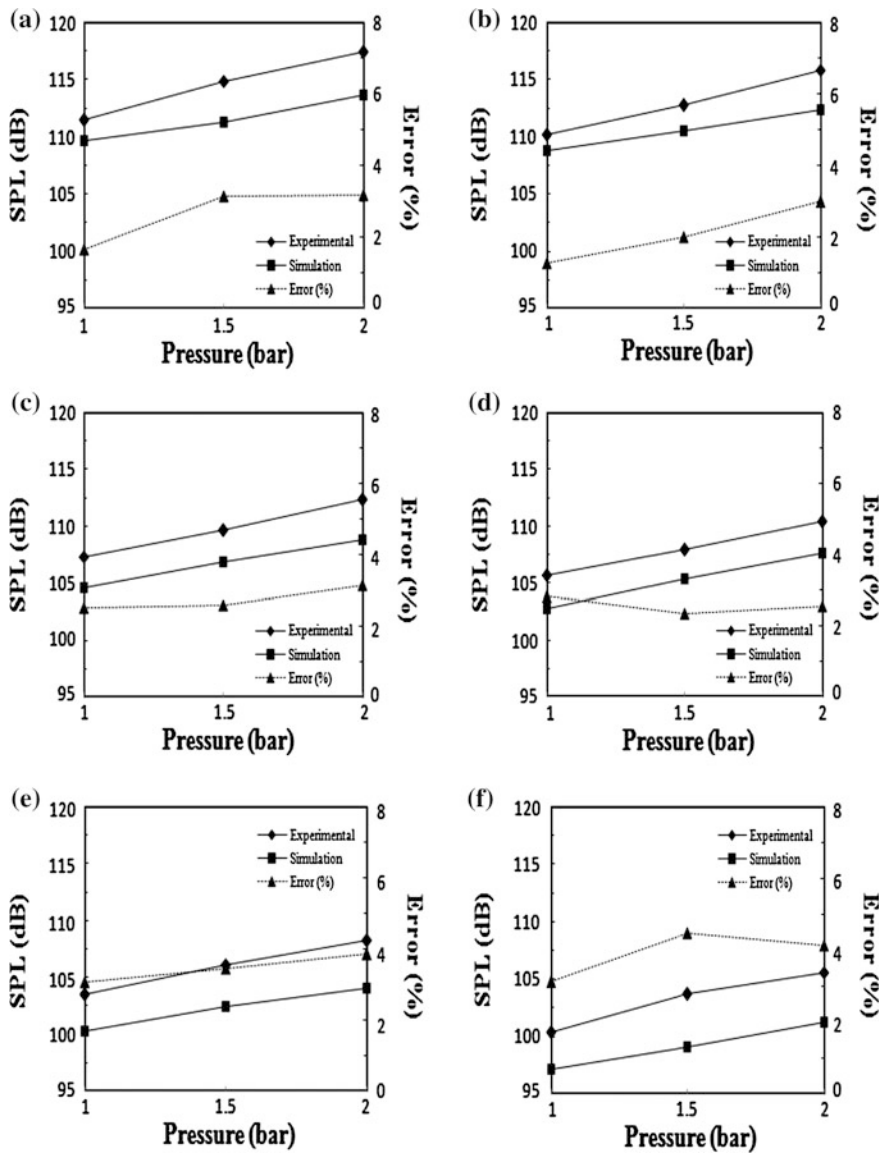
Fig. 11 SPL obtained at different pressures for horn attached to **a** 0 bend **b** 2 bends **c** 4 bends **d** 6 bends **e** 8 bends **f** 10 bends
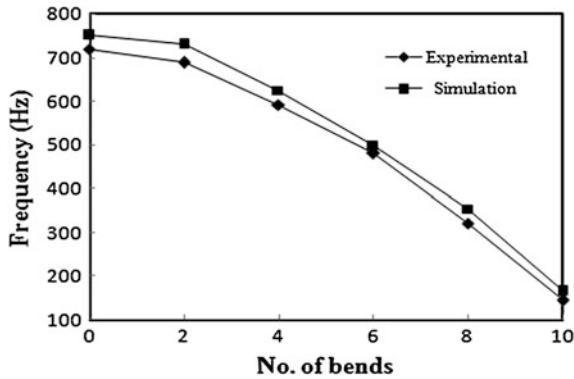
Fig. 12 Frequency obtained at different lengths

Table 3 Frequency obtained from experimentation and simulation

No. of bends	Experimental frequency (Hz)	Simulation frequency (Hz)	% error
0	720	750	−4.17
2	688	729.17	−5.98
4	592	625	−5.57
6	480	500	−4.17
8	320	354.17	−10.68
10	144	166.17	−15.40

6.3 Comparison of SPL With Increase in Length and at Different Pressures

Figure 13a–c shows variation of SPL at different lengths and at different pressures obtained from experimental and simulation study. It is seen that as length is increasing SPL is gradually reducing. As input air pressure increases, SPL increases.

6.4 Percentage Reduction in Frequency Obtained With Increase in Length

Figure 14a, b shows percentage reduction in frequency versus increase in the number of bends when compared with the frequency of plain horn. As length of the acoustic horn is increasing, frequency is reducing.

Fig. 13 SPL at different lengths at **a** 1 bar **b** 1.5 bar **c** 2 bar
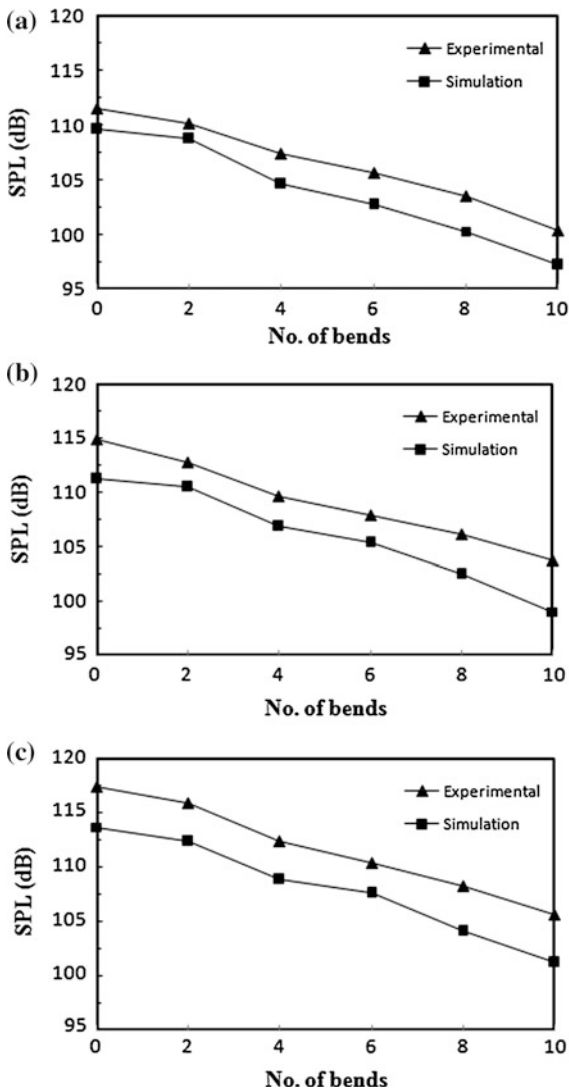
7 Conclusions

It is concluded from experimental and simulation study that, when the overall length of the acoustic horn is increased, the SPL and frequency both decreased. The sound pressure level increases with an increase in pressure. It is further observed that frequency is independent of pressure for the same length. The maximum percentage reduction obtained in frequency is about 80 % for horn attached to 10 bends when compared to plain horn. On comparing simulation and experimental

Fig. 14 Percentage reduction in frequency. **a** Simulation. **b** Experimental
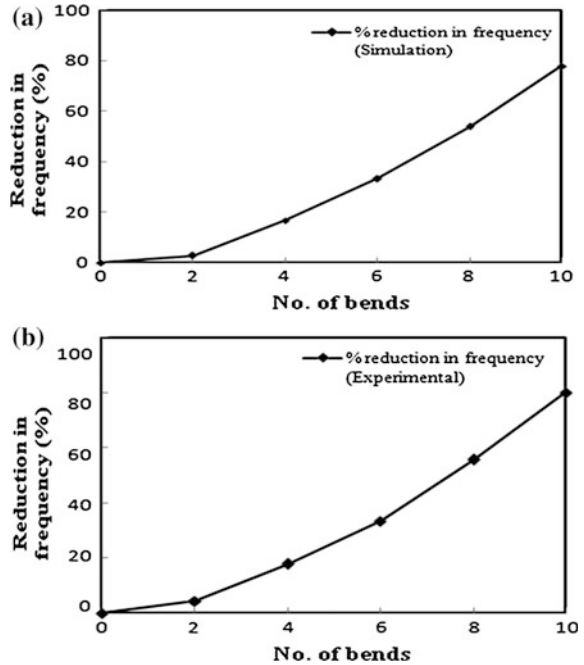
results, it is found that they are in good agreement and within acceptable limits. The frequency obtained in the cases of horn attached to 6, 8, and 10 number of bends, i.e., 480, 320, and 144 Hz, respectively, fall within the range of frequency of acoustic soot blowers. The desired SPL can be easily achieved by increasing the air pressure and this trend has been seen from the experimental and simulations results. This study has been carried out at lower pressure for human safety. Practically, in process equipments high sound pressure level can be used to increase sound pressure level.

References

1. R. Hatt, (1990), "*Understanding Boiler Slag*", Coal combustion. Inc, Versailles, pp 3.
2. H. Naganuma, (2013), "*Reduction mechanisms of ash deposition in coal and/or biomass combustion boilers*", Journal of fuel processing technology, Vol 106, pp 303–309.
3. L. Buhl, Steen Drue and Leif Lind, (1996), *"Field Testing of Acoustical Cleaning of Electrostatic Precipitators"*, ICESP VI Conference on Air Toxics Series, Budapest, Hungary, pp 18–21.
4. G. Yu, JIN BS, XIAO G, (2009), *"The Fouling Characteristics and Comparative Analysis of Cleaning Technology of SCR"*, 11th International Conference on Electrostatic Precipitation, Hangzhou, pp 624–626.
5. T. Jing, (2004), *"Applications of the Sonic Soot Cleaning Technique in Boilers"*, International conference on ultrasonics, ferrorelectrics conference, Beijing, pp 2211–2212.

6. W. Ronghui, Han Ke, Tan Ruitian, (2004) *"Acoustic Horn Made Electrostatic Precipitator Collecting Plate and Hopper Clean in Zhanjiakou Power Plant"*, International Conference on Electrostatic Precipitation, Lianoning zhongxin Automatic Instruments Co. Ltd, China, pp 1–6.
7. M. King, (2008), "*Horn physics"*, Section 5, pp 1–29.
8. G. Seiffert, Barry Gibbs, (2006), *"Removal of Charged Powder Deposits by High Intensity Low Frequency Sound: The Role of Inertial and Drag Forces"*, 13th International Conference on Sound and Vibration, Vienna, Austria, pp 2–6.
9. P. Mirek, (2013), *"Field testing of acoustic cleaning system working in 670 MW CFB boiler"*, Journal of chemical and process engineering, Vol. 34, No. 2, pp 283–291.
10. R. Hall, (1984), *"Sonic cleaning device and method"*, United States Patent Publication, Patent No. 44,61,651.
11. T. Zhang, (2012), *"Acoustic cleaning device with variable length to compensate application temperature"*, United States Patent Publication, Patent No. 01,45,182.
12. S. Dequand, (2003), *"Acoustics of 90 degree sharp bends"*, Journal of sound and Vibration, Vol. 89, pp 1025–1037.
13. E. Bangtsson, D. Noreland, (2002), *"Shape optimization of an acoustic horn"*, Comsol Multiphysics tutorial, acoustics module, pp 2002–2019.
14. I. Wygant, M. Kupnik, (2008), *"Analytically calculating membrane displacement of a circular CMUT cell"*, IEEE International Ultrasonics Symposium Proceedings, pp 2111–2114.
15. L. Beranek, (2012), "*Acoustics: Sound fields and transducers"*, Chaoter 9, Academic press, San Deigo, pp 407–448.
16. F. Alton, K. Pohlmann, *"Master handbook of acoustics"*, Fifth edition, Mc Graw Hill, pp 3–38.
17. V. A. Krasil'nikov, (1963), *"Sound and ultrasound waves in air, water and solid bodies"*, pp 26–27.
18. Hall, (1984), *"Sonic cleaning device and method"*, United States Patent Publication, Patent No. 44,61,651.
19. V. A. Krasil'nikov, (1963), *"Sound and ultrasound waves in air, water and solid bodies"*, pp 26–27.
20. R. Hatt, (1990), "*Understanding Boiler Slag"*, Coal combustion. Inc, Versailles, pp 3.

Fuzzy Logic Simulation for Brake-by-Wire Control System

Pajarla Saiteja and S. Jeyanthi

Abstract Brake-by-wire technology describes the replacement of conventional components such as the pumps, brake fluids, and vacuum servos and master cylinders with electronic control unit, sensors and actuators. This paper shows designing of an electromagnetic braking system which is controlled by fuzzy logic technique, here electromagnetic braking system is controlled by two input parameters, they applied brake pressure and load acting on a vehicle. These input components are connected to ECU. When the sensors sense the brake pressure and load it is given to controller. And controller undergoes fuzzification and finally it gives the required voltage of front and rear axle brakes. Mechanical braking system is efficient but it has some drawbacks such as mechanical components causing high vibrations, higher stopping distance, and brake fluid which cause corrosion and have effect on environment and occupy more space. All these drawbacks are overcome by brake-by-wire system.

Keywords Electromagnetic braking system · ECU · Fuzzy logic · LabVIEW software

1 Introduction

1.1 Brake-by-Wire

Brake-by-wire technology in automobile industry has the ability to regulate the brakes through electrical means. Brake-by-wire technology in automobile industry describes the replacement of conventional components such as the pumps, hoses, brake fluids, and master cylinders with electronic sensors and actuators [1]. Similarly, drive-by-wire technology came to automobile technology which displaces the conventional mechanical, hydraulic, and pneumatic control systems with elec-

P. Saiteja (✉) · S. Jeyanthi
VIT University, Chennai, India
e-mail: pajarla.saiteja@gmail.com

tronic control systems using electromechanical sensors and actuators, and here we are using human–machine interfaces, such as pedal and steering feel emulators [1].

Brake-by-wire technology was introduced by FIA in 2014 with some rules. FIA found a lot of speculations about its working, it describes what does it mean and why it is brought into formula 1 races [2]. Formula 1 technical people are making brake pedal simulation and controlling system for BBW. They are technically very good in working simulation and f1 drivers drive the hybrid car with BBW system; they feel it as a high-efficient hybrid braking system and are more comfortable working with it. After that so many owners came forward to install the hybrid braking system in their F1 cars. After one separate team started analyzing the control system day by day, they found new aspects in brake-by-wire [2].

1.2 Electromagnetic Brakes

An electromagnetic braking system is one of the high-efficient braking systems; generally it uses magnetic force to engage the brakes, but for the generation of magnetic force, it requires power and braking is transmitted by manually. Here in electromagnetic brakes disc is connected to a rotating shaft and the electromagnet is mounted on the brake frame. When we applied electricity to the copper coils, it develops a magnetic field across the armature, this magnetic field occurs because of the supplying current across the coil and causes the armature winding to get attracted toward the coil [3]. And by this process high torque develops, because of this negative torque (opposite direction) the vehicle comes to rest position. This electromagnetic braking system is used for studying purpose [3].

The electromagnetic braking system works on the electric power and magnetic power and also on the principle of electromagnetism. These electromagnetic brakes are totally friction-less controlling system. Due to friction-less character, brakes are more durable and have longer life span and there is less maintenance in braking system. Due to the advantages of these brakes, BBW controlling system is an excellent replacement for convectional braking system.We can reduce the ware and tear problem of brakes by EMB system. In these brakes, we would not get any heat loss [4]. This electromagnetic braking system is much effective than conventional braking system and the time taken for applying of brakes is also very less. But here we need lubrication for reduction heat during braking. This electromagnetic braking system gives much better performance than conventional braking system with low cost, which is more important commercial element in today's need. There are also many advantages of electromagnetic brakes [4].

Today's automobile marketplace electromagnetic braking system is one of the greatest prevalent braking systems. This is more efficiently used in cars, and it is an effective braking system for heavy vehicles also. By consuming this electromagnetic braking system, we can raise the life of the whole braking system [4]. The

general working principle of this EMB system is that the magnetic flux will get generated in the opposite direction of the rotating wheel because of the eddy current flowing opposite to the rotating wheel direction in the coils. This eddy current tries to stop the rotating wheel of the vehicle.

1.3 Fuzzy Logic

The Fuzzy Logic concept was initiated in the year 1965 [5, 6, 7], by a computer science professor called A. Zadeh. He was working at the University of California in Berkeley. Basically, fuzzy logic (FL) has multivalued logic characteristics that allow to get intermediate values. Those values lie in between conventional evaluations like true/false, yes/no, high/low, etc. Everything in on way of programmed to the computers [5]. The fuzzy system is an advanced level replacement of conventional membership functions and this logic originated from ancient Greek philosophy. Generally the fuzzy logic system explains complex answers like humans. Normal systems give answers like true/false or any numbers as output. Here fuzzy logic gives answers for more complex questions also. For example conventional system we programmed like if the value is $2n + 1$ the output will be odd number and it's an $2n$ then output will be even if we are getting value as 0 it's not in both conditions it will think like human and gives the appropriate answer as even number like humans so it's called as fuzzy logic. In their exertions to devise a succinct theory of reason, and later mathematics, the so-called "Laws of Thought" were suggested [6]. One of these is the "Law of the Excluded Middle," that states every proposition must either be true or false.

The membership functions operate in the fuzzy set of membership function with value lying in between 0.0 and 1.0. For example, a membership value is 0.3 has a membership value of 0.5 to the set low coherence. It is a very important point which distinguishes between fuzzy logic and probability concept. Both operate over the same numeric range, and have like values: 0.0 representing False (or non-membership), and 1.0 on behalf of True. Though, there is a division to be complete between the two statements: First Statement is probabilistic tactic yields the natural language "There is a 50 % casual that g is low," while the fuzzy vocabulary agrees tog's degree of membership within the set of low interferometry coherence is 0.50." Second Statement is the semantic difference is the first view presumes that g is or is not low; it is just that we only have a 50 % chance of knowing which set it is in.

Fig. 1 Architecture of BBW
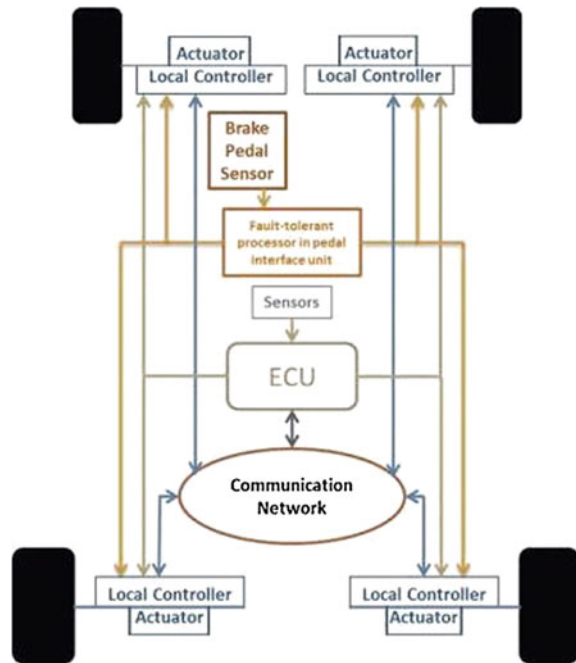
2 Architecture

This BBW control system contains electromagnetic actuators, brake pedal sensor, load sensing valve, ECU with fuzzy microcontroller, and communication networks (Fig. 1).

BBW control system works on the fuzzy logic technique. The fuzzy logic controller can give more precise output. Here load sensing valve and brake sensors are the inputs to the fuzzy logic and finally it will give voltage for electromagnetic brakes for front and rear axle. By this fuzzification technique, we are getting different voltage values for different load conditions.

3 Mathematical Calculations

Mathematical calculation for mechanical braking torque

Torque $\tau = F \times \mu \times R$

F = Force acting on wheel

μ = coefficient of friction

R = Radius of the wheel

Fig. 2 Reaction force diagram
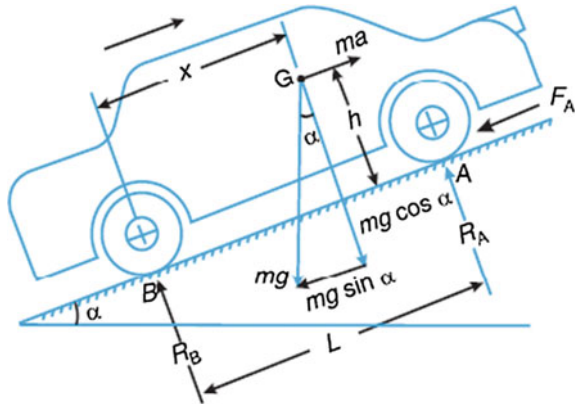
Reaction forces at front and rear wheels:

This is the most common way of applying brake on the vehicle, in which braking force acts on both rear and front wheels (Fig. 2).

Let F_A = Braking force provided by the front wheels = $\mu \times R_A$. F_B = Braking force provided by the rear wheels = $\mu \times R_B$.

$$R_A = m \cdot g \cos \alpha \left(\frac{\mu h + x}{L}\right) \quad R_B = m \cdot g \cos \alpha \left(\frac{L - \mu h - x}{L}\right)$$

R_A = Reaction force at front wheels

R_B = Reaction force at rear wheels

If vehicle moving on plain surface ($\alpha = 0$):

$$R_A = m \cdot g \left(\frac{\mu h + x}{L}\right) \quad R_B = m \cdot g \left(\frac{L - \mu h - x}{L}\right)$$

Let's apply the same phenomena to heavy vehicle. Contemplate Ashok Leyland 222″ vehicle.

See Fig. 3.

Overall Length OL = 10,859 mm

Rear Overhead ROH = 3308 mm

Front Overhead FOH = 1912 mm

Wheel Base WB = 5640 mm
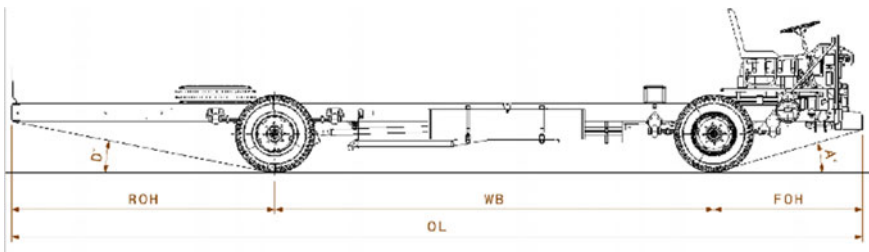
Fig. 3 Dimensions of Ashok Leyland 222″ vehicle

Braking Torque Calculation for 222″ Vehicle:

$R_A = m \cdot g \left(\frac{\mu h + x}{L}\right)$ $R_B = m \cdot g \left(\frac{L - \mu h - x}{L}\right)$

At maximum condition

Mass of the vehicle = 16,200 kg

RA = 10,700 N m; RB = 5499.35 N m

B.FA = 3745 N m; B.FB = 1924.77 N m

TA = 3745 × 0.50 = 1902 N m; TB = 1924.77 × 0.508 = 978 N m

Braking Torque (Bτ) for diff Load conditions:

See Tables 1 and 2.

Here the max braking torque is divided into five conditions, as brake pressure. Let us consider an example, at max load condition 16,200 kg required front axle braking torque is 978 N m and rear axle braking torque is 1902 N m. This is the max torque to stop the vehicle. In practical applications, we do not want maximum braking torque for all braking conditions sometimes, we need to reduce the speed and sometimes we need to stop the vehicle that is why I divided the max torque into different brake pressure conditions.

Applying the Mechanical Braking Torque in Electromagnetic Braking Torque Calculations:

DC Motor Torque Equation

$V = Kv \times \omega \frac{\tau}{Kt} Ra$

V = Voltage Supply

ω = Angular Velocity

Kv = Back EMF Const

Kt = Torque Const

τ = Torque

Ra = Resistance across the circuit

Table 1 Bτ at max load

Load	Brake Pr	Front	Rear
16,200	2	586	1141
	3	684	1331
	4	782	1521
	5	880	1711
	6	978	1902

Table 2 Bτ at min load

Load	Brake Pr	Front	Rear
6000	2	218	423
	3	254	493
	4	290	564
	5	327	635
	6	363	705

Table 3 Front and rear EMB voltages at different loads

Load	Brake Pr	Front	Rear
16,200	2	1981	3829
	3	2311	4467
	4	2642	5106
	5	2972	5744
	6	3302	6382
6000	2	751	1435
	3	876	1674
	4	1001	1913
	5	1126	2152
	6	1252	2392

See Table 3.

4 Applying Fuzzy Logic

See Table 4.
Step-1 Tabulation in fuzzy logic technique
Step-2 Forming Into Sub Iterations
Step-3 Forming into fuzzy sets
See Tables 5 and 6.

Table 4 Step 1 tabulation in fuzzy logic technique

	Front	Rear	Load	Brake Pr
Min	751	1435	6000	2
Max	3302	6382	16,200	6
Diff	2551	4947	10,200	4
Diff/2	1276	2474	5100	2
Min	751	1435	6000	2
	2027	3909	11,100	4
Max	3302	6382	16,200	6
Low	751.751.2027	1453.1453.3909	6000.6000.11100	2.2.4
Medium	751.2027.3302	1453.3909.6382	6000.11100.16200	2.4.6
High	2027.3302.3302	3909.6382.6382	11100.16200.16200	4.6.6

Table 5 Step 2 tabulation in fuzzy logic technique

Low low				Medium low				High low			
Load	Brake Pi	Front	Rear	Load	Brake Pr	Front	Rear	Load	Brake Pr	Front	Rear
16,200	2	1981	3829	16,200	2	1981	3829	11,500	2	1413	2701
	3	2311	4467		3	2311	4467		3	1648	3152
	4	2642	5106		4	2642	5106		4	1884	3602
15,500	2	1895	3655	15,500	2	1895	3665	11,000	2	1353	2608
	3	2211	4276		3	2211	4276		3	578	3043
	4	2527	4887		4	2527	4887		4	1804	3478
15,000	2	1787	3522	15,000	2	1787	3522	10,500	2	1293	2491
	3	2085	4109		3	2085	4109		3	1508	2905
	4	2383	4696		4	2383	4696		4	1724	3321
14,500	2	1704	3429	14,500	2	1704	3429	10,000	2	233	2347
	3	1988	4000		3	1988	4000		3	1438	2739
	4	2272	4572		4	2272	4572		4	1644	3130
14,000	2	1690	3288	14,000	2	1690	3288	9500	2	1173	2257
	3	1972	3836		3	1972	3836		3	1368	2633
	4	2254	4384		4	2254	4384		4	1564	3009
13,500	2	1628	3170	13,500	2	1628	3170	9000	2	1113	2139
	3	1899	3698		3	1899	3698		3	1298	2495
	4	2170	4226		4	2170	4226		4	1484	2852

Table 6 Step 3 tabulation in fuzzy logic technique

Condition	Axle			
Lowest low	Front	Low	Medium	High
	Rear	Low	Medium	High
Lowest medium	Front	Low	Medium	High
	Rear	Low	Medium	High
Lowest high	Front	Low	Medium	High
	Rear	Low	Medium	High
Medium low	Front	Low	Medium	High
	Rear	Low	Medium	High
Medium medium	Front	Low	Medium	High
	Rear	Low	Medium	High
Medium high	Front	Low	Medium	High
	Rear	Low	Medium	High
High low	Front	Medium	Medium	High
	Rear	Medium	Medium	High
High medium	Front	Low	Medium	High
	Rear	Medium	Medium	High
Highest high	Front	Low	Medium	High
	Rear	Medium	High	Low
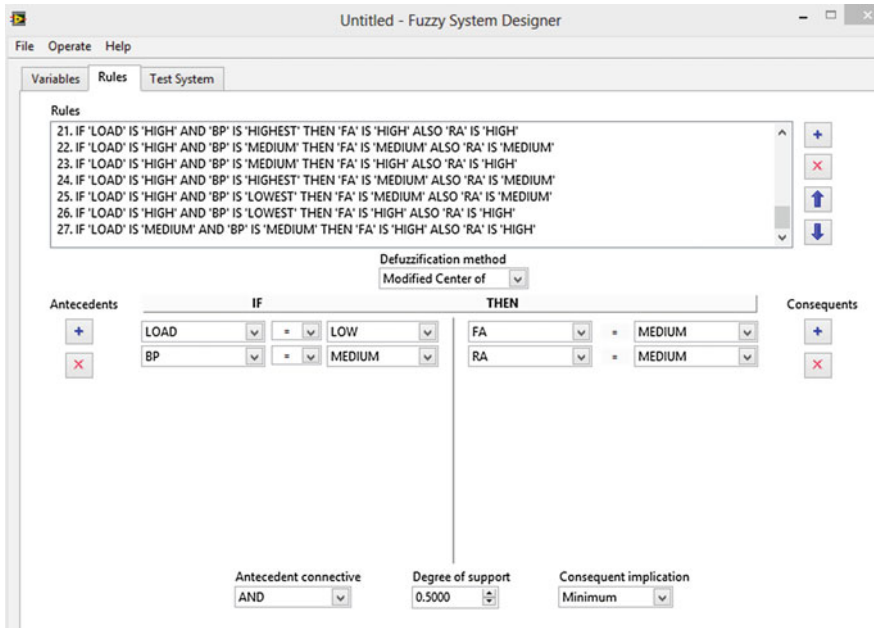
Fig. 4 Fuzzy rules in LabVIEW software

5 Forming of Fuzzy Rules in LabVIEW Software

See Fig. 4.

6 Input/Output Values for Triangular Membership Function in LabVIEW Software

See Fig. 5.

7 Output Verification

See Fig. 6.

Verification Practical values with LabVIEW Software Values (Fig. 7):
At load 12,250 and Bp 6 the Practical values are FA = 1912; RA = 3682.
LabVIEW Fuzzy Software Values are FA = 1912.75; RA = 3687.92.

Here practical values are very closer to the LabVIEW fuzzy simulation values.
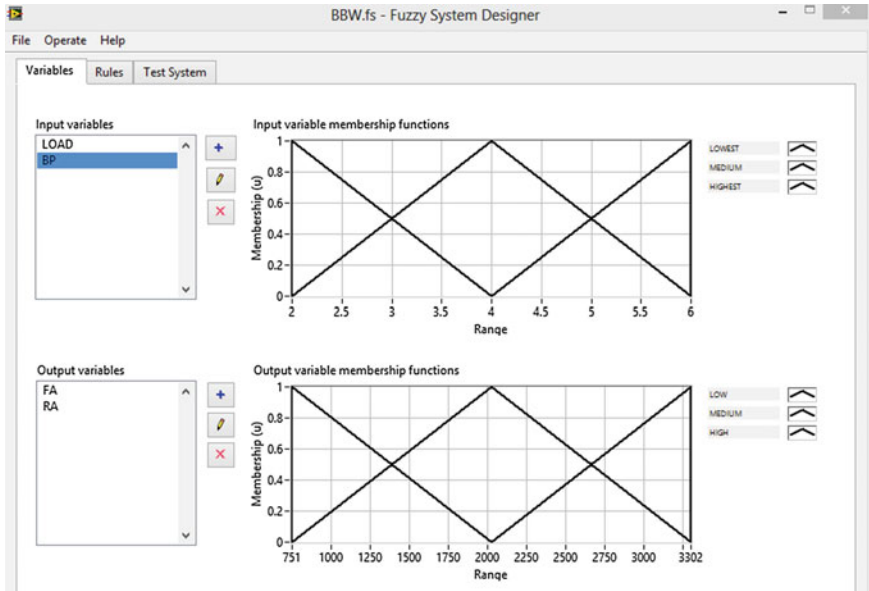
Fig. 5 Loading of input/output values in LabVIEW software
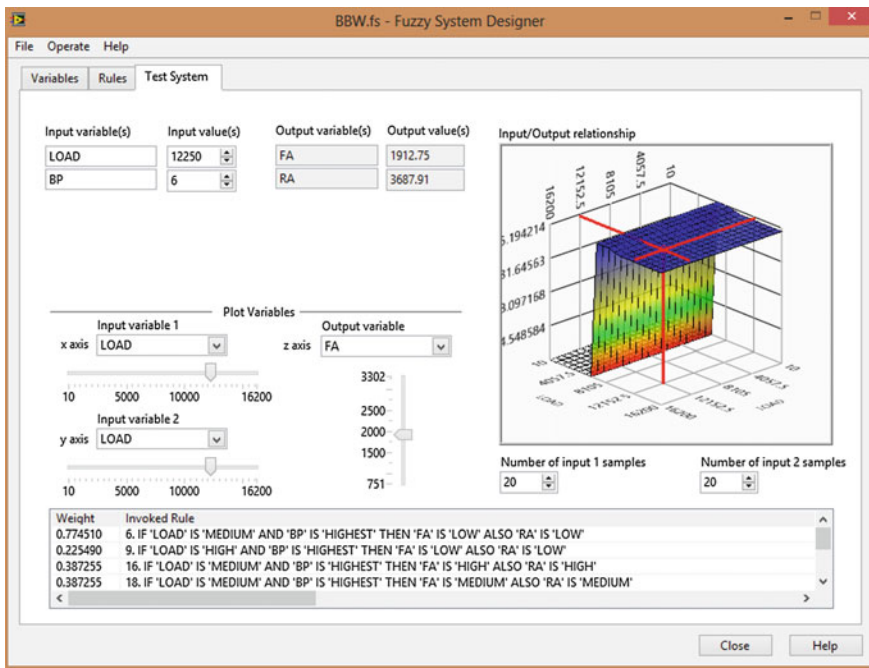
Fig. 6 Output verification at load 12,250 and Bp 6
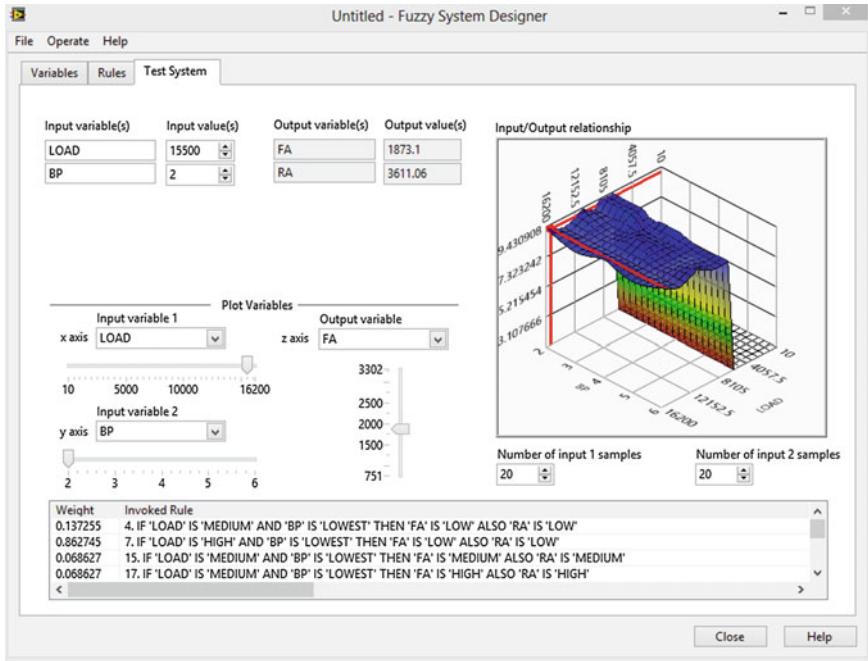
Fig. 7 Output verification at load 15,500 and Bp 2

By this result, we can say fuzzy logic simulation for brake-by-wire control system is successfully verified.

Verification Practical values with LabVIEW Software Values:
At Load = 15,500 and Bp = 2 the Practical Values are FA = 1895; RA = 3665. LabVIEW Software Values are FA = 1873; RA = 3611.06.

Here practical values are very closer to the LabVIEW fuzzy simulation values. By this result, we can say fuzzy logic simulation for brake-by-wire control system is successfully verified.

8 Conclusion

Brake-by-wire technology in automotive industry represents the replacement of traditional components such as the pumps, hoses, fluids, and vacuum servos, and master cylinders with electronic sensors and actuators. There are many brake control techniques, in which electromagnetic braking system is one of the best braking systems. There are many advantages compared to disc and drum brakes. EMB is less complex, requires less maintenance, and it can give more accurate

precise output and high braking torque and also can archive. For getting accurate output for different input values, we applied fuzzy logic to the controller. Here we applied Triangular membership function for making easier operation. Here we have given brake pedal sensor and load sensing valve as the inputs to the triangular membership functions. Outputs are front and rear axle electromagnetic brake voltage. Fuzzy logic is applied for getting precise output for different load conditions.

References

1. R. Schwar, R. Iserman, J. Bohm, J. Nell and P.Rieth, "Modeling and Control of an Electromechanical Disk Brake", SAE Paper 980600, 1998.
2. Youngsong Lee and Woon-Sung Lee, "Hardware-in-the-loop Simulation for Electro-mechanical Brake", SICE-ICASE International Joint Conference 2006.
3. Jeong-Woo Jeon, Gui-Aee Woo, Ki-Chang Lee, Don-Ha Hwang and Yong-Joo Kim, "Real-Time Test of Aircraft Brake-By-Wire System with HILS & Dynamometer System".
4. Tanner J. A., "Review of NASA Anti-skid Braking Research," NASA Langley Research Center, Virginia, SAE 821393, Oct. 1982.
5. R. Isermann, Fault-Diagnosis Systems: An Introduction from Fault Detection to Fault Tolerance: Springer Berlin Heidelberg, 2006.
6. P. E. Dumont, A. Aitouche, and M. Bayart, "Fault Detection of Actuator Faults for Electric Vehicle", in Control Applications, 2007. CCA 2007. IEEE International Conference on, 2007, pp. 1067–1072.
7. C. D. Gadda, S. M. Laws, and 1. C. Gerdes, "Generating Diagnostic Residuals for Steer-by-Wire Vehicles", Control Systems Technology, IEEE Transactions on, vol. 15, pp. 529–540, 2007.

Effect of Permeability
on the Rayleigh-Type Acoustic Streaming

Neetu Srivastava

Abstract A theory is developed for the boundary layer analysis of the passive methods to control the noise. The emphasis through the present treatment is on the materials where fluid and solid are of comparable densities for instance in case of water-saturated rocks. It is found that the flow may be described by two non-dimensional parameters and a characteristic frequency.

Keywords Porous media · Acoustic wave · Boundary layer

1 Introduction

Changing the environment for propagation of sound without losing the energy as well as less induction of noisy discomfort is the challenge faced by technologists. Our purpose is to investigate and establish a boundary layer theory of propagation of sound waves in a transport system composed of fluid saturated porous media. The propagation of sound wave through porous particles reduces the reflection of sound. Sound transmission through this type of structures has been studied by many researchers. Many industrial devices as well as air/surface transportation devices have a double-walled panel. The problem of sound transmitted through two identical plates is addressed by London [1] in which he compared the theoretical results with experimental measurements in a reverberant sound field. Propagation of sound through curved aircraft panels under the influence of over pressure at the concave side was studied by Liu [2]. Lee et al. [3] investigated and examined the sound transmission through single- and double-walled cylindrical shells by using the acoustic wave equations and Love's theory of thin shell vibration. Bolton et al. [4] built an analytical model to predict the sound transmission through flat doubled panels lined in the poroelastic media in the absence of any mean flow using Biot's

N. Srivastava (✉)
Department of Mathematics, Amrita School of Engineering, Bengaluru,
Amrita Vishwa Vidyapeetham, Amrita University, Bangalore, India
e-mail: s_neetu@blr.amrita.edu

model [5]. This model is used for the wave propagation in fluid saturated porous materials where the interaction of sound wave and viscosity was not considered.

The present study has incorporated this important physical effect on sound transmission. Here in this paper, we investigated the interaction of acoustic wave with a porous media in part A and derived an approximate solution to the acoustical wave problem through porous region in the vicinity of the wall in the part B. It is found that outside the boundary layer there is a steady flow whose velocity is independent of viscosity but depends on porosity. It has been shown that the Darcy number is zero then the solution is same as that of the solution of Landau and Lifschitz [6].

2 Formulation of the Problem

In this section, we mainly focus on the mathematical formulation of flow induced in the fluid due to an oscillatory motion of an acoustic wave with small amplitude. Velocity is small due to small oscillations, so in equation of motion the quadratic terms are neglected. Assuming that a sound wave in an ideal fluid is adiabatic, we assume that the pressure variation is related to the small change in density and is given by $p' = \left(\frac{\partial p}{\partial \rho_0}\right)_s \rho'$. Substituting this in the equation of continuity we can rewrite the equation as,

$$\frac{\partial p'}{\partial t} + \rho_0 \left(\frac{\partial p}{\partial \rho_0}\right)_s \operatorname{div} \vec{v} = 0, \tag{1}$$

1-D Standing Wave in a Planar Porous Channel:

Consider an acoustic wave in the fluid in which all quantities depend on only one coordinate 'x' and the flow is homogeneous in yz plane. Since the oscillations are small, so quadratic terms in the Euler equation can be neglected and reduced to,

$$\frac{\partial v_x}{\partial t} + \frac{\operatorname{grad} p'}{\rho_0} + \frac{v}{\kappa} v_x = 0 \tag{2}$$

where v_x and v_y are the velocity components in x and y direction. In order to express all the unknowns in the terms of one variable, let us introduce the velocity potential by $\bar{v} = \nabla \emptyset$. The Eq. (2) will take a form,

$$\nabla \left[\frac{\partial \emptyset}{\partial t} + \frac{v}{\kappa} \emptyset\right] = -\frac{\operatorname{grad} p'}{\rho_0} \tag{3}$$

Sound speed in air varies with pressure, density, temperature, humidity, wind speed, etc. The expression for the speed of sound in a fluid is given in terms of its thermodynamic properties. Defining wave velocity by $c = \sqrt{\left(\frac{\partial p}{\partial \rho_0}\right)_s}$ and substituting (3) in (2), the modified equation can be written as,

$$-\left[\frac{\partial^2 \emptyset}{\partial t^2} + \frac{v}{\kappa}\frac{\partial \emptyset}{\partial t}\right] + c^2 \frac{\partial^2 \emptyset}{\partial x^2} = 0, \tag{4}$$

Substituting $\emptyset(x,t) = F(x)e^{-i\omega t}$ in (4) and introducing the dimensionless number Ro is the Roshko number and σ is a Darcy Number, the solution for $F(x)$ will be written as,

$$F(x) = c_1 \cos Ax + c_2 \sin Ax, \quad A = \frac{\omega}{c}\sqrt{\left[1 + i\left(\frac{\sigma^2}{Ro}\right)\right]}. \tag{5}$$

The constants in the solution can be evaluated from the conditions,

$$x \to 0, \quad v = v_0 \text{ (finite value)}, \tag{6}$$

As x approaches to infinite then velocity should be finite. Hence the solution is

$$U = Re(v_0 \cos \omega t \cos Ax) \tag{7}$$

where $A = \frac{\omega}{c}\sqrt{\left[1 + i\left(\frac{\sigma^2}{Ro}\right)\right]}$. For an infinite permeability $A = \frac{\omega}{c} = k$ and the solution (7) will reduce to Landau Lifschitz solution. The required velocity v in the boundary layer and can be expressed in the terms of stream function $\psi(x,y,t)$ by,

$$v_x = \frac{\partial \psi}{\partial y} \quad \text{and} \quad v_y = -\frac{\partial \psi}{\partial x} \tag{8}$$

3 Acoustic Streaming at a Flat Plate Bounded Above by Porous Region

Let us consider the acoustics boundary layer at a plane solid wall (the xz-plane), assuming two-dimensional flow in the xy-plane. Assuming the boundary layer approximation valid for this non-steady flow under consideration, the resulting boundary layer equation can be written as

$$\frac{\partial v_x}{\partial t} + v_x \frac{\partial v_x}{\partial x} + v_y \frac{\partial v_x}{\partial y} - v \frac{\partial^2 v_x}{\partial y^2} - \frac{v}{\kappa}v_x = U\frac{\partial U}{\partial x} + \frac{\partial U}{\partial t}. \tag{9}$$

Here (dp/dx) is expressed in terms of the flow velocity $U(x, t)$ outside the boundary layer. In the present case

$$U = Re(v_0 \cos \omega t \cos Ax) \quad \text{where } A = \frac{\omega}{c} \sqrt{\left[1 + i\left(\frac{\sigma^2}{Ro}\right)\right]}. \tag{10}$$

Now we will solve the Eq. (9) by successive approximations with respect to the small quantity v_0, the amplitude of the velocity fluctuations in the sound wave.

First Approximation:

For the first approximation, the quadratic terms in Eq. (9) are all omitted together. The solution of the equation

$$\frac{\partial v_x^{(1)}}{\partial t} - v \frac{\partial^2 v_x^{(1)}}{\partial y^2} - \left(\frac{\sigma^2}{Ro}\right) v_x^{(1)} = -i\omega v_0 \cos Ax \cos \omega t \tag{11}$$

which satisfies the necessary conditions at $y = 0$ and $y \to \infty$ can be solved by the variable separable method. Substituting $v_x^{(1)} = F(y)e^{-i\omega t}$ in (11), the solution will be

$$v_x^{(1)} = Re\{v_0 \cos Ax(1 - e^{-\varepsilon y})e^{-i\omega t}\} \tag{12}$$

where $\varepsilon = \kappa \sqrt{\left[1 - i\left(\frac{\sigma^2}{Ro}\right)\right]}$, $\kappa = \sqrt{-\frac{i\omega}{v}} = \frac{(1-i)}{\delta}$.

Second Approximation:

In the second approximation, solving the equation for $v^{(2)}$ in a steady state with the condition that corresponding solution must satisfy the boundary conditions at $y = 0$ and the condition far from the surface. The velocity as $y \to \infty$ can be given as,

$$v_x^{(2)}(\infty) = Re\left\{\frac{3v_0^2}{8c_a} \sqrt{1 + i\left(\frac{\sigma^2}{Ro}\right)} \sin 2Ax\right\}, \tag{13}$$

which will go back to the solution in Landau and Lifschitz for $N = 0$. This shows that outside the boundary layer, there is a steady flow whose velocity is independent of viscosity but depends on permeability.

4   Model, Results and Discussion

Figure 1 shows a model: a two-dimensional porous channel flow domain satisfying the condition for generation of classical Rayleigh streaming, $\lambda \gg h \gg \delta$, where is the sonic wavelength. The standing wave W_s' defined in Eq. (13) is implemented in a spanwise direction to this simple shear flow through the porous region. To solve
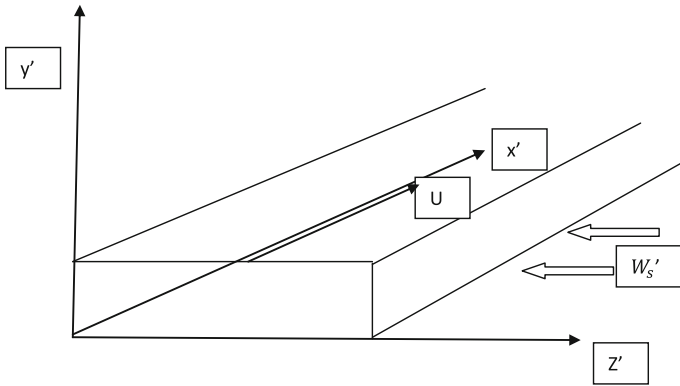
Fig. 1 Flow domain with coordinates. Here h is the distance between the two walls, U is the velocity of the upper wall and W'_s is the velocity of the imposed standing wave

Fig. 2 Rayleigh acoustic streaming between the walls when the ratio of permeability parameter and Roshko number is less than one
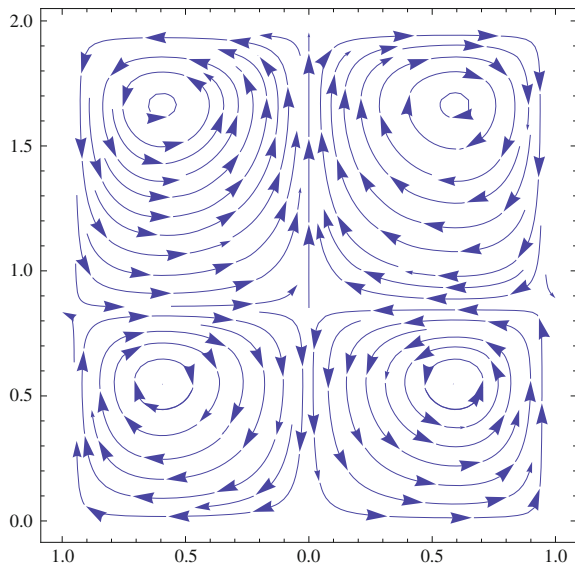
the flow governing equation, we implement the perturbation method. It is found that the streaming pattern developed in this problem is a function of porosity and the solution obtained will be reduced to Vainshtein [7] for an infinite permeability. Figures 2 and 3 shows that due to the porosity, the centre of vortices as well as the stagnation point is affected.

Fig. 3 Streaming patterns
when the ratio of permeability
parameter and the Roshko
number is zero
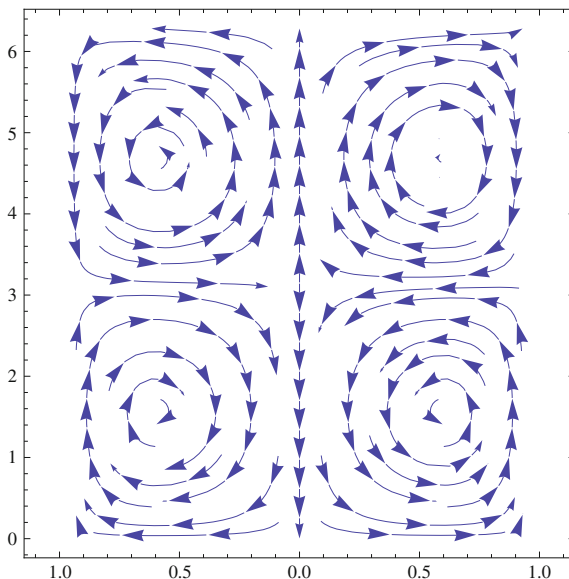
5   Conclusions

The boundary layer theory is developed in the transport system comprises of fluid
saturated porous media. It is found that the standing wave velocity is a function of
permeability. Also, it is found that outside the boundary layer there is a steady flow
whose velocity is independent of viscosity but depends on the two non-dimensional
parameters. The presence of porous media will affect the streaming patterns, peri-
odicity and number of vortices as well as stagnation point.

References

1. A. London (1950) Transmission of reverberant sound through double walls. J. Acoust. Soc.
   Am.; 22(2):270–9.
2. B.L. Liu et al. (2007) Influence of overpressure on sound transmission through curved panels.
   J. Sound Vibration; 302: 760–76.
3. J.H. Lee et al., (2002) Analysis and measurement of sound transmission through a
   double-walled cylindrical shell, J. Sound Vibration; 251:631–649.
4. J.S. Bolton et al. (1996) Sound transmission through multi-panel structures lined with elastic
   porous materials, J. Sound Vibration; 191:317–347.

5. M.A. Biot, Theory of propagation of elastic waves in a fluid saturated porous solid. I. Low-frequency range-II, Higher frequency, J. Acoust. soc. Am., 28; 179–191.
6. L.D. Landau and E.M. Lifschitz, (1993) Fluid Mechanics, Vol. 6, Course of theoretical physics. Oxford: Pergamon Press, Second Ed., 1993.
7. Peter Vainshtein (1995) Rayleigh streaming at large Reynolds number and its effect on shear flow. J. Fluid Mech., 285, 249–269.

Effect of Print Angle on Mechanical Properties of FDM 3D Structures Printed with POM Material

Yi-Ta Wang and Yi-Ting Yeh

Abstract Fused deposition modeling (FDM) is currently the most popular form of 3D printing. Using this technique, the materials are stacked layer by layer. This study investigates how to increase the mechanical strength of the structure by changing the direction of structure using ANSYS Workbench, SolidWorks 3D Computer Aided Design software (CAD) software, and Umaker (3D printer). The study was divided into two parts. In the first part, model data samples were imported into ANSYS for analysis prior to printing. The models were drawn using the SolidWorks software. The second part used the Umaker 3D printer to print the samples using the polyacetal material (POM). The structures were made using three different directions, 0°, 45°, and 90° of the fused deposition modeling machine. Test specimens were fabricated according to the ASTM D638 165 mm × 19 mm × 7 mm [1], type I standard. The mechanical integrity of the samples was assessed using tensile strength tests. The tensile strengths at specified angles of the structure were compared across specimens of each direction type. The results showed that the strength values of the 45° direction type were 65–72 % of those of specimen in the 0° direction type demonstrating that direction is a relevant factor in the mechanical integrity of 3D printed structures. Using the results of this study, the life span and mechanical strength of 3D printed structures can be increased.

Keywords Fused deposition modeling · 3D printing · Anisotropic · POM

1 Introduction

Subtraction processing is refining a block of original material through cutting, polishing, and drilling to produce a final product. The main disadvantage of this process is that it often produces waste. If this waste cannot be recycled, then, it is a

Y.-T. Wang (✉) · Y.-T. Yeh
Department of Mechanical and Electromechanical Engineering,
National Ilan University, 1, Sec. 1, Shennong Road, Yilan 26041, Taiwan, ROC
e-mail: ytwang@niu.edu.tw
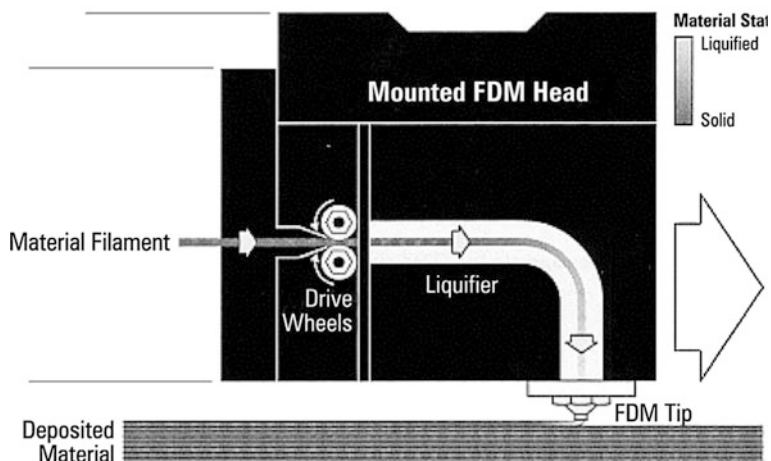
Fig. 1 FDM schematic [2]

not only a waste of resources but also a manufacturing cost to vendors. Since the Industrial Revolution, the traditional industry approach to machining has been to use computer numerical control (CNC), which uses subtraction processing.

However, if the product is too complex, then the subtraction processes cannot meet the specifications and objectives of the product. Over time, through increasing precision and complexity of technology, conventional CNC machining subtraction has been able to keep up with the needs of society. Conversely, addition processing, also known as additive manufacturing has advantages that subtraction processing lacks. For example, Rapid prototyping (RP) technology is a powerful tool in providing initial working models, and melt deposition modeling (or fused deposition modeling, FDM) forms products by heating a raw material until a molten state is reached, and expelling this material through a nozzle onto a working platform to manufacture products layer by layer, as shown in Fig. 1 [2]. This manufacturing method does not produce waste, is environmentally friendly, and can quickly and effectively meet the custom demands.

2 Methodology

This study used ASTM D638 for polyacetal material (POM) process specifications. The specimen models were designed using SolidWorks software and printed at different angles using the Umaker 3D printer. The user interface software is developed by Umaker Co. Ltd., which provides the functions of modal layering and printer control. The FDM system consists of an X–Y table to control the horizontal

motion of substrate and a Z-axis to control the vertical motion of nozzle. Print a minimum thickness of each layer is 0.1 mm, and the maximum printing speed of 300 mm/s. The user can adjust the speed of printing in accordance with their needs. The specimens were printed at angles of 0°, 45°, and 90°, and tensile tests were conducted to observe the differences in mechanical strength. ANSYS Workbench software was used to perform simulations of the mechanical testing, and the results were compared with the experimental data. The experiment flowchart is shown in Fig. 2. When the cost and time requirement to develop the object is larger, the manufacturing entity for the data is discussed. In business today, the development of the simulation software has lowered costs and time requirements of research. The software used for simulation analysis in this study was ANSYS.

Models for tensile testing per ASTM D638 were designed using SolidWorks CAD software, and had a dimension of 165 mm × 19 mm × 7 mm [1]. The model used in the ANSYS simulation for structural mechanics analysis had a boundary condition of 665 N applied at the 20 mm position, while the other end of the specimen was fixed. Eliminating the sides and the part of the sample past the fixed end, the sample was divided equally into 10 segments, and mechanical properties of

Fig. 2 Experimental structure
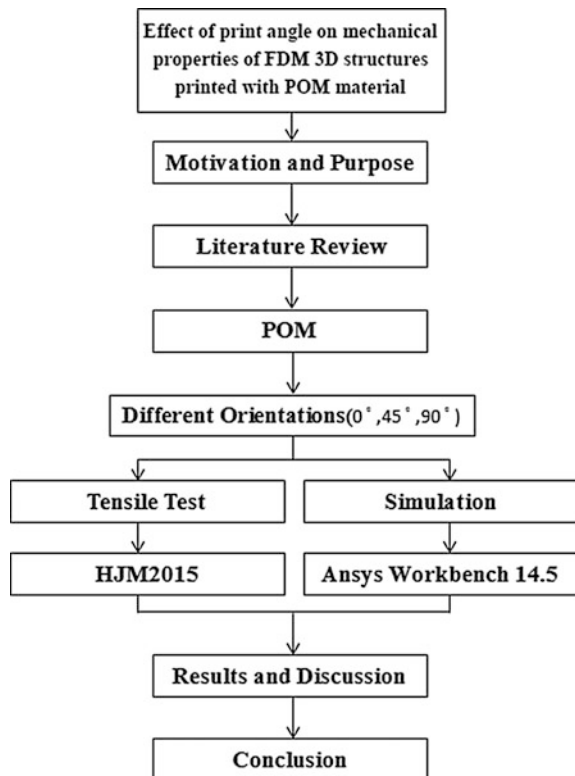
each segment were measured to provide analog data. FDM is a favorable RP technique [3–5] because of its low-cost equipment and durable products, and is therefore widely used. In FDM, a thermoplastic material is heated to a semi-molten state, and extruded into a thin filament by means of a deposition modeling object. The extrusion nozzle path is defined to create a 2D profile, which becomes a 3D structure, as the material is stacked through layering. The stacking process uses heat dissipation; the lower temperature surrounding the filaments leads to a fast cure, creating a platform for the new layer to yield a third dimension. Semi-molten material fuses with cured filaments to create a bonded structure [6].

Results verified by tensile test and experiment specimen models were designed using the SolidWorks software to comply with the tensile test piece size requirements of ASTM D638 (165 mm × 19 mm × 7 mm) [1]. After file conversion to STL file format, the files were imported into Cura software for pre-printing preparation. POM was used as the test material, and the Umaker 3D printer was applied to print 0°, 45°, and 90° three different angles stacked 26 layers of test specimens. For 0° specimen, the 3, 13, 23 layer are stacked three-layer deposition in 90° direction as the supporting layer. For 90° specimen, the 3, 13, 23 layer are stacked three-layer deposition in 0° direction as the supporting layer.

3   Results and Discussion

In anisotropic materials, the tensile strength is different for different directions [7]. Figure 5 shows a simulation of stress using a sample created with a 0° direction of lamination. The maximum stress in the stacking direction of the 0° piece of 10.4×10^6 Pa occurred in the middle, and gradually decreased toward the left and right sides. Figure 6 shows a simulation of stress for a sample having a 45° stacking angle. The maximum stress value was 3.99×10^6 Pa. Figure 7 shows a simulation of stress for a sample created with a 90° stacking angle. The maximum stress value was 3.69×10^6 Pa. The comparison of Figs. 5, 6, and 7 shows that the diagonal stacking direction of the 0° analog test piece had a greater maximum stress (red area) than the 45° or 90° test piece. This shows that the mechanical strength of the test piece created with a 0° angle was better than both the 45° and 90° test pieces. The 45° angle of orientation of the maximum stack simulation stress is second. Analog stress differences between each of the three test piece types fabricated with POM melt deposition confirmed the anisotropic nature of the mechanical properties. The differences in stress orientations between the three test samples (axial for the 0° piece, and radial for the 90°) shows that it can be used to bear the load in different directions [8] (Figs. 3 and 4).

Figure 8 is a strain simulation analysis graph for a specimen stacked at an angle of 0°, the left side of the 20 mm fixed end and another 665 N force toward right side. The maximum strain of the test piece created in the 0° direction was 5.83×10^{-3} mm/mm, and gradually decreased from the right side to the left side. Figure 9 is a strain

Fig. 3 The FDM system

simulation analysis graph of the test piece created with a 45° stacking angle. The maximum strain was 2.20×10^{-3} mm/mm. Figure 10 is a strain simulation analysis graph of the test piece created with a 90° stacking angle. The maximum strain value was 1.45×10^{-3} mm/mm.

The comparison of Figs. 8, 9, and 10 shows the maximum analog strain area of the 0° stacking angle test piece to be greater than those of the 45° and 90° stacking angle test pieces. Both analog strain areas have a stacking direction angle of 0°. The tensile strength of stacking direction of 0° is better and the 45° angle direction stacked maximum analog strain between 0° and 90°. At directional strengthening material textures, although 0° angle stacking direction than the other two high tensile strength, but a 45° angle to the direction of stacking capacity of objects is the best direction. The object security is preferably 45° when the angle of the direction of the stack. Object at different angles molding tiered stack, its mechanical strength is better than all the way molding an angle [9].

A material having different properties in different directions is non-isotropic (anisotropic). Polymer materials generated by heat melt are anisotropic; thus, the stacking direction has a great influence on the strength of the product, and stacking

Fig. 4 Heating board
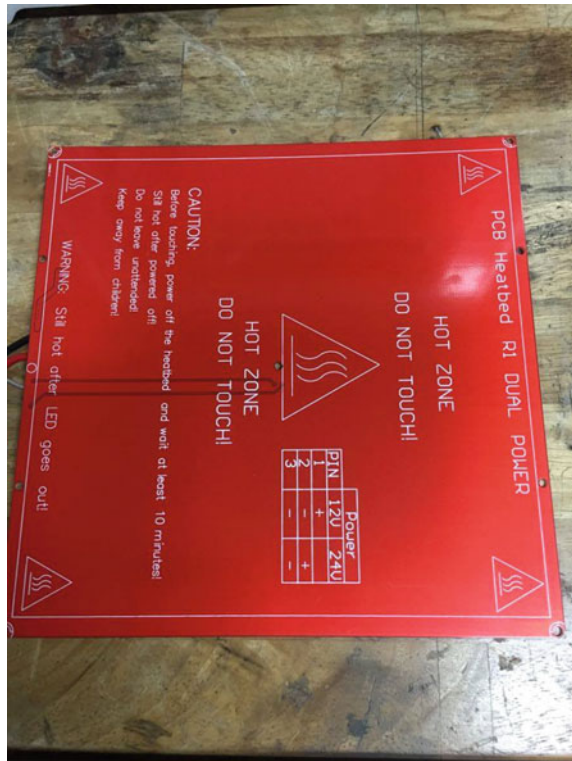
Fig. 5 Stacking direction of 0°, stress simulation analysis chart
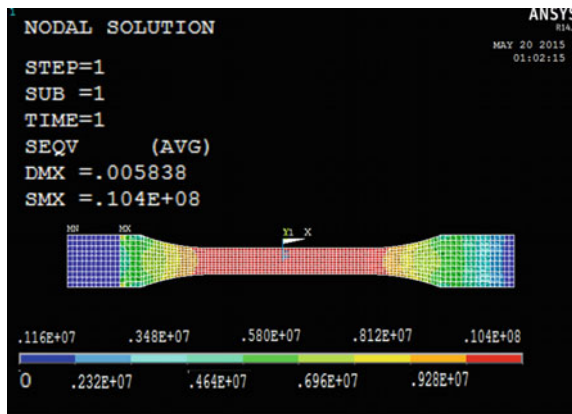
Fig. 6 Stacking direction of 45°, stress simulation analysis chart
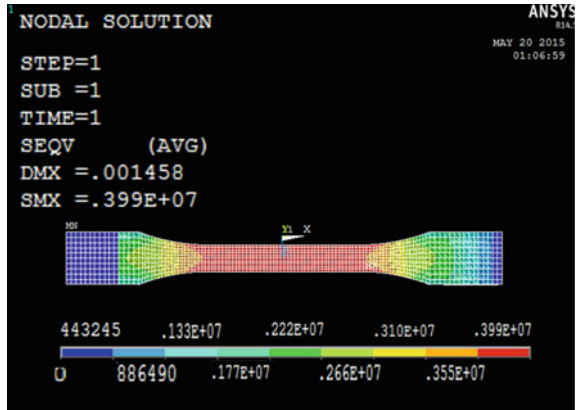
Fig. 7 Stacking direction of 90°, stress simulation analysis chart
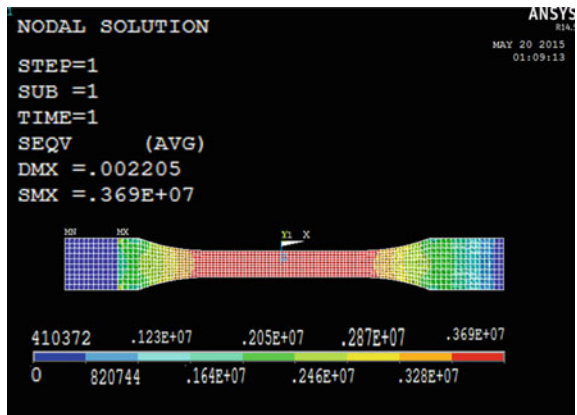
Fig. 8 Stacking direction of 0°, strain simulation analysis chart
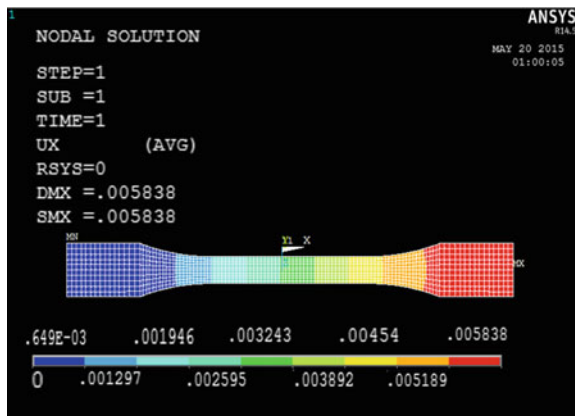
Fig. 9 Stacking direction of 45°, strain simulation analysis chart
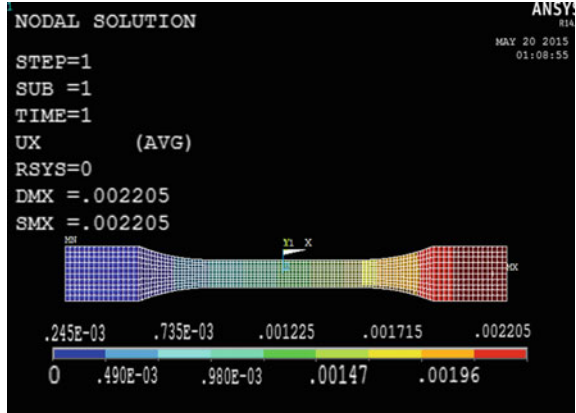
Fig. 10 Stacking direction of 90°, strain simulation analysis chart
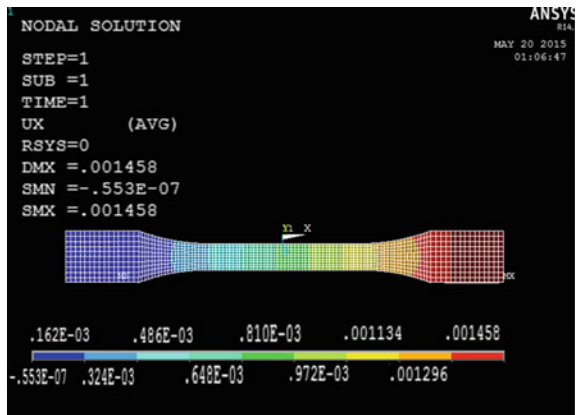
in different directions may result in different mechanical strengths [10]. In order to predict the mechanical properties of prototyped objects, measuring such material properties is very important. Material parameters, such as air gap spacing, model, or color temperature, will produce different characteristics [11].

Figure 11 shows POM deposited at angles of 0°, 45°, and 90°. The maximum strength of the specimens were 665.64 N, 485.07 N, and 258.47 N, respectively. The breaking strength of these pieces were 662.10 N, 251.38 N, and 233.68 N, respectively. This shows that the mechanical strength is significantly different for FDM stacked using different angles. A study conducted by Ahn et al. noted that stacking at different angles affected van der Waals forces of binding molecules [2]. Specifically, the study showed that stacking at a 0° angle demonstrated the greatest forces followed by stacking at a 45° angle, and lastly stacking at a 90° angle.

Fig. 11 The maximum
power point of view of
different angles corresponding
to the stack under elongation,
fracture strength
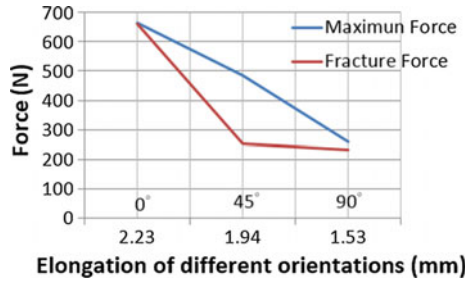
Fig. 12 A stack of different
angles maximum stress,
maximum strain comparing
chart
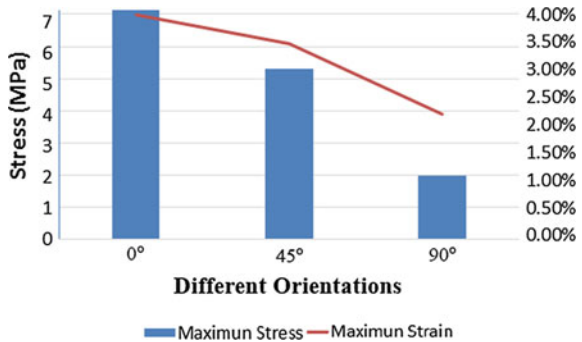
Figure 11 also shows the maximum strength at different stacking angles corresponding to the elongation, fracture strength comparison graph. The 45° displayed in a stack in a diagonal direction of the tensile strength of the specimen can be achieved with an amount of stacked 0° side of the tensile test piece 72 % power. Figure 12 shows the maximum stress for a stack of different angles, the maximum strain comparison chart, X-axis for various angles stacked, the left Y-axis is the stress value; right of the Y-axis as a percentage of stretch. The maximum stress is blue line, the tensile stresses were 7.31, 5.29, and 1.98 Mpa for the 0°, 45°, and 90° specimens, respectively. The maximum strain is the red line, 0°, 45°, and 90°, the strain of the specimen was 3.92, 3.42, and 2.20 %, respectively. It shows that the maximum tensile stress is 0° angle stacking of the test piece, followed by 45°, then to 90°. Comparing Figs. 11 and 12 shows that the mechanical strength of the 0° angle direction specimen to be the highest, followed by the 45° specimen. This result supports Chen's work [12], which points out specimens with a stack angle of 45° angle to have mechanical strength values falling between specimens with stack angles of 0° and 90°.

4   Conclusions

1. Polyacetal can be used for successful melt deposition modeling upon proper adjustment of the 3D printer parameters. The stacking direction has a great influence on the strength of the specimens, and stacking in different directions may result in different mechanical strengths.
2. In anisotropic materials, the tensile strength and strain simulation analysis shows that the diagonal stacking direction of the 0° analog test piece had a greater maximum stress than the 45° or 90° test piece. The mechanical strength of the test piece created with a 0° angle was better than both the 45° and 90° test pieces. The main reason should be at 0° specimen dominant force van der Waals forces, separation requires a large force of two molecules that conducted by Ahn et al. noted [2].
3. Tensile verified test results show that the tensile strength values are greatest for 0° specimens and smallest for 90° specimens, and that the strength values of the 45° direction type were 65–72 % of those of specimen in the 0° direction type demonstrating that direction is a relevant factor in the mechanical integrity of 3D printed structures.

References

1. ASTM (1997), ASTM D638-97, Test Method for Tensile Properties of Plastics, ASTM.
2. S.-H. Ahn, M. Montero, D. Odell, S. Roundy, and P. K. Wright, "Anisotropic material properties of fused deposition modeling ABS," Rapid Prototyping Journal, vol. 8, pp. 248–257, 2002.
3. Sung-Hoon Ahn,Caroline S. Lee and Woobyok Jeong, "Development of translucent FDM parts by post-processing," Rapid Prototyping Journal, Vol. 10 Iss: 4, pp. 218–224.
4. J. Jones, D. Wimpenny, R. Chudasama, and G. Gibbons, "Printed circuit boards by selective deposition and processing," *nanoscale,* vol. 22, p. 23, 2011.
5. C. B. Arnold, P. Serra, and A. Piqué, "Laser direct-write techniques for printing of complex materials," *Mrs Bulletin,* vol. 32, pp. 23–31, 2007.
6. Y. Zhang and K. Chou, "A parametric study of part distortions in fused deposition modelling using three-dimensional finite element analysis," Proceedings of the Institution of Mechanical Engineers, Part B: Journal of Engineering Manufacture, vol. 222, pp. 959–968, 2008.
7. Zong wei Wang, Computer Simulation on the Growth of Fatigue Crack in Laminate Composites, Thesis, Power Mechanical Engineering (PME) of National Tsing Hua University, Taiwan, 2000.
8. Xin Zhang, Xingping Xu, Lei Wang, Di Zhang, Yugui Wu, Design of composite continuous tubular, Petroleum Machinery, Vol. 11, pp. 1001–4578.

9. FENG-MIN LAI, CHUN-TENG HSUEH, YU-WEI CHEN and CHI-HAN TSAO, Stress Intensity Factors of Composite Laminates with Different Types of Cracks and Patch Test Fragments, Journal of Science and Engineering Technology, Vol. 6, No. 1, pp. 57–74,2010.
10. http://www.linkupon.com/T-t15.html
11. C. Lee, S. Kim, H. Kim, and S. Ahn, "Measurement of anisotropic compressive strength of rapid prototyping parts," Journal of materials processing technology, vol. 187, pp. 627–630, 2007.
12. Chung-Wen Chen, Jia-Lin Tsai, Predicting Tensile Strength of Fiber Composite With/Without Crack, Thesis, Engineering of National Chiao Tung University, Taiwan, 2006.

Finite Element Analysis of Surface Grinding Process Using Nanofluids

Ongolu Suresh Babu, Venkata Ramesh Mamilla and G. Lakshmi Narayana Rao

Abstract The main aim is to investigate on the grinding process and to improve the surface characteristics such as surface finish and micro-cracks and surface topography from micro-level to nanolevel using carbon nanotube based on nanofluids. Carbon nanotubes have high mechanical and electrical properties particularly, more heat transfer capacity of 6000 w/mk. By using this property, the multi-walled carbon nanotubes are mixed with the coolant of SAE20W40 oil during grinding process to investigate the surface characteristics like surface roughness of AISI D2 tool steel work piece materials which are used more in moulds and dies. Carbon nanotubes increase the heat carrying capacity, thermal conductivity of the lubricating oil and therefore prevent any scratch to the work as well as the nano particles participating in the machining process and fill the micro-voids generated during the machining operation and give a better surface finish.

1 Introduction

The high-chromium high-carbon Cold Work tool steel D2 is considered. During the tempering procedure, we considered the steel as it is high in both chromium and carbon for the purpose of forming large volumes of secondary chromium carbides forming the precipitation of the carbides which further gave rise to high wear resistance steel.

In order to utilize for punch as well as dies or injection mould tools, D-2 steel is vacuum heat treated. In this heat treatment process, the steel is heated to an elevated temperature further to make it as perfect steel and is rapidly cooled by vacuum process. A special wheel has been adopted for surface grinding on the perfect steel.

O.S. Babu · V.R. Mamilla (✉) · G. Lakshmi Narayana Rao
Department of Mechanical Engineering, QIS Institute of Technology, Ongole,
Andhra Pradesh, India
e-mail: maa_ram@yahoo.co.in

Table 1 Specifications of MWCNTs

OD	10–20 nm
Length	10–30 μm
Purity	>95 wt%
Ash	<1.5 wt%
Specific surface area	>233 m^2/g
Electrical conductivity	>10^{-2} S/cm

During the treatment process, parts of 2 mm thin can be manufactured and 0.004 mm leaving for finish grinding.

For high abrasive wear applications, D2 steel is manufactured and can exist the position of heat treated to RC 64 which has a short tempering temperature.

In the plastic moulding industry, it is used for barrel liners, die workings in the metal stamping industry as well as in several other applications which require high wear resistance.

Carbon nanotubes have a lot of structures, inconsistent in length, thickness, and number of layers. Even though they are formed from basically the same graphite sheet, their electrical characteristics are at variance depending on these variations, acting either as metals or as semiconductors (Table 1).

2 Design of Grinding Wheel and Work Piece

The grinding wheel selected for design is A60K5V10. The aluminium oxide grinding wheel is selected which is manufactured by universal carbodium. The properties of the grinding wheel and the work piece are tabulated below (Tables 2 and 3).

Table 2 Properties for grinding wheel

Properties	Values
Young's modulus(N/mm^2)	2×10^{-9}
Poisson ratio	0.29

Table 3 Properties for D2-tool steel work piece

Properties	Values
Young's modulus(N/mm^2)	188000
Poisson ratio	0.26
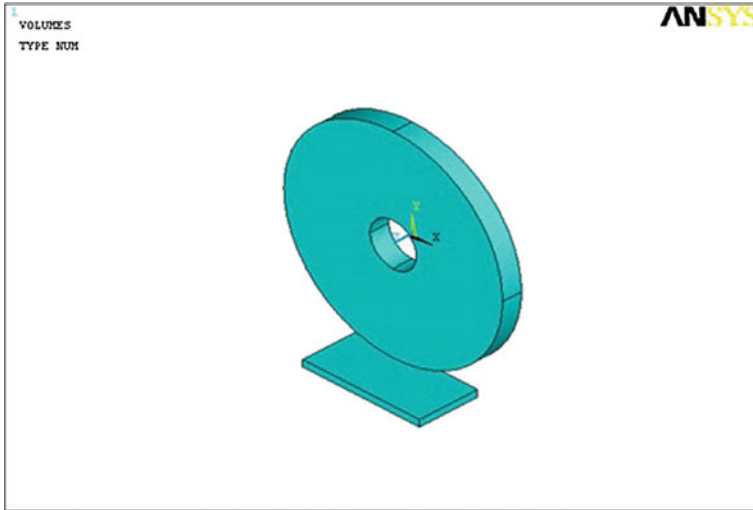
Fig. 1 Modelling of grinding wheel and work piece

2.1   Dimensions Used for Modelling

Grinding Wheel:
   Diameter of the wheel: 150 mm
   Thickness of the wheel: 13 mm
   Internal Diameter of the wheel: 31.75 mm
Work piece
   Length: 80 mm
   Breadth: 50 mm
   Thickness: 5 mm

Modelling of the work piece and grinding wheel was done through Ansys software as per the above specifications. Here the grinding wheel is assumed to be made up of aluminium oxide. The design was made according to A60K5V10 (Fig. 1).

3   Results and Discussion

See Fig. 2, Tables 4 and 5.
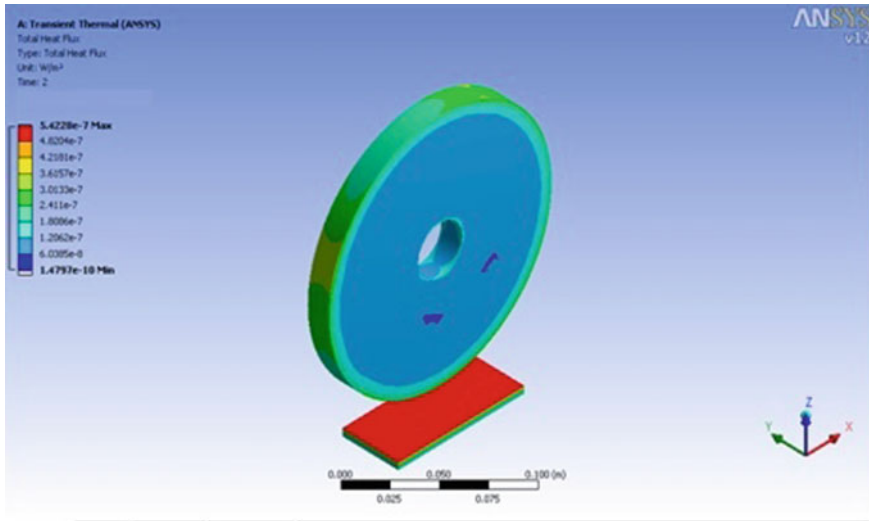
Fig. 2 Heat flux on the work piece with out using nanofluids

Table 4 Results show the variation of heat flux without mixing of nanofluids

Depth of cut (mm)	Heat flux (w/m$^{2)}$)
0.1	1.44e-6
0.2	1.86e-6
0.3	3.27e-6
0.4	5.42e-7

Table 5 Results show the variation of heat flux mixing of nanofluids

Depth of cut (mm)	Heat flux (w/m$^{2)}$)
0.1	8.845e-4
0.2	1.03e-5
0.3	1.404e-6
0.4	2.346e-6

Table 6 Shows the parameters used for Taguchi Analysis in grinding process

Parameters	Level 1	Level 2	Level 3
Speed (C)	2400	2400	2400
Feed (A)	0.2	0.3	0.4
Depth of Cut (B)	0.01	0.02	0.03

4 Taguchi Analysis

In Taguchi analysis, we can find out the optimum parameters used in grinding process. Taguchi involves with orthogonal arrays to systematize the parameters affecting the development and the levels at which they are supposed to be different.

Main Effects Plot for SN ratios without CNT
Data Means
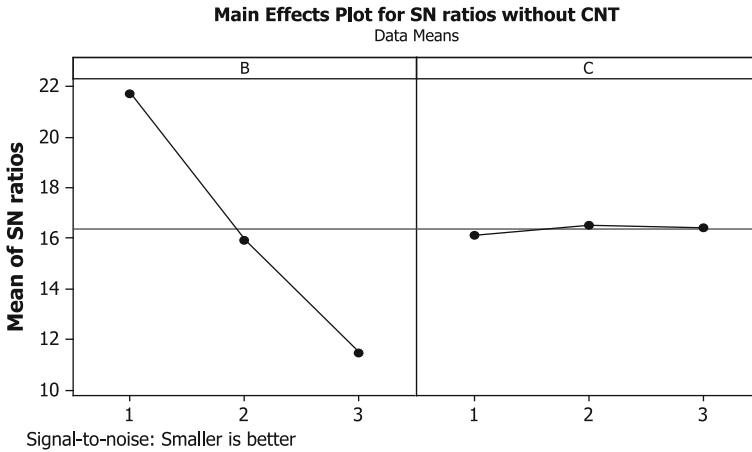
Fig. 3 Factor effect diagram without CNT coolant

Table 7 Results for XRD Analysis

Sample	Peak Height (cts)	D-Spacing (a)	Displacement (2θ)
With CNT	198.055400	1.30254	0.300
Without CNT	408.386	2.02974	0.420

To optimize the performance characteristic, Taguchi involves design of experiments for analysis of variance on the collected data which is used to choose new parameter values (Table 6).

From the Fig. 3, Level 3 of A and Level 1 of B give the maximum effect of improving surface roughness. Naturally A3 and B1 are the best combination, i.e., a feed 0.4 mm/rev and depth of cut 0.01 mm furnish the smallest amount of surface roughness. From the factor outcome, graph shows that feed generous additional impact to improve the surface finish without using CNT coolant. Based on the experiment, the optimal level setting of parameters is A3B1 (Table 7).

Above results show that the asperities on the work piece for which nanofluids are not used are more when compared to the work piece for which nanofluids are used. By using nanofluids in grinding process, the height of the asperities is decreased. The atoms size reduces and the properties of the work piece are improved.

5 Conclusion

Surface roughness and the temperature evolved are more for the work piece for which normal fluids are used. The parameters which will affect the grinding process were studied. Micro-cracks evolved is more for the work piece for which nanofluids

are not used and is identified by using S.E.M analysis. By X.R.D analysis, we can identify that the asperities are more for the work piece for which nanofluids are not used. Nanofluids form a thin layer on the work piece which will minimize the micro-cracks and improve the surface finish of the work piece.

References

1. H. K. Tonshoff, J. Peters. I. lnasaki, T. Paul, "Modeling and Simulation of Grinding Processes". Material processing technology. Pp 677-688, (1992).
2. R.A. Irani, R.J. Bauer, A. Warkentin (2005), "Cutting fluid application in the grinding process". Material processing technology. Pp 1696–1705, (2005).
3. S. Shaji, V. Radhakrishnan., "Analysis of process parameters in Surface Grinding with Graphite as lubricant". Material processing technology Pp 965-972,(2003).
4. S. Prabhu and B.K. Vinayagam, "Nano Surface Generation in Grinding Process using Carbon Nano Tube with Lubricant Mixture."Machine tools and Manufacturing. Pp 747–760, (2008).
5. Rudiger Rentsch, lchiro lnasaki,"Investigation of Surface Integrity by Molecular Dynamics Similation". Machine tools and Manufacturing. Pp 295-298,(1993).
6. BrahimBenFathallah, NabilBenFredj a, HabibSidhom a,"Effects of abrasive type cooling mode and peripheral grinding wheel speed on the AISI D2 steel ground surface integrity." Machine tools and Manufacturing.Pp 126-128,(2005).
7. D.A. Doman, A. Warkentin, R. Bauer, "Finite element modeling approaches in grinding". Machine tools and Manufacturing. Pp 109-116, (2001).
8. A.G. Mamalis, et al., "Nanotechnology and nanostructured materials: trends in carbon nanotubes," Precision Engineering,v 28, (2004),Pp 16–30.

Resonance Behavior of Steam Turbine Blades with Zigzag Lacing Pins

B.L. Jaiswal

Abstract The paper highlights the contribution of zigzag lacing pins, which are assembled in LP stages of some of the steam turbines. The result of experimental investigations on a prototype rotor establishes that these zigzag pins play a major role in forming a disk-like structure at high speeds. For such blades, conventional Campbell diagram does not give the complete dynamic behavior and hence SAFE diagram/Impulse diagram need to be generated. Due to the complex fixity conditions, analytical modeling is not very accurate and hence experimental investigation is a must to determine the exact behavior of the bladed disk. The paper describes the details of telemetry instrumentation used during the test. Detailed analysis procedure has been highlighted to retrieve and interpret the recorded data for generation of SAFE diagram.

Keywords Steam turbine blades · Zigzag lacing pins · SAFE diagram · Modeling · Telemetry instrumentation

1 Introduction

Turbomachinary blades are normally subjected to a very severe vibration environment due to which, they are subjected to periodic forces with frequencies equal to the rotational speed and its harmonics because of imbalances in the steam flow. These blades being flexible members are liable to be excited at their resonant frequencies during the operation whenever the excitation frequency coincides with one of the natural frequencies of the blade. It is possible in small machines to design the blades and tune them so that no resonance occurs in the operating range. For machines of large capacity, sometimes this is not possible, since they comprise of several thousands of blades distributed over several stages. Though in such cases also it may be possible to design the blading to avoid resonance at the steady

B.L. Jaiswal (✉)
Vel Tech Dr.RR & Dr.SR Technical University, Chennai, India
e-mail: jaiswalbl@gmail.com

operating speeds; the blade may experience resonance during acceleration and deceleration of rotor during starting and shutting operations. Hence, the only way is to live with this resonance but control the level of resonant response by providing damping for dissipation of the vibratory energy at transient resonant conditions.

Thus damping becomes an important aspect of blade design and it is a common practice to deploy damping pins, damping wires, zigzag lacing pins, etc., in turbines of many designs. The paper describes the behavior of blades in LP rotor of one of the turbines, where zigzag lacing pins are assembled. Zigzag lacing pins pass through holes of two successive blades and are loosely fitted between the blades and are extensively used in LP stage of various designs for providing frictional damping which limits the amplitude of vibration in the event of resonance at the operating speed. However, these zigzag pins, in addition to providing damping, play a major role in forming a disk-like structure at high speeds, thereby completely illiminating free standing blade modes.

Analytical studies for above configuration of bladed disk is very difficult due to the complex fixity conditions associated with the zigzag pins and also due to the complex fir-tree type of profile at the blade root. Conventional experimental modal analysis cannot be carried out on this stage of the rotor, since in the static condition blades and zigzag pins are loose, due to which disk type of structure does not exist. Due to the above limitations of analytical work, experiments were carried out on a prototype turbine by the application of the telemetry system. Measurements were carried out by installing strain gauges on four diametrically opposite blades and data was recorded up to 3400 RPM. Experimental data collected from instrumented blades at various speeds was analyzed using sophisticated instrumentation and software, which helped in identification of all relevant disk modes. It was established that these pins in addition to providing damping, completely changed the characteristics of the stage by the formation of disk-like structure near the operating speed. Due to this transformation resonance characteristics of the stage completely change and sustainable resonance condition is completely eliminated. The paper highlights the details of the instrumentation, test procedure, and the analysis technique to retrieve the salient information.

2   Disk Modes and Resonance Condition

Packetted bladed disks and blades with zigzag pins require specialized dynamic analysis. A Campbell diagram is very commonly used to analyze the resonance of a freestanding blade. However, the Campbell diagram does not contain enough information to analyze a complete bladed disk due to which it only reveals possible resonance. To help understand and analyze packetted bladed disk resonance, the SAFE diagram [1] is used which confirms if a true resonance exists in the disk. This diagram is plotted to take care of nodal diameter showing the mode shape, and resonance is sustainable only when the nodal diameter line cuts the corresponding excitation or the engine order line near the operating speed. Only when this

condition is satisfied the energy buildup is the maximum. However, there are two simultaneous conditions for the energy buildup per cycle to be the maximum.

These conditions are

1. The frequency of the exciting force equals the natural frequency of vibration, and
2. The exciting force profile has the same shape as the associated mode shape of vibration.

Thus for a resonance to occur, both of the above conditions must be met and this situation is best illustrated only by the SAFE diagram.

3 Determination of Nodal Diameter

Nodal diameter pattern of the vibrating disk can be determined by plotting the amplitude and phase at various locations. For the case of 1xND and 2xND modes, this technique can be applied without any problems, if the blades are selected at two diametrically opposite locations. In this case, strain spectrum of two diametrically opposite blades will be out of phase for 1xND mode and in phase for 2xND modes. However, this technique can be applied only for low nodal diameter modes since for higher nodal diameters it becomes very cumbersome, mainly due to nonsymmetrical mode shapes. For such cases, AC magnet excitation [2] provides a simple method for identifying the nodal diameter associated with a particular frequency. The technique is based on the fact that if a disk is excited by a stationary AC magnet with either of the frequency fe, then the blades on the disk will vibrate at a frequency f. Hence by determining fe, f at a particular speed S, the number of nodal diameter N can be identified, from the expression

$$\text{fe} = f \pm N \times S$$

where, N = Number of nodal diameters
$\qquad$ S = rotational speed

This technique was used for the identification of nodal diameters and the rotor during this test was run at constant speed of 2400, 2700, and at 3000 RPM. Blades at each of these constant speed runs were excited with variable frequency AC magnet.

4 Telemetry Instrumentation and Test Setup

Tests in rotating condition were carried out by the use of FM telemetry instrumentation. In this technique [3], the signal from a sensor (which could be a strain gauge, a thermocouple or an accelerometer) modulates a RF carrier being emitted

by the miniature transmitter. These FM transmitters are mounted on the rotating shaft and are connected to the sensor. The rotating antenna, connected to the transmitters and mounted on the rotating structure, enables telemetering of the modulated signal from transmitters. This antenna is capacitively coupled to a stationary antenna placed very close (50 mm max.) to the rotating antenna. The receiver receives the signal from the stationary antenna and demodulates to retrieve the information. The receiver signal, in the form of DC/AC voltage, is analyzed using conventional signal analyzers or can be recorded on an instrumentation tape recorder for later analysis. Figure 1 shows the rotor in the balancing tunnel, FM transmitters assembled in the balancing groove and some of the instrumented blades. Figure 2 shows the instrumented stage with the receiving antenna and AC/DC electromagnets for giving excitation to the blade in rotating conditions.

Fig. 2 Instrumented blades, FM transmitters and antenna
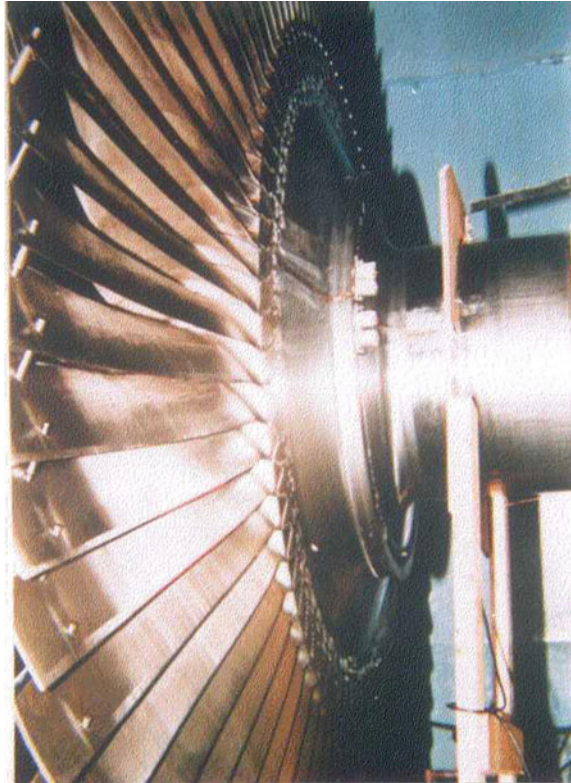
5   Sensor Installation and Measurements

Last stage of the LP rotor under investigation comprises of 78 blades having fir-tree root and these blades are assembled with zigzag lacing pins. Blades for detailed investigation were selected based on the results of static frequency analysis, which was carried out by conventional impact test to identify the blades with the lowest and highest frequencies. From this test results, four blades were selected so as to include one blade with the lowest frequency of 51.25 Hz and one with the highest frequency of 61.25 Hz. Two adjacent blades satisfying the frequency requirements were identified and the other pair was selected so as to lie at 180° position to the first one.

All the four blades were instrumented with semiconductor strain gauges. These gauges were connected to telemetry transmitters assembled in special housings, which were mounted, on the balance weights placed in the balancing groove. DC magnet and AC magnet placed close to the blade were used for giving excitation to blades in the rotating condition.

Subsequently, measurements were carried out under rotating condition after evacuating the vacuum tunnel. During this spin test, coast-up and coast down

signatures were recorded up to a speed of 3400 RPM and during this period, blades were excited by a DC magnet. For the determination of nodal diameter pattern, signal was also recorded at constant speed of 2400, 2700, and 3000, and during this test blades were excited by AC magnet with variable frequency power supply in the frequency range of 5–130 Hz.

6   Analysis of Test Results

Frequency spectrums of all the blades were obtained by carrying out FFT of the data recorded during impact test under stationary condition. Signals recorded at various speeds were also analyzed using FFT to study the increase in natural frequencies due to speed effects.

Data recorded during AC magnet excitation were analyzed to get the nodal diameter information at the speed of 2400, 2700, and 3000 RPM. Data acquisition system and data analysis software were also used to get a clear representation of phase change, as the rotor speed increases and the nodal diameter changes from 1xND to 2xND. Salient results are highlighted below.

Figure 3 shows the fundamental frequencies of blades in static condition, obtained by conventional impact test. Under static condition blade assembly in the root and also the zigzag pins between the blades are loose.

Figure 4 shows the presence of two dominant resonance, which are obtained at the speed of 3110 RPM and at 3300 RPM. It is also seen from the results that all the four instrumented blades exhibit exactly identical resonance frequencies, i.e., 103.5 and 110 Hz, as seen in the waterfall diagram of Fig. 4.

Figure 5 show two spectrums obtained for determination of nodal diameter. These spectrums show the response of the blade at the speed of 2700 RPM due to the excitation of blade with the AC magnet. These figures were obtained by
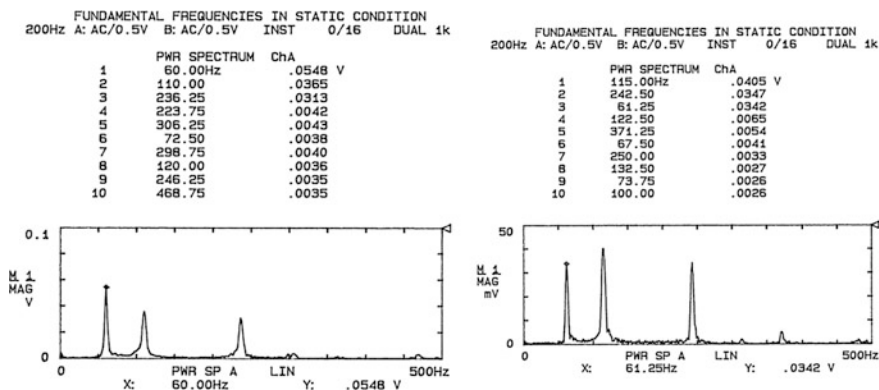
Fig. 3 Fundamental frequency of two typical blades in static condition
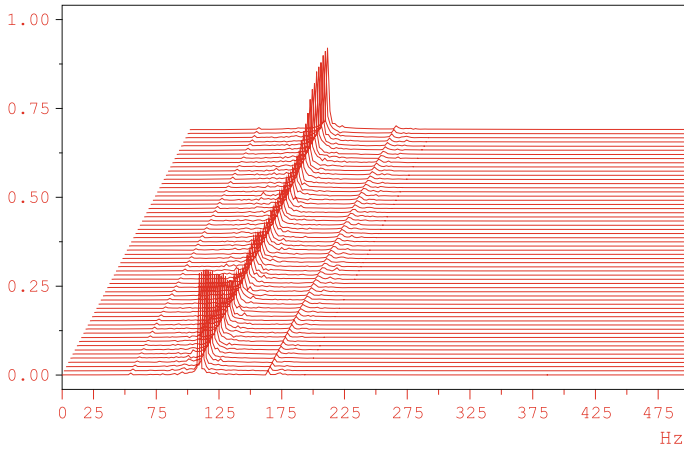
Fig. 4 Water fall diagram of blade resonance at 3105 RPM and at 3300 RPM
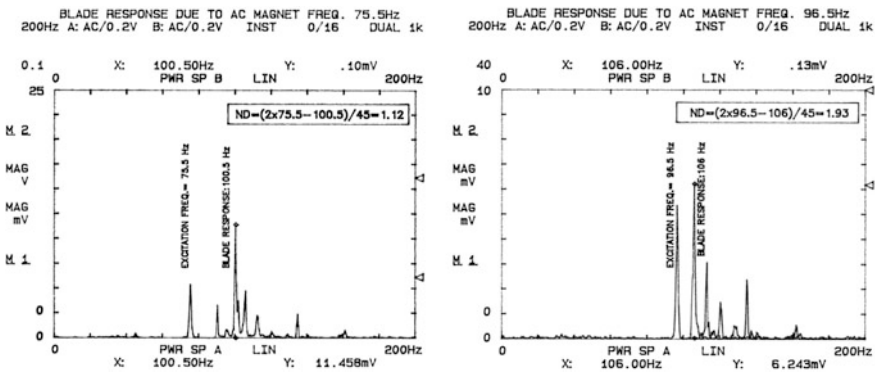
Fig. 5 Nodal diameter through AC excitation

overlapping the instantaneous blade excitation frequency (AC magnet) and the blade response and show the excitation of a specific nodal diameter at a particular frequency of AC magnet excitation.

Calculation procedure for the nodal diameter is highlighted in these figures and is as per the procedure highlighted in Sect. 3.

Interpretation of data recorded during AC magnet excitation at the speed of 2400 and 3000 RPM also showed similar trend.

For further verification of nodal diameter patterns as obtained by the use of AC magnet excitation, phase variation due to change of nodal diameters pattern was also studied. Since the blades selected are in diametrically opposite positions, this exercise can be used to derive very definite conclusions for 1xND and 2xND modes.
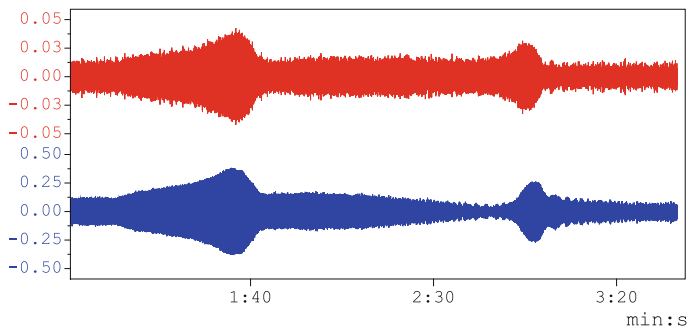
Fig. 6 Time spectrum of two diametrically opposite blades during resonance

Figure 6 shows the time spectrums of two diametrically opposite blades high-lighting resonance at two different intervals during coast-up when the speed is increased from 3000 to 3400 RPM. As seen from this figure both the blades resonant at the same speed and the corresponding frequencies obtained from the frequency analysis are 103.5 and 110 Hz.

To obtain the phase pattern, time spectrums for both the blades were captured during the peak amplitude as is seen from Fig. 7 for the first resonance at 103.5 Hz.
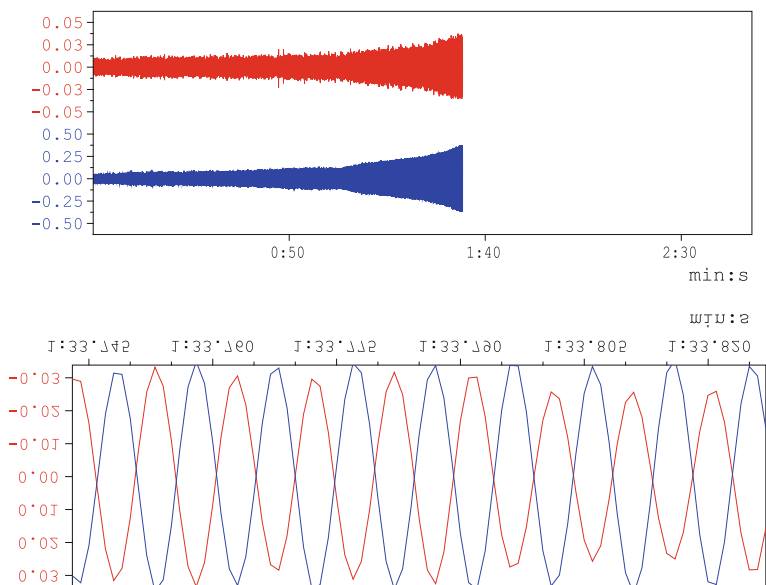
Fig. 7 Time spectrum showing out of phase displacement of two diametrically opposite blades
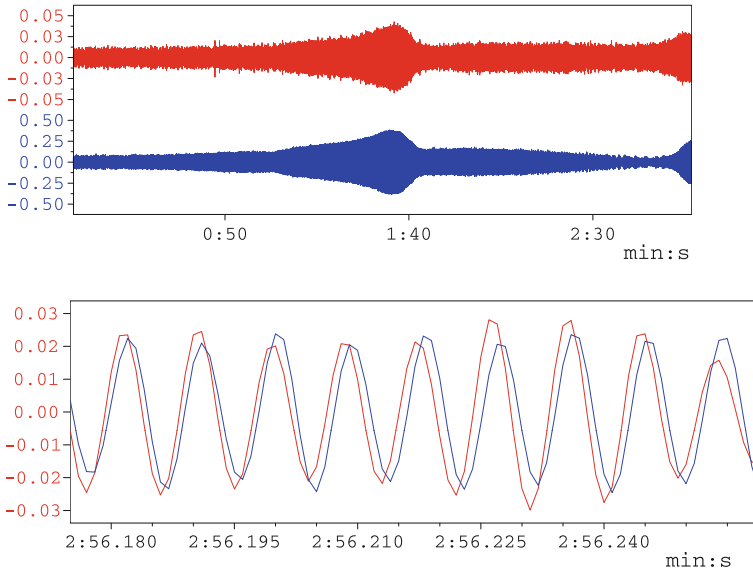
Fig. 8 Time spectrum showing in phase displacement of two diametrically opposite blades

Out of phase spectrum as seen from the expanded time waveform clearly shows 1xND disk mode of vibration.

The exercise is repeated for the second resonance point at the frequency of 110 Hz and in phase spectrum for 2xND mode is clearly seen from Fig. 8.

Since these are disk modes, the resonance condition gets confirmed only after studying the matching between the mode shape and shape of the excitation force. For this purpose SAFE diagram shown in Fig. 9 is drawn, where nodal diameter points are projected on the corresponding engine order line.

As is clearly seen from this, figure 103.5 Hz corresponding to 1xND will not come under resonance near the operating speed since the nodal line projection does not cut 1xEO line near the operating speed.

2xND mode of 110 Hz with 2xEO at the speed around 3300 RPM, which is far away from the operating regime.
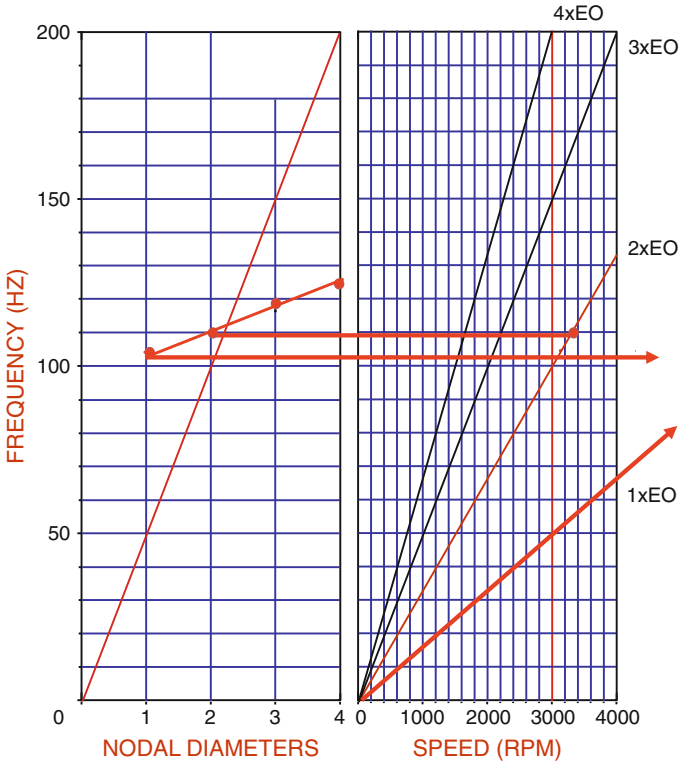
Fig. 9 Safe diagram of bladed disk

7   Conclusions

- SAFE diagram clearly indicates that this frequency of 103.5 Hz, which happens to be 1xND mode does not cut the 1xEO line, anywhere near the operating speed and confirms that there is no possibility of any resonance. There exists a possibility of resonance for 2xND mode (110 Hz), but at speeds much beyond the normal operating regime.
- Spectrums of blades show that the dominant frequencies of blades near the operating speed are almost identical (103.5 and 110 Hz) even for blades having different frequencies in the static conditions. This happens since blades are having varying degree of interference fit or looseness at the root in the stationary condition which disappears at high speeds. Hence the dynamic characteristics of the stage can be established only by spin test and not with the tests in static condition.

References

1. "Reliability evaluation of shrouded blading using SAFE interference diagram", M.P. Singh, J. J. Vargo, Journal of Engineering for Gas Turbines and Power", October 1989, Vol. 111
2. "The development of turbine blading to achieve optimum vibration characteristics" McGuire P. M., Knipe W.H. Technical Report, GEC Alsthom
3. "Data Handbook Wireless Data Corporation", WDC-100, U.S.A. (1989)

Optimization of GTAW Process Parameters on Mechanical Properties of AA 7075-T6 Weldments

K.S. Pujari and D.V. Patil

Abstract This works mainly pertains to improvement in the mechanical properties of AA 7075-T6 aluminium alloy welds through gas tungsten arc welding (GTAW) process. Design of experimental technique Taguchi was applied to optimize GTAW process parameters of AA 7075-T6 aluminium alloy welded joints for improving the mechanical properties. Mathematical model was developed by Regression. Adequacy of developed model was checked by analysis of variance. The effect of heat treat on mechanical properties was also studied and an improvement in the mechanical properties was observed. Metallography of heat treated and non-heat treated welded joints correlated with the mechanical properties.

Keywords AA 7075-T6 · GTAW · Optimization · Taguchi method

1 Introduction

Among aluminium alloys, AA 7075 alloy has many attractive properties compared to other alloys; it is economical and versatile to use and high strength and light weight are the reasons it is very widely used in the aerospace, automobile and other industries [1–3]. Balasubramanian et al. [4, 5] says that there are many situations where in AA 7075-T6 plates are joined together with fusion welding in particular Butt welding. Karunakaran et al. [6] and Balasubramanian et al. [7] and Kumar et al. [8] found that pulsed current welding is beneficial to enhance the mechanical properties of the GTAW joints and grain refinement of welded joints, and are better compared to the continuous current welded joints. It is also found by Balasubramanian et al. [9] and Campana et al. [10] that AC pulsing current in GTAW is beneficial and frequency is more effective on the hardness.

K.S. Pujari (✉)
Department of Mechanical Engineering, KLS VDRIT, Haliyal 581329, India
e-mail: kalmesh49@gmail.com

D.V. Patil
Department of Mechanical Engineering, SDMCET, Dharwad 580003, India

Senthil Kumar et al [11] analyzed the influences of pulsed current parameters on tensile properties of pulsed current TIG-welded AA 6061 aluminium alloy, and it is found that peak current and pulse frequency have direct proportional relationship with the tensile properties of the welded joints. On the other hand, base current and pulse on time are having inversely proportional relationship with the tensile strength.

Karunakaran et al. [6] and Balasubramanian et al. [7] found that the maximum current gives sufficient penetration and bead contour, while the minimum current is set to maintain a stable arc. But Yarmuch et al. [13] found that maximum penetration occurs on the maximum cleaning setting, where the majority of each AC cycle is on electrode positive polarity. This is opposite to conventional expectations and occurs principally because the field emission characteristics of cold cathode materials that increase the energy input to the cathode [14].

From the literature review, it may be observed that, among all the optimization techniques Taguchi technique is most widely used, because of less number of experiments with more number of factors. The main objective of the present investigation is to optimize the GTAW process parameters for increasing mechanical properties of AA 7075-T6 alloy welded joints using Taguchi method.

2 Scheme of Investigation

In order to increase the mechanical properties of the welded joint, the present investigation has been carried out in the sequence. (a) Selection of the base material and filler wire material. (b) Identifying the important GTAW process parameters. (c) Finding the range of identified process parameters. (d) Selection of orthogonal array. (e) Conducting the experiment as per the selected orthogonal array. (f) Recording the mechanical properties. (g) Finding the optimal process parameters for increasing the mechanical properties. (h) Conducting the confirmation test. (i) Developing regression model for predicting the mechanical properties within the range. (j) Identifying significant process parameters. (k) Checking the adequacy of developed model and its validation. (l) PWA to the welded joints.

2.1 Selection of the Base Material and Filler Wire Material

In this investigation, AA 7075-T6 aluminium alloy of thickness 3.46 mm is selected as a base material. After exhaustive literature review, commercially available ER5356 is selected as filler material for welding AA 7075-T6.

2.2 Identifying the Important GTAW Process Parameters

From the literature review [9–12], the most important process parameters which are having greater influence on the mechanical properties of AC pulse GTAW process are: peak current (I_p), base current (I_b), welding speed (S), pulse frequency (F), pulse on time (P_{on}) and gas flow rate (GF).

2.3 Finding the Range of Identified Process Parameters

A several number of trials are conducted using 3.46 mm thick AA 7075-T6 samples to find out the feasible working range of AC pulsed current GTAW process parameters. Different combinations of AC pulse current parameters with argon gas are used to perform the trial runs. The working range of process parameters are selected by observing the bead contour, penetration, bead appearance. The working range of process parameters selected in the present study are shown in the Table 1a.

2.4 Selection of Orthogonal Array

In this study, six process parameters are selected that mainly affect the quality of welded joints. All the six process parameters are considered at three levels as shown in the Table 1, and three interactions are selected namely ($I_p \times I_b$), ($I_p \times S$) and ($I_b \times S$). The close three level orthogonal array accessible for satisfying the condition of selecting the OA is L_{27}. There are two trials for every experiment to reduce the noise.

Table 1 Working range and levels of the process parameters

Symbol	Process parameter	Units	Level-1	Level-2	Level-3
I_p	Peak current	Amps	195	200	205
I_b	Base current	Amps	93	98	105
S	Welding speed	mm/min	200	300	400
F	Frequency	Hz	4	6	8
P_{on}	Pulse on time	%	40	50	60
GF	Gas flow rate	Lit/min	9	10	11

2.5 Conducting the Experiment as Per the Selected Orthogonal Array

The base metal (AA 7075-T6) of size 250 mm × 150 mm × 3.14 mm have been prepared by chemical cleaning. The butt joint welds were made as per the orthogonal array L_{27}. Automatic GTAW machine has been employed for conducting the experiments. Welding was performed by preplacing the filler wire into the groove with mild steel back plate.

2.6 Recording the Mechanical Properties

The specimens for tensile test are taken from the middle of the weld joints. The specimens are prepared as per the ASTM-E8 specifications [12]. Tensile test is conducted on 60 ton universal testing machine (Model: FIE-Bluestar, UTES-60) at room temperature. Microhardness testing of the welded joint is done using Vickers Microhardness tester (Model: FMV-1: FSA-Make). The response values UTS, (YS), %EL and VHN of the welded joints were evaluated for all the conditions.

2.7 Finding the Optimal Process Parameters for Increasing the Mechanical Properties and Conducting the Confirmation Test

The Taguchi technique is applied to study the effect of individual process parameters independent of other process parameters, and also their interactions on the selected responses UTS, YS, %EL and VHN. The contribution of each process parameter and its interactions on responses is analyzed by statistical tool ANOVA. The optimal process parameter combination for each response was determined and it was found that same combination process parameters for all responses. Optimal responses values for optimal combination are presented in the Table 2. For validation of the optimal results, two trial experiments are conducted as per the optimal

Table 2 Optimum values of responses and validation of optimum results

Optimum condition	Responses	Optimum value	Experimental value
I_p-205A, I_b-93A, S-200 mm/min, F-6 Hz, Pon-60 % GF-11lit/min	UTS	367.38 MPa	365 MPa
	YS	276.826 MPa	275 MPa
	%EL	2.59 %	2.2 %
	VHN	118	114

combination, and results are presented in the Table 2. It is found that experimental values are closer to the optimal results.

2.8 Developing Regression Model for Predicting the Mechanical Properties Within the Range

The mechanical properties responses are function of peak current (I_p), base current (I_b), welding speed (S), frequency (F), pulse on time (P_{on}) and gas flow rate (GF). As per the ANOVA of means, for all mechanical properties responses UTS, YS.% EL and VHN, the significant process parameters are I_p, I_b, S, F, P_{on}. So the response function of mechanical properties is expressed as

$$\text{UTS}/\text{YS}/\%\text{EL}/\text{VHN} = f(I_p, I_b, S, F, P_{on})$$

2.9 Identifying Significant Process Parameters

The significant process parameters are determined by statistical tool ANOVA. From the ANOVA, it is found that except GF all other process parameters and their interactions are maximum percentage of contributions. The following empirical relationship is obtained to predict mechanical properties UTS/YS/%EL/VHN.

$$
\begin{aligned}
\text{UTS} = {}& 220.523 + 32.496(I_p) - 9.296(I_b) - 45.969(S) - 34.210(F) \\
& + 86.275(P_{on}) + 65.546(I_P^2) - 13.487(I_b^2) + 2.911(S^2) + 6.672(F^2) \\
& + 10.514(P_{on}^2) + 18.175(I_pI_b) + 25.942(I_pS) + 40.487(I_pF) - 64.546(I_pP_{on}) \\
& - 7.513(I_bS) + 5.643(I_bF) + 4.347(I_bP_{on}) + 38.391(SF) + 27.965(SP_{on}) \\
& R^2 = 94.78
\end{aligned}
$$

$$
\begin{aligned}
\text{YS} = {}& 203.528 + 29.944(I_p) - 4.769(I_b) - 24.468(S) - 6.766(F) \\
& + 62.421(P_{on}) + 20.566(I_P^2) + 12.365(I_b^2) - 24.385(S^2) - 30.098(F^2) \\
& - 12.165(P_{on}^2) + 10.494(I_pI_b) + 11.861(I_pS) + 37.903(I_pF) + 7.513(I_pP_{on}) \\
& - 30.661(I_bS) + 26.249(I_bF) - 2.123(I_bP_{on}) + 29.201(SF) + 38.268(SP_{on}) \\
& R^2 = 87.26
\end{aligned}
$$

$$\% \ EL = 1.361 + 0.003\left(I_p\right) + 0.113(I_b) - 0.325(S) - 0.002(F)$$
$$+ \ 0.358(P_{on}) + 0.500(I_P^2) + 0.09694(I_b^2) + 0.134(S^2) + 0.022(F^2)$$
$$- \ 0.047(P_{on}^2) + 0.035(I_pI_b) + 0.071(I_pS) + 0.152(I_pF) + 0.038(I_pP_{on})$$
$$+ \ 0.238(I_bS) + 0.093(I_bF) + -0.131(I_bP_{on}) + 0.177(SF) + 0.198(SP_{on})$$
$$R^2 = 90.45$$

$$VHN = 81.638 + 6.00(I_p) - 0.916(I_b) - 10.250(S) - 4.625(F)$$
$$+ \ 15.500(P_{on}) + 11.500(I_P^2) - 0.916(I_b^2) + 4.250(S^2) + 2.125(F^2)$$
$$+ \ 2.500(P_{on}^2) + 3.925(I_pI_b) + 6.421(I_pS) + 6.500(I_pF) - 10.4167(I_pP_{on})$$
$$- \ 2.083(I_bS) + 1.886(I_bF) - 2.119(I_bP_{on}) + 6.197(SF) + 2.300(SP_{on})$$
$$R^2 = 92.44$$

2.10 Checking the Adequacy of Developed Model and Its Validation

It is observed that coefficient of correlation (R^2) for all the developed mathematical model is more than 80 %. Hence, developed mathematical models are adequate and can be used to predict the mechanical properties. An observation is made at different combinations of AC pulse GTAW process parameters within the limit of investigation and corresponding predicted value as per the Taguchi technique and Regression model are determined by the developed mathematical model and it is given in the following Table 3. It is observed that the difference between predicted values and actual values is small. Hence the developed model is adequate within the selected range of investigation.

Table 3 Predicted values of mechanical properties

AC pulse GTAW process parameters	Responses	Predicted value		Actual value
		Taguchi	Regression	
I_p-205A, I_b-93A, S-200 mm/min, F-6 Hz, P_{on}-60 % GF-11 lit/min	UTS (MPa)	367.38.	362.23	365
	YS (MPa)	276.82	265.82	275
	%EL	2.59	2.01	2.2
	VHN	118	120	114

3 Heat Treatment of Welded Joints

The base metal AA 7075-T6 contains Copper (Cu) and has a wide melting range with a low solidus temperature [12, 13] and it is very sensitive to weld cracking. During welding, the Weld zone (WZ), Interaction (IZ) and Heat affected zone (HAZ) comes across heating and cooling at high temperature. So, ageing is sufficient to improve the strength of welded joints. The ageing treatment T6 temper is carried out at temperature −140 °C, and time 10 h on welded joints. Table 4 shows tensile properties of as welded (AW) and postweld age (PWA) joints. Significant improvements in YS, UTS and %EL are observed for the PWA joints over the AW joints. The joint efficiency of AW joint is 57.40 %. After PWA treatment, the joint efficiency is increased to 58.00 %. This indicates that there is increase in strength of weld joint values due to the changes in microstructures. This increase in strength due to a higher amount of precipitates in PWA joints is compared to AW joints (Fig. 1). In AW condition, the %EL with filler wire ER5356 is 1.240. After PWA treatment, the %EL is increased to 3.751. There is significant increase in %EL due to PWA of welded joints; this is because of the variation in the microstructure (Fig. 1).

It has been studied and the following conclusions were made. The similar optimal combination (i.e. I_p-205 A, I_b-93 A, S-200 mm/min, F-6 Hz, P_{on}-60 %, and GF-11 lit/min) observed in all the mechanical properties of welded joints.

Table 4 Tensile properties of as welded (AW) and post weld age (PWA) joints

Joint type	YS (MPa)	UTS (MPa)	EL (%)	Joint efficiency (%)	Region of failure
BM	473.875	527.227	8.858	–	–
AW joint	164.418	302.663	1.240	57.40	WZ
PWA joint	178.875	306.187	3.751	58.00	WZ

(a)   **(b)**
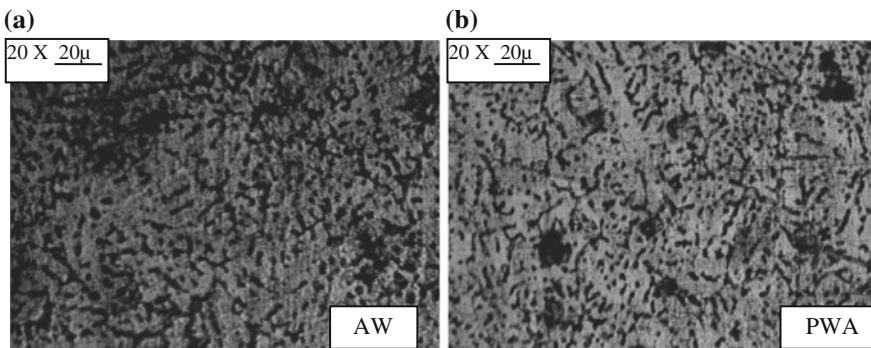
Fig. 1 The micrograph of AW and PWA weld zone

4 Discussion

The main objective of the paper is to emphasize on the quality responses namely UTS, YS, %EL and VHN with minimum number of experiments. Similar optimum condition is observed for all responses. After conducting tensile test over the welded specimen, it was observed that the entire welded specimen fails at weld zone. So, tensile properties are the properties of the weld joint. From the ANOVA, it is found that process parameter 'Pon' shows higher percentage of contribution on all responses compared to other process parameters. Hence, the effect of pulse on time has more influence on mechanical properties of the welded joints. Also it is found that interactions $(I_p \times I_b)$, $(I_p \times S)$ and $(I_b \times S)$ are moderately effective on all quality responses; so they also significant.

5 Conclusion

The effect of pulsed GTAW process parameters such as I_p, I_b, F and P_{on} mechanical properties UTS, YS, %EL and VHN of AA 7075-T6 weld joints. The behaviour of the welded joints in optimal condition (i.e. I_p-205 A, I_b-93 A, S-200 mm/min, F-6 Hz, P_{on}-60 %, and GF-11 lit/min) leads to increase in mechanical properties of the welded joints; this is due to the formation of Mg_2Al_3 precipitates as shown in the metallographic view Fig. 1a. From the metallographic (Fig. 1b) view, it also reveals the fine grain structure at the weld zone which leads to increase in mechanical properties. It is also observed that there is improvement in the mechanical properties of the welded joint after heat treatment. The mechanical properties YS increases from 164.418 to 178.875 Mpa and UTS increases from 302.663 to 306.187 MPa, %EL increases from 1.240 to 3.75 %; this is mainly due to the increased precipitation of the weld zone as shown in the Fig. 1a. Mathematical models were developed to predict mechanical properties such as UTS, YS, %EL and VHN within the selected range of GTAW process parameters. The developed model is very useful in the industry for predicting mechanical properties pulse GTAW joints of AA 7075-T6 alloy.

References

1. D. Reddy A, (2007) "Characterization of Mechanical properties and study of microstructures of stir welded joint" PhD thesis. University Of Missouri.
2. Alcoa mill products, Bettendorf, IOWA 52722,(800)523-9596, www.mill-alcoa.com
3. Alexander Grant Paleocrassas, (2009) "Process Characterization of Low Speed, Fiber Laser Welding of AA 7075-T6 PhD thesis". North Carolina State University, Raleigh.

4. V. Balasubramanian,V. Ravisankar, "Effect of Postweld Aging Treatment on Fatigue Behavior of Pulsed Current Welded AA 7075" Journal of Materials Engineering and Performance Volume 17(2) April 2008—225.
5. V. Balasubramanian, V. Ravisankar. "Effect of pulsed current and post weld aging treatment on tensile properties" Materials Science and Engineering A 459 (2007) 19–34.
6. N. Karunakaran, V. Balasubramanian. "Effect of pulsed current on temperature distribution, weld bead profiles and characteristics of gas tungsten arc welded aluminum alloy joints" Trans. Nonferrous Met. Soc. China 21(2011) 278 − 286.
7. M. Balasubramanian, V. Jayabalan. "Prediction and Optimization of Pulsed Current Gas Tungsten Arc Welding Process Parameters" Journal of Materials Engineering and Performance. Volume 18(7) October 2009—871.
8. A. Kumar, S. Sundarrajan "Optimization of pulsed TIG welding process parameters on mechanical properties of AA 5456", Materials and Design 30 (2009) 1288–1297.
9. M. BalasubramanianV. Jayabalan V. Balasubramanian "Effect of Pulsed Current Gas Tungsten Arc Welding Parameters" *J. Manuf. Sci. Eng.* 131(6), 064502 (Nov 05, 2009)
10. M.A.R. Yarmuch and B.M. Patchett "Variable AC Polarity GTAW Fusion Behavior in 5083 Aluminum" Welding Research 200-s July 2007, Vol. 86.
11. T. Senthil Kumar,V. Balasubramanian, M.Y. Sanavullah. "Influences of pulsed current tungsten inert gas welding parameters on the tensile properties" J Mater Materials and Design 28 (2007) 2080–2092.
12. Welding Robots technology" system issues and application, Pires J. N. Lourerio,VIII,180p,88, Hardcover,ISBN-978-1-85233-953-1, 978-1-953-1
13. M.A.R. Yarmuch and B.M. Patchett "Variable AC Polarity GTAW Fusion Behavior in 5083 Aluminum" Welding Research 200-s July 2007, Vol. 86
14. Ahmed Khalid Hussain, Abdul Lateef, Mohd Javed,. "Influence of Welding Speed on Tensile Strength of Welded Joint in TIG Welding Process". International Journal Of Applied Engineering Research, Dindigul Volume 1, No 3, 2010.

Experimental Investigation on the Effectiveness of Active Control Mechanism on Base Pressure at Low Supersonic Mach Numbers

Zakir Ilahi Chaudhary, Vilas B. Shinde, Musavir Bashir and Sher Afghan Khan

Abstract In the current investigation, the experiments were carried out to evaluate the effectiveness of microjets in controlling the base pressure from a convergent-divergent nozzle at low supersonic Mach at different expansion level. Tests were carried out for low supersonic Mach numbers 1.25, 1.3, 1.48, and 1.6 while nozzle pressure ratio ranges from 3 to 11. The jets are augmented abruptly into an axisymmetric circular channel with different cross-sectional areas as that of nozzle exit area. The results show that the proficiency of the microjets is only marginal in controlling the base pressure even under the influence of favorable pressure gradient at lower NPRs namely 3 and 5. It was also observed that for higher values of the NPRs such as 7, 9, and 11, the dynamic control by very small jets results in rise of base pressure for the different values of the *L/D* ratios of these investigations. For NPRs 5 and 7, the trend differs due to the level of expansion, nature of waves present in the base region, relief available to the flow, length to diameter ratio of the enlarged duct, and the Mach numbers. It is seen that most of the cases exhibit similar behavior for higher as well as the lower length to diameter ratios, which

Z.I. Chaudhary (✉)
Department of Mechanical Engineering, Datta Meghe College of Engineering,
Airoli, Navi Mumbai, India
e-mail: zakirilahi@gmail.com

V.B. Shinde
NHITM, Thane, India

V.B. Shinde
Mechanical Engineering, DMCE, Airoli, Navi Mumbai, India

M. Bashir
School of Aerospace Engineering, University Sains Malaysia,
Penang, Malaysia

S.A. Khan
Faculty of Engineering, Department of Mechanical Engineering, IIUM,
Kuala Lumpur, Malaysia
e-mail: sakhan@iium.edu.my

means; that the back pressure has not adversely influenced the flow field in the base region as well as in the duct. With this it can be stated that the microjets can be an alternative for the experimentalist for base pressure control in the form of microjets.

1 Introduction

The discipline of "Base Flow Aerodynamics" is capturing a lot of attention in the past few years. The examination of base flow behind aerodynamic vehicles is necessary to know the flow separation phenomenon, which leads to the formation of a low-pressure circulation region near the base. The rocket's exhaust will interact with the supersonic external flow and worsen the performance of launchers and projectiles, and base flow is the trigger. The role of base flow will be even more important to decide the performance relative to the external flow, if the advanced future nozzle mechanics, such as spike nozzle, is considered. In order to comprehend the parameters of base flow aerodynamics, more experiments are carried out and new applications are chosen. In case of flow separation, the notable difference in pressures is ample compared to the total drag on the body at Transonic Mach numbers. It is observed that the base drag is around 10 % of the skin-friction drag in the sub-sonic flow as the wave drag will be zero. To further increase the base pressure, which decreases the base drag, one can think of different geometrical shapes like boat tails, additional cavities, vented cavities, ribs, splitter plate, sting and disks, or application of base bleed and base combustion. However, the studies of base drag reduction with active control has not been studied much, therefore we will study the problem with an internal flow.

As stated, numerous techniques have been analyzed to control the flow separation, hence base drag either by preventing it or by reducing its effects. Quite a few researchers have used the passive techniques like splitter plate, ribs at the base region of the enlarged duct, acoustic excitation, step body, locked vortex, but very less efforts have been put in on dynamic control approaches. Therefore, in the present work, an effort is made to examine the base pressure manipulation with active control with the help of microjets under the effect of favorable, unfavorable pressure gradient and for ideally expanded cases; at high supersonic Mach numbers with microjets (Fig. 1).

Considering the accomplishment of efficient designs in order to minimize drag, control the separation phenomenon, and insight of complex flow fields, numerous flow control methods have been envisioned in the past two decades [1]. The aerodynamic forces are mainly lorded by separation over the posterior slope, the base region, and two longitudinal vortices developed on the side [2–4]. The sudden augmentation of air in a duct results in base pressure and noise [5]. When the flow remains attached, the base pressure showed minimum value, which depends mainly
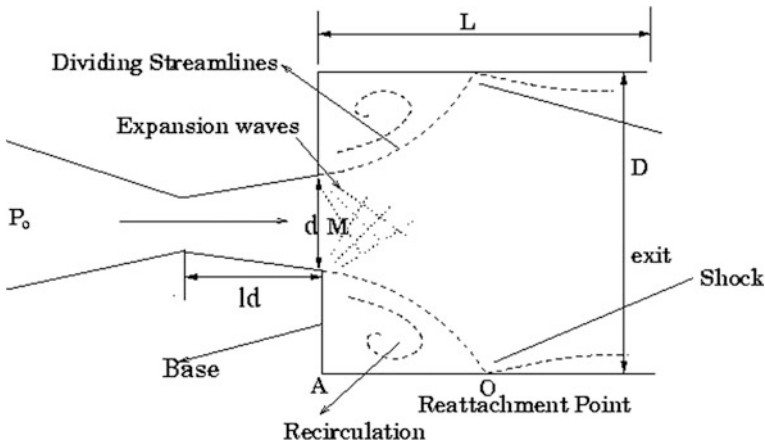
Fig. 1 Flow pattern in abrupt expansion

on the duct to nozzle area ratio and on the geometry of the nozzle. A specific configuration of jet flow has found applications as a combustion burner in many industries [6]. To accomplish the aforesaid goals, various passive [7] and active control methods [8] have been adopted over the past two decades to mitigate the challenging factors. Among these techniques, the most assenting design was the use of active control mechanism of microjets because of its versatility and cogency.

The proficiency of microjets to restrain the base pressure in abruptly augmented axisymmetric ducts is studied by Khan et al. [9–13]. From the experimental results, it was found that the microjets can serve as active controllers for base pressure. Also, the very small jets do not upset the flow pattern in the enlarged duct as seen while scanning the wall pressure distribution. Syed Ashfaq et al. [14, 15] investigated the effect of nozzle parameters correctly and under expanded jets, and concluded that the control in the form of the very small jets is quite successful. One of the reason for this behavior could be due to the lowest area ratio; the space available for the flow to create the suction is the lowest and the vortex sitting at the base whose strength is constant is able to influence the base region very effectively leading to very low level of base pressure and also; when we observed the wall pressure it is found that the wall pressure is low and oscillatory in nature and this trend of wall pressure having waviness was observed for all the NPRs and Length to Diameter ratio. It is also observed that this waviness nature is very strong at higher NPRs as compared to the lower NPRs. The investigated results were presented to restrain the base pressure from a convergent nozzle under the influence of favorable pressures variation at sonic Mach number.

In this study, we examine the use of microjet-based control in a suddenly expanded axisymmetric duct; especially the aim is to control the base pressure in the supersonic regime, which appears to be very promising. We will evaluate the microjet efficiency to reduce the base drag and to gain some insight in the mechanism behind this approach.

2   Experimental Method

A schematic of the experimental setup is depicted in the Fig. 2. Eight very small jet holes were used for dynamic flow control of base pressure. The pressure energy was extracted from the main settling chamber by utilizing a tube coupling the main settling chamber with the control chamber. To measure the wall pressure distribution, wall pressure taps were provided on the enlarged duct. Starting from the base region, initially nine holes were made at a small gap (as the major activity will take place within the reattachment length) and remaining holes were made at a comparatively bigger gap.

Further, the experimental setup consisted of an axisymmetric convergent-divergent nozzle having exit diameter as D_1 followed by a concentric axisymmetric duct of larger diameter of diameter D_2, and the ratios of the diameter (i.e., D_2/D_1) are in the range from 1.6 to 2.5. Eight microjets of 1 mm diameter were used as control mechanism. The maximum Mach number at the exit of the orifice of the microjets will be unity. At the exit, diameter of the nozzle was kept fixed (i.e., 10 mm) and the diameter ratio of the model was 1.6, 1.8, 2.2, and 2.5. Brass pipe was used to fabricate the suddenly expanded ducts. The duct has a maximum $L/D = 10$ and the lower L/Ds were achieved by cutting the length after testing a particular L/D. However, the results presented in this paper are for Length to Diameter ratio of 10, 8, 6, and 5, though the experiments were performed for 10–1.

PSI model 9010 pressure transducer was employed to measure the pressure in the control chamber, the stagnation pressure in the main settling chamber and the pressure at the base as well as wall pressure for ten locations. It has 16 channels and pressure range is 0–300 psi. It displays the reading after averaging 250 samples per
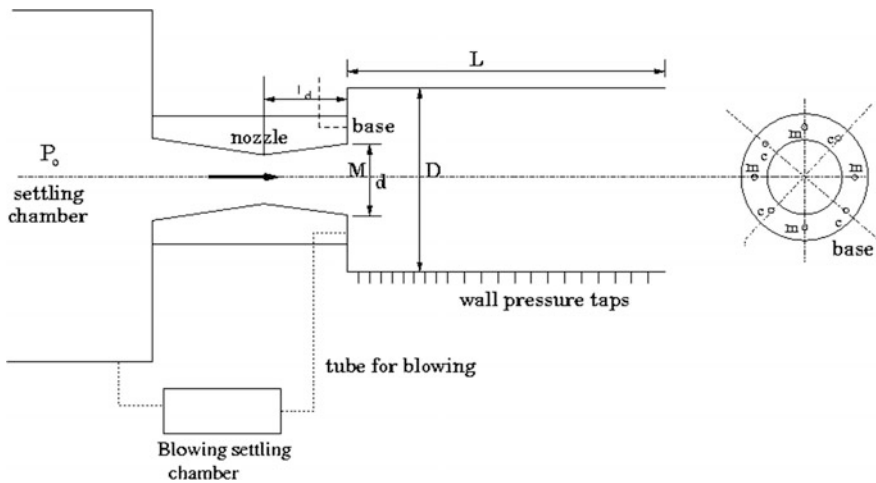
Fig. 2 Experimental setup

second. To interface the transducer with the computer, software is provided by the manufacturer. The user-friendly menu-driven software obtains data and displays the pressure readings from all the 16 channels simultaneously on the computer screen.

3   Results and Discussions

The plots of base pressure with length to diameter ratio are presented in Figs. 3 and 4, for four area ratios for NPRs in the range from 3 to 11 for Mach numbers 1.25, 1.3, 1.48, and 1.6. It is already acknowledged that when the sub-sonic jets leave the nozzle, they are always correctly expanded whereas, when the supersonic jets are exiting from the nozzle the jet will be under, over, or correctly expanded depending upon the level of expansion. We have calculated the values of the NPRs for correct expansion from the isentropic relations and the NPR values are 2.59, 2.71, 3.57, and 4.25 for the Mach numbers as stated above. While presenting the results of base pressure, we have taken minimum Length to Diameter ratio as 3. This minimum value of $L/D = 3$ was selected from the point view to ensure that the flow remained attached with the enlarged duct wall. While scanning the wall pressure results, it was observed that $L/D = 3$ is sufficient for the flow to remain attached with the abruptly expanded duct for all the Mach numbers and NPRs of the present investigations. While analyzing the results, it is also to be kept in mind that the reattachment length is function of the area ratio to which the jet is exhausted; the reattachment length will increase progressively with increase in the area ratio. Since for a given Mach number and the NPR, only the area ratio is changing and hence the effect of area ratio is clearly reflected in the results. Therefore, with the increase in area ratio, the relief to the flow will increase but the strength of the vortex will be the same, hence the value of the base pressure will be varying even though the inertia level and the level of expansion remains the same.

It is well known from the literature that the active/passive controls perform better in the presence of favorable pressure gradient. In the present study, the combined effect of favorable pressure gradient and the relief due to area ratio on the active control effectiveness is investigated. The percentage variation in base pressure as function of L/D ratio and area ratio are depicted for NPR 3, 5, 7, 9, and 11. Figure 3 presents the results of base pressure for Mach 1.25 and 1.3 for various NPRs and area ratios for L/D ratio in the range from 3 to 10 for NPR 3 (Fig. 3a, b). It is seen that at this NPR, the jets are slightly under-expanded and an expansion fan will be present at the nozzle exit, for lowest area ratio, the gain is marginal and for the remaining area ratio the microjets are not effective.

When we see the results for NPR = 5 the jets are under-expanded and the level of under-expansion are 1.93 and 1.84, respectively, and the effectiveness of the microjets has improved considerably. The general trend is that, for lower area ratio
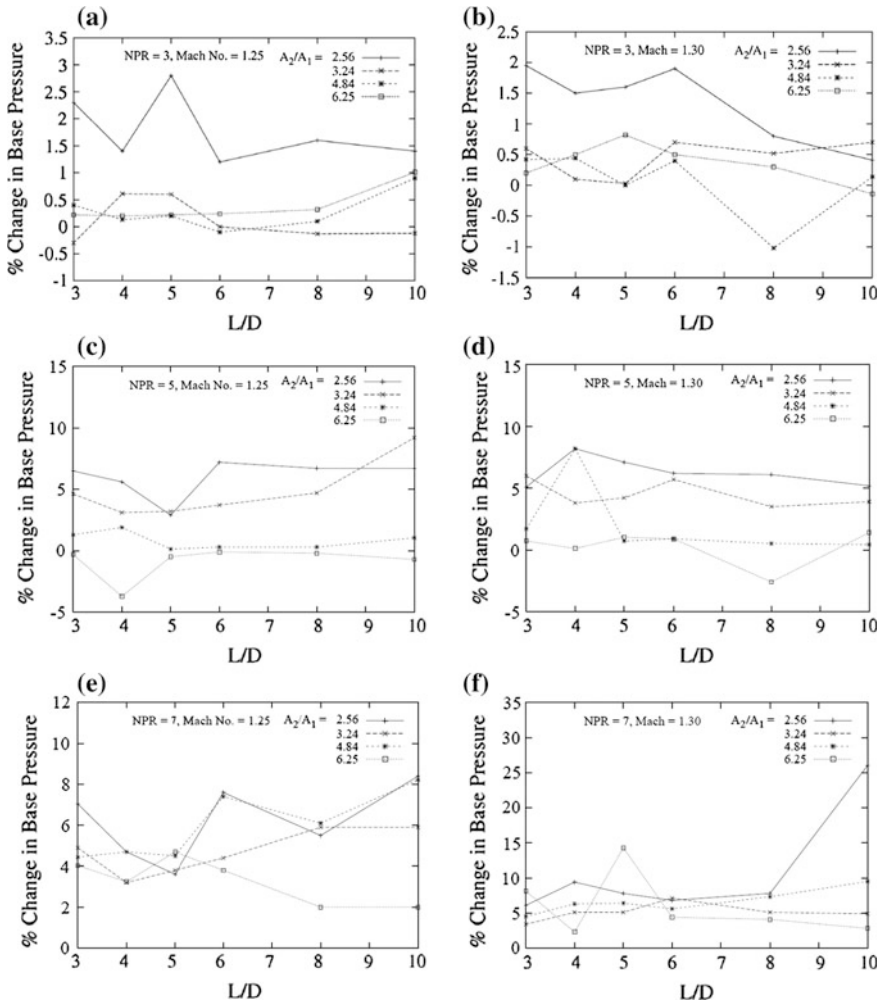
Fig. 3 Base pressure versus *L/D* ratio

2.56 and 3.24 the gain is on the positive side however, for remaining area ratios the control results in decrease of base pressure. When the NPR is further increased to the values 7, 9, and 11 there is no appreciable increase in the base pressure. The reason for this trend could be that though the control becomes effective under the influence of favorable pressure gradient as mentioned in the literature, if we go on increasing the level of under-expansion the control effectiveness will not increase in the same proportion, and hence; the same is reflected in the base pressure results at NPR 7, 9, and 11.
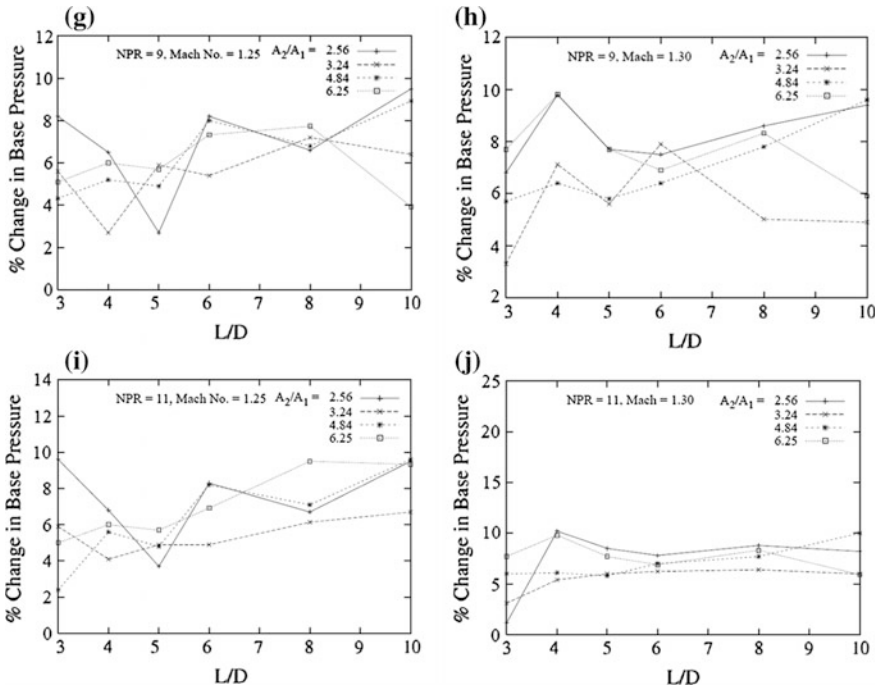
Fig. 3 (continued)

The results for Mach numbers 1.48 and 1.6 are illustrated in Fig. 4i–x. From the figure, it is observed that at NPR = 3, results show similar trends as discussed except the marginal increase in the magnitude of the base pressure and this increase is attributed due to the increase in the inertia level at the nozzle exit and at this situation there will be a weak shock at the nozzle exit and the shear layer coming out of the nozzle will hardly be deflected towards the nozzle center line by the shock. It may cause delayed reattachment and a longer reattachment length compared to a case without a shock. It is well known that the reattachment length is a parameter, which strongly influences the base vortex, the increase or decrease of reattachment length will modify the base pressure level in the base region. From the figure it is seen that control effectiveness is only marginal and the reason for this trend is mainly due to the level of expansion. At this NPR, jets are over expanded and the level of expansion is 0.84 and 0.71. The results at NPR 5, jets are under-expanded and there is substantial improvement in the effectiveness of the microjets for the last two higher area ratios and for the lower area ratios the gain is only marginal.

However, at higher NPRs such as 7, 9, and 11 there is observable rise in the level of under-expansion but the same is not reflected in the effectiveness of the microjets
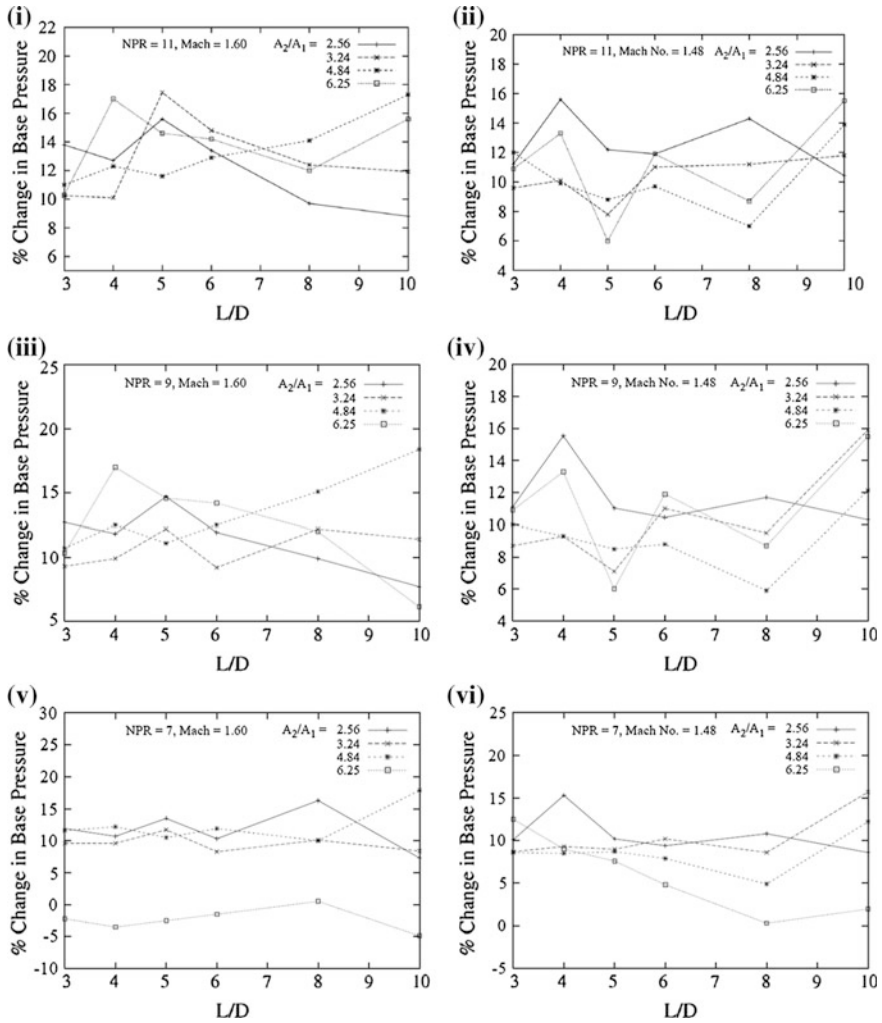
Fig. 4 Base pressure versus *L/D* ratio

and the gain remains between 15–20 % and further increase in NPRs does not yield any fruitful results. The change in the behavior is due to the higher NPRs and making jets highly-under expanded does not ensure that the effectiveness will get enhanced in the same ratio as discussed earlier. This indicated that once the level of under-expansion is in the range of 1.5–20 and will yield the best results. Figure, further indicates that the results show oscillatory nature; this may be due to the
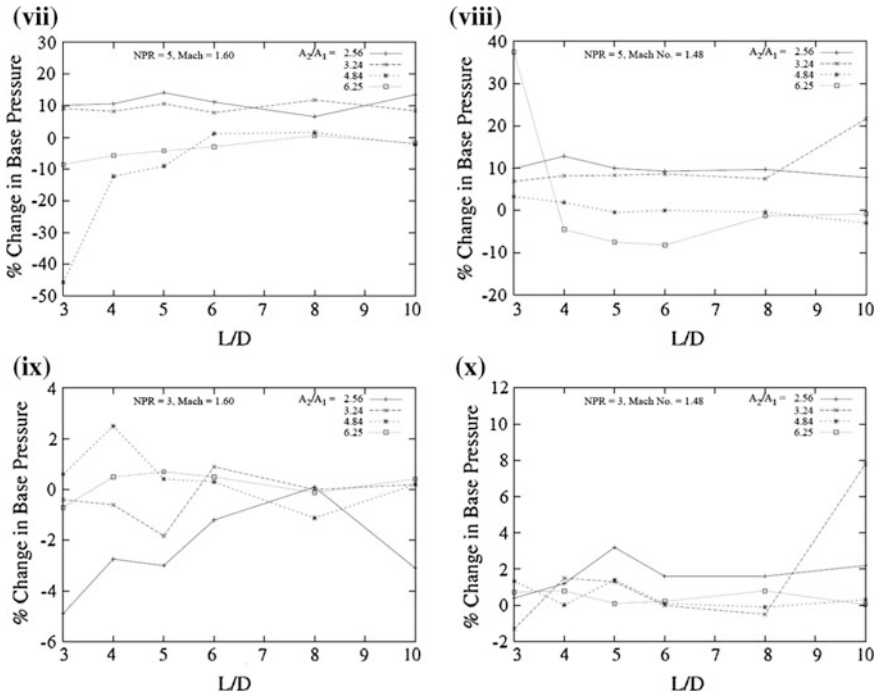
Fig. 4 (continued)

presence of oblique shock waves, weak waves, and expansion fan at different NPRs depending on the level of expansion. These results are clearly visible in Fig. 4i–x. It is evident that increase in relief to the flow simply indicates that relaxation space existing for the flow is increasing. This sort of relief will make the shock/expansion waves at the nozzle lip to spread relatively more freely with increase of relief at the lip of nozzle/area ratio.

Figure 5a–h presents the base pressure results as a function of NPR for all the Mach numbers and L/D ratios for the lowest area ratio of the present study. In this case, the NPR ranges are such that the flow remains under-expanded except at Mach 1.48 and 1.6 and NPR = 3, and it is also seen that the level of under-expansion increases with progressive increase in the NPR but there is such enhancement in the performance of the microjets; this could be due to the fact that the reattachment length is very small and the vortex positioned at the base remains powerful and the control is able to influence marginally. A maximum increase in the base pressure achieved is around 18 % at Mach 1.6, and for the all other Mach numbers this remains around 8–10 %.

Wall pressure results are shown in Fig. 6a–f. We have selected only Mach 1.25 to show a qualitative representation. Further, it is seen that wall pressure remains the same with and without control. Hence, we can say that the control in the form of microjets does not make the flow oscillatory.
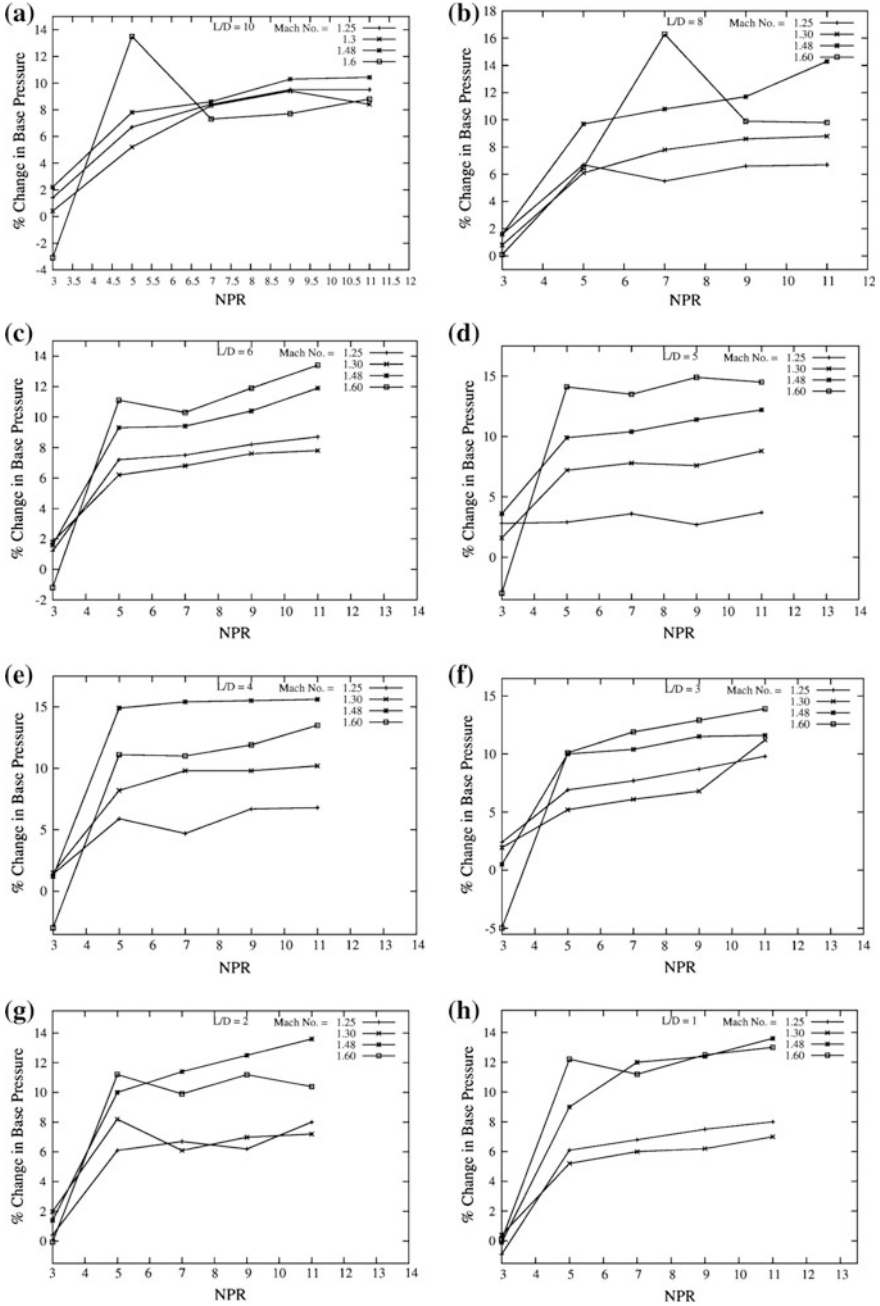
Fig. 5 Base pressure versus NPR
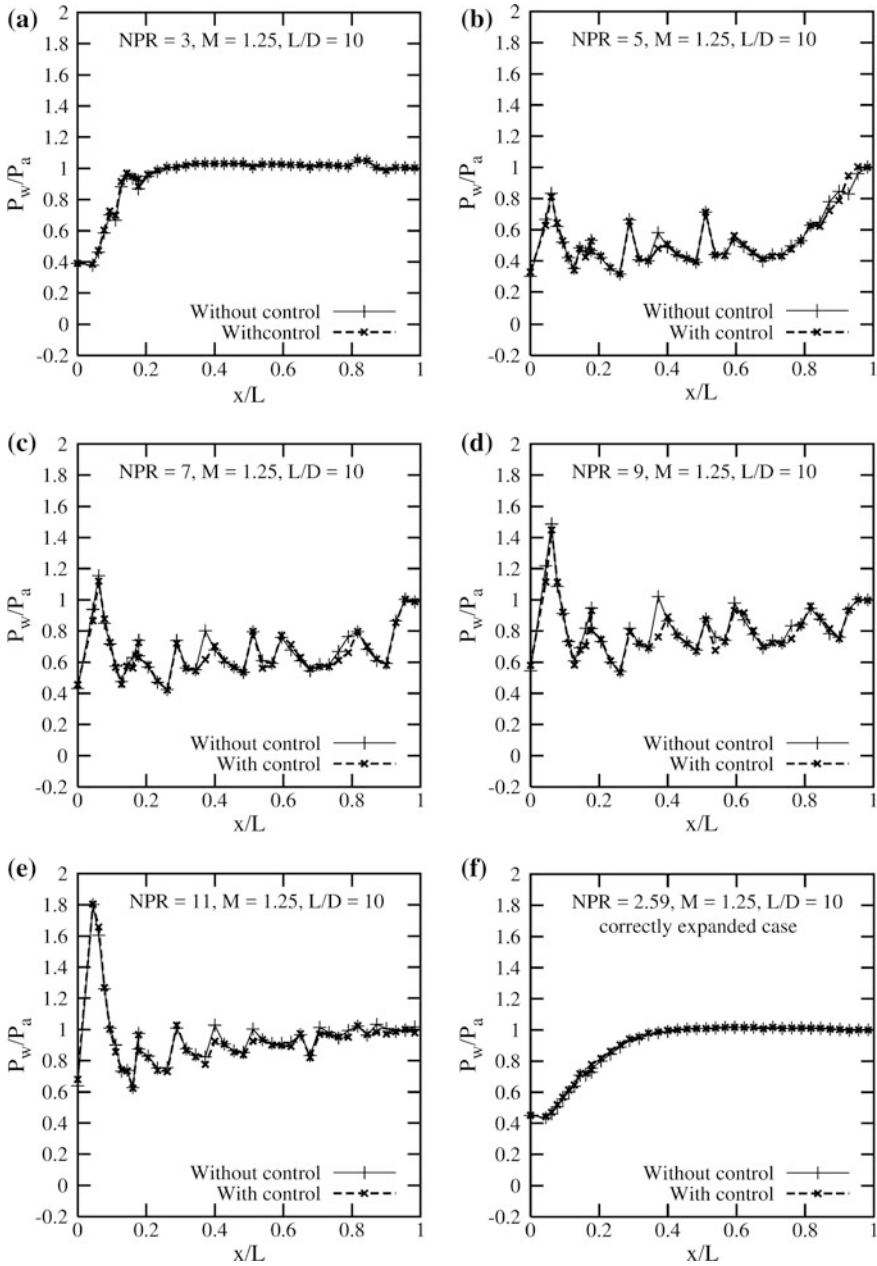
Fig. 6 Wall pressure distribution in the enlarged duct

4   Conclusion

The results show that the effectiveness of the very small jets is minimal in controlling the base pressure whenever jets are over expanded at NPR 3 for higher Mach numbers. It is also seen that even under the influence of favorable pressure gradient at lower Mach numbers NPRs namely 3 and 5, results maximum gain in the base pressure and further increase in NPR unable to moderate the base pressure value. An important point to be observed is that, unlike passive controls, the favorable pressure variation would not necessarily give expected results for dynamic control in the form of very small jets. At NPRs 5, the trends are different due to the level of expansion, nature of waves present at the base, relief available, Length to Diameter ratio, and Mach numbers.

It is seen that most of the cases show the similar trend for higher as well as the lower *L/Ds*, which means that the back pressure has not badly affected the flow field in the base region as well as in the duct. With this it can be stated that the microjets can be an alternative for the researchers, as base pressure control by microjets do not impose any adverse impact in the flow field at the base region as well as in the enlarged duct.

References

1. M. Gad-el Hak and A. Pollard. Flow Control: fundamentals and practices. Lecture notes in physics. New series m, Monographs, m53. Springer, 1998.
2. J. Favier, L. Cordier, A. Kourta, Sur l'optimisationD'actionneurs pour le contrôled' écoulements Mécanique & Industries 8, n° 3, 259–265, 2007.
3. M. Rouméas, P. Gilliéron, A. Kourta, "Drag Reduction by flow separation control on a car after body", *Int. J. Numer. Meth. Fluids* (2008) doi 10.1002/fld.1930
4. V. Boucinha, P. Magnier, A. Leroy-Chesneau, R.Weber, B. Dong et D. Hong, "Characterization of The Ionic Wind Induced by a Sine DBD Actuator Used for Laminar-to-Turbulent Transition Delay By LDV", 4th AIAA Flow Control Conference Seattle (USA), 23–26/06 2008
5. S. J. Anderson T. J. Williams. Base pressure and noise produced by the abrupt expansion of air in a cylindrical duct. *Archive Journal of Mechanical Engineering Science* 1959–1982 (VOLS 1–23) 10(3):262–268 · JUNE 1968
6. Green S (ed) (1995) Fluid vortices. Kluwer Academic Publishers, the Netherland.
7. R. Elavarasan, A. Krothapalli, L. Venkatakrishnan, and L. Lourenco. Suppression of self-sustained oscillations in a supersonic impinging jet. *AIAA Journal*, 39(12):2366–2373, 2002.
8. F. S. Alvi, C. Shih, R. Elavarasan, G. Garg, and A. Krothapalli. Control of supersonic impinging jet flows using supersonic microjet. *AIAA Journal*, 41(7):1347–1355, 2003.
9. S. A. Khan and E. Rathakrishnan, Active Control of Suddenly Expanded Flows from Over expanded Nozzles, *International Journal of Turbo and Jet Engines (IJT)*, Vol. 19, No. 1–2, pp. 119-126, 2002.
10. S. A. Khan and E. Rathakrishnan, Control of Suddenly Expanded Flows with Micro Jets, *International Journal of Turbo and Jet Engines (IJT),* Vol. 20, No. 2, pp. 63–81, 2003.

11. S. A. Khan and E. Rathakrishnan, Active Control of Suddenly Expanded Flow from Under Expanded Nozzles, *International Journal of Turbo and Jet Engines, (IJT),* Vol. 21, No. 4, pp. 233–253, 2004.
12. S. A. Khan and E. Rathakrishnan, Control of Suddenly Expanded Flow from Correctly Expanded Nozzles, *International Journal of Turbo and Jet Engines (IJT),* Vol. 21, No. 4, pp. 255–278, 2004.
13. S. A. Khan and E. Rathakrishnan, Control of Suddenly Expanded Flow, Aircraft Engineering and Aerospace Technology: *An International Journal,* Vol. 78, No. 4, pp. 293–309, 2006.
14. Syed Ashfaq, S. A. Khan and E. Rathakrishnan, Active Control of Flow through the Nozzles at Sonic Mach Number, *International Journal of Emerging Trends in Engineering and Development,* Vol. 2, Issue-3, pp. 73–82, 2013.
15. Syed Ashfaq, S. A. Khan and E. Rathakrishnan, Control of Base Pressure with Micro Jets for Area Ratio 2.4, *International Review of Mechanical Engineering (IREME),* Vol. 8. n. 1, pp. 1–10, January 2014.

A Review on the Trends and Developments in Hybrid Electric Vehicles

C. Parag Jose and S. Meikandasivam

Abstract The paper aims at reviewing the history, the development, and the current scenario of hybrid electric vehicle (HEV). HEVs have their origin back in the mid-nineteenth century and even though it had gone through a lot of ups and downs, today it is at a revolutionary stage. The excessive usage of fossil fuels and the depleting atmospheric conditions has proven HEVs to be the most viable alternative. This paper goes in detail analyzing the origin of HEVs, their growth and debacle, the current stage of HEVs, and the social and economic impact it can have on the modern world. The paper also draws light on the future technologies that can be implemented in HEVs which can hence make Earth greener. The advancement in the field of power electronics and drives, and new fast charging and slow discharging, durable batteries have in fact made the HEVs to be more economical and more efficient.

Keywords HEV · PHEV · Energy storage systems · Power converters · Wireless power transfer

1 Introduction

The invention of wheel has been the turning point in the history of mankind when man identified that there were faster means by which they could move from one place to another. Being food gatherers and agriculturists, this gave man an insight that unexplored ideas and paths existed, which would make their harsh life easier. But the trails were tiring and cumbersome. It was not until late seventeenth century that the first steam-powered vehicle was invented. A member of a Jesuit mission in

C. Parag Jose (✉) · S. Meikandasivam
Power System Division, School of Electrical Engineering (SELECT),
Vellore Institute of Technology, Vellore, India
e-mail: paragjose@gmail.com

S. Meikandasivam
e-mail: meikandasivam.s@vit.ac.in

China, Ferdinand Verbiest, built the first steam-powered toy vehicle around 1672 for the Chinese Emperor. But it was not until late eighteenth century that Nicolas-Joseph Cugnot developed steam-powered vehicles capable of goods and human transport. It was in the year 1789 that the first automobile patent in the United States was granted to Oliver Evans. By 1801, Richard Trevithick, a British engineer and mining expert was running a full-sized vehicle on the roads in Camborne, England. The nineteenth century saw a big boom in the field of vehicle industry. In 1807, François Isaac de Rivaz designed the first car powered by an internal combustion engine fuelled by hydrogen. By this time, lots of new features like hand brakes, multi-speed transmission, horns, better steering, and even four wheel drives were added in the vehicles. In 1886, the first petrol or gasoline-powered automobile, the Benz Patent-Motorwagen, was invented by Karl Benz [1]. This was the first mass production vehicle and became the brand of vehicle industry. The vehicle industry grew from there and by the end of twentieth century V8 engines, multiaxle vehicles, power breaks, power steering, and other features were developed which made driving vehicle more popular. But with increase in popularity and cheap vehicles, the business improved and many car companies came up. The vehicles were sought out for comfort travel, for transporting goods, and even for racing. But the main victim of this boom in vehicle industry was the environment. The fuel for operating the vehicle was mostly fossil fuels, which was extracted in abundance. But this proved to be a big mistake as humans became completely dependent on fossil fuels for vehicle powering. The reckless usage not only depleted the amount in huge quantities, but also started bringing about atmospheric consequences [1–4].

2 History of Hybrid Electric Vehicles

The dependency on fossil fuels were so huge that during mid-1960s to mid-1970s, when the OPEC nations imposed an oil embargo on the Western countries in response to their involvement in the Yom Kippur War lead to the increase in oil prices form $3 per barrel to nearly $12 globally. It proved to be an eye opener to the world countries as they understood that too much dependency on fossil fuels can prove to be of very bad consequences as their economy was held at ransom by the decision of the OPEC countries. This lead to a surge in finding viable alternatives for fuel resources and vehicle industry in particular. Electric vehicle was sought out. Even though the history of electric vehicles ranges back to the early nineteenth century, it was not popular among the general masses. A Hungairan, Ányos Jedlik, developed a model car powered by an electric motor in 1828. In 1834, Vermont blacksmith Thomas Davenport built a similar electric vehicle which operated on a short, circular, electrified track [5].

In 1835, Professor Sibrandus Stratingh, from the Netherlands and his assistant Christopher Becker created a small-scale electrical car, powered by non-rechargeable primary cells. The first-known electric car was built in 1837 by chemist

Robert Davidson of Aberdeen. It was powered by galvanic cells (batteries). Even though during this period the electric vehicle could draw a lot of attention, it soon proved to get notorious as the batteries had to be replaced as it got exhausted very fast. This proved to be a big economic burden for the vehicle owners. The electric vehicle had suffered a big blow. But in 1859, a French physicist Gaston Planté developed rechargeable lead–acid batteries that provided a viable means for storing electricity on-board a vehicle. By 1881, another French scientist Camille Alphonse Faure, significantly improved the design of the battery which greatly increased the capacity of such batteries and led directly to their manufacture on an industrial scale. With this, the interest in electric vehicles returned. Walter C. Bersey, a British entrepreneur designed a fleet of such cabs and introduced them to the streets of London in 1897. They were called as 'Hummingbirds' due to the idiosyncratic humming noise they made [6]. The first hybrid car was developed by the Woods Motor Vehicle Company of Chicago. It was a gasoline-electric hybrid car. But the hybrid car proved to be a commercial failure as it was too slow for its price, and too difficult to service. But still the hybrid car had a lot of positives compared to its predecessors. They did not have the vibration, smell, and noise associated with gasoline cars. They also did not require gear changes and was very easy to start, unlike the gasoline cars which required to be cranked to start. But by the beginning of twentieth century with better road facilities, more crude oil sources were being discovered and need for faster vehicles soon replaced the slower electric vehicles with IC engine-based high-speed fuel-based cars.

3 Current Hybrid Scenario

The increase in global warming caused by greenhouse gas is turning out to be a significant problem. Figure 1 shows the amount of CO_2 emitted into the atmosphere by various factors. The transportation industry is contributing about 23 % and increasing as per the data collected by the International Energy Agency (IEA) [7]. Countries including India, the United States of America (USA), the European Union (EU), China, Japan, South Korea, and other countries, therefore have proposed and established new fuel economy policies and car CO_2 emission standard which are revolutionary compared with the former regulations. Recent measures taken by governments like Delhi, the limiting of vehicles based on the even and odd registration numbers, and in China where, to reduce the air pollution, vehicle bans were introduced and pointed towards what the world is seriously considering to overcome these sides effects of global warming. On 1 October 2015, India submitted its Intended Nationally Determined Contribution (INDC), including the targets to lower the CO_2 emissions by 33–35 %, to increase the share of nonfossil-based power generation capacity to 40 % of installed electric power capacity by 2030 and to create an additional (cumulative) carbon sink of 2.5–3 GtCO2e through additional forest and tree cover by 2030. On the other side the Environmental Protection Agency (EPA), USA has decided to have 58 % reduction in CO_2 emission by 2025. In this scenario, electric vehicles and hybrid electric
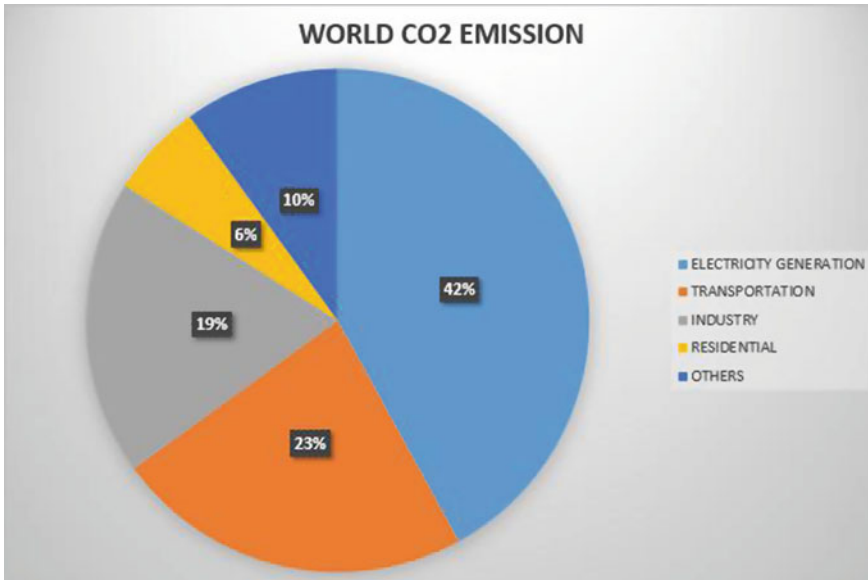
Fig. 1 World CO_2 emission level

vehicles have great importance. Hybrid vehicles, as the name indicates is a vehicle which makes use of more than one fuel source and which when optimized provides a very economic and environment friendly vehicle. The conventional hybrid vehicle makes use of battery as one fuel source along with the conventional fossil fuels. It was in 1899 that the first commercial hybrid car was developed by Lohner-Porsche. It was called the Lohner-Porsche Mixte Hybrid. Today the hybrid vehicle has advanced to plug-in hybrid electric vehicles. Dr. Andy Frank, who is the inventor of the modern PHEV began his work on PHEVs in 1971. By 1989, a plug-in parallel hybrid was developed by Audi. This car had a 12.6 bhp (9.4 kW) Siemens electric motor which drove the rear wheels. A trunk-mounted nickel–cadmium battery supplied energy to the motor that drove the rear wheels. The vehicle's front wheels were powered by a 2.3–l five-cylinder engine with an output of 136 bhp (101 kW). By the year 2000, The Electric Power Research Institute (EPRI) sponsored the Hybrid Electric Vehicle Alliance to promote and develop original equipment manufacturer commercialization of plug-in hybrid electric vehicles.

In 2001, The U.S. Department of Energy created the National Center of Hybrid Excellence at UC Davis. Ever since there has been a tremendous growth in the field of hybrid vehicles, many leading car manufacturing companies have joined the race in producing the most economical and efficient hybrid. Companies like BMW, Tesla, Audi, Nissan, Chevrolet have made a mark in the hybrid car industry. The plug-in technology has also grown which has led a lot of electrical companies to join in the race to build the most user friendly charging stations. Various companies like GE, NRG Energy, AeroVironment, Better Place, Sema Connect, and Tesla are

some of the famous contenders in the field of development of charging stations [8–11]. The world market is seeing a boom in the hybrid car industry. Big automotive companies have started to invest in electric vehicles and hybrid electric vehicles. Companies like Renault have come up with refreshing designs and models including the Renault Twizy which is a low-cost compact car, and would be a leader in its segment. Renault Zoe is the compact family car in its segment and was launched in 2015. Bolloré Bluecar, Mitsubishi I, Smart Electric Drive, Chevy Spark EV, Nissan Leaf, Volkswagen e-golf, Ford Focus Electric are few of the leaders till date in the alternate car scenario.

4 Hybrid Electric Vehicle Configurations

The hybrid electric vehicles are driven by a combination of an IC engine and an electric motor. The electric motor draws the power for its operation from the batteries provided. The IC Engine draws its power by the combustion and expansion of fuels in the combustion chamber. Based on the various combinations of IC engine and electric motor, the hybrid electric vehicle configurations are

- Series Hybrid Electric Vehicle
- Parallel Hybrid Electric Vehicle
- Series–Parallel Hybrid Electric Vehicle

4.1 Series Hybrid Electric Vehicle

The series hybrid electric vehicle has the power from the IC engine and the electric motor fed in series to the transmission and drive system. The IC engine operates using fuel and the rotary power generated is used to operate a generator. The generator produces power which is fed along with power from the battery to the ac motor after being converted from dc to ac using an inverter. The motor is coupled to a gear system which transmits the power to the drive wheels through the transmission system, thereby driving the vehicle. The operation is depicted in Fig. 2.

4.2 Parallel Hybrid Electric Vehicle

The parallel hybrid electric vehicle is shown in Fig. 3. In parallel hybrid electric vehicle configuration both the IC engine and the electric Motor is coupled to a gear system which is in contact with the wheels. The IC Engine is coupled to the gear system through the transmission system. The motor is driven by the battery. The battery which supplies dc power is converted to ac using a bidirectional inverter.

Fig. 2 Series hybrid configuration
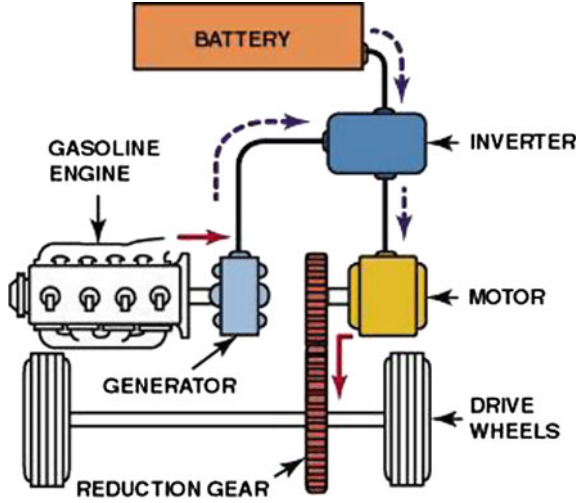
Fig. 3 Parallel hybrid configuration
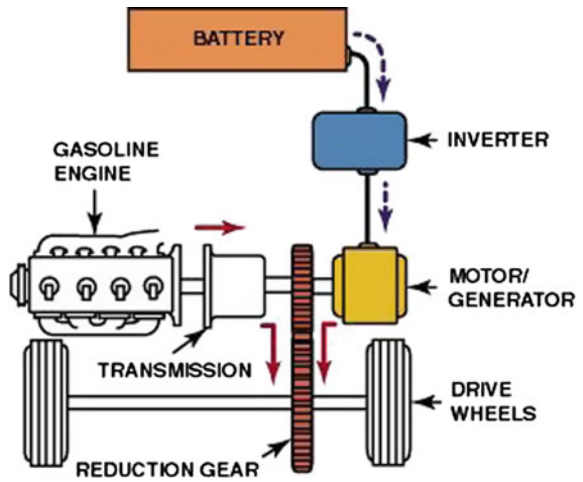
The system makes use of bidirectional inverter so that regeneration of power can be performed. In the regeneration process, while the vehicle undergoes braking, the gear system provides a mechanical rotation in the opposite direction. This rotation in the opposite direction makes the electric machine to operate in generator mode. The power thus generated by the generator is then fed to the bidirectional inverter which now operates in rectifier mode and feeds the battery with dc power, thus enabling charging of the batteries.

Fig. 4 Series–Parallel hybrid
configuration
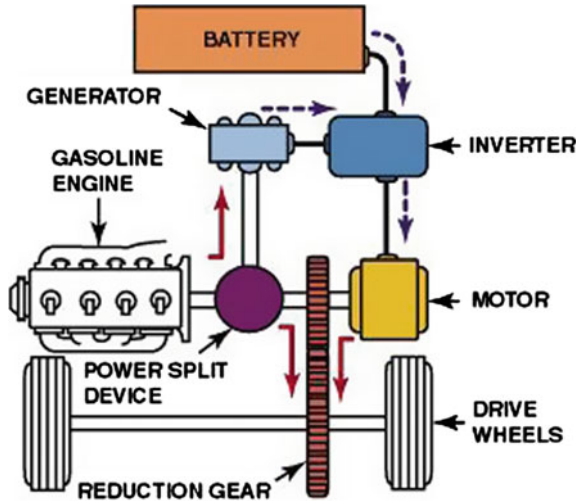
4.3 Series–Parallel Hybrid Electric Vehicle

A series–parallel hybrid electric scheme is a combination of properties of both series hybrid electric vehicles and parallel hybrid electric vehicles as shown in Fig. 4. The system makes use of a power split device which enables both the series and parallel operation. The power split device transfers a portion of the mechanical power from the IC Engine to the generator which converts the power into electrical energy and through the inverter is fed to the ac motor. Another portion of the mechanical power from IC Engine is coupled to the gear system. The ac motor drive system is also coupled to the gear system. The power from the IC Engine and the motor is fed to the transmission system and the wheels through the gear system.

5 Power Electronics Converters in Hybrid Systems

Power electronics is an interdisciplinary branch which is made use for different applications ranging from agriculture to industries. Power electronic circuits are miniaturized electronic controller circuits that can handle high-power applications. In hybrid electric vehicles, different power converters are vital in the generation, sharing a load and transmission of power to operate the vehicle. The operations include dc–dc conversion, ac–dc bidirectional conversion, soft switching applications, frequency conversion operations, and voltage control operations. For this, different kinds of converters are implemented.

5.1 DC–DC Converters

A converter that can convert dc input voltage at one magnitude to dc voltage of another magnitude is called as a dc–dc converter. The operations range from step-up to step-down on the dc voltage. For more flexibility, buck–boost dc converters are preferred. In a topology discussed in [12], the bidirectional dc–dc buck–boost converter is implemented. The bidirectional buck–boost dc/dc converter circuit consists of two switches. The power electronic switch S1 is used for boost converting while the switch S2 is used for the buck conversion mode, where the two modes control power flowing in opposite directions. The novelty of the design is that the buck converter mode is used for engine starting while the boost converter mode is used to control the electric current from the generator into the batteries and the motor drive.

When using batteries as the dc source, for the purpose of galvanic isolation for safety reason and high voltage ratio, another topology of dc–dc converter is introduced [13] which is based on the use of three-port isolated dc–dc converters. In this discussed system, three energy sources are used where each energy source is connected to other sources and loads via an identical module of dc–dc converter. The converters used are three-port isolated bidirectional dc–dc converters.

5.2 AC–DC Bidirectional Converters

The Bidirectional converters plays a vital role in hybrid electric vehicles. The converter is capable of converting the dc supply from the battery to ac to operate ac motors which are connected to the wheel base through a set of differentials. The advantage of such converters is that if the vehicle is equipped with proper regenerative braking technique the bidirectional converters can aid in charging back of the batteries.

5.3 Resonant Converters

Resonant converters are the future of power electronic applications in hybrid electric vehicles. The aim of the hybrid electric vehicle is to be an alternative for the fossil-based vehicles. But if the efficiency of such vehicles is less, then no one would opt for them. So, it is highly required to have the best and optimized performance. One of the main drawbacks of electric vehicles is the large amount of switching losses involved. While switching power electronic switches there is a lot of power loss in the form of heat. Also, the switching occurs at very high frequency which also increases the amount of power being lost. This can be overcome using resonant circuits. The resonant circuits make use of a resonant tank circuit which is

a capacitor inductor combination which enables to have zero voltage points or zero current points. If the switching is done at these points, the power loss can be minimized to zero. This kind of switching is known as zero voltage switching and zero current switching. By implementing resonant circuits it can make the vehicles more power saving.

6 Electrical Machines in Hybrid Systems

6.1 Brushed DC Motor

Conventional Direct Current (DC) motors have stators made up of permanent magnets while the rotor has windings-brushed dc Motors are considered as the simplest and user friendly electric motor that can be used in a hybrid electric vehicle for propulsion. The main advantage of such a machine over the IC Engine is that it has its maximum torque at low speed and the torque steadily falls as the speed increases compared with the IC Engine which has its maximum torque at somewhat high speed. However, the drawbacks of Brushed dc motors have reduced its reach. Low efficiency, reliability concerns, and bulky nature of the machine reduced its popularity. The temperature due to the heat generated also turned out to be a drawback as these losses limited the amount of power that the motor can deliver.

Due to the nature of design of brushed dc motor virtually all losses occur in the rotor at the centre of the motor. This meant that the heat generated was much more difficult to remove. The brushed dc motor was of different classes like separately excited, series motor, and shunt motor. These classifications were based on the powering and positioning of the field excitation winding [14].

6.2 Brushless Direct Current Motor (BLDC)

The motors which operated using Alternating Current (AC) are known as synchronous motors. BLDC motor is an ac motor. It is also called as permanent magnet synchronous motor, electronically commutated motor and self-synchronous motor. This machine is called as brushless, because the armature has no brushes connected to it. This enables the removal of wear and tear to the machine and also avoids brush drop. The rotor consists of a permanent magnet. The stator coil takes alternative supply from a dc source which generates magnetic field. The motion of the rotor is due to the interaction of the generated magnetic field with the field of the permanent. However due to back emf generated in the stator coil, the torque reduces as the speed increases (the back emf reduces the current in the coil). The advantage of this motor is that currents do not need to be induced in the rotor (like in induction motor), making them somewhat more efficient and giving slightly greater specific

power. The notable disadvantage is that it is costlier due to the presence of permanent magnet [14].

6.3 Switched Reluctance Motor (SRM)

SRM is also called as doubly salient machine; this is because both the stator and rotor are having salient poles. The stator and the rotor are made up of iron which is magnetized by the current through the coil on the stator. The stator windings are constituted by stator coils placed on the stator poles. Each pole has one coil over it [14]. Now, the rotor wound on the salient pole would be such that it is out of orientation with the magnet field; this causes the production of a torque to minimize the air gap and make the magnetic field symmetrical. When it is compared to the BLDC motor, there is no need for the current in the coil to alternate. The drawback that is faced in the proper design of an SRM is that the timing of the turning on and off of the stator currents must be much more carefully controlled. Another drawback of the SRM is that it is noisy due to the variable nature of the torque. This disadvantage can however be drastically reduced by adding more coils to the stator. It is always maintained that the number of salient poles is always two less than the number of coils. SRM is capable of providing a higher power density.

6.4 Axial Flux Ironless Permanent Magnet Motor

The most modern kind of machine used in hybrid electric vehicles are axial flux ironless permanent magnet motors which have a slotless, ironless, and outer rotor axial flux permanent magnet machine. Along with being a variable speed machine, the absence of stator core also enables to reduce the weight of the motor. The machine has a radial field type air gap. This enables to provide a more power density to the machine. There are many advantages for this permanent machine configuration, which are that these double magnet rotors could be fixed on the wheel lateral sides, thereby providing better position for the motors to operate. The stator windings could also be mounted centrally on the axle. The usage of slotless winding enabled to improve the efficiency compared with toothed structures. A high field is achievable with new permanent magnet materials and special magnet arrangement. There is a reduced copper loss due to availability of more space [14].

6.5 Permanent Magnet Synchronous Motor

The permanent magnet synchronous generators are one of the most modern types of generator used. These are variable speed generators which could be operated for

different speeds without using any gear system, which makes them more compact and more efficient. For applications like in vehicle industry where higher torque is required for in-wheel drive operations, new design has been done where permanent magnet synchronous motor with an outer rotor. But while doing the outer rotor design, the constraint is to give the best fit to the wheel rim and for the purpose of simpler construction, since the outer rotor does not require its own bearings compared to inner rotor type traction motor. The permanent magnet material which is normally used is NdFeB because of its high energy density. The sinusoidal nature of the flux linkages in the air gap makes it possible for the motor to be controllable by a sinusoidal supply voltage and by vector control method. The torque developed when plotted against the rotor position shows that the machine develops high torque at very low speeds too. The only notable loss in the otherwise advantageous machine is that when the machine is used for in-wheel drive application it causes high iron loss for the machine at higher speeds which makes the machine operation unstable [15].

7 Energy Sources and Soc Optimization Techniques

The battery powered electric and hybrid electric vehicles developed and used today uses nickel metal hydride (NMH) batteries and lithium–ion. When comparing batteries for hybrid electric vehicles and electric vehicles priority is given to high power batteries for hybrid electric vehicles (HEVs) as compared to high energy density batteries for electric vehicles (EV). For HEVs, the high power capability means to have the resistance of the battery to be low. Therefore, knowing the resistance of a battery is critical to assess its power capability. It is found that the energy densities of the HEV batteries are significantly lower than that of the EV batteries of the same chemistry. For example, a lithium–ion EV battery would have an energy density of 100–150 Wh/kg and that of a HEV battery would be 60–75 Wh/kg. Therefore for proper operation of HEVs, it is necessary that proper optimization is to be performed by having a tradeoff between energy density and power density. Even though nearly the entire hybrid vehicles in the market are using batteries as the technology of choice for energy storage, research is done to develop ultracapacitors in vehicles, which has been successfully implemented in transit buses which have been used in the United States of America, Japan, and China. The research for developing ultracapacitors for vehicle applications has been underway since early 1990s. The initial research and development has been on double-layer capacitors using microporous carbon in both of the electrodes. Soon after, the aim was to achieve an energy density of at least 5 Wh/kg for high power density discharges [16]. But one of the main challenges for ultracapacitors is that it is critical that their power and life cycle characteristics be significantly better than the high power batteries because the energy density of the capacitors will be significantly less than that of batteries. Research has also been done on ultracapacitors that use pseudocapacitive or battery-like materials in one of the electrodes with

microporous carbon in the other electrode. This approach enables to increase the energy density of the devices. There are presently commercially available carbon/carbon ultracapacitor devices (single cells and modules) from several companies VMaxwell, Ness, EPCOS, Nippon Chem-Con, and Power Systems [17–19]. An ideal battery for a HEV will be such a battery that would have an energy density close to that of an EV battery and the power capability close to that a HEV battery. When the cell size (Ah) of the PHEV battery is compared with the cell size of a EV battery, it will be smaller than for EVs as the energy stored will be less by a factor of 3–4. When PHEV batteries are compared with the HEVs it is required to be designed for deep discharge, long cycle life batteries rather than shallow discharge batteries like those in HEVs. Therefore it is found that PHEV batteries will have energy density characteristics closer to the EV batteries than HEV batteries, but with higher power capability than the larger EV cells. The main aim of researchers today is to be able to increase the power of the EV batteries with a minimum sacrifice in cycle life.

The electric and hybrids even though attractive replacements to the conventional fossil fuel vehicles are affected by few drawbacks; the primary one including the range of the vehicle. An electric car with a range above 200 km is not too feasible even with the technologies available today. The limited space available in vehicles and high cost of battery systems is the spoilers. The battery capacity cannot be increased much and the viable options like lithium sulfur and lithium air batteries are until now limited to laboratories and are not much reliable for mass production. The increase in the battery quantity to increase the backup means more charging time, which is a huge drawback. So understanding these to be the key issues to be addressed, a lot of research is being undertaken to have viable replacements. Fuel cell-based range extension methods are being researched on [19]. The advantage of the fuel cell-based systems includes having no waste gases polluting the atmosphere as the only byproduct which is produced is water. State of charging of a battery or cell stack is the parameter which determines the proper working of a battery for a defined application. It is necessary that all the batteries or cell stack charging–discharging is optimized. The hybrid electric vehicles require a stack of cells which are used to power the motor. So it is highly required that the charging and discharging of the cell stack should be optimized. For the optimization process, different techniques or algorithms are developed. Cell balancing is the process which is undertaken as a result. Cell balancing is classified into two broad divisions which are Passive cell balancing and Active cell balancing [20–23].

7.1 Passive Cell Balancing

Passive cell balancing technique is the method where the system takes a sample of the cell voltages of each cell in the stack at specific intervals. This is then used for determining the lowest voltage cell within the stack. Once the identification process is over, the cell potential of other cells is leveled to the lower potential cell by

discharging from the higher potential cells. The process of passive cell balancing can be easily implemented and it is cheap and reliable. However, this technique is wasteful and due to its discharge method it can generate large amounts of unwanted heat. The problem is in dissipating the heat as the cells will be concealed inside a pack. Such a method is slow to equalize and requires large areas of PCB coating to allow for typically surface mount resistor cell load heat dissipation.

7.2 Active Cell Balancing

Active cell balancing is used for overcoming the drawbacks of the passive cell balancing technique. In this method, the sample cell voltages are measured and then instead of choosing the lowest cell voltage as the base, the system takes the average of the instantaneous cell voltage. Once this average is identified, the higher voltage cells are made to drain out their charges which are then transferred to the cells whose cell voltage value is lower than the average voltage value which has been calculated. This optimization technique is however complex than the passive cell balancing technique as it uses a lot of power electronic components for switching and regulation process. However, the losses involved in active cell balancing are minimal. The only losses would be due to the presence of the power electronic switches which, while their switching process produces loss of power in the form of heat. However, if proper zero voltage or zero current switching resonant circuits are implemented it will enable to reduce the switching losses thus making active cell balancing the most optimized technique. Active balancing can be sub-divided into further topologies based on the usage of capacitor and/or inductive component.

8 Hybrid Design Considerations and Performance Analysis

The world is affected daily by the volatility of fuel prices. The conventional vehicles run on fossil fuel derivative and hence the future prices of fossil fuels can have a significant impact on the cost effectiveness of electric vehicles. Studies agree that petrol and diesel prices will likely rise in the long term even though it is at a reduced rate now. The U.S. Energy Information Administration and IHS Global Insight, a leading forecasting firm, are predicting that both fossil fuels and electricity will be more expensive in 2035. A rising world population, and more economically stabilizing people, especially in developing countries, will push up demand for cars and thus of fossil fuels. Therefore, HEVs are a viable alternative. Many world countries are developing policies to support the PEVs includes both supply side and demand side incentives. Supply side incentives would provide assistance to manufacturers and suppliers who wish to enter the PEV market,

increase their market share, or conduct research and development in the hybrid electric vehicle market. When comparing the HEVs with the conventional vehicles, one of the chief consumer issues is regarding the range of the vehicle. The range of the vehicle is of critical concern as there are chances of running out of power without the ability to recharge a PEV's batteries. Most of the conventional vehicles can travel over 500 kms between fueling, while the range of most electric vehicles tops out at 200–350 kms. In addition to this, the usage of air conditioning and radio further lowers the range capacity. The driving public is used to a technology where range is almost never a concern, as fuel pump stations are available at every few kilometres. But with very few charging stations and that too the infrastructure is still scattered, customers may worry about not being able to take PEVs on long road trips, particularly away from urban core areas. Another disadvantage of the HEVs over the conventional vehicles is the acceptability of the technology. The consumers always doubt about the reliability of the vehicle and its technology. If a breakdown of the HEV occurs it would be very difficult to have it fixed at local workshops or service stations as the technology would be out of the grasp of local units.

Another concern would be regarding the safety features of the HEVs over the conventional vehicles. The usage of battery entirely to run the vehicle may not be safe in the eyes of few customers. And the most important concern for HEVs is the cost involved. The high end cost is not much attracting the customers towards HEVs and so prefer the conventional vehicles. However, these types of fears will become less as customers become more familiar with PEVs. Most of the leading automotive manufacturers typically specializes in engine and transmission systems and outsources other components. But as the vehicle become more electric, the more value the battery holds [24]. Most of the leading manufacturers are therefore having their own research wings or are associating with specialized PEV and battery research firms to develop their technology. Formulae E, the racing division is currently partnering with Qualcomm and is using the Qualcomm Halo technology. Qualcomm is also teaming up with Daimler as well as Swiss Electric car parts manufacturer Brusa for developing new and innovative models equipped with wireless charging features. The key points of the new HEV industry are to build a better battery, achieve a good market, and provide the customer with the best and valued product [25]. But importance is also given to the electronics and software of power and thermal management systems.

Design for hybrid electric vehicle is a complex process. The first requirement in the design is to identify the load that the vehicle should be able to handle and what would be the speed and range that is expected during its performance. Assume a four-seater family car, which has a range of 200 km powered by the batteries. The acceleration should be 0–100 km/h under 15 s with a top attainable speed of 120 km/h. The kerb weight should be maintained to be below 1000 kg. These are some basic requirements that will be expected from a vehicle, which has to be attained while designing. When designing the power to weight ratio of the vehicle is to be considered. The maximum torque is produced at a lesser speed than the speed required to have maximum engine power. The other requirement is to have an

optimized aerodynamic system, thereby the drag coefficient is to be optimized. The vehicle should be equipped with specially developed tyres with a very low rolling resistance. If the chassis and the body is developed using aluminum (e.g., side doors, rear door, bonnet, front sills, frame of chairs, disk/drum brakes) or magnesium (e.g., steering wheel, rims, parts of the rear door) it could enable a better power density of the vehicle. Thinner glass can be used for all windows. Other weight optimization techniques could also be made use, like, amount of rust protection wax could be maintained at bare minimum, PVC undercover, door rubbers, seat rails, could be optimized in their content.

9 Future Hybrid Vehicles

The future of hybrid electric vehicles is vast. There is a lot of space for better and more efficient vehicles to be developed. Today, the world is fast changing towards the usage of renewable energy sources for the sustainment of the environment along with growth. Therefor vehicles which could be operational using renewable energy systems could be developed. Even though bio-fuel was developed long before, it could not find any viable market. Proper marketing and educating the people towards the better alternate is very important. Two of the most researched area today dealing with application of renewable energy systems in hybrid electric vehicle is solar-powered and wind-powered electric vehicles.

9.1 Solar-Powered Hybrid Electric Vehicles

Solar powered hybrid electric vehicle could be one of the better alternatives for fossil fuel cars. Today, a lot of researchers have tried to develop such vehicles. The solar panel-powered plug-in hybrid electric vehicle is a reality today. However designs and developments are performed to mount the solar panel onto the vehicle which could enable to charge the batteries of the vehicle on the run. The main drawback that these designs face is the reduced efficiency of the solar panels. It can hardly convert up to 20 % of the input power to useful power. Research on developing better efficient, more durable, and more user friendly solar panels could revolutionize the hybrid vehicle industry.

9.2 Wind-Powered Hybrid Electric Vehicle

Many research works have been performed to harness the wind power to power up the vehicle. The most modern technology however is limited to PHEV powered by wind. However, mounting up of the wind turbine on the vehicle is also being

pursued. The main drawback of such designs is that the drag force acting on the vehicle reduces the efficiency drastically thereby making the wind turbine a liability. To overcome this, design could be performed in such a manner that the wind turbine is concealed; thereby enabling the wind to be streamlined to the turbine without invoking much of drag force. Mounting the wind turbine inside the bonnet of a vehicle could be a viable solution. Also developing an alternate wind turbine for the conventional wind turbine which is limited to Betz limit could prove to be a boon to the inclusion of renewable energy systems to hybrid electric vehicle.

9.3 Wireless Power Transmission

Today the power transmission through wireless technology is emerging. This could be a viable source of charging the vehicles in the near future. Companies like Qualcomm is performing pioneering work in developing such wireless power transfer (WPT) technologies. The methods involved in such power transfer include through electromagnetic resonance, by inductance or through radiation. The technologies until now were limited to double pole wireless charging but research is being done and single pole charging pads with single or multiple coils have been developed [26]. Development is happening such that asymmetric designs are replacing conventional designs. The conventional four-coil system which has a symmetric coil configuration where the primary side has the source and transmitter coils, and the secondary side contains receiver and load coils. The new asymmetric four-coil system has the primary side that consists of a source coil, and two transmitter coils acts as intermediate coils while in the secondary side, a load coil serves as a receiver coil. In the design, primary side and the two intermediate coils boost the apparent coupling coefficient at around the operating frequency. Due to this double boosting effect, the system with an asymmetric four-coil resonator has a higher efficiency than the conventional symmetric four-coil system [27]. However, the main concerns regarding the system are alignment issues, foreign object detection, and safety concerns. The technology could also be extended to on-the-run charging systems. A series of such wireless charging stations could be placed along the sides of the roads. Thus, as the vehicle moves, the charging stations can transmit the power which can be harnessed on the go. However, this is a concept that requires a lot of research work to be done. It could prove to be a revolutionary technology in the future.

9.4 Grid Integration of Hybrid Electric Vehicles

Electric power is never excess and so, however the power received could be utilized. Electric hybrid vehicles uses the charge that is stored in its battery which is received either from grid in the form of PHEV or from renewable energy sources

like solar or wind to operate the drive and propel the vehicle. However, at times when there is a shortage of power in the grid for house-hold applications or powering a building and the vehicle is having stored energy in its battery, the opposite operation of powering the grid from the batteries of the electric vehicle can be performed. This process of grid to vehicle and vehicle to grid integration is a novel method which enables sustainability for the vehicle as well as the grid. However, few of the challenges that may arise are proper integration without conceding much power loss and ability to maintain the power quality to its optimum required range.

10 Conclusion

The paper discussed in detail the origin, the development, and the recent trends in hybrid electric vehicles. The vehicle industry from time immemorial has been dependent on the fossil fuels. Even though the first vehicles developed were also giving prominence to the electric version, low capacity non-rechargeable batteries caused the electric vehicles to have a bad impression among the masses. Along with the development of combustion engine and finding of large quantities of fossil fuels enabled the vehicle industry to fully focus on harnessing the fossil fuels, as they were more simple and easier to operate. But the increasing atmospheric pollution and the fast-depleting fossil fuel storage has made world countries to look up for alternatives. Even though we are abundant in alternative energy sources, the right way of harnessing is still eluding the world. Better classes of electric vehicles called the hybrid electric vehicles are having better demand now. People have started to understand the requirement of maintaining the atmosphere and the fossil fuel for future generations. Hybrid electric vehicle today is limited to plug-in technology where the vehicle has to be parked for recharging for long durations. However, there are researches being done to have technology to charge the vehicle on the run. This could prove to be a game changer for the vehicle industry. This paper highlights the recent trends in usage of power electronics and drives in vehicles. This integration of power electronics to the mechanical portion of the vehicle has not only improved the efficiency of the system, but has also proven to enable retaining and reusing the lost power including techniques like regenerative braking, wireless charging, and thermos-coupled exhaust power generation. The hybrid electric vehicles would in future be used more and enable a sustain development of the world.

References

1. Today in Technology History: July 6, The Center for the Study of Technology and Science, retrieved 2009-07-14
2. Guarnieri, M. (2012). "Looking back to electric cars". Proc. HISTELCON 2012 - 3rd Region-8 IEEE HISTory of Electro - Technology CONference: The Origins of Electrotechnologies:#6487583. doi:10.1109/HISTELCON.2012.6487583
3. "Planté Battery". National High Magnetic Field Laboratory. Retrieved 14 December 2014.
4. "Development of the Motor Car and Bicycle". TravelSmart Teacher Resource Kit. Government of Australia. 2003. Retrieved 2009-04-24.
5. Timeline: Life & Death of the Electric Car, NOW on PBS, Public Broadcasting Service, 9 June 2006, retrieved 2009-04-24.
6. "Hailing the History of New York's Yellow Cabs".
7. International Energy Agency: CO2 Emissions from Fuel Combustion, www.iea.org
8. http://www.earlyelectric.com/carcompanies.html Accessed August 16, 2010.
9. Valdes-Dapena, Peter (18 April 2006), "Hybrid cars are so last century", CNN, retrieved 14 July 2009
10. "History of Hybrid Vehicles". HybridCars.com. 2006-03-27. Archived from the original on 2009-02-08.
11. Kirsch, David A. (2000). The Electric Vehicle and the Burden of History. New Brunswick, New Jersey, and London: Rutgers University Press. pp. 153–162. ISBN 0-8135-2809-7.
12. Northcott, D.R.; Westward Ind. Ltd., St. Francois, MB, Canada; Filizadeh, S.; Chevrefils, A.R. "Design of a Bidirectional Buck-Boost DC/DC Converter for a Series Hybrid Electric Vehicle Using PSCAD/EMTDC", Vehicle Power and Propulsion Conference, 2009. VPPC '09. IEEE
13. Matheepot Phattanasak, Roghayeh Gavagsaz-Ghoachani, Jean-Philippe Martin, Babak Nahid-Mobarakeh, Serge Pierfederici, and Bernard Davat "Control of a Hybrid Energy Source Comprising a Fuel Cell and Two Storage Devices using Isolated Three-Port Bidirectional DC-DC Converters". 2013 Eighth International Conference and Exhibition on Ecological Vehicles and Renewable Energies (EVER)
14. Omonowo D. Momoh and Michael O. Omoigui. "An Overview of Hybrid Electric Vehicle Technology." IEEE Conference on Vehicle Power and Propulsion Conference, 2009. VPPC '09.
15. F. Magnussen, "On design and analysis of synchronous permanent magnet for field – weakening operation," Ph.D. dissertation, Royal Institute of Tech., Sweden, 2004.
16. A. F. Burke, B Electrochemical capacitors for electric vehicles: A technology update and recent test results from INEL, [presented at the 36th Power Sources Conf., Cherry Hill, NJ, Jun. 1994.
17. A. F. Burke and M. Miller, BSupercapacitor technology-present and future,[presented at the Advanced Capacitor World Summit, San Diego, CA, Jul. 2006.
18. A. F. Burke, B The present and projected performance and cost of double-layer and pseudo-capacitive ultracapacitors for hybrid vehicle applications,[presented at the IEEE Vehicle Power and Propulsion System Conf., Chicago, IL, Sep. 8–9, 2005.
19. A. F. Burke and M. Miller, BUltracapacitor update: Cell and module performance and cost projections,[presented at the 15th Int. Seminar on Double-Layer Capacitors and Hybrid Energy Storage Devices, Deerfield Beach, FL, Dec. 5–7, 2005.
20. Active battery balancing comparison based on MATLAB Simulation', 7th IEEE Vehicle power and propulsion Conference, VPPC'11, 2011
21. S. Moore and P. Schneider, 'A Review of cell equalization methods for Lithium Ion and Lithium polymer battery systems', In proceedings of the SAE 2001 World Congress, 2001
22. N. Kutkut, and D. Divan, "Dynamic equlization techniques for series battery stacks", IEEE Telecommunications Energy Conference, INTELEC'96, pp. 514–521, 1996
23. Vehicle Power Management: Modeling, Control and Optimization By Xi Zhang, Chris Mi.

24. International Economic Development Council: Electric Vehicle Industry, www.iedconline.org
25. Qualcomm: Formulaes for the future, www.qualcomm.com
26. G. Ombach, 'Design considerations for wireless charging system for electric and plug-in hybrid vehicles', Institution of Engineering and Technology Hybrid and Electric Vehicles Conference 2013 (HEVC 2013) - London, UK (6–7 Nov. 2013)
27. SangCheol Moon, Gun-Woo Moon, 'Wireless Power Transfer System with an Asymmetric 4-Coil Resonator for Electric Vehicle Battery Chagers', IEEE 2015 IEEE Applied Power Electronics Conference and Exposition (APEC) - Charlotte, NC, USA

Design of Expert Combustion Monitoring System

S. Yuvaraj, K.M. Kiran Babu, P. Kaleeshwaran and S. Tamilselvan

Abstract It is identified that the monitoring systems can be used, not only for statistics and data processing calculations, but also for combustion, unburned pollutant components. This situation allows us to realize AFT calculation. It is demonstrated that the AFT equations could be solved efficiently using LabView software. The cells in the spreadsheet are viewed as either natural grids or elements of a matrix [1]. The Symphony spreadsheet program is applied to calculate the AFT of combustion systems. A design template which contains the necessary formulae is constructed so that very little knowledge of the program is required to obtain impressive results. This template becomes a powerful tool by providing a fast and efficient means of designing stable closed-loop system as well as predicting its performance [2]. The computational domain corresponds to the real physical shape and/or the computational space by grid generation. The results can be visualized on the same LabView with inherent graphics. The pre- and post-processors are all in one SAFT.

Keywords SAFT · Combustion · Adiabatic flame temperature

1 Solution of the Combustion Equation

Q_p is heat evolved, or the heat given off by the system, or the heat of combustion or heat of reaction.

S. Yuvaraj (✉) · P. Kaleeshwaran
Department of Aerospace Engineering, Karpagam Academy of Higher Education,
Coimbatore 642120, India
e-mail: Syuva91@gmail.com

K.M. Kiran Babu
Department of Aeronautical Engineering, Karpagam Institute of Technology,
Coimbatore 642120, India

S. Tamilselvan
Department of Aeronautical Engineering, Sri Ramakrishna Engineering College,
Coimbatore 641022, India

$$H_{\text{reac}}(T_i, P) = H_{\text{prod}}(T_{\text{ad}}, P)$$
$$h_{\text{reac}}(T_i, P) = h_{\text{prod}}(T_{\text{ad}}, P)$$

$$\Delta H = \sum_{i,\text{prod}} n_i \left[\left\{ \left(H_{T_2}^\circ - H_0^\circ \right) - \left(H_{T_0}^\circ - H_0^\circ \right) \right\} + \left(\Delta H_f^\circ \right)_{T_0} \right]_i$$

$$- \sum_{i,\text{react}} n_j \left[\left\{ \left(H_{T_0'}^\circ - H_0^\circ \right) - \left(H_{T_0}^\circ - H_0^\circ \right) \right\} + \left(\Delta H_f^\circ \right)_{T_0} \right]_j = -Q_p$$

$$\sum_{i,\text{prod}} n_i \left[\left(H_{T_{\text{ad}}}^\circ - H_{T_0}^\circ \right) + \left(\Delta H_f^\circ \right)_{T_0} \right]_i = \sum_{i,\text{react}} n_j \left[\left(H_{T_1}^\circ - H_{T_0}^\circ \right) + \left(\Delta H_f^\circ \right)_{T_0} \right]_j$$

The use of Solver for combustion problems provides students with an intuitive method for obtaining finite difference solutions. Its advantages over the circular reference approach become even more apparent when the staggered grid formulation for the Glassman equations is utilized, as described in the next section [3 and 5].

As mentioned earlier, the usefulness of the method lies in its visual presentation and straightforward solution process. The students, unencumbered by programming details, can develop a clear conceptual understanding of how the grid variables relate to one another before moving on to writing code.

In order to demonstrate how the Solver function in Excel is used to solve systems of equations, consider the following conduction problem, given to students in an undergraduate heat transfer class. The problem is to calculate the energy distribution in a combustion chamber of an automotive system as seen in Fig. 1

From the reference we came to know the following equation through which the total temperature produced and consumed can be described. These are the factors affecting the engine performance during flight [6].

1.1 Factors Affecting Combustion of the Engine

i. Pressure Loss
ii. Combustion Intensity
iii. Combustion Efficiency
iv. Vibrations
v. Materials
vi. Aging of the system and its components

$$T_{\text{ad}} = xT_c + yT_v + zT_{\text{ce}} + aT_p + bT_m + cT_i + dT_a$$

	A	B	C	D	E	F	G	H
8	Eqn in Terms of Unit Mass	1	4	13.16	2.75	2.25	13.16	
9								
10	Mass x Specific Heat (J/K)				3576.209	5471.614	16062.79	
11								
12	Summation of Mass x Specific Heat for all species (J/K)							25110.6154
13								
14	Heat Released From Combustion (CH4) (J/Kg)							50050000.0000
15								
16	Adibatic Temperature - Ref Temperature (T2-Tref) (K)							1993.1809
17								
18	T Ref (K)							298.0000
19								
20	T Guess (K)							2291.1809
21								
22	T Mean (K)							1294.5905
23								
24	Adiabatic Flame Temperature T2 (K)							2291.1809
25								

Fig. 1 Adiabatic flame temperature

xT_c Combustion products temperature
yT_v Temperature changes due vibration
zT_{ce} Temperature changes due to combustion efficiency loss
aT_p Temperature changes due to pressure loss
bT_m Temperature changes due to material effect
cT_i Temperature changes due to combustion intensity
dT_a Temperature changes due to aging of the system

**Temperature changes is with respect to heat loss/gain
Pressure loss factor, $PLF = K_1 + K_2 (T_{02}/T_{01} - 1)$
Combustion intensity = Heat release rate/combustion volume * Pressure
Combustion efficiency = (Actual total – Head temperature rise)/(Theoretical total – head temperature rise)

For an adiabatic combustion process, with no change in KE or PE, temperature of products is called Adiabatic Flame Temperature, Tad-Maximum temperature that can be achieved for given concentrations of reactants' incomplete combustion or heat transfer from the reactants act to lower the temperature. The adiabatic flame temperature is generally a good estimate of the actual temperature achieved in a flame, since the chemical time scales are often shorter than those associated with

transfer of heat and work conceptually simple, but in practice difficult to evaluate because it requires detailed knowledge of product composition, which is function of temperature [7].

2 Expert System

2.1 Methodology-Flow Chart

See Fig. 2.

Fig. 2 Methodology flow chart
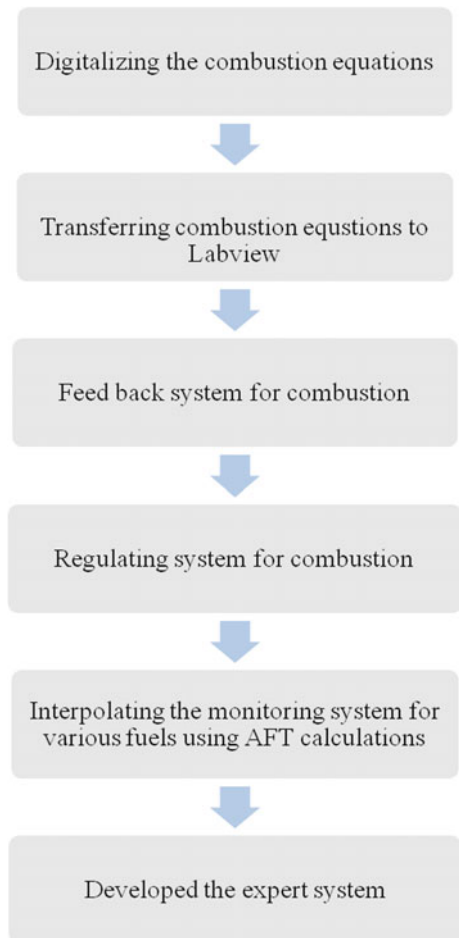
3 Expert Combustion Monitoring System

The combustion problems are studied by experience and from the literatures of various experts in the area of combustion, the collected reference problems are studied and the cause of problems focusing single unique reason is identified, hence it is taken as the area of research focus. The solving techniques for the same problems found by various experts are verified and their suggestions were collected for the future developments.

From the studies, it is found that, digitalizing the combustion system for complete monitoring of every reaction inside the combustion chamber [4].

In order to digitalize and develop the expert system, it is mandatory to develop a database with benchmarked values, and knowledge base for verifying the system also it makes regulation of combustion process.

Then for the development of display system, the user interface is designed with the feedback system which is enabled with sensors and control units. A set of LabView programme is used in the development of knowledge base and feedback system of the expert system.

3.1 Design of Expert Combustion Monitoring System

See Fig. 3.

3.2 The Knowledge Base of the Expert System

See Fig. 4.
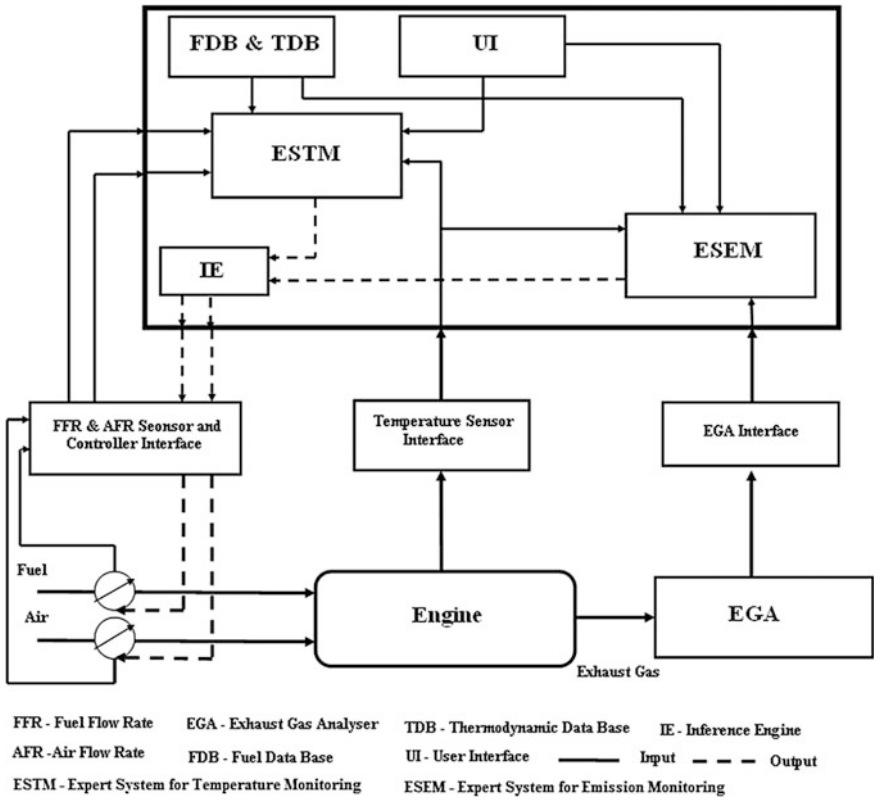
Fig. 3 Block diagram of Expert combustion monitoring system
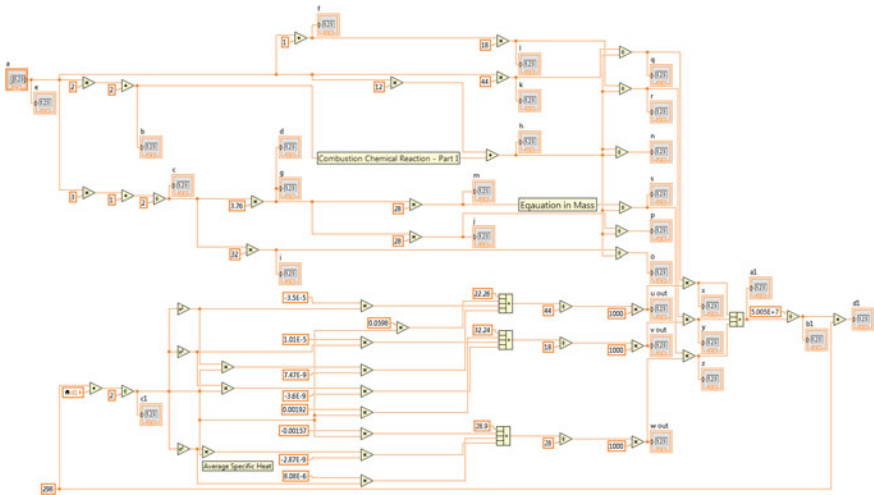
Fig. 4 AFT calculator—LabView

4 Conclusion

The Solver tool in Excel provides an intuitive way for students to learn the fundamentals of computational fluid dynamics and heat transfer. A spreadsheet solution allows students to clearly conceptualize the interrelationships among the nodal variables in the discretization without the burden of having to write and debug code. The spreadsheet links between plots and cell values allows instant visualization of parametric changes.

The combustion process can be monitored for its proportion of combustion and the unburned products are taken into consideration and it will be burned by supplying the adequate necessary products the signals received from the feedback system (Fig. 5).

The expert system makes maximum possible burning of combustion products inside the combustion chamber. Also, it is found that the combustion can be controlled as per the requirement by controlling the Air–Fuel mixture passing inside the combustion chamber.
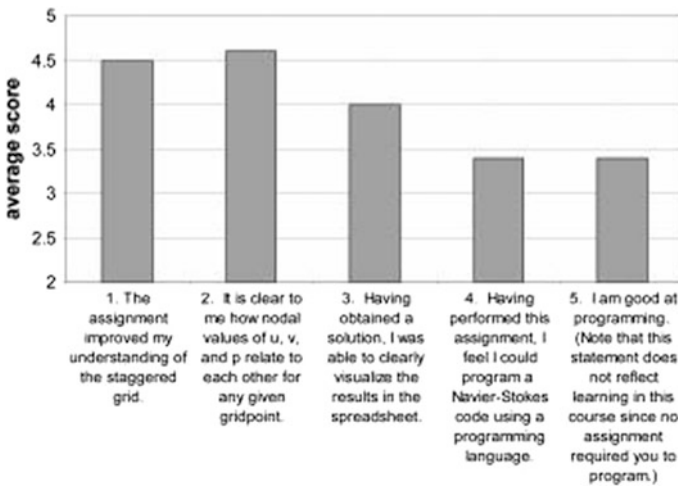
Fig. 5 Student assessment of using Solver to solve the driven combustion problem. Possible scores were *5* strongly agree, *4* agree, *3* neutral, *2* disagree, *1* strongly disagree

5   Future Works

5.1   Measuring System for Vibration Effect

A lamp is made to burn with aviation fuel with static condition. A lamp is made to burn with aviation fuel when it is placed in vibration generator and supposed to the frequency ranges from 20–60 Hz. The results are tabulated and the equation is generated by rehearsal method.

5.2   Measuring System for Material Effect

The combustion of a candy lamp is made to burn with different materials as outer cover and the percentage of changing with average is notified and tabulated. The average is considered as the effect of material.

References

1. E.M.A. Mokheimer and M. A. Antar, on the use of spreadsheets in heat conduction analysis, Int. J. Mech. Eng. Educ., 28(2), 1998, Pp. 113–139.
2. M.A. Antar and E. M. Mokheimer, Spreadsheet modeling of transient three dimensional heat conduction with various standard boundary conditions, Int. J. Mech. Eng. Educ., 30(1), 2000, Pp. 17–34.
3. M. R. Schumack, Teaching heat transfer using automotive-related case studies with a spreadsheet analysis package. Int. J. Mech. Eng. Educ., 25(3), 1997, Pp. 177–196.
4. R. Kumar and A. Al-Shantaf, Spreadsheet analysis of fluid mechanics problems, 1997 ASEE/IEEE Frontiers in Education Conf. Proc.
5. J.D.Martinez-Morales, Elvia Palacios, G.A.Velazquez Carrillo, Modeling Of Internal Combustion Engine Emission by Lolimot Algorithm, Science Direct, Elsevier, 2012.
6. Analysis of capillary diffuser for micro jet engine, Yuvaraj S, et al, Discovery, 2015, 29(115), 179–183.
7. S. Shreyas Krishna, C.J Thomas Renald Numerical analysis of a turbocompounded Diesel – Brayton combined cycle, ISBN: 978-960-474-158-8-2010.Pp 258-261

Structural Performance Analysis of SAE Supra Chassis

Shubham Thosar, Antriksh Mutha and S.A. Dharurkar

Abstract The objective of this study is to analyse the design of a Formula SAE roll cage by analytical and numerical methods based on dynamic loads experienced by the roll cage under normal driving conditions. Torsional stiffness of the roll cage has also been studied. Good designs demand a light chassis which has to sustain the racing environment. In this study, static and dynamic load distributions were calculated analytically followed by extensive study of various boundary conditions to be applied during Finite Element Analysis (FEA) carried out in Ansys. Stress distributions, lateral displacements during static, dynamic conditions and frequency modes were analysed and a high factor of safety made the design favourable for use.

Keywords Structural performance analysis · Finite element analysis · SAE supra chassis · Dynamic conditions · Frequency modes · High factor safety

S. Thosar (✉) · A. Mutha · S.A. Dharurkar
Department of Mechanical Engineering, MGM Jawaharlal Nehru Engineering College, Aurangabad, India
e-mail: shubham.thosar81@gmail.com

A. Mutha
e-mail: mutha.antriksh@gmail.com

S.A. Dharurkar
e-mail: sudarshan7565@gmail.com

1 Introduction

The chassis structure must safely support the weight of the vehicle components and transmit loads that result from longitudinal, lateral and vertical accelerations that are experienced in a racing environment without failure. This paper probes the various aspects of chassis design. Some crucial questions addressed are: What is the best way to transfer the loads through the structure? How stiff should the frame be? How a chassis has effect on different race condition? What is the effect of pipe diameter and cross section on the stiffness of the chassis? What should be the appropriate factor of safety while designing a frame?

2 The Chassis

The primary objective of the chassis is to provide a structure that connects the front and rear suspension without excessive deflection. When considering a race car chassis, a frame that is easily twisted will result in significant handling problems. The lateral loading on a vehicle is taken up in two places; the frame and the suspension. The suspension can be adjusted, the frame cannot. So to get required handling, the frame should be stiffer to compensate lateral loading on the car. On the whole, a frame that is able to sustain torsional loads resulting from inertial accelerations of components experienced during cornering or from applied loads acting on one or opposite corners of the vehicle will almost always be sufficiently strong.

3 Design Methodology
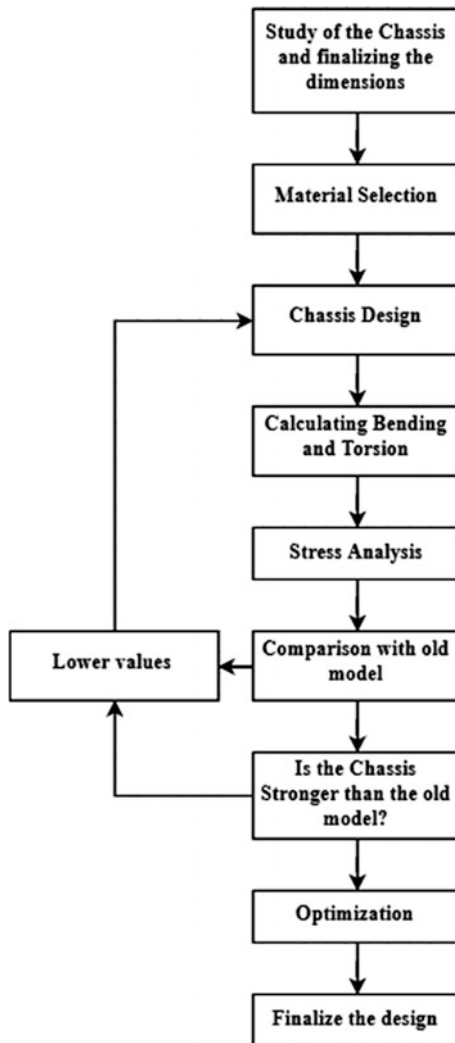
4 Material Selection

The integrity of a design can be ensured only after a systematic material selection procedure. Since the chassis has to be designed for harsh driving conditions, the selection of material becomes a vital part of design process. The mechanical

properties such elasticity modulus E, the shear modulus G, density ρ and yield stress f_y are important from design point of view.

For selection of appropriate material for chassis, prepare a decision matrix of crucial factor which can affect the performance of the car's mechanical properties, cost and availability.

	AISI 1010	AISI 4130	AISI 1018
Tensile strength	3	5	3
Cost	4	3	4
Availability	4	3	3
% Elongation	3	4	3
Machinability	4	4	4
Density	3	5	3
Total	21	24	20

Thus the material AISI 4130 proves to be most desirable even with the higher cost for a greater safety.

5   Vehicle Loading

Frame is defined as a fabricated structural assembly that supports all functional vehicle systems. This assembly may be a single welded structure, multiple welded structures or a combination of composite and welded structures. Depending upon application of loads and their direction, chassis is deformed in respective manner shown below.
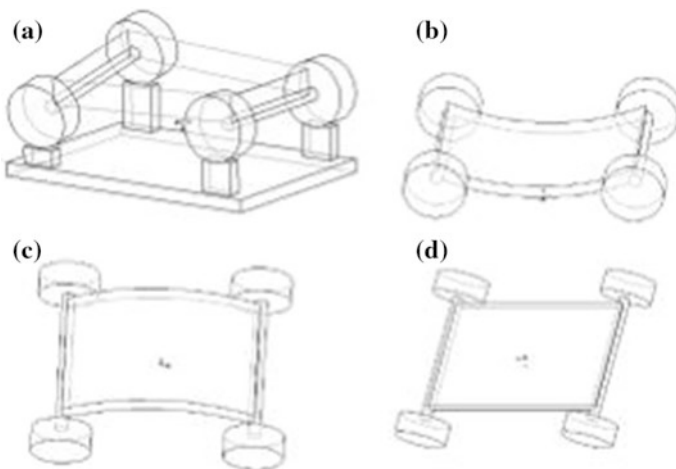
(a) Longitudinal Torsion—created mainly by a cornering vehicle or bumps in the racetrack. It is the chassis' ability to resist deformation under this load that defines torsional stiffness.

(b) Vertical Bending—Vertical bending is created by the weight of the drive and vehicle's components, these forces can be boosted by vertical acceleration produced.

(c) Horizontal Bending—This deformation mode is caused by the centrifugal forces created by the cornering of the vehicle.

(d) Horizontal Lozenging—occurs when the car deforms into a parallelogram-like shape, this is caused by the uneven or opposing application of force on the wheels on opposite sides of the car.

6 Effect of Chassis on Different Race Condition

The SAE Supra competition is scored based on two areas, static and dynamic testing, with both having various sub-categories. The dynamic section consists of four events; acceleration, skid pad, autocross and endurance. Each of these events demand different performance from the chassis. It is a balancing act to achieve optimum performance from the vehicle.

Acceleration: This event simply needs a car that can reach high speeds quickly, thus looking at Newton's second law of motion $F = ma$; thus low mass of chassis will give higher acceleration.

Skid pad: This event is a measure of the car's cornering ability around a flat corner. To achieve this, the chassis is required to have a high value of torsional stiffness that is well balanced throughout the chassis.

Autocross: The Autocross event is a standard race track comprising of a straight, constant turns and some other types of turns. Cars run on the track with the average speed between 40–48 km/h. This event is designed to measure the vehicle's desired performance outcomes of handling, acceleration and breaking. Thus higher torsional rigidity of the chassis will yield higher handling.

Endurance: The final event is the measure of the car's reliability, endurance and fuel economy. The fuel economy however will be influenced by the car's chassis, as any superfluous weight will slow the car down thus reducing economy.

7 Dynamic Loading

Lateral Load Transfer: When cornering in a steady turn, load is transferred from the inside pairs of the wheels to the outside pair due to centrifugal force. This load transfer is called lateral load transfer.

$$\text{Lateral Load Transfer}\ (L_b) = \frac{\text{Lat.Accn.} \times \text{C.G.} \times \text{Weight}}{\text{Track Width}}$$

$$L_b = 1.5 \times 10 \times 705.479/48 = 220\ \text{lbs} = 99\ \text{kg}$$

$$\text{Force} = 99 \times 9.8 = 970.2\ \text{N}$$

8   Lateral Bending

Lateral bending is due to the load transfer while cornering which is equal to centrifugal force and thus the force of 4774.3 N is acted on the side impact member in cockpit, thus the equivalent stress is calculated (246 MPa) which is well under permissible limit. Thus material will not start to yield during lateral bending (Figs. 1, 2, 3, 4, 5, 6, 7, 8, 9, 10 and 11).

Longitudinal Load Transfer: Such load transfer occurs in a longitudinal plane under linear acceleration or deceleration

$$\text{Long.Load Transfer}\ (L_b) = \frac{\text{Accn.} \times \text{C.G.} \times \text{Weight}}{\text{Track Width}}$$

$$L_b = 1.5 \times 10 \times 705.479/68 = 170\ \text{lbs} = 77.14\ \text{kg}$$

$$\text{Force} = 77.14 \times 9.8 = 755.9\ \text{N}$$

Fig. 1 Lateral acceleration loading
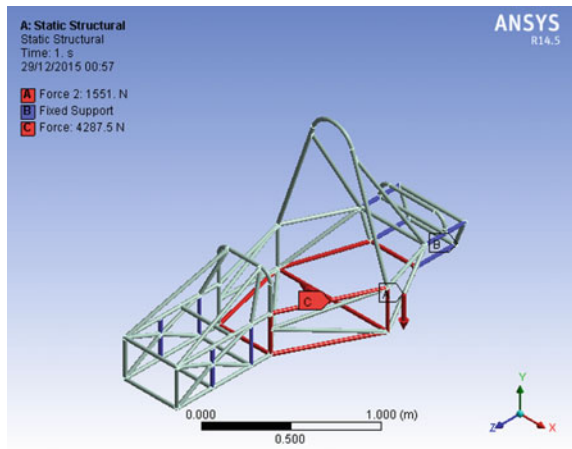
Fig. 2 Lateral acceleration stress analysis
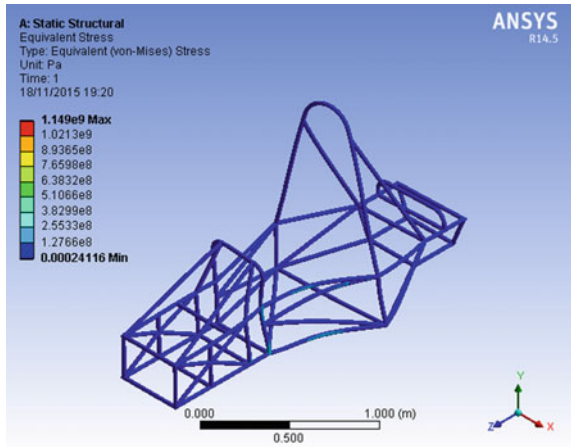
Fig. 3 Long. acceleration loading
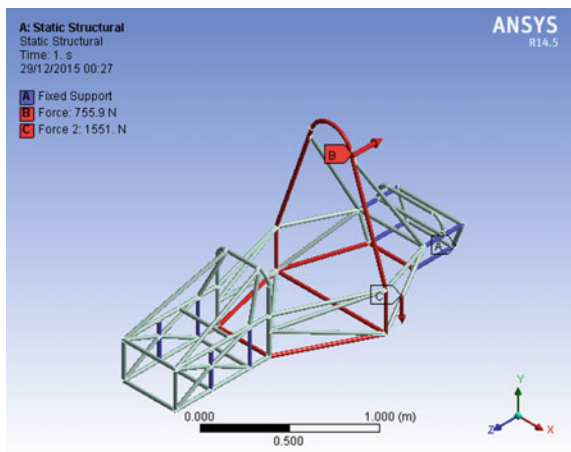
Fig. 4 Long. acceleration stress analysis
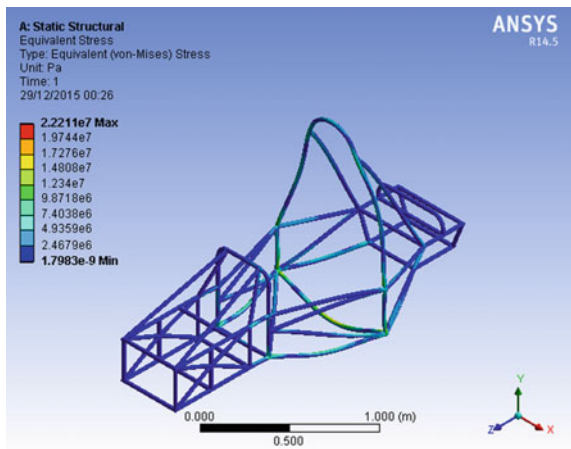
Fig. 5 Front impact loading
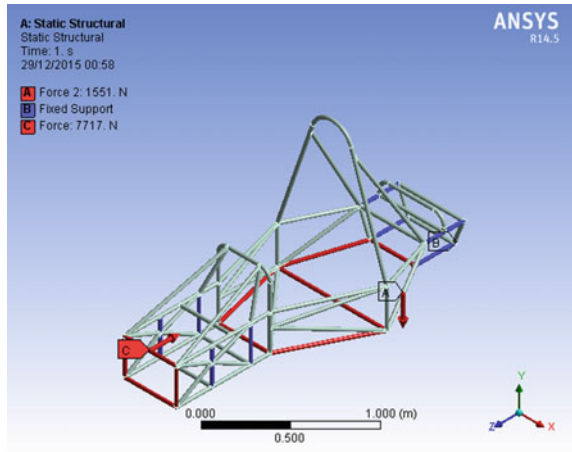
Fig. 6 Front impact stress analysis
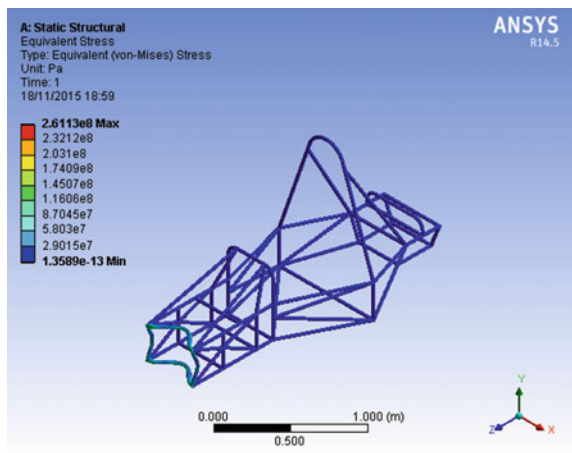
Fig. 7 Side impact loading
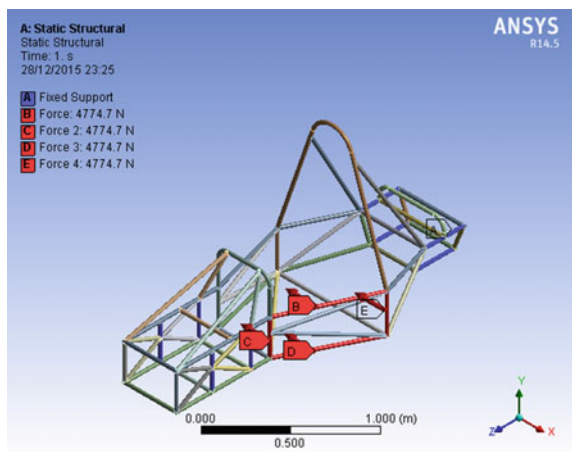
Fig. 8 Side impact stress analysis
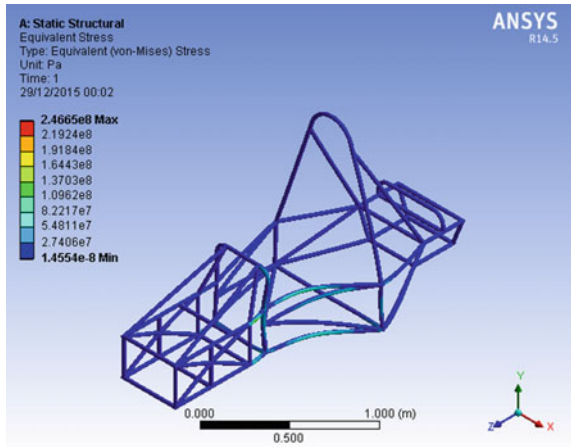
Fig. 9 Torsional rigidity loading
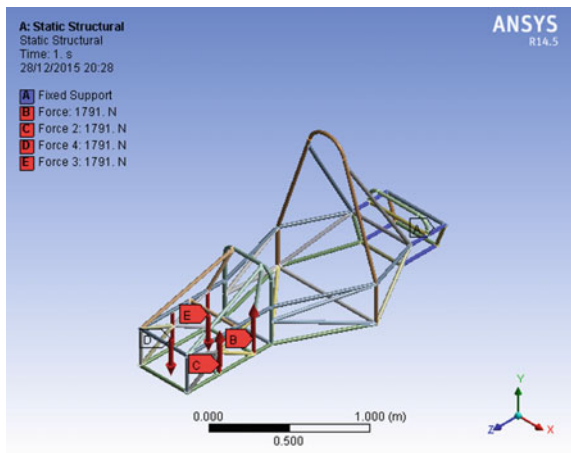
Fig. 10 Torsional rigidity stress analysis
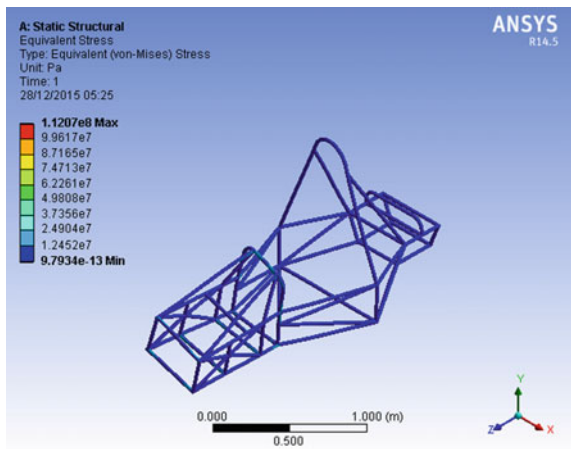
Fig. 11 Torsional rigidity total deformation
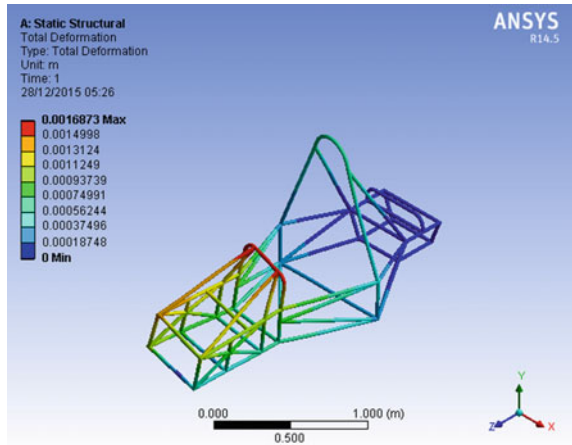
9 Acceleration and Brake Test

Due to inertia effect, acceleration forces tend to act in opposite direction to the motion of body. The mass of driver is assumed 70 kg and drive train 50 kg and acceleration of engine is 3.7 m/s^2.

As calculated above, longitudinal force is applied on the main hoop; and simultaneous static load due to drive and drive train is acted downward in cockpit area. Equivalent stress is calculated for this dynamic test which comes as 221 MPa. This is less than the permissible stress 435 MPa, thus chassis is safe.

10 Impact Loading

Type of impact forces	Boundary conditions	Force that chassis can withstand after the impact	Von mises stress (MPa)	FOS
Front impact	Clamping all suspension pickup points and applying force on front bulk head	9G	261	1.76
Side impact	Clamping all suspension pickup points and applying force on side impact member	5G	114	4.03

The function of the frame is to provide the vehicle strength, structural integrity and to protect the driver (in case of serious impacts and rollover) and support front and rear suspension systems, engine, drive train, steering system and other systems in the vehicle. It must be of adequate strength to protect the driver in case of an accident.

11 Selection of Theory of Failure

Since all the tests are carried out under static structural, the cross section of the component is assumed to be uniform throughout, but in practise due to some irregularities, fluctuating load can lead to fatigue failure. These fluctuating loads are very hard to calculate and so it is always preferred to have a higher factor of safety. It is seen that Distortion Energy Theory (Huber Von Mises and Hencky's Theory) predicts yielding with precise accuracy in all four quadrants. Moreover, Distortion Energy Theory is used for ductile materials, when the factor of safety is to be held in close limits and the cause of failure of the component is being investigated. This theory predicts failure most accurately. Thus, among the three theories, i.e. Max. Principle Stress Theory, Max. Shear Stress Theory and Distortion Energy Theory, Distortion Energy Theory was selected for designing the chassis.

12 Torsional Rigidity

It is the torsional response of a structure to an applied torque loading. A best possible chassis would be one that has high stiffness; with low weight and cost. If there is significant twisting, the chassis will vibrate, complicating the system of the vehicle and sacrificing the handling performance. It is desirable to design a chassis with maximum torsional rigidity. This allows the suspension to do their job correctly.

In order to design a car of maximum torsional stiffness, the basis or generalised equation for torsion must be examined. Figure below is a basic shaft constrained at one end and an applied torque T at the other, with Φ denoting the resultant twist of the shaft.
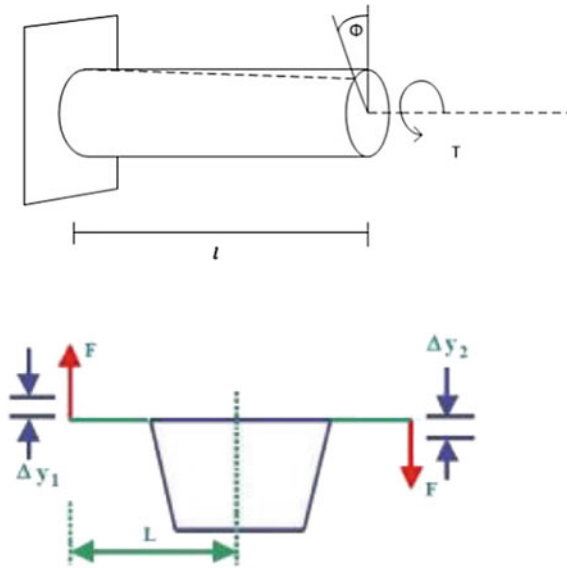
$$T = \Phi JG/l$$

This equation can then be rearranged to express torsional stiffness,

$$T/\Phi = JG/l.$$

This expression displays that torsional stiffness in proportion to both the polar moment inertia and material shear modulus, whilst being inversely proportional to the length.

The torsional rigidity can be calculated by finding the torque applied to the frame and dividing by the angular deflection.

$$K = \frac{R}{\theta}$$

$$K = \frac{F \times L}{\tan^{-1}\left[\frac{\Delta y_1 + \Delta y_2}{2L}\right]}$$

where, K Torsional Stiffness
T Torque
θ Angular deformation
F Shear Force
$y1, y2$ Translational displacement

Table 1 Deflection and stiffneszs

	Applied moment (Nm)	Deflection (m/deg)	Stiffness (Nm/deg)
2.4 mm wall thickness	450	0.10368	480
3.4 mm wall thickness	450	0.034	1470

Force applied   1130 N
$y_1 = y_2$ 1.68 mm = 0.00168 mm
L 0.20

$$K = \frac{1130 \times 2}{\tan^{-1}[\frac{0.00168 + 0.00168}{2 \times 0.20}]}$$

$$K = 482 \frac{\text{Nm}}{deg}$$

Deakin et al. concluded that a Formula SAE racer, which has a total suspension roll stiffness of 500–1500 Nm/deg, requires chassis stiffness between 300 and 1000 Nm/deg to enable the handling to be tuned.

13   Effect of Wall Thickness on Torsional Stiffness

From the given table, it can be inferred that the thickness of the frame has the maximum effect on the torsional stiffness. The torsional stiffness increases 3 times with 1 mm increase in frame thickness. Thus, it increases stiffness drastically with no significant increase in the weight of the chassis and increasing the stiffness to weight ratio of the chassis enhancing the handling of the car (Table 1).

14   Conclusion

The aim of this project was to design a chassis for a competition, a goal that has been accomplished. In the work done, a frame is designed which is rigid enough not to deform under acceleration and braking loads and at the same time hold all the parts together. The work was started with a basic design of frame which would meet the entire design requirement. Chassis was found to be safe significantly in static (bending) and dynamic (acceleration) modes with stress values noticeably less than the yield strength. The dominant characteristic of structural behaviour viz. torsional rigidity increased three times with an average increase in the wall thickness.

Reference

1. SUPRA SAEINDIA Rulebook 2015.
2. Design, Analysis and Testing of a Formula SAE Car Chassis, SAE TECHNICAL PAPER SERIES, 2002-01-3300.
3. Structural Performance Analysis of Formula Sae Car, Jurnal Mekanikal, December 2010, No. 31, 46 – 61.
4. Milliken, William F. and Milliken, Douglas L., "Race Car Vehicle Dynamics", Society of Automotive Engineers, 1997.
5. Design of Machine Elements by V. B. Bhandari.
6. Data Records – Team VAAYU 4.0, J.N.E.C., Aurangabad, SUPRA SAEINDIA 2015.
7. Design, Analysis and Manufacture of 2011 REV Formula SAE Vehicle Chassis.
8. Jacob I. Salter 20247771 School of Mechanical and Chemical Engineering the University of Western Australia.
9. World Academy of Science, Engineering and Technology International Journal of Mechanical, Aerospace, Industrial, Mechatronic and Manufacturing Engineering Vol: 6, No: 5, 2012 The Frame Analysis and Testing for Student Formula.

Parametric Optimization of FSAE Restrictor for Random Vibrational Analysis

A.V. Pavankumar, R. Suraj, Puneet Kumar, H.S. Shiva Prasad
and Kumar K. Gowda

Abstract The air intake restrictor of an FSAE car is associated with the fluid flow analysis of the system. Structural integrity of the restrictor plays a major role in the optimization of the system thus obtaining aero-structural interaction. This paper aims at the optimization of the restrictor holistically. Fluid flow conditions are modeled for different convergent and divergent angle of the restrictor using choking condition, the lowest pressure difference model is chosen as the optimum solution. The pressure inside and the environment pressure is coupled to the structural analysis and then to vibrational model. A random vibrational analysis is performed to obtain the random probability of stresses due to undulations in the road. A 3-σ stress is considered and parametric optimization of the random vibration is used to optimize the thickness of the restrictor to get best possible thickness.

Keywords Convergence · Design of experiments · Modal analysis · Optimization · Probabilistic stress · Restrictor · Random vibration · Sigma · Sampling points

1 Introduction

FSAE is a student formula racing event held every year, across the world. SAE SUPRA is one such conducted by SAE-INDIA every year, which gives students, a platform to design and fabricate a formula style racecar, governed by the rules of SAE. In order to restrict the power of the engine, SAE has come up with a rule, wherein, the air going to the engine should pass through a neck whose diameter should not exceed 20 mm [1]. For the fabrication, we have selected a

A.V. Pavankumar (✉) · Puneet Kumar
Kshipra Simulations, Bangalore, India
e-mail: pavanku222@gmail.com

R. Suraj · H.S. Shiva Prasad
Nitte Meenakshi Institute of Technology, Bangalore, India

K.K. Gowda
Vivekananda Institute of Technology, Bangalore, India

KTM duke 390 engine which delivers a power of 43 BHP at 9500 rpm [2]. It is noted that the engine head has the diameter of 54 mm at its throttle body so that one end of the restrictor is fixed, whereas the other end is connected to an air filter whose fitting has a diameter of 55 mm. Placing the restrictor thus reduces the area of fluid flow drastically. When the engine is running at higher RPM, the engine burns more fuel which requires more air for combustion, thus the velocity of the air reaches its maximum velocity of Mach 1 leading to critical flow condition [3]. As the engine RPM is less, mass flow rate is compensated by the increase in the velocity of air through restrictor [3–5].

Also, when the vehicle is moving on the road, it undergoes a lot of random vibrations. Due to which there is a possibility that the natural frequency of the restrictor matches with the forced vibrations which may cause possible resonance. Or many modes can resonate simultaneously causing catastrophic failure of the component.

2 Research Methodology

2.1 Computational Fluid Dynamics Optimization

The basic design parameters that have to be considered while designing any CFD problem lie in boundary conditions. The air intake manifold of the vehicle lies between the air filter and the throttle body of the engine hence, the inlet and the outlet of the manifold have predetermined diameter. Therefore, length is considered to optimize the fluid flow in the system.

Any CFD problem is solved by using finite volume methods where the appropriate boundary conditions are put in the Navier stoke equations, these equations along with the momentum and energy equations are solved to find the resulting pressure, velocity vector, and density. As the system has less Reynolds number, there is no Reynolds stress and eddy viscosity remains constant hence it can be considered as laminar flow system. Any boundary value problem needs feasible boundary conditions else a numerical instability is achieved [6]. Keeping above factor in mind, the choking conditions have been calculated (Fig. 1).

Where
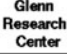
T = 300 K (Room Condition)
A = 0.001256 (20 mm diameter)
P_t = 101325 Pa (1 Atm)
R = Gas constant = 0.286 K/Kg-k
M = 1 (Choked Conditions)
γ = 1.4

Calculated mass flow rate is = 0.0703 kg/s.

Fig. 1 Mass flow choking
equation [7]

The mass flow rate acts as a Neumann boundary condition acting on outlet and atm pressure of 101,325 Pa acts as Dirichlet boundary condition acting on inlet side thus fulfilling all the required boundary conditions. In order to reduce the error, care must be taken while meshing which can give a residual truncation error and may lead to numerical instability

3 Fluid Flow Analysis

In order to capture the structural stresses due to fluid flow, fluid domain is modeled inside the structural domain (solid manifold) for the reason that fluid flow exerts difference in pressure due to inside fluid flow pressure and outside atm pressure. By varying the convergent and divergent angle, 20 possible restrictor systems are modeled and analyzed for the fluid flow.

Fig. 2 shows the CFD Analysis for the restrictor to capture the pressure over the manifold. From Fig. 3, it is clear that the pressure is minimum at neck and velocity is maximum reaching Mach 1. The iterative results of possible restrictor are shown in the Tables 1 and 2.
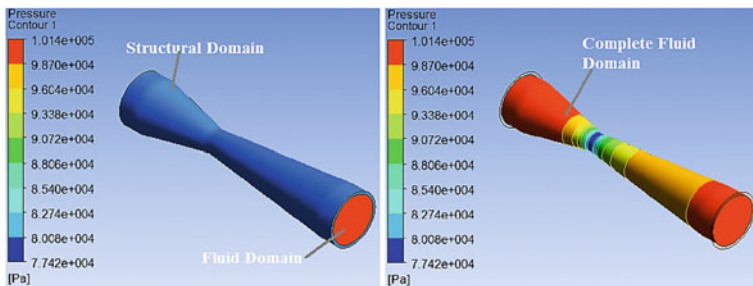
Fig. 2 Fluid and structural domain in CFD and fluid domain

Fig. 3 Imported pressure from CFD
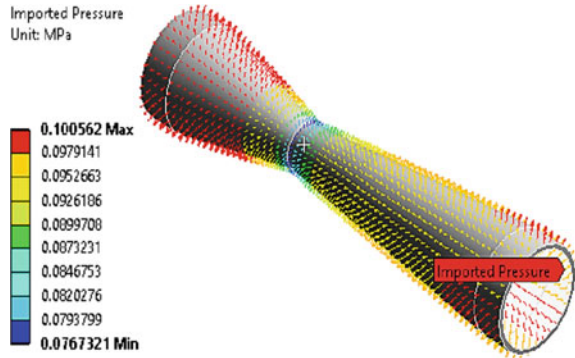
Table 1 Total pressure at throttle

Convergent angle/divergent angles (degree)	10	12	14	16	18
6	77598.4	77312.2	76554	75674.1	74860.5
8	78010.6	77374.1	76484.6	75889.1	750148
10	76899.6	96374.6	75969.1	75197.6	74487.5
12	76431.4	75020.6	74584.4	74293.4	73578.9

Table 2 Total pressure at engine head

Convergent angle/divergent Angle (degree)	10	12	14	16	18
6	97939.4	98016.1	96922.7	97393.3	97142
8	96701.6	97138	96983.2	96778.4	96581.5
10	95662.5	95060.4	95078.1	95097.8	94838.2
12	95095.7	94105	94076	93815.7	93955.9

From the table, it is inferred that the pressure difference is low for 12° convergent angle and 6° divergent angle and length of restrictor is 246 mm, 50 mm clearance is given on either side to fit air filter and engine head.

4 Structural Interaction

The optimized angles along with the length are taken for the structural analysis. The pressure obtained in the CFD is coupled to the structural analysis to simulate real-time environment. Different materials have been considered to optimize the structural part of the manifold. The stresses due to fluid pressure are captured and tabulated in Table 3.

Table 3 Material properties

Material	Density kg/m³	Yield stress (MPa)	Young's modulus (MPa)	Poisson's ratio	Obtained stress (MPa)
Structural steel [8]	7850	250	2e⁵	0.3	29.377
Aluminum [9]	2770	280	71000	0.33	20.11
Copper [10]	8300	280	1.1e⁵	0.34	24.379
Gray cast iron [10]	7850	250	2e⁵	0.3	14.896

It can be seen that different material shows different stresses due to the reason that Young's modulus and Poisson's ratio are different for different materials; the stresses obtained are in the radial direction and hence can be treated as Hoop stress. Figure 5 shows the variation of hoop stress in the structural steel, the stresses generated are due to difference in pressure of one atmospheric pressure and the imported fluid pressure (Fig. 4).

Fig. 4 Stress due to pressure from CFD
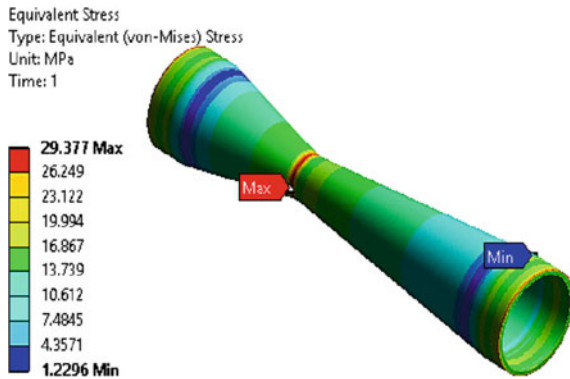
Fig. 5 Variation of stress (MPa) with mesh size(mm)
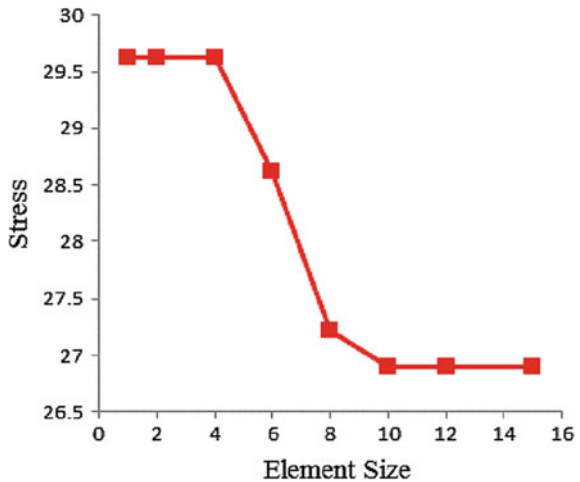
4.1 Convergence Criteria

Without checking the results to be convergent, it is not appropriate to conclude the results; hence in order to get proper results the forthcoming analysis has been tested for mesh convergence for all case.

In this analysis, the convergence is obtained by varying space step as the analysis is time independent form. When the stress anomaly with respect to stress stops, the convergence is achieved. Figure 6 shows the variation of the stress with respect to mesh size, when the mesh size becomes 4 mm, the results are converged. Hence a mapped mesh of 4 mm is used in all the analysis to bolster the claim.

4.2 Random Vibration Analysis

When the car is in motion, the natural frequencies of the chassis, suspension, engine, and transmission have to be taken care of, for the whole system to be safe. But as the car is moving on the road, the motion will be of nondeterministic type whereas the future behavior of any component cannot be predicted. There exists randomness as characteristics of the excitation or input, not the natural frequency.

A measurement of acceleration spectral density can measure random vibration, the root mean square acceleration is used to express the overall energy of random vibration and this can be treated as statistical value which can be used for design and analysis purpose [11, 12] (Table 4).
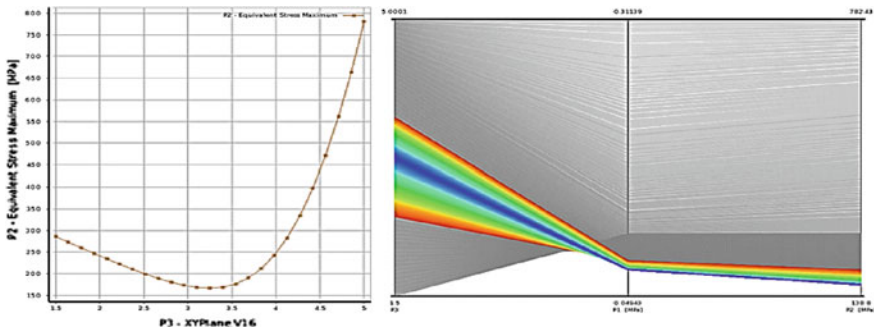
Fig. 6 Response surface for structural steel

Statement	Probability ratio	Percent probability (%)
−σ < x <+ σ	0.6827	68.27
−2σ < x <+2 σ	0.9545	95.45
−3σ < x <+ 3σ	0.9973	99.73

Table 4 Probability for a random signal with normal distribution and zeros mean [13]

Because of the mathematical complexity of working of overlapped sine curves to find instantaneous amplitude, statistical process can be used to find the probability of occurrence of particular amplitude; there might be chances that the random vibration of the road can directly match with one or more natural frequencies of the system and create resonance, hence before doing random vibration, we conducted modal analysis with the prestressed modal and the boundary conditions simulating exact road scenario to find out natural frequencies. Hence random analysis is carried out for the range of frequencies from 1 to 8000 Hz which covers 5 modes of the restrictor (Tables 5 and 6).

As thickness of the restrictor changes, it strongly affects the natural frequencies as well as random vibrations. In order to understand this variation, a design of experiment has been created coupling fluid flow static structural to random vibration with the help of modal analysis.

$$F = \frac{1}{2\pi}\sqrt{\frac{K}{m}} \tag{1}$$

As the thickness of the material increases, mass increases. But stiffness depends on various other parameters which decides the natural frequency, thus makes it unpredictable to calculate by continuum method. The frequency response curve shows that as the thickness increases, stresses due to random vibration decreases till a break even point. After that the stresses keep on increasing due to variation in stiffness (Fig. 7).

From screening method, five values of thickness are chosen to find interpolating function. Later 1000 samples have been calculated using the interpolating functions and response surface is plotted according to the objectives and constraints thickness

Table 5 Natural frequencies for 3 mm thickness manifold

Restrictor material		Structural steel	Copper	Aluminum	Gray cast iron
Frequencies Hz/No. of modes	1	3911.6	2811.2	3912.4	3034.7
	2	3911.7	2811.3	3912.4	3034.7
	3	5597.6	4073.3	5651.3	4318.5
	4	5600.4	4075.4	5654.2	4320.7
	5	7421.2	5321.	7409.6	5764.1

Table 6 Natural frequencies for 4 mm thickness manifold

Restrictor material		Structural steel	Copper	Aluminum	Gray cast iron
Frequencies Hz/No. of modes	1	3945.2	2836.	3946.6	3060.4
	2	3945.4	2836.1	3946.8	3060.6
	3	6646.4	4838.2	6711.7	5126.4
	4	6649.6	4840.6	6714.9	5128.9
	5	7478.6	5363.2	7468.1	5808.2
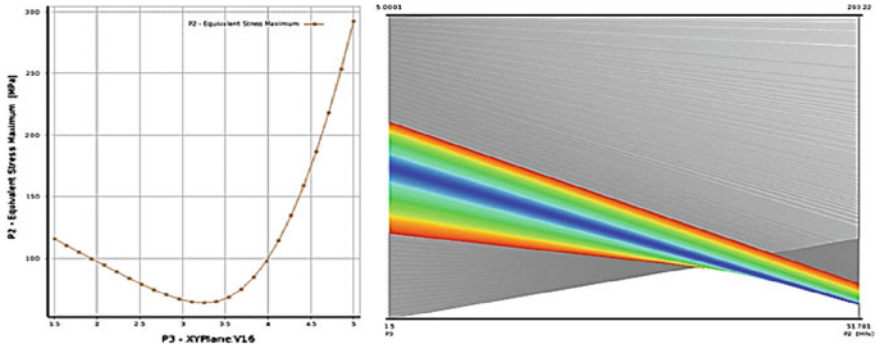
Fig. 7 Response surface for aluminum

is minimum and stress is minimum, one best candidate point is selected from 1000 samples.

From the above Figs. 8, 9, 10, 11, 12, 13 and 14, it can be inferred that all the stress values are minimum when the thickness of the restrictor is between 3 and
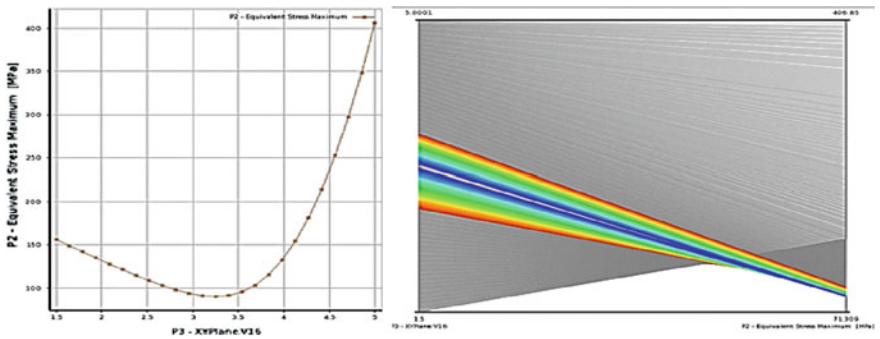
Fig. 8 Response surface for copper
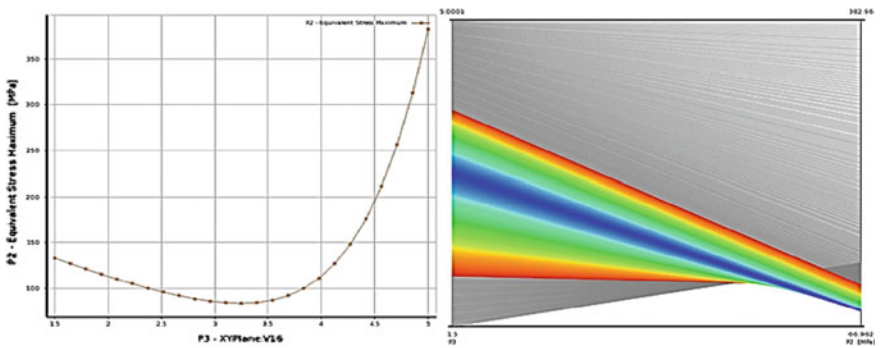
Fig. 9 Response surface for gray cast iron

Fig. 10 Random stresses for structural steel model
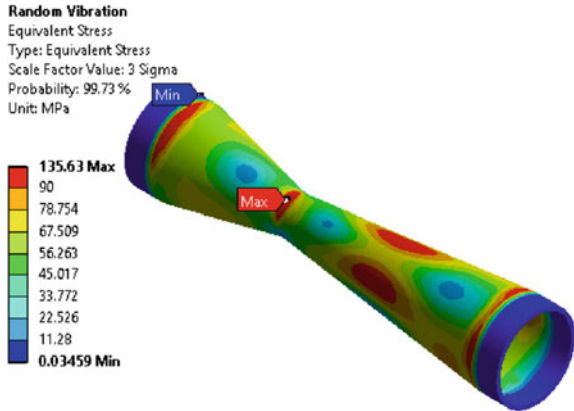
Table 7 Resulting stresses

Material	Thickness (mm)	Random stress (MPa)	Probability (%)	Sigma value
Structural steel	3.25	135	99.73	3σ
Aluminum	3.25	68	99.73	3σ
Copper	3.25	83	99.73	3σ
Gray cast iron	3.25	75	99.73	3σ

3.5 mm. Response surfaces show the variation between thickness and stress values (Table 7).

5 Conclusion

CFD results clearly show that pressure difference is lowest for convergent angle of 6° and divergent angle of 12°.

Any material can be used for the restrictor, but we have considered only four materials for the analysis. Even though the stresses are different for different materials, thickness is always 3–3.5 mm for a random frequency range of 1–8000 Hz. Spectral analysis shows minimum stresses compared to random vibrational stresses which can be neglected.

References

1. SAE rule book-2015.
2. KTM Duke Specification.
3. Farrugia M., Cauchi J., "Engine Simulation of a Restricted FSAE Engine, Focusing on Restrictor Modelling,". SAE Technical Paper Series, vol. 01, no. 3651, Dec 2006.

4. Section 8, "Sonic Flow Nozzles and Venturi -Critical Flow, Choked Flow Condition", ASME Publication.
5. B. Jawad, A. Lounsbery, and J. Hoste, "Evolution of intake design for a small engine formula vehicle," in SAE Technical Paper 2001-01-1211, SAE World Congress, Detroit, MI, 2001.
6. Computational Fluid Dynamics by Malalashekhar and veersteeg.
7. NASA, mass flow choking, Glenn research center.
8. Fatigue Data at zero mean stress comes from 1998 ASME BPV Code, Section 8, Div 2, Table 5–110.1.
9. General aluminum alloy. Fatigue properties come from MIL-HDBK-5H, page 3–277.
10. Copper Development Association Inc.
11. Analyzing random Vibration fatigue, By Santhosh, M kumar, Technical support Engg, ANSYS.
12. Random Vibration, An overview, by Barry controls, Hopkinton, MA.
13. An introduction to random vibration, Revision B, by Tom Irvine, Oct 26, 2000.

Taguchi's Parametric Approach in Optimizing Selective Inhibition Sintering Process Variables

P. Arunkumar and E. Balasubramanian

Abstract Selective Inhibition Sintering (SIS) is novel additive manufacturing process wherein wide array of indigenous polymers can be used to produce high strength parts. The contemporary approach has many parameters that need to be optimized. The proposed work considers layer thickness, heater speed, and amount of heat as candidate options to optimize using Taguchi's single response method. The thermo-structural Finite Element Analysis (FEA) provided the maximum displacement and temperature of the structural model. Design of experiment is conducted for three levels of considered factors and corresponding orthogonal array and responses are obtained. Further, Analysis of Variance (ANOVA) studies are steered to evaluate the influence of these parameters on parts dimensional accuracy. The simulation analysis results of this work demarcated that layer thickness is one of the important factor in SIS process for dimensional stability. Finding from this study enables us to perform experiments on suitable layer thickness that leads to production of parts with adequate strength.

Keywords Selective inhibition sintering · Polymer sintering · Finite element analysis · Taguchi method · Optimization

1 Introduction

1.1 Selective Inhibition Sintering Process

Selective Inhibition Sintering (SIS) process is an emergent technique in rapid prototyping (RP) field which ensures the part strength, surface quality, and dimensional accuracy. It is cost effective than other RP process [1] and inexpensive polymers, metals are used to create the parts [2, 5]. It is a layer deposition method in which the sintering process followed by inhibition is a core procedure to obtain SIS

P. Arunkumar · E. Balasubramanian (✉)
Department of Mechanical Engineering, Vel Tech University, Avadi, Chennai, India
e-mail: esak.bala@gmail.com

part from the computer-aided design model. The consecutive layer deposition and sintering of powders are performed until the parts produced. There were few works concentrated on SIS process in the literature. Khoshnevis et al. [2] have constructed the alpha machine to build the 3D objects such as plastic parts using sintering process of powder materials. Khoshnevis et al. [4] have developed the SIS process for the fabrication of metallic parts. Khoshnevis et al. [5] investigated on fabrication of parts using ceramic material in SIS process. It is evident from these literatures that, SIS parameter optimization studies are vital and they have to be performed beforehand of real-time experiments to save the time and cost. Hence, this work concentrated on optimizing the SIS process parameters using Taguchi's principle and also validating with analysis of variance (ANOVA).

1.2   Taguchi Method

Taguchi method offers systematic way to determine optimal parameters of multi-faceted manufacturing process with regard to performance and cost. There are three quality characteristics that are identified by Taguchi [9] to perform the analysis of signal-to-noise (S/N) ratio. Lipin et al. [9] have optimized the factors such as hardness, composition, stiffness of work piece/tool, and tool life for CNC drilling technique. The few studies [10–13] were focused on multi response optimization for their manufacturing process. Pai et al. [14] approached the Taguchi method and response surface methodology (RSM), for the proper selection of factors in grinding process. There are plenty of studies that have been carried out in analyzing and optimizing the various manufacturing process parameters. However, research on evaluating and optimizing SIS process parameters are quite few. Asiabanpour et al. [3] conducted design of experiments using response surface methodology to validate the optimal parameters in SIS process. In this paper, the finite element study has been carried out for single layer SIS process to evaluate the thermal and structural behavior of the part. Taguchi's approach is adopted to identify the effect of each process parameters such as layer thickness, heater speed, and amount of heat in arriving an optimal solution.

2   Design of Experiments

The conduct of experiments and obtaining an optimal solution is a tedious and time-consuming process. Before performing real experiments, the complete knowledge of the product or process and identifying the key factors which are likely to stimulus the process is necessary. In view of this, design of experiment (DoE) is primarily conducted to obtain optimal process parameters which in turn will be useful for evaluation.

	S. No	Parameter	Level	Values
Table 1 Process variables and levels	1	Layer thickness (t)	3	1.5, 2 and 2.5 mm
	2	Heater speed (s)	3	180, 200 and 220 mm/s
	3	Amount of heat (Q)	3	30, 40 and 50 W

2.1 Orthogonal Array

In this study, layer thickness, heater speed, and amount of heat are the three parameters that are selected each at three levels (Table 1).

The present study considers three parameters and three levels, L9 Orthogonal array can be selected for further investigations. Since the DOF of L9 orthogonal array is nine which are greater than the DOF obtained for the various levels and process parameters that confirm the execution of number of experiments to be carried out.

2.2 FEA Modeling

In order to evaluate the structural and thermal behavior of SIS process to perform further investigation of DoE, a finite element model of 30×30 mm is taken into account [6]. The inner layer shown as light gray is considered to be the polymer material and the outer periphery is an inhibitor which is shown as dark region in Fig. 1. The present study considers polyamideimide (PAI) polymer with potassium iodide (KI) as inhibitor for further simulation.

The multiple layer sintering phenomenon [7, 8] is analyzed through element birth and death technique using finite element analysis (FEA) solver ANSYS. With respect to L9 orthogonal array, nine iterative simulations are performed and the results are given in Table 2.

| t=1.5mm | t=2mm | t=2.5mm |
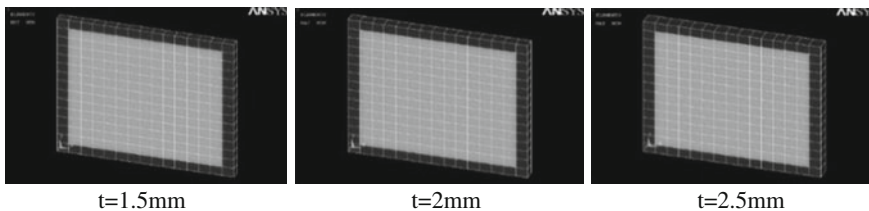
Fig. 1 Part and inhibitor model

Table 2 S/N ratio for displacement and temperature

S. No	Layer thickness (m)	Heater speed (mm/S)	Amount of heat (W)	Disp (mm)	Temp (K)	S/N ratio (Disp)	S–N ratio (Temp)
1	0.0015	180	30	0.030393	308.4153	30.3445	49.7827
2	0.0015	200	40	0.030474	309.5360	30.3215	49.8142
3	0.0015	220	50	0.030159	310.3740	30.4117	49.8377
4	0.0020	180	40	0.039183	308.5220	28.1380	49.7857
5	0.0020	200	50	0.039229	309.2293	28.1279	49.8056
6	0.0020	220	30	0.039041	306.3740	28.1697	49.7250
7	0.0025	180	50	0.047963	308.5707	26.3818	49.7871
8	0.0025	200	30	0.047761	306.0193	26.4186	49.7150
9	0.0025	220	40	0.047808	306.6300	26.4099	49.7323
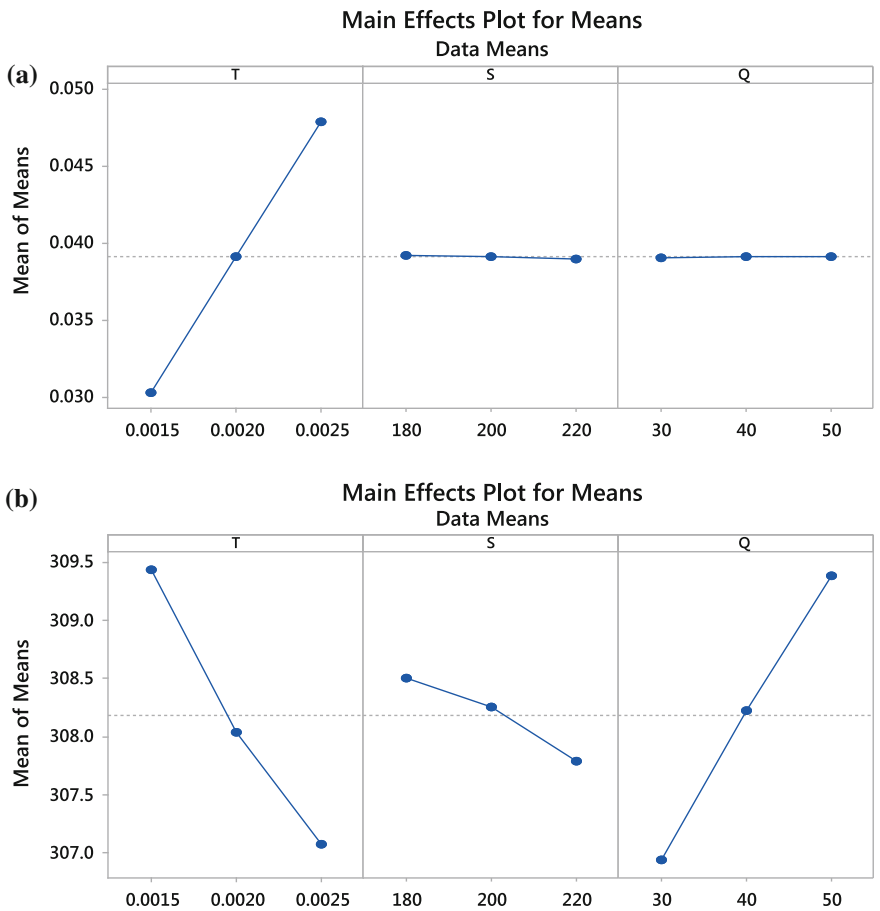
Fig. 2 **a** Mean effect plots for displacement. **b** Mean effect plots for temperature

Table 3 (a) Response table for S–N ratio (disp). (b) Response table for S–N ratio (temp)

Level	ST	SS	SQ
Response table for S–N ratio (disp)			
1	30.36	28.29	28.31
2	28.15	28.29	28.29
3	26.4	28.33	28.31
Delta	3.96	0.04	0.02
Rank	1	2	3
Response table for S–N ratio (temp)			
1	49.812	49.785	49.741
2	49.772	49.778	49.777
3	49.745	49.765	49.81
Delta	0.067	0.02	0.069
Rank	2	3	1

Table 4 Nominal levels of factors for output responses

Factors	Temperature	Displacement
T	Level 1	Level 1
S	Level 1	Level 3
Q	Level 3	Level 1/level 3

2.3 S/N Ratio

The quality characteristics can be effectively identified through the logarithmic functions subjected to optimal criteria. In this investigation for minimal displacement, lower the better S/N ratio and nominal the better for temperature study is considered.

The mean effect plots for displacement and temperature are shown in Fig. 2a, b. It clarifies that the displacement greatly depends on layer thickness rather than other factors. In addition, it is identified that the temperature variation regards to the factors are shown at Fig. 2b.

The layer thickness and amount of heat are predominantly affecting the thermal behavior of the structure than heater speed.

The greater S/N value gives better performance and it may not depend on the category of performance characteristics. The optimum parameters and their levels are estimated from Table 3 and it is summarized in Table 4.

3 Analysis of Variance (ANOVA)

ANOVA is a statistical-based tool which helps in evaluating the significance of considered process parameters. Based on that, ANOVA table is constructed for temperature (Table 5) and displacement (Table 6) profiles. It is evident from these

Table 5 ANOVA results for temperature

Source	DOF	Adj SS	Adj MS	F-ratio	P-value	Percentage (%)
T	2	8.51	4.25371	119.3	0.008	46.2
S	2	0.79	0.39105	10.97	0.084	4.24
Q	2	9.05	4.524	126.30	0.008	49.15
Error	2	0.07	0.0356	–	–	–
Total	8	18.41	–	–	–	–

Table 6 ANOVA results for displacement

Source	DOF	Adj SS	Adj MS	F-ratio	P-value	Percentage (%)
T	2	0.000459	0.00023	16551.41	0	99.78
S	2	0	0	1.99	0.335	0.12
Q	2	0	0	0.44	0.692	0.1
Error	2	0	0	–	–	–
Total	8	0.00046	–	–	–	–

Table 7 Optimal parameters for SIS process

S. No	Parameters	Structural field	Thermal field
1	Layer thickness	1.5 mm	1.5 mm
2	Heater speed	200 mm/s	180 mm/s
3	Amount of heat	30 W	50 W

tables that, thickness and amount of heat are more influencing in the distribution of temperature and thickness alone playing vital role in minimizing the structural displacement.

The results also suggested the nominal values of selected parameters to perform further experimental studies which are given in Table 7.

4 Conclusion

The present work concentrated on Taguchi method of optimizing the process parameters of SIS process with L9 orthogonal array. The FEA study provided regions of maximum temperature and displacement of the structure which is further taken into account to perform Design of Experiments. Rigorous simulations are carried out to obtain the responses of temperature and displacement. The inference on the simulation studies identified the key influencing parameters of SIS temperature and displacement of the polymer structure. The amount of heat about 50 % induces thermal gradient than layer thickness and heater speed. The layer thickness predominantly affected the displacement of the structure than other parameters. It is concluded that, with the layer thickness of 1.5 mm and 30 W applied heat, minimal thermal stress and structural displacement are experienced.

References

1. Chua CK, Leong KF (1998) Rapid Prototyping. Principles and Applications in Manufacturing, John Wiley & Sons.
2. Khoshnevis B, Asiabanpour B (2006) Selective Inhibition of Sintering. Rapid Prototyping, Springer US, 197–220.
3. Asiabanpour B, Khoshnevis B, Palmer K and Mojdeh M (2003) Advancements in the SIS process. 14th International Symposium on Solid Freeform Fabrication, Austin, TX.
4. Khoshnevis B, Yoozbashizadeh M and Chen Y (2012) Metallic part fabrication using selective inhibition sintering. Rapid Prototyping Journal 18.2: 144–153.
5. Khoshnevis B, Zhang J, Fateri M, and Xiao Z (2014) Ceramics 3D printing by selective inhibition sintering. In Solid Free Form Symposium (SFF).
6. Arunkumar P, Balasubramanian E, and Chandrasekhar U (2015) Thermo mechanical modeling of selective inhibition sintered thermoplastic parts. Journal of Applied Mechanics and Materials, In press.
7. Roberts IA, Wang CJ, Esterlein R, Stanford M, and Mynors DJ (2009) A three-dimensional finite element analysis of the temperature field during laser melting of metal powders in additive layer manufacturing. International Journal of Machine Tools & Manufacture, 49: 916–923.
8. Arunkumar P, Balasubramanian E, and Chandrasekhar U (2016) Investigation on multi-layer selective inhibition sintering process using finite element analysis. 5th International Conference of Materials Processing and Characterization.
9. Lipin K, and Govindan P, A review on multi objective optimization of drilling parameters using Taguchi methods.
10. Sibalija, Tatjana V, and Majstorovic V.D (2010) Novel approach to multi-response optimisation for correlated responses. FME Transactions 38.1: 39–48.
11. Ic, Tansel Y, Dengiz B, Dengiz O, and Cizmeci G (2014) Topsis based Taguchi method for multi-response simulation optimization of flexible manufacturing system. In Simulation Conference (WSC) winter. IEEE.
12. Gaitonde VN, Karnik SR, Achyutha BT, Siddeswarappa B (2006) Multi-response optimization in drilling using Taguchi's quality loss function, Indian Journal of Engineering and Materials Sciences, 13.6: 484.
13. Refaie AA, Wu TH, and Li MH (2010) An effective approach for solving the multi-response problem in Taguchi method, Jordan Journal of Mechanical and Industrial Engineering, 4.2: 314–323.
14. Pai, Dayananda, Rao SS, and Shetty R (2012) Application of Taguchi and response surface methodologies for metal removal rate and surface roughness in grinding of drac's. International journal of Engineering and Management, 3.1.

Design of an Aircraft Wing for Given Flight Conditions and Planform Area

H.P. Bharath, H.K. Narahari and A.T. Sriram

Abstract Wing design is crucial in order to get required performance during flight. Wing design includes selection of airfoil, planform shape with a host of parameters like leading edge sweep, thickness to chord ratio and twist. Design of wing for a 20 ton class combat air-craft, capable of supersonic cruise ($M = 1.3$ at an altitude 6 km) and for short take-off and landing is considered as a test case. A sequential selection method is used in this study as a first step before full DoE-based optimization. NACA 64A series airfoils are used for construction of various wing geometries by varying (a) camber 0–5 % (b) leading edge sweepback angle of $42° \pm 3°$ (c) maximum thickness to chord ratio of 4–5 %, and (d) geometric twist angle of about 0°–1°. CATIA software is used for creating the wing geometry. ANSYS-Fluent software is used for CFD simulations. The plain wing geometry is arrived by sequentially analyzing each geometric parameter. Simulations are also performed for wing with high-lift devices, HLDs, like leading edge slat and trailing edge flap for take-off and landing condition. For required flight condition plain wing with airfoil NACA 64A204, 42° leading edge sweepback, −0.53° twist and 0.23° wing incidence angle showed improved aerodynamic performance than baseline wing. The selected plain wing with HLDs of +12.5° deflection at $M = 0.25$ has slightly more lift coefficient and $(L/D)_{max}$ than wings with HLDs at other deflection and Mach number.

Keywords Supersonic cruise · NACA 64 series airfoil · Sweepback wing · Symmetric and cambered wing · Wing twist · High-lift devices

1 Introduction

Research and development of supersonic aircraft are quite important due to its current use in military and future use in commercial aircraft. Design of any aircraft generally involves an integrated approach of considering various subsystems,

H.P. Bharath · H.K. Narahari · A.T. Sriram (✉)
Department of Automotive and Aeronautical Engineering,
M. S. Ramaiah University of Applied Sciences, Bangalore 560 054, India
e-mail: atsriram@gmail.com

independently first and then interconnecting them to meet specified requirements. Among various subsystems, wing design plays a major role in order to provide adequate lift and also to improve handling qualities.

The aerodynamic design of supersonic wing itself is complicated due to the presence of shock waves. They cause additional drag, which leads to higher fuel consumption. It is also preferable to have short take-off and landing. This brings in additional complexity in design. Hence it is important to consider various aspects during design stages. The complexity of structural aspects can be considered separately before analyzing the wing for aerodynamic performance.

Generally, the wing design starts with mission requirement with overall weight of aircraft. For simplicity, cruise speed at particular altitude is considered in this study. Also, wing area and related parameters are assumed based on existing data/configuration which serve as baseline configuration for the wing. In this study, geometric variation is considered to identify its effects and also for better wing design.

The fundamental effects of various geometric parameters like camber, sweepback, and thickness to chord (t/c) ratio of wing are known [1–4]. Wing twist (aerodynamic as well as geometric) is given in order to ensure that the stall occurs in the root regions first than wing tip regions. For supersonic aircraft, it is desirable to have minimal camber and small (t/c) ratio to minimize wave drag and use leading edge slat and or trailing edge flap (HLDs) for short take-off and landing.

The flow physics associated with supersonic airplane was reviewed in the past [5], mostly based on experimental measurements and theoretical analysis. Also, DoEs method was used [6] for better design. In this study, CFD simulations are performed with the use of ANSYS-Fluent software to obtain performance characteristics and better understanding before proceeding to optimization methods.

2 Design Methodology and Simulation Cases

The design methodology followed in the present study is shown in Fig. 1. It has five phases. In the first phase, a baseline airfoil of NACA 64A004 airfoil is selected. The selected airfoil is analyzed for four cambers with varying angle of attack to obtain drag polar. Generally two or three better airfoils are selected based on lift characteristics for the construction of wing.

The baseline wing is constructed from the baseline airfoil. It has leading edge sweepback angle of 42° and uniform (t/c) of 4 % along the span without any twist.

Based on the airfoil analysis, three wings are proposed. In the second phase, the leading edge sweep angle is varied as 39°, 42°, and 45°. It gives nine different wings geometries (Wing-A to Wing-I). In each wing geometry, the drag polar is constructed with five different angles of attack.

In third phase of wing design, the variation of (t/c) along the span is considered. For this study, NACA 64A204 airfoil with LE sweepback angle 42° (Wing-E) is considered as reference wing. Two more wing geometries are constructed (Wing-J and Wing-K) for this study.
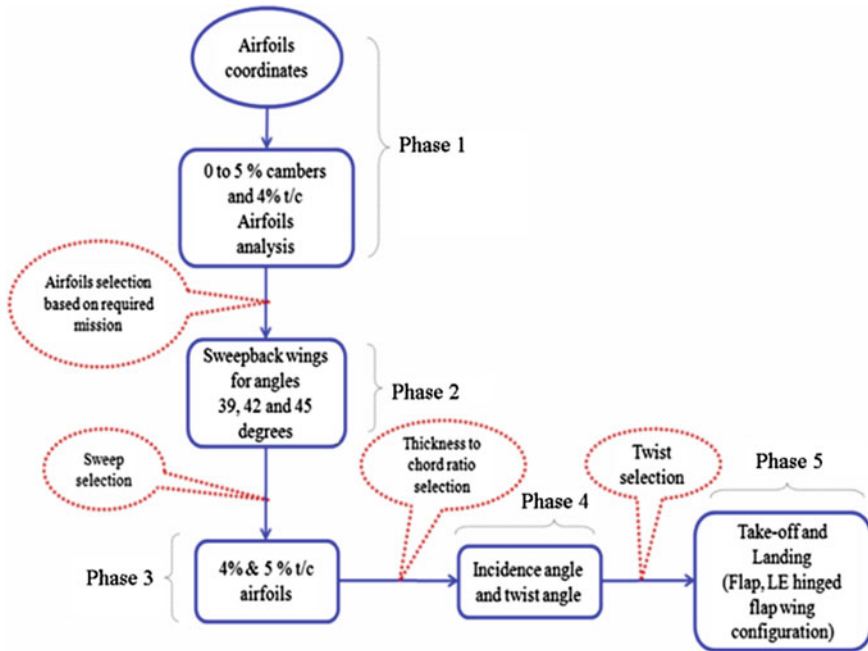
Fig. 1 Flow chart showing the methodology for wing design consideration

In the fourth phase of the design, the wing twist is varied. Different twist is given for Wing-E and Wing-K. Based on the simulations, the better wing is selected (Wing-N for the present study).

The selected wing in the fourth phase is analyzed with HLDs of LE hinged flap and TE flap for take-off and landing. Some wing configurations are given in Appendix and details are given in reference [7].

3 CFD Simulations for Validation and Verification

Initially, NACA 0012 airfoil is simulated for inflow Mach number, $M = 0.7$ and Reynolds number 9×10^6 with angle of attack of 1.49° for validation. The predicted results have shown good agreement with experiments.

The wing planform with variation in sweep, computational domain, structured mesh, and the boundary conditions for the baseline wing is shown in Fig. 2. Three grids of 1.3, 1.45, and 1.9 millions are chosen for grid study. The results are shown less difference among various grids. Hence, grid size of 1.45 million is used in this study.
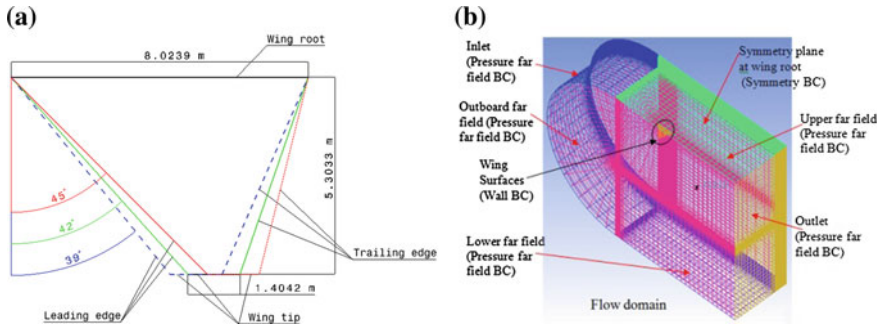
Fig. 2 Wing configurations and computational domain. **a** Wing planform. **b** Structured mesh and boundary conditions

4 Results and Discussion

The simulations were carried out at different angles of attack for various airfoils and wing geometries for flight condition of $M = 1.3$ at an altitude of 6 km. Then aerodynamic performance parameters like lift coefficient, drag coefficient, and pressure distributions were extracted from simulations for analysis.

4.1 Effect of Camber on 2D Airfoil

The baseline airfoil is of zero camber (NACA 64A004). The camber is varied to get four additional airfoils. Simulations are performed by varying the angle of attack (from 1° to 7°).

Figure 3 shows the plot of C_L against C_D. It is seen that the C_D for zero lift is more for cambered airfoil. However, it can be seen from the figure that for the same drag coefficient C_D the cambered airfoil can sustain higher C_L. Based on this, NACA64A204 airfoil is selected for wing design.

Mach number contour for symmetric and cambered airfoil at 0° angle of attack are shown in Fig. 4a, b, respectively. It clearly captures shock structure and flow turning along the cambered airfoil and associated compression and expansion waves.

4.2 Effect of 3D Wing Sweep and Thickness to Chord Ratio, t/c, Along the Span

The effect of sweep on aerodynamic characteristics for NACA 64A204 airfoil is alone show in Table 1. The $(C_L/C_D)_{max}$ and C_L at 0° AoA increase with sweepback angle. However, lift-curve slope decreases. By considering combined effect, 42° sweep has better advantage. Hence, Wing-E is considered for further design.
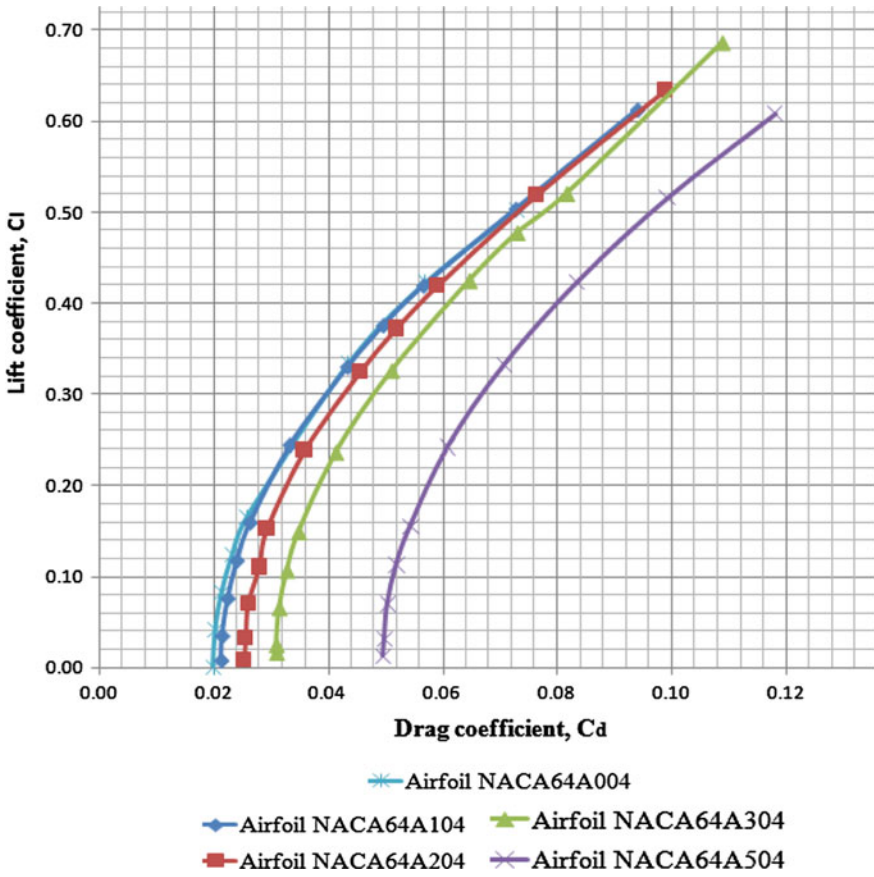
Fig. 3 Drag polar of symmetrical and cambered airfoils
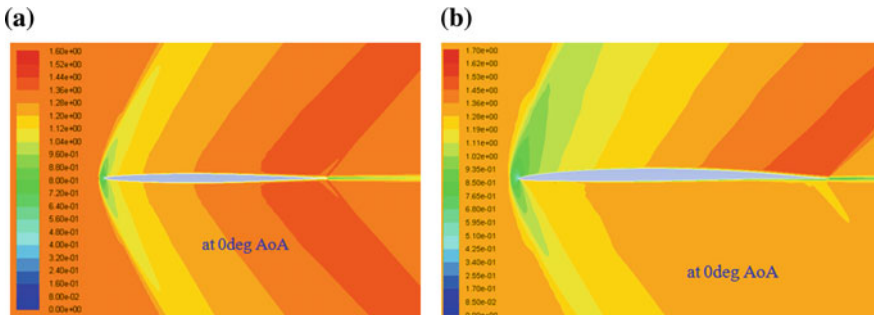
Fig. 4 Mach number contours to show the effect of camber. **a** Symmetrical NACA 64A004 airfoil. **b** Cambered NACA 64A204 airfoil

Table 1 Effect of LE sweepback angle

Sl. No	Wing type	LE Sweepback angle (degree)	Lift-curve slope (per degree)	$(C_L/C_D)_{max}$	C_L at 0° AoA
1	Wing-D	39	0.0606	8.00	0.0253
2	Wing-E	42	0.0599	8.20	0.0271
3	Wing-F	45	0.0587	8.31	0.0295

Wings with 4–5 % variation in (t/c), (Wing-J and Wing-K), are simulated. Further, calculations are made for wing weight and fuel volume to estimate range and endurance. The results show there is no significant benefit from increasing (t/c) of wing from 4 to 5 %.

4.3 Effect of Twist

The wing geometries with three different twists were created for Wing-E and Wing-K. Wing-N and Wing-Q have shown better C_L at 0° AoA of about 0.0358. This helps in cruise condition.

The lift distribution over semi-span of Wing-E, Wing-N, and Wing-Q are compared (not shown here) and it is observed that the Wing-Q has negative C_L near the wing tip regions. Hence, the Wing-N is selected as required plain wing.

Figure 5 shows pressure coefficient for baseline wing and Wing-N. It is observed that pressure coefficients at wing root have more positive values than the tip. It is also observed that the Wing-N has better elliptical lift distribution so it is safer.
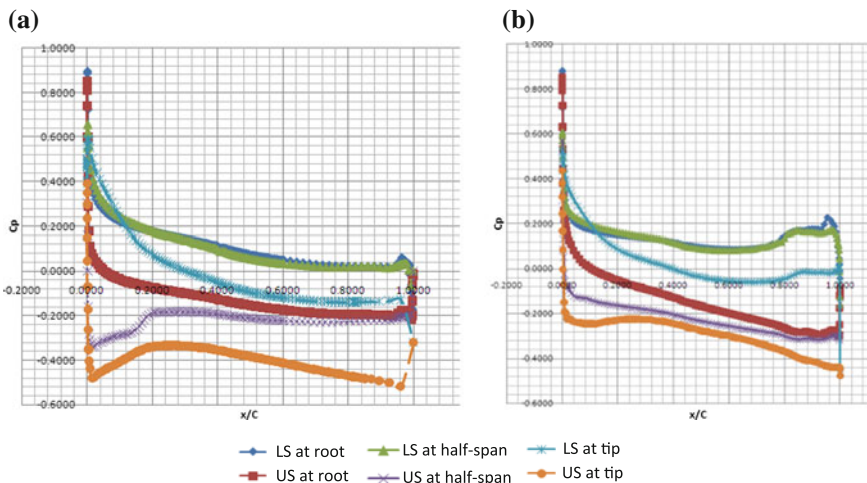
Fig. 5 Pressure coefficient. **a** Baseline wing for 5° AoA and **b** Wing-N at 5° AoA
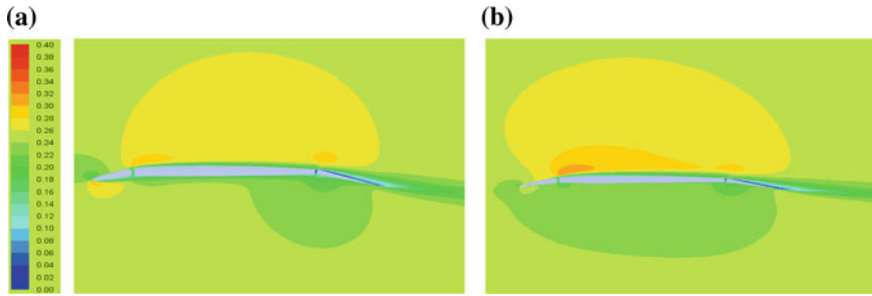
Fig. 6 Mach contours of Wing-R. **a** $M = 0.25$ and 0° AoA. **b** M = 0.25 and 4° AoA

4.4 Subsonic Simulations for Cruise, Take-off, and Landing

Simulation is performed for selected Wing-N for subsonic performance. It is observed that the drag coefficient at $M = 0.7$ at an altitude 6 km and 0° AoA is about half of drag coefficient at $M = 1.3$.

LE hinged flap and TE flap were created on selected plain Wing-N with deflection of +12.5° and +20° and simulations are performed at $M = 0.1$ and $M = 0.25$ at sea level condition.

The results have shown that C_L/C_D is maximum at HLD's deflection of +12.5° and at $M = 0.25$. So, Wing-R (i.e., Wing-N with +12.5° HLD's deflection) at $M = 0.25$ is considered for climbing and descending flight conditions.

The Mach contours of flow over Wing-R at $M = 0.25$ for 0° and 4° AoA are shown in Fig. 6a, b, respectively. It is observed that the flow at LE of wing is smooth at 4° AoA than at 0° AoA. So there will be less chances of flow separation at increased angle of attack which is below stall angle. Hence, it is preferable to fly at a higher AoA while using HLD's, especially while using leading edge flap.

5 Conclusions

A sequential way of designing supersonic wing is proposed and demonstrated with CFD simulations. Wing constructed from cambered airfoil is preferable due to its lift characteristics. At various phases of design, the noticed observations are summarized below.

- While wing LE sweepback helps for supersonic flight conditions, higher sweepback tends to increase wing structural weight as well as adversely impact take-off and landing performance. Keeping the above trade-off in view, a sweepback angle of 42° is selected in the present study.

- The t/c ratio is one of the important design parameters which influences the weight of wing, fuel storage, and hence the range and endurance. The value of t/c between 4–5 % t/c is recommended.
- The twist of wing is studied and wing is suggested with twist of −0.53° to provide delay in tip stall.
- In order to establish subsonic performance, studies were carried out with HLDs. A combination NACA 64A204 airfoil with 42° LE sweptback, 0.23° incidence angle and −0.53° twist and flap deflection +12.5° gave the suitable take-off, climb and landing performance.

Appendix: Selected Wing Configurations

Baseline wing: NACA 64A004 airfoil, LE sweepback angle 42°· No Twist
Wing A: NACA 64A104 airfoil, LE sweepback angle 39°, No Twist
Wing B: NACA 64A104 airfoil, LE sweepback angle 42°, No Twist
Wing C: NACA 64A104 airfoil, LE sweepback angle 45°, No Twist
Wing D: NACA 64A204 airfoil, LE sweepback angle 39°, No Twist
Wing E: NACA 64A204 airfoil, LE sweepback angle 42°, No Twist
Wing J: NACA 64A205 (at root) and NACA 64A204 (at tip) airfoils, 42° LE sweepback, No Twist
Wing K: NACA 64A205 (at root), NACA 64A204 (MAC span or 2.651 m span) and NACA64104 (at tip) airfoils, 42° LE sweepback, No Twist
Wing N: Wing E with −0.53° Twist and 0.23° incidence angle
Wing Q: Wing K with −0.65° Twist and 0.25° incidence angle
Wing R: Wing N with +12.5° HLD's deflection

References

1. Daniel P. Raymer (1992) *Aircraft Design: A Conceptual Approach*, AIAA Education Series.
2. Nicolai and Carichner(2010) *Fundamentals of Aircraft and Airship Design,Volume I — Aircraft Design,* AIAA, INC. 1801 Alexander bell drive, Reston, VA 20191-4344.
3. Sadraey, Mohammad H. (2013) *Aircraft Design – A Systems Engineering Approach* John Wiley & Sons Ltd.
4. Whitford, Ray (1989) *Design for Air Combat* Jane's Information Group, Surry, England.
5. Kulfan, R. M. and Sigalla, A (1979) Real Flow Limitations in Supersonic Airplane Design, *J. Aircraft,***16** (10) pp 645–658.

6. Giunta, A., Balabanov, V., Haim, D., Grossman, B., Mason, W. H., Watson, L. T., and Haftka, R. T. (1996) Wing Design for a High-Speed Civil Transport Using a Design of Experiments Methodology, *AIAA* 96-4001.

7. Bharath H. P. (2015) *Design of an Aircraft Wing for Given Flight Conditions and Planform by Varying Other Geometric Parameters,* M.Sc. Thesis, Dept. of Automotive and Aeronautical Engineering, M. S. Ramaiah School of Advanced Studies, Bangalore, INDIA.

Investigations on the Influence of Mechanical Behaviour of Copper Aluminium Nickel Powder Compacts Processed Through Powder Metallurgy

Abirami, K. Thiruppathi and S. Raghuraman

Abstract Optimization is proved proficiency method, which is used for finding required process conditions to give the maximum or minimum value of the function. A new metal based alloy with a defined composition of Copper (84 %) Aluminium (12 %) Nickel (4 %) is proposed. The powder has synthesized by a powder metallurgy process for the production of near net-shaped components through mechanical alloying. It is more complex to attain the properties in the making of materials for marine applications. The main objective of this study was to obtain an alloy compact with high density and hardness and consider a set of optimal process parameters like sintering temperature, holding time and compaction pressure. The alloy has a set of desired properties to suit the needs of the marine applications, porous material filters and electric friction equipments. The combination of Cu–Al–Ni offered in marine applications like rotary hydraulic actuator, hydraulic tube due to high mechanical strength, good corrosion resistance. Copper, Aluminium and Nickel powders are mixed by ball milling equipment and compacted at pressures 550, 590 and 630 MPa using Universal Testing Machine (UTM). These compact specimens have been sintered in an electric muffle furnace at temperatures 640, 695 and 750 °C at different holding times of 30, 60 and 90 min. The L9 orthogonal array was designed with the combination of input factors and their levels. The experiments were conducted at each level to measure the maximum hardness and density. Grey Relational Analysis was applied to find the optimum input parameter configuration. ANOVA was adopted to determine the level of significance of input factors. Confirmatory experiments were done to verify the optimal results.

Keywords Powder metallurgy · Powder compacts · Mechanical properties · Taguchi method · Grey relational analysis

Abirami (✉) · K. Thiruppathi · S. Raghuraman
School of Mechanical Engineering, SASTRA University, Thanjavur, Tamil Nadu, India
e-mail: abiramimechanical@gmail.com

1   Introduction

Powder metallurgy is the art and science technology for producing metal alloy, ceramic powders for blending the powders, compaction and sintering of compacted powder to get a specimen with the desired properties [1]. Cu–Al–Ni alloy products are used in porous material filters and electric friction equipments with better mechanical strength (up to 400 Mpa) [2]. Nickel was used to enhance the chemical stability of Cu. The microstructure of the Cu–Al–Ni alloy has to be evaluated in different percentage of Ni. The Ni content is increased to get a smooth decrease of the grain size of structure [3]. Cu–Al alloy has better mechanical and strength properties; when the Ni is added to these alloys it increases the permeability of the alloy [4]. Taguchi method was designed to determine the optimal input parameters of Titanium alloy foams and to maximize the density of titanium alloy foams [5]. Copper-aluminium-nickel alloy is a corrosion-resistant material which is used in marine hardware, dental post and core applications with the reasonable cost. The copper alloys blended with 9 wt% Al and 2–4 wt% Ni to be used in dental post and core applications [6]. The quality of a product is the main factor for showing the growth of a company. The quality of the product mainly depends upon the material and process parameters. Optimization technique plays a vital role to increase the quality of the product at reasonable cost [7]. Grey Relational Analysis (GRA) has been used by many researchers for machining processes, which implicate chemical, mechanical polishing [8], turning [9], to optimize the significant input parameters.

The specimen strength is increased through the reduction of grain size, and grain size in the micrometre range is suitable for industrial application because of good balance between strength and ductility [17]. The porosity of the sintered specimens decreases with an increase in the sintering temperature and decrease in loading pressure [18]. Cu–Al–Ni shape memory alloys, negligible porosity, excellent interparticle bonding, and fine grain size are primary requirements to realize desired shape memory and mechanical properties [19]. The objective of this paper is to determine the optimal levels of the process parameters for metal alloy compacts using Taguchi approaches.

2   Materials and Methodology Used

2.1   Experimental Material

The Copper and Aluminium powders were procured from the Metal Powder Company LTD (MEPCO), Thirumangalam and Nickel powder was procured from Ponmani & Co, Trichy. The particle size of the powder is 75–125 µm (Copper), 150–180 µm (Aluminium) and 100 mesh (Nickel).

2.2 Specimen Production

The weight of the powders were measured by an electronic balance (SH1MADZU) with a least count of 0.001 mg and an accuracy of ±0.01 mg. 504 g of Copper, 72 g of Aluminium and 24 g of Nickel were used to prepare a 600 g powder to blend of 84 % Copper 12 % Aluminium and 4 % Nickel by weight. 60 g of powder were required to produce a single specimen. The material is handled carefully to avoid the process of oxidation.

Therefore,
Copper content in a single specimen = 0.84 × 60 = 50.4 g
Aluminium content in a single specimen = 0.12 × 60 = 7.2 g
Nickel content in single a specimen = 0.04 × 60 = 2.4 g.

2.2.1 Ball Milling Process

The 600 g of powders were required to produce the nine specimens and these powders were subjected to ball milling process in order to obtain a uniform blend of Copper, Aluminium and Nickel powders. The process was carried out without any interruption for 8 h. Figure 1 shows the apparatus used for the ball milling. This apparatus is used to grind or mix metal powders for further processing.

The Copper, Aluminium and Nickel powder and ceramic balls are poured into the mill drum and rotated at 80 RPM. The motor rotated at 520 RPM.

2.2.2 Compaction

The blended powders were subjected to compaction process using UTM machine. The shape of the specimen is cylindrical. 25 mm diameter of mild steel die was used for the production of the compacts. The compaction pressure was selected from the American Standard for Materials (ASM) manual for powder metallurgy. The powder should be compacted from 250 to 635 MPa. The compaction pressure range was taken as 550–630 MPa because below a pressure of 550 MPa results in surface crack.

Fig. 1 Ball milling equipment process

Fig. 2 Compacted specimen

During the compaction process, the punch speed was carefully controlled since high force will produce a very less density of the specimen so the life of the specimen is less. The dimensions of the specimen are 25 mm × 30 mm. A compacted specimen is shown in Fig. 2. The compaction process was carried out in three different levels of pressure. The compaction force is calculated using

$F = P \times A$
where,
P = Compaction pressure
$A = \pi r^2 = \pi \times 12.5^2 = 490.873 \text{ mm}^2$
$P = 550 \text{ MPa } F = 270 \text{ KN}$
$P = 590 \text{ MPa } F = 290 \text{ KN}$
$P = 630 \text{ MPa } F = 310 \text{ KN}$

2.2.3 Sintering of Powder Compact

Sintering is the process of bonding the powder particles to get the strength of a compact specimen. Sintering temperature is taken as 0.6 times to 0.7 times on the melting point of the alloy.

Melting point of the alloy = 1067.8 °C [6]

$$\text{Sintering Temperature range} = 0.6 \times 1067.8 \text{ to } 0.7 \times 1067.8$$
$$= 640.6 \text{ to } 747.46$$

The sintering temperature of the alloy was taken in the range of 640–750 °C. The sintering time was selected in the range of 1800 s (30 min) to 5400 s (90 min) based on previous experiments [2]. The muffle furnace used for sintering process is shown in Fig. 3. The three different response parameters and three different levels are recommended for experimental work and shown in Table 1.

Fig. 3 Muffle furnace

Table 1 Input factors and levels

Factor	Notation	1	2	3
Compaction pressure (MPa)	A	550	590	630
Sintering temperature (°C)	B	640	695	750
Holding time (min)	C	30	60	90

2.3 Experimental Method

Orthogonal array which is basically highly fractioned factorial layouts becomes useful in terms of minimizing the number of trials to be conducted. The frequency of occurrence of the symbols will be same for all the columns. Taguchi's L9 orthogonal array was designed with the combination of input factor and their levels. The Table 2 shows the L9 orthogonal array.

2.3.1 Measurement of Hardness

The Brinell hardness test method as used to determine the hardness of the specimens. The specimens were polished using four grades of emery sheet before the

Table 2 L9 orthogonal array

Exp No	Pressure (MPa)	Temperature (°C)	Holding time (min)
1	550	640	30
2	550	695	60
3	550	750	90
4	590	640	60
5	590	695	90
6	590	750	30
7	630	640	90
8	630	695	30
9	630	750	60

hardness testing process. A carbide ball indenter was used in Brinell hardness machine for measuring the hardness of the specimen. The hardness values were measured at two different points, and the average value of the hardness was taken.

2.3.2 Measurement of Density

Sintered specimens density was measured by Archimedes principle using SH1MADZU machine. The sintered specimen, fully immersed in a fluid is sustained by a force equal to the weight of the fluid removed from the water.

Theoretical Density is calculated using

$$\text{Theoretical Density of the Cu}-\text{Al}-\text{Ni} = \frac{100}{\dfrac{\% \text{ of Cu}}{\rho_{\text{Cu}}} + \dfrac{\% \text{ of Al}}{\rho_{\text{Al}}} + \dfrac{\% \text{ of Ni}}{\rho_{\text{Ni}}}} = \frac{100}{\dfrac{84}{8.96} + \dfrac{12}{2.699} + \dfrac{4}{8.88}}$$
$$= 7.0069515 \, \text{g/cc}$$

3 Analysis Technique

Taguchi method is useful to measure the single output parameter. The advantage of Taguchi's method has to reduce the experimental time, reduces the cost and easily identifies the significant output parameter. ANOVA is used to determine the level of significance of input factors. Taguchi's contribution is the S/N ratio. There are six different S/N ratios, (a) Higher-the-better (b) Lower-the-better (c) Nominal-the-best (d) Classified attribute (e) Dynamic.

The objective is to obtain the high density and high hardness. It is concerned with obtaining the larger value of density and larger value of hardness. Hence, the required quality characteristics of high density and high hardness are higher-the-better, because the output must be large. Higher-the-better S/N ratio is calculated by

$$\text{S/N ratio} \, (\eta_{HB}) = -10 \log_{10} \left(\frac{1}{j}\right) \sum_{i=1}^{n} \frac{1}{y_i^2}$$

where, j—number of recurrence of the experiment, y_i—average of output response value and $i = 1, 2, 3 \dots n$.

3.1 Experimental Results

The values of the output parameters (Density and Hardness) for the nine experiments that have been carried out and the values are presented in Table 3.

Table 3 Experimental output

Exp No	Pressure (MPa)	Temperature (°C)	Holding time (min)	Density (g/cc)	Hardness (HB)	S/N ratio for density	S/N ratio for hardness
1	550	640	30	5.8343	96	15.3198	39.6454
2	550	695	60	5.9042	105	15.4232	40.4238
3	550	750	90	5.9543	110	15.4966	40.8279
4	590	640	60	5.6749	97	15.0792	39.7354
5	590	695	90	5.9985	119.5	15.5609	41.5474
6	590	750	30	6.0031	120	15.5675	41.5836
7	630	640	90	5.9139	110	15.4375	40.8279
8	630	695	30	5.7868	96	15.2488	39.6454
9	630	750	60	5.4271	100.5	14.6914	40.0433

3.2 Optimization Using Grey Relational Analysis

A grey relational technique is used for optimizing single response problem. Grey Relational Analysis was employed to determine the optimal input parameter configuration. The main objective of Taguchi method is (a) To reduce the changes in product design (b) To improve fitness to use.

The steps are

Step 1: Normalizing S/N ratio in the Range 0–1.

The normalized Signal to Noise ratio is computed using the formula, $x_i(k) = \dfrac{\eta_i(k) - \min \eta_i(k)}{\max \eta_i(k) - \min \eta_i(k)}$ where, $\eta_i(k) = $ Current S/N ratio value for the kth response, $\min \eta_i(k) = $ Least value of $\eta_i(k)$ for the kth response $\max \eta_i(k) = $ Higher value of $\eta_i(k)$ for the kth response.

S/N ratio and Normalized S/N ratio for the density and hardness is shown in Table 4.

Table 4 Normalized S/N ratio for density and hardness

Exp No	Density (Response I)		Hardness (Response II)	
	S/N Ratio	Normalized S/N Ratio	S/N Ratio	Normalized S/N Ratio
1	15.3198	0.7173	39.6454	0
2	15.4232	0.8353	40.4238	0.4016
3	15.4966	0.9191	40.8279	0.6101
4	15.0792	0.4426	39.7354	0.0464
5	15.5609	0.9925	41.5474	0.9813
6	15.5675	1	41.5836	1
7	15.4375	0.8516	40.8279	0.6101
8	15.2488	0.6362	39.6454	0
9	14.6914	0	40.0433	0.2053

Step 2: Computation of deviation

The deviation is computed using the formula, $\Delta = 1 - x_i(k)$ where $x_i(k)$ = Normalized S/N ratio.

Step 3: Determination of grey relational coefficient

The grey relational coefficient is calculated using the formula, $\chi = \frac{\Delta\min + \gamma\Delta\max}{\Delta + \gamma\Delta\,max}$ where Δ = Deviation of the current response, Δmin = Minimum deviation, Δmax = Maximum deviation, γ = Distinguishing coefficient, which is taken as 0.5.

Step 4: Ranking of grey relational grade

The grade is computed using, $G = \sum_{i=1}^{n} \frac{\chi_i}{n}$ where, n = Number of responses, χ = Grey relational coefficient.

Deviation, Grey relational coefficient and Grey relational grade are shown in Table 5 (Fig. 4).

Step 5: Computation of mean grey relational grade for individual input parameter

The mean grey relational grade for each level of an input parameter is computed by the following method.

(a) To take the average value of the grey relational grade for each column of the input parameters at a corresponding level
(b) Tabulate the mean grey relational grades for three input parameters at a corresponding level (Table 6, Fig. 5).

Step 6: Determination of an optimal input parameter. The optimized input parameter level is selected corresponding to the rank of the Grey relational grades.

Compaction pressure = Level 2 = 590 MPa, Sintering Temperature = Level 3 = 750 °C and Holding Time = Level 3 = 90 min. The optimal parameter configuration is **A2 B3 C3**. The rank implies that the corresponding factor has a high impact on the output parameters. The significant input parameters from the

Table 5 Deviation, grey relational coefficient and grade for each experiment

| Exp No	Deviation sequences		Grey relational coefficient		Grey relational grade	Rank
	Density	Hardness	Density	Hardness		
1	0.2827	1	0.6388	0.3333	0.4861	6
2	0.1647	0.5984	0.7522	0.4552	0.6037	5
3	0.0809	0.3899	0.8607	0.5619	0.7113	3
4	0.5574	0.9536	0.4729	0.3440	0.4085	8
5	0.0075	0.0187	0.9852	0.9639	0.9746	2
6	0	0	1	1	1	1
7	0.1484	0.3899	0.7711	0.5619	0.6665	4
8	0.3638	1	0.5788	0.3333	0.4561	7
9	1	0.7947	0.3333	0.3862	0.3598	9
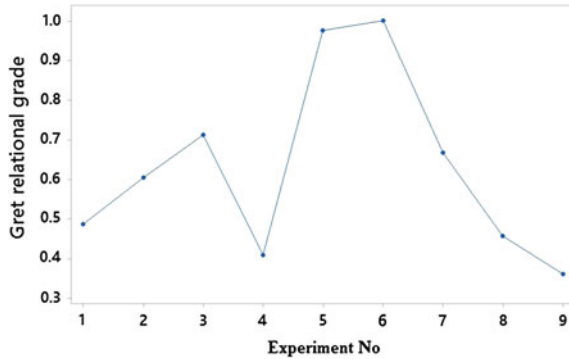
Fig. 4 Grey relational grade for each experiment

Table 6 Mean grey relational grade for individual input factor

Input factor	Level 1	Level 2	Level 3	Max-Min	Rank
Compaction pressure (MPa)	0.6004	**0.7944**	0.4941	0.3003	2
Sintering temperature (°C)	0.5204	0.6781	**0.6904**	0.17	3
Holding time (min)	0.6474	0.4573	**0.7841**	0.3268	1

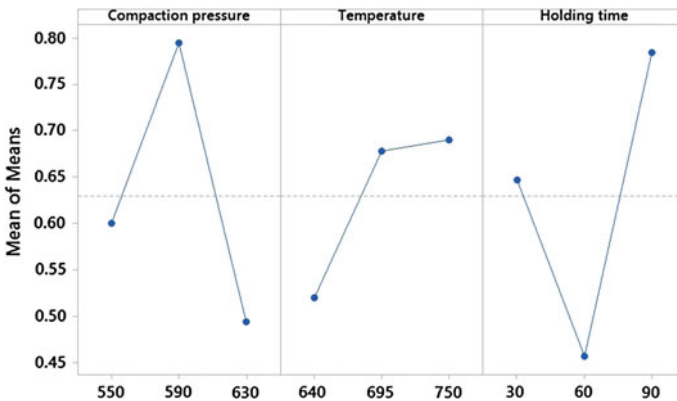**Fig. 5** Average grey relational grade for individual input factor

Max-Min values can be concluded as Factor C = Holding time, Factor A = Compaction Pressure, Factor B = Sintering temperature.

ANOVA was also adopted to determine the percentage significance of input factors. ANOVA method was carried on the Signal to Noise ratio values for the density. Table 7 shows the result of order of significance in ANOVA technique.

Table 7 ANOVA results

Input parameter	DOF	Sum of squares	Mean sum of squares	F test	% of contribution
Compaction pressure	2	0.13906	0.06953	1.68	31.8
Sintering temperature	2	0.05394	0.02697	0.65	12.337
Holding time	2	0.16162	0.08081	1.95	36.959
Error	2	0.08268	0.04134		18.907
Total	8	0.43730			100

Table 8 Confirmation test

Exp No	Compaction pressure (MPa)	Sintering temperature (°C)	Holding time (min)	Density (g/cc)	Hardness (HB)
1	590	750	90	5.9923	123.3926
2	590	750	90	5.9464	123.4586

Table 9 Comparison results

Process parameter	Predicted result	Experiment result
Optimal Parameter	A2 B3 C3	A2 B3 C3
Density (g/cc)	5.9766	5.9694
Hardness (HB)	123.5001	123.4256

3.3 Confirmation Test and Results

The calibration experiment is to validate the conclusion of an output parameter during the analysis phase, after identifying optimal levels of input parameters. The optimal input parameter configuration is **A2 B3 C3**. The predicted response value is calculated by

$$\text{Predicted Value} = [\text{Mean value of A2 + Mean value of B3 + Mean value of C3}]$$
$$- [2 \times \text{Mean value of an output parameter}]$$

The confirmation test for the optimum input parameter configuration and the response values are shown in Table 8.

The comparison of predicted value and experimental value is shown in Table 9.

4   Conclusions

Taguchi's design of experiments and Grey Relational Analysis were employed in this paper to maximize the output parameters like Density and Hardness of metal-based alloy compacts processed through a powder metallurgy route.

The conclusion of this research work is listed below

- The optimum input parameters configuration was concluded as A2 B3 C3. A = Compaction pressure at 590 MPa, B = Sintering Temperature at 750 °C and C = Holding time at 90 min.
- The confirmation test was done and compared with the predicted result.
- ANOVA was also adopted to determine the percentage significance of input factors
- The percentage significance of input factors was obtained using ANOVA.

The further work can be extended to analyze the microstructure of the Cu–Al–Ni powder compacts.

References

1. G.S Upadhyaya, *Powder Metallurgy Technology*, Department of Materials and Metallurgical Engineering, IIT Kanpur, ISBN 1 898326 40 1.
2. W.A Monteiro, J.A.G Carrio (2010) *Structural and Electrical Properties of Copper-Aluminium-Nickel alloys obtained by Conventional Powder Metallurgy Method*, Material Science, Vols 660–661, pp 41–45.
3. Martina Hafner, Wolfgang (2015) *Aluminium-Copper-Nickel Thin film compositional spread Nickel influence on fundamental alloy Properties and Chemical Stability of Copper,* Material Science, Thin solid films 580, 36–44.
4. P.Wenschot (1997) *A New Ni-Al Bronze alloy with Low Magnetic Permeability,* Metallurgical and Materials Transactions, Volume 28A, 689.
5. S. Ahmad, N. Muhamad (2009) *Taguchi Method for determination of optimised sintering parameters of Titanium alloy foams,* International Advances in Materials and processing Technologies, Vol 53.
6. Apiwat Rittapai1, SomchaiUrapepon (2014) *Properties of Experimental Cu-Al-Ni alloy for Dental post and Core Applications,* Journal of Advanced Prosthodontics, Volume 6.2, 15–23.
7. Venkata Rao. R., *Advanced Modelling and Optimization of Manufacturing Processes*, Springer. 2011.
8. Lin, Z.C., Ho, C.Y (2003)*Analysis and application of grey relation and ANOVA in chemical-mechanical polishing process parameters*, International Journal of Advanced Manufacturing Technology, Vol. 21, pp. 10–14.
9. M. Kaladhar (2012) *Determination of optimum process parameters during turning of AISI 304 Austenitic Stainless steels using Taguchi method and ANOVA,* International Journal of Lean Thinking, Volume 3, Issue 1.
10. J.Crane, J.Winter (1986) *Copper – Properties and Alloying,* Material Science and Engineering, Vol 2, p. 848–855.

11. ASM Specialty Handbook (2001) *Copper and Copper alloys, Metals,* Chapter 1 section 1, 56–60.
12. S.M. Tang, C.Y. Chung (1997) *Preparation of Cu-AI-Ni-based Shape Memory Alloys by Mechanical Alloying and Powder Metallurgy Method,* Journal of Materials Processing Technology 63, 307–312.
13. W.A. Badawy, M.M Rabiee (2010) *Effect of Ni Content on the electrochemical behaviour of Cu-Al-Ni alloys in Chloride free neutral solutions,* Chemical Engineering Act 56, 913.
14. M. Gojie, L.Vrsakovic (2011) *Electrochemical and Microstructural Study of Cu-Al-Ni shape memory alloy,* Material Science and Design, Compd 509, 9782.
15. S. Raghuraman, K.Thiruppathi (2013) *Optimization of EDM Parameters using Taguchi Method and Grey Relational Analysis for Mild Steel IS2026,* IJIRSET Vol 2, Issue 7.
16. Sachiko Masuoka, Yosiro (2008) *Preparation of well sintering Cu-Al powders and Properties of its sintered compacts,* Japan Society of Powder Metallurgy, Volume 55, Number 6.
17. G.M. Le a, A. Godfrey a, N. Hansen (2013) "*Structure and strength of aluminium with sub-micrometer/micrometer grain size prepared by spark plasma sintering*"Materials and Design 49, 360–367.
18. Guoqiang Xie, Wei Zhang (2006*) "Fabrication of porous Zr–Cu–Al–Ni bulk metallic glass by spark plasma sintering process*"Scripta Materialia 55,687–690.
19. Mohitsharma, sanjaykumar (2010) *"Processing and Characterization of Cu-Al-Ni Shape Memory Alloy Strips Prepared from Elemental Powders via a Novel Powder Metallurgy Route"* The Minerals, Metals & Materials Society and ASM International.

Investigations on the Performance of Various Bio-Fuels Along with Low Thermal Conductivity Piston Crown in a Diesel Engine

Akkaraju H. Kiran Theja and Rayapati Subbarao

Abstract In this work, combustion chamber of the engine is modified with brass piston crown and air gap insulation of 2 mm between the crown and the piston body. After modification, experiments are carried out with bio-fuels like jatropha, karanja and palmolein on a single cylinder diesel engine with constant speed and an injection timing of 29° bTDC. Comparison of performance parameters, heat balance details and exhaust emissions is done in case of all the fuels at various loads. Brake thermal efficiency increased appreciably with karanja than diesel, while fuel consumption is more in bio-fuels. Heat utilized for brake power is more with karanja when compared to all other fuels. Heat carried away by exhaust gases remained same for all the fuels for all the load conditions. Also, heat rejected to the coolant is low for karanja compared to diesel. Furthermore, CO and HC emissions are fewer with karanja. Thus, the present work identifies karanja as a suitable alternate fuel and with more engine modifications the performance of the engine can be further enhanced.

Keywords Diesel engine · Bio-fuels · Karanja · Engine modification · Piston crown · Performance · Emissions

1 Introduction

Emission control for greener environment and global fuel crisis leads to the search for alternate fuels obtained from different techniques. Greater attention has been drawn to bio-fuels derived from animal fats and vegetable oils prepared with little effort. Apart from increased emissions, there are drawbacks associated with the

A.H.K. Theja (✉)
Department of Mechanical Engineering, KL University, Guntur, India
e-mail: ahkirantheja@gmail.com

R. Subbarao
Department of Mechanical Engineering, NITTTR, Kolkata, India
e-mail: rsubbarao@hotmail.com

Table 1 Properties of the fuels tested

Parameter	Diesel	Karanja	Jatropha	Palmolein
Lower calorific value (kJ/kg)	42700	34900	38450	39750
Specific gravity	0.83	0.809	0.87	0.875

direct use of bio-fuels such as low calorific value and high viscosity. But, it is essential to search for renewable fuels in the present world's economic front to save foreign exchange and to create energy security [1]. Biodiesels derived from vegetable oils are used by many researchers in diesel engines as demand is increasing in developing countries [2]. Transesterification is the most popular processing technique to reduce the high viscosity in the vegetable oils [3]. In the recent past, many researchers found that the brake thermal efficiency is slightly improved by the use of biodiesels in diesel engine without engine modification, however, emissions being higher. Only 1/3rd of the supplied heat in the engine is utilized for work and the same amount is taken away by the cooling system. Minimizing the heat loss to such systems could improve the performance and reduces their size and volume [4]. Heat rejection can be minimized by ceramic coating and air gap insulation. Krishna et al. [5] made comparative studies between conventional engine and engine with low heat rejection combustion chamber with various test fuels, which showed improvement in brake thermal efficiency with reduced exhaust gas temperature and coolant load. Reddy et al. [6] observed higher performance with low heat rejection engine. From the earlier works, it is observed that large amount of heat produced in the combustion chamber is rejected to coolant and exhaust of the engine. Any modification to the engine may lead to improved performance with bio-fuels. In the present study, a brass crown insert is screwed to aluminium piston with an air gap insulation of 2 mm. Tests are conducted on the modified engine with diesel along with bio-fuels, whose properties are shown in Table 1.

2   Experimental Setup

Brass is selected as the piston crown material, which is an alloy made of copper–zinc with low thermal conductivity and heat capacity. The new piston crown along with the optimized air gap insulation (2 mm) acts as a heat barrier. Initially, brass rod of 85 mm diameter is prepared using turning operation on lathe. Later, standard hemispherical piston crown is prepared using proper turning tool and a recess for the valve clearance is arranged. Inserts are drilled at four locations with seating to facilitate screws. Aluminium piston is cut with suitable thickness and drilled at the same locations in order to fix the brass crown with screws on the top portion, since the high-speed reciprocating movement of piston demands very secure method of
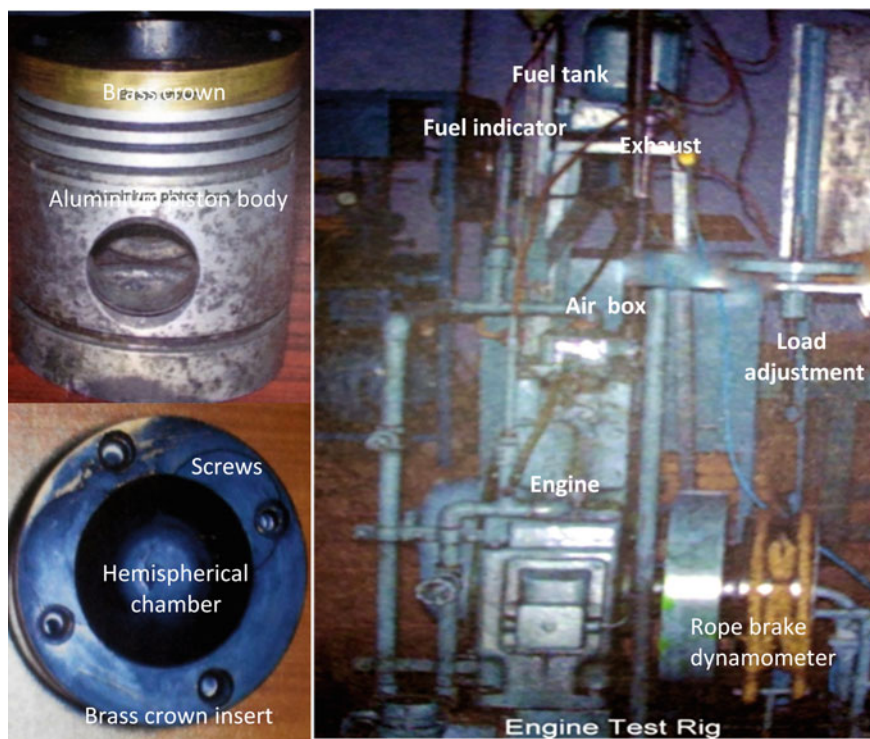
Fig. 1 Experimental setup and piston with brass crown

fastening the crown to the piston. Experiments are carried out on a single cylinder, four-stroke, water cooled, naturally aspirated DI diesel Kirloskar engine as shown in Fig. 1. Compression ratio is 16:1 with bore of 80 mm and stroke of 110 mm. Engine speed is maintained at 1500 rev/min and injection timing of 29° bTDC at all the load conditions. Rope brake dynamometer is attached to accomplish loading on the engine by adding weights in incremental steps of 2 kg from no load to a maximum load of 12 kg. Engine is run idle for ten minutes after the start, in order to stabilize the conditions before the readings are taken. Air drawn into the engine is measured using a U-tube manometer. Time elapsed for 20 cc of fuel level dropped in a burette is noted to estimate the fuel consumption. The inlet and outlet temperatures of water and exhaust gas are noted with the help of thermocouples placed at appropriate locations on the engine. Exhaust emissions are detected with the help of a standard five-gas analyser.

3   Results and Discussion

Experimental results are plotted in terms of performance, heat balance and emissions. Performance plots demonstrate the variation of each parameter with respect to brake power. Heat balance charts are used to compare the heat utilized and lost for all the cases. Emissions of CO, HC, NO_x and O_2 are considered.

3.1   Performance Parameters

Specific fuel consumption (SFC) is reducing with increment in load as shown in Fig. 2a. SFC is lowest for diesel. For karanja, it is slightly higher at all loads. Jatropha is consumed more by the engine. Figure 2b shows the Total Fuel Consumption (TFC) by the engine per hour. Similar to the case of SFC, diesel showed less TFC, followed by karanja, jatropha and palmolein. Only difference being that TFC increased in proportion to the increased load. Brake thermal efficiency is getting better with load as shown in Fig. 3a. For karanja, the performance is distinctly more when compared to diesel. Efficiency is almost same in case of palmolein and jatropha for most of the loads. Figure 3b shows the exhaust gas temperature variation with brake power. Karanja and palmolein have highest gas temperature than diesel and jatropha. From these plots, it is clear that the performance of the bio-fuel is more with similar fuel consumption. This can be attributed to the modification of the combustion chamber.
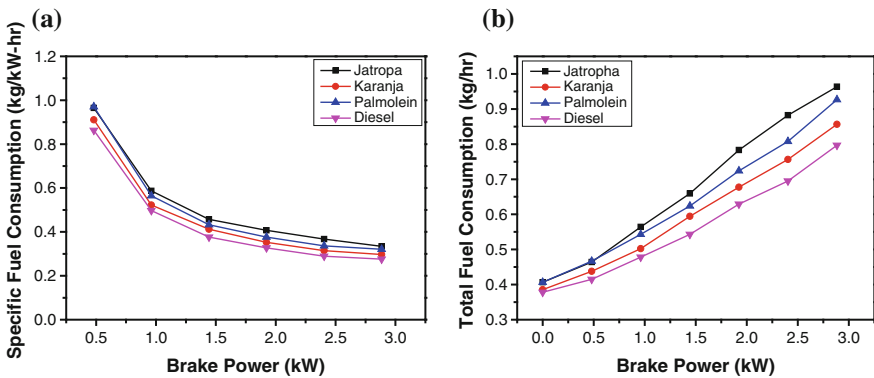

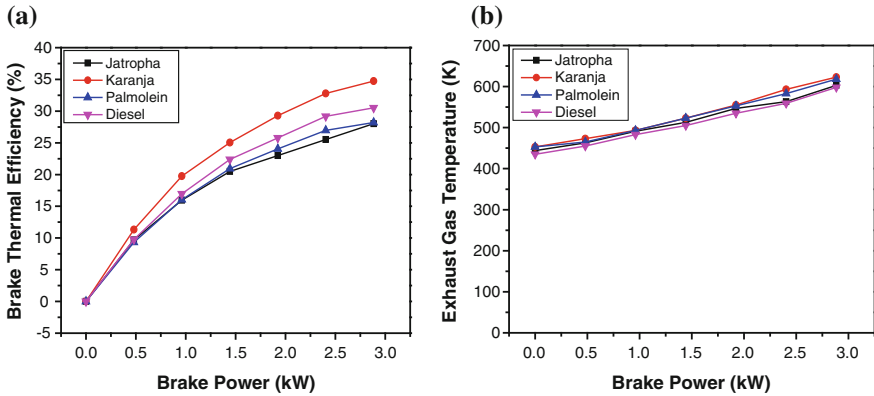**Fig. 2** Specific and total fuel consumption for all the fuels

(a)

(b)

Fig. 3 Brake thermal efficiency and exhaust gas temperature for all the fuels

3.2 Heat Balance Details of the Engine

Table 2 shows the amount of heat converted into power output, heat lost to exhaust gases and coolant in case of diesel and karanja. Heat corresponding to the brake power gradually enhanced with load when engine is tested with diesel. Similar pattern is observed in all the fuel cases. The highest amount of heat corresponding to the brake power is 31 % at full load operation in case of diesel. Heat carried away by the exhaust gases remained identical at all the loading conditions. The amount of heat rejected to the coolant varied with load in both the cases. It is also seen that the amount of heat utilized in brake power has improved significantly for karanja. On the other hand, the amount of heat rejected to the coolant is not as much as diesel. Karanja has shown excellence in minimizing the amount of heat equivalent to unaccounted losses with rise in brake power. The amount of heat carried by exhaust gases is not beyond 26 %, in all the cases of karanja. The percentage of heat supplied in unaccounted losses by jatropha fuel has dropped as shown in

Table 2 Heat balance details for diesel and karanja

Brake Power (kW)	Heat equivalent to brake power (%)		Heat rejected to coolant (%)		Heat carried away by exhaust gases (%)		Heat equivalent to unaccounted losses (%)	
	Diesel	Karanja	Diesel	Karanja	Diesel	Karanja	Diesel	Karanja
0	0	0	55.99	44.78	17.24	22.77	26.76	32.43
0.48	9.76	11.32	61.86	43.39	18.24	23.48	10.13	21.79
0.96	16.95	19.75	61.53	43.00	18.69	23.05	2.18	14.18
1.44	22.38	25.03	54.14	43.59	18.35	22.46	5.11	8.90
1.92	25.77	29.28	46.76	40.58	17.89	22.20	9.57	7.95
2.40	29.16	32.78	50.80	41.52	17.97	23.01	2.06	2.68
2.88	30.52	34.74	44.30	41.25	17.96	22.28	7.21	1.73

Table 3 Heat balance details for jatropha and palmolein

Brake Power (kW)	Heat equivalent to brake power (%)		Heat rejected to coolant (%)		Heat carried away by exhaust gases (%)		Heat equivalent to unaccounted losses (%)	
	Jatropha	Palmolein	Jatropha	Palmolein	Jatropha	Palmolein	Jatropha	Palmolein
0	0	0	31.54	37.32	19.55	19.48	48.91	43.20
0.48	9.70	9.33	30.72	41.40	18.92	18.43	40.66	30.86
0.96	15.95	16.03	35.36	38.08	18.46	18.74	30.21	27.13
1.44	20.48	20.94	35.67	44.21	17.80	19.05	26.05	15.8
1.92	22.99	24.05	35.04	43.98	16.93	18.34	25.02	13.62
2.40	25.51	26.95	35.54	46.95	16.11	18.29	22.83	7.80
2.88	28.02	28.20	32.54	49.12	16.92	17.62	22.52	5.06

Table 3. The impact is seen in the form of increased heat corresponding to the brake power. Moreover, it is less when compared with diesel and karanja. The performance of the engine is poor with palmolein fuel. It draws utmost 28 % of total heat equivalent to the brake power at the highest load. The amount of heat equivalent to unaccounted losses is also more when compared with diesel and karanja. Heat carried by exhaust gases continued to be same at all loads for both the fuels.

3.3 Exhaust Emissions

Carbon monoxide is due to partial combustion and its emissions get intensified with richer mixtures. From Fig. 4a, it is clear that contribution of karanja is less in CO emissions except at 0.48 kW of the brake power. At all the loads, palmolein fuel is the highest contributor of CO. For diesel, the values are markedly higher when compared to karanja. In general, unburned hydrocarbons are specified in terms of
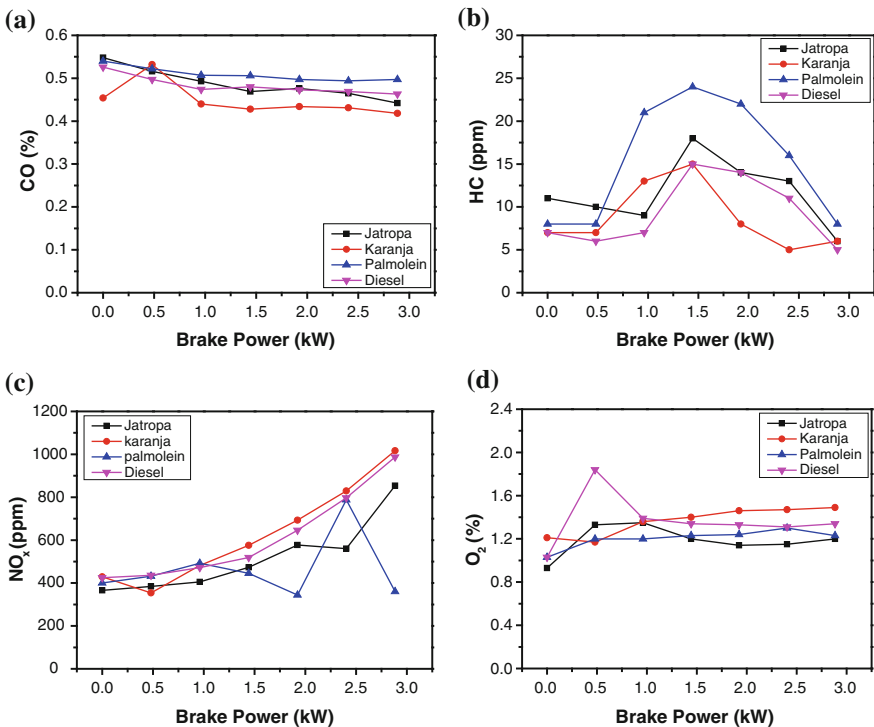

Fig. 4 Exhaust emissions of CO, HC, NO_x and O_2 for all the fuels

total hydrocarbon concentration, expressed in parts per million (ppm). From Fig. 4b, it is evident that HC emissions are higher for the intermediate loads. Up to these load positions, diesel has less ppm when compared to karanja. At higher loads, karanja gave less HC emissions. Except at 0.48 kW of the brake power, both jatropha and karanja fuels emitted more hydrocarbons than diesel. The nitric oxide emissions with bio-fuels are less when compared to diesel as shown in Fig. 4c. Karanja showed more NO_x, but comparable to the case of diesel. Figure 4d demonstrates the release of oxygen when the fuels are burnt. Jatropha is the least contributor of oxygen whereas karanja is the major one, which is advantageous.

4   Conclusions

Experimentation is carried out on a diesel engine with changed piston crown material and air gap. Various bio-fuels are tested along with diesel on the modified engine and results are compared. Plots of performance, heat balance and emissions are drawn against brake power. It is clear that karanja showed highest performance among all the fuels considered here. Also, the exhaust gas temperature is considerably more for karanja, when compared to diesel. SFC and TFC are higher for bio-fuels. But for karanja, fuel consumption is only slightly higher than diesel. The amount of heat rejected to the coolant is also less in case of karanja, when compared to diesel. For diesel, CO emissions are distinctly higher when compared to karanja. Karanja showed low CO and HC and higher O_2 emissions. Overall, bio-fuels showed better or comparable characteristics with engine modification. This is not achieved by earlier works. More engine modifications may still improve the performance of bio-fuels. Thus, the present analysis leads the researchers to make engine modifications while using bio-fuels in order to enhance the engine performance further.

References

1. Vinay Kumar.D., Ravi Kumar. P., Santosha Kumari, M.: Prediction of performance and emissions of a biodiesel fuelled lanthanum zirconate coated direct injection diesel engine using artificial neural networks. Procedia Engineering. 64, 993–1002 (2013).
2. Nanthagopal, K., Subbarao, R.: Experimental investigation and performance evaluation of DI diesel engine fueled by waste oil-diesel mixture in emulsion with water. J. of Therm. Sci. 13, 83–89 (2009).
3. Agarwal, A.K., Das, L.M.: Biodiesel development and characterization for use as a fuel in compression ignition engines. J. Eng. Gas Turbines Power. 123 (2), 440–447, (2000).
4. Parker,D.A., Donnison, G.M.: The development of an air gap insulated piston, SAE Technical Paper. 870652 (1987).

5. Krishna, M.V.S.M., Rao, V.R.R.S., Reddy, T.K.K., Murthy, P.V.K.: Comparative studies on performance evaluation of DI diesel engine with high grade low heat rejection combustion chamber with carbureted alcohols and crude jatropha oil. Renew. Sustainable Energy Reviews. 36, 1–19 (2014).
6. Reddy, C. K., Krishna, M.V.S.M., Murthy, P.V.K., Reddy, T.R.: A comparative study of the performance evaluation of a low heat rejection engine with three different levels of insulation with crude pongamia oil operation. Can. J. Mech. Sci. and Eng. 3 (2012).

Design and Development of FPGA-Based MAGLEV System for a Low-Speed Wind Tunnel

Sumukh Surya and D.B. Singh

Abstract The present work seeks to develop a magnetic levitation (MAGLEV) system suitable for a low-speed wind tunnel to support light weight models using FPGA controller. The concept of Pulse Width Modulation (PWM) was used to control single degree of freedom. The reference voltage set and the differential voltage from linear Hall Effect sensors (SS 494B) are compared. The duty cycle varies from 0 to 100 % based on the position of the object. These sensor outputs were connected to NI 9239 and the output (PWM) was obtained from NI 9472. This output was given to the driver circuit to achieve appropriate action. A MOSFET was used to boost the current required for levitation. A diode was connected in parallel with the electromagnet to avoid reverse current flow. A LabVIEW FPGA program was built in order to generate PWM and finally levitate the object. FPGA-based control is event-based control and provides microsecond delay.

Keywords MAGLEV · FPGA controller · PWM

1 Introduction

In wind tunnels, scaled down model of the prototype of flight article is rigidly held using a support system and air is made to flow over the model at desired speeds. The reactions (forces and moments along and about all the three axes) due to flow of air on the test article (object) are measured using an internal strain gauge balance. Figure 1 shows a photograph of a low-speed wind tunnel at NAL, Bangalore. In this method, interference of the support system on the air-flow over the object cannot be avoided. However, if the object can be rigidly held in the test section without any physical support, there would be no support interference. On the other hand, a magnetic levitation system has the potential to permit the rotation of the test article by externally controlling the magnitude and orientation of magnetic flux. In

S. Surya (✉) · D.B. Singh
CSIR- National Aerospace Laboratories, Bangalore, India
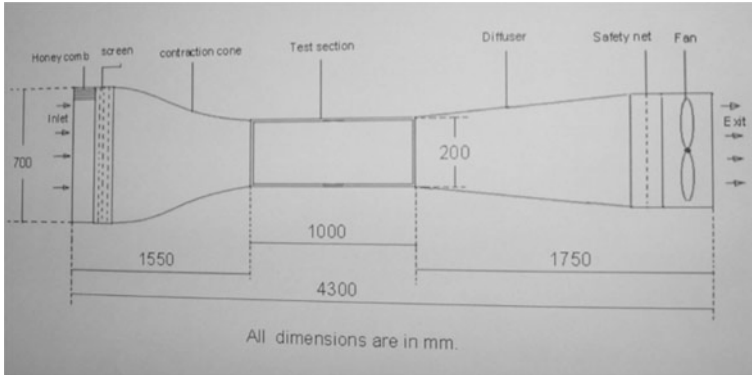e-mail: sumukhsurya@gmail.com

Fig. 1 Photograph of a low-speed wind tunnel at NAL, Bangalore

the present work, attempt is made to develop a magnetic levitation system which can support a small weight in wind-off condition. Here, the object is rigidly held at a controlled attitude by external magnetic forces using multiple electromagnets mounted external to the wind tunnel. During the air flow, the object changes its attitude due to the air loads. The current required to bring the object back to its initial position is offline calibrated against known loads. Thus, the aerodynamic loads can be obtained without a conventional support system and conventional strain gauge balance. A real-time controller, NI cRIO 9033 was used to achieve magnetic levitation. In case of MAGLEV systems, real-time controller plays an important role as microsecond timing and high reliability is required. The PWM output was obtained from NI 9472 at every 100 μs. The basics of electromagnetic levitation and the design of electromagnet are discussed in Ref. [1, 2, 3].

2 Description of MAGLEV System

Figure 2 shows the block diagram of the FPGA controlled MAGLEV System used in the present work.

1. **Object**
   This consists of a diamagnetic substance in it, which helps in repelling the magnetic field produced by the electromagnets.
2. **Electromagnet**
   Used to levitate the object; it is continuously excited by current using the power circuit.
3. **Linear Hall Effect Sensors**
   Senses the position of the object and ensures that the desired position of the object (center of the wind tunnel is maintained throughout the testing). In the
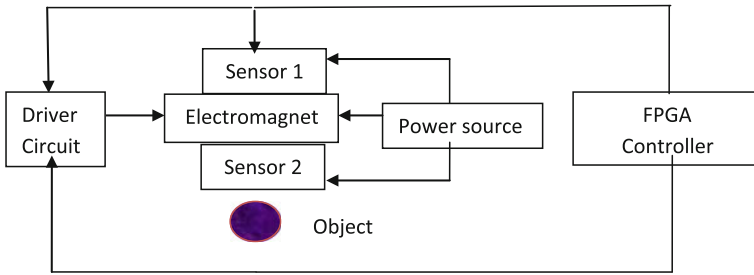
Fig. 2 Block diagram of FPGA-controlled MAGLEV system

present work, two linear Hall Effect sensors (above and below the electro-magnet) are used to determine the differential signal.

4. **FPGA Controller cRIO 9033**

   It contains 1.33 GHz Intel processor and Xilinx Kintex-7 160T FPGA processor with one USB drive and two USB hosts. This controller has 4 slots and is the largest and most powerful FPGAs in the Compact RIO product family.

5. **NI 9239-Input Card**

   It has four channels and has inbuilt 24 bit ADC. The sampling rate is 50 ks/s. The Hall sensor outputs are connected to this card.

6. **NI 9472-Output Card**

   It is an eight channel and 100 µs digital output card. One of the important features is that it can handle 2300 Vrms of transient voltage between the input and the output channels. The PWM generated in this channel was given to the MOSFET to boost the current level. The output from the MOSFET was given to the electromagnet to generate appropriate flux based on the current level.

3 Experimentation

Linear Hall Effect sensors (2nos) were placed above and the below the electro-magnet. The sensor placed above the electromagnet measured the total magnetic field, i.e. the magnetic field of the electromagnet + magnetic field of the object to be levitated (permanent magnet). The other sensor measured the magnetic field of the permanent magnet. A difference of these two signals resulted in the magnetic field of the electromagnet. Reference voltage of ∼1 V was set by placing the sensor at a particular distance from the electromagnet.

LabVIEW was used a platform to compare the differential signal and reference signal and generate PWM accordingly. The PWM varied from 0 to 100 % duty cycle based on the position of the object to be levitated. Based on the PWM signal, the electromagnet produced appropriate flux required for levitation. Figure 3 shows the PWM generation using FPGA-based control program. Figure 4 shows the
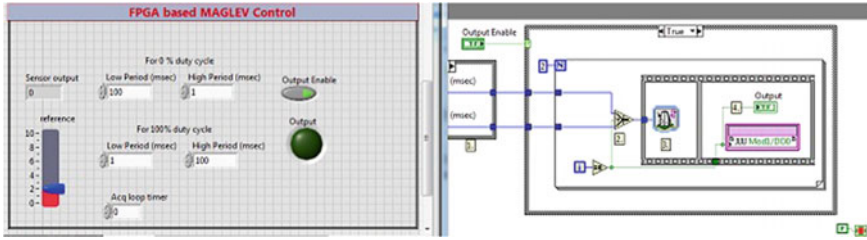
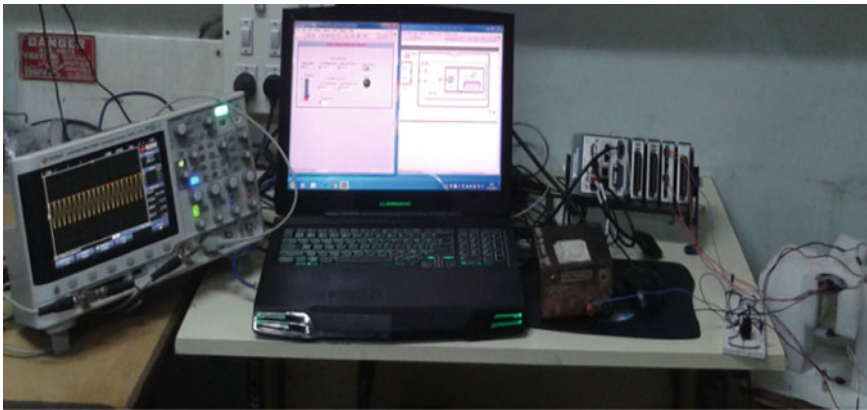**Fig. 3** Screen shot of PWM generation using FPGA technique

Fig. 4 Photograph of experimental setup of FPGA-based MAGLEV system

experimental set up of MAGLEV system. A common voltage supply was used to excite the sensors and electromagnet, 10 V and 2 A.

4 Results

The object was levitated but distortions were observed in the waveform due to the inductor (electromagnet) in the circuit. Figure 4 shows the levitation of the object. However, by using appropriate filters these distortions can be eliminated. During the levitation process, lateral oscillations were observed. The reasons are as follows:

1. The weight acting on the center of gravity and the center of flux were not collinear. Hence, the magnet was subjected to an unrestrained side force.
2. A phase lag was created between the electromagnet and the object to be levitated. This problem can be solved by using a lead compensator (Fig. 5).

Fig. 5 Photograph of levitating object

Electromagnet

Levitated object
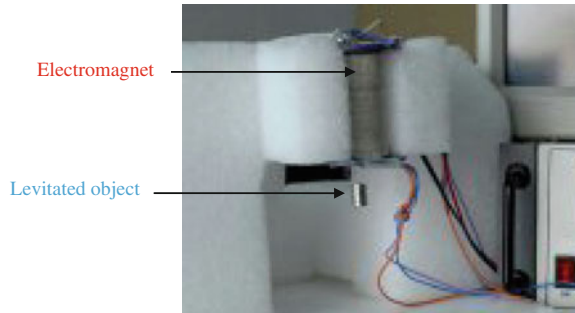
5 Conclusion

1. For proper levitation, cross sectional area of electromagnet should be greater than that of the cross sectional area of the object, so that the CG of the object lies well within the high-flux region of the electromagnet.
2. If two electromagnets with appropriate offset, with the object configured as a bar magnet, stability of the levitated object can be ensured. Alternately, a horseshoe electromagnet can also be used with appropriate polarity to provide the necessary repulsive forces.
3. For better control and stability, multiple electromagnets can be used. Vectored magnetic force can be obtained when multiple electromagnets are used. Sliding mode control can also be adopted for efficient control Ref. [4, 5].

References

1. Sumukh Surya, Ramyashree. S, Rashmi Nidhi, D B Singh, Aparna R J, "Development of a simple MAGLEV system for a low-speed wind tunnel", IEEE Xplore978-1-4799-8371-1/15.
2. Lance Wiiliams, "Electromagnetic Levitation Thesis", 2005.
3. www.signalpath.com
4. Hamid Yaghoubi and Yousfi Khemissi, "Sliding Mode Of The Magnetic Suspension System, Practical Application of Magnetic Levitation Technology", *Dept. of Electrical Engineering, Najran University, Saudi Arabia.*
5. Tejinder Kumar, Shimi S.L., Dnyaneshwar, ShakshiRana, "Modeling, simulation and control of single actuator magnetic levitation system".

Performance Investigation of High Temperature Combustion Technology (HiCOT) Using CFD Simulation

T. Yokesh, M. Manjunath, P. Prithivi, S. Ravi Shankar and P.S. Premkumar

Abstract Combustion is the process of converting the energy stored in chemical bonds to heat energy that can be utilized in a various ways. A good engine is a one which has high efficiency that leads to better performance of the aircraft. In this fast emerging field, fuel exhaust emission has become a hazardous thing to be considered by all leading industries. In addition, the oil crisis has become a problem to aircraft industries. According to the international statistics, both the developed and developing countries are contributing their efforts to important emission of greenhouse gases. In order to improve the efficiency of the combustion process, energy conservation reduces the global oil crises and the emission of harmful gases, HiCOT would be a better technology to produce favorable results. High temperature Combustion Technology (HiCOT) is a promising technology for energy saving, flame stability enhancement and NO_x emission reduction. In a conventional HiCOT system, the combustion air is highly preheated by using the recuperative or regenerative heat exchangers. In this project, the combustion air is heated using the recirculation process. Numerical studies have been carried out to investigate the combustion performance of methane–air mixture in a cylindrical combustor using High Temperature Combustion Technology (HiCOT) to predict thermal efficiency and pollutant emission levels of NO_x and CO_2 at various air inlet temperatures and velocities using CFD simulation. The design process is carried out through ANSYS DESIGN MODULAR. Flow domain, grid generation, CFD simulation, and the post-processing results are obtained using ANSYS WORKBENCH and FLUENT.

T. Yokesh · M. Manjunath · P. Prithivi · S. Ravi Shankar · P.S. Premkumar (✉)
Department of Aeronautical Engineering, Kumaraguru College of Technology,
Coimbatore 641049, India
e-mail: cadesprem@gmail.com

1   Introduction

Combustion is a chemical process in which a substance reacts rapidly with oxygen and gives off heat. The original substance is called the fuel, and the source of oxygen is called the oxidizer. The fuel can be a solid, liquid, or gas, although for airplane propulsion the fuel is usually a liquid.

During combustion, new chemical substances are created from the fuel and the oxidizer. These substances are called exhaust. Most of the exhaust comes from chemical combinations of the fuel and oxygen. When a hydrogen–carbon-based fuel (like gasoline) burns, the exhaust includes water (hydrogen + oxygen) and carbon dioxide (carbon + oxygen). But the exhaust can also include chemical combinations from the oxidizer alone. If the gasoline is burned in air, which contains 21 % oxygen and 78 % nitrogen, the exhaust can also include nitrous oxides (NO_x, nitrogen + oxygen). The temperature of the exhaust is high because of the heat that is transferred to the exhaust during combustion. Because of the high temperatures, exhaust usually occurs as a gas, but there can be liquid or solid exhaust products as well. Soot, for example, is a form of solid exhaust that occurs in some combustion processes.

During the combustion process, as the fuel and oxidizer are turned into exhaust products, heat is generated. Interestingly, some source of heat is also necessary to start combustion. Gasoline and air are both present in your automobile fuel tank; but combustion does not occur because there is no source of heat. Since heat is both required to start combustion and is itself a product of combustion, we can see why combustion takes place very rapidly. Also, once combustion gets started, we do not have to provide the heat source because the heat of combustion will keep things going. We do not have to keep lighting a campfire, it just keep burning.

To summarize, for combustion to occur three things must be present: a fuel to be burned, a source of oxygen, and a source of heat. As a result of combustion, exhausts are created and heat is released. We can control or stop the combustion process by controlling the amount of fuel available, the amount of oxygen available, or the source of heat.

1.1   HiCOT

High Temperature Combustion Technology (HiCOT) is a combustion process in which the inlet air temperature is higher than the auto ignition temperature of the air–fuel mixture. Aircrafts, Automobiles and Rocket combustion process plays a major role in Global oil crises and for the environmental pollution by the emission of greenhouse gases such as CO_X, NO_x, SO_X, etc. In order to improve the efficient combustion process, energy conservation, to reduce the global oil crises and the emission of harmful gases HiCOT would be better technology to produce positive results.

2 Project Methodology

2.1 Problem Description

Combustion of methane gas is carried out in a turbulent diffusion flame furnace. The flame is considered to be a turbulent diffusion flame. A small nozzle in the center of the combustor introduces the methane at a velocity of 10 m/s. Ambient air enters the combustor coaxially at 0.3 m/s. The overall equivalence ratio is 0.7. The high-speed methane jet initially expands with little interference from the outer wall and entrains and mixes with the low-speed air at various temperatures of 300, 500, 750, and 1000 K.

2.2 Numerical Calculation

Equation,

$$CH_4 + 2(O_2 + 3.76N_2) \rightarrow CO_2 + 2H_2O + 7.52N_2$$

We have taken 21 % of oxygen and 79 % of nitrogen present in the air (Table 1).

Equivalence Ratio: 0.7

2.3 Fluent Setup

See Table 2.

2.4 Boundary Condition

See Table 3.

2.5 2D Model

See Figs. 1 and 2.

The dimensions of the above model are,

- Air Inlet Diameter = 97.5 mm
- Fuel Inlet Diameter = 2.5 mm
- Combustor Total Diameter = 200 mm
- Combustor Length = 1800 mm

Table 1 Mass Fractions of CH_4, O_2 and N_2

	Mass	Mass fraction
CH_4	16	0.0550
O_2	64	0.2200
N_2	210.6	0.7240

Table 2 Fluent setup

Type	Pressure-based
Condition	Steady state
Model	κ-ε (K-Epsilon), Standard wall function
Combustion type	Species transport
Turbulence model	Eddy dissipation

Table 3 Boundary Conditions

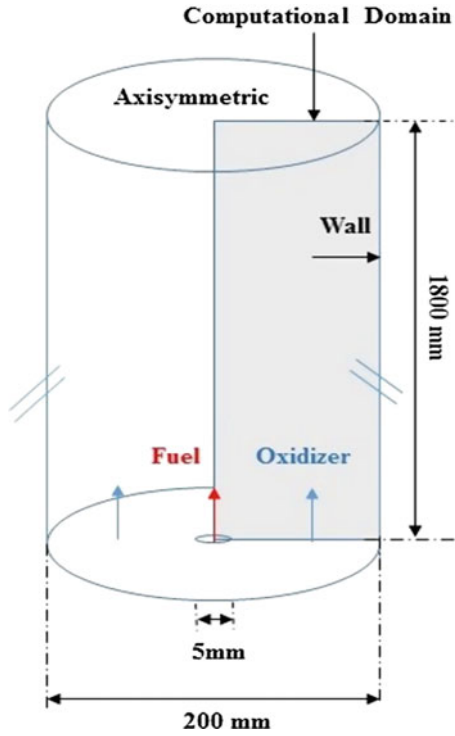| Air velocity	0.3 m/s
Fuel velocity	10 m/s
Air inlet temperature	300 K, 500 K, 750 K, 1000 K
Air inlet temperature	300 K
Equivalence ratio	0.7

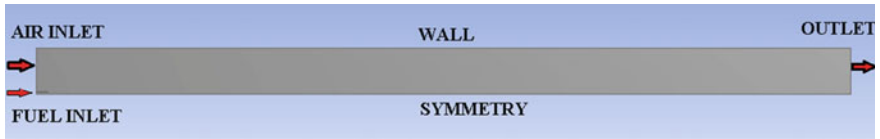**Fig. 1** Axisymmetric wall-confined jet geometry for HiCOT

Fig. 2 Model done in ANSYS design modular

2.5.1 Mesh Model and Mesh Details

See Fig. 3 and Table 4.
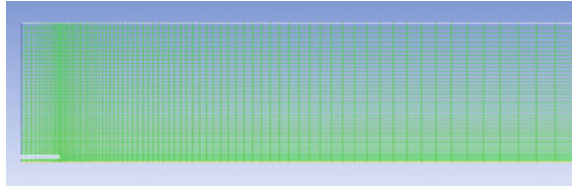
Fig. 3 Meshed model of 2D combustor

Table 4 Mesh details

Mesh type	Non-uniform mesh
3D meshing	Mapped face meshing
Minimum edge size	1 mm
Maximum edge size	20 mm
Nodes	7014
Cells	6819
Orthogonal quality	1

2.5.2 Results and Discussion

Static Tempeature

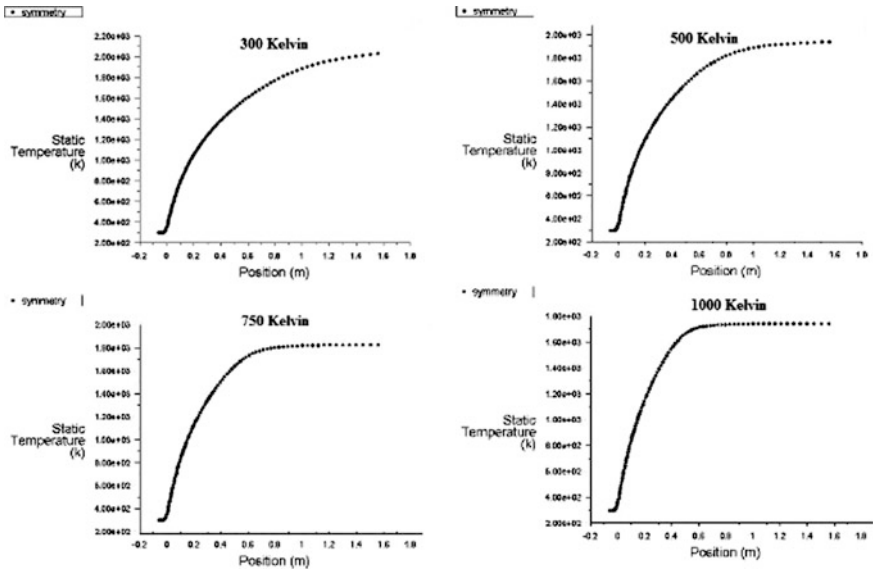See Figs. 4 and 5.
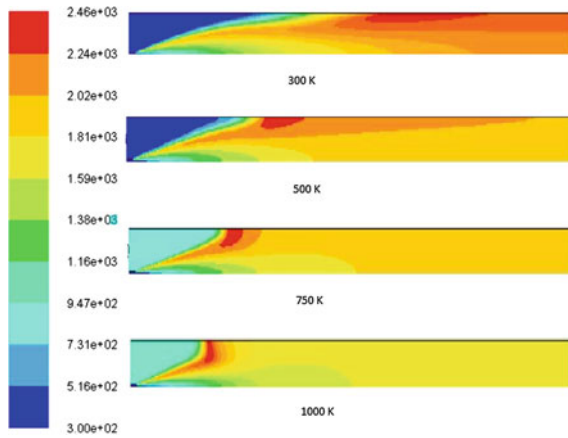
Fig. 4 Contours of static temperature

Fig. 5 Static temperature variation graph
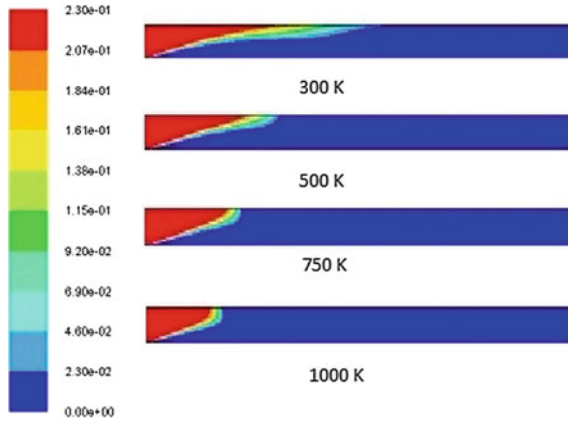
O_2

See Figs. 6 and 7.

Fig. 6 Contours of O_2
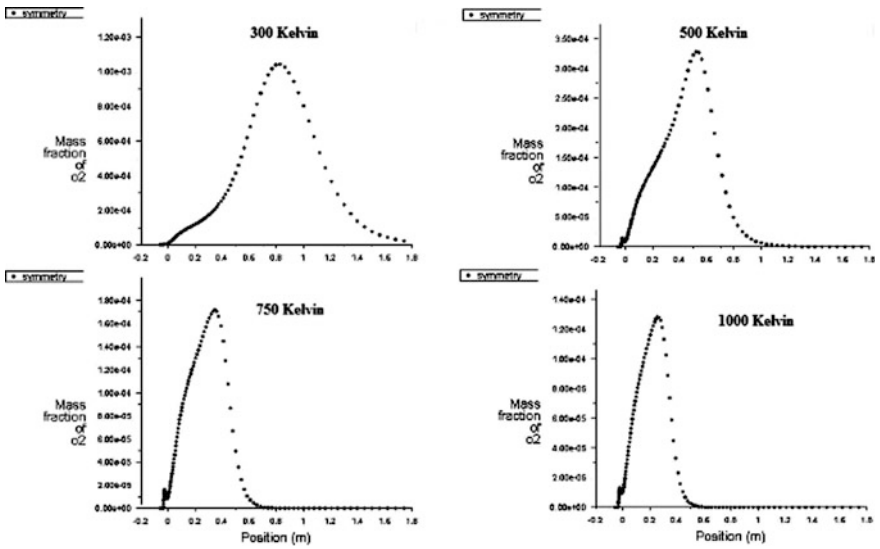

Fig. 7 Mass fraction of O_2 variation graph

CO_2

See Figs. 8 and 9.
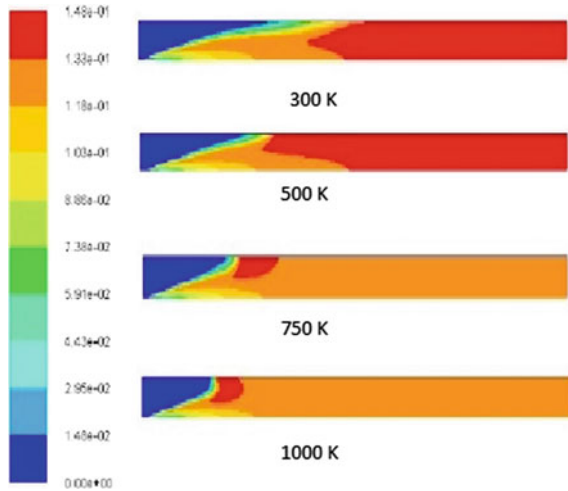
Fig. 8 Contours of CO_2
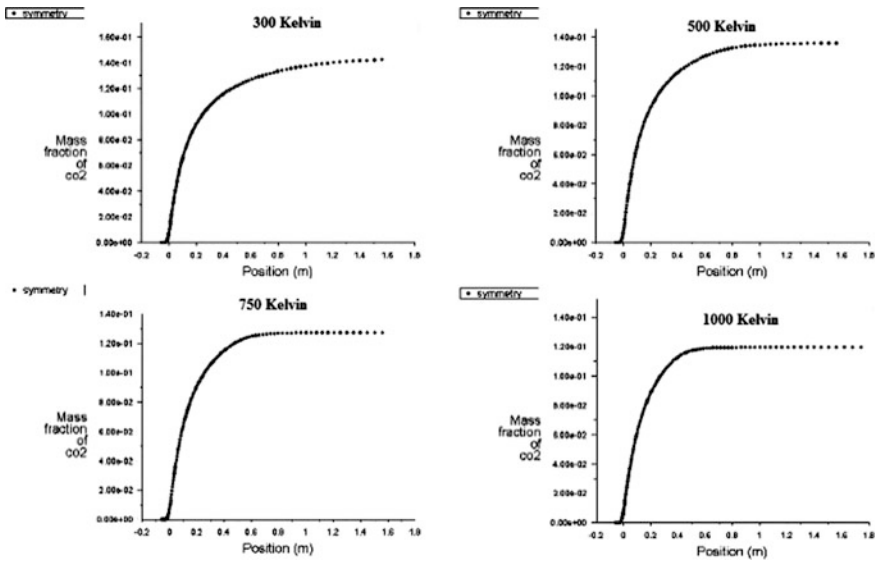

Fig. 9 Mass fraction of CO_2 variation graph
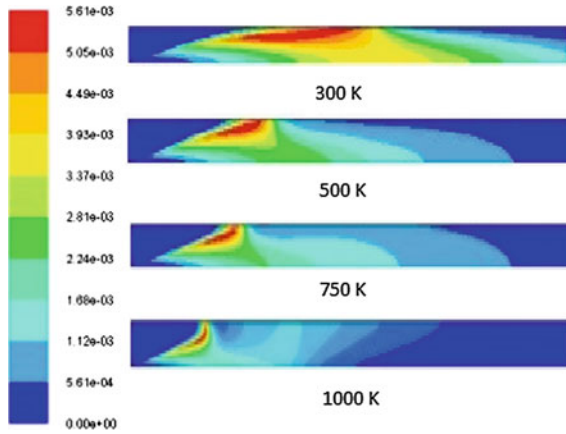
NO_x

See Figs. 10 and 11.

Fig. 10 Contours of NO_x
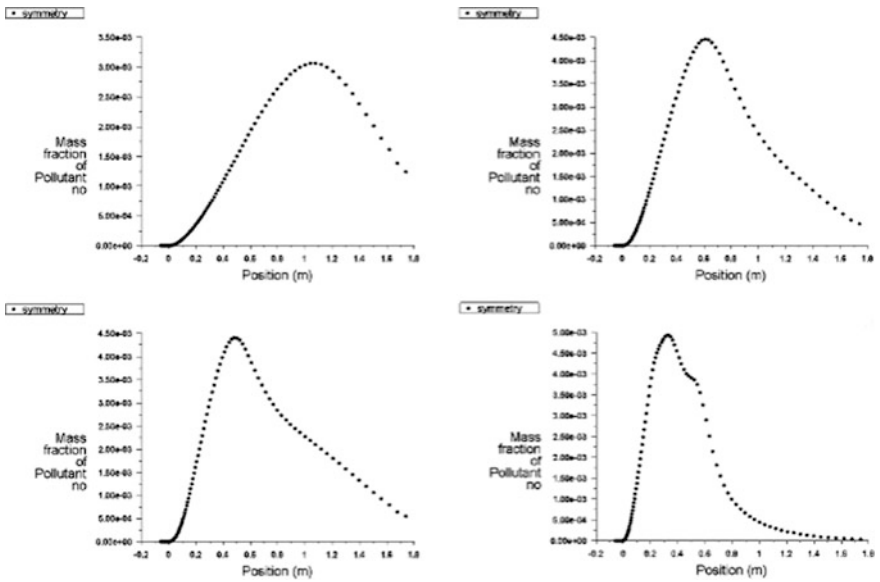
Fig. 11 Mass fraction of NO_x variation graph

Table 5 Dimensions of 3D Combustor

Air Inlet diameter	195 mm
Fuel Inlet diameter	5 mm
Combustor total diameter	200 mm
Combustor length	1800 mm

Fig. 12 Model done in ANSYS design modular
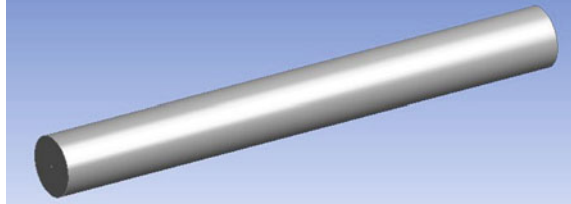
Fig. 13 Mesh model
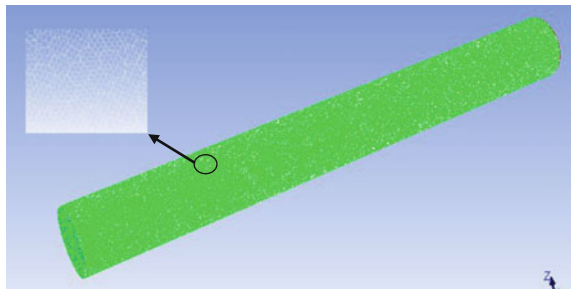
2.6   3D Combustor Model

Dimensions are,
See Table 5 and Fig. 12.

2.6.1   Mesh Model of 3D Combustor & Mesh Details

See Fig. 13.

2.6.2   Mesh Details of 3D Combustor

See Table 6.

Table 6 Mesh Details of 3D Combustor

Mesh type	Structured mesh
3D meshing	Poly hedra mesh
Minimum edge size	1 mm
Maximum edge size	20 mm
Nodes	1153322
Elements	762062
Orthogonal quality	0.87

2.6.3   Results and Discussion

Static Tempeature

See Figs. 14 and 15.

Fig. 14 Contours of static temperature

Fig. 15 Static temperature variation graph

O$_2$

See Figs. 16 and 17.

Fig. 16 Contours of O$_2$

Fig. 17 Mass fraction of O$_2$ variation graph

CO_2

See Figs. 18 and 19.

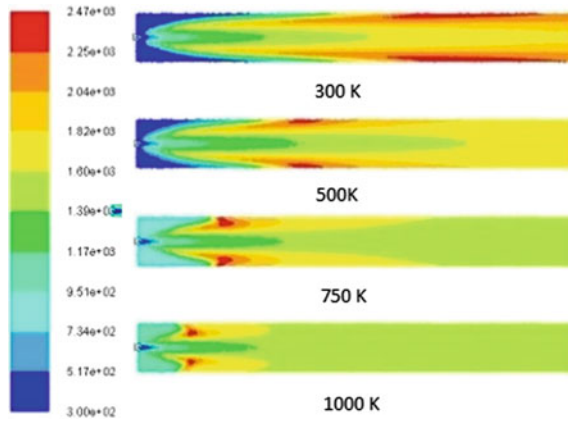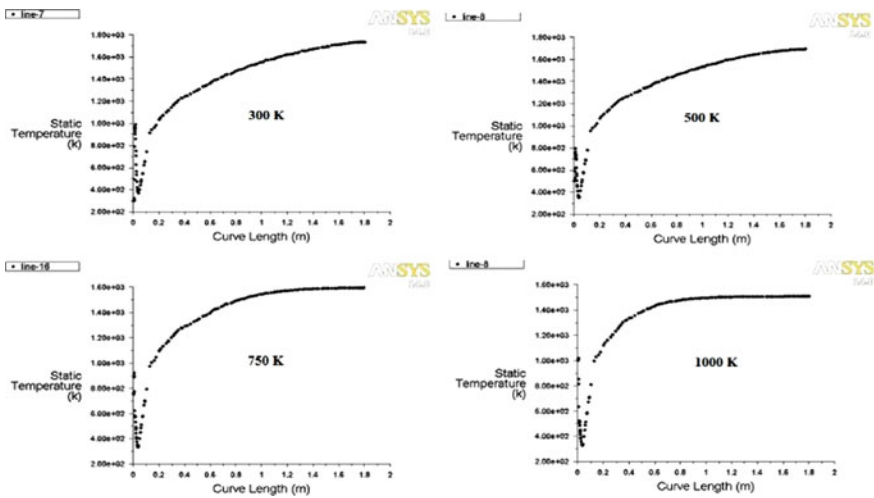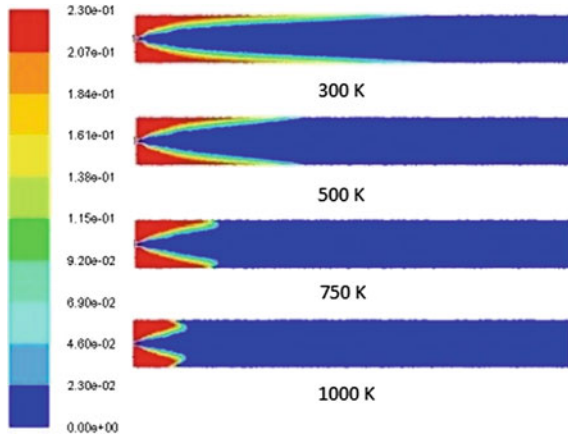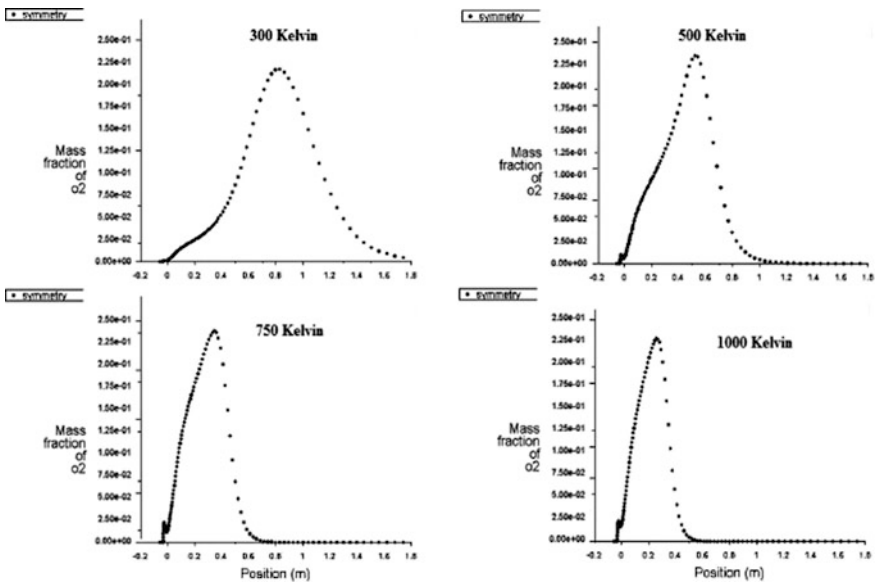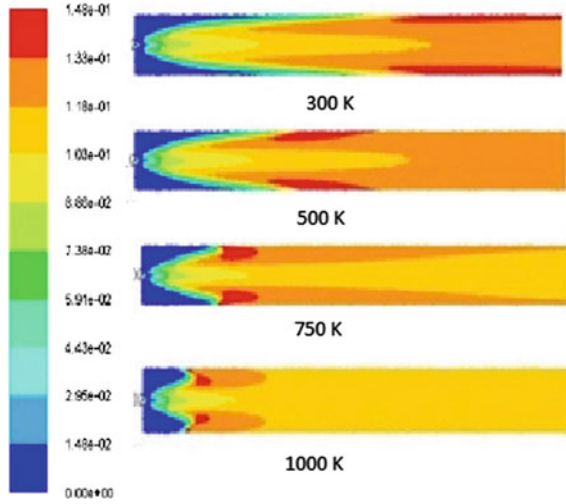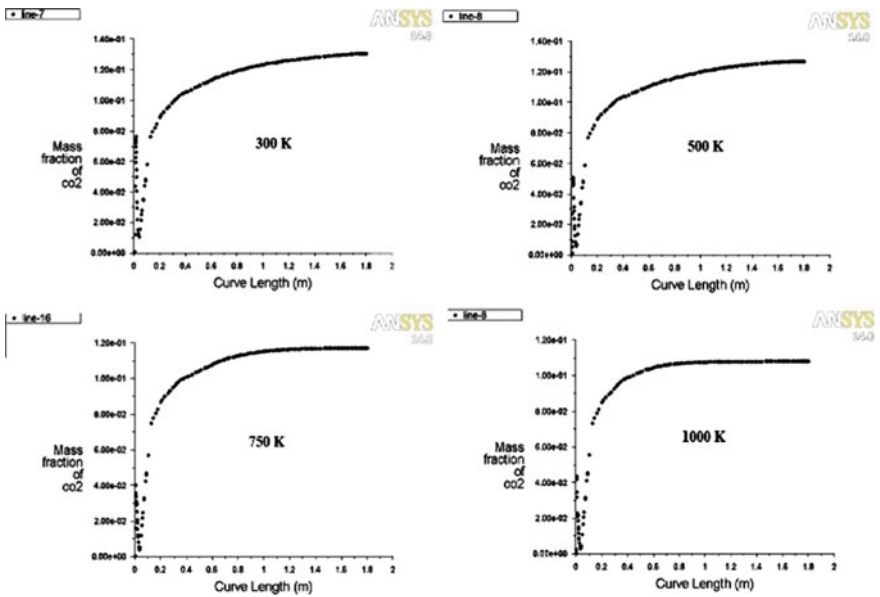**Fig. 18** Contours of CO_2

Fig. 19 Mass fraction of CO_2 variation graph

2.7 Discussion of Results

From both the results of 2D and 3D combustor analysis, the efficiency of combustion was investigated for four cases; it is shown in Figs. 4, 5, 6, 7, 8, 9, 10, 11, 12, 13, 14, 15, 16, 17, 18 and 19. Mesh quality of 2D axisymmetric combustor is 1 and the result of 3D model was validated with 2D model. In these cases, the air mixture is composed of 21 % oxygen and 79 % nitrogen on mass basis. The fuel is 100 % Methane on mass basis. The mean inlet velocity of hot co-flow is set to 0.3 m/s and the fuel velocity is 10 m/s. Initially, the methane–air mixture gets momentum at the Inlet. After ignition process the momentum getting reduced and diffusion process takes place. While comparing the four contours, we can observe that temperature in the air inlet is very low at 300 K whereas the temperature at 1000 K is very high. The maximum value of the temperature is above 2500 K. So that we can conclude that combustion process is taking place. Each contours show that when we increase the temperature of air, the complete combustion process takes place due to complete burning of Oxygen. At 300 and 500 K temperatures, the exhaust gas consists of large amount of CO_2. If we increase the temperature of air, the emission of CO_2 relatively reduced. The emission of N_2 can also be reduced by increasing the temperature. The formation of carbon inside combustor can also be reduced to low by using this technology. Comparing the variation of CH_4 at different temperatures, we could see, at low temperatures, the formation of CH_4 is low but it is exhausted due to incomplete burning. At 1000 K, the CH_4 is more but it is not exhausted because of high temperature combustion.

2.8 Comparison of 2D and 3D Combustor

See Figs. 20, 21, 22 and 23.

Fig. 20 Variation of NO_x at various air inlet temperature
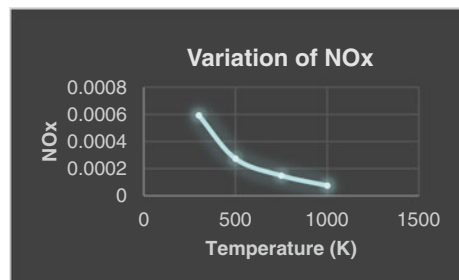
Fig. 21 Variation of CH_4 at various air inlet temperature
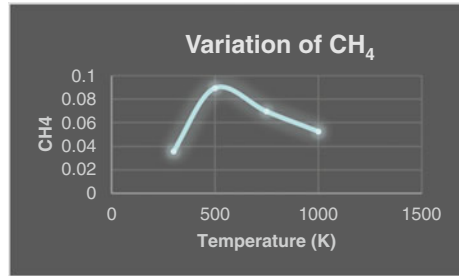
Fig. 22 Variation of O_2 at various air inlet temperature
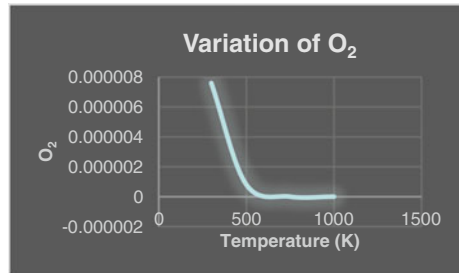
Fig. 23 Variation of N_2 at various air inlet temperature
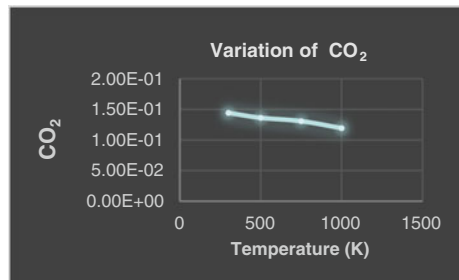
3 Comparison of Results

While comparing the 2D and 3D results, from Figs. 20, 21, 22 and 23, there are no variation of results at lower temperature. But there are some variations at higher air temperature. These results show that the accuracy of the results in CFD depends on the mesh quality. For the four cases the value of mass weighted average is calculated throughout the cylinder and it is plotted against the different air temperatures with fuel lean mixture. While seeing the NO_x plot, as temperature increases, the NO_x emission is reduced. In the CH_4 plot, initially CH_4 increases but at high temperatures, it is reduced. The amount of O_2 emitted is comparatively reduced

with increase in temperature shows the complete and efficient combustion process taking place. CO_2 emission decreases linearly as temperature increases. The emission of N_2 is partially reduced. With the help of these plots we can conclude that HiCOT increases the combustion efficiency as well as it reduces the emission of N_2, CO_2 and NO_x in order to avoid the air pollution.

4 Advantages

- High-temperature combustion air easily provides stable flame with even low calorific value gases or fuel, provided the temperature of combustion air is high (above auto ignition temperature).
- Energy conservation.
- High thermal efficiency by an efficient combustion process.
- Reduced emission of pollutants such as NO_x, CO_X and Soot. It reduces the environmental pollution.
- High temperature air has higher heat flux than normal air.
- Decrease SFC—High temperature is achieved without much fuel consumption
- Thrust gets increased.

5 Conclusion

From the results of 2D and 3D combustor, it is evidenced that we are able to reduce the exhaust of gases like NO_x, N_2 and CO_2 Using HiCOT. Also we have utilized the methane—air mixture completely for the combustion. Thus, this technology improves the combustion efficiency thereby increasing the overall efficiency. HiCOT may bring impact in jet propulsion by adopting it to gas turbine engines.

References

1. M.M.Noor, Andrew P.Wandel and Talal Yusaf 2013. Detail guide for CFD on the simulation of biogas combustion in bluff-body mild burner.
2. Acon, C. H. J., Sala, J. M. and Blanco, J. M. 2007, Investigation on the design and optimization of a low NO_x-CO Emission burner both experimentally and through CFD simulations, Energy and Fuels.
3. G.Sorrentino, D.Scarpa, A.Cavaliere 2012. Transient inception of MILD combustion in hot diluted diffusion ignition (HDDI) regime: A numerical study.
4. Flame Characteristics and Challenges with High Temperature Air Combustion by Ashwani K. Gupta, University of Maryland, Department of Mechanical Engineering, College Park, MD 20742, USA.

5. A. Cavaliere and M. de Joannon, "Mild combustion," Progress in Energy and Combustion Science, vol. 30, no. 4, pp. 329–366, 2004.
6. M. Katsuki and T. Hasegawa, "The science and technology of combustion in highly preheated air," Symposium (International) on Combustion, vol. 27, no. 2, pp. 3135–3146, 1998.
7. T. Niioka, "Fundamentals and applications of high temperature air combustion," in Proceedings of the 5th ASME/JSME Joint Thermal Engineering Conference, San Diego, Calif, USA, 1999.

Calculation of Theoretical Performance of Boron-Based Composite Solid Propellant for the Future Applications

Syed Alay Hashim, Manu Lahariya, Srinibas Karmakar and Arnab Roy

Abstract Elemental boron is a highly attractive high energy material and it is a metalloid chemical element. Boron possesses the second greatest heating value of any element that can be adopted as an energetic material in the processing of propellants and explosives. In the present work, boron-based composite solid propellants are examined theoretically. In the actual condition, boron has problems during the ignition and combustion due to the coating of B_2O_3 layer on its surface. The vacuum-specific impulse and the specific impulse are calculated for several boron-based propellants with the help of NASA Lewis Code, Chemical Equilibrium with Applications (CEA). Several other elements such as aluminium, iron, magnesium and titanium are also considered in this study as additives in boron-based propellants. The performance values of boron-based propellants are compared with that of pure aluminium-based composite propellant. In the CEA simulation hydroxyl terminated polybutadiene (HTPB) and ammonium perchlorate (AP) are taken as binder and oxidizer, respectively. Although pure boron-HTPB-AP has the highest theoretical performance, it is observed that presence of any small percentage of boron in aluminized propellant can give higher performance than that of pure aluminium-based propellant.

Keywords Propellant ingredients · Boron combustion · Specific impulse · NASA CEA thermodynamic simulation

S.A. Hashim (✉) · M. Lahariya · S. Karmakar (✉) · A. Roy
Department of Aerospace Engineering, Indian Institute of Technology, Kharagpur, India
e-mail: aviator123hash@gmail.com

S. Karmakar
e-mail: skarmakar@aero.iitkgp.ernet.in

1   Introduction

The main desirable characteristics for a solid propellant are high specific impulse, burning rate based on predetermined ignition properties, low cost processing, high density, and good storage ability. Other than these qualities, the propellant should not produce excess smoke in the exhaust and also free from combustion instability. Here, we are discussing about boron and other fuels for composite solid propellant. The composite propellants are less hazardous and easy handling than double-based propellants. As a fuel ingredient, boron has extremely high gravimetric and volumetric heating values when compared with aluminum, magnesium, and other energetic fuels. Therefore, boron is considered as an energetic fuel for the propellants which are used in rocket and air-breathing propulsions such as ducted rocket and ramjet engines [1]. Some fuels which are used in rocket propulsion are shown in the Table 1.

The boron quality is such that, it can be introduced as a fuel in the solid propellant and in future it will be considered as a high potential fuel for the rocket propulsion. On the other hand the ignition process of boron is complex due to the presence of liquid layer of boron oxide (B_2O_3) at temperature between (723–2316) K, which is the melting and the boiling point of the oxide. In the boron combustion, the convective and the radiative heat flux will be transferred to the boron particle; therefore, reaction starts at the B–B_2O_3 interface. In the next step of the reaction there will be an evaporation of B_2O_3 at the gas-liquid interface and then the diffusion of oxygen stars through the oxide layer to the B–B_2O_3 interface. The combustion product finally produces HBO_2 when B_2O_3 reacts with the water vapour [3].

Boron has excellent heating values on both gravimetric and volumetric basis. Although boron has very high theoretical energy potential, the presence of local oxide layer on the particle surface inhibits its ignition and hence its utilization of full energetic potential is not achieved. The past research conducted by Macek and Sample noticed that boron combustion can be explained by a two stage-processes. In the first stage, the boron particles start burning, although it is coated with the oxide layer. Once the particle temperature reaches above the B_2O_3 boiling point (2300 K at 1 atm), the oxide layer is entirely vanished by evaporation; results, the ignition process is delayed remarkably [4]. In the second stage, the energy which is

Table 1   Heating values of various fuels [2]

S. nos.	Fuel	Gravimetric heating values (KJ/g)	Volumetric heating values (KJ/cm^3)
1.	Boron	59.3	131.6
2.	Graphite	32.8	73.8
3.	Aluminum	31.1	83.9
4.	Magnesium	24.7	43.0
5.	Titanium	19.7	88.8
6.	Zirconium	12.0	78.2

released in the hydrogen containing gases is significantly lowered due to the formation of HBO_2. This phenomenon creates problem when boron is mixed with fuels or binder, in which hydrocarbons are generally present [5].

If we are talking for a solid fuel-based ramjet engine the specific impulse (I_{sp}) of a propulsive system describes the energetic performance of the propellant for a given thrust value and the flight conditions. The specific impulse of the propulsive system is almost directly proportional to the heating value per unit mass of the propellant. And for those systems having limited volume such as air to air missiles and SFRJ, the volumetric specific impulse ρI_{sp} is more important. Due to these reasons, boron-based fuel-rich propellant is very demanding for SFRJ [6–8]. The combustion process of the fuel rich propellants can be explained by primary and secondary combustion processes. The presence of oxidizer in the propellant helps the primary combustion which is initiated in the gas generator and generates high energy. The secondary combustion process starts when the primary combustion products move to the secondary combustion zone and reacts with the oxygen which comes from the inlet of the engine (SFRJ). Therefore, these studies are not only demanding for the researchers working only in the combustion mechanisms of a fuel-rich propellant but also provides a valuable research in both the primary and the secondary combustion processes [9, 10].

The main objective of this study is to evaluate the rocket performance parameters, specially the specific impulse of the propellant. For the satisfactory research work, we are trying to understand the burning characteristics of boron-based propellants with the help of thermodynamics simulation.

2 Methodology

The thermochemical evaluation of boron, boron with other fuels along with the oxidiser is performed by using NASA Lewis Code, Chemical Equilibrium with Applications (CEA) [11]. Table 2 shows the ingredients of the composite solid propellant which will be used here for the CEA inputs. The propellants are processed theoretically for pure boron and also mixture of fuels along with the oxidiser (AP). The CEA results give the performance for the different combinations and finally some energetic propellants are selected for applications in rocket propulsion.

Table 2 Propellant ingredients [12]

S. nos.	Ingredients	Chemical formula	Type
1.	Aluminum (AL)	Al	Fuel
2.	Boron (B)	B	Fuel
3.	Ammonium perchlorate (AP)	NH_4ClO_4	Oxidizer
4.	Hydroxyl terminated polybutadiene (HTPB)	$(C_4H_6(OH))_n$	Polymer

3   Result and Discussion

The following tables and plots give the rocket performance parameters for the different ingredient's percentage available in the propellant. The propellant combinations are evaluated at different chamber pressures, these are 50, 100, and 150 bar, respectively. It is assumed here a small scale missile and the supersonic area ratio (A_e/A_t) is taken as 10. In the CEA code, the ingredient's initial temperature is maintained at 298.15 K for all the cases which will be discussed here (Figs. 1 and 2).

Table 3 shows five different types of propellants. The oxidizer to fuel ratio is taken as 2.125 but it is not constant for all other combinations. The last row has non metallic propellant, i.e., only HTPB is burned with the help of AP. It is observed from the Table 3 that the first row has the best performance among the other combinations. So, the first row of Table 3 combination is taken here as a reference propellant for the further discussions. In Table 4, we are compared with five different types of propellant combinations. The pure aluminium values are taken from the Table 3 and the pure boron column is simulated by the replacement of aluminum to boron. In the remaining three columns, boron is added with aluminum. In this table pure boron column shows the best performance. The percentage of aluminum in the propellant is decreasing and it is filled by boron. We reduced the aluminum percentage from 18 to 10, and mixed with boron from 3 to 8 % in the pure aluminum-based propellant. We have concluded that the performance of the propellant is improved, although the boron percentage is low. Finally, we observed that the last combination (Al-10 %, B-8 %, HTPB-14 % and AP-68 %) has maximum performance parameter than B-3 % and B-5 %, and these are also greater than that of pure aluminum case. Figures 3 and 4 show vacuum I_{sp} and I_{sp} of the investigations which are discussed in Table 4. Consequently, it is noticed that small amount of

Table 3   Different ingredient's percentage and CEA results [13]

S. nos.	Propellant ingredients	Vacuum specific impulse (Ns/Kg)		
		50 Bar	100 Bar	150 Bar
1.	AL-18 %, HTPB-14 %, AP-68 %	2824.8	2830.4	2833.0
2.	AL-20 %, HTPB-14 %, AP-66 %	2827.0	2833.5	2836.8
3.	AL-25 %, HTPB-14 %, AP-61 %	2750.0	2755.9	2759.1
4.	AL-30 %, HTPB-14 %, AP-56 %	2617.4	2628.0	2634.4
5.	AL-00 %, HTPB-14 %, AP-86 %	2634.5	2635.7	2636.3

Table 4   CEA results for different boron and aluminum percentage

S. nos.	P_{cc} (Bar)	Vacuum specific impulse (Ns/Kg)				
		Pure AL	Pure B	B-3 %	B-5 %	B-8 %
1.	50	2824.80	3777.10	3017.30	3124.80	3273.60
2.	100	2830.40	3810.80	3028.60	3139.50	3292.00
3.	150	2833.00	3829.70	3034.60	3147.40	3302.00

boron is mixed with the aluminum particle which enhances the burning properties of the propellant. It is observed that aluminum–boron propellant combinations have higher energy level than the pure aluminized propellants. In this evaluation, aluminum is acted as a combustion booster for the boron to release its complete energy to enhance the performance of the composite propellant.

Now, we are considering pure boron propellant which has 18 % boron by weight. The boron percentage is reduced from 18 to 15 % and this part is filled with other elements having fuel properties to evaluate the performance. The boron ignition has problems; therefore, we can find with which combination of the element, the performance will be very close to the pure boron combination. These elements are Al, Cu, Ni, Zr, W, Cr, Mn, Ti, Mg, and Fe. Table 5 shows a set of propellants based on iron as an additive. Here we observed that first row gives maximum values of vacuum I_{sp} as well as I_{sp}. In the same way of tabulation, we observed that a similar type of results is produced for the other nine elements combinations which are not separately tabulated here. Based on performance the first row of Table 5 is taken as a reference propellant where the additive is only 0.3 %. Table 6 shows the performance for twelve different combinations of propellants including pure aluminum and pure boron. As we have discussed earlier, that pure boron-based propellant has problems during ignition and combustion; therefore, other elements are added individually to the pure boron-based
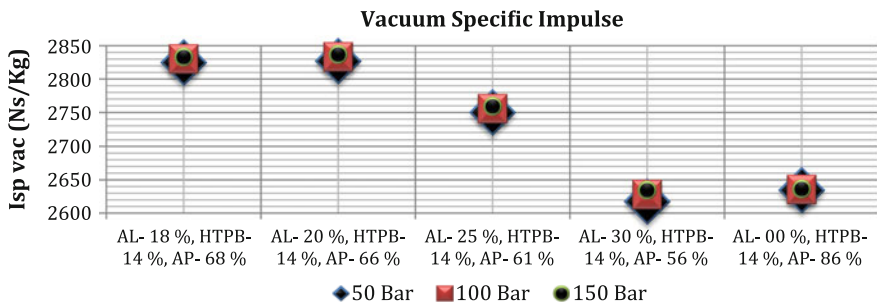

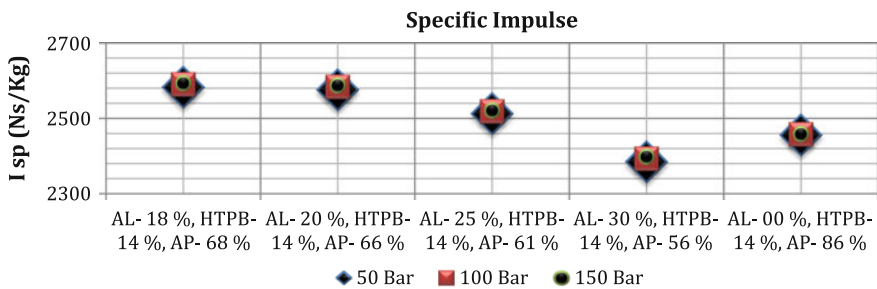**Fig. 1** CEA plot for different ingredient's percentage

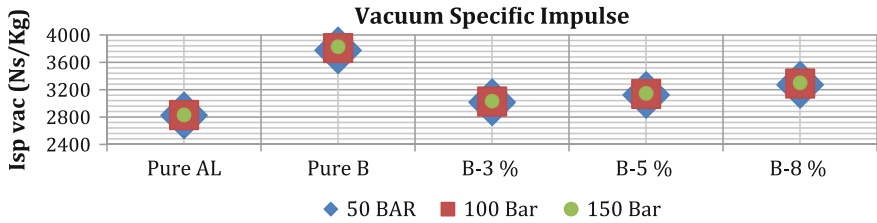**Fig. 2** CEA plot for different ingredient's percentage

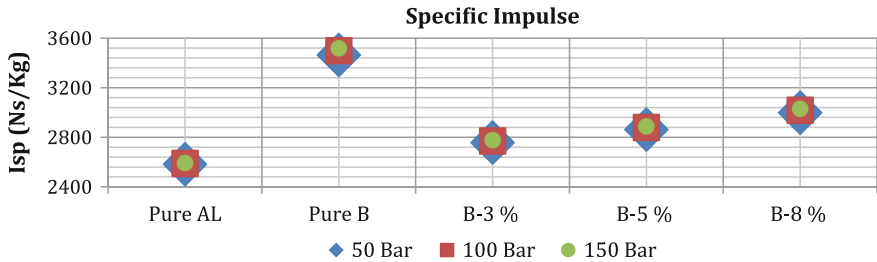**Fig. 3** CEA plot for different boron and aluminum percentage

Fig. 4 CEA plot for different boron and aluminum percentage

Table 5 CEA results for different iron and boron-based propellants

Vacuum-specific impulse (Ns/Kg)				
S. nos.	Ingredients	50 Bar	100 Bar	150 Bar
1.	Fe-0.3 %, B-17.7 %, HTPB-14 %, AP-68 %	3770.2	3803.7	3822.5
2.	Fe-0.5 %, B-17.5 %, HTPB-14 %, AP-68 %	3765.6	3799.0	3817.7
3.	Fe-1 %, B-17 %, HTPB-14 %, AP-68 %	3754.0	3787.1	3805.6
4.	Fe-2 %, B-16 %, HTPB-14 %, AP-68 %	3733.1	3765.0	3782.8
5.	Fe-3 %, B-15 %, HTPB-14 %, AP-68 %	3714.1	3744.9	3762.0

Table 6 CEA results for various combinations

Vacuum-specific impulse (Ns/Kg)				
S. nos.	Ingredients	50 Bar	100 Bar	150 Bar
1.	Al-18 %, HTPB-14 %, AP-68 %	2824.8	2830.4	2833.0
2.	Al-0.3 %, B-17.7 %, HTPB-14 %, AP-68 %	3764.8	3798.1	3816.7
3.	Cu-0.3 %, B-17.7 %, HTPB-14 %, AP-68 %	3765.5	3798.9	3817.6
4.	Ni-0.3 %, B-17.7 %, HTPB-14 %, AP-68 %	3765.6	3799.0	3817.6
5.	Zr-0.3 %, B-17.7 %, HTPB-14 %, AP-68 %	3765.6	3799.0	3817.7
6.	W-0.3 %, B-17.7 %, HTPB-14 %, AP-68 %	3765.7	3799.0	3817.7
7.	Cr-0.3 %, B-17.7 %, HTPB-14 %, AP-68 %	3765.7	3799.1	3817.7
8.	Mn-0.3 %, B-17.7 %, HTPB-14 %, AP-68 %	3765.7	3799.1	3817.7
9.	Ti-0.3 %, B-17.7 %, HTPB-14 %, AP-68 %	3767.1	3800.4	3819.1
10.	Mg-0.3 %, B-17.7 %, HTPB-14 %, AP-68 %	3767.4	3800.8	3819.4
11.	Fe-0.3 %, B-17.7 %, HTPB-14 %, AP-68 %	3770.2	3803.7	3822.5
12.	B-18 %, HTPB-14 %, AP-68 %	3777.1	3810.8	3829.7

propellants. These elements improve the ignition capability of the boron in the propellants by changing the amount of HBO_2, and the individual performance of the propellants is very close to the pure boron combination. It is also noticed that these combinations have higher values than pure aluminum-based propellants and also higher than aluminum–boron-based propellants which are discussed in Table 4. Table 6 results are observed deeply with the help of Table 7. In Table 7, we have chosen three propellants, namely pure boron, B–Fe, and B–Mg combinations. These two combinations are very close to the pure boron which is shown in Figs. 5 and 6.

The dominant species of the combustion product which has major role in the propellant performance are shown in Table 7. We have selected pure boron and two

Table 7 Combustion products of the propellants

| S. nos.	Species	Chamber mole fractions (at 50 Bar)		
		Pure B	B-Fe	B-Mg
1.	BO	1.0905×10^{-1}	1.0934×10^{-1}	1.0824×10^{-1}
2.	B_2	1.9295×10^{-4}	1.8308×10^{-4}	1.7657×10^{-4}
3.	BO_2	4.7950×10^{-4}	4.9351×10^{-4}	4.8890×10^{-4}
4.	B_2O	2.6452×10^{-3}	2.5869×10^{-3}	2.5533×10^{-3}
5.	B_2O_2	2.4958×10^{-2}	2.5148×10^{-2}	2.5354×10^{-2}
6.	B_2O_3	2.6578×10^{-4}	2.7514×10^{-4}	2.7881×10^{-4}
7.	HBO	8.0108×10^{-2}	8.0741×10^{-2}	8.1044×10^{-2}
8.	HBO_2	5.3587×10^{-4}	5.5472×10^{-4}	5.5876×10^{-4}
9.	HBOH	2.9933×10^{-5}	3.0202×10^{-5}	3.0024×10^{-5}
10.	CO	1.9473×10^{-1}	1.9584×10^{-1}	1.9569×10^{-1}
11.	CO_2	3.0359×10^{-5}	3.1328×10^{-5}	3.1246×10^{-5}
12.	H_2O	3.0751×10^{-4}	3.1814×10^{-4}	3.1747×10^{-4}
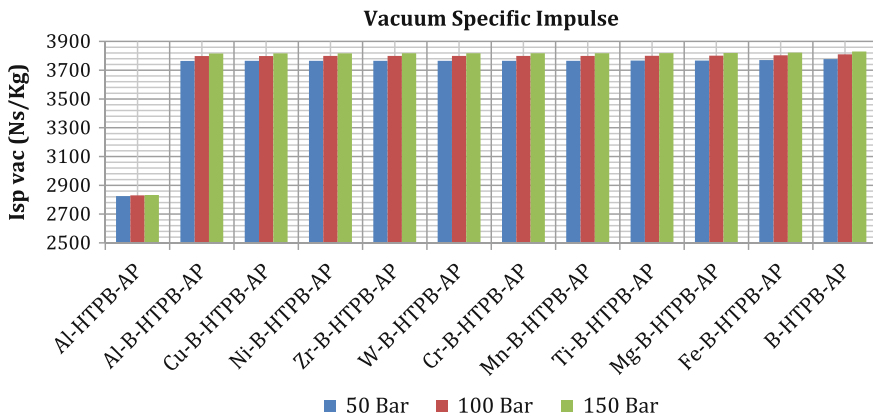
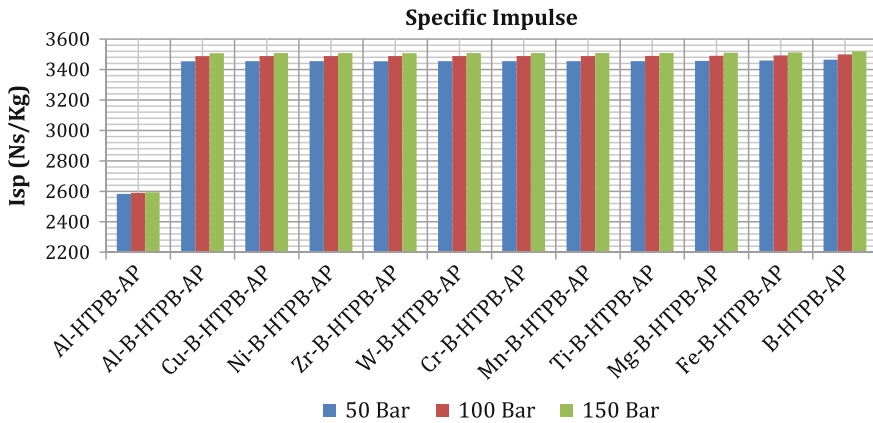**Fig. 5** CEA plots for various combinations

Fig. 6 CEA plots for various combinations

other combinations such as B–Fe and B–Mg. In case of fuel-rich condition the dominant species are BO, HBO, and B_2O_2. The dominant species under oxygen-rich condition are BO_2, B_2O_3, HBO_2, and HOBO. The B_2O_3 coating on the boron particle minimizes the diffusion of oxygen. The species containing hydrogen are H_2O, OH, H, and H_2; these are available above 1800 K. These species initially enhance the combustion, but further as their concentrations increase, start forming HOBO. It is observed that the species HBO and the long residence metastable intermediate HOBO are the dominant products. In other word it can be called as thermodynamic sink because it prevents full release of combustion energy. So, the condensation of B_2O_3 to liquid from gaseous state requires more time, but in between this duration the combustion product will leave the thrust chamber (i.e., B_2O_3 condenses from the gases to liquid state too late in the combustion process). In the actual condition these phenomena have a disadvantage over the pure boron combustion, because a part of the motor propulsive efficiency is destroyed [14, 15].

4 Conclusion

In Table 7 we have observed that the mole fraction of B_2O_3 is the lowest for the pure boron case compared to other combinations. It is clear from the above discussions that pure boron combination suffers less kinetic problems than others. Hence, by these theoretical researches, pure boron-based propellant has higher specific impulse than that of other eleven propellants combination as shown in Figs. 5 and 6. We have also seen that how the boron-based propellants stand with higher energy than that of pure aluminized propellants. The above discussions confirm that boron can be considered as a high energy fuel or ingredient for the high performance futuristic propellants. Eventually, in this theoretical research work we

have concluded that pure boron bags first, B–Fe second, and B–Mg is at third position on the basis of rocket performance parameters which is shown in Table 6. It is also observed here that for the pure boron case maximum energy cannot be released due to the oxide layer, but with the help of iron and magnesium we can get nearly the same performance parameters what we got for the pure boron case. In the present day, many researchers are involved in nano particle-based propellant processing and its testing. In order to enhance the explosive and rocket performance parameter of boron-based propellant; it is required to process the propellant in a nanoparticulate form.

References

1. Wen Ao, Weijuan Yang., Yang Wang., Junhu Zhou., Jianzhong Liu., and Kefa Cen., "Ignition and Combustion of Boron Particles at One to Ten Standard Atmosphere" Zhejiang University, 310027 Hangzhou, People's Republic of China.
2. Davenas Alain., "Solid Rocket Propulsion Technology" Pergamon Press, ISBN-0-08-040999-7 (1993).
3. Kenneth K. Kuo., and Ragini Acharya., Application of Turbulent and Multiphase Combustion, John Wiley & Sons USA, INC, ISBN 978-1-118-12756-8.
4. Gregory Young., Colin W. Roberts., and Chad A. Stoltz., "Ignition and Combustion Enhancement of Boron with Polytetrafluoroethylene," Journal of Propulsion and Power, Vol. 31, No. 1, January–February 2015.
5. Ulas, A., Kuo, K. K., and Gotzmer, C., "Ignition and Combustion of Boron Particles in Fluorine-Containing Environments," Combustion and Flame, Vol. 127, Nos. 1–2, 2001, pp. 1935–1957. doi:10.1016/S0010-2180(01)00299-1.
6. Gany. A., and Timnat. Y. M., "Advantages and Drawbacks of Boron—Fueled Propulsion," Acta Astronautica, Vol. 29, No. 3, 1993, pp. 181–187.
7. Netzer. D., Gany. A., Karadimitris. A., and Scott. C. II, "Regression and Combustion Characteristics of Boron Containing Fuels For Solid Fuel Ramjets," Journal of Propulsion and Power, Vol. 7, No. 3, 1991, pp. 341–347.
8. Besser. H. L., and Strecker. R., "Overview of Boron Ducted Rocket Development During the Last Two Decades," Combustion of Boron-Based Solid Propellant and Solid Fuels, CRC Press, Inc., Boca Raton, FL, 1993, pp. 133–178.
9. Bao. F. T., Huang. J. X., Integral Solid Propellant Ramjet Rocket Motor (in Chinese), Beijing, China Astronautic Publishing House, 2006.
10. Miyayama. T., Oshima. H., Improving Combustion of Boron Particles in Secondary Combustor of Ducted Rockets, 42nd AIAA/ASME/SAE/ASEE Joint Propulsion Conference & Exhibit, Sacramento, California, 2006.
11. Gordon. S and McBride. B., "Computer program for calculation of complex chemical equilibrium composition and applications". http://www.grc.nasa.gov/WWW/CEAWeb/ceaWhat.htm. NASA RP 1311, 1994,
12. Sumit Verma., Ramakrishna. P. A., "Dependence of density and burning rate of composite solid propellant on mixer size". Acta Aeronautica 93 (2014) 130–137.
13. Mukunda. H. S., "Understanding aerospace chemical propulsion" Interline publishing, ISBN-81- 7296- 087- 5 (2004).
14. Bellott. B. J., "Synthesis, characterization, and reactivity of volatile compounds for material applications". PhD thesis, University of Illinois at Urbana–Champaign (2010).
15. Yetter. R. A., Rabitz. H., Dryer. F. L., Brown. R. C., Kolb. C. E., "Kinetics of high temperature B/O/H/C chemistry". Combustion and flame 83: 43–62 (1991).

PreSTo Wing Module Optimization for the Double Trapezoidal Wing

Karunanidhi Ramachandran and Dieter Scholz

Abstract This paper explains the Aircraft Preliminary Sizing Tool (PreSTo) developed at the Hamburg University of Applied Sciences. From the different modules of PreSTo, PreSTo wing, and its sweep angle have been taken as the key feature to explain further. In order to figure out the necessary values for the double trapezoidal wing a loop has been created between the kink chord, inner taper ratio, inboard leading edge sweep angle, and inboard 25 % chord sweep angle. By the end of the loop all the major chords, sweep angles, and taper ratios are calculated and a 2D representation of the wing is given. PreSTo will interact with the user by giving suggestions and during certain parameter conflicts; it can give warning to the user concerning his previous made design choices. Values of wing parameters generated in the wing module are finally stored into PreSTo central database. OpenVSP Connect retrieves values from PreSTo central database and visualizes the aircraft and its wing in 3D with NASA's tool Open Vehicle Sketch Pad (OpenVSP).

Abbreviations

A	Aspect ratio
AAA	Advanced Aircraft Analysis
ACSYNT	Aircraft Synthesis
AERO	Aircraft Design and Systems Group
APD	Aircraft Preliminary Design
c	Chord (index: t = tip, r = root, k = kink)

K. Ramachandran (✉) · D. Scholz
Aircraft Design and System Group (AERO), Hamburg University of Applied Sciences, Berlinor Tor 11, 20099 Hamburg, Germany
e-mail: chandran.ramk@gmail.com

D. Scholz
e-mail: info@profscholz.de

337

CATIA V5	Computer-Aided Three-Dimensional Interactive Application Version 5
CAPDA	Computer Aided Preliminary Design of Aircraft
CEASIOM	Computerized Environment for Aircraft Synthesis and Integrated Optimization Methods
d_f	Fuselage diameter
FLOPS	Flight Optimization System
GUI	Graphical User Interface
HAW Hamburg	Hamburg University of Applied Sciences
MAC	Mean Aerodynamic Chord
OPerA	Optimization in Preliminary Aircraft Design
OpenVSP	Open Vehicle Sketch Pad
PrADO	Preliminary Aircraft Design and Optimization Program
PreSTo	Aircraft Preliminary Sizing Tool
RDS	Raymer Design System
SAS	Simple Aircraft Sizing
y_k	Distance between kink chord and fuselage centerline

1 Introduction

The aircraft design process has its own different phases. In each phase, we need to deal with all of the main parts of the aircraft like wing, fuselage, and empennage. Where the basic needs of the aircraft figured out by the strategic planning and market analysis group and the design engineers will continue their work later on. The whole design process has an iterative character. Every change will cause an alteration of some other value [1].

Design engineers at different aircraft industries are using their own kinds of preliminary design software. Such software is not openly available and shrouded in secret. There are also many private research groups and Universities with their own design tools. Commercial aircraft design tools which are available online for use are RDS, AAA, APD, and CEASIOM [2–5]. Daniel Raymer developed RDS Integrated Aircraft Design and Analysis based on his book "Aircraft Design: A Conceptual Approach." Jan Roskam created the software tool AAA (Advanced Aircraft Analysis) based on his book "Airplane Design." Pacelab GmbH in Berlin developed APD (Aircraft Preliminary Design). The CEASIOM (Computerized Environment for Aircraft Synthesis and Integrated Optimization Methods) developed by SimSAC is an aircraft design software openly available. CFS Engineering provides support for the tool.

Aircraft design tools that are made by universities and research organizations are PrADO, CAPDA, FLOPS, and ACSYNT. CAPDA (Computer Aided Preliminary Design of Aircraft) was developed at Technical University Berlin as a tool for the analysis and Conceptual Design of commercial aircraft [6]. PRADO (Preliminary Aircraft Design and Optimization) program was developed for many years as a

modular Aircraft Design tool at Technical University Braunschweig [7]. FLOPS (Flight Optimization System) is a multidisciplinary tool (with nine modules) for designing and evaluating advanced aircraft concepts. It was developed by NASA [8]. ACSYNT (Aircraft Synthesis) started as an initiative of Ames research center to improve the conceptual design process. It is now Joint Sponsored Research Agreement by Ames Research Center, NASA, and Virginia Tech [9].

Tools developed at the Hamburg University of Applied Sciences follow a different approach. SAS (Simple Aircraft Sizing) is only the first step in the tool chain of preliminary aircraft design. SAS allows manual analysis of basic preliminary sizing parameters; OPerA (Optimization in Preliminary Aircraft Design) allows optimizing conceptual design parameters and PreSTo (Aircraft Preliminary Sizing Tool) offers a modular, manual, interactive, and more detailed approach of every conceptual design step. The complexity and the features increase gradually from SAS to PreSTo. The tool chain follows in this way:

SAS => OPerA => PreSTo => Further Tool Evaluation and Display Tools

2 Simple Aircraft Sizing (SAS)

The philosophy of SAS is to support the aircraft designer converting certain mission requirements into important aircraft parameters. The program is set up as a spreadsheet in Excel. An advantage using a spreadsheet over the use of programming languages is its efficient integration of input, calculation, and output. Excel is easy to understand and does not need an expert to operate. It is easy to store and compatible with most of the operating systems and computers.

SAS consists of well-proven equations and calculation sequences from the lecture of Prof. Scholz. From basic input parameters to aircraft design like payload and range, landing, and take-off field length the outputs like required thrust and wing area are calculated, complemented by maximum take-off mass, fuel mass, and other mass parameters. On the way to these results aerodynamic and other parameters like Oswald factor, maximum glide ration, zero-lift drag coefficient, minimum drag lift coefficient, specific fuel consumption are calculated, to name only a few [10].

3 OPerA—Optimization in Preliminary Aircraft Design

The main aim of OPerA was to apply formal optimization to aircraft preliminary design and preliminary aircraft cabin design. Aircraft basic parameters like aspect ratio, maximum lift coefficients are the engineer's choice. Especially for inexperienced aircraft designers it is difficult to choose all required parameters in the best way. The challenge is to find that combination of design parameters which is an optimum for the design. However, this optimum combination of design parameters found by formal optimization is only a starting point to a further detailed design

described by more parameters in PreSTo. Adding PreSTo to OPerA means to combine formal optimization with a subsequent interactive and experienced-driven aircraft design environment [11].

OPerA goes way beyond Preliminary Sizing. It deals with many more parameters and offers many features only found in Conceptual Design. It includes drag and mass estimations, derivation of main geometrical parameters, a specific fuel consumption model, direct operating cost (DOC) calculation and even evaluation of Added Values. Nevertheless, it stays a simple tool, although allowing a complete Aircraft Design analysis. OPerA is limited to conventional aircraft configurations, but includes innovative concepts and cabin parameters that are normally not part of conceptual design. OPerA requires only Microsoft Excel 2007 and makes use also of Excel's built-in optimizer know as the Solver [12].

4 Overview of PreSTo

PreSTo is still under development, but progressing. PreSTo is a modular and interactive tool that requires manual input. It stretches from preliminary sizing to conceptual design. It will ultimately contain a module for each step of classical Aircraft Design:

- Sizing (PreSTo-Sizing)
- Cabin and Fuselage Layout (PreSTo-Cabin)
- Wing Layout
- Design for High Lift
- Empennage Layout
- Landing Gear Layout
- Mass and CG Estimation
- Drag Estimation
- DOC Calculation
- Results, Interfaces to other Tools, 3D Visualization (OpenVSP-Connect).

Each module has its own Excel file. The idea is to open in a first step the desired aircraft project contained in an Excel file by means of a Graphical User Interface (GUI). This file also stores the database describing the project. Figure 1 shows the central GUI of PreSTo. When the aircraft project is opened, parameters are set in Excel. Once the user interactively generated new values for further design parameters, the values are written back into the database with help of the graphical user interface. The only file necessary to store the project is the database file (with the GUI, Fig. 1). When future developments of PreSTo come with improved modules, these updated modules will be available on the Internet for download. The aim is to keep all existing databases compatible with new versions of the modules [13].
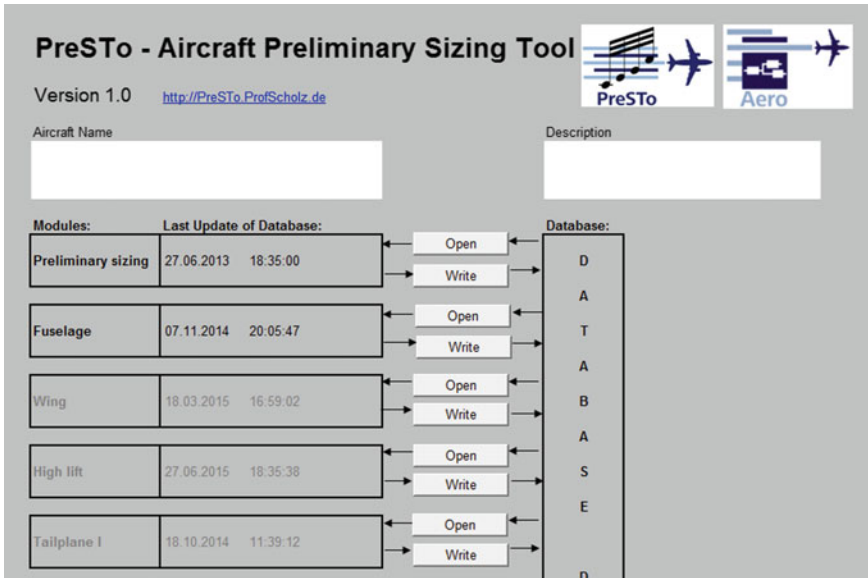
Fig. 1 Graphical User Interface (GUI)

5 PreSTo Wing Design

The wing section of an aircraft is a fundamental part of aircraft design. Initial input of parameter required to begin with the PreSTo wing optimization. Written VBA codes imports parameters from the database of PreSTo. When users click the 'Open' button in the GUI for the wing module, the VBA program opens the wing module and inserts the basic parameter into this module. These basic parameters are from the previous modules, which are stored in the database. Typically, users have defined a certain range and number of passengers and other fundamental parameters in the very beginning. Based on these fundamental parameters inserted by the user the fuselage length, fuselage diameter, the lift coefficient in cruise, a first fuel estimation, and other parameters are set. The wing module that now follows consists of several worksheets with only one being visible for the end user. The other worksheets contain plane data, graphs, airfoil data, and constants [13]. Several wing parameters are calculated as detailed in the Sects. 5.1 and 5.2.

5.1 Sweep Angle

Wing sweep reduces the negative effects on the wing from transonic and supersonic flow. Wing sweep also improves roll stability of the aircraft. A double trapezoidal wing has two different sweep angles—a sweep angle for the inner wing and a sweep

angle for the outer wing. Wing sweep may be forward or aft, but in most of the cases, it is aft swept and defined with respect of the 25 % chord line. Two sweep angle suggestions are given in PreSTo based on Howe [14] and Raymer [15] to the user. The different sweep angles give freedom to the user to choose, because both authors' suggestions come from experience and are free to be adapted. The inner wing sweep is calculated as follows:

$$\tan = (\varphi_i) = \frac{x}{y_k - d_f/2} \tag{1}$$

This inner sweep calculation is for the 25 % chord line. 'X' is found from the taper ratio of the inner wing. This states the increase toward the wing root.

$$\frac{3}{4}c_r = \frac{3}{4}c_k + x$$

$$\Leftrightarrow \frac{3}{4}(c_r - c_k) = x \quad \text{with} \quad \lambda_i = \frac{c_k}{c_r} \rightarrow x = \frac{3}{4}c_k\left(\frac{1}{\lambda_i} - 1\right)$$

Leads to the final formula (2),

$$\varphi_{i,25} = \arctan\left(\frac{\frac{3}{4}c_k\left(\frac{1}{\lambda_i} - 1\right)}{y_k - \frac{d_f}{2}}\right) \tag{2}$$

Inner taper ratio

The overall taper ratio is depicted with suggestions from Howe [14] or Torenbeek [1]. The outer taper ratio depends on the overall taper ratio and the inner taper ratio (3)

$$\lambda_o = \frac{\lambda}{\lambda_i} \tag{3}$$

The inner taper ratio is the ratio of the kink chord to the root chord according to Eq. (4), but can also be geometrically derived to be dependent on the kink chord and wing sweep according Eq. (5).

$$\lambda_i = \frac{c_k}{c_r} \tag{4}$$

$$\lambda_i = \frac{c_k}{c_k + \left(y_k - \frac{d_f}{2}\right)\tan\left(\varphi_{0,i}\right)} \tag{5}$$

Equation (6) considered in case of different inboard trailing edge sweep,

$$\lambda_i = \frac{c_k}{c_k + \left(y_k - \frac{d_f}{2}\right)\left[\tan\left(\varphi_{0,i}\right) - \tan\left(\varphi_{100,i}\right)\right]} \tag{6}$$

Kink chord

The intersection of the two trapeziums is called the "kink." The area of double trapezoidal wing calculated according to Eq. (7).

$$S = 2\left[c_r\frac{d_f}{2} + \frac{(c_r + c_k)\left(y_k - d_f/2\right)}{2} + \frac{(c_k + c_t)(b/2 - y_k)}{2}\right] \tag{7}$$

Equation (7) written as follows,

$$S = \frac{d_f}{2}(c_r - c_k) + y_k(c_r - c_t) + \frac{b}{2}(c_k + c_t) \tag{8}$$

By taking c_k out in common, Eq. (9) modified in terms of taper ratios,

$$S = \frac{d_f}{2}c_k\left(\frac{c_r}{c_k} - 1\right) + y_k c_k\left(\frac{c_r}{c_k} - \frac{c_t}{c_k}\right) + \frac{b}{2}c_k\left(1 + \frac{c_t}{c_k}\right) \tag{9}$$

Substituting, $\lambda_i = \frac{c_k}{c_r}$, $\lambda_o = \frac{c_t}{c_k}$
c_k can be found with the formula (10):

$$c_k = \frac{s}{\frac{d_f}{2}\left(\frac{1}{\lambda_i} - 1\right) + y_k\left(\frac{1}{\lambda_i} - \lambda_o\right) + \frac{b}{2}(1 + \lambda_o)} \tag{10}$$

The kink chord is dependent on the inner taper ratio only. The outer taper ratio is calculated from the overall taper ratio. The other values are present already.
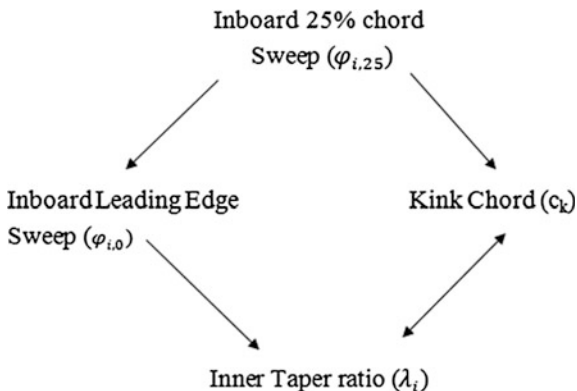
Inboard sweep
The inboard sweep is calculated via Eq. (11).

$$\varphi_{i,25} = \arctan\left(\frac{\frac{3}{4}c_k\left(\frac{1}{\lambda_i} - 1\right)}{y_k - \frac{d_f}{2}}\right) \tag{11}$$

Only inboard taper ration is required in the above formula. It is calculated from the Eq. (5). Sweep angle at different percentage of chord given in Eq. (12) [16].

$$\tan(\varphi_n) = \tan(\varphi_m) - \frac{4}{A}\left[\frac{n - m}{100} \cdot \frac{1 - \lambda}{1 + \lambda}\right] \tag{12}$$

**Fig. 2** Loop created for optimization of Taper ratio

Equations (5), (10), (11), and (12) will form the loop to find all the necessary values. The kink ratio $\eta_k = y_k/(b/2)$ is a percentage of semi span where the kink chord is located. It follows from statistics. With these two values the iteration process starts and values for inner and outer taper ratios, inner sweeps, and all chords are given. In essence, following values are dependent in the loop (Fig. 2). In the loop, double arrow between kink chord and inner tapper ratio indicates that both are sharing the same unknowns.

The settings in the Excel solver can be manually changed or automatically when incorporated in the VBA code during startup. When the PreSTo workbook is opened, the settings will automatically be configured to allow for iterations with a maximum of 100 or a maximum discrepancy of 0.001 [17].

5.2   Wing Geometry Results

The basic wing geometry of the double trapezoidal wing is drawn using inner, kink, and outer chord, inner and outer sweep angle, and inner and outer taper ratio. The resultant wing diagram is shown in Fig. 3. The red dot indicates the Aerodynamic Center (AC) located on the Mean Aerodynamic Chord (MAC), and the pink line shows the kink chord.

Fig. 3 Wing geometric results
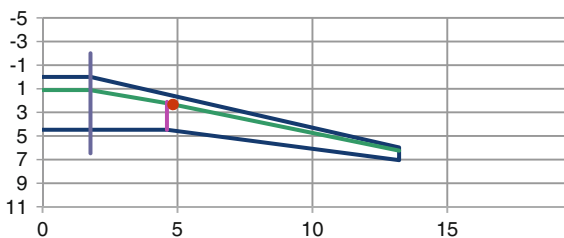
6 OpenVSP Connect

OpenVSP Connect is primarily intended as an interface tool between any aircraft design tool and Open Vehicle Sketch Pad (OpenVSP) from NASA [18]. OpenVSP Connect needs OpenVSP for the display of the aircraft. In the order of 50 core parameters of the aircraft are used to calculate the many input parameters required by OpenVSP to sketch a passenger aircraft. For each of the core parameter, a proposed value is given in the user interface and automatically applied as long as the user does not specify his/her own value. This is a fundamental principle of the program. The user will always get assistance from the PreSTo. This too proposes values to fill the required fields. The program works in "automatic mode" by using all proposed or default values. Based on the minimum of just two input values "cruise Mach number" and "number of passengers" an aircraft can be sketched automatically [19].

7 Summary and Future Steps

In this report, main task was designing a double trapezoidal wing. Various extra parameters used to get the required double trapezoidal plan form. There is a dependency between taper ratio, kink chord, root chord, tip chord, and sweep. With the use of an Excel solver, loop created and implemented in order to find the suitable values for designing the trapezoidal wing. Besides these suitable values, the end users still have the choice to use another number of preferences. OpenVSP connect is one of the important features of PreSTo. OpenVSP connect helps to visualize the 3D view of the complete aircraft and the separate modules.

PreSTo is still under development phase. Most of the modules are already finished and some of it has to be updated with the latest design options (Extra features). In future, possibilities for connecting some complicated analysis software's (CFD, MATLAB…, etc) with PreSTo will be studied.

References

1. E. Torenbeek, *Synthesis of Subsonic Airplane Design*. Delft University Press, 1982.
2. D. P. Raymer, "Conceptual Design Modeling in the RDS-Professional Aircraft Design Software," *49th AIAA Aerosp. Sci. Meet. Incl. New Horizons Forum Aerosp. Expo.*, pp. 1–11, 2011.
3. W. a. J. Anemaat and J. Roskam, "Advanced Aircraft Analysis," *DARcorporation*, no. 785, 2014.
4. PACE, "Pacelab Aircraft Priliminary Design (APD)," 2011. [Online]. Available: https://www.pace.de/products/preliminary-design/pacelab-apd.html. [Accessed: 20-Sep-2015].

5. SimSAC, "CEASIOM (Computerized Environment for Aircraft Synthesis and Integrated Optimization Methods)," 2015. [Online]. Available: http://www.ceasiom.com/index.php. [Accessed: 27-Dec-2015].

6. M. Schmid, "CAPDA-Computer Aided Preliminary Design of Aircraft," 2009. [Online]. Available: https://www.luftbau.tu-berlin.de/menue/forschung/abgeschlossene_projekte/visual_capda/. [Accessed: 04-Sep-2015].

7. Wolfgang Heinze, "PrADO—Preliminary Aircraft Design and Optimization," 2008. [Online]. Available: https://www.tu-braunschweig.de/ifl/simulationswerkzeuge. [Accessed: 20-Dec-2015].

8. T. M. Lavelle and B. P. Curlett, "Graphical user interface for the NASA FLOPS aircraft performance and sizing code," 1994.

9. NASA, "ACSYNT—Aircraft Synthesis," 1997. [Online]. Available: https://www.nasa.gov/ames/spinoff/aircraft_design_software/#.VoSQkvkrLIU. [Accessed: 22-Dec-2015].

10. Dieter Scholz, "SAS-Simple Aircraft Sizing," 2008. [Online]. Available: http://fe.profscholz.de/. [Accessed: 19-Dec-2015].

11. Dieter Scholz, "OPerA—Optimization in Preliminary Aircraft Design," 2011. [Online]. Available: http://opera.profscholz.de/. [Accessed: 10-Dec-2015].

12. M. F. Nita, "Contributions to Aircraft Preliminary Design and Optimization," 2013.

13. AERO, "Aircraft Design and Systems Group," 2015. [Online]. Available: http://aero.profscholz.de/. [Accessed: 20-Dec-2015].

14. D. Howe, *Aircraft conceptual design synthesis*. Professional Engineering Publishing Limited, 2000.

15. D. P.Raymer, *Aircraft Design: A Conceptual Approach*. American Institute of Aeronautics and Astrinautics, Inc., 1992.

16. Dieter Scholz, *Aircraft Design Lecture Notes*. Hamburg: HAW Hamburg, 2012.

17. Ozgrid, "Excel Training," 2014. [Online]. Available: http://www.ozgrid.com/forum/showthread.php?t=187310. [Accessed: 25-Dec-2015].

18. J. R. Gloudemans, "OpenVSP," 2012. [Online]. Available: http://www.openvsp.org/.

19. Dieter Scholz, "OpenVSP Connect," 2013. [Online]. Available: http://openvsp.profscholz.de/. [Accessed: 19-Dec-2015].

Optimization Technique Applied for Method of Evaluation of a Controllable Factor of FSAE Car Chassis

R. Suraj, A.V. Pavan Kumar, Abhilash P. Kulkarni, S. Kiran Aithal and R. Vinutha

Abstract Design of any system is imperfect without optimization. The common problem faced for any design engineer during designing of a tubular race car chassis is the determination of optimum parameter for the tube. This optimization technique is specifically applied to the chassis of FSAE car. This technique provides the most optimum equation which relates all the controllable factors of the chassis. The optimum equation is found using *point-set topology, surface fitting methods, iterations in analysis softwares.* Controllable factors like diameter, wall thickness, deflection, yield strength are made a 3D surface function in the form of $z = (ax^n)$ $(y^m) + (bx^{n-1})(y^m) + (cx^n)(y^{m-1}) + \dots px + cy$. The obtained equation is the most optimum equation which relates all the controllable factors for a specific loading condition. Considering loading condition as side impact condition, if the optimum parameter has to be chosen (say diameter), the priority of deflection and the yield strength of the material is input into the equation, which contains the deflection and yield strength as other parameters. The equation is solved to obtain the most optimum diameter for the specified inputs. If all the inputs are given to the equation and if the equation is satisfied, the given inputs are said to be optimum inputs (Zero deviation from the given equation). Any variation either below or above the equation are considered to be positive or negative deviation measured from a reference of the optimum equation.

R. Suraj (✉) · A.P. Kulkarni · S. Kiran Aithal
NMIT, Bangalore, India
e-mail: surajraju42@gmail.com

A.V. Pavan Kumar
Kshipra R&D Simulations, Bangalore, India

R. Vinutha
SEACET, Bangalore, India

1 Introduction

Formula SAE is a competition conducted by SAE where the main aim is to build and race formula cars under certain rules and regulations [1]. The competitors undergo certain tests including virtual rounds where their respective designs are critiqued and their viability is ensured.

The formula SAE car being considered is designed and built on certain rules and regulations. The car engine for example must contain a cylinder volume less than 610 cc [1]. The chassis being used in most of the Formula SAE cars is a Tubular Space frame for much obvious reasons as monocoque would be costlier and not viable in current conditions. So for any car, the SAE rulebook specifies certain minimum diameters for cross section of tubing in order to prevent rolling and related accidents, and to ensure safety of the driver.

The main objective is to obtain an equation containing many variables which is an optimum diameter solution during designing provided the needed loading condition is given with the material being used for an appreciable Factor of Safety.

2 Adopted Design Procedure of Chassis

2.1 Material Selection

We felt that the key for the good chassis is to select good materials, in fact the best. The material is key factor for the optimisation of the design. This made us to think twice before selecting the material. For this purpose we did extensive research on the materials. The main factors for our comparison were completely based on strength, weight, cost and weld ability [2]. We found out AISI SAE 1018 is suitable for our application [3].

A chassis having the following properties are considered for the fabrication (Table 1).

2.2 Frame Design

While designing the beams hallow tubes are more advantageous than the solid shaft.

Whenever a bending load is applied on the rod, it tries to bend in the direction of action of force. The maximum stress always occurs at the end of the rod, i.e. at the extreme radius of the bar. The end where force is allied undergo compression and the downwards end undergoes tension stress. But the centroidal axis of the bar is always remains to be unchanged without any compression and tension and hence called as neutral fibres. Thus, it does not matter if we keep the material near the

Table 1 Material properties

Material	SAE 1018
Tensile strength	630 MPa
Yeild strength	385 Mpa
Poisson's ratio	0.29
Modulus of elasticity	210 GPa
% elongation	27
Carbon	0.182 %
Manganese	0.645 %
Sulphur	0.64 %
Phosphor	0.03
Geometry	Circular Hallow tube
Weld ability	Good

neutral fibre or remove it, still it will have same strength. This can be interpreted mathematically maximum stress depends on the section modulus of the member. The section modulus of hollow member is high when compared to solid member having same weight. Hence hallow shaft is better for the chassis [4, 5].

We always prefer in structural engineering a tubular or space frame chassis which is a truss light in weight and rigid. Before designing the chassis few factors needs to be considered and are listed below [6]:

- Less the length, the more it can take bending forces.
- Chassis is always designed for conditions like impact, roll over and torsional rigidity.
- Chassis exactly acts like truss and distribute the force.
- The more outer diameter less is the stress.
- The more thickness less is the bending.
- The chassis should be symmetrical otherwise induces unavoidable vibrations/ undulations.

2.3 Methodology

First and foremost step for the design of the chassis is to find the boundary condition and the placing of the components. Keeping this in mind we have started to draw line diagram and then transferred them into a modeling software. Chassis is to be decided based on the track width and wheelbase dimensions. But the relation between them are profoundly complicated, but few of them can be realised very easily, few of them are listed are below [7].

A long wheel base should have more stability during braking, and if it is polar moment of inertia is not so high should produce more yaw moment in the corners

entry. On the other hand, in slow corners it should have more "under steering tendency" asking for more steering angle and should be less agile [7, 8].

A wide track will produce less weight transfer and so should give a higher cornering grip potential, but the vehicle will tend to follow wider lines on the track and to have, for example, bigger frontal area [7, 8].

A wheel base of 1600 mm and track width of 1250 at front and 1300 mm at rare has been achieved with the wheel base to track width ratio of 1.33. Stability does not only depend on these two but also depends on the height of the vehicle. The total height of our vehicle is 1000 mm whose ratio to wheel base is 1.6 which is golden ratio. This property is very useful for straight line stability [7, 8].

2.4 Loading Conditions [7, 8]

Side impact loading conditions are considered for the problem. In this case, a side impact to an obstruction is considered wherein a car rams into stationary vehicle.

Assumption made:

1. Maximum Speed of car = 22.7 $\frac{m}{s}$
2. Mass of car = 300 kg

From the equations of motions such as, $v = u + a * t$ and Newton's first law of motion, $= ma$, the force (F) for the above mentioned boundary condition is calculated to be 13885 N.

The calculated force 13885 N will be acted upon the side impact structures of the chassis.

2.5 Analysis

Theoretical calculations using FEM for the complete chassis will be highly time consuming and cumbersome [9]. In order to reduce the human effort, the computational methods have been widely used for analysis and validation. Finite Element Analysis is one among the prominent type of computational methods which are available in the market for commercial use. Thus, a commercially available FEA package has been chosen to do analysis of the chassis.

Few points of our understanding on how the software works is as follows:

1. It does not have units to sense itself; it is purely user justified units.
2. Slope of stress strain curve is young's modulus is sufficient to specify with optional of Poissons ratio.
3. Young's modulus will take care of the stress-strain and Poissons ratio will take of deflections in translation and rotation.

4. Slope of the stress–strain is tends to infinity without any yielding point or breaking point.
5. Density is the factor which decides the natural frequency of the chassis.
6. Node connectivity is very strong, even infinite force cannot break the node connectivity.
7. Strain energy has to be monitored for the optimization instead of the stress or strain to obtain better comparison.
8. There is no deviations and jumble in the stress–strain curve.
9. For the chassis, time step is always negotiated. That is, the variation in the time step in software 1D analysis doesn't give any difference between time steps.
10. As the stress strain curve is linear, the strain energy is integration under the curve.
11. The interpolation is linear.

Following assumptions are made during the analysis of chassis [10–12]:

1. Boundary conditions are first calculated by using motion equations and after analysis converted to G forces.
2. MIG Welding has one ton holding capacity which made us to negotiate the effect of welding on the chassis.
3. The material is assumed to be isotropic.
4. There is no initial cracks on the material (in order to come to this conclusion, A FOS of 2 minimum have been chosen).
5. The forces are acting on the key points or edges.
6. Fixed points arrest all 6 degree of freedom.
7. Complete chassis can be represented as a 1 dimensional truss.
8. Applying the section to the truss makes the chassis three dimensional.
9. Young's modulus is 210 GPa and Poissons ratio are 0.29.
10. Beam 188 is the 3D linear finite strain beam element used for the analysis (property of the element has been discussed in later stages).

3 Finite Element Analysis of the Chassis

The load of 13885 N is applied along on the side impact structures and the opposite side structures are constrained for motion of all DOF (fixed condition) (Fig. 1).

The results are documented and further iterations are carried out by varying the outer and inner diameter and keeping the wall thickness constant with a value of 1.65 mm for roll hoops and 1.25 mm for the other members. The diameter of roll hoops and side impact structures are varied within a range of 25.4–32 mm.

Figure 2 shows stress concentration of 190 Mpa for outer radius being 0.015 m and inner radius 0.01335 m.

Further iterations are carried out in a similar way and the results are shown. Results tabulated for 20 iterations are shown in the excel sheet (Fig. 3).
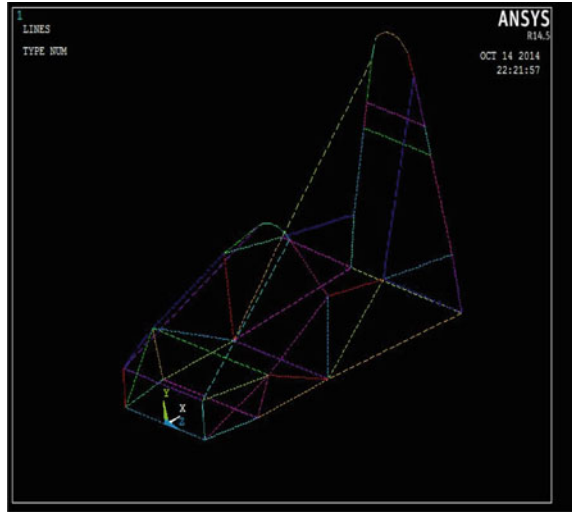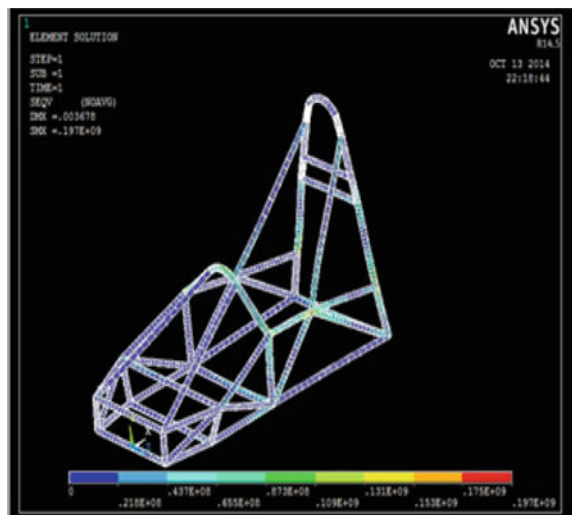
Fig. 1 Line diagram of the
chassis

Fig. 2 Results showing
deflection and stress
concentration

3.1 Surface Response

As the optimisation has different input and no specific outputs, it is very important
to note that several surface responses can be added together to get a simpler
understanding of the behaviour. In the nominal methods of optimisation like
Taguchi, only best possible solution is obtained. But to get continuous results for in
between points, we have to opt for higher order model like screening method. On

Sl.no	d1	d2	y(mm)	Stress(mpa)
1	25.4	25.4	4.859	243
2	26	25.4	4.669	234
3	27	25.4	4.379	221
4	28	25.4	4.12	208
5	29	25.4	3.888	198
6	30	25.4	3.678	197
7	31	25.4	3.488	195
8	25.4	26	4.703	240
9	26	26	4.52	232
10	27	27	4.022	214
11	28	27	3.782	203
12	30	27	3.37	180
13	30	28	3.201	177
14	31	27	3.194	173
15	31	28	3.041	170
16	28	26	3.985	206
17	29	27	3.564	191
18	29	28	3.3389	187
19	31	28	3.033	168
20	31	29	2.887	166

Fig. 3 Results for 20 iterations

the other hand, parameterising the thickness and diameter is complicated compared to this method.

Sampling points are used to find the relation between by plotting a surface, goodness of the fit is ensured to use the equation for the further purpose. Usually 1000 samples are considered to generate the trade-off points and the candidate points which is time consuming, hence in this method, instated of point, one equation is considered which has to be solved to get the optimum results by defining the constrains of upper boundary, lower boundary or seeking target value.

The results obtained are used as sampling points which are input into a Mathematical Software to generate the first 3D surface [13–15]. It is plotted by taking parameters d_1, y and induced stress. The dia (d_1) is taken in the X-axis, deflection (y) along the Y-axis and induced stress (σ_i) along the Z-axis [16] (Fig. 4).

The equation of the surface is extracted; the equation is computed to be

$$f(x, y) = z = P00 + P10*x + P01*y + P20*x^2 + P11*xy + P02*y^2 \qquad (1)$$

where $y = d_1$, $z = $ deflection (y) and $x = $ stress induced (σ_i).

With coefficients being as follows:

P00 = −308.1
P10 = 1.015

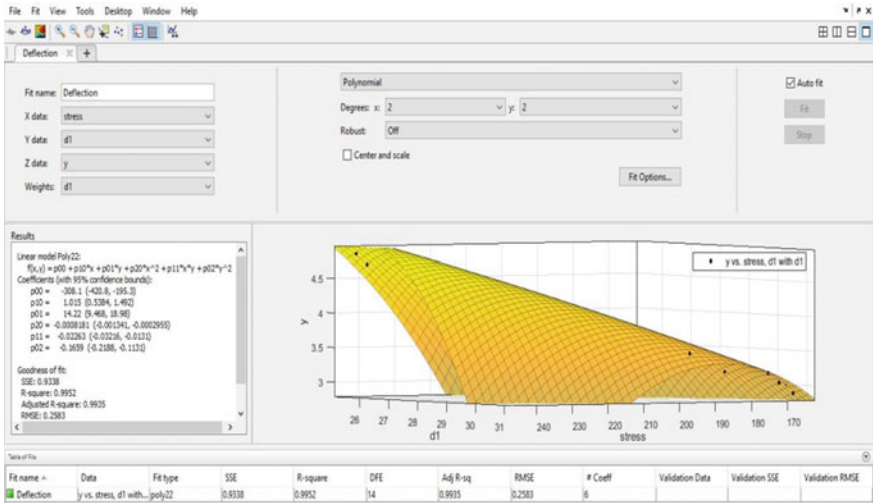**Fig. 4** 3D Surface 1

P01 = 14.22
P20 = −0.0008181
P11 = −0.02263
P02 = −0.1659

   The second surface is plotted by the taking the parameters d_2, d_1, induced stress. d_1 is taken in the X-axis, d_2 in the Y-axis and induced stress in the Z-axis [16] (Fig. 5).
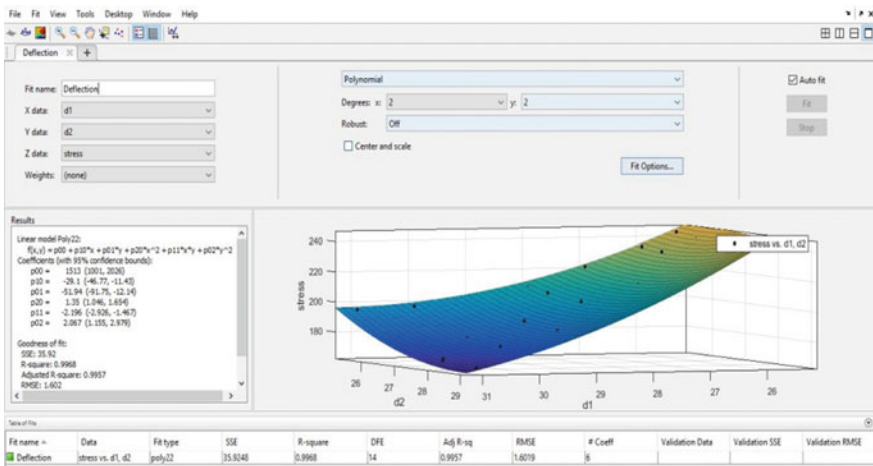

Fig. 5 3D Surface 2

The equation of the surface is extracted; the equation is computed to be

$$f(x,y) = z = P00 + P10*x + P01*y + P20*x + P11*xy + P02*y \qquad (2)$$

where $x = d_1$, $y = d_2$ and $z =$ stress induced (σ_i).
With the constants being

P00 = 1513
P10 = −29.1
P01 = −51.94
P20 = 1.35
P11 = −2.196
P02 = 2.607

We can see that Eqs. 1 and 2 is a function of induced stress. These functions can be written as follows,
From Eq. 1,

$$\sigma_i = f(d_1, y) \text{ Say P}$$

From the Eq. 2,

$$\sigma_i = f(d_1, d_2) \text{ Say A}$$

$$P = \sigma_i = f(d_1, y)$$
$$= 3371 - 175.9 * d_1 - 374.9 * y + 2.298 * d_1^2 + 11.46 * d_1 * y + 11.05 * y^2$$
$$(3)$$

$$A = \sigma_i = f(d_1, d_2)$$
$$= 1827 - 17.82 * d_1 - 85.67 * d_2 + 0.3504 * d_1^2 - 04337 * d_1 * d_1 + 1.699 * d^2$$
$$(4)$$

Let,

$$P + A = Y$$

$$f(d_1, y) + f(d_1, d_2) = 2\sigma_i \text{ from Eqs. 3 and 4}$$

$$\gg 2\sigma_i = f(d_1, d_2, y)$$

$$\gg 2\frac{\sigma_{yt}}{\text{FOS}} = f(d_1, d_2, y)$$

Thus we can write,
$d_1 = f(\sigma_{yt}, \text{FOS}, d_2, y)$. This is the optimum equation.

$P + A = Y$ can be written as,
From Eqs. (3) and (4)

$$2\sigma_i = 3371 - 175.9 * d_1 - 374.9 * y + 2.298 * d_1^2 + 11.46 * d_1 * y + 11.05 * y^2$$
$$+ 1827 - 17.82 * d_1 - 85.67 * d_2 + 0.3504 * d_1^2 - 04337 * d_1 * d_2 + 1.699 * d^2.$$

$$2\frac{\sigma_{yt}}{\text{FOS}} = 5198 - 193.72 * d_1 - 85.67 d_2 - 374.9 y + 2.6484 d_1^2 - 0.4337 * d_1 * d_2$$
$$+ 11.46 * y * d_1 + 1.699 d_2^2 + 11.05 y^2. \tag{5}$$

The above equation is the optimum equation.

Now, in order to determine the diameters of the roll hoop and side impact structures. We just enter the required Yield Strength of the material chosen and required deflection of the side impact structures into the optimum equation.

The following are supporting equations which give relations between all the parameters in order to determine the required diameters. The derivation of these equations are given in Appendix D.

1. Equation Relating d_2, Stress and deflection

$$y = f(d_2, \sigma_i)$$
$$= -48.41 + 3.492 * d_2 + 0.03509 * \sigma_i - 0.603 * d_2^2 - 0.001429 * d_2$$
$$* \sigma_i + 0.00006388 * \sigma_i^2 \tag{6}$$

2. Equation relating d_1, d_2, deflection

$$y = f(d_1, d_2)$$
$$= 54.96 - 1.578 * d_1 - 1.709 * d_2 + 0.01491 * d_1^2 - 0.01883 * d_1$$
$$* d_2 + 0.01811 * d^2 \tag{7}$$

3.2 Goodness of Fit

$$R^2 = 0.9952 \ (\text{in the range of } 3\sigma)$$

$$\text{RSME (root mean square error)} = 0.2583$$

$$\text{SSE (sum of squares of error)} = 0.9338$$

As the R^2 value is in 3 σ range and SSE and RSME are approaching towards zero the surface equation can be directly considered without normalisation and can be used for further purposes [6].

4 Conclusion

It can be seen that the equations are easy to handle than compared to large number of points which can be utilised to do optimise the system. In this we tried to come up with a method which can give optimum solutions. Collection of sampling points plays a major role in the optimisation.

References

1. Supra SAEINDIA rulebook 2015.
2. Material science and metallurgy by Goel.
3. Engineering Handbook by G.L.Huyett.
4. Mechanics of materials by Johnston and beer.
5. Mechanics of materials by K Ramamrutham.
6. Structural performance analysis of formula SAE car, jurnal Mekanikal, December 2010, No31, 46-61.
7. Introduction to vehicle dynamics by William F Milliken and Douglas L Milliken.
8. Tune to win by Carroll Smith.
9. Finite elements methods, by G R LIU and S.S. Quek.
10. Mathematical Modeling Handbook from teachers college, Columbia university.
11. Machine Design Data Handbook, Volume 1 and 2, 2nd edition by Dr. K. Lingaiah.
12. Design of Machine Elements by V B Bhandari.
13. Numerical Methods in engineering with Matlab by Jaan kiusalaas.
14. Oxford concise dictionary of Mathematics by Christopher Clapham and James Nicholson.
15. Mathematical Modeling and Simulation by Nguyen V M Man, Ph.D.
16. Effective Optimisation Technique Using Bivariate Interpolation Methods by Pavan Kumar AV, Yeshodhara B, Vinayaka N,

Multi-objective Optimization of EDM Process Parameters Using PCA and TOPSIS Method During the Machining of Al-20 % SiC$_p$ Metal Matrix Composite

N. Pallavi Senapati, Rawnak Kumar, S. Tripathy and Amruta Rout

Abstract The present experimental study deals with the machining of Al-SiC$_p$ metal matrix composite (MMC) (with 20 % SiC reinforcement) by using a brass tool electrode using electric discharge machining (EDM) process. The aim of the research work is to analyze the effect of process parameters namely input current (I_p), pulse on time (T_{on}), duty cycle (DC) and gap voltage (V_g) on the response variables' material removal rate (MRR), tool wear rate (TWR), diametral overcut (DOC) and surface roughness (SR). The experiments were performed using Taguchi's L$_9$ orthogonal array. Multi-objective optimization has been applied using a hybrid approach by combining principal component analysis (PCA) and Technique for Order Preference by Similarity to Ideal Solution (TOPSIS) to obtain maximum MRR and minimum TWR, DOC and SR.

1 Introduction

Over the past few decades, aluminium-based MMCs have wide range of application in the military, aerospace and nuclear engineering as they light in weight and resistant to high temperature [1]. Al MMCs are difficult to machine as they contain hard and brittle reinforcements. High tool wear and cost have been reported while

N.P. Senapati (✉) · R. Kumar · S. Tripathy · A. Rout
Department of Mechanical Engineering, ITER SOA University,
Bhubaneswar 751030, India
e-mail: npallavisenapati@gmail.com

R. Kumar
e-mail: rawnak.iter@gmail.com

S. Tripathy
e-mail: sasmeetatripathy@soauniversity.ac.in

A. Rout
e-mail: amruta.rout@gmail.com

machining these composites using traditional techniques [2]. Hence EDM is considered as an effective method for machining such materials where better surface finish and high dimensional accuracy can be acquired. EDM is a thermo-electrical route in which removal of material occurs by a sequence of succeeding discharges between the tool and the workpiece separated by a dielectric medium. In this experiment, electric discharge machining is done on the workpiece material AlSiC-MMC (20 % SiC reinforcement) by brass tool electrode.

Sushant Dhar et al. [3] evaluated the influence of input parameters on MRR, TWR, ROC while machining Al–4Cu–6Si alloy 10 wt% SiC_p composites using EDM process and developed a second order, non-linear mathematical model. Mohan et al. [4] studied the outcome of SiC rotation of electrode on EDM of Al-SiC composite by varying volume percentage of SiC and speed of rotating electrode. Gopalakannan and Senthilvelan [5] machined Al-SiC nano composites with Cu tool using face centred central composite design of response surface methodology. Hu et al. [6] analysed the surface micro-topography, elements and wear resistance of SiC_p/Al composite by powder-mixed EDM in which PMEDM process gives reduced surface roughness, better corrosion resistance and wear resistance as compared to EDM process. Puhan et al. [7] investigated on machinability characteristics of Al-SiC composite on EDM. Optimization of multiple responses by combining PCA and fuzzy inference system and merging it with Taguchi technique was done.

It was observed from the literature survey that no substantial work has been done on AlSiC-MMC with 20 % SiC reinforcement. The present study is a step in this route. The present aim of research work is to analyze the effect of input parameters such as input current (I_p), pulse on time (T_{on}), duty cycle (DC) and gap voltage (V_g) on the performance variables Metal removal rate (MRR), Tool wear rate (TWR), Diametral Overcut (DOC) and Surface Roughness (SR) during machining of AlSiC-20 % SiC_p reinforcement using EDM process and finding the optimum set of input parameters.

2 Experimentation

2.1 Experimental Setup

The EDM machine used for the experiment is model Electronica Smart ZNC, EDM (Die sinking type EDM) with servo-head and positive polarity for electrode. The dielectric liquid used in EDM machine was commercial grade EDM oil. Brass tool of 15 mm diameter was selected as the electrode to machine the workpiece AlSiC (20 % SiC as reinforcement) metal matrix composite. After machining, the surface roughness of the specimen was measured using a portable stylus type profilometer (Table 1).

Table 1 Machine specifications of EDM

Parameters	Input current (I_p) (A)	Pulse on time (T_{on}) (μs)	Duty Cycle (DC) (%)	Gap voltage (V_g) (V)	Flushing pressure (p) (bar)
Range	0–50	0.5–4000	1–12 %	0–250	0–2

2.2 Electrode and Workpiece Material

Brass tool of 15 mm diameter and 60 mm length was taken as the tool electrode. The workpiece material chosen for the experiment was AlSiC metal matrix composite with aluminium as the base metal and 20 % SiC as reinforcement. The AlSiC-MMC was fabricated by stir-casting process in which initially the aluminium and silicon carbide powder were preheated for 3–4 h at 450 and 900 °C, respectively, and then the powders were mixed mechanically below their melting points. This AlSiC mixture was then allowed to pour into the graphite crucible and put into the coal-fired furnace at 760 °C temperature. After heating, the slurry was taken into the sand mould and allowed it to solidify within 30 s. Finally the samples were prepared as per the requirement.

2.3 Design of Experiments

The Taguchi technique was used to determine the design of experiments and L_9 OA was chosen to conduct the experiments. So Table 2 shows the factors and levels chosen for the experiment.

2.4 Principal Component Analysis (PCA)

The PCA method is used for multi-objective optimization of the responses MRR, TWR, SR, and DOC and a set of optimum values are obtained for maximum MRR and minimum TWR, SR and diametral overcut. The steps for PCA are described as follows:

Step-1: The normalization 'higher-the-better' and 'lower the better' criteria is done by Eqs. (1) and (2):

Table 2 Input parameters and their levels

Parameters	Level-1	Level-2	Level-3
Input current (I_p)	3	5	7
Pulse on time (T_{on})	50	75	100
Duty cycle (DC)	7	8	9
Gap voltage (V_g)	30	40	50

$$x_i^*(j) = \frac{x_i - [\min(x_i(j))]}{[\max(x_i(j))] - [\min(x_i(j))]} \qquad (1)$$

$$x_i^*(j) = \frac{[\max(x_i(j))] - x_i(j)}{[\max(x_i(j))] - [\min(x_i(j))]} \qquad (2)$$

where, $i = 1, 2, \ldots, m$ no. of experiments $j = 1, 2, \ldots, n$ output responses

Step-2: The correlation between each pair of quality characteristics (j and k) has been inspected using Eq. (3)

$$\rho_{jk} = \frac{\text{Cov}(Q_j, Q_k)}{\sigma_{Qj} * \sigma_{Qk}} \qquad (3)$$

where, $j = 1, 2, \ldots, n$, $k = 1, 2, 3, \ldots, n$, $j \neq k$

where, ρ_{jk} is correlation coefficient, σ_{Qj} and σ_{Qk} indicates standard deviation of j and k, respectively.

Eigen value and Eigen vector can be obtained by using the Minitab 16 software.

Step-3: Evaluation of principal component score:

The normalized reference sequence and the Eigen vectors are written in matrix form say [A] and [B], respectively. The principal component scores can be calculated by the matrix multiplication of [A] and [B].

$$P_i(k) = \sum_{j=1}^{n} N_i^* \beta_{kj} \qquad (4)$$

where, $i = 0, 1, 2, 3, \ldots n$, $k = 1, 2, 3, \ldots n$

$P_i(k)$ = principal component score of the kth element in the ith sequence
$N_i^*(j)$ = normalized value of the jth element in the ith sequence
β_{kj} = jth element of the Eigen vector β_k

Step-4: The quality estimate loss is calculated using $[Y_0(k)Y_i(k)]$ if the responses are correlated.

2.5   TOPSIS

The optimum set of values obtained in PCA method is combined with TOPSIS method to get the optimal parameter setting. The principal components PC_1, PC_2 and PC_3 are written in matrix form which is called as decision matrix. The steps are explained below.

Step-1: Decision matrix which consist of 'n' attributes and 'm' alternatives which is represented as [8, 9]:

$$D_m = \begin{bmatrix} x_{11} & x_{12} & x_{13} & \cdots & \cdots & x_{1n} \\ x_{21} & x_{22} & x_{23} & \cdots & \cdots & x_{2n} \\ x_{31} & x_{32} & x_{33} & \cdots & \cdots & x_{3n} \\ \vdots & \vdots & \vdots & \ddots & \ddots & \vdots \\ \vdots & \vdots & \vdots & \ddots & \ddots & \vdots \\ x_{m1} & x_{m2} & x_{m3} & \cdots & \cdots & x_{mn} \end{bmatrix} \quad (5)$$

where x_{ij} is the performance of ith alternative with respect to jth attribute.

Step-2: Normalized matrix is obtained from the following expression

$$r_{ij} = \frac{x_{ij}}{\sqrt{\sum_{i=1}^{m} x_{ij}^2}} \quad j = 1, 2, \ldots, n. \quad (6)$$

Step-3: The weighted normalized decision matrix $V = [v_{ij}]$ can be obtained by

$$V = w_j r_{ij} \quad (7)$$

where, $\sum_{j=1}^{n} w_j = 1$.

Step-4: In this step, the ideal (best) and negative-ideal (worst) solutions were obtained from using Eqs. (12) and (13)

$$V^+ = \left\{ \left(\sum_i^{max} v_{ij} | j \in J \right), \left(\sum_i^{min} | j \in J | i = 1, 2, \ldots . m \right) \right\} \quad (8)$$
$$= \{ v_1^+, v_2^+, v_3^+, \ldots, v_n^+ \}$$

$$V^- = \left\{ \left(\sum_i^{min} v_{ij} | j \in J \right), \left(\sum_i^{max} | j \in J | i = 1, 2, \ldots . m \right) \right\} \quad (9)$$
$$= \{ v_1^-, v_2^-, v_3^-, \ldots, v_n^- \}\}$$

Step-5: In this step the separation between alternatives were determined. The separation of each alternative from 'ideal' solution is given by

$$S_i^+ = \sqrt{\sum_{j=1}^{n} (v_{ij} - v_j^+)^2}, \quad i = 1, 2, \ldots m. \quad (10)$$

The separation of each alternative from 'negative-ideal' solution is given by

$$S_i^- = \sqrt{\sum_{j=1}^{n} (v_{ij} - v_j^-)^2}, \quad i = 1, 2, \ldots m. \quad (11)$$

Step-6: In this step, the relative closeness of particular alternative to the ideal solution is calculated which is expressed as

$$P_i = \frac{S_i^-}{S_i^+ + S_i^-} \quad i = 1, 2, \ldots m. \tag{12}$$

Parameters corresponding to the highest P_i value were considered as optimum set of input parameters.

3 Results and Discussion

3.1 Effect of Current, Pulse on Time and Gap Voltage on MRR

The material removal occurs due to the spark created which melts and erodes the material from the workpiece. Figure 1 shows the variation of MRR with Input Current. Figure 2 shows the variation of MRR with Pulse on Time. Figure 3 shows the variation of MRR with Gap Voltage.

Fig. 1 Effect of current on MRR
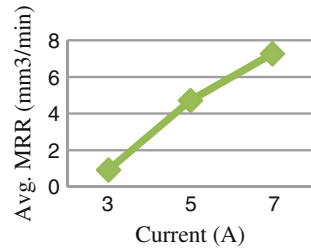
Fig. 2 Effect of pulse on time on MRR
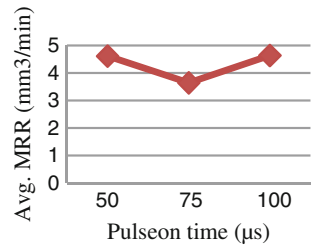
Fig. 3 Effect of gap voltage on MRR
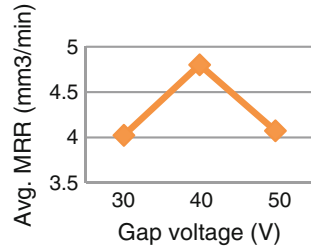
Fig. 4 Effect of current on TWR
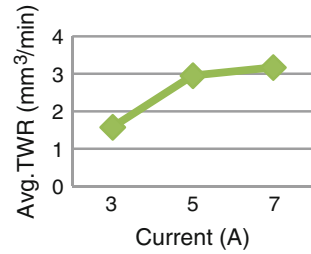
3.2 Effect of Current, Pulse on Time and Gap Voltage on TWR

During machining, not only material removal from work piece occurs but also the tool wear occurs due to the high temperature created by spark. Figure 4 shows the variation of Input Current with TWR. Figure 5 shows the variation of Pulse on Time with TWR. Figure 6 shows the variation of Gap Voltage with TWR.

Fig. 5 Effect of pulse on time on TWR
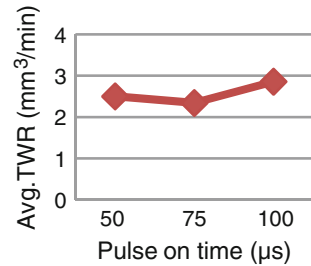
Fig. 6 Effect of gap voltage on TWR
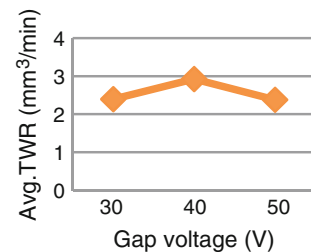
Fig. 7 Effect of current on SR
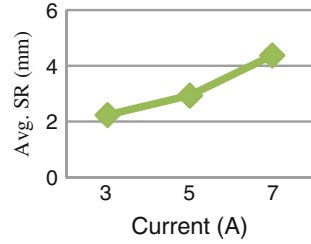
Fig. 8 Effect of pulse on time on SR
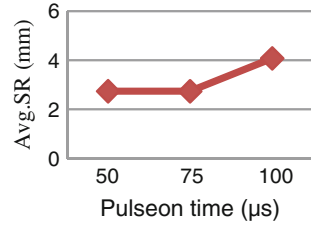
Fig. 9 Effect of gap voltage on SR
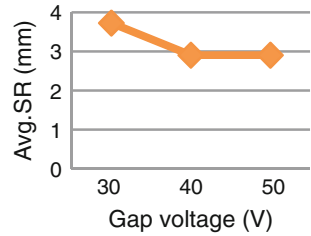
3.3 Effect of Current, Pulse on Time and Gap Voltage on Surface Roughness

Surface roughness occurs due to increase in spark energy which causes surface pits resulting from the removal of material to enlarge. Figure 7 shows the variation of Input Current with Surface Roughness. Figure 8 shows the variation of Pulse on Time with Surface Roughness. Figure 9 shows the variation of Gap Voltage with Surface Roughness.

4 Conclusion

After conducting the experiment on AlSiC-Metal Matrix Composite, the important conclusions are as follows:

(1) The feasibility of machining AlSiC-MMC (20 % SiC Reinforcement) was evaluated and the effect of process parameters on the response variables was studied.
(2) Maximum MRR was obtained for high Input Current, low Pulse on Time, high Duty Cycle and intermediate Gap Voltage.
(3) For minimum TWR, MRR was found closer to its minimum value.
(4) Multi-objective optimization was done by combining PCA with TOPSIS and the optimal set of parameters obtained were at input current = 5 A, pulse on time = 100 μs, Duty cycle = 70 % and gap voltage = 40 V.

References

1. N. Mohd Abbas, D.G. Solomon, Md. Faud Bahari, A review on current research trends in electric discharge machining, Int. J. Mach. Tool Manuf. 47 (2006) 1214–1228.
2. L. Cronjäger, Machining of fibre and particle-reinforced aluminium, Ann. CIRP 41 (1) (1992) 63–66.
3. Sushant Dhar, Rajesh Purohit, Nishant Saini, Akhil Sharma, G. Hemanth Kumar, Mathematical modelling of ED machining of cast Al-4Cu-6Si alloy-10 % SiC_p composites, Journals of Materials Processing Technology 194 (2007) 24–29.
4. B Mohan, A Rajadurai, K. G. Satyanarayana, Effect of SiC and rotation of electrode on Electric Discharge Machining of Al-SiC composite, Journal of Materials Processing Technology 124 (2002) 297–304.
5. S. Gopalakannan, T Senthilvelam, Application of response surface method on machining of AlSiC nano-composites, Al-SiC nano-composites with Cu electrode by adopting face centred central composite design of RSM, Measurement 46 (2013) 2705–2715.
6. F.Q. Hu, F.Y. Cao, B.Y. Song, P.J. Hou, Y. Zhang, K. Chen, J.Q. Wei, Surface properties of SiCp/Al composite by powder-mixed EDM, Procedia CIRP 6 (2013) 101–106.
7. Debaprasanna Puhan, Siba Sankar Mahapatra, Jambeswar Sahu, Layatitdev Das," A hybrid approach for multi-response optimization of non-conventional machining on AlSiCp MMC", Measurement 46 (2013) 3581–3592.
8. S. Opricovic and G.H. Tzeng "Compromise solution by MCDM methods: A comparative analysis of VIKOR and TOPSIS". European Journal of Operational Research, vol. 156, (2004), pp. 445–455.
9. N.D. Chakladar and S. Chakraborty "A combined TOPSIS-AHP-method-based approach for non-traditional machining processes selection". Journal of Engineering Manufacture, vol. 222, (2008), pp. 1613–1623.
10. F. Mˆuller, J. Monaghan, Non-conventional machining of particle reinforced metal matrix composite, Int. J. Machine Tools Manuf. 40 (2000) 1351–1366.

Study of Static Stall Characteristics of a NACA 0012 Aerofoil Using Turbulence Modeling

Aarjav Malhotra, Arpan Gupta and Pradeep Kumar

Abstract Static stall of a NACA 0012 aerofoil has been studied by simulating a two dimensional, incompressible flow over the aerofoil section at various angles of attack for a Reynold's number of three million. An $SST\,k-\omega$ turbulence model is used to capture the turbulence, flow separation, and associated pressure changes. The lift coefficient is plotted with the angle of attack to determine the stall angle and the results are compared with experimental results. The computation is done on a structured mesh comprising of 229,376 cells (with refined regions near the aerofoil and extending till the edge of the domain for the part above and below its front of to capture the boundary layer and turbulence over the aerofoil) by solving the steady-state momentum and continuity equations along with the two equations of the $SST\,k-\omega$ turbulence model. The angle of attack is varied by changing the flow direction of air; no changes are made to the air speed. This study shows that modeling turbulence with the $SST\,k-\omega$ model can yield an estimate of the stall angle of aerofoils at high Reynold's number flows.

Keywords Reynolds number · Airfoil · Turbulence model · Boundary layer · Static stall · NACA 0012

1 Introduction

Flows around aerofoils can be described by theoretical models that are fairly accurate under laminar flow conditions. The lift produced by a thin aerofoil section (l) is said to be directly proportional to the angle between the air flow and the aerofoil chord, i.e. the angle of attack (AoA) as given by the equations

$$l = \frac{1}{2}\rho v^2 c c_l$$

A. Malhotra (✉) · A. Gupta · P. Kumar
School of Engineering, Indian Institute of Technology, Mandi, India
e-mail: aarjav_malhotra@students.iitmandi.ac.in

$$c_l = c_{l0} + a_0\alpha_0$$

where ρ is the air density, v is the free stream air velocity relative to the aerofoil, c. is the chord length of the aerofoil section, c_l is the section lift coefficient, c_{l0} is the section lift coefficient at zero angle of attack, a_0 is the section lift curve slope, α is the angle of attack [1]. However, this relation is valid only up to a certain value of angle of attack: the lift characteristics start to diate from the linear model once the flow starts transitioning from laminar to a turbulent one and become unpredictable for highly turbulent flows.

Turbulence can arise when the angle of attack becomes large enough for the flow to get separated from the upper surface of the aerofoil. As the turbulence and flow separation increase, pressure on the upper surface starts to increase resulting in a situation where the lift being produced by the aerofoil decreases with increasing AoA. The angle of attack at which lift starts to decrease is called the Critical AoA and the aerofoil is said to have 'stalled.' Static stall is a steady state phenomenon in which the stalling is observed beyond the critical AoA. The steady flow simulations are carried out at various angles of attack using the commercial Computational Fluid Dynamics (CFD) software, Fluent, and the value of the lift coefficient is observed.

The lift generated by an aerofoil is practically controlled by varying the angle of attack. Knowing the critical angle AoA for static stall is hence important as it puts a limit on the operational range of the aerofoils. In this study, we examine the flow over a NACA 0012 aerofoil. We have chosen this aerofoil in particular because it has been subjected to extensive experimental studies which allow for reliable validation of results. Also, this aerofoil section has been used extensively in various forms, such as the personal aircraft Cessna 152, Sikorsky S-67 Blackhawk, Sikorsky SH-3 Sea King, Vortech Skylark and some wind turbines as well which makes it a good candidate for a simulation-based study.

CFD is a simulation-based approach for visualizing flow features and determining various parameters such as pressure and velocity fields. Due to the recent advances in computing technology and rapid evolution of computational techniques, CFD is becoming more reliable and in some applications (ex. those in which flow features cannot be determined experimentally) even being the go-to choice for the design of components. For carrying out a CFD simulation, the conservation equations of mass (also called the continuity equation) and momentum are solved over a discretized domain (called the mesh). For turbulent flows, the fluctuating parameters are not calculated directly (as in DNS) but instead they are modeled using additional equations which are then solved simultaneously with the mass and momentum conservation equations.

The general form of the continuity equation is

$$\frac{\partial \rho}{\partial t} + \nabla \cdot (\rho \vec{u}) = S_m$$

where S_m denotes the source term. The conservation equation for momentum is given by

$$\frac{\partial(\rho\vec{u})}{\partial t} + \nabla \cdot (\rho\vec{u}\vec{u}) = -\nabla p + \nabla \cdot (\tau) + \rho\vec{g} + \vec{F}$$

where $\vec{F}$ is the external body force (per unit volume), $\rho\vec{g}$ is the gravitational body force, p is the static pressure and τ is the stress tensor given by

$$\tau = \mu\left[(\nabla\vec{u} + \nabla\vec{u}^T) - \frac{2}{3}\right]\nabla \cdot \vec{u}I$$

where μ is the molecular viscosity and I is the identity matrix. Since we are simulating 2D, steady and incompressible flow (without any external forces), the above equations can be reduced to

$$\frac{\partial u}{\partial x} + \frac{\partial v}{\partial y} = 0 \quad \text{(Continuity equation)}$$

$$\rho\frac{Du}{Dt} = -\frac{\partial p}{\partial x} + \frac{\partial \tau_{xx}}{\partial x} + \frac{\partial \tau_{yx}}{\partial y} \quad \text{(Momentum conservation in } x \text{ direction)}$$

$$\rho\frac{Dv}{Dt} = -\frac{\partial p}{\partial y} + \frac{\partial \tau_{xy}}{\partial x} + \frac{\partial \tau_{yy}}{\partial y} \quad \text{(Momentum conservation in } y \text{ direction)}$$

Since the flow leading up to static stall is turbulent, the simulation needs to model the turbulence appropriately and solve the associated additional equations as well. In this simulation, we have used the $SSTk - \omega$ turbulence model, which is a refined version of the $k - \omega$ model that makes the model relatively independent of the inlet free stream turbulence while ensuring accurate near-wall solution. This model is used because it gives good results in adverse pressure gradients and separating flows, which is expected in the case of stall of an aerofoil.

2 Solution Method

The aerofoil used in this study, NACA 0012, is a member of the four digit wing section described by the National Advisory Committee for Aeronautics (NACA). This is a symmetric aerofoil (i.e. 0° camber as indicated by the first two digits) with a maximum thickness equal to 12 % of the given chord length. The thickness distribution is given by the equation

$$y_t = \frac{T}{0.2}\left[0.2969(x/c)^{0.5} - 0.126(x/c) - 0.3516(x/c)^2 + 0.2843(x/c)^3 - 0.1015(x/c)^4\right]$$

Fig. 1 a C domain.
b Aerofoil closeup
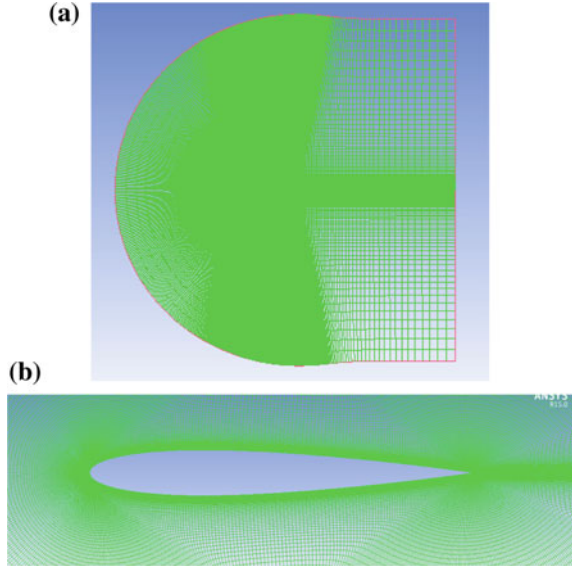
where T denotes the last two digits of NACA 00XX, c is the cord length and x is the position along the chord from 0 to c. The constant in the last term (i.e. -0.1015) can also be set to -0.1036 to ensure a zero thickness trailing edge with smallest change to the overall shape of the aerofoil. This thickness distribution can then give the profile of the aerofoil for the chosen chord length [2].

A C-type domain was taken with boundaries about 500 chords away from the aerofoil to eliminate the effect of far-field boundaries. The structured mesh has been refined in areas where high gradients were expected, such as near the wake region and aerofoil walls (particularly going from the leading and trailing edges to the boundaries) (Fig. 1). The final grid comprises of 229,376 cells [3].

Pressure far-field boundary condition was used with ambient pressure and temperature of 101,325 Pa and 300 K, respectively, at a Mach number of 0.13 (which implies an incompressible flow and hence the energy equation was not solved). This particular Mach number was chosen to get a Reynold's Number of three million (approx.) for density and viscosity values of 1.225 kg/m^3 and 1.7894×10^{-5} kg/m s, respectively, for a 1 m chord length. A coupled solver was used with second order scheme for pressure and power law scheme for momentum. The simulations were done at various angles of attack ranging from 4° through 20° and various parameters such as the lift coefficient (c_l), static pressure (p) and velocity magnitude were observed.

3   Results and Discussion

Simulations were performed at 4°, 6°, 8°, 10°, 12°, 14°, 15°, 16°, 17° and 20° angles of attack and the corresponding lift coefficients, static pressure contours and velocity magnitude contours were observed. Lift coefficient is a dimensionless form of the lift force that is the force acting on the aerofoil in a direction perpendicular to the relative free stream velocity.

3.1   Lift Coefficients

After increasing linearly with the angle of attack, the lift coefficient reaches a maximum value at the critical angle for static stall. Static stall can be said to have occurred when the lift coefficient starts to decrease with increasing angle of attack. Figure 2 shows the variation of lift coefficient according to the simulation versus the experimental data at a Reynold's number of three million [1].

The lift coefficient drops from about 1.3320 to about 1.2993 as the AoA is increased from 16°–17°. It can thus be concluded that according to the simulation static stall occurs around 16°, which is close to the experimental observation at the same Reynold's number of three million [1].

Comparable results are obtained for the lift coefficient at low angles of attack. However, deviation is observed as the angle of attack approaches the critical value. Several reasons can be assigned to the deviation of simulation predictions from the experimental data. First, the simulations have been done for fully turbulent boundary layer, which causes some deviation in results since realistically the boundary layer undergoes a gradual transition from laminar to fully turbulent as the angle of attack is increased [4]. Moreover, flow separation is a complex three dimensional phenomenon that needs three dimensional models and more refined grids [4].
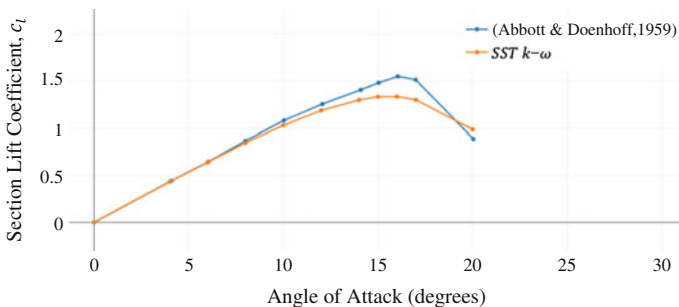
Fig. 2 Lift polar at Re = 3,000,000 [1]

(a)

(b)

(c)

(d)
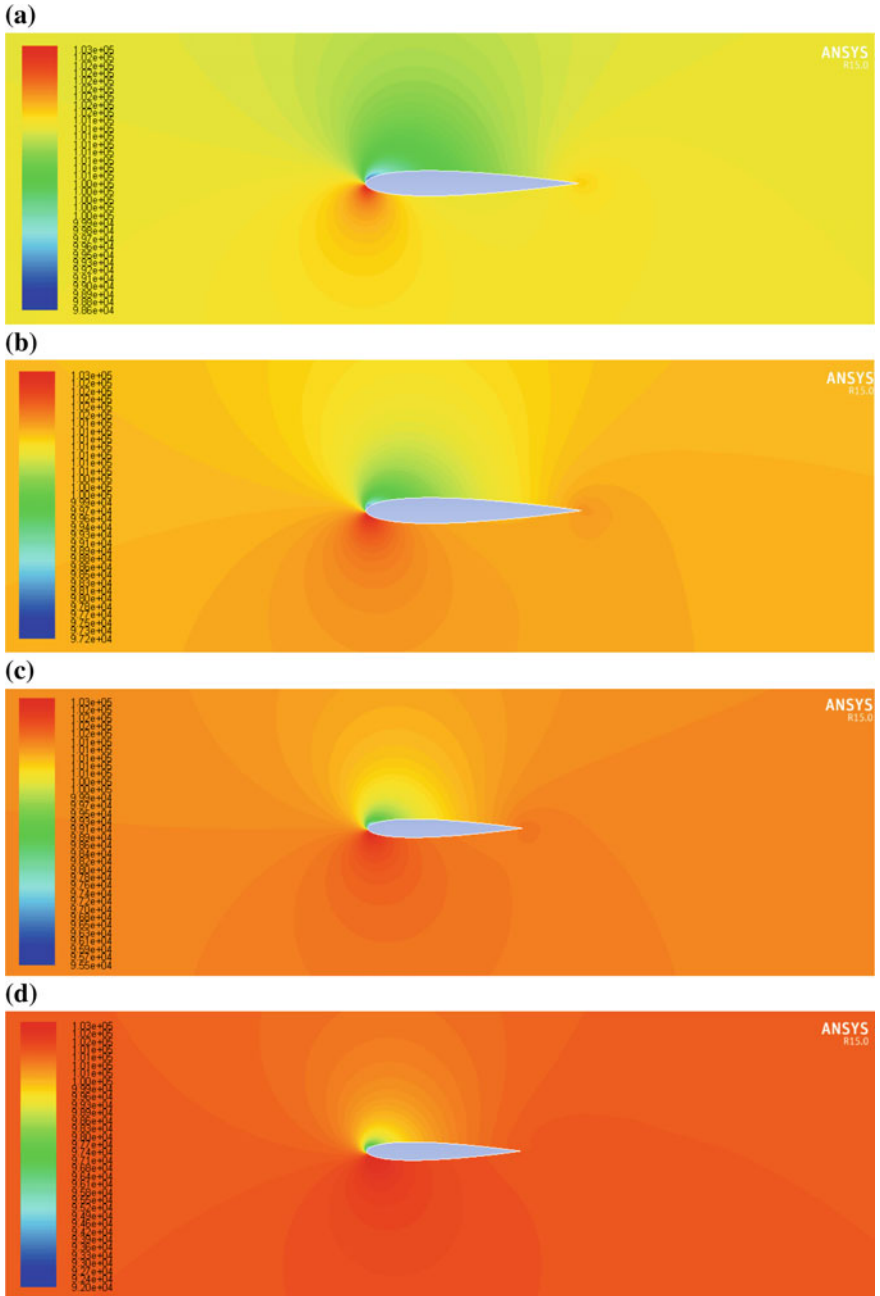
Fig. 3 Static pressure at **a** 6°, **b** 8°, **c** 10°, **d** 14°, **e** 15°, **f** 16°, **g** 20°
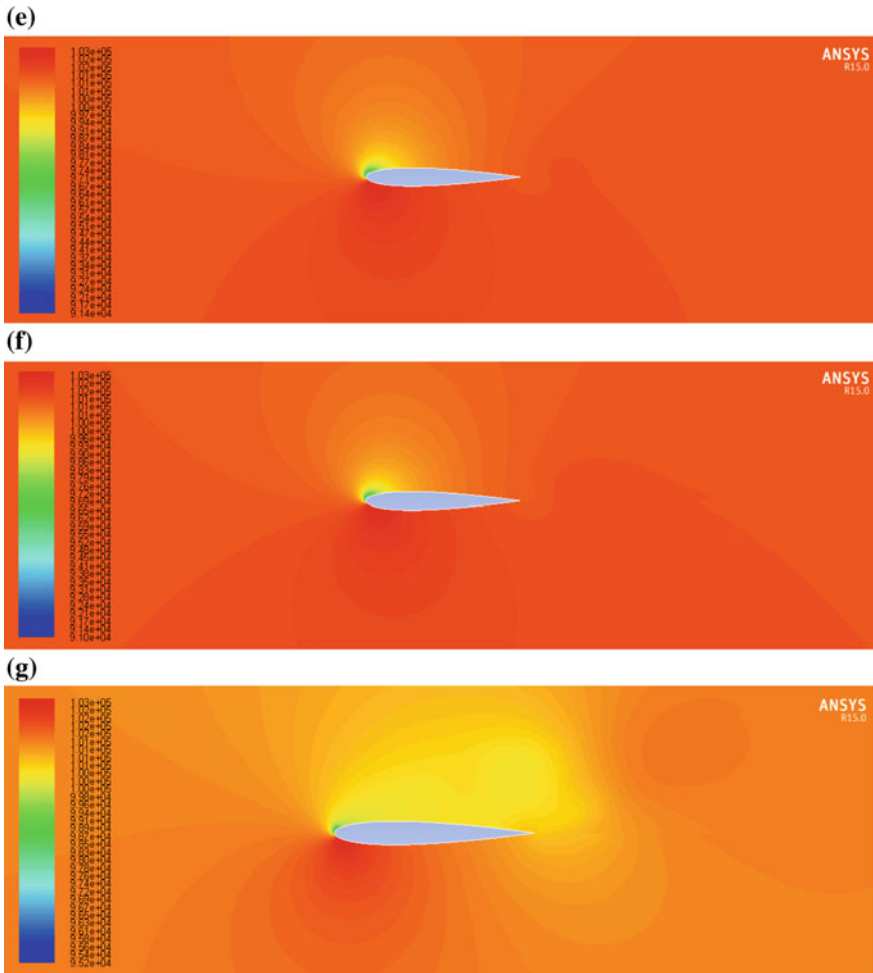
(e)

(f)

(g)

Fig. 3 (continued)

3.2 Static Pressure Contours

The following are the static pressure contours obtained for the various angles of attack. It can be seen that for all angles of attack, the pressure at the lower surface is higher than that at the upper surface which explains the lift being produced by the aerofoil (Fig. 3).
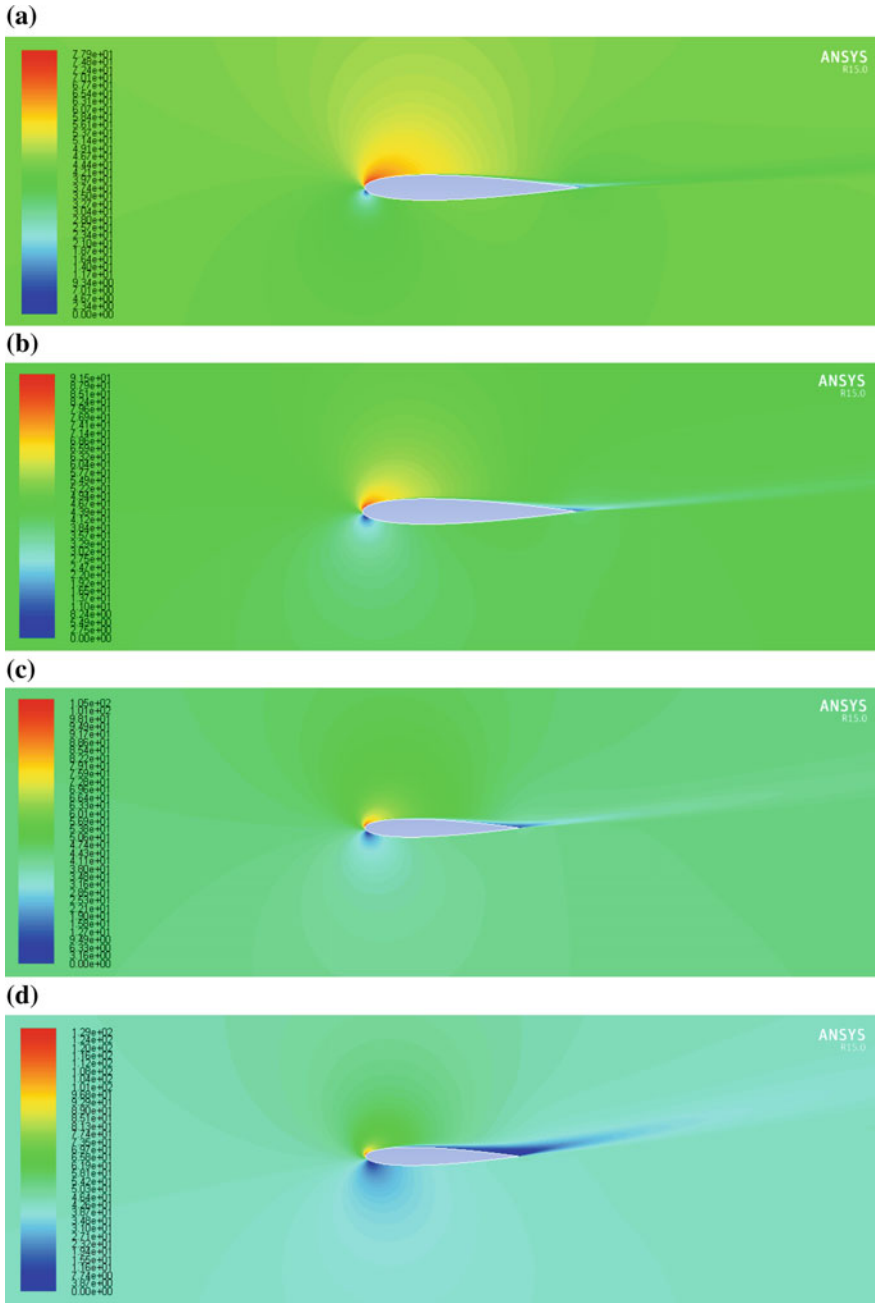
Fig. 4 Velocity magnitude at **a** 6°, **b** 8°, **c** 10°, **d** 14°, **e** 15°, **f** 16°, **g** 20°

(e)

(f)

(g)
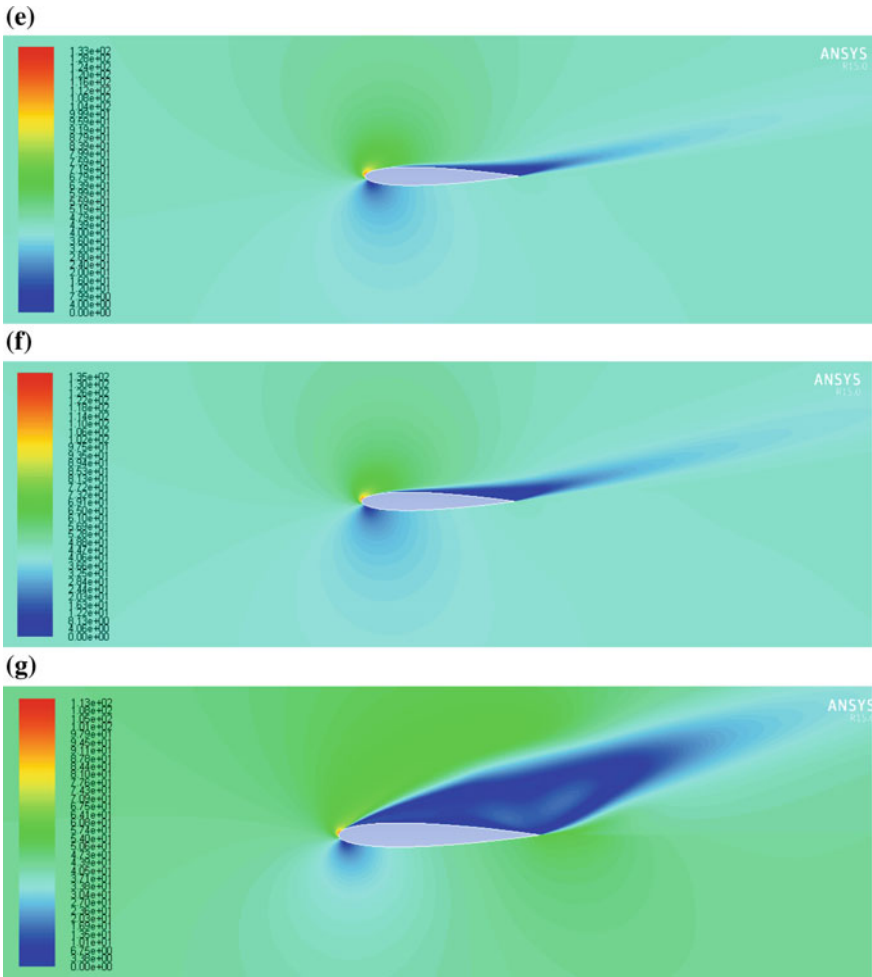
Fig. 4 (continued)

3.3 Velocity Magnitude Contours

The following are the velocity magnitude contours obtained from the simulations. It can be seen that near the critical angle, the flow separation is very pronounced and the low speed of flows can be related to increased static pressure which causes a decrease in the lift (Fig. 4).

4   Conclusions

Through this study, we conclude that the $SSTk - \omega$ turbulence model can be used for predicting the critical angle of attack for static stall of aerofoils in case of high Reynold's number flows. For better agreement with experimental observations, transition to turbulence in the boundary layer should also be accounted for. Use of three dimensional models is also suggested.

References

1. Abbott, I. H. & Doenhoff, A. E. V., 1959. *Theory of Wing Sections*. New York: Dover Publications.
2. Moran, J., 1984. *An Introduction to Theoretical and Computational Aerodynamics*. s.l.:Dover Publications.
3. Langley Research Center (NASA), 2015. *Turblence Modeling Resource*. [Online]. Available at: http://turbmodels.larc.nasa.gov/NACA0012_grids/n0012_449-129.p2dfmt.gz [Accessed 27 11 2015].
4. Eleni, D. C., Athanasios, T. I., & Dionissios, M. P. 2012. Evaluation of the turbulence models for the simulation. *Journal of Mechanical Engineering Research*, 4(3) (10.5897/JMER11.074), pp. 100–111.

Effect of Compaction Aspect Ratio on Wear Characteristics of Sinter Extruded Pure Copper Processed Through Powder Metallurgy Route

S. Shruthi, S. Venkatakrishnan, S. Raghuraman and R. Venkatraman

Abstract Powder metallurgy is widely used, unique manufacturing process resulting in a near-net shape. The parameters like, the compaction pressure, aspect ratio (height to diameter ratio), sintering conditions can be varied in order to achieve the required properties of the end product. In this research work, all the above parameters except the aspect ratio are fixed. Wear analysis is carried out on sinter-extruded copper samples are made for two different aspect ratios, i.e., 0.5 and 1. The experiments are conducted based on Taguchi's L18 orthogonal array by taking the aspect ratio, speed, and load as three important factors. The mass loss and COF (coefficient of friction) are the main results studied in this work and are supported by hardness and density measurements.

1 Introduction

Powder metallurgy is a method of producing components of metals and composites from their powdered form. Components that are difficult to manufacture by conventional metal forming techniques due to its complex shape and geometry are manufactured in the powder metallurgy (PM) route, making the process simple, highly accurate, and facilitates for near-net shape manufacturing. Extensive studies in powder metallurgy are carried out to improve properties and behavior of metals tailor made for specific practical and industrial applications. As powder metallurgy process is a near-net shape manufacturing process it makes use of certain aspects of shake-making technology for powder compaction and it is followed by a consoli-

S. Shruthi · S. Venkatakrishnan · S. Raghuraman (✉)
School of Mechanical Engineering, SASTRA University, Thanjavur 613 401, India
e-mail: raghu@mech.sastra.edu

R. Venkatraman
Shanmuga Precision Forging, Thanjavur 613 401, India

dation process and further secondary processing is done on the material depending on the requirement. In this work, compacted samples are further subjected to sinter-extrusion. Size and shape of the initial compact, compaction pressure, sintering conditions, and soaking time are a few important factors that influence the properties of the end product. The factors like compaction pressure, sinter extrusion conditions, and soaking time are kept constant, while the compaction aspect ratio is varied. Compaction is done in two different aspect ratios, i.e., 0.5 and 1.

Taguchi experimental designs, often called orthogonal arrays (OAs), consist of a set of fractional factorial designs which ignore interaction and concentrate on main effect estimation. This procedure generates the most popular set of Taguchi designs. Taguchi uses the following convention for naming the orthogonal arrays: La(b^c), where a is the number of experimental runs, b is the number of levels of each factor, and c is the number of variables. Designs can have factors with several levels, although two and three level designs are the most common. The L18 design is the most popular. The L18 OA consists of one factor at 2 levels and up to seven factors at 3 levels each [1]. The first factor with 2 levels in this experiment is aspect ratio and speed and load are factors with 3 levels each.

Various experiments have been conducted by various researchers to find the effect of parameters like temperature, sliding velocity, surface finish on the wear characteristics of copper. Copper and its alloys have good wear resistance as it finds its application in construction, automobile, and aircraft industries. Copper, due to its high wear resistant, gives promising results when used as a material for bearings. Wear resistance of copper further gets enhanced when it is alloyed. The ranking of sliding wear resistance in descending order is CuBeNi > CuBe > CuCrZr $\sim$ CuNiSiCr > CuZr $\sim$ CuCr > Cu [2]. It is also found that the wear resistance of the copper-based alloys increases with decrease in normal load and the increase in hardness [2]. Dewan Muhammad Nuruzzaman and et al. have found that during friction process, copper or aluminum specimens takes less time to stabilize as the normal load or sliding velocity increases [3]. Recently it is found that, powdered materials impregnated with the inorganic fullerene like IF-WS2 nanoparticles allow to improve considerably the tribological behavior of powder materials. Confinement of the IF in the pores of the powder matrix and its gradual furnishing to the contact surface decreases the ploughing of the rubbed surfaces [4].

This work primarily concentrates on the wear analysis of sinter-extruded copper samples that are made from compacts of two different aspect ratios. Copper used in this experiment is processed through powder metallurgy route and is used for studying the effect of aspect ratio on COF and mass loss by pin-on-disk apparatus. With regard to copper it is expected to have low coefficients of friction. It must also be understood that, a greater mass loss means that a lot of debris gets collected on the bearing surface, degrading the surface properties and thereby increasing the friction between the surfaces as COF is a function of surface finish also. This shows that it is vital to study the wear characteristics of Copper with stringency. Powder metallurgy is a growing field and it is under wide research, to manufacture bearings through powder metallurgy route.

Table 1 Wear test parameter specifications

S. no	Factors	Levels		
		1	2	3
1	Speed (rpm)	300	600	900
2	Load (Kgf)	0.5	1.0	1.5
3	Aspect ratio	0.5	1.0	–

2 Experiment

The experiments are performed using 99.95 % pure copper powder with particle size 50 μm. The copper powders are compacted to a cylindrical form of diameter 25 mm and heights 12.5 and 25 mm. The amount of powder required by mass for compaction is found using the compressibility chart for copper powders from the ASM Handbook Vol. 7 [5]. The compacted copper samples are then sinter-extruded at a temperature of °C [5] to a diameter of 12 mm and then later annealed at 425 °C for 2 h [6]. The density after each stage is found by Archimedes principle, through a density measuring device, Shimadzu AUX 220. Also, the hardness of samples were tested for both 1 and 0.5 aspect ratio samples.

The wear test is conducted based on Taguchi's L18 orthogonal array, with three factors. The factors considered are aspect ratio, speed, and normal load and are shown in Table 1.

As per American Society for Testing and Materials (ASTM), G-99 is the standard test method for wear testing using Pin-on-Disk apparatus. This standard procedure is followed during this experimentation [7].

3 Result and Discussion

The extruded specimens are subjected to sliding wear test on pin-on-disk instrument. The values of coefficient of friction and mass loss for different aspect ratios, speed, and load are shown in Table 2. From the values of coefficient of friction obtained for 0.5 aspect ratio specimens, it can be inferred that, for a constant speed, coefficient of friction increases till load is 1 Kilo gram force (Kgf) and decreases when load is 1.5 Kgf; but this trend is not seen for 1 aspect ratio sample. It is found that the Vickers micro hardness value 0.5 and 1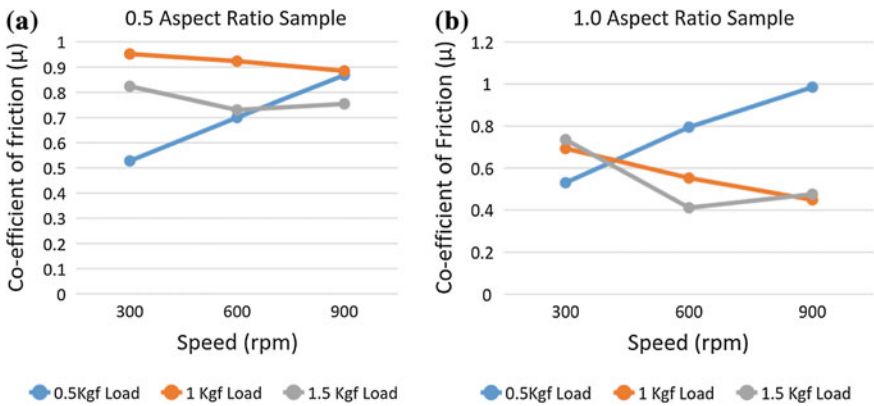 aspect ratio specimens are 96.8 and 90.9, respectively. Figure 1 shows the line plot of coefficient of friction versus load and angular speed for (a) 0.5 aspect ratio sample (b) 1.0 aspect ratio sample.

For 60–40 brass with steel, it is found that wear rate varies independently with speed [8]. In this study, Fig. 2 shows irregular trend in variation of mass loss with respect to angular speed. It can also be inferred from the same graph that, mass loss also varies irregularly even with load. The results of this experiment are in accordance with [8]. With the experimental results, it can be concluded that wear test of pure copper processed through powder metallurgy route also exhibits the

Table 2 Values of coefficient of friction for different aspect ratio, speed and Load

	Coefficient of friction (μ)					
Aspect ratio	0.5			1		
	Speed (rpm)					
Load (kgf)	300	600	900	300	600	900
0.5	0.527835	0.700282	0.867933	0.530062	0.794674	0.985044
1	0.952104	0.923539	0.884621	0.693131	0.552685	0.448697
1.5	0.823486	0.730414	0.75434	0.735431	0.411171	0.475493
Average	0.79607			0.62515		

Fig. 1 Coefficient of friction versus load and angular speed for **a** 0.5 aspect ratio sample **b** 1.0 aspect ratio sample
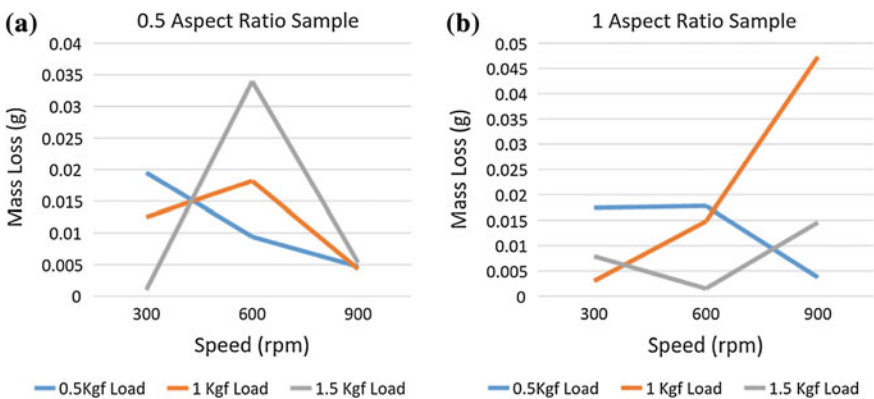
Fig. 2 Mass loss versus load and angular speed for **a** 0.5 aspect ratio sample **b** 1.0 aspect ratio sample

Table 3 Values of mass loss for different aspect ratio, speed, and load

	Mass loss (g)					
Aspect ratio	0.5			1		
	Speed (rpm)					
Load (kgf)	300	600	900	300	600	900
0.5	0.0195	0.0094	0.0047	0.0174	0.0178	0.0037
1	0.0125	0.0182	0.0043	0.003	0.0148	0.0473
1.5	0.001	0.034	0.0053	0.0079	0.0015	0.0146
Average	0.00870			0.01422		

Table 4 Vickers hardness and density values for different aspect ratio

Aspect ratio	Vickers hardness (HV)	Density (g/cc)	Relative density in % (with respect to solid copper density)
0.5	96.8	8.8446	98.71
1.0	90.9	8.5011	94.88

same trend. Table 3 shows the values of mass loss for different combinations of aspect ratio, speed and load parameters.

Densification achieved by 0.5 aspect ratio sample is greater than 1.0 aspect ratio sample which is evident from the form the density values shown in Table 4. In unidirectional compaction, powders close to the punch and die walls experience much more force than those at center and hence the lower half. The pressure difference increases with length of the specimen and there is no uniformity in the green density of the specimen [9]. In other words, 1.0 aspect ratio specimens have higher porosity content than 0.5 aspect ratio sample. Due to the reasons: high porosity content, lesser densification, and low hardness values, mass loss in wear test is higher for 1.0 aspect ratio than 0.5 aspect ratio specimens. Thus, for manufacture of powder metallurgical components for lower wear rate and higher densification, lesser aspect ratio can be preferred.

4   Conclusion

- Coefficient of friction and mass loss due to wear varies irregularly with variation in load and speed conditions.
- For pure copper specimens processed through powder metallurgy route, higher densification is achieved for lower aspect ratio.
- Porosity content in powder metallurgical specimens increases with aspect ratio.
- Density and hardness values are higher for samples of lower aspect ratios.
- Specimens of higher aspect ratios exhibit higher values of mass loss during wear test.

References

1. Ranjit K. Roy (2001) Design of Experiments using the Taguchi approach: 16 Steps to Product and Process Improvement. John Wiley and Sons, United States.
2. C.T. Kwok, P.K. Wong, H.C. Man and F.T. Cheng (2010) Sliding Wear and Corrosion Resistance of Copper-based Overhead Catenary for Traction Systems. Vol. 3(1). IJR International Journal of Railway. p. 19–27.
3. Dewan Muhammad Nuruzzaman and Mohammad Asaduzzaman Chowdhury (2013)Friction Coefficient and Wear Rate of Copper and Aluminum Sliding against Mild Steel. Vol 4. International Transaction Journal of Engineering, Management, & Applied Sciences & Technologies. p. 29–40.
4. M. Lvovsky, I. Lapsker, Yu. Volovik, Y. Feldman, R. Popovitz-Biro and R. Tenne(2003) Wear. Superior tribological properties of powder materials with solid lubricant nanoparticles. p. 794–800.
5. Vol 7.ASM Handbook (1992) p. 2162.
6. Vol 4.ASM Handbook (1991) p. 1962.
7. ASTM G99. Standard Test Method for Wear Testing with pin-on-Disk Apparatus. Designation: G-99–5a.
8. A.W.J. DeGee and J.H. Zaat(1962)Vol 5. Wear. p 257.
9. P.C. Angelo and R. Subramanian (2012). Powder Metallurgy; Science, Technology and Applications. PHI Learning Private Limited, India.

Optimization of Process Parameters and Investigation on Surface Characteristics During EDM and Powder Mixed EDM

S. Tripathy and D.K. Tripathy

Abstract Electro Discharge Machining (EDM) is an extensively used non-conventional process for material removal in die manufacturing and aerospace industries. The present work investigates the effect of process parameters like graphite powder concentration (C_p), peak current (I_p), pulse on time (T_{on}), duty cycle (DC) and gap voltage (V_g) on the performance characteristics of material removal rate (MRR), tool wear rate (TWR), surface roughness (SR) and recast layer thickness (RLT) during EDM and PMEDM of H-11 die steel. Taguchi's L_{27} orthogonal array was used to carry out the experiments. Investigation of microstructures was done using scanning electron microscope (SEM) to examine alterations and defects on the machined surface.

Keywords EDM · PMEDM · Optimization · Material removal rate · Surface roughness · Recast layer thickness · SEM

1 Introduction

Electrical Discharge Machining (EDM) process is being widely used to impart intricate shapes to conductive metals and alloys possessing high hardness and toughness which find wide application in the mould and die making industries, aerospace, automobile and electronic industries. Powder Mixed Electro Discharge Machining (PMEDM) has enhanced the machining potential of EDM which involves mixing of a proper material in a fine-powdered form to the dielectric fluid which in turn decreases the insulating strength of the dielectric fluid and increases the interelectrode gap causing an effortless removal of debris.

S. Tripathy (✉)
Mechanical Engineering Department, ITER, SOA University, Bhubaneswar, India
e-mail: sasmeetatripathy@soauniversity.ac.in

D.K. Tripathy
KIIT University, Bhubaneswar, India
e-mail: provc@kiit.ac.in

Pecas et al. [1] investigated that the performance of the PMEDM process depends upon characteristics like powder type, concentration, particle size, electrode area, workpiece constituents and properties. Kumar et al. [2] reported reviews on the effect of mixing different powders and additives to the dielectric. Kansal et al. [3, 4] studied the effect of process parameters and found the optimal setting of parameters for PMEDM using response surface methodology, Taguchi, utility concept and multi-objective optimization. Singh et al. [5] evaluated the role of input parameters on SR while machining H-11 die steel using copper tool and by adding Al powder to the dielectric. Effect of adding silicon and aluminium powders to the dielectric has also been investigated [6–8].

The past studies show less work on the performance characteristics of H-11 die steel using PMEDM. Comparative studies between EDM and PMEDM using graphite powder on H-11 work material has not been much investigated. The recast layer formation with difference in concentration of powder on H-11 die steel needs to be investigated experimentally. The alterations occurring in the surface characteristics due to the addition of powder have to be understood in depth. The present work is a step in this direction. Furthermore, optimum set of parameters has been obtained to increase the efficiency of the process.

2 Experimental Details

2.1 Machine Setup

Experiments were performed on die sinking type EDM. The workpiece material selected for the experiment is H-11 die steel having a composition of 0.39 %C, 1 % Si, 0.5 %Mn, 0.03 %P, 0.02 %S, 4.75 %Cr, 1.1 %Mo, 0.01 %Co, 0.01 %Cu, 0.5 %V and Fe as balance.

2.2 Design of Experiments

Taguchi's Technique was implemented to find the effect of process variables on the PMEDM performance. The important input parameters selected were concentration of graphite powder (gm/l), I_p, T_{on}, DC and V_g varying at three levels respectively based on certain pilot experiments performed for selection of parameters and their levels as shown in Table 1. Considering the number of factors and their levels, an L_{27} Taguchi's orthogonal array was used to perform the experiments.

Table 1 Selection of levels for the factors

Factors with units	Levels		
	Level 1	Level 2	Level 3
Concentration of graphite powder (gm/l)	0	3	6
Peak current (Amp)	3	6	9
Pulse on time (µs)	100	150	200
Duty cycle (%)	7	8	9
Gap voltage (Volts)	30	40	50

3 Results and Discussion

3.1 Material Removal Rate and Tool Wear Rate

The machining efficiency of the process can be characterised by the MRR and TWR. Experimental observations of MRR and TWR show that when graphite powder is added in 3 gm/l, the MRR increases and the TWR decreases. As the concentration of powder increases to 6 gm/l, the MRR further increases and the TWR decreases with less damaged surfaces. When no powder is added to the dielectric, it is apparent that the MRR increases with increase in current and pulse on time. It can be observed from Fig. 1a–d that with the increase in concentration of powder from 3 to 6 gm/l, the MRR is showing an increase and TWR decreases followed by a minor increase resulting in improved surface quality for H-11die steel.

3.2 Effect of Input Parameters on Surface Roughness

The surface roughness examined using a surface roughness tester in Fig. 2a shows that the increase in pulse current increases the roughness of the surface. The SR is maximum during EDM, when no powder is added to the dielectric fluid. The SR remarkably reduces during PMEDM when the powder is added in the concentration of 3 gm/l. Adding powder in a concentration of 6 gm/l to the dielectric fluid, slightly increases the SR as shown in Fig. 2b.

3.3 Effect of Input Parameters on Recast Layer Thickness

The faster machining rates produce higher recast layer thickness. It can be seen from Fig. 3a that the RLT value rises with the rise in I_p. Figure 3b shows that the RLT increases with the increase in powder concentration, the flushing pressure remaining the same.

Fig. 1 Variation of MRR
and TWR with the important
input parameters
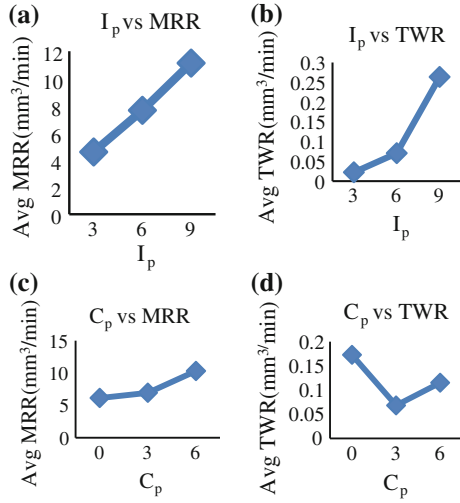
Fig. 2 Variation of SR with
the important input
parameters
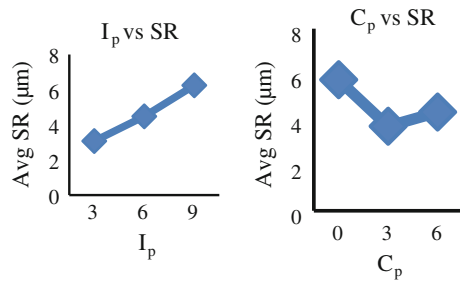
Fig. 3 Variation of RLT
with the I_p and C_p
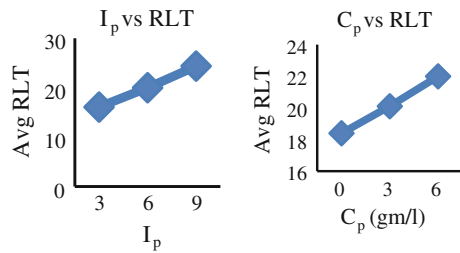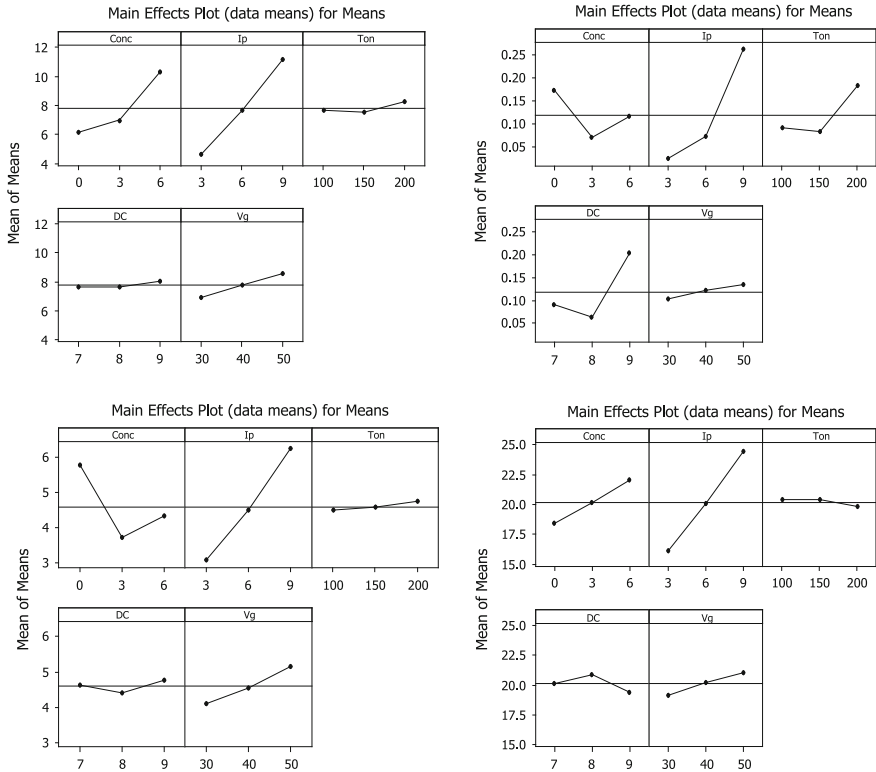
Fig. 4 Main effects plot for mean values of MRR, TWR, SR and RLT

3.4 Single Objective Optimization

By studying the main effects plot of each of the factors, the trend showing the influence of different factors towards the process can be distinguished. The relative importance of the parameters with respect to MRR, TWR, SR and RLT was investigated to determine the optimum combinations of parameters from the results obtained using Minitab software. Figure 4 presents the main effects plot for mean values of MRR, TWR, SR and RLT with various input parameters.

3.5 Confirmatory Tests

The confirmation experiments are carried out to authenticate the results drawn during the analysis. The machining was again carried out with the same set of input parameters and the output responses under consideration were again calculated which was found to be approximately same as the previous values.
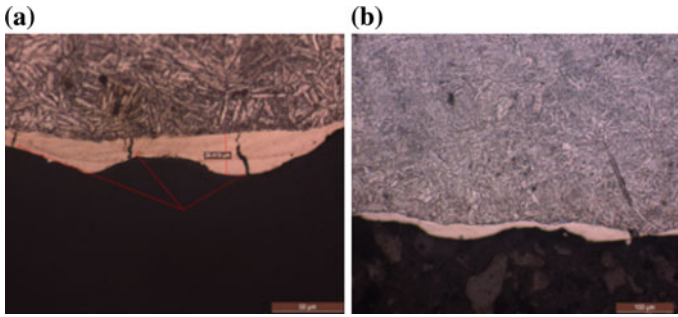
Fig. 5 Profile of Material surface during EDM and PMEDM

3.6   Microstructure Analysis

It could be seen from the microstructural studies that the profile of the material surface beneath the recast layer varies as shown in Fig. 5a, b during EDM and PMEDM, respectively.

4   Conclusion

The following are the major findings from the present work

1. The third level of parameters for powder concentration, third level of I_p, third level of T_{on}, third level of DC and third level of V_g produce maximum MRR when machined using EDM and PMEDM.
2. The second level of parameters for powder concentration, first level of I_p, second level of T_{on}, second level of DC and first level of V_g provide minimum TWR when machined using EDM and PMEDM.
3. The second level of parameters for powder concentration, first level of I_p, first level of T_{on}, second level of DC and first level of V_g offer minimum SR when machined using EDM and PMEDM.
4. The first level of parameters for C_p, first level of I_p, third level of T_{on}, third level of DC and first level of V_g offer minimum RLT when machined by EDM and PMEDM.
5. The surface texture showed enormous improvement with reduced RLT and improved the surface quality with the increase in C_p.

References

1. Pecas, P., Henriques, E.: Electrical discharge machining using simple and powder mixed dielectric: The effect of the electrode area on the surface roughness and topography. Jour. of Mat. Proces. Technol. 200. (2008) 250–258.
2. Kumar, S., Singh, R., Singh, T.P., Sethi, B.L.: Surface modification by electrical discharge machining: A review. Jour. of Mat. Proces. Technol. 209. (2009) 3675–3687.
3. Kansal, H.K., Singh, S., Kumar, P.: Parametric optimization of powder mixed electrical discharge machining by response surface methodology. Jour. of Mat. Proces. Technol.1699. (2005) 427–436.
4. Kansal, H.K., Singh, S., Kumar, P.: Performance parameters optimization (multi-characteristics) of powder mixed electric discharge machining (PMEDM) through Taguchi's method and utility concept. Ind. Jour. of Eng. and Mat. Sci.13. (2006) 209–216.
5. Singh, Baljinder., Singh, Paramjit., Tejpal, Gaurav., Singh, Gurtej.: An experimental study of surface roughness of H-11 in EDM process using copper tool electrode. Int. Jour. of Adv. Manuf. Technol. 3(4). (2012) 30–33.
6. Kansal, H.K., Singh, Sehjipal., Kumar, Pradeep.: Effect of Silicon powder mixed EDM on machining rate of AISI D2 die steel. Jour. of Manuf. Proces.9. (2007) 13–22.
7. Batish, Ajay., Bhattacharya, Anirban., Singla, V.K., Singh, Gurmail.: Study of Material Transfer Mechanism in Die steels using powder mixed Electrical Discharge Machining. Mat. and Manuf. Proces.27. (2012) 449–456.
8. Wu, K.L., Yan, B.H., Huang, F.Y., Chen, S.C.: Improvement of surface finish on SKD steel using electro-discharge machining with aluminium and surfactant added dielectric. Int. Jour. of Mach. Tools and Manuf. 45. (2005) 1195–1201.

Evaluation of Tensile Properties of Natural Silk and Coir Fibers

S. Gowthaman, C. Gowri Sankar and P. Chandrakumar

Abstract This paper evaluates the tensile properties of naturally available BM silkworm silk and coir fibers. Tensile experiments are conducted to evaluate the tensile properties of the fibers over a variation of lengths ranging from 10 to 30 mm, wherein the effect of machine compliance is also taken into account. The gauge length does not seem to affect the Young's modulus of fibers. The tensile strength and modulus of silk fiber is 6 and 2 times, respectively, higher than that of coir fiber. The failure strain of both the fibers is comparable having high value in the range of 15–20 %. The results are promising for application of silk and coir fibers as reinforcements in hybrid composites.

Keywords Silk fiber · Coir fiber · Tensile modulus · Tensile strength · Elongation

1 Introduction

Among different natural fibers, silk, and coir fibers have very high extensibility and are considered highly potential for hybridization of composites [1–3]. The dragline silk of certain spiders has excellent tensile properties and toughness and considered as the perfect candidate for high elongation fibers [4]. However, harvesting and implementing of spider silk on a large scale has been found difficult due to the carnivorous and cannibalistic nature of spider. On the other hand, harvesting of highly domesticated Bombyx mori (BM) silkworm silk is very easy and this silk has been implemented on a large scale for manufacturing of commercial silk textiles. The tensile strength and toughness of this silkworms' silk fiber is high after the spider silk, and has been considered as an alternative candidate material for HE fibers. Cheung et al. [5] investigated the mechanical properties of BM, twisted BM

S. Gowthaman (✉) · C.G. Sankar · P. Chandrakumar
Vel Tech University, Avadi, Chennai, India
e-mail: gowthaman@veltechuniv.edu.in

and Tussah silkworm silk fibers using tensile testing. The tensile strength, modulus, and failure strain for these fibers were 216, 171, and 252 MPa; 6.1, 3.8, and 5.8 GPa; and 20, 21, and 33 %, respectively. Poza et al. [6] studied and reported the tensile strength, modulus, and failure strain of BM, A atlas and A trifasciata silk fibers as 650, 200, and 600 MPa; 16, 5, and 7 GPa; and 15, 18, and 30 %, respectively. Zhu et al. [7] reported the tensile strength, modulus and failure strain of regenerated and natural BM silk fibers as 175 and 400 MPa; 6 and 7 GPa; and 21 and 27 %, respectively. Another favorable natural HE fiber for hybridization is brown coir fiber that is derived from the husk of the ripe coconut (*Cocos nucifera*). Defoirdt et al. [8] compared the tensile properties of coir, bamboo, and jute fibers using mini tensile testing machine. Among the three, the coir fibers presented low mechanical strength (177 MPa), low modulus of elasticity (3.44 GPa), and high failure strain (37.85 %), while the jute fibers presented high mechanical strength (353 MPa), high modulus of elasticity (26.25 GPa), and low failure strain (3.5 %).

   As evidenced from the above literature review, tensile testing of individual fibers has shown a wide range of properties. This has been attributed to different approaches in experiments and/or negligence of the effect of machine or grip compliance on the properties of fibers. This necessitates employing an efficient method for the evaluation of the fiber modulus and the prediction of its size dependence. In the current paper, the authors present a study on the tensile behavior of naturally available BM silkworm silk and coir fibers. Tensile experiments were conducted to evaluate the properties of the fibers over a variation of lengths ranging from 10 to 30 mm, wherein the effect of machine compliance was taken into account. The measured properties are useful for micromechanics analysis and development of hybrid composites.

2 Materials and Methods

2.1 Materials

The silk fibers used in this research belong to Bombyx mori (BM) silkworm silk category. The brown coir fibers were obtained from a local vendor and were also used in their natural form. The diameter of the all fibers was measured by using a polarizing microscope (Dewinter Classic PI) at 100× magnification. For each individual silk and coir fiber, the diameters were measured at three different locations along its gauge length. The minimum area was used for measurement of tensile strength, while the average of all the values was used for measurement of Young's modulus. The average diameter of silk fiber was 17.4, 18.7, and 18.1 µm

for 10, 20, and 30 mm gauge length, respectively. The average diameter of coir fiber was 142.1, 149.1, and 169 μm for 10, 20, and 30 mm gauge length, respectively.

3 Tensile Test

The tensile test specimens were prepared according to ASTM C1557 [9]. The tensile tests were performed in a universal testing machine Shimadzu, model EZ-SX equipped with 20 N load cell. For all fibers and for all gauge lengths (10, 20, and 30 mm), the tests were carried using the displacement control at a rate of 0.05 mm/min. A total of 15 samples were tested for each type of fiber. The compliance of the loading and gripping system was determined by obtaining the force versus displacement behavior of the fiber at various gauge lengths as described in ASTM C1557. The total cross-head displacement during fiber testing, ΔL, can be expressed by

$$\frac{\Delta L}{F} = \frac{L}{EA} + c,$$ (1)

where c is the machine compliance, F is the applied force, E is the Young's modulus of the fiber, and A is the cross-sectional area of the fiber. Thus, a plot of $\Delta L/F$ (indicated compliance) versus guage length L will yield a straight line of slope $1/EA$ and intercept c, the compliance of the load train.

4 Results and Discussion

The load versus displacement curves for silk and coir fibers for all gauge lengths are shown in Figs. 1 and 2, respectively. From the chart obtained for each specimen, the indicated compliance $(\Delta L/F)$ for each specimen was calculated by extrapolating the initial straight line portion of the load displacement curve. Figure 3 shows the plots of indicated compliance versus gauge lengths for the fibers, in which the Y-intercept represents the system compliance. From the calculated compliances and measured average cross-sectional area for fibers, the Young's modulus for all the fibers at different gauge lengths was calculated using Eq. (1). Table 1 presents the Young's modulus of the fibers for different gauge lengths, wherein the gauge length does not seem to affect the Young's modulus of the fibers. Similar results have been reported by other authors also [10, 11]. The average Young's modulus of silk and coir fibers was 5.0 and 2.2 GPa, respectively.
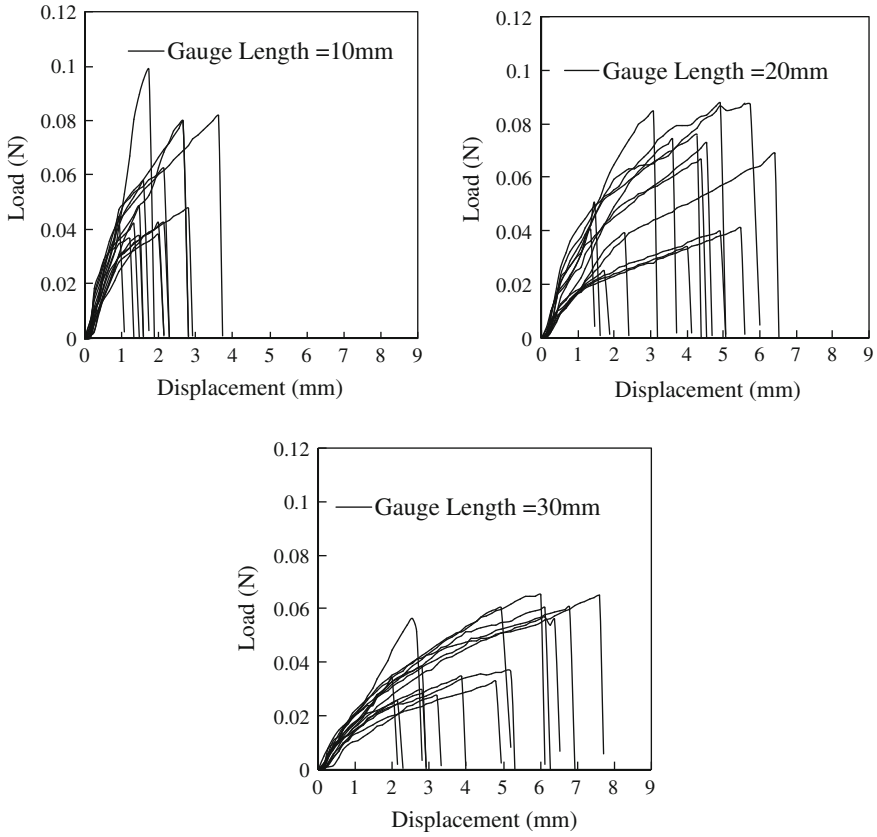
Fig. 1 Load-displacement curves for silk fibers

Typical tensile behavior of fibers is presented in Fig. 4. It is interesting to notice that silk and coir fibers presented a nonlinear region starting at stress levels of 150 MPa or below. This nonlinear region, following the initial portion of the stress–strain curve has been hypothesized to be due to a collapse of the weak primary cell walls and delamination between fiber cells [10]. The average tensile strength and failure strain for all fibers at different gauge lengths are summarized in Table 1. Among silk and coir fibers, the silk fiber (tensile strength ∼300 MPa) was found to be almost 6 times stronger than coir fiber (tensile strength ∼50 MPa).
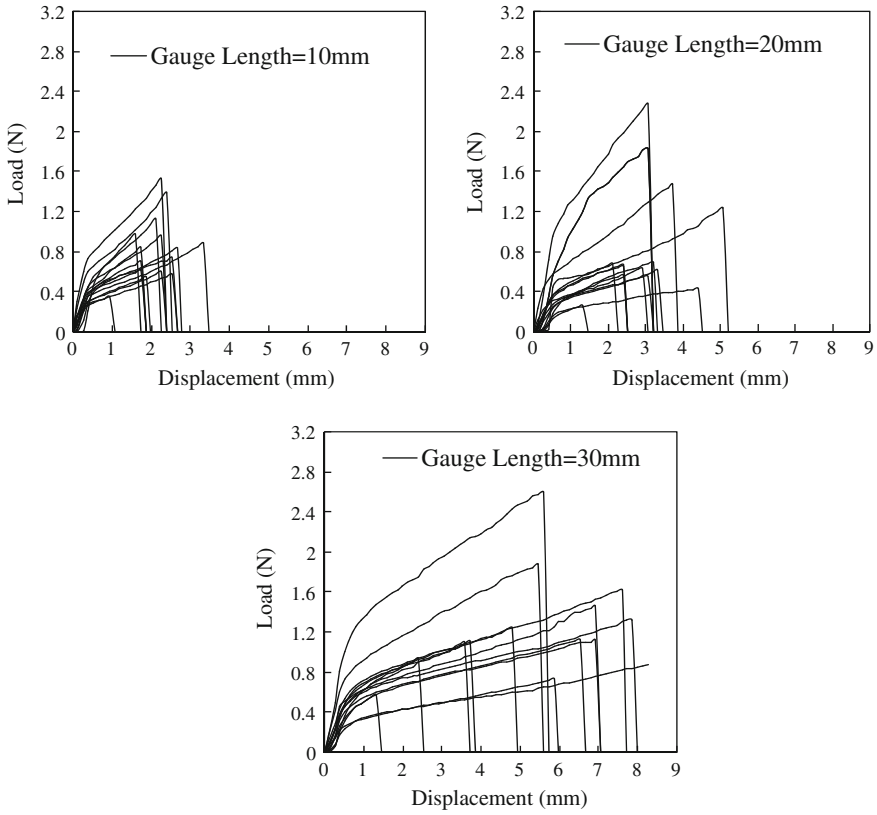
Fig. 2 Load-displacement curves for coir fibers
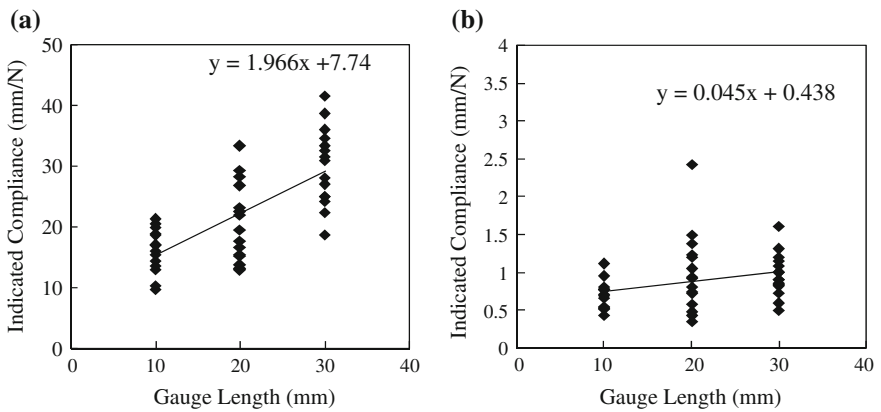
Fig. 3 Indicated compliance versus gauge length curves for **a** silk and **b** coir fibers

Table 1 Tensile properties of fibers

Fibers	Gauge length (mm)	No. of samples	Mean strength (MPa)	Young's modulus (GPa)	Failure Strain (%)
Silk	10	15	0330.24 ± 092.97	5.043	21.13
	20	15	0296.55 ± 066.57	5.079	20.04
	30	15	0266.61 ± 093.98	5.061	15.37
Coir	10	15	0056.36 ± 014.25	2.209	21.27
	20	15	0055.88 ± 020.54	2.183	15.24
	30	15	0055.85 ± 013.89	2.247	17.71

Fig. 4 Typical tensile stress–strain curves for fibers
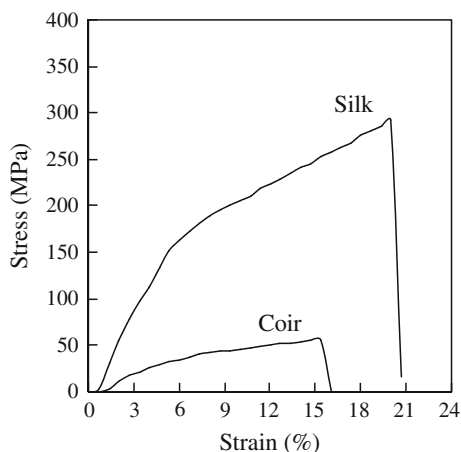
5 Conclusions

The paper presented a study on the evaluation of tensile behavior of naturally available BM silkworm silk and coir fibers. Tensile experiments were conducted for the fibers at different gauge lengths ranging from 10 to 30 mm, wherein the effect of machine compliance was also included. The stress–strain curves for silk and coir fibers presented a nonlinear region starting at stress levels of 150 MPa or below due to potential collapse of the weak primary cell walls and delamination between fiber cells. The average strength and modulus of silk and coir fibers were 300 MPa and 5 GPa, and 50 MPa and 2.2 GPa, respectively. Both the silk and coir fibers exhibited high elongation with failure strain values of 15–20 %. The results are promising for application of silk and coir fibers in hybridization and provide a step forward for micromechanical analysis and development of hybrid composites.

References

1. H Ku, H Wang, N Pattarachaiyakoop, M Trada, A Review on the Tensile Properties of Natural Fiber Reinforced Polymer Composites, Composites Part B: Engineering, 42, 2011, p. 856–873.
2. US Bongarde, VD Shinde, Review on Natural Fiber Reinforcement Polymer Composites, International Journal of Engineering Science and Innovative Technology, 3, 2014, p. 431–436.
3. J Sahari, SM Sapuan, Natural Fiber Reinforced Biodegradable Polymer Composites, Reviews on Advanced Materials Science, 30, 2011, p. 166–174.
4. X Liu, K Zhang, Silk Fiber—Molecular Formation Mechanism, Structure-Property Relationship and Advanced Applications, http://dx.doi.org/10.5772/57611, 2014.
5. H Cheung, K Lau, M Ho, A Mosallam, Study on the Mechanical Properties of Different Silkworm Silk Fibers, Journal of Composite Materials, 43, 2009, p. 2521–2531.
6. P Poza, JP Erez-Rigueiro, M Elices, JL Lorca, Fractographic Analysis of Silkworm and Spider Silk, Engineering Fracture Mechanics, 69, 2002, p. 1035–1048.
7. ZH Zhu, K Ohgo, T Asakura, Preparation and Characterization of Regenerated Bombyx mori Silk Fibroin Fiber with High Strength, eXPRESS Polymer Letters, 2, 12, 2008, 885–889.
8. N Defoirdt, S Biswas, L Vriese, LQN Tran, JV Acker, Q Ahsan, Assessment of the Tensile Properties of Coir, Bamboo and Jute Fiber, Composites Part A: Applied Science and Manufacturing, 41, 2010, p. 588–595.
9. ASTM. ASTM C1557, Standard Test Method for Tensile Strength and Young's Modulus of Fibers. West Conshohocken, PA, USA: American Society for Testing and Materials; 2008.
10. MEA Fidelis, TVC Pereira, OFM Gomes, FASilva, RDT Filho, The Effect of Fiber Morphology on the Tensile Strength of Natural Fibers, Journal of Materials Research and Technology, 2, 2013, p. 149–157.
11. PK Ilankeeran, PM Mohite, S Kamle, Axial Tensile Testing of Single Fibres, Modern Mechanical Engineering, 2, 2012, p. 151–156.

Comparison of Turbulence Models in Simulating Axisymmetric Jet Flow

B.T. Kannan, S. Karthikeyan and Senthilkumar Sundararaj

Abstract The present work is a comparison of various turbulence models available in ANSYS-Fluent in simulating an axisymmetric jet flow. A large domain is chosen for simulation of the jet flow with an intention to avoid errors due to the computational boundaries. The simulations are carried out at a fixed Reynolds number for facilitating comparisons. This work considers various first-order closure models such as standard k-epsilon model, standard k-omega model, RNG k-epsilon, Realizable variants of k-epsilon model, SST k-omega model, and a second-order closure model namely Reynolds stress model. The simulated results are compared with reference literature to understand the applicability of models using various parameters such as inverse mean axial velocity decay, turbulence intensity, turbulent kinetic energy, and streamlines. Large variations are found in all the parameters between first and second-order turbulence closure models. The streamlines also show reverse flow patterns near the nozzle for second order turbulence model. The first-order closure models are found to be better than the second-order closure models in predicting the flow field of axisymmetric jets.

Keywords Numerical simulation · Jets · Axisymmetric · Turbulence models · ANSYS-Fluent

1 Introduction

Turbulent jets are fundamental flows and they have a variety of applications in industries. Axisymmetric jets are the simplest to be studied extensively in the past [1]. The simulation of axisymmetric jets is used to assess the turbulence models by

B.T. Kannan
Department of Aerospace Engineering, Indian Institute of Technology – Madras,
Chennai, India

S. Karthikeyan · Senthilkumar Sundararaj (✉)
Department of Aeronautical Engineering, Vel Tech University, Chennai, India
e-mail: ssenthil@veltechuniv.edu.in

comparing them with experimental data. Due to the simplicity in geometry, axisymmetric jets have been extensively tested and the behavior of different models has been reported. The advantages and disadvantages of using a turbulence model are clearly mentioned in the literature [2]. The effect of choosing a particular turbulence model with respect to the flow field physics is not clearly mentioned for axisymmetric jet case. Hence, there is a need to investigate why the turbulence models behave in a particular fashion by looking into the flow field and various parameters representing the physics.

2   Computational Method

2.1   Computational Domain and Grid

The computational domain (refer Fig. 1) is a rectangular domain with axial and lateral boundaries extending more than 200 nozzle diameters 'D.' The domain is divided into a nonuniform mesh with fine resolution toward the wall and the axis.

2.2   Flow Details

The flow is representing a highly turbulent air jet similar to a physical situation mentioned in the literature [3]. The Reynolds number of the flow is high enough such that there will be no dependence based on the nondimensional number. Uniform velocity profile is assumed to represent the top-hat velocity profile as in experiments. The flow is considered isothermal and steady state assumptions are considered.

Fig. 1 Computational domain and grid with boundary conditions
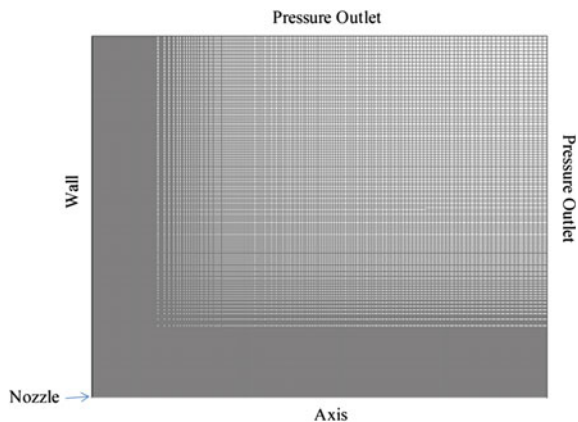
2.3 Simulation Details

The simulation is carried out in a commercial solver ANSYS-Fluent for all the cases considered in the study. The grid is created using Gambit and exported to the solver for simulations. The boundary conditions used are

- Velocity Inlet with uniform velocity value—for the nozzle
- Pressure outlet—for the right outlet and top entrainment surface
- Wall—for no slip
- Axis for the jet axis

The SIMPLE algorithm is used for coupling velocity and pressure equations. Standard relaxation factors were maintained for all the models. Convergence criteria for residuals were set to 10^{-06} for all the variables. The governing equations used are Reynolds Averaged Navier Stokes (RANS) equations along with the turbulence models.

2.4 Turbulence Models

Equivalent area-based method of defining half width velocity is required when geometry based method is not applicable.

The various turbulence models used in this work are listed as below.

- Standard k-epsilon model (SKE)
- Realizable k-epsilon model (RKE)
- RNG k-epsilon model (RNGKE)
- Standard k-omega model (SKO)
- SST k-omega model (SST)
- Reynolds Stress Transport Model (RSTM)

3 Results and Discussion

3.1 Inverse Mean Axial Velocity Decay

The inverse mean axial velocity decay is plotted against the axial distance for various turbulence models and it is shown in Fig. 2. The experimental data of Quinn [4] is also provided for comparison purposes. The standard k-epsilon model results from the present simulation matches well with the OpenFOAM results of Kannan [3] which was also simulated with the same model. The comparison shows that the first-order closure models are better than the second order closure models. The Realizable k-epsilon model predicts the decay very close to experiments

Fig. 2 Comparison of inverse mean axial velocity decay for all models
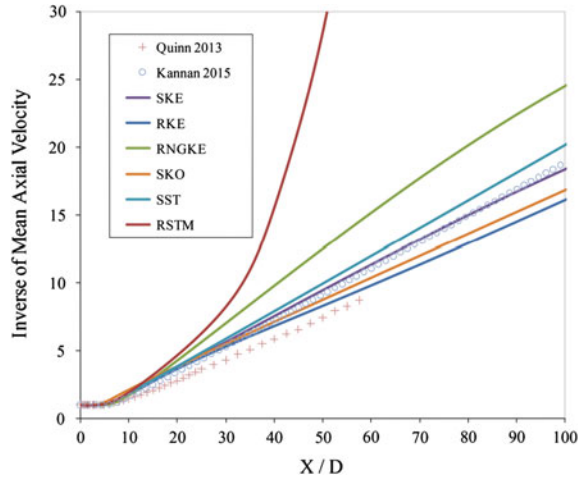
followed by standard k-omega model and standard k-epsilon model. It is to be noted that the first-order model results were in good agreement with experiments for a noncircular jet case at high Reynolds number [5]. The second-order closure model deviates significantly after 30 diameters downstream the nozzle and the solution becomes unphysical. The other parameters have to be examined for realizing the real cause of the deviation.

3.2 Turbulent Intensity

The turbulent intensity values are plotted along the jet axis for various models and compared with the reference data. The turbulent intensity extracted from the fluent includes both intensities in comparison to two intensities from OpenFOAM. The intensities show that the second-order turbulence model has deviated from representing the physics of the jet. The jet should have nearly constant intensity in the potential core region followed by increase and attaining a steady value. The SST k-omega model and the standard k-epsilon model reproduce the physically possible solution. Realizable k-epsilon and standard k-omega models are found to underestimate Turbulence intensity (Fig. 3).

3.3 Turbulent Kinetic Energy (TKE)

The turbulent kinetic energy is non-dimensionalized with the axial kinetic energy and plotted against the jet axial coordinate. The plot compares the various turbulence models and clearly shows the deviation predicted by the second-order closure

Fig. 3 Comparison of turbulent intensities
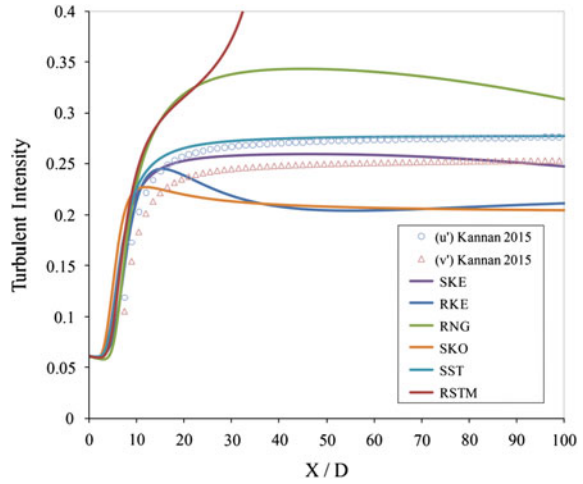
turbulence model. The first-order closure models predict better than the second-order closure models. The standard k-epsilon model along with SST k-omega model predicts the physical flow behavior, whereas the RNG version of k-epsilon over estimates the TKE. Realizable k-epsilon and standard k-omega models are found to underestimate TKE (Fig. 4).

Fig. 4 Comparison of turbulent kinetic energies
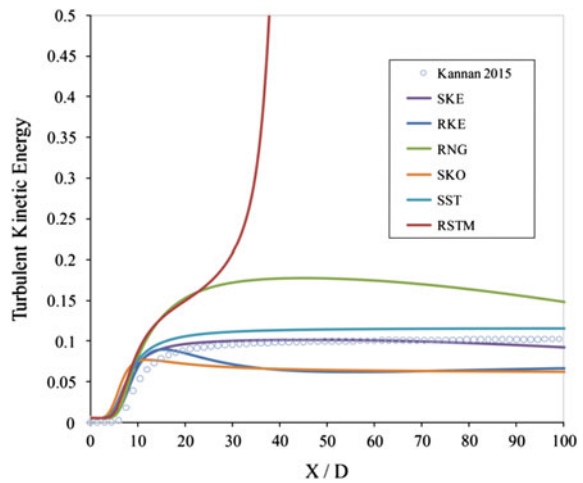
3.4 Streamlines

The streamlines are visualized to check the entrainment patterns of the simple jet flow and it is shown in Figs. 5 and 6 for the standard k-epsilon model and the Reynolds Stress Transport Model respectively. The standard k-epsilon model shows slight recirculation near the outlet which will not influence the core jet.

The Reynolds Stress Transport Model shows slight recirculation near the nozzle and the unphysical entrainment patter throughout the entire domain. This unphysical behavior is generated due to the numerical instabilities caused due to the usage of higher order model with the same conditions that are used for first-order models.

Fig. 5 Streamlines for standard k-epsilon model
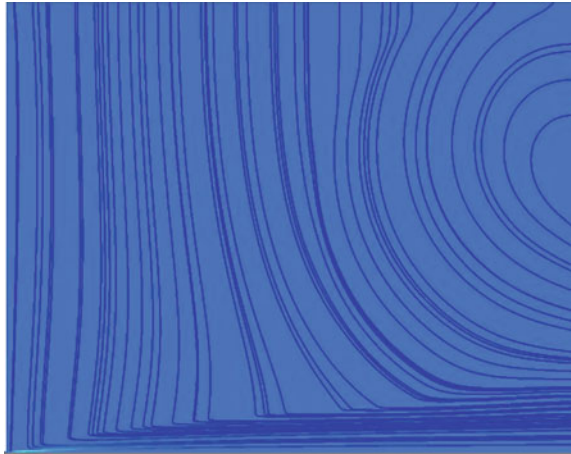
Fig. 6 Streamlines for reynolds stress transport model
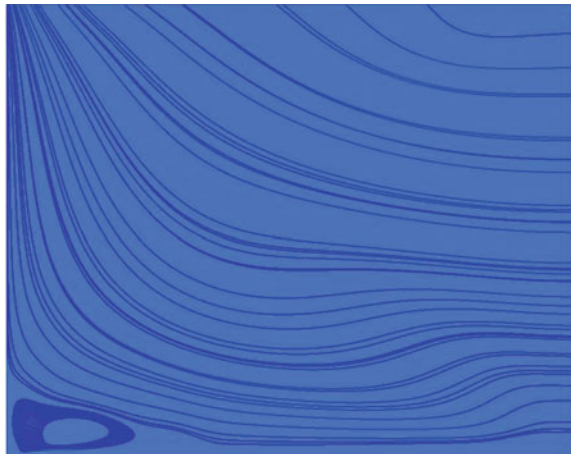
4 Conclusion

The present work compares various turbulence models available in ANSYS-Fluent in simulating an axisymmetric jet flow. The results from the two solvers (Fluent and OpenFOAM) match well with each other. The first-order closure models like standard k-epsilon model and Realizable variant of k-epsilon model are found to better than the second-order Reynolds Stress Transport Model. The streamlines show reverse flow patterns near the nozzle for second-order turbulence model. This is due to the numerical instability of the solver while using higher order models. The corrections for using solvers with higher order models can be done by adjusting the relaxation factors and/or adding stability terms in the model equations.

References

1. C.G. Ball, H. Fellouah, A. Pollard, Prog. Aerosp. Sci. 50 (2012).
2. S.B. Pope, Turbulent Flows, (2000).
3. B.T. Kannan, Procedia Engineering. 127 (2015) 1292.
4. W.R. Quinn, Flow, Turbulence and Combustion. 91 (2013) 773.
5. B.T. Kannan, S. Senthilkumar, in A.K. Saha, Debopam Das, Rajesh Srivastava, P. K. Panigrahi, K. Muralidhar (eds.), Fluid Mechanics and Fluid Power—Contemporary Research, Springer India, India, 2016, paper no: 47.

Finite Element Analysis of High Strength Polymers Interaction with Inhibitors in Selective Inhibition Sintering Process

A. Aravind, T.N. Siddiqui, P. Arunkumar and E. Balasubramanian

Abstract Selective Inhibition of Sintering (SIS) is a predominant Additive Layer Manufacturing (ALM) technique to produce parts out of polymers and metals. The present work considers sintering interaction phenomenon between high strength polymers and inhibitors using Finite Element Analysis (FEA). Transient thermal coupled with structural analysis is performed for various high strength polymers such as Polyamideimide (PAI), Polyetherimide (PEI), Polyphthalamide (PPA), and Poly Tetra Fluoro Ethylene (PTFE) with inhibitors Potassium iodide (KI), Potassium chloride (KCl), and Sodium chloride (NaCl). Simulation results suggested that the effect of heat is more influencing on PAI which obtained minimal structural displacement in comparison with other polymers. Compared with NaCl, the inhibitors KCl and KI provided greater inhibition effect which will be employed in SIS additive manufacturing process to manufacture high strength and dimensionally stable plastic parts.

Keywords High strength polymers · Inhibition · Sintering · Finite element analysis · Additive layer manufacturing

1 Introduction

An evolution in Additive Layer Manufacturing (ALM) (RP) is progressing rapidly in many fields such as medical technology, automotive and aerospace technology, arts, and archaeology. Among the various RP techniques that are currently being used, the processes such as Fused Deposition Modeling, Selective Laser Sintering, Stereolithography, 3D Printing and Laser Engineered Net Shaping [1] have emerged as preferred options in many Indian industries, academia and research laboratories. All the above referred RP processes permanently depend upon foreign sources for the consumable materials. However, Selective Inhibition Sintering (SIS) has been proven to be an effective additive manufacturing process in utilizing

A. Aravind · T.N. Siddiqui · P. Arunkumar · E. Balasubramanian (✉)
Department of Mechanical Engineering, Vel Tech University, Avadi, Chennai, India
e-mail: esak.bala@gmail.com

indigenous polymer powders and producing the parts of high strength. It works with sintering and inhibition phenomena, where the build part is subjected to sintering process using heating element. Since the inhibitor is at the periphery of working materials and their high melting temperature causes the inhibition [2]. Due to the low cost and high quality of SIS printing, the impact of SIS in 3D printing industry could be disruptive [3]. Asiabanpour et al. conducted statistical experiments and enumerated the effective factors of SIS process such as heater feed rate, heater temperature, build tank temperature, and layer thickness [4]. They have also explained about the machine path generation systems and fabricated several 2.5- and 3-dimensional parts. The tool path generation is relatively slower than the disk input/output controller and the speed can be improved using advanced controllers [5]. They have also investigated in the selection of materials, optimization of process variables, and subsequently developed alpha machine [6]. In order to perform optimization of process variables, Asiabanpour et al. conducted design of experiments and validated with analysis of variance (ANOVA) technique to achieve superior surface quality [7]. Khoshnevis et al. investigated the fundamentals of SIS process of metallic parts and explained about the basic functions behind the working of SIS process [8]. They have experimented with various low strength polymer powders and inhibition materials and also inhibitor reactions with polymer were discussed [9]. Recently, Arunkumar et al. [2] examined the effect of sintering phenomenon for polyester and polyamide through FEA. Deepak Kumar et al. [10] evaluated the sintering behavior of various polymers and selection of suitable heat source to obtain effective sintering. These studies were concentrated on low strength polymers interaction with inhibitors. However, applications pertaining to high temperature needs to produce greater strength parts that necessitate high strength polymers. Hence, the present study explores on the various high strength polymers with interaction of different inhibitors using Finite Element Analysis.

2 Finite Element Analysis

2.1 Simulation Model

The thermo-structural evaluation of SIS process using FEA is an effective methodology to analyze the performance characteristics of high strength polymers and interaction with inhibitors. The present study considers 30 × 30 × 2 mm structured Finite Element (FE) model as shown in Fig. 1 where in the light gray indicates the polymer region and dark gray specifies inhibitors.

For the present model, the considered working materials are high strength polymers such as Polyamideimide (PAI), Polyetherimide (PEI), Polyphthalamide (PPA), Poly Tetra Fluoro Ethylene (PTFE), and inhibitors are Potassium iodide (KI), Potassium chloride (KCl), Sodium chloride (NaCl). The standard material

Fig. 1 FE modeling of SIS part
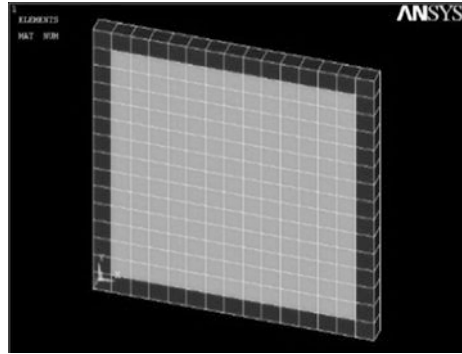
reference is used to acquire thermal and structural properties of high strength polymers [11] and for inhibitors [ref].

The present study considers high strength polymers such as Polyamideimide (PAI), Polyetherimide (PEI), Polyphthalamide (PPA), Poly Tetra Fluoro Ethylene (PTFE) and inhibitors Potassium iodide (KI), Potassium chloride (KCl), Sodium chloride (NaCl). The thermal and structural properties of high strength polymers [11] and inhibitors are given in Tables 1 and 2 respectively. The heating is applied longitudinally; convection from the top surface and radiation is neglected. Phase change during the sintering and solidification is considered to be negligible.

2.2 Boundary Conditions

The sequential coupling method is employed to analyze the thermo-structural behavior of sintering phenomenon. The heater speed, spot size of heater, and heat flux are considered to be 200 m/s, 2 mm, and 6.67e−6 w/m^2 respectively. The initial temperature of part and surrounding temperature is taken as atmospheric (303 K) and natural convection is assumed to be 30 W/m^2 K. Discretization of the structure is performed with solid 70 thermal element and solid 185 for the respective analysis. Heat input is applied in equal intervals of time ranging from 10 to 150 ms.

Table 1 Properties of polymers

Polymers	Thermal conductivity (W/m K)	Specific heat (J/kg K)	Density (kg/m^3)	Melting temperature (C)	Young's modulus (N/m^2)	Poisson ratio	Coefficient of thermal expansion (/K)
PEI	0.22	2000	1270	232	3.3e9	0.44	56e−6
TEFLON	0.24	1050	2160	335	0.55e9	0.46	125e−6
PPA	0.15	1400	1130	310	2.2e9	0.41	54e−6
PAI	0.4	1000	1410	275	4.5e9	0.38	30e−6

Table 2 Properties of inhibitors

Polymers	Thermal conductivity (W/m K)	Specific heat (J/kg K)	Density (kg/m^3)	Melting temperature (C)	Young's modulus (N/m^2)	Poisson ratio	Coefficient of thermal expansion (/K)
KI	2.1	313	3123	682	31.49e9	0	43e−6
KCl	6.53	690	1980	1050	29.63e9	0.250	36.6e−6
NaCl	6.5	854	2165	801	39.96e9	0.216	44e−6

3   Results and Discussion

Simulations are carried out using ANSYS solver to examine the sintering and inhibition interaction phenomenon of polymers and inhibitors.

3.1   Temperature Distribution

The effect of applied heat on the SIS structure is examined through FEA and its characteristic behavior is assessed. The variation of temperature in these polymers are very small, however, PAI attained maximum temperature than other polymers because of its higher thermal conductivity and low coefficient of thermal expansion as seen in Fig. 2.
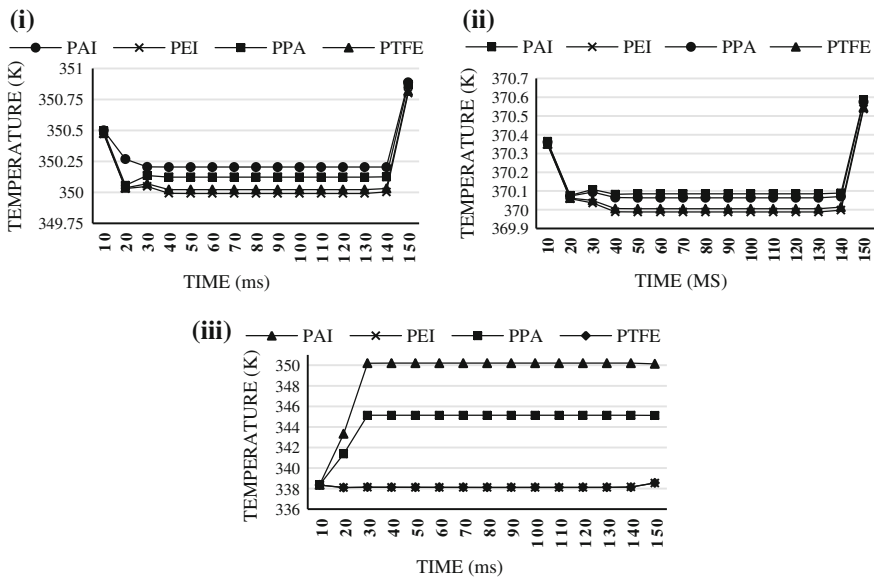
Fig. 2 Variation of temperature for various polymers and inhibitors. **i** KCl, **ii** KI, **iii** NaCl
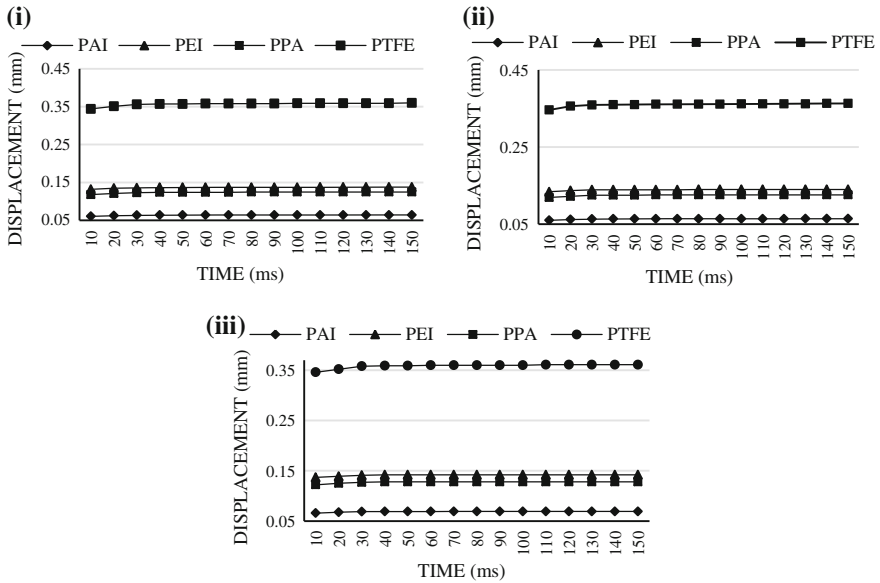
Fig. 3 Displacement variation for various polymers and inhibitors. **i** KCl, **ii** KI, **iii** NaCl

The interaction behavior of various inhibitors reveals that, KCl and KI provided similar trend where the NaCl has abrupt change in the temperature which may affect the part body temperature. It is also observed in Fig. 2(ii) that, KI induce more temperature than KCl and hence, PEI with KCl can be an effective choice than other materials.

3.2 Effect of Displacement Variation Using Various Inhibitors

The structural displacement of various polymers was observed through coupling the effect of thermal load into the structural field using FEA. The effect of inhibitors does not influence the displacement of the structure as shown in Fig. 3. The maximum displacement is observed in PTFE of 0.35 mm and PAI attained about 0.05 mm which is comparatively very minimal. Hence, dimensionally stable parts can be made out of PAI in comparison with other polymers.

4 Conclusion

The performance evaluation of various high strength polymers with multiple inhibitors is investigated using finite element analysis. Thermal behavior of PEI with KCl achieved minimal temperature and there by reduction of thermal stress

and strain can be attained. The structural displacement is predominant in PTFE compared with other polymers and minimal displacement is experienced in PAI which can be suitable for manufacturing dimensionally stable plastic parts. In future, experimental studies will be carried out to evaluate the thermo-structural behavior of PAI and PEI with KCl as inhibitor to produce the parts of high strength at elevated temperature.

References

1. Chua CK, Leong KF (1998) Rapid Prototyping. Principles and Applications in Manufacturing, John Wiley & Sons
2. Arunkumar P, Balasubramanian E, and Chandrasekhar U (2015) Thermo mechanical modeling of selective inhibition sintered thermoplastic parts, Journal of Applied Mechanics and Materials, 813–814: 791–795
3. Khoshnevis B, Zhang J, Fateri M, and Xiao Z (2014) Ceramics 3D printing by selective inhibition sintering. In Solid Free Form Symposium (SFF).
4. Asiabanpour B, Palmer K, and Khoshnevis B (2003) Performance factors in the selective inhibition of sintering process. Institute of Industrial Engineering Research Conference, Portland, OR.
5. Asiabanpour B, Khoshnevis B (2004) Machine path generation for the SIS process, Robotics and Computer-Integrated Manufacturing, 20.3: 167–175
6. Asiabanpour B, Palmer K (2004) Systematic approach for Rapid Prototyping processes development, IIE Annual Conference. Proceedings, Institute of Industrial Engineers-Publisher.
7. Asiabanpour B, Palmer K and Khoshnevis B (2004) An experimental study of surface quality and dimensional accuracy for selective inhibition of sintering. Rapid Prototyping Journal, 10.3: 181–192
8. Khoshnevis B, Yoozbashizadeh M, and Chen Y (2012) Metallic part fabrication using selective inhibition sintering (SIS), Rapid Prototyping Journal, 18.2: 144–153.
9. Asiabanpour B, Khoshnevis B, Palmer K, and Mojdeh M (2003) Advancements in the SIS process. 14th International Symposium on Solid Freeform Fabrication, Austin, TX.
10. Deepak kumar K, Prasanth N, Arunkumar P, Balasubramanian E, and Abilash A (2015) Coupled field transient thermo - structural analysis of inhibited sintering process. Journal of Applied Mechanics and Materials, 813–814: 663–667.
11. Mark JE (1999) Polymer Data Handbook. 3rd Edition, Oxford University Press.
12. Udroiu, Razvan, and Nedelcu A (2011) Optimization of Additive Manufacturing Processes Focused on 3D Printing. INTECH Open Access Publisher.
13. Ding J, Colegrove P, Mehnen J, Ganguly S, Almeida PS, Wang F, and Williams S (2011) Thermo-mechanical analysis of Wire and Arc Additive Layer Manufacturing process on large multi-layer parts, Computational Materials Science, 50.12: 3315–3322
14. Pulak, Senthilkumaran PKJK, and Rao MPP, Advances in Materials for Powder based Rapid Prototyping.

Optimization of Process Parameters of Powder Additive-Mixed Electrical Discharge Machining

Pallavi Chaudhury, Sikata Samantaray and Sibakanta Sahu

Abstract Powder-mixed EDM is a prominent methodology for enhancing surface quality as well as MRR. The objective of this experiment is to optimize the PMEDM process parameters for machining EN19 work piece by Cu electrode with tungsten powder additives. In this experiment, three levels of current, powder concentration, and pulse on time are kept as the main variables for which Taguchi single objective methodology has been adopted to design the experiment. ANOVA has been done to show powder concentration is the significant variable for high MRR. The conclusions arrived for an optimum value of different parameters has also been verified and the error was found to be 0.64 %.

Nomenclature

EDM	Electrical Discharge Machining
PMEDM	Powder-Mixed EDM
MRR	Material Removal Rate
TON	Pulse on Time
TWR	Tool Wear Rate
SR	Surface Roughness
W/Pc	Work Piece
IP	Peak Current

P. Chaudhury (✉) · S. Samantaray
Department of Mechanical Engineering, I.T.E R S'O'A University,
Bhubaneswar, Odisha 751030, India
e-mail: pallavi.chaudhury@gmail.com

S. Sahu
Department of Mechanical Engineering, G.I.T.A, Bhubaneswar,
Odisha, India

1 Introduction

EDM as a reliable and precise machining process proved to be a novel method for machining of hard material. These machining techniques were first invented by Joseph Priestly in 1770. However, EDM was not fully used for machining until 1943 when two Russian scientists with the help of a spark generator studied how the erosive effects of the technique could be controlled and used for machining purposes in future. When in conventional EDM kerosene was used as dielectric liquid, it creates several problems during machining, such as degradation of dielectric liquid properties, pollution of air, and adhesion of carbon particles on to the work piece surface. All these phenomena lead to unstable discharge between the tool and work piece, which result in lower machining efficiency. Powder-mixed electric discharge machining (PMEDM) is one of the new methodologies for enhancing the capabilities of EDM by enhancing the machining efficiency. A suitable material as powder additives is mixed into the dielectric fluid of EDM. When a suitable voltage is applied, the spark gap between tool and work piece filled up with powder additive particles, creates a cluster. The gap distance increased from 25–50 to 50–150 mm [15]. This cluster formation helps in increasing the gap between both the electrodes, which leads to early explosion, faster erosion from the work piece surface. The material used in this study is EN-19 Steel which is a low alloy steel. It has a property to undergo heat treatment through hardening and posses a good combination of physical property strength, ductility, and toughness in quenched and tempered condition.

The objectives of this paper are stated as follows:

1. To analyze the effect of powder additives with dielectric over Conventional EDM.
2. To evaluate the efficiency of PMEDM on EN-19 with respect to responses such as MRR, TWR, Over Cut.

Fig. 1 Powder-mixed EDM
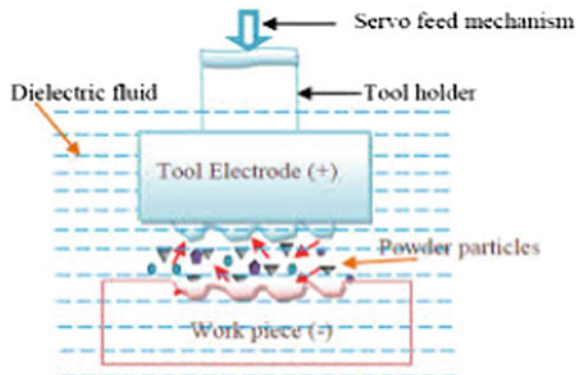
3. To determine the global solutions for optimal cutting parameters of PMEDM operation Taguchi methodology has to be adopted.
4. ANOVA method has been adopted to analyze the experimental results using the signal to noise(S/N) ratio.

1.1 Literature Review

From literature review, it is clear that when powder additive mixed in dielectric it successfully helpful to overcome the limitation of conventional EDM machining process. It was observed from review, although a lot of work has been done in the field of PMEDM using various powders such as titanium, silicon, aluminum, graphite etc., tungsten powder has high melting point and high conductivity, but less work has been performed using it (Table 1).

2 Experimental Setup and Procedure

In this study, set of experiments were carried out on Elecktra Plus electrical discharge machine; model SMART ZNC with modifications which has to be done for PMEDM method as shown in Fig. 1. A new container was developed with a capacity of 6.5 L for EDM oil which has to be placed in the empty machining tank shown in Fig. 2. Experiments were performed in that container with EN-19 (specimen 51 mm × 26 mm × 5 mm) as work piece, cylindrical copper tungsten electrode (φ 15.0 mm) as an electrode. The flow system of dielectric was modified for circulation of powder additives in dielectric medium in small quantities to prevent contamination of whole of dielectric fluid for conducting the experiments. According to Cause–Effect diagram powder concentration, current and pulse on time by keeping other variables as constant. These three design variables have been selected for orthogonal array (L9) methodology. The machining process parameters for this setup as shown in Table 4 (keeping all other parameters constant) (Table 2).

Table 1 (Review of PMEDM)

Author/year	Process parameters	Tool electrode	Work piece	Powder	Research finding
Batish et al. [4]	Current Pulse on time Powder Over cut	Graphite, W-Cu, Brass	H11 HCHCr AISI1045	Si Graphite W	• The MRR & Over cut increases with addition of the powder • TWR reduced by adding powder additives
Batish et al. [4]	Pulse on Pulse off time current powder	Cu, W-Cu	EN-31, H11, HCHCr	Graphite, Al	• 80 % increase in micro hardness after PMEDM • Graphite powder was found to be most suitable for achieving higher micro hardness
Reddy et al. (2014)	Peak current pulse on time duty factor gap voltage powders	Cu	AISID3, EN 31	Al, Cu	• MRR increases by metal powder additives • SR improves by adding Al powder in dielectric fluid than that of Cu powder and without powder
Singh et al. (2009)	Powder Concentration Peak Current Pulse ON Duty Cycle	Cu	EN24	W	• MRR increases in Powder-Mixed EDM
Kumar et al. (2010)	Polarity Peak Current Pulse on time Gap voltage Powder concentration Duty cycle	Cu, Cryogenically cooled Cu	Inconel 718	Graphite	• MRR increases due to powder additives
Lal et al. [9]	Polarity Peak Current Pulse on time Gap voltage Powder concentration	Cu	SKD11	Ti	• MRR increases and TWR decreases using Titanium powder additives
Singh et al. (2013)	Peak current, powder concentration	Cu	Al6063	Si	• SR decreases with the addition of silicon powder in the dielectric
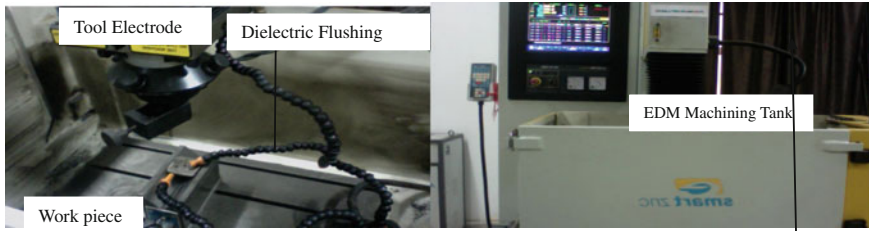
Fig. 2 Experimental setup for PMEDM

Table 2 Composition of work piece-EN-19

Elements	C	Si	Mn	Cr	Mo
Composition (wt. in %)	0.035–0.045	0.1–0.35	0.5–0.8	0.9–1.5	0.2–0.4

2.1 Experimental Design and Procedure

(Table 3)

2.2 Result and Discussion

A. MRR calculation

MRR is selected as a response variable as it is directly proportional to the machining efficiency which has to be calculated by weight loss method. For calculating MRR, the specimen has to be weighed before and after each run using electronic balance having a resolution of 0.01 gm (Tables 4 and 5).

Table 3 Process parameters with their Levels

Sl. No.	Designation	Factors	Level-1	Level-2	Level-3
1	A	Current	3	5	7
2	B	Pulse on time (μs)	20	50	100
3	C	Work piece	EN-19		
4	D	Duty factor (%)	50 %		
5	E	Powder type	W		
6	F	Powder Conc. (G/L)	0	5	10
7	G	Flushing pressure (kg/cm^2)	100		
8	Open-circuit voltage		70 ± 5 %		
9	Polarity straight		Electrode positive polarity		
10	Machining time		10 min		

Table 4 Experimental design matrix OA L9

Powder concentration	Current	Pulse time	MRR	TWR	Over Cut
0	3	20	4.085	1.56	0.01
0	5	50	4.4	2	0.07
0	7	100	8.93	3.75	0.07
5	3	50	0.89	0.69	0.1
5	5	100	9.2	1.2	0.17
5	7	20	7.93	0.31	0.1
10	3	100	17.25	1.55	0.24
10	5	20	15.33	0.03	0.16
10	7	50	14.47	1.27	0.22

$$\frac{W_i - W_f}{\rho \times t} \times 1000 \, \text{mm}^3 / \min \tag{1}$$

where

W_i Initial weight of work piece material (grams)
W_f Final weight of work piece material (grams)
t Time period of trails in minutes
ρ Density of work piece in grams/cm^3

As this experimental design is orthogonal (L9), now it is possible to separate out the effect of each parameter at different levels. All observations are transformed into S/N ratio and mean S/N ratio also has been calculated using MINITAB-17. The analysis and graphical presentations are being also done by MINITAB.

B. Taguchi Analysis for MRR

The S/N ratios have been calculated to identify the major contributing factors and its interactions with other process parameters due to which variation in MRR possible. MRR is "Larger is better" type response given by

$$(\text{S/N}) \, \text{HB} = -10 \log (\text{MSD}) \, \text{HB} \tag{2}$$

MSDHB = Mean Square Deviation for higher-the-better response.
ANOVA Analysis For MRR, TWR

To study the significance of the process parameters affecting the quality characteristic, i.e. MRR, TWR, ANOVA test has been done by General Linear Model. For $\alpha = 0.05$, the value of $F_{0.05}, 1.8 = 3.46$ [10]. Now if the value of F_0 is greater than 3.46 than it shows the significant (For lower p-value) (Table 6).

General Linear Model

Empirical expressions have been developed to evaluate the relationship between process and response variables. ANOVA analysis showed that powder

Table 5 Main effect for means: MRR, TWR, and Over Cut

Response Table for S/N Ratios for MRR, TWR, Over Cut

For MRR "Larger is better"				For TWR "Smaller is better"				For OC "Smaller is better"			
Level	Concentration	Current	Pulse ON	Level	Concentration	Current	Pulse ON	Level	Concentration	Current	Pulse ON
1	14.79	17.75	17.97	1	−7.79	3.93	12.79	1	27.83	24.91	25.38
2	19.01	18.89	18.35	2	2.86	7.43	−1.98	2	17.72	18.13	18.3
3	22.98	20.15	20.47	3	14.47	−1.82	−1.27	3	15.15	17.67	17.02
Delta	8.19	2.41	2.49	Delta	22.26	9.25	14.78	Delta	12.68	7.24	8.36
Rank	1	3	2	Rank	1	3	2	Rank	1	3	2

Table 6 Analysis of Variance (ANOVA) for MRR and TWR, using Adjusted SS for Tests

ANOVA For MRR

Source	DF	Seq SS	Adj SS	Adj MS	F	P
Current	2	19.4	19.4	9.7	68.39	0.02
Powder Concentration	2	2.13	2.13	1.07	7.53	0.01
Pulse on time	2	6.51	6.51	3.25	22.94	0.04
Residual Error	2	0.28	0.28	0.14	–	–

Total 8 28.3253

S = 0.3766 R-Sq = 99.0 % R-Sq(adj) = 96.0 %

Regression Equation is MRR = 1.92 + 0.825 Concentration + 0.498 IP + 0.0201 TON (3)

ANOVA For TWR

Source	DF	Seq SS	Adj SS	Adj MS	F	P
Current	2	64.07	64.07	32.04	64.49	0.03
Powder Concentration	2	4.54	4.54	2.27	4.57	0.02
Pulse on time	2	11.69	11.69	5.84	11.77	0.08
Residual Error	2	0.99	0.99	0.5	–	–

Total 8 81.3018

S = 0.7048 R-Sq = 98.8 % R-Sq(adj) = 95.1 %

The regression equation is TWR = −0.137−0.226 Concentration + 0.316 IP + 0.0189 TON (4)
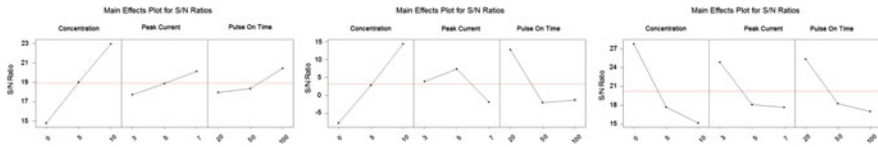
Fig. 3 Graph for main effect plot for MRR, TWR, Over Cut

concentration is the most significant in controlling MRR. From Fig. 3 graph optimum combination of factors for MRR is: A3, B3, F3. For optimum combination for higher machining efficiency theoretical optimum MRR is required to be calculated. The estimated S/N ratio using the optimal level of the design parameters can be calculated as follows:

$$n_{opt} = n_m + \sum a_{i=1}(n_i - n_m) \tag{3}$$

where

n_m Total mean S/N ratio = 20.92
n_i Mean S/N ratio at optimum level
a Number of main design parameter
N_{opt} 20.92 + (17.97 − 20.92) + (19.01 − 20.92) + (22.98 − 20.92) = 18.12
    Optimal value of S/N ratio = 18.12.
    The formula used for calculating the theoretical optimal value of MRR is given as

$$y^2 = \frac{1}{10^{\frac{-nopt}{10}}}$$
$$y_{opt} = 0.122 \, mm^3/min \tag{4}$$

Theoretical optimal value of MRR for this experiment is 0.122 mm³/min. To verify the improvement in MRR a confirmation experiment has been performed (Table 7).

As shown in the above table, the experimental values for optimal condition of MRR nearly related with prediction. The maximum deviation of predicted values from experimental values is nearly equals to 1 %. Hence, the experimental values

Table 7 Results of confirmation experiments

Optimal condition	MRR Predicted mm³/min	MRR Experiment mm³/min	Error MRR %
A3 B3 F3	0.122	0.338	0.64

confirms the optimization of MRR using Taguchi single objective factor analysis method and the resulting numerical model seems to be capable of predicting MRR.

3   Conclusion

A simplified model of PMEDM has been developed to enhance machining efficiency. The optimal setting of the parameters for a multicharacteristic process done by Taguchi's approach and utility concept. The conclusions of this work are summarized as follows:

Performance parameters	Optimal condition	Process parameters
MRR	A3 B3 F3	Current at 7A, pulse ON time at 100 μs, powder Concentration at 10 g/lt
TWR	A2 B1 F3	Current at 5A, pulse ON time at 20 μs, and powder Concentration at 10 g/lt
Over Cut	A1 B1 F1	Current at 3A, pulse ON time at 20 μs, powder Concentration at 0 g/lt

References

1. S.K Choudhary, Dr. R.S Jadoun, Current Advanced Research Development of Electric Discharge Machining (EDM): A Review (2014), International Journal of Research in Advent Technology, Vol. 2, No. 3, E-ISSN: 2321–9637.
2. G. Talla, D. K. Sahoo, S. Gangopadhyay, C.K. Biswas, Modeling and multi-objective optimization of powder mixed electric discharge machining process of aluminum/alumina metal matrix composite, Engineering Science and Technology, an International Journal 18 (2015) 369–373.
3. S. Singh, C.S. Kalra, Experimental Study of PMEDM on EN 24 Steel with Tungsten Powder in Dielectric, (2014), International Journal on Emerging Technologies 5(1): 153–160, ISSN No. (Online) : 2249–3255.
4. A. Batish, A. Bhattacharya, V. K. Singla, and G. Singh. Study of material transfer mechanism in die steels using powder mixed EDM. (2012,) Materials and Manufacturing Processes 27:449–456.
5. S. Goyal, R. K. Singh, Parametric Study of Powder Mixed EDM and Optimization of MRR & Surface Roughness (2014), International Journal of Scientific Engineering and Technology 3 (1), 56–62.
6. F.Q. Hu, F.Y. Cao, B.Y. Song, P.J. Hou, Y. Zhang, K. Chen, J.Q. Wei, Surface properties of SiCp/Al composite by powder-mixed EDM (2013), Procedia CIRP 6, 101–106.

7. A. Agrawal, A. Dubey, P. K. Shrivastava, Modeling and Optimization of Tool Wear Rate in Powder Mixed EDM of MMC, (2013), 2nd International Conference on Mechanical and Robotics Engineering, pp. 1–6.
8. A. Singh, R. Singh, Effect of Silicon Powder Mixed EDM on Surface Roughness of Al6063 Aluminium Alloy, IJIRST –International Journal for Innovative Research in Science & Technology| Volume 2 | Issue 03 | August 2015 ISSN (online): 2349–6010.
9. H. Lal, V. Sharma, P. Singh, Study of Wear Ratio of SKD11 Steel in Titanium Abrasives Mixed Electrical Discharge Machining, (2015), International Journal of Emerging Research in Management &Technology ISSN: 2278–9359 (Volume-4, Issue-7).
10. A. Bhattacharya, and A. Batish, Effect of process variables on micro hardness, grain size and strain during machining of various die steels with PMEDM using dummy treated experimental design.(2012), Proceedings of the Institution of Mechanical Engineers, Part B: Journal of Engineering Manufacture 226(7):1192–1204.
11. A. Bhattacharya, A. Batish, and N. Kumar. (2013). Surface characterization and material migration during surface modification of die steels with silicon, graphite and tungsten powder in EDM process. Journal of Mechanical Science and Technology 27(1):133–140.
12. A. Bhattacharya, A. Batish, and G. Singh. (2011). Surface modification of high carbon high chromium, EN31 and hot die steel using pow der mixed EDM process. Materials Science Forum 701:43–59.
13. A Bhattacharya., A. Batish, G. Singh, and V. K. Singla. (2012). Optimal parameter settings for rough and finish machining of die steels in powder mixed EDM. International Journal of Advanced Manufacturing Technology 61(5–8):537–548.
14. H. Kansal, K., S. Singh, and P. Kumar. Effect of silicon powder mixed EDM on machining rate of AISI D2 die steel. (2007) Journal of Materials Processing Technology 9:13–21.
15. A. Kumar, S. Maheshwari, C. Sharma, and N. Beri. Research developments in additives mixed electrical discharge machining (AEDM): a state of art review. (2010), Materials and Manufacturing Processes 25(10):1166–1180.
16. S. Kumar, R. Singh, T. P. Singh, and B. L. Sethi. Surface modification by electrical discharge machining: a review. (2009) Journal of Materials Processing Technology 209:3675–3687.

A Spring-Activated Quick-Response Mechanism for Legs of a Mooring Mast: Conceptual Design and Analysis

Utsav Bhardwaj, Syed Khaleelullah and Rajkumar S. Pant

Abstract A mooring mast is used for safe and secure ground-handling of airships. It occupies space, and hence there is a need to make it foldable and portable. The mast is provided with long legs to have adequate ground-stability; hence it is important for the legs to be quickly foldable. This paper describes a mechanism designed to enable quick unlocking and folding as well as quick unfolding and locking of the legs, in an appropriate orientation. The mechanism employs a spring-activated quick-response rod. Kinematic analysis of the mechanism and stress analysis of its key components have also been carried out.

Keywords Mooring mast · Ground-stability · Flexibility · Spring-activated · Kinematic analysis · Stress analysis

Nomenclature

L_N	Length of the notch = Radius of curvature of the circular periphery of the notch (m)
D_L	Outer diameter of the mast-leg (m)
k	Stiffness of the compression spring (N/m)
F_N	Constant force required to be applied by the operator on the mast-leg during unfolding process (N)
θ	Angle measured from the vertical reference line in the anticlockwise direction, at which the leg touches the circumferential periphery of the notch (Degree)
x	Instantaneous compression of the spring (m)

U. Bhardwaj (✉) · S. Khaleelullah · R.S. Pant
Department of Aerospace Engineering, Indian Institute of Technology Bombay,
Powai, Mumbai 400076, India
e-mail: u.bhardwaj88@yahoo.in

S. Khaleelullah
e-mail: syedkhaleelullah1990@gmail.com

R.S. Pant
e-mail: rkpant@aero.iitb.ac.in

σ_c	Axial compressive stress and bending stress, respectively, for the situation under consideration (N/m^2)
A_{NM} and A_{NL}	Maximum and minimum stress-resisting area for the notch respectively (m^2)
S_{yt}, S_{yc} and S_{sy}	Yield-tensile strength in tension, compression and shear, respectively, of the material/joint under consideration (N/m^2)
F.O.S.	Factor of safety

1 Introduction

Airships belong to a family of Lighter-Than-Air (LTA) systems, which develop a principle part of their lift force by the buoyancy of an LTA gas filled in their envelopes. Airships had gone into oblivion due to the connotation of being unsafe, and also because their operations are very much dependent on ambient weather conditions. However, they are making a comeback for specific roles and applications, such as a long endurance aerial platform for surveillance and aerial photography. Several agencies all over the world are exploring the use of small remotely controlled airships for these and other interesting applications.

Due to the large size and buoyant nature of airships, their ground-handling is usually considered as a serious problem [1]. A structural module known as "mooring mast" is needed for its safe and secure ground-handling. When the mast is not to be used for a long period of time, it is recommended to keep it at a suitable location to avoid damage due to corrosion. However, a mooring mast consumes a lot of storage space. Portability and foldability are the key design requirements for a mooring mast. To ensure adequate ground-stability, the legs of the mast are generally made quite large, and hence foldability of the mast legs is one of the most important factors that affect the overall foldability of the mooring mast. Several mooring masts [2–4] have already been designed, fabricated and field-tested at Lighter-Than-Air Systems Laboratory, Department of Aerospace Engineering, IIT Bombay, but none of them is having the provision for quick folding and unfolding of the legs with ease. In this paper, we present a simple mechanism that can allow quick unlocking and folding of the legs, when the mast is not to be used; and quick unfolding and locking of the legs, when the mast is to be used.

2 Conceptual Design of the Quick-Response Mechanism

The quick-response mechanism has been modeled and designed taking into consideration the two mooring masts, designed, fabricated and tested at LTA Systems Lab, IIT Bombay, as shown with the moored airships in Fig. 1a, b [5].
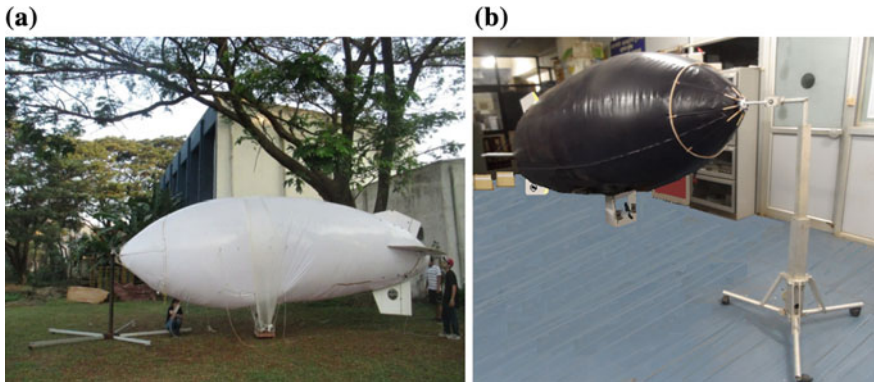
Fig. 1 **a** Mooring mast for outdoor airship [5], **b** mooring mast for indoor airship [5]

Figure 2a shows the conceptual design of the quick-response mechanism. The casing is a U-shaped strip having two aligned circular holes in its two lateral (side) strips "S_1" and "S_2", one in each. The base-strip of the casing has four holes in it, to allow mounting of the mast legs. For the present case, modules are to be mounted over some extensions of the mast-base, as shown in Fig. 2b. Across "S_1" and "S_2", there is a rod passing throughout. One end of this cross-rod contains a knob, and at the other end, a curved notch is attached, as can be seen in Fig. 2a.

The mechanism is to be mounted over the extension of the mast-base in such a way that the axis of the cross-rod is perpendicular to the axis of the mast-leg. The profile of the notch surface is almost a quarter-circle, geometrically same as the cross-section of the mast-leg with which this mechanism is to be used, i.e., we have, $L_N = D_L/2$.

A through slot of rectangular cross-section is made in each leg, exactly where the notch faces the fully opened leg. This slot is to be in a vertical plane, when the leg is in fully unfolded orientation. A compression spring is mounted over the cross-rod
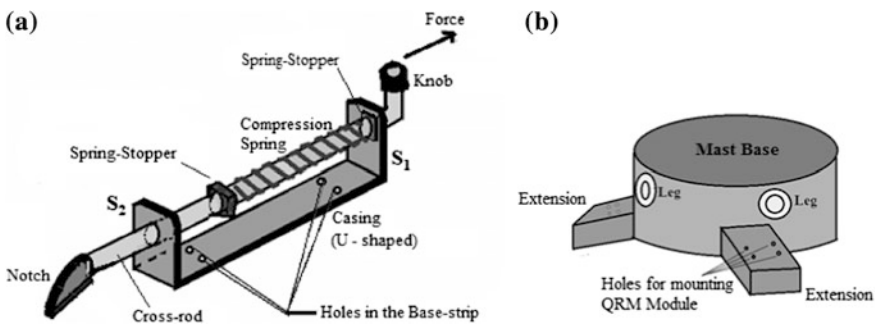
Fig. 2 **a** Conceptual design of the Spring-activated quick-response mechanism, **b** extensions of the mast-base for mounting the QRM module

between the stoppers. This spring can easily be designed using various design equations [6]. This quick-response mechanism is applicable only for masts with legs of circular cross-sections, which are hinged permanently near their end, where they are joined with the mast-base [2]. Thus, in order to use this mechanism with the currently existing masts, these masts need some modifications at their respective legs.

3 Operation of the Quick-Response Mechanism

When the leg is unfolded as shown in Fig. 3, its bottom curved surface touches the notch, pushing it backwards. Rod "R" will slide backwards through the casing and the spring will be compressed.

The leg pushes notch backwards very smoothly and gently, rubbing its lower surface at the notch. During this course of action, whatever force acts on the notch perpendicular to the axis of cross-rod, will be balanced by an equivalent reaction from the mounting arrangement, and only the force-component along the cross-rod will be the dynamic one. Now, as soon as the rectangular hole in the leg will come in front of the sliding notch, the notch will suddenly and quickly get into it with a jerk and hence, will lock the leg in that position. The spring will be released. The knob will again get its initial position. The notch will now be lying in one-half of the rectangular hole of the leg. Even this cavity in the leg can be made only up to axis of the leg for better strength. Note that the rectangular hole is along the lateral side of the leg, so that rectangular hole will exactly face the notch thoroughly only after the leg would have become horizontal. This ensures the locking of legs in the horizontal position, ensuring the horizontality of the mast-base too. The
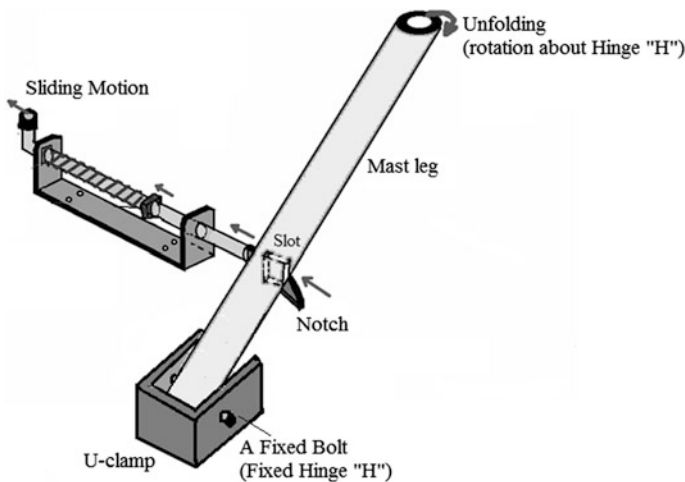
Fig. 3 Unfolding of the mast leg

longitudinal axis of the mooring mast will be perpendicular to the ground then. This leads to stability and accuracy of the mooring mast on the ground during its field application. To fold the leg back and to make it touch to the vertical portion of the mast in the folded position, the knob can be pulled backwards by hand. As soon as the notch comes out of the rectangular hole of the leg, the leg can be folded. The effort required in folding and unfolding of the leg depends solely on the stiffness of the compression spring and mass of the leg. This effort is very small, owing to the stiffness of the compression spring, which is taken small, as the stiffness of the spring has no role to play in deciding the strength and stability of the legs of the mooring mast. Also, the mechanism has been named as "quick-response", since, as soon as the leg is straightened and made parallel to the ground, the contoured bolt responds back very quickly to lock the leg.

4   Mechanical Analysis of the Quick-Response Mechanism

As one starts unfolding a leg, it will touch the uppermost curved surface of the notch at its end "N_1". Till this stage, the person unfolding the leg had to take care only of the self-weight of the mast-leg. But, as soon as the leg touches the notch at "N_1", the true operation of the quick-response mechanism starts. Compression of the spring becomes maximum when the point "N_2" of the notch comes in front of the leg. The line of contact between the leg and the curved surface of the notch slides from the point "N_1" to the point "N_2". A constant force (assumed to be constant for analysis) "F_N" is required to be continuously applied over the leg by the operator during the course of unfolding the leg, and the force exerted by the leg on the notch also equals "F_N". It will always be normal to the circular periphery of the notch. Thus, the point of application of force "F_N" over the notch slides from point "N_1" to the point "N_2" as the leg is unfolded and locked, as shown in Fig. 4a. The force "F_N" acting on the notch at any general point "N", which is at any angle "θ" measured in the anticlockwise direction from the reference line "OM", can be resolved into two components, one component (F_H) parallel to the axis of the contoured bolt and another one (F_V) perpendicular to the axis of the contoured bolt. These components have been shown in Fig. 4b. These components are mathematically given by
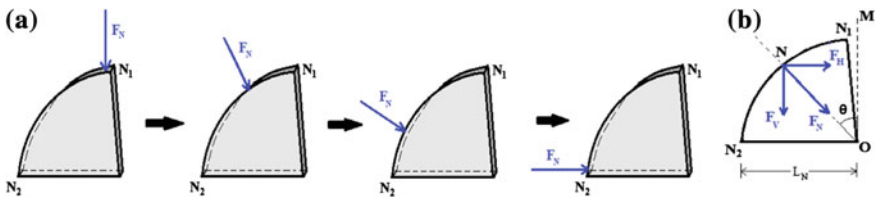
Fig. 4   a Sliding of the point of application of force "F_N" over the notch, **b** resolution of the force "F_N"

$$F_H = F_N \sin \theta \qquad (1)$$

$$F_V = F_N \cos \theta \qquad (2)$$

"OM" is being taken as the reference line to specify any point over the notch as a function of its angle "θ" measured from "OM" in the anticlockwise direction. "OM" is a line perpendicular to the base of casing. It is to be worth noted that angle "MON_1" is not to be taken as $0°$. Otherwise, it would not be practically possible at all to give a start to the sliding motion of the contoured bolt backwards by moving and forcing the leg over the notch. Thus, some suitable nonzero value, say $5°$–$10°$ can be chosen for angle "MON_1". For simplicity in the stress analysis, angle "MON_2" has been taken as equal to $90°$. The results will not be having any error practically, if the F.O.S. is taken a little bit more.

Suppose, when the leg touches the notch at point "N", the spring has been compressed by an amount "x" till that time. At that instant,

$$F_H = k\, x \qquad (3)$$

$$\text{implying} \quad F_N = \frac{kx}{\sin \theta} \qquad (4)$$

At the very initial stage, the situation is specified by these set of conditions, $\theta = \text{close to}\, 0°, x = 0$ and $F_V \approx F_N$.

Also, at that instant, when the leg is at the verge of getting locked, we have $\theta = 90°, x = L_N$ and $F_V = 0$.

We have

$$F_N = (k)(L_N) \qquad (5)$$

$$\text{and} \quad F_{HM} = (k)(L_N) \qquad (6)$$
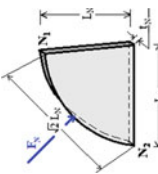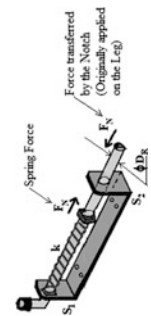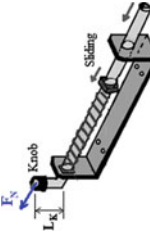
Equation (5) gives the value of constant force "F_N" required to be applied by the operator on the leg.

Also, "F_V" varies from a maximum value "F_{VM}" (approximately "F_N") to zero.

5   Stress Analysis of the Quick-Response Mechanism
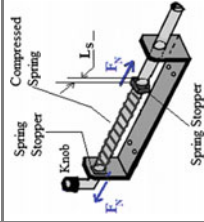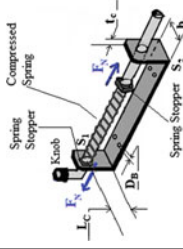
The stress analysis for the different parts of the mechanism and the various joints used within the mechanism has been carried out in details. The force diagrams, stresses involved and the recommended materials have been shown in Table 1. There are almost no chances of buckling [7] of the cross-rod owing to its small length and restrictions. Further, the knob should be made with the cross-rod itself by upsetting forging process leading to the bending of the grains [8]. For stresses

Table 1 Component wise stress analysis

Component	Dimensions and forces	Maximum stress (nature)	Design equation	Suggested material
Notch		$\sigma_{NcM} = \dfrac{k}{t_N}$ (compressive)	$\sigma_{NcM} = \dfrac{k}{t_N} = \dfrac{S_{yc}}{\text{F.O.S.}}$	Mild steel [MS-2062 (MS-Bright)]
Joint of notch and cross-rod	Separate figure not required	$\tau_N = \dfrac{F_N}{L_N t_N}$ (shear stress)	$\tau_N = \dfrac{S_{sy}}{\text{F.O.S.}}$	Ductile material like mild steel $(S_{yc} = S_{yt})$ [6]
Cross-rod		$\sigma_{Rc} = \dfrac{F_N}{(\pi D_R^2/4)}$ (axial compressive stress) (to be used for design as per maximum shear stress theory [6]) $\tau_R = \dfrac{F_N}{4\left(\frac{\pi D_R^2}{4}\right)} = \dfrac{F_N}{\pi D_R^2}$ (quarter-shear)	$\sigma_{Rc} = \dfrac{S_{yc}}{\text{F.O.S.}}$ $\tau_R = \dfrac{S_{sy}}{\text{F.O.S.}}$	Ductile material like mild steel $(S_{yc} = S_{yt})$ [6]
Knob		$\sigma_b = \dfrac{32 M_K}{\pi D_R^3} = \dfrac{32 F_N L_K}{\pi D_R^3}$ (bending stress) $\tau_K = \dfrac{F_N}{(\pi D_R^2/4)}$ (shear stress at 90° bend) (to be used for design)	$\sigma_b = \dfrac{S_{yc}}{\text{F.O.S.}}$ $\tau_K = \dfrac{S_{sy}}{\text{F.O.}}$	Mild steel [MS-2062 (MS-Bright)]

(continued)

Table 1 (continued)

Component	Dimensions and forces	Maximum stress (nature)	Design equation	Suggested material
Spring-stopper		$\tau_S = \dfrac{F_N}{\pi D_R L_S}$ (shear stress at the joint between one spring-stopper and the cross-rod)	$\tau_S = \dfrac{S_{sy}}{\text{F.O.S.}}$	Mild steel [MS-2062 (MS-Bright)]
Casing		$(\sigma_c)_{\text{Net}} = \sigma_b + \sigma_c$ $= \dfrac{6 F_N L_C}{\pi D_R^3} + \dfrac{F_N}{2(b_c t_c)}$ (net compressive stress) $\tau_C = \dfrac{F_N}{4 D_B t_c}$ (shear stress in the base-strip)	$(\sigma_c)_{\text{Net}} = \dfrac{S_{yc}}{\text{F.O.S.}}$ $\tau_C = \dfrac{S_{sy}}{\text{F.O.S.}}$	Mild steel [MS-2062 (MS-Bright)]

involved in the casing, though the compressive stress due to normal loading and bending load are maximum at different instants of time, still, to get net compressive stress, the maximum values of these two have been added, to have better safety. Using the stated design procedure, dimensions of the various components of the mechanism can be found out. The mechanism is to be designed mast specific. The actual dimensions will depend upon the actual weight and size of the mast legs. Also, the final dimensions are to be kept considerably larger than those found out using this procedure to give a very high F.O.S., since the effect of stress concentration [6] has not been taken into account.

6 Summary and Conclusions

The basic conceptual design of the spring-activated quick-response mechanism has been established which allows the quick unlocking and folding, and quick unfolding and locking of the legs of a mooring mast, to induce in it the properties of foldability and portability. This mechanism in conjunction with the mast legs is not at all readily available yet. Broadly speaking, it has some features common with a generic spring loaded bolt, but, there are far more additional and beneficial features added in order to make it implementable for the purpose of controlling the operations of folding and unfolding of mast legs. The notch serves the purpose of establishing one-to-one interaction of the mechanism with the leg. It adds a good mechanical advantage to it, enabling quick operations needing very small human efforts.

References

1. D. Howe, Mooring in: G.A. Khoury (ed.), Airship Technology, second ed., Cambridge Aerospace Series: 10, Cambridge University Press, London, 2012, pp. 258–277.
2. S. Khaleelullah, U. Bhardwaj, and R.S. Pant, "Design and Fabrication of the Mooring Masts for Remotely Controlled Indoor and Outdoor Airships", *Proceedings of the 20th AIAA Lighter-Than-Air Systems Technology Conference*, Daytona Beach, FL, USA, March 2013.
3. S.M. Kale, and R.S. Pant, "Structural Design of Mooring Mast for a Remotely Controlled Airship", *Proceedings of the 5th International Convention of The Airship Association*, Oxford, England, August 2004.
4. A. Goyal, D. Pandey, and R.S. Pant, "Design of a Portable Mooring Mast with Drag Force Measuring Device for Remotely Controlled Airships", *Proceedings of the 19th AIAA Lighter-Than-Air Systems Technology Conference*, Virginia Beach, Norfolk, Virginia, USA, September 2011.

5. S. Khaleelullah, U. Bhardwaj, and R.S. Pant, "Design, Fabrication and Testing of Mooring Masts for Remotely Controlled Indoor and Outdoor Airships", *Journal of The Institution of Engineers (India): Series C*, Springer, ISSN: 2250-0553 (electronic version) (to appear).
6. VB Bhandari, Design of Machine Elements, Tata McGraw Hill Education Private Limited, 8th reprint of 3rd edition, ISBN-13: 978-0-07-068179-8, New Delhi, 2012.
7. G.H. Ryder, Strength of Materials, Macmillan Publishers India Limited, reprint of 3rd edition with SI units (1969), ISBN-13: 978 0333-93536-1, Chennai, 2009.
8. P.N. Rao, Manufacturing Technology: Foundry, Forming and Welding, Tata McGraw Hill, 21st reprint of 2nd edition, ISBN 0-07-463180-2, New Delhi, 2007, pp. 254–255.

Aluminum Agglomerate Size Measurements in Composite Propellant Combustion

K. Jayaraman and G. Boopathy

Abstract Experimental and numerical investigation have been done to evaluate the aluminum agglomerate size in AP/HTPB/Aluminum propellants and compared it with burning rate results. Bimodal AP particle size distribution is considered in the present work. The effect of aluminum size, aluminum content, fine AP size, fine AP/binder ratio and coarse AP size in aluminum ignition, accumulation and agglomerate formation during combustion, typically in their ranges, are focused. The burning rates were found to be higher for the propellants with lower fine AP/binder ratio. The agglomerate sizes for the propellants with 10 % Al was found to be higher than those with 15 and 18 % aluminum. Observing the agglomerate sizes and the burning rate trends, it can be concluded that the agglomerate sizes vary inversely as the burning rates.

Keywords Agglomerate · Composite propellant combustion · Aluminum propellant · Burning rates

1 Introduction

Aluminum is the most widely used metal due to its abundance, nonreactivity during mixing and storage, nontoxicity, and its ability to reduce H_2O and CO_2 to lower molecular weight gases such as H_2 and CO. Compared with other ingredients, the A1 particles have a unique tendency of igniting reluctantly and accumulating on the burning surface, thus forming relatively large agglomerates that burn relatively slow after leaving the burning surface.

K. Jayaraman (✉)
IIT Madras, Presently at ICARE-CNRS, Olreans, France
e-mail: jayaraman78@gmail.com

G. Boopathy
Department of Aeronautical, Vel Tech University, Chennai, India

2 Experimental Details

2.1 Propellant Samples

Ammonium perchlorate (AP) used in the present work is obtained from Tamil Nadu Chlorates Ltd, Madurai, India. The purity of AP is >99 %, and it does not contain any anticaking agents. The micro-aluminum of 15 μm in size is obtained from MEPCO, Madurai, India. Hydroxyl terminated polybutadiene (HTPB) is used as a prepolymer, which functions as the hydrocarbon fuel. Di-octyl adipate (DOA) acts as plasticizer and toluene di-isocyanate (TDI) or isophorone di-isocynate (IPDI) plays the role of a curing agent. Three baseline formulations are taken for each case, i.e., non-aluminized, nano-aluminized, and normal aluminized: (1) fine AP/binder ratio = 60/40 and fine AP size of 20 μm; (2) fine AP/binder ratio = 60/40 and fine AP size of 5 μm; and, (3) fine AP/binder ratio = 65/35 and fine AP size of 5 μm. The effects of aluminum content, aluminum size and variation are studied.

2.2 Burning Rate Measurement

Burning rate measurements were performed over the pressure range from 1 to 12 MPa with the step of 1 MPa by using combustion photography method. The samples were ignited using hot nichrome wire. A window bomb is used for this purpose; it is a pressure vessel consisting of two windows, one to illuminate the sample and another used to view the combustion process by CCD camera. More than 60 % of the tests are repeated at least once, and burning rates obtained within a repeatability of 5 % is considered acceptable.

2.3 Agglomerate Collection and Size Analysis

The quench collection bomb is a stainless steel pressure vessel which is designed to withstand a maximum working pressure of 20 MPa. The Sauter mean diameter (SMD), which is a representative of the ratio of volume to the surface area, is considered to represent the nominal size of the agglomerates. Similarly, the arithmetic mean diameter (AMD) of the agglomerates is also presented in the nominal size plots.

3 Results and Discussions

3.1 Observations on Burning Rate Trends

1. Effect of Aluminum Content

Figure 1 shows the burning rate trends of the IPDI-cured propellant with fine AP/binder ratio 65/35, fine AP size of 5 µm, coarse AP size of 450 µm and total solids loading of 87.5 %.

2. Effect of Aluminum Size

The burning rate trends of IPDI-cured propellant formulation with a fine AP/binder ratio of 60/40 and the fine AP and coarse AP sizes of 20 and 450 µm is shown in Fig. 2.

3. Effect of Coarse AP Size

The effect of coarse AP size of the propellant is examined for coarse AP sizes of 450, 350 and 250 µm with 5/75 µm fine AP/binder ratio of 60/40 with the TDI-cured. The burning rates of the propellants are shown in Figs. 3 and 4.

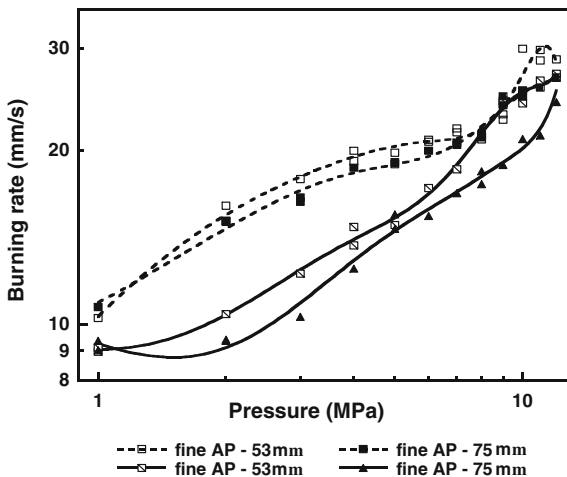**Fig. 1** Effect of aluminum content on the burning rates of IPDI – cured propellants with a fine AP/binder ratio of 65/35, m respectively µ the coarse and fine AP and Al sizes being 450 µm, 5 µm and 15
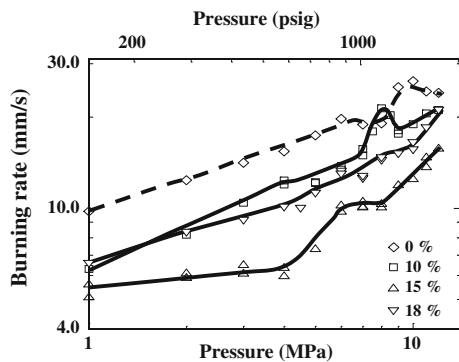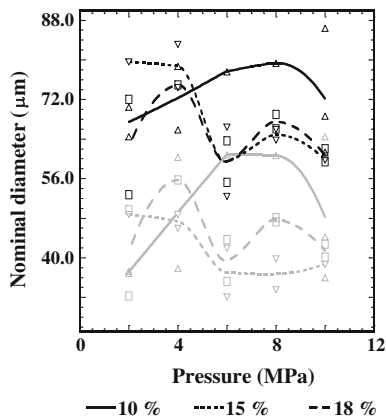

Fig. 2 Effect of aluminum size on the burning rates of IPDI-cured propellants with a fine AP/binder ratio of 60/40, containing 15% Al, with the coarse and fine AP sizes being 450 µm and 20 µm respectively
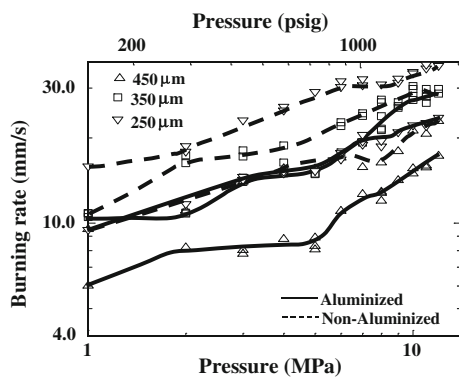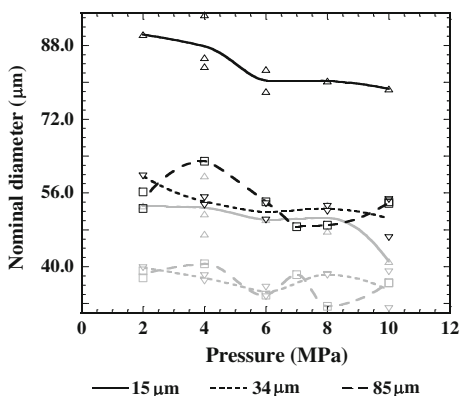
3. Effect of Fine AP/Binder Ratio

The burning rates of two propellant formulations with fine AP/binder ratios of 65/35 and 60/40, with TDI-cured and IPDI-cured are shown in Figs. 5 and 6 respectively.

4. Effect of Fine AP Size

Figures 5, 6 and 7 show the effect of fine AP size on the burning rates of propellants, with the variation in that parameter as 5, 20, 53 and 75 µm.

Observations in agglomerate sizes

The Sauter mean diameter (SMD) D_{32} and the arithmetic mean diameter (AMD) D_{10} are derived, and plotted against the pressure for comparison of variations in different formulation parameters.

Fig. 3 Effect of coarse AP size on the burning rates on TDI-cured propellants with a fine AP/binder ratio of 60/40, m size. µthe fine AP size being 5 µm, containing 15% Al of 15
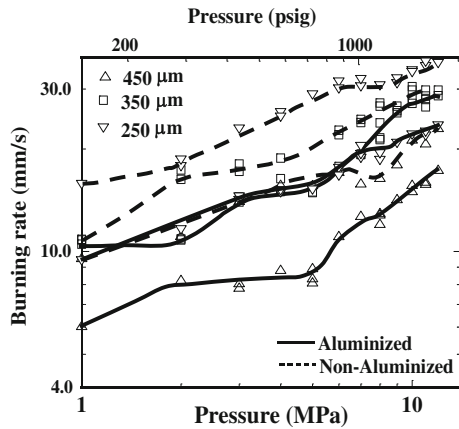
**Fig. 4** Effect of coarse AP size on the burning rates on TDI-cured propellants with a fine AP/binder ratio of 60/40, m size. µ the fine AP size being 75 µm, containing 15% Al of 15
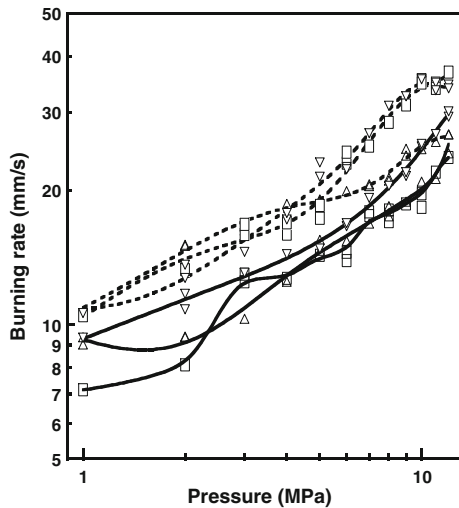
Fig. 5 Effect of fine AP/binder ratio and fine AP size on the burning rates for TDI-cured propellants with 450 μm coarse AP along with the non-aluminized burning rates

△ fine AP/binder-65/35; fAP- 5 μm
□ fine AP/binder-60/40; fAP- 5 μm
▽ fine AP/binder- 60/40; fAP- 20 μm
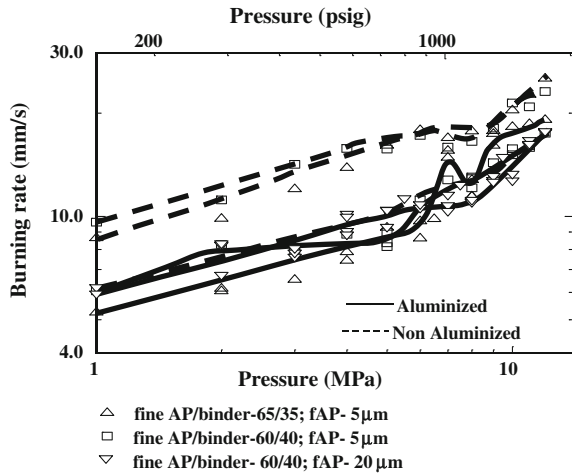
Fig. 6 Effect of fine AP/binder ratio and fine AP size on the burning rates for IPDI-cured propellants with 450 μm coarse AP along with the non-aluminized burning rates (Aluminized propellant-15% of 15 μm.)

△ fine AP/binder-65/35; fine AP- 5 μm
□ fine AP/binder- 60/40; fine AP- 5 μm
▽ fine AP/binder-60/40; fine AP- 20 μm
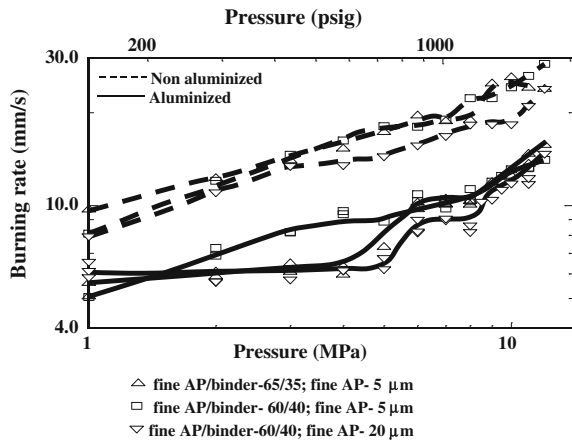
1. Effect of Aluminum Content.
The influence of aluminum content on the agglomerate sizes can be seen in Fig. 8.

Effect of Aluminum Size
The arithmetic and Sauter mean diameters of agglomerate sizes are shown in Fig. 9, for various sized Al propellants.

2. Effect of Coarse AP Size
The agglomerate sizes are plotted against the operating pressure in Figs. 10 and 11.

Effect of Fine AP/Binder Ratio
The influence of fine AP/binder ratio can be seen in Figs. 12 and 13, for TDI and IPDI-cured propellants, respectively.

Fig. 7 Effect of fine AP size on the burning rates for TDI-cured propellants with 450 μm coarse AP along with the non-aluminized burning rates (Aluminized propellant-15% of 15 μm.) (Non-aluminized – dotted line; Aluminized – solid line)

Fig. 8 Effect of aluminum content on the agglomerate sizes of IPDI – cured propellants with a fine AP/binder ratio of 65/35, the m respectively.(Grey – μ coarse and fine AP and Al sizes being 450 μm, 5 μm, 15 AMD and Black – SMD)

Fig. 9 Effect of aluminum size on the agglomerate sizes of IPDI-cured propellants with a fine AP/binder ratio of 60/40, containing 15% Al, with the coarse and fine AP sizes being 450 μm and 20 μm respectively. (Grey–AMD and Black–SMD)

Fig. 10 Effect of coarse AP size on the burning rates on TDI-cured propellants with a fine AP/binder ratio of 60/40, m size. (Grey–AMD and ◻ the fine AP size being 5 μm, containing 15% Al of 15 Black–SMD)
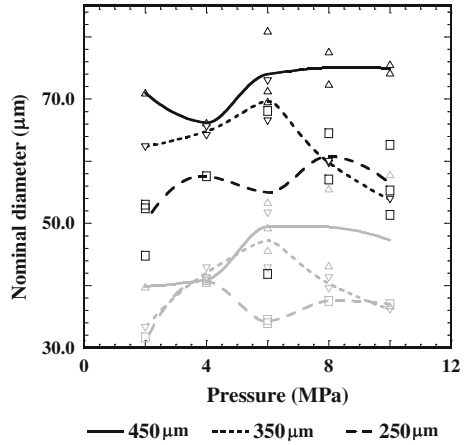
Fig. 11 Effect of higher size fine AP size on the agglomerate sizes for TDI-cured propellants, containing 15% of Al with 15 μm size (SMD – dotted line ; AMD – solid line)
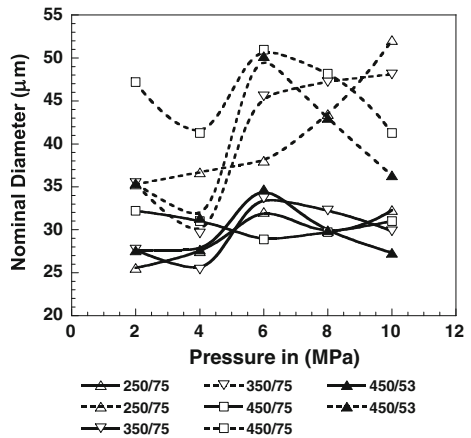
Fig. 12 Effect of fine AP/binder ratio and fine AP size on the agglomerate sizes for TDI-cured propellants with 450 μm coarse AP, containing 15% of Al with 15 μm size (Grey–AMD and Black–SMD)
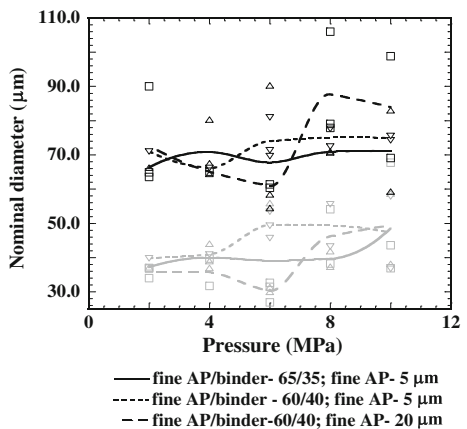
Fig. 13 Effect of fine
AP/binder ratio and fine AP
size on the agglomerate sizes
for IPDI-cured propellants
with 450 µm coarse AP
containing 15% of Al with 15
µm size (Grey–AMD and
Black–SMD)
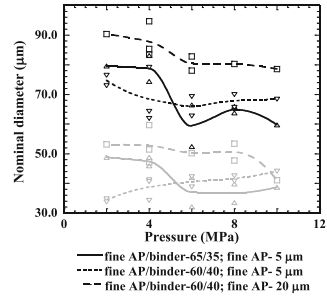
3. Effect of Fine AP Size

The effect of fine AP size on agglomerate size is shown in Figs. 11, 12 and 13 by comparing the agglomerate trends between the propellants with 5, 20, 53, and 75 µm fine AP sizes.

4   Conclusions

When Al is added to the non-aluminized propellant keeping the fine AP/binder ratio constant, the burning rates dropped. This is due to accumulation of aluminum on the burning surface, which acts as a heat sink. The reduction is nonmonotonic with Al content; an increase from 10 to 15 % further reduces the burning rate, but a further increase to 18 % restores the burning rate somewhat. When 15 µm Al is used in the propellant, the burning rates dropped with respect to the non-aluminized propellant. When the size of the Al is increased to 34 µm, the burning rates have been increased. Further increase in the Al size to 85 µm did not increase the burning rates significantly. As the coarse AP size decreased from 450 to 350 µm, the burning rates of the propellant increased, but did not significantly change with further decrease in the coarse AP size to 250 µm. The agglomerate sizes were observed to be lower for higher parent aluminum size used in the propellant. With a decrease in the coarse AP size from 450 to 350 µm, the agglomerate sizes reduced considerably. But with further reduction in the coarse AP size to 250 µm, the agglomerate sizes are not appreciably varied. The agglomerate sizes were found to increase with increase in the fine AP/binder ratio. The propellants with smaller fine AP sizes showed lower agglomerate sizes; this is due to the restricted movement of the Al particles on the propellant surface due to tightly packed fine AP-binder matrix and the higher rates of reactions due to higher exposed oxidizer surface areas.

References

1. Babuk, V. A., Belov, V. P., and Khodosov, V. V. (1988), Study of the structure of Agglomerates with Combustion of Aluminized Mixed Condensed Systems, *Physics of Combustion and Explosion*, **24(4)**, 552–557.

2. Babuk, V. A., Vasilyev, V. A. and Malakhov, M.S. (1999), Condensed Combustion Products at the Burning Surface of Aluminized Solid Propellant, *Journal of Propulsion and Power,* **15 (6)**, 783–793.

3. Babuk V. A. and Vasilyev V. A. (2002), Model of Aluminum Agglomerate Evolution in Combustion Products of Solid Rocket Propellant, *Journal of Propulsion and Power*, **18(4)**, 814–823.

4. Cohen N. S. (1983), A Pocket Model for Aluminum Agglomeration in Composite Propellants, *AIAA Journal*, **21**, 720–725.

5. Dokhan A., Price E. W., Seitzman J. M. and Sigman R. K. (2001), The Effects of Aluminum Particle Size on the Burning Rate and Residual Oxide in Aluminized Propellants, *A. AIAA/ASME/SAE/ASEE Joint propulsion conference and Exhibit,* AIAA-2001–3581.

6. Grigoriev, V. G., Kutsenogy, K. P. and Zarko, V. E. (1981), Model of Aluminum Agglomeration in Combustion of Double-Base Composition, *Physics of Combustion and Explosion*, **14(4)**, 9–17 (in Russian).

7. Grigoriev, V. G, Zarko, V. E. and Kutsenogy, K. P. (1981), Experimental Investigation of Aluminum Particle Agglomeration in Condensed System Combustion, *Physics of Combustion and Explosion*, **17(3)**, 3–10 (in Russian).

8. Jayaraman K., Anand K.V., Bhatt D.S., Chakravarthy S.R., and Sarathi R. (2009), Production, Characterization, and Combustion of Nanoaluminum in Composite Solid Propellants, *Journal of Propulsion and Power*, **25(2)**, 471–481.

9. K. Jayaraman, K. V. Anand, S. R. Chakravarthy, and R. Sarathi, "Effect of Nano-Aluminium in plateau-burning and catalyzed solid propellant combustion", Combustion and Flame, 2009, Vol. 156, No. 8, pp. 1662–1673.

10. K. Jayaraman, S. R. Chakravarthy, and R. Sarathi, "Accumulation of nano-aluminium in the combustion of composite solid propellant mixtures", Combustion, Explosion and Shockwaves, 2010, 46, 21–29.

11. K.V. Anand, A. Roy, I. Mulla, K. Balbudhe, K. Jayaraman, S.R. Chakravarthy, Experimental data and model predictions of aluminium agglomeration in ammonium perchlorate-based composite propellants including plateau-burning formulations, *Proceedings of the Combustion Institute,* 34, 2013, 2139–2146.

12. Povinelli, L. A. and Rosenstein, H. A. (1964), Alumina Size Distributions from High Pressure Composite Solid Propellant Combustion, *AIAA,* **2**, 1754–1760.

13. Price, E. W. (1984), Combustion of Metallized Propellants, chapter 9 in *Fundamentals of Solid Propellant Combustion*, Kuo, K. K. and Summerfield, M. (eds.), Progress in Astronautics and Aeronautics, **91**, AIAA, Washington, DC.

14. Sambamurthi J. K., Price E. W., and Sigman R. K. (1984), Aluminum Agglomeration in Solid Propellant Combustion, *AIAA Journal*, **22**, 1132–1138.

15. Zarko, V. E. (1998), Metal Combustion in Rockets, Chapter 10, 301–353, *Modeling and Performance Prediction in Rockets and Guns*, Chakravarthy, S. R. and Krishnan, S. (eds.), Allied Publishers, Chennai, India.

Handling Simulation and Experimentation of an Armoured Multi-axle Vehicle with Multi-axle Steering

V.V. Jagirdar, V.P. Maskar and M.W. Trikande

Abstract A 8 × 8 vehicle has better performance in terms of its obstacle crossing capabilities and off-road manoeuvring. In this study, a comprehensive multi-body model of the vehicle with multi-axle steering was developed. Vehicle handling is studied by first quantifying the steady-state behaviour of vehicles and then relating steady-state principles to transient dynamics. Vehicle handling characteristics depends on suspension and steering linkages configuration, tyre properties, sprung/unsprung mass of vehicle and road loads. A MBD model for handling was developed and steer angle versus lateral acceleration was plotted. Handling characteristics of a multi-axle vehicle were carried out objectively as per SAE test procedure and the model was validated through conduct of actual experiments. It was concluded that understeer characteristics as desired were achieved.

Keywords Eight-wheeled armoured vehicle · Steering lock angles · Multi-body dynamics · Handling · Understeer · Oversteer

1 Introduction

Handling refers to a general overall quality of a vehicle comprising of subjective impression of the driver regarding the vehicle's behaviour and vehicle response to directional commands. Several studies have been carried out for the handling evaluation of cars and four-wheeled vehicle. However, there is a dearth of such studies for multi-axle 8 × 8 vehicles. 8 × 8 vehicles have better stability and produce more traction than commercial vehicles, hence multi-axle vehicles are preferred by military. Pacejka's [1] handling diagram was used for studying handling of multi-axle vehicles by Winkler [2]. Yaw rate control has been used for 6 × 6 vehicle's manoeuvring. Steering mechanism used in this vehicle is a complex one. Four out of eight wheels are made steerable to take care of tyre scrub and

V.V. Jagirdar (✉) · V.P. Maskar · M.W. Trikande
Vehicles Research and Development Establishment (DRDO), Ahmednagar, India
e-mail: vinit.jagirdar@gmail.com

Fig. 1 Steering geometry of an 8 × 8 vehicle
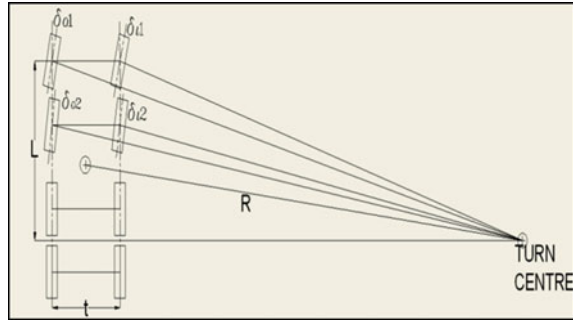
reduce the turning circle diameter. The vehicle model is constructed using commercial Software (MSC ADAMS). Handling performance of armoured multi-axle 8 × 8 vehicles with independent double wishbone suspension system for front two axles and trailing arm independent suspension for rear two axles is examined. In this study, SAE recommended test practise as given in SAE J2181 [4] for determination of steady-state directional properties with more than one steerable axle has been used. Objective of this test was to study the effect of change in lateral acceleration with respect to steering angle of 8 × 8 armoured vehicle. To evaluate the handling characteristics of the vehicle, it was tested at steering pad of NCAT at VRDE. Test results obtained from actual tests were then compared with those obtained with MBD simulation study. The turning path of a vehicle depends on its speed, wheel base, suspension and steering system characteristics. At higher speeds, understeer is desired since vehicle requires more steering angle than the Ackermann steering angle. This is result of lateral compliance of the front being lower than rear. To study vehicle handling and stability we have to consider driver as the vehicle system and the driver are inseparably connected in a closed loop system. By handling tests it is possible to attach an objective measure to a subjective phenomenon (Fig. 1).

2 Cornering Equations

The steady-state cornering equations are derived from the application of Newton's second law with the equation describing geometry. For simplification vehicle is represented by the bicycle model as in Fig. 2 for higher speed turning radius is much larger as compared to wheel base of vehicle where small angles can be assumed, but steering wheel angle difference for outer and inner wheel of vehicle is negligible thus for simplification single wheel is considered at a steer angle 'δ' with equivalent cornering force of both inner and outer wheel, Similar assumption is made for rear two axles.

Fig. 2 Steering of a bicycle model
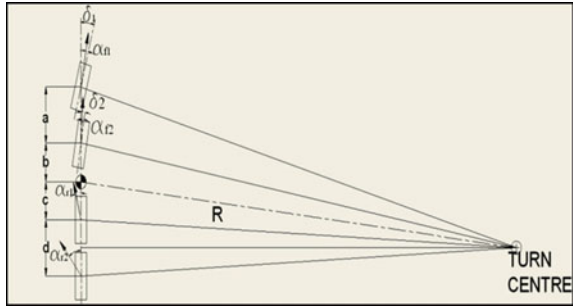
Notations used

R Turning radius

b Spacing second axle and CG

d Spacing third and fourth axle

V Vehicle speed

a Spacing first and second axle

c Spacing CG and third axle

t Track width

Small steering angles are assumed (in radians)

$$\text{Ackerman angle} = (a + b + c + d/2)/(R) = L/R \tag{1}$$

Applying Newton's second law of motion, the centripetal acceleration is equated with total lateral forces generated at wheels

$$F_y = F_{yf1} + F_{yf2} + F_{yr1} + F_{yr2} = MV^2/R \tag{2}$$

Also, the total moment of the lateral forces at CG must be zero.

$$F_{yf1}(a+b) + F_{yf2}(b) - F_{yr1}(c) - F_{yr2}(c+d) = 0 \tag{3}$$

Under cornering conditions, tyre experiences lateral slip when it develops lateral force.

$$F_y = C_\alpha \alpha \tag{4}$$

where, F_y Lateral force (Cornering), C_α Cornering stiffness of tyre, α Slip angle.

$$C\alpha_{f1} + C\alpha_{f2} + C\alpha_{r1} + C\alpha_{r2} = MV^2/R \tag{5}$$

$$C\alpha_{f1}\alpha_{f1}(a+b) + C\alpha_{f2}\alpha_{f2}(b) - C\alpha_{r1}\alpha_{r1}(c) - C\alpha_{r2}\alpha_{r2}(c+d) = 0 \tag{6}$$

From the geometry of the vehicle in the turn to c

$$\delta = L/R + \alpha_{f1} + (a+b)/R - [\alpha_{r1} - c/R - (\alpha_{r2} - (c+d)/R] \tag{7}$$

$$\delta = L/R + \alpha_{f1} - \alpha_{r1} + \alpha_{r2}(a+b)/R + c/R - (c+d)/R \tag{8}$$

$$\delta = L/R + \alpha_{f1} - \alpha_{r1} + \alpha_{r2}(a+b-d)/R \tag{9}$$

But from the vehicle geometry $a = d$ and b is $\ll R$, hence the third term can be neglected.

$$\text{i.e.} \quad \delta = L/R + \alpha_{f1} - \alpha_{r1} \tag{10}$$

$$\alpha f1 = W_{f1} V2 / C\alpha_{f1} \, g \, R \tag{11}$$

$$\alpha r1 = W_{r1} V2 / C\alpha_{r1} g \, R \tag{12}$$

where W_f front axle weight (FAW), W_r rear axle weight (RAW).

$$\delta = L/R + (W_{f1}/ C\alpha_{f1} - W_{r1}/ C\alpha_{r1}) \, V^2/g \, R \tag{13}$$

The steering angle, δ, is given by following equation

$$\delta = L/R + K_{ay} \tag{14}$$

where, K is understeer gradient (deg/g), ay is lateral acceleration (g)

$$W_f/ C\alpha_f > W_r/ C\alpha_r \rightarrow K > 0 \rightarrow \alpha_f > \alpha_r \tag{15}$$

Ackerman turn radius is modified by tyre slip angles and steer angles. Slip angles greater in the front than in the rear increase path radius from the Ackerman condition and produce understeer. Methods for measurement of understeer gradient are all based on the above equation. The derivation of this equation assumes the vehicle in steady-state operating condition, therefore understeer is defined as a steady-state property. Handling evaluations of test vehicle have been carried out as per steady-state circular test procedure by performing constant speed test. The objective of this test is to understand the handling characteristics of the vehicle under steady-state conditions. In this test forward speed and steering angle of the vehicle are measured on preselected paths. Based on the relationship between steering angle and lateral acceleration obtained during the test the handling characteristics (understeer/oversteer) of the high mobility vehicle are evaluated. For understeer vehicle the steer angle needed to maintain constant radius increases as the vehicle speed increases. For oversteer vehicle the steer angle needed to maintain constant radius turn decreases as the vehicle speed increases. For neutral steer vehicle the steer angle needed is independent of forward velocity to maintain
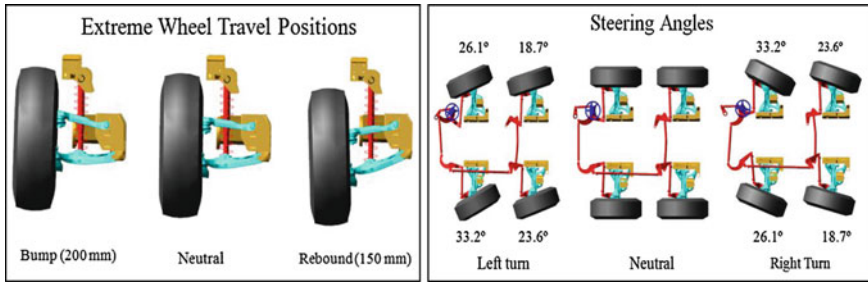
Fig. 3 Wheel travel and steering lock angles for each wheel

constant radius turn. The neutral and understeer vehicle are considered stable when compared with an oversteer vehicle.

3 Steering Kinematics Verification

The dual axle steering system with double wishbone independent suspension for front axles and trailing arm suspension systems for rear axles has been modelled in MSC ADAMS View s/w. Hydropneumatic suspension's non-linear stiffness characteristics have been modelled as a spine curve from the data points. Single wheel, opposite and parallel wheel travel analysis to check the system for interference was carried out. Steering angles achieved by simulation is compared with angles required for Ackerman steering to achieve the desired wheel lock angles (Fig. 3).

4 Test Procedure

The procedure for the objective assessment of handling has been carried out in accordance with SAE J2181 [4] and SAE J266 [3]. This test measures changes in steady-state cornering characteristics as a function of lateral acceleration. Five methods have been given in the standard of which constant speed with variable steer has been used for experimentation. With the vehicle being driven in an initially straight line at the test speed, a preselected steering input is applied and maintained at that value of 4 to 5 s until vehicle speed reaches a steady-state condition. When the steering is applied, the vehicle is maintained at a constant speed at steady-state throughout the remainder of the run. Then, the vehicle is driven for different sets of steering wheel angles and turning radius is measured. The lateral acceleration is calculated from the speed and turning radius. Results in terms of lateral acceleration are plotted against steer angle. The test vehicle is driven over a path at constant speeds at range of turning radii. The data is recorded when a steady-state is achieved. The vehicle is driven at successively increasing speeds and radii and data is taken for steady-state conditions for each speed.
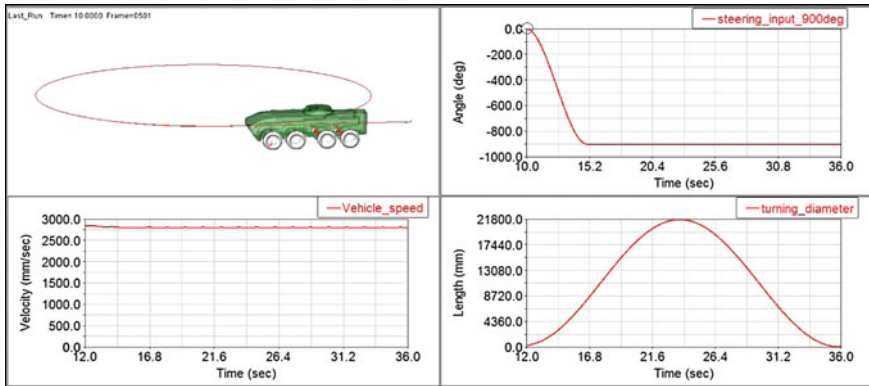
Fig. 4 Handling simulation 10 km/h speed steering angle 900°
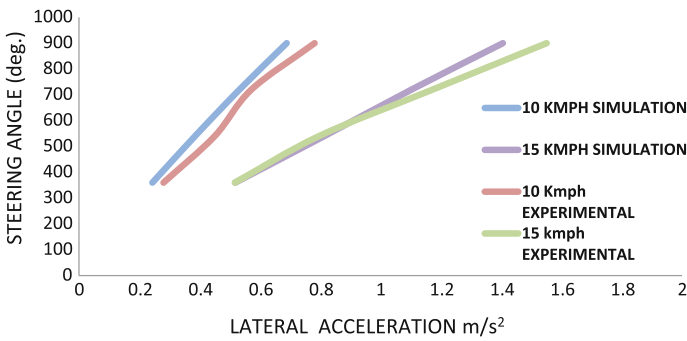
Fig. 5 Steer angle V/s Lateral acceleration curve for constant speed Simulation and Experimental data

In this test, the turning radius is changed by changing the steer angle at 360°, 540°, 720° and 900° and the data is collected for a steady-state response at constant speed (Fig. 4).

The results are plotted as shown in Fig. 5. Slope of steer angle lateral acceleration curve determines vehicle handling behaviour.

5 Conclusions

A comprehensive experimental investigation and MBD simulation on handling of vehicle was carried out by doing constant speed with variable steer test as per SAEJ266 [3] and SAEJ2181 [4]. Slope of the curves is positive, that implies that the vehicle is understeer, which is desirable. Good correlation has been obtained in

simulation and experimental results. This validated model can be used to predict handling performance of the vehicle in different conditions and vehicle variants (change in axle weight distribution) will result in saving a lot of time and money.

References

1. H. Pacejka, Tire and Vehicle Dynamics, 2012.
2. C. B. Winkler, "Simplified analysis of the steady-state turning of complex vehicles," Vehicle System Dynamics, vol. 29, pp. 141–180, 1998.
3. Steady-state directional control test procedures for passenger cars and light trucks SAEJ266 SAE INTERNATIONAL.
4. steady-state circular test procedure for trucks and buses SAE J2181 SAE INTERNATIONAL.

Analysis of Air-to-Air Rotary Regenerator for HVAC Systems Using CFD

S. Mahesh, B. Jayaraman and R. Madhumitha

Abstract Air-to-air heat exchangers play a crucial role in mechanical equipment, due to potential primary energy savings both, in the case of commercial properties and economic zones. This paper studies computational fluid dynamics (CFD) simulation in a rotary regenerator achieving a capacity of 90 ton by heating ventilation air conditioning systems The modelling is done using the commercial code ANSYS FLUENT ©. The operating parameters like rotational speed, porosity of mesh and dimensions of rotary regenerator like length, diameter were studied and compared with literature. Effects of variation of pressure, velocity and temperature at different sections of the rotary regenerator which accounts for the effectiveness of rotary regenerator and the percentage increase in coefficient of performance (COP) of HVAC plant are discussed.

Nomenclature

ρ	Density (kg/m^3)
σ_k	Prandtl-Schmidt number for k
t	Time (s)
K	Turbulence kinetic energy (m^2/s^2)
ϵ	Dissipation rate of turbulent kinetic energy (m^2/s^3)
x	Horizontal displacement (m)
u, v, w	Velocity (m/s)
μ	Molecular viscosity (Pa s)
C	Friction coefficient
μ_ς	Eddy viscosity (Pa s)
S	Mean strain rate tensor
G_k	Destruction of turbulent kinetic energy
G_b	Destruction of turbulent dissipation

S. Mahesh (✉) · B. Jayaraman · R. Madhumitha
School of Mechanical Engineering, SASTRA University, Thanjavur, India
e-mail: sivamahesh80@gmail.com

V	Volume (m^3)
$\mathcal{T}$	Stress, internal energy per unit mass (m^2/s^2)
$\frac{V^2}{2}$	Kinetic energy per unit mass (m^2/s^2)
K	Thermal conductivity (energy equation) (W/mK)
T	Local temperature (K)
P	Pressure (Pa)
F	Force (N)

1 Introduction

There has been an increase in the demand of heat recovery applications in recent years due to consistent rise in energy prices. One of the solutions to this concern is that heat exchangers are considered to play a pivotal role in contemporary requirement. Several research initiatives have been carried out on the heat transfer by single film transfer coefficient [1]. Among various types of heat exchangers, gas-to-gas was employed commonly in applications such as furnaces, air conditioning systems and power plants [2]. There have been a number of studies and statistics relating to the methodology used in estimating the performance of regenerative preheaters [3]. Also, the sterling cycle regenerator with wire mesh screens and fluid thermal equations have been correlated to this study [4]. Screen mesh is used to filter or capture particles of larger size than of the mesh size from a fluid system containing a mixture of particles [5]. A heat wheel consists of a cylindrical rotating device which results in rolling up corrugated sheets of a metallic material in order to achieve a large number of parallel channels with a typical sinusoidal cross-sectional geometry [6]. It is crucial to determine the conduction in the matrix to predict the effectiveness of the heat wheel [7]. In order to reduce the contamination of the fresh air flow, a purge sector was introduced between exhaust and supply air stream. The principle employed is a transfer of heat from one air stream to the wheel matrix and vice versa. It was also revealed from the literature study, that regenerators with hygroscopic matrix materials were emphasised to generate heat, moisture recovery and dehumidification of moist air [8]. The present study is focused primarily on the CFD simulation in a rotary regenerator achieved at a high capacity of 90 ton by heating ventilation air conditioning systems.

2 Governing Equations

CFD simulation has been carried out considering the Eqs. (1)–(3).
A. Continuity equation

$$\frac{\partial \rho}{\partial t} + \Delta \cdot (\rho V) = 0 \qquad (1)$$

B. Momentum equation
X-Component

$$\frac{\partial pu}{\partial t} + \Delta(\rho u V) = -\frac{\partial p}{\partial x} + \frac{\partial \tau xx}{\partial x} + \frac{\partial \tau yx}{\partial y} + \frac{\partial \tau zx}{\partial z} + \rho fx \tag{2}$$

C. Energy equation

$$\rho \frac{\partial}{\partial t}\left(e + \frac{V^2}{2}\right) + \nabla\left[\rho\left(e + \frac{V^2}{2}\right)V\right]$$
$$= \rho q + \frac{\partial}{\partial x}\left[k\frac{\partial T}{\partial x}\right] + \frac{\partial}{\partial y}\left[k\frac{\partial T}{\partial y}\right] + \frac{\partial}{\partial z}\left[k\frac{\partial T}{\partial z}\right] + pfv \tag{3}$$

Turbulence Model
Turbulence model used in this analysis is a renormalisation group (RNG) k-ε model. It is basically a two equation model based on the model transport equation for the turbulence kinetic energy (k) and its dissipation rate (ε).

3   CFD Model and Description

Rotary Regenerator Model Geometry and Meshing
The rotary regenerator rotates at a constant speed and therefore meshing of the wheel has been considered as rotating a mesh. Six different volumes were considered for the analysis of the rotary regenerator wheel as shown in Fig. 1. A typical rotary regenerator with geometrical parameters shown in Table 1 has been considered for the study. Among the six volumes, volume 1, 2, 3 and 4 have been considered as the duct volume and that zone as the zone of fluid with fixed mesh. The volume numbers 5 and 6 are considered as the rotary regenerator wheel volume and that forms the zone of fluid with moving mesh. A three-dimensional model has also been developed for the practical mesh structure. The mesh used for analysis is a tetrahedral mesh (Fig. 2) for ease of meshing and convergence of the solution. The mesh sizingis 0.03 m and total number of meshing tetrahedrons is 36,482.

Fig. 1 2D model of rotary regenerator

1,2,3 & 4 are duct volumes, stationary mesh, 5 & 6 are wheel volumes, rotation mesh
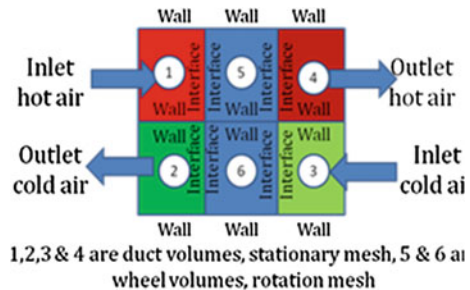
Table 1 Material properties

Wheel diameter (m)	1
Wheel length (m)	0.4
*Duct diameter (m)	0.4
*Duct length (m)	0.4
Thermal diffusivity (m²/2)	84.18×10^{-6}
Specific heat (kJ/kg K)	0.896
Thermal conductivity(W/mK)	204.2

Fig. 2 Isometric view of the rotor with duct system
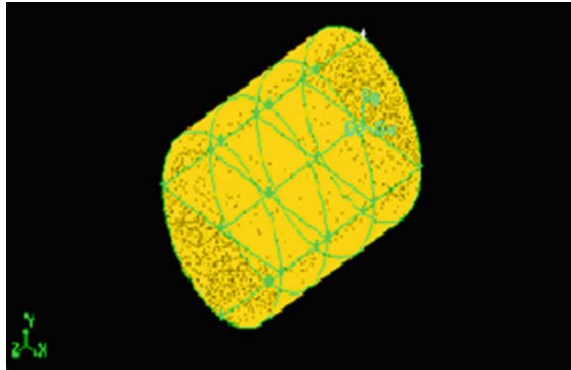
Boundary condition

Inlet boundary conditions are given in Tables 2 and 3 to predict the effectiveness of the rotary regenerator with varying porosity, rotational speed keeping other parameters like temperature and velocity constant. The boundary conditions were applied with FLUENT software as given in Table 2. The boundary conditions shown in Table 2 have all parameters remaining constant except the porosity of the matrix material to predict the outlet temperatures of the hot and cold fluids. Table 3 shows the boundary conditions used in the analysis for predicting the effect of RPM on temperature and velocity distribution.

Table 2 Boundary condition—the effect of porosity

Speed (rpm)	Porosity	Hot air inlet		Cold air inlet	
		Temperature (K)	Velocity (m/s)	Temperature (K)	Velocity (m/s)
10	0.4	313	0.1	298	0.1
10	0.5	313	0.1	298	0.1
10	0.6	313	0.1	298	0.1
10	0.7	313	0.1	298	0.1

Table 3 Boundary condition to predict the effect of rotational speed

Speed (rpm)	Porosity	Hot air inlet		Cold air inlet	
		Temperature (K)	Velocity (m/s)	Temperature (K)	Velocity (m/s)
6	0.6	313	0.1	298	0.1
7	0.6	313	0.1	298	0.1
8	0.6	313	0.1	298	0.1
9	0.6	313	0.1	298	0.1

4 Results and Discussion

Temperature Profiles

As hot air enters the rotor, its temperature reduces from 313 to 307 K, when the hot air passes the exit of the rotor. The temperature is further reduced to 305 K as heat is stored in the matrix. Similarly, as the cold air enters the rotor and temperature increases from 298 to 304 K. When the cold air passes the exit of the rotor the temperature is further increased to 305 K due to the reason that heat is absorbed by the cold air from the matrix. It can be inferred that the hot air temperature remains unchanged till the duct end. As the hot air enters the rotor, heat will be absorbed by the matrix and as a result temperature gradually reduces until it completely passes the rotor. It was found from the temperature curves that, the variation of cold and hot air temperature occurs in a similar fashion for the curves $z = 0.45$, $z = 0.5$, $z = 0.55$, $z = 0.6$ but not for the curves $z = 0$ and $z = 0.4$ as there is significant variation in temperature of cold air from the outer surface towards the centre of the rotor than the variations in hot air temperature.

Velocity Profiles

Figure 3 illustrates the variation of cold air velocity along the length of the duct and rotary wheel at various radial locations. Line at $y = 0.4$ m, $y = 0.3$ m, $y = 0.2$ m and $y = -0.1$ m represent the variation of cold air velocity at 0.4, 0.3, 0.2 and 0.1 m, respectively. By comparing these curves it may be concluded that, the variation of cold air velocity occurs in a similar fashion up to mid plane and the velocity increases from inlet duct to rotor and reaches a maximum of 0.25 m/s and then

Fig. 3 Variation of cold air velocity along the length
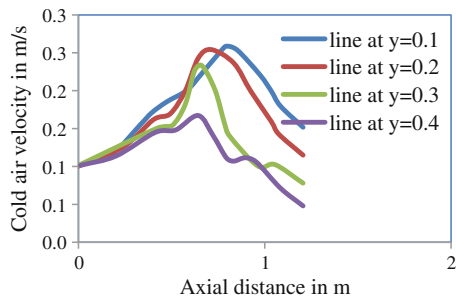
decreases gradually through the duct and the velocity is not uniform for these curves when it comes out of the outlet duct. The magnitude of velocity remains unchanged till the cold air has passed through the inlet duct. As the cold air enters the rotor the relative velocity increases up to 0.5 m/s. Then the magnitude of velocity decreases to 0.1 m/s as it passed through the rotor and exit duct. There is a small increase in the hot air velocity along the length of the rotor alone from 0.8 to 0.4 m due to rotation of the air flow across the separation wall at various radial locations.

5 Pressure Profiles

The plane at an axial distance of 0.4 m resembles the upper half face as the rotor inlet for the cold air flow and the lower half face as the rotor outlet for the hot air flow. Therefore, heat absorbed by the matrix from hot air will be recovered by the cold air as the rotor outlet of hot air has become the rotor inlet of cold air. It was seen that the cold air pressure is uniform over the inlet face but the hot air pressure varies at different points of the hot air outlet face since the hot air has passed through the porous medium the pressure is not uniform for hot air. By comparing the pressure plots along various radial direction it was also concluded that the variation of cold air pressure is same for all the curves but it is not true for the curves showing the variation of hot air pressure as there is more variation of the hot air pressure.

Effect of Porosity on Effectiveness
Inlet conditions are given based on the journals prepared by several research people who are specific to air conditioning application. In the present work, the value of porosity alone was varied during each trial by keeping all other parameters such as hot air inlet temperature, cold air inlet temperature and velocity of both hot and cold air and rotational speed constant to study.

Figure 4 shows the effects of porosity on heat transfer and effectiveness. It also shows that heat loss of hot air is equal to heat gain of cold air according to heat transfer process of counter flow heat exchanger. In the graph, it is clearly shown that effectiveness decreases as porosity increases. From the heat transfer point of

Fig. 4 Effectiveness versus speed
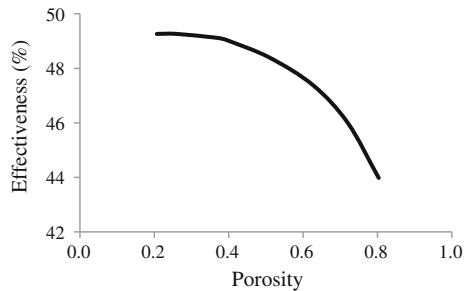
view, the value of porosity should be kept at minimum wherever possible in order to achieve large heat transfer which in turn will be helpful to increase the effectiveness of the heat exchanger.

Effect of Rotational Speed on Effectiveness

Figure 5 illustrates the effect of rotational speed on the effectiveness of the heat exchanger. In the graph, it is clearly shown that effectiveness increases as speed increases. From the heat transfer point of view, the value of speed should be kept at maximum but within the practical limit wherever possible in order to achieve large heat transfer which in turn will be helpful to increase effectiveness of the heat exchanger.

Figure 6 shows good agreement with the literature as shown. The effectiveness value in literature is greater than the effectiveness value of this analysis. This is due to difference in the boundary conditions and carryover leakage. In literature, carryover leakage is considered and therefore better effectiveness is achieved. The effects of important process parameters on the rotary regenerator effectiveness were also investigated for the different porosity values of 0.2–0.8 while the velocity (0.1 m/s) and rotational speed (10 RPM) are kept constant. Similarly, for different rotational speeds (6–12 RPM), the effectiveness of rotary regenerator was calculated for the same velocity (0.1 m/s) and constant porosity value of 0.6. Maximum effectiveness of 49.3 is obtained for constant rotational speed of 10 RPM and low

Fig. 5 Effectiveness versus porosity
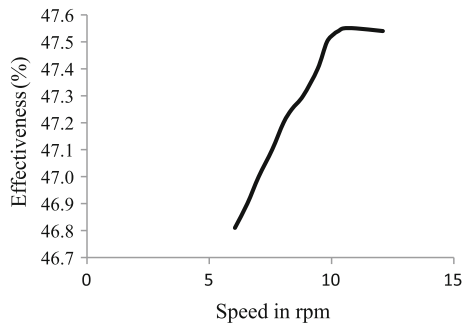
Fig. 6 Effectiveness of regeneration temperatures (Rabah A.A.)
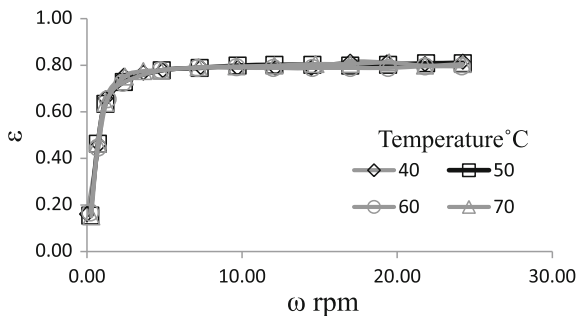
porosity value of 0.2. Also, maximum effectiveness of 48.05 is obtained for constant porosity of 0.6 and maximum rotational speed of 11 RPM. Further increasing the rotational speed to 12 RPM increases the effectiveness to 48.06.

6 Conclusion

Modelling of rotary air-to-air energy wheel with ducts for supply and exhaust air was developed and the performance analysis carried out using FLUENT software. Simulation models of symmetric-balanced energy wheel were developed to estimate the effectiveness of the rotary heat exchanger with aluminium as porous medium (matrix). Conclusions of results of model simulations are the following:

1. The effectiveness of the rotary heat exchanger increases with increase in the speed of the rotary wheel.
2. Both heating and cooling modes are equally sensitive to the changes in porosity of the matrix.
3. The effectiveness of the rotary heat exchanger decreases with increase in the porosity of the matrix.
4. Effectiveness is almost constant for low porosity values and it decreases for high porosity of the matrix.

References

1. Maclaine-Cross, I.L. and Banks, P.J., "Coupled heat and mass transfer in regenerators – Predictions using an analogy with heat transfer"; International Journal of Heat and Mass Transfer, Vol. 15, No. 6, pp. 1225–1242 (1972).
2. Abdulmajeed Al Ghamdi, S., "Analysis of air to air rotary energy wheels"; Dissertation to Russ College of Engineering and Technology, Ohio University, (2006).
3. SandiraAlagic, Nikola Stosic, Ahmed Kovacevic and Indira Buljubasic, "Numerical analysis of heat transfer and fluid flow in rotary regenerative air preheaters"; Journal of Mechanical Engineering 517–8, 411–417(2005).
4. Sercan OZ Bay, "Thermal Analysis of Stirling Cycle Regenerator"; Thesis submitted to the Graduate School of Natural and Applied Sciences of The Middle-East Technological University, (2011).
5. Swanepeol, DC, Kroger, DG, Rotary regenerator design theory and optimization, R and D Journal, Vol. 12, No. 3 (1996).
6. Stefano De Antonellis, Manuel Intini, Cesarl Maria Joppolo and Calogero Leone, "Design optimization of heat wheels"; Energies 2014, 7, 7348–7367, (2014).
7. Porowski, M. and Szczechowiak, E.,, Inference of longitudinal conduction in the matrix on effectiveness of rotary heat regenerator used in air conditioning, Heat Mass Transfer, 43: 1185–1200. (2007).
8. Holmberg, R. B.. Combined heat and mass transfer in regenerators with hygroscopic materials, Journal Heat transfer, 101, 205–210, (1979)

Design and Optimization of a Steering Knuckle of FSAE Car

Antriksh Mutha, Shubham Thosar and Nikhil Ghodmare

Abstract Steering knuckle is that component of a vehicle which connects the suspension system, braking system and the steering system to the chassis of the vehicle. A steering knuckle should have high precision, durability and low weight. The purpose of this study is to design a knuckle which is low in weight and has better performance with considerable factor of safety. The study is divided into two steps. The first step involves the designing of a steering knuckle with the help of designing software and by estimating the loads which are acting on the component. The second part is carrying out FEA on the component to find out the stresses induced and the deformation. This will help in optimising the knuckle. After the analysis is done, the knuckle can be optimised by removal of materials where the induced stress is low.

Keywords Steering knuckle · FEA · Optimisation

1 Introduction

Formula SAE is a student level competition organised by Society of Automotive Engineers, wherein it is expected that students design and manufacture a prototype of an open wheel race car. Hence, weight is an important criterion while designing any component for such vehicles. A steering knuckle plays a very important role in an automobile. Thus, the goal is to design a knuckle which has weight as low as possible. Thus, the power to weight ratio of the car can be increased. The function of a steering knuckle is to convert the linear motion of the tie rods to the angular motion of the stub axle. The designing of the knuckle depends upon the suspension and

A. Mutha (✉) · S. Thosar · N. Ghodmare
Department of Mechanical Engineering,
MGM Jawaharlal Nehru Engineering College, Aurangabad, India
e-mail: mutha.antriksh@gmail.com

S. Thosar
e-mail: shubham.thosar81@gmail.com

N. Ghodmare
e-mail: nikster005@gmail.com

steering geometries, as well as, brake mountings. A reduction in weight also helps in improving the handling of vehicle. A knuckle is to be designed in such a way that it sustains the forces and torques acting on it because of the bumps, braking, acceleration and steering action. In design optimisation, it is expected that the weight should be minimised and satisfactory strength, stiffness and durability is achieved.

2 Research Procedure
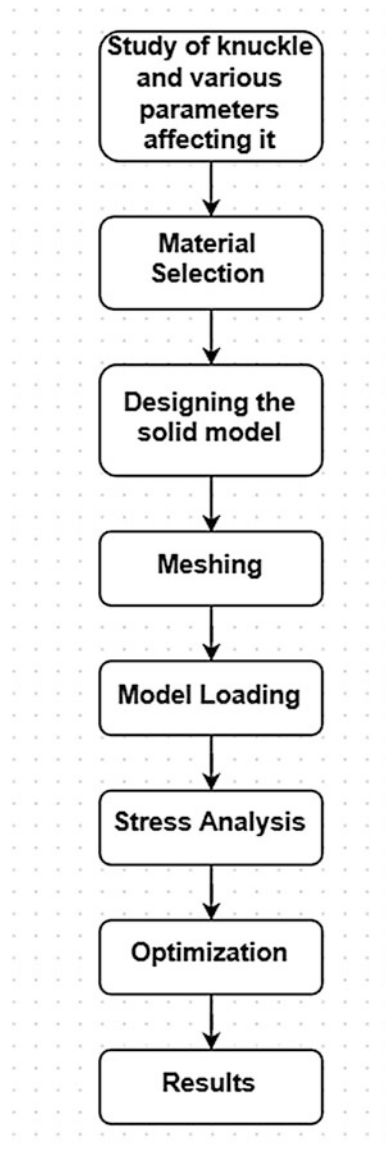
3   Material Selection

Aluminium 7075-T6	
Aluminium (Al)	90 %
Zinc (Zn)	5.6 %
Magnesium (Mg)	2.5 %
Copper (Cu)	1.6 %
Chromium (Cr)	0.23 %
Material properties	
Density	2.81 g/cc
U.T.S.	572 MPa
Yield strength	503 MPa
Young's modulus	71.7 GPa
Machinability	70 %

4   Selection of Manufacturing Process

Forging
It is a manufacturing process in which the shaping of the material is done by using localised compressive forces. This can be done either by a hammer or dies.

Casting
It is process in which liquid metal is poured into the mould of desired shape and allowed to solidify. The solidified part is called as casting.

Machining
It is a process in which a block of metal is machined with the help of various machines, i.e. VMC, CNC, etc. to achieve the desired shape.

Manufacturing Process	Advantages	Disadvantages
Forging	Higher strength, Reduced material cost	Costly, warping
Casting	Economical for mass production	Poor surface finish, cracks, pores
Machining	Good surface finish, accuracy	High wastage, costly

Machining process was selected as it is preferred when the quantity of the production is low.

5 Analysis of Forces Acting on Knuckle

While designing a knuckle, it is important to analyse the forces acting on it. The values of the forces acting on the knuckle are calculated in Newton and then are converted into 'G forces' by dividing the value by mass of the vehicle, so that these values can be applied for designing the knuckle of another vehicle of similar type.

The various types of forces acting on the knuckle are as follows:

1. Weight of the vehicle.
2. Lateral force due to turning.
3. Braking force.
4. Weight transfer during braking, acceleration and turning.
5. Forces due to steering effect.
6. Bump force.

6 Calculations

The values of the forces obtained are as follows:

Force	Value (N)	G force (G)
Weight of vehicle	735.75	0.25
Lateral force due to turning	18041.11	6.13
Braking force	1275.71	0.43
Lateral load transfer	4963.66	1.68
Long load transfer	503.41	0.17
Steering force	585.144	0.19
Bump force	1270	0.43

7 Stress Analysis

The FEA on the knuckle was carried out on ANSYS and following result was obtained.

Meshing
The element used for meshing is hexahedron.
The component was meshed with various mesh sizing and a graph was prepared.
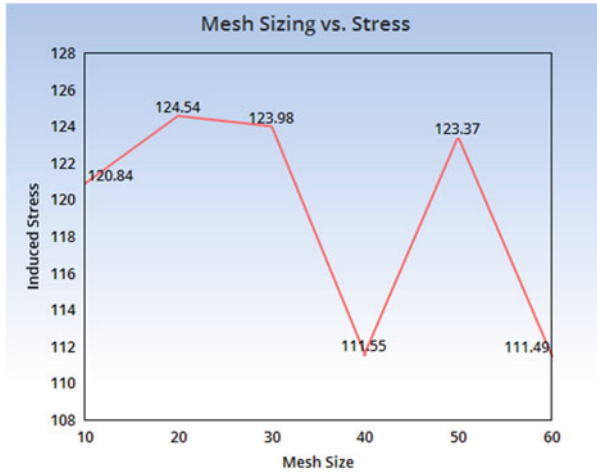
Mesh sizing	10	20	30	40	50	60
Nodes	59,523	52,157	49,562	49,943	48,097	47,099
Elements	39,794	35,273	33,841	34,004	33,007	32,425
Stress (MPa)	120.84	124.54	123.98	111.55	123.37	111.49
Deformation (mm)	0.057	0.056	0.055	0.055	0.055	0.055

From the table, it can be seen that the stress induced in the component when the mesh size is 10 mm is 120.84 MPa, whereas, that induced when the size is 30 mm is 123.98 MPa. Also it can be seen that the difference in the stress induced at different mesh sizing is not more than 10 %. So any mesh size can be chosen. But it can be seen that if the mesh size is kept as 10 mm, the nodes generated are 59,523 and are 49,562 when the mesh size is 30 mm, and the difference in stress value is not large. But the time required to solve 59,523 nodes will be more as compared to 49,562 nodes. Hence, a mesh size of 30 mm was selected.

During the analysis, the suspension mountings were constrained as they are in direct contact with the chassis. The force acting on the knuckle because of the weight of the car was applied on the bearing support step provided on the knuckle. The lateral and longitudinal forces because of weight transfer and turning were also applied on the bearing support step provided on the knuckle. The force due to braking was applied on the calliper mounting. The forces due to steering effect were applied on the steering arm bolting point. As the spring is directly connected to the lower arm, the bump forces were applied on the lower arm bolting point (Figs. 1, 2 and 3).
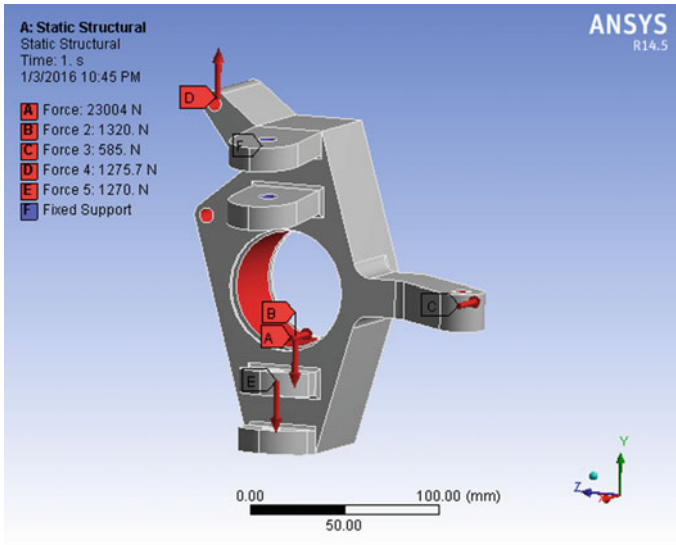
Fig. 1 Knuckle loading
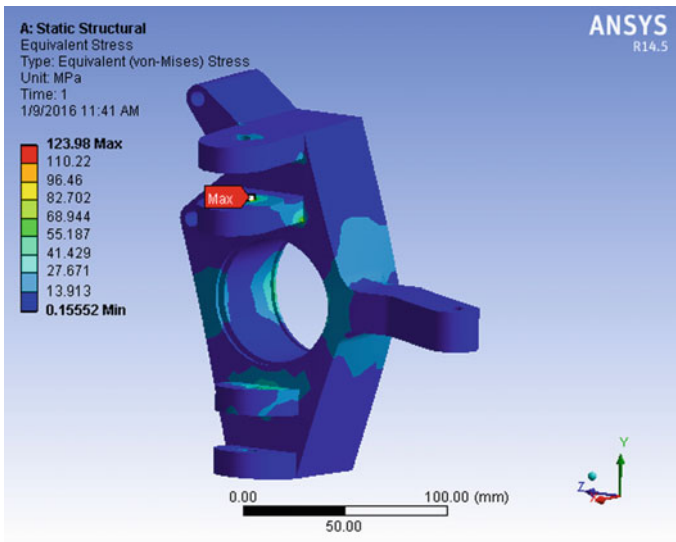
Fig. 2 Equivalent stress on original design
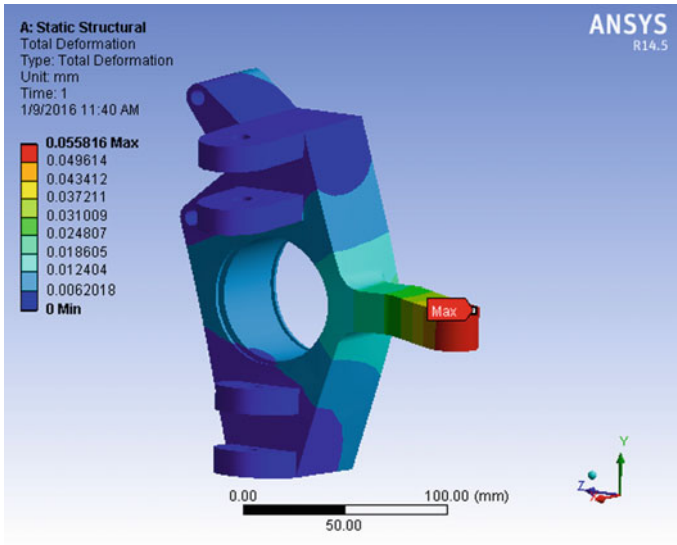
Fig. 3 Total deformation of original design

| Equivalent stress (Von Mises) | 123.98 MPa |
| Total deformation | 0.055 mm |

From the table it can be seen that the factor of safety comes out to be 4.05. It is clear that the component is over designed and can be optimised. There is lot of scope for reducing the weight as well as the material from the knuckle. One way of optimising the geometry was by removing the material from the parts where there was very less stress concentration. This method was adopted and an optimised geometry was prepared. Stress analysis was carried out on the optimised knuckle and results were noted down (Figs. 4, 5 and 6).

| Equivalent stress (Von Mises) | 292.27 MPa |
| Total deformation | 0.166 mm |

After the optimization of the model the stress concentration in the model has increased resulting in lowering the factor of safety. The factor of safety comes out to be 1.72. The factor of safety has reduced but is satisfactory. The weight of the optimised knuckle is much lower than that compared to the original one and hence, with appreciable factor of safety and lesser weight the design is finalised.
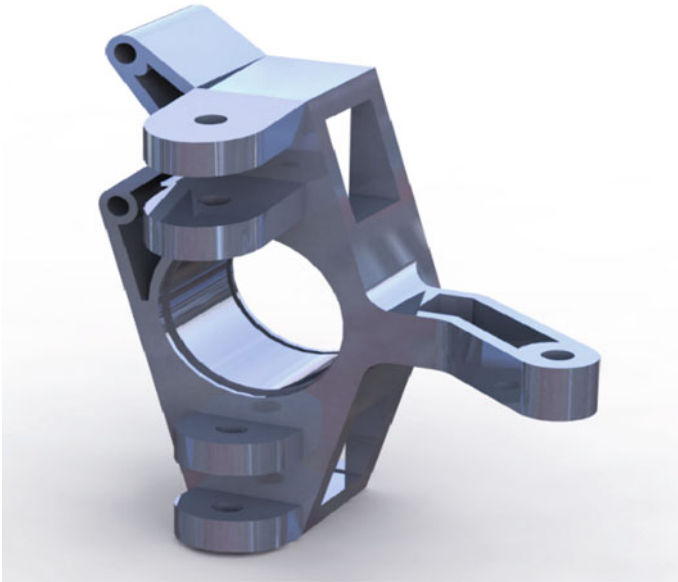
Fig. 4 Optimised design
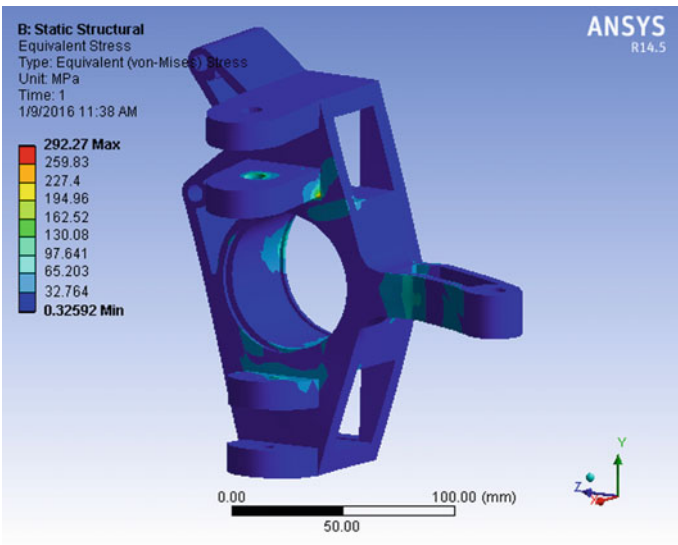
Fig. 5 Equivalent stress on optimised design
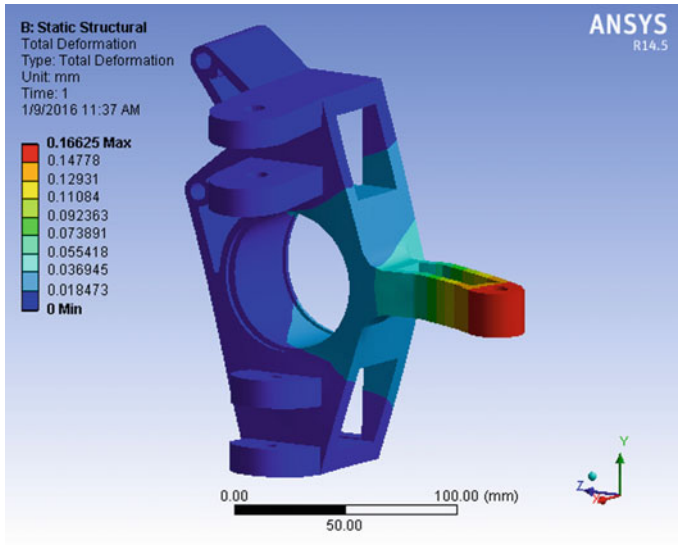
Fig. 6 Total deformation of optimised design

	Old	Optimised
Mass	1590.52 g	940.35 g
Deformation	0.0556 mm	0.166 mm
Stress	123.98 MPa	292.27 MPa
F.O.S.	4.05	1.72
Volume	566.020 cc	334.643 cc

8 Conclusion

The Knuckle was designed as per the procedure, but it was overdesigned. Hence, the design was optimised. The optimised design showed 40.87 % reduction in weight as well as in material volume when compared to the earlier design. The equivalent stress induced in the new design was 292.27 MPa providing a F.O.S. of 1.72, which is well within the limits. The deformation is also satisfactory. Hence, the new design can be concluded safe.

References

1. Milliken & Milliken, "Race Car vehicle dynamics", SAE International, 1995, ISBN I56091-526-9
2. Thomas Gillespie, "Fundamentals of vehicle dynamics", SAE publications, 1992, ISBN 97881-89401, pp 5–6
3. http://asm.matweb.com/search/SpecificMaterial.asp?bassnum=MA7075T6
4. http://www.azom.com/article.aspx?ArticleID=6652
5. FEA & Optimisation of Steering Knuckle of ATV, http://iraj.in/up_proc/pdf/187-144402791633-38.pdf
6. STRESS ANALYSIS ON STEERING KNUCKLE OF THE AUTOMOBILE STEERING SYSTEM, IJRET: International Journal of Research in Engineering and Technology eISSN: 2319-1163 | pISSN: 2321-7308
7. Design and optimization of hub and knuckle for Formula SAE car, http://www.ijerd.com/paper/vol10-issue10/Version_2/G10106569.pdf
8. Data Records-Team VAAYU 4.0, MGM Jawaharlal Nehru Engineering College, Aurangabad.

CFD Analysis of Flapping Wing for MICAV Application

P. Srinivasa Murthy

Abstract CFD analysis of flapping wing is required for the design of MICAV configuration. The basic aerodynamic phenomenon for MICAV flapping wing flight is unsteady flow, spiraling leading edge vortex formation which is responsible for sustained flight at low speeds, wake capturing which adds additional lift, and fast pitch up which generates positive lift at the time of stroke reversal. In this paper, an investigation has been done for a typical MICAV flapping wing configuration. Wing is subjected to sinusoidal flapping oscillations with a frequency 25 Hz, amplitude of 45° up-stroke, and 35° down-stroke; span of the wing, 45 cm; chord, 15 cm; thickness is varied from 0.025 to 0.1 mm; leading edge is straight and trailing edge is curved. CFD unsteady solution is obtained and analyzed. It has been found that 0.025 mm thick wing tends to generate more lift and thrust than 0.1 mm thick wing.

Keywords Unstructured grid · Dynamic Mesh · Unsteady flow · MICAV flow field

1 Introduction

In the design of MICro Aerial Vehicle (MICAV), the flapping wing unsteady aerodynamics at low Reynolds number has to be analyzed. The main aerodynamic features of flapping wings are spiral leading-edge vortex, rotational lift due to pitch up rotation, and wake capturing [1]. Also, in the case of natural flying objects the tip of the flapping wing generates the "Figure 8" motion during flapping. The developments of these features are to be captured through CFD analysis in unsteady mode. It is required to optimize the lift by maximizing the production of spiraling leading-edge vortex, pitch up rotation during the transition of upward and downward strokes, and capturing the shed wake vortex left behind by the previous

P. Srinivasa Murthy (✉)
Aeronautical Development Establishment, Bangalore, India
e-mail: dr_ps_murthy@yahoo.co.in

strokes. The production of thrust can also to be maximized by changing the camber of the wing with time and synchronizing with flapping frequency. More details on aerodynamics features of flapping wings are available in open literatures [2, 3].

In the present paper an investigation of CFD analysis of rigid flapping wing of typical MICAV configuration with different thicknesses are presented and results are compared for better efficiency to implement in the realistic design.

2   Computation Method

A CFD tool has been used to solve both the steady and unsteady flows. Mesh generator has been used to generate the unstructured tetrahedral mesh around MICAV configuration.

3   CFD Computation

Cases analyzed were the following for flapping wing configuration (Fig. 1):

1. $M = 0.03$, frequency, $f = 25$ Hz, U/S = 45°, D/S = 35°, thickness, $t = 0.1$ mm. Cruise condition
2. $M = 0.03$,   frequency, $f = 25$ Hz,   U/S = 45°,   D/S = 35°,   Thickness, $t = 0.025$ mm. Cruise condition

Mesh consisting of 2.5 million tetrahedral elements is generated for the flapping wing configuration for unstructured grid system; computer used dual processor quad core Xeon with 32 GB RAM work station; CPU time taken for each case is around 15 days for half flapping cycle.

Fig. 1 Flapping wing geometry with leading-edge straight, trailing edge curved
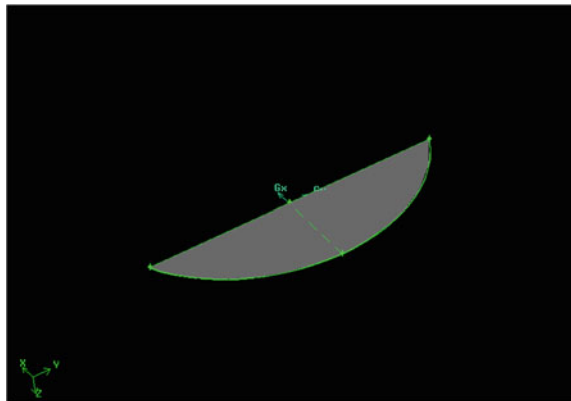
4 Results and Discussion

Most of the natural flying objects have the wing planform of semi-elliptic type with leading-edge straight and trailing edge curved. The purpose of choosing such a configuration for flapping wing is to generate spiraling leading-edge vortex at the apex during down-stroke and propagate the vortex toward the tip without break-down and finally shed once it reaches the tip. For efficient cruise the leading edge vortex system should be stable without break down anywhere between root and tip. Another aspect of flapping wing aerodynamics is 'wake capture'. At the end of the stroke the tip is influenced by the shed vortex that means, tip captures the shed vortex and generates additional lift. When the wing reverses the stroke the local angle of attack changes sign due to which fast pitch up generates additional lift. So these three effects, namely, spiral leading-edge vortex, wake capture, and fast pitch up are to be maximized in any flapping wing design. To meet this futuristic objective a study has been taken up for CFD analysis. A typical planform chosen for the CFD analysis of flapping wing for MICAV Configuration is shown in Fig. 1. Total span is 45 cm with root chord of 15 cm. Grid generated over the wing is around 2.5 million tetrahedral cells. CFD solution is generated for laminar flow. Typical cpu time taken by the Intel work station with octa core processor, 64 bit, 24 GB RAM is around 15 days to capture half cycle unsteady solution.

Kinematic motion considered for the flapping wing analysis is a sinusoidal motion with amplitude 45° up-stroke and 35° down-stroke with a frequency of 25 Hz. Time history of flapping motion is shown in Fig. 2.

Wing is modeled as a rigid flat plate with constant thickness for the present analysis. Although the real flapping wing is a membrane wing made of fabric materials which are highly flexible and deformable during flapping motion, the analysis of such a wing are highly complex to handle at the present moment. Figure 3 shows thrust coefficient versus time for right wing flapping at a rate of 25 Hz. The wing is modeled as a rigid flat plate with a constant thickness of

Fig. 2 Flapping angle time history, $M = 0.03$, $f = 25$ Hz, thickness = 0.1 mm, U/S = 45°, D/S = 35°
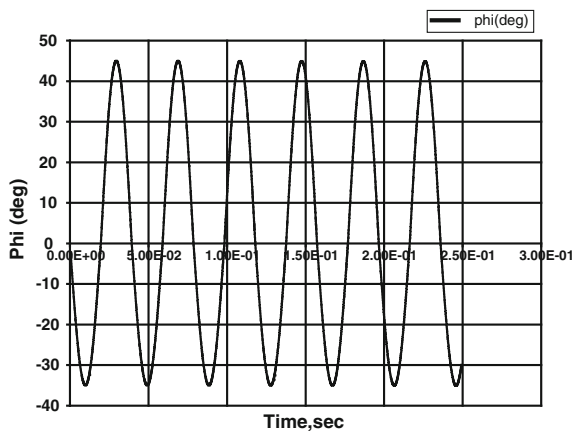
Fig. 3 Thrust coefficient
time history, $M = 0.03$,
$f = 25$ Hz,
thickness = 0.1 mm,
U/S = 45°, D/S = 35°
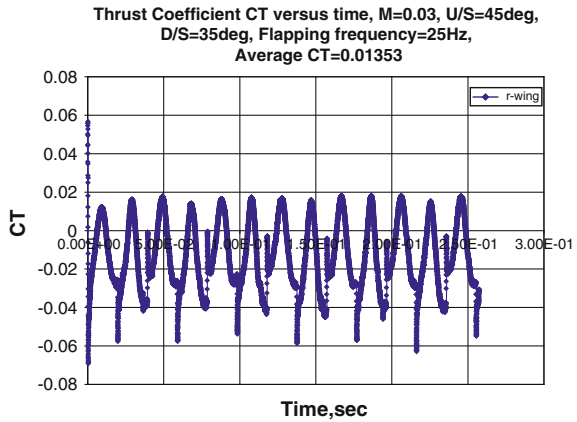
0.1 mm. The Mach number is 0.03 with up-stroke of 45° and down-stroke of 35°. The time average thrust coefficient is 0.01353.

Since the flow is unsteady during flapping motion the time history of lift coefficient for right wing flapping at a rate of 25 Hz is shown in Fig. 4. The wing is modeled as a rigid flat plate with a constant thickness of 0.1 mm. The Mach number is 0.03 with up-stroke of 45° and down-stroke of 35°. The time average lift coefficient is −0.0518

Next case analyzed is for 0.025 mm thick rigid wing. Figure 5 shows thrust coefficient versus time for right wing flapping at a rate of 25 Hz. The wing is modeled as a rigid flat plate with a constant thickness of 0.025 mm (25 μm). The Mach number is 0.03 with up-stroke of 45° and down-stroke of 35°. The time average thrust coefficient is 0.034291.

Figure 6 shows lift coefficient versus time for right wing flapping at a rate of 25 Hz. The wing is modeled as a rigid flat plate with a constant thickness of

Fig. 4 Lift coefficient time
history, $M = 0.03$, $f = 25$ Hz,
thickness = 0.1 mm,
U/S = 45°, D/S = 35°
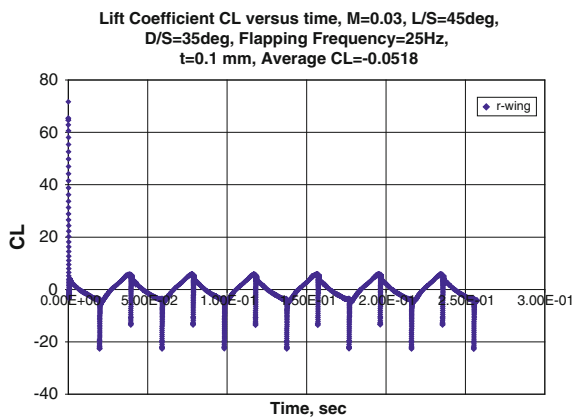
Fig. 5 Thrust coefficient time history, $M = 0.03$, $f = 25$ Hz, thickness = 0.025 mm, U/S = 45°, D/S = 35°
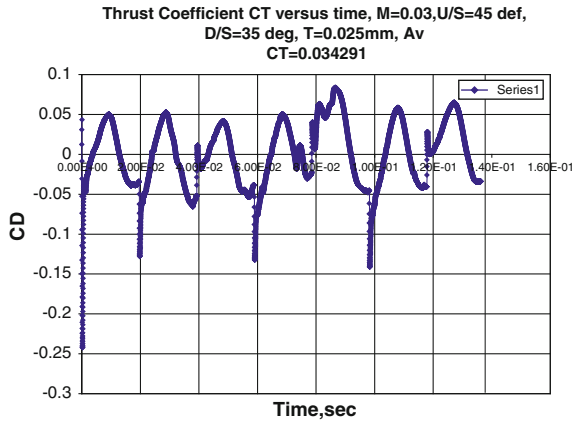
Thrust Coefficient CT versus time, M=0.03,U/S=45 def, D/S=35 deg, T=0.025mm, Av CT=0.034291

Fig. 6 Lift coefficient time history, $M = 0.03$, $f = 25$ Hz, thickness = 0.025 mm, U/S = 45°, D/S = 35°

Lift Coefficient CL versus time, M=0.03, U/S=45 deg, D/S=35 deg, t=0.025mm, Av CL=1.17520
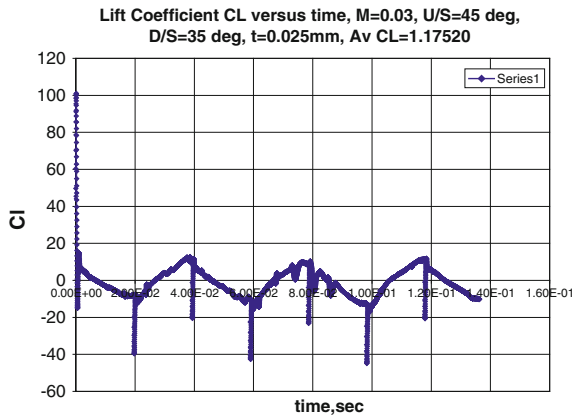
0.025 mm (25 μm). The Mach number is 0.03 with up-stroke of 45° and down-stroke of 35°. The time average lift coefficient is 1.1752.

Figures 7, 8 and 9 show the pressure coefficient contour plot for down-stroke, mid-stroke, and up-stroke, respectively. Down-stroke position indicates formation of spiral leading edge vortex at the root. Mid-stroke position indicates progression of leading edge vortex to mid span region and up-stroke position indicates progression of leading edge vortex to tip region. The sequence of spiral leading edge vortex formation at the root, growth and span wise progression to mid-span and further to tip, finally shedding at the tip region will repeat in each flapping cycle.

It has been found that 0.1 mm thick rigid wing flapping at a rate of 25 Hz with 45° up-stroke and 35° down-stroke produces time average thrust of 0.01353 and 25 μm thick wing produces average thrust of 0.034291. Since thinner wing is susceptible for large deformation dynamic wing flexure are required to be considered

Fig. 7 Pressure coefficient
contour at down-stroke


```
1.16e+0[
1.01e+0[
8.47e-01
6.89e-01
5.31e-01
3.73e-01
2.14e-01
5.62e-02
-1.02e-0
-2.60e-0
-4.18e-0
-5.77e-0
-7.35e-0
-8.93e-0
-1.05e+0
-1.21e+0
-1.37e+0
-1.53e+0
-1.68e+0
-1.84e+0
-2.00e+0
```
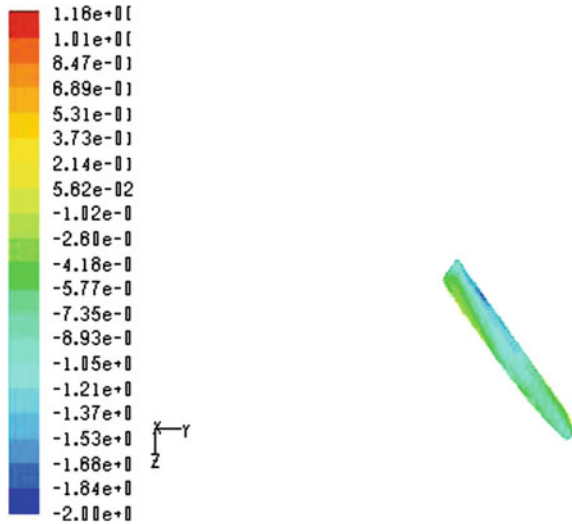
Fig. 8 Pressure coefficient
contour at mid-stroke


```
1.58e+00
1.35e+00
1.12e+00
8.87e-01
6.57e-01
4.27e-01
1.98e-01
-3.23e-0
-2.62e-0
-4.92e-0
-7.22e-0
-9.52e-0
-1.18e+0
-1.41e+0
-1.64e+0
-1.87e+0
-2.10e+0
-2.33e+0
-2.56e+0
-2.79e+0
-3.02e+0
```
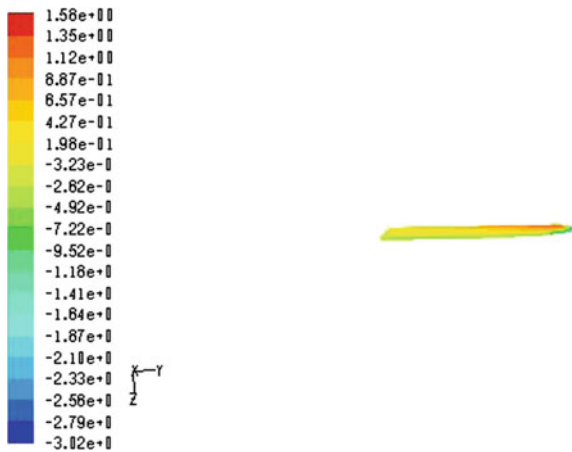
for detailed analysis. The dynamic flexure adds to the camber of the wing and
aerodynamic efficiency will be more if the camber is designed favorably for
aerodynamics. Similarly time average lift produced by 0.1 mm thick wing is
−0.0518 and 0.025 mm thick wing is 1.1752. It has been found from the time
history of lift and thrust plots that thinner rigid flat plate wing generates more lift
and thrust than thicker wing. The reason could be due to the high leading edge
curvature of thinner wing which generates strong spiraling leading edge vortex and
hence more lift and thrust.

Fig. 9 Pressure coefficient
contour at up-stroke


```
1.44e+00
1.28e+00
1.13e+00
9.74e-01
8.20e-01
6.66e-01
5.11e-01
3.57e-01
2.03e-01
4.89e-02
-1.05e-0
-2.59e-0
-4.14e-0
-5.68e-0
-7.22e-0
-8.76e-0
-1.03e+0
-1.18e+0
-1.34e+0
-1.49e+0
-1.65e+0
```
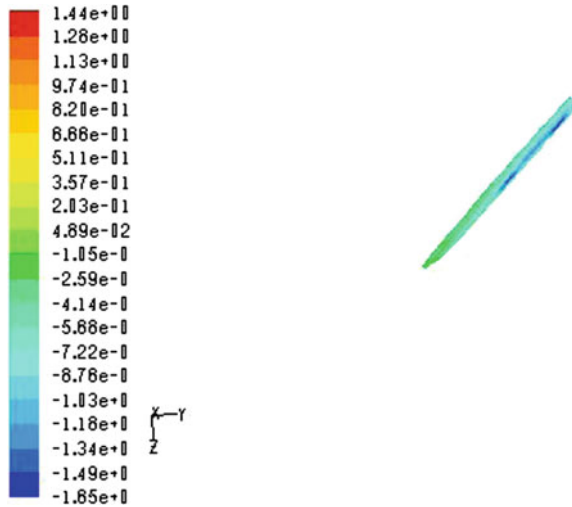
5 Conclusion

CFD analysis for a typical MICAV flapping wing configuration for two different thicknesses is carried out. Results indicate essential features of unsteady aerodynamic phenomenon of flapping wing, such as formation of spiral-leading edge vortex, span wise growth, and finally shedding at the tip region are captured in the CFD solution. It has been found that 0.025 mm thick flapping wing is more aerodynamically efficient than 0.1 mm thick flapping wing in producing lift and thrust.

References

1. Dragos Viieru, Jim Tang, Yongsheng Lian, Hao Liu and Wei Shyy, 'Flapping and Flexible Wing Aerodynamics of Low Reynolds Number Flight Vehicles' 44th AIAA Aerospace Sciences Meeting and Exhibit, AIAA 206-503, 9–15 January 2006, Reno, Nevada
2. T.N. Pormsin-Sirirak, Y.C. Tai, H. Nassef, C.M. Ho,'Unsteady-State Aerodynamic Performance of MEMS Wings' Caltech Micromachining Laboratory, 136–93, CA 91125, USA
3. Yuan Lu, Gong Xin Shen, 'Three-dimensional flow structures and evolution of the leading-edge vortices on a flapping wing', The Journal of Experimental Biology 211, 1221–1230, Published by The Company of Biologists 2008

GA-Based Multi-objective Optimal Control of Nonlinear Quarter Car Suspension

M.P. Nagarkar and G.J. Vikhe Patil

Abstract Multi-objective optimization of optimal control of quarter car suspension system is presented in this paper. A quarter car having quadratic stiffness of tire and cubic stiffness of suspension stiffness is modeled for control application. In optimization, the variables, weight matrices parameters are searched to satisfy objectives, namely, RMS sprung mass acceleration, RMS control force, RMS suspension/rattle space, tire deflection, and unsprung mass displacement and constraints on RMS acceleration and maximum control force. As the nature of the problem is of multi-objective type and objectives are of conflicting nature, hence GA is implemented to search the weight matrices parameters. During optimization and simulation, acr is traveling on class E road at 80 kmph. Trade-off front is obtained from optimization and three cases I, II, and III are selected and simulated further up to 120 kmph. These three cases provide ride comfort by keeping RMS sprung mass acceleration below ISO 2631 limit, i.e., 0.315 m/s^2. Amongst the three cases designer may prefer Case II as it follows all constraints up to 120 kmph.

Keywords Genetic algorithm · Multi-objective optimization · Optimal control · Quadratic tire stiffness · Cubic stiffness in suspension spring

Notations

A	System Matrix
A_w	Frequency weighted RMS sprung mass acceleration (m/s^2)
a_{max}	Maximum sprung mass acceleration (m/s^2)
a_w	Frequency weighted sprung mass acceleration (m/s^2)
B_f	Control input matrix
B_w	Disturbance matrix
c_s	Suspension damping coefficient (Ns/m)

M.P. Nagarkar (✉)
SCSM Nepti, A'Nagar CoE, A'Nagar 414005, MS, India
e-mail: maheshnagarkar@rediffmail.com

M.P. Nagarkar · G.J. Vikhe Patil
AVCoE, Sangamner, A'Nagar, MS, India

F	Control force (N)
f_{max}	Maximum LQR control force (N)
f_{obj}	Objective function
J	Performance Index
k_s	Spring stiffness (N/m)
k_{snl}	Nonlinear Spring Stiffness (N/m^3)
k_t	Tire stiffness (N/m)
k_{tnl}	Nonlinear tire stiffness (N/m^2)
m_s	Sprung mass (kg)
m_{us}	Unsprung mass (kg)
N	Number of samples
P	Symmetric positive definite matrix
Q, R	Weighting matrices
f	Control vector
VDV	Vibration dose value (m/s$^{1.75}$)
x	State Vector
x_r	Road profile (m)
x_s	Sprung mass displacement (m)
x_s	Sprung mass displacement (m)
$\dot{x}_s$	Sprung mass velocity (m/s)
$\ddot{x}_s$	Sprung mass acceleration (m/s^2)
x_{us}	Unsprung mass displacement (m)
$\dot{x}_{us}$	Unsprung mass velocity (m/s)
$\ddot{x}_{us}$	Unsprung mass acceleration (m/s^2)

1 Introduction

Ride quality improvement and to support the entire vehicle's weight, along with stability and road holding are the requirements of a vehicular suspension system. A typical vehicle suspension system consists of parallel mounted coil spring and damper. While mathematical modelling, the suspension system is considered as linear in nature. But springs stiffness and tire stiffness exhibit nonlinear nature [1]. Narayana and Senthil [2] presented nonlinear quarter car model and its optimal control. Nonlinear model comprises of nonlinearities in damping and stiffness. McGee et al. [3] presented 2 DoF nonlinear quarter car model having tire and spring nonlinearities in frequency domain. Lixia and Wanxiang [4] implemented a nonlinear 2 DoF suspension model having nonlinear tire stiffness and suspension spring stiffness. Author presented chaotic response and study of bifurcation of a suspension system. Bucak and Öz [5] studied a quarter car model having with cubic nonlinearity in suspension stiffness for active control application. Authors had shown bifurcation and chaotic response in presence of nonlinearities [3–5].

To the changing road surface, active suspension system supply external energy to respond dynamically. Thus, in active suspension system, relative motion is achieved between the body and wheel. Performance criterions such as ride quality, body displacement and acceleration, rattle space requirement and tire force are improved using active suspension system. In active suspension system actuator supplies force which depends on control signal [6]. Active control methods from classical, robust to intelligent and hybrid control algorithms had proposed by researchers to achieve improved ride and comfort by minimizing sprung mass acceleration.

This paper implements optimal control of nonlinear quarter car model with quadratic performance indices. Selection of weighting matrices Q and R is the key issue while designing LQR controller as control action is directly affected by weight matrices parameters. Elmadany and Al-Majed [7] had selected the weighting constants for Q and R as per the preferences of designer. Authors [8–11] had chosen weight matrices parameters of LQR arbitrarily or authors [12, 13] had adjusted LQR parameters by trial and error to achieve desired performance.

Optimal control of nonlinear quarter car (NLQC) model is presented in this paper. Nonlinear quadratic stiffness of tire and nonlinear cubic suspension spring stiffness is considered. For optimal control the objectives functions are—minimize frequency weighted RMS sprung mass acceleration (hereafter called as RMS sprung mass acceleration), RMS optimal control force, RMS rattle/suspension space requirement, maximum tire deflection, and maximum unsprung mass displacement. Maximum control force, RMS and maximum sprung mass acceleration, maximum rattle space, maximum deflection of tire, and maximum displacement of unsprung mass are used as constraints. As the optimization problem is multi-objective and of conflicting type, hence trial and error method to select the weight matrices, Q and R, is very time consuming and cumbersome. Hence to search weight matrices Q and R, GA-based optimization technique is used.

2 Mathematical Modeling of NLQC

In the presence of nonlinearities, vehicle shows chaotic behavior and complex relation between the ride's comfort [5]. Vehicle shows large vibration intensity at low periodic motion state and driving comfort. During control applications linear model is studied commonly. But it is concluded that suspension has quadratic and cubic suspension nonlinearities [3–5]. Hence in this study, a NLQC model quadratic stiffness in tire and cubic suspension spring stiffness nonlinearities is implemented for ride control application. The complete vehicle mass is divided into two masses, i.e., the sprung mass and the unsprung mass with springs and damper as shown in Fig. 1. NLQC is modeled the vertical plane while its transverse or longitudinal deflections are considered negligible.

Fig. 1 Nonlinear quarter car model
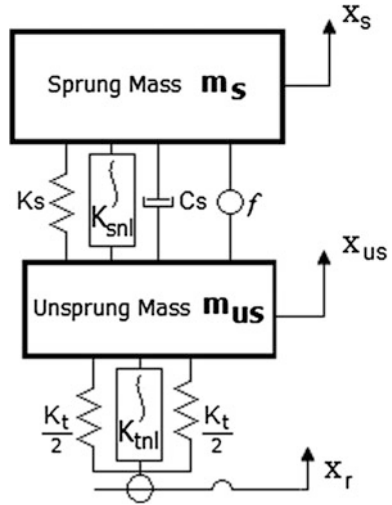
According to D'Alembert's principle, the governing equations of motion are

$$
\left.
\begin{array}{l}
m_s \ddot{x}_s + c_s(\dot{x}_s - \dot{x}_{us}) + k_s(x_s - x_{us}) + k_{snl}(x_s - x_{us})^3 + F = 0 \\
m_{us}\, \ddot{x}_{us} - c_s(\dot{x}_s - \dot{x}_{us}) - k_s(x_s - x_{us}) - k_{snl}(x_s - x_{us})^3 + k_t(x_{us} - x_r) \\
+\, k_{tnl}(x_{us} - x_r)^2 - F = 0
\end{array}
\right\}
\quad (1)
$$

Defining state variable as $x_1 = x_s$, $x_2 = \dot{x}_s$, $x_3 = x_{us}$, $x_2 = \dot{x}_{us}$, $F = f$, and $x_r = w$, in state space form (1) can be represented as

$$
\dot{x} = Ax + G(x) + B_w w + B_f f
\quad (2)
$$

where

$$
x = \begin{bmatrix} x_1 \\ x_2 \\ x_3 \\ x_4 \end{bmatrix};\;
A = \begin{bmatrix}
0 & 1 & 0 & 0 \\
\frac{-k_s}{m_s} & \frac{-c_s}{m_s} & \frac{k_s}{m_s} & \frac{c_s}{m_s} \\
0 & 0 & 0 & 1 \\
\frac{k_s}{m_{us}} & \frac{c_s}{m_{us}} & \frac{-(k_s + k_t)}{m_{us}} & \frac{-c_s}{m_{us}}
\end{bmatrix};\;
B_w = \begin{bmatrix} 0 \\ 0 \\ 0 \\ \frac{k_t}{m_{us}} \end{bmatrix};\;
B_f = \begin{bmatrix} 0 \\ \frac{-1}{m_s} \\ 0 \\ \frac{1}{m_{us}} \end{bmatrix}
$$

$G(x)$ containing nonlinear terms is

$$
G_x = \begin{bmatrix}
0 \\
\frac{-k_{snl}(x_1 - x_2)^3}{m_s} \\
0 \\
\frac{-k_{snl}(x_1 - x_2)^3 + k_{tnl}(x_s - w)^2}{m_{us}}
\end{bmatrix}
\quad \text{where } G(0) = 0.
$$

The parameters of a NLQC are.

m_s = 240 kg, m_{us} = 40 kg, k_s = 20,000 N/m, c_s = 1000 N.s/m,

k_{snl} = 2,000,000 N/m^3 [6], k_t = 140,000 N/m, k_{tnl} = 1.25 k_t N/m^2 [5].

3 Multi-objective Optimal Control of NLQC

Optimal Control

The control law is full state feedback with disturbance rejection. Let us consider nonlinear system described in (2). The linear feedback control is given by

$$f = \left[-R^{-1}B^T P\right] x \qquad (3)$$

which is optimal to transfer system (4) from initial state to final state. Design involves determination of control input f to minimize performance index J. Performance index J represents control input limitations and requirement of performance characteristic [11]. The quadratic performance index is

$$J = \int\limits_0^t \left[L(x) + f^T R f\right] \mathrm{d}t, \qquad (4)$$

where $L(x)$ containing $G(x)$ is positive definite, then Q and R are positive definite. The error and performance index expenditure is determined by Q and R [11, 14].

Matrix P, symmetric and positive definite, is solution of nonlinear algebraic Riccati Eq. (5). Refer [11] for optimal control analysis.

$$AP + A^T P - PBR^{-1}B^T P + Q = 0 \qquad (5)$$

Malab function *lqr* is used to solve (5) for A, B_f, Q, and R.

Problem Formulation in GA Environment

GA-based optimization technique is implemented to search optimal control weighting matrices Q and R. GA is invented by Holland [15] for optimization and global search. Due to conflicting nature of objective functions, NGPM [16] (A NSGA-II Program in Matlab) is implemented for multi-objective optimization. In NSGA-II non-dominated sorting is done. For this each individual is compared with remaining solutions of a population. NSGA-II had introduced a new parameter, called as crowding distance (CD). In the non-dominated population, CD gives measure of individuals' diversity. Selection of parents from non-dominated front is based tournament selection and CD. Crossover and mutation operators are used to create new off-springs. Current population/parents and new off-springs are combined to generate population for next generation.

Algorithm is repeated till to reach some convergence criterion such as fitness or stopping criterion such as number of generations or CPU time. Here algorithm is stopped after 100 numbers of generations.

During optimization, objective functions are ride comfort (RMS sprung mass acceleration as per ISO 2631 [17]), RMS suspension travel, tire deflection, road holding and RMS control force. Optimization problem is formulated as follows

$$f_{obj1} = \text{Minimize (RMS F)}; \; f_{obj2} = \text{Minimize (Aw)}; \; A_w = \left\{ \int_{o}^{T} [a_w(t)]^2 dt \right\}^{1/2}$$

$$f_{obj3} = \text{Minimize (RMS Suspension Travel)}; \; f_{obj4} = \text{Minimize (max } |x_{us} - x_r|)$$
$$f_{obj5} = \text{Minimize (max } |x_{us}|))$$

Subject to constraints [18]
$A_w \leq 0.315 \, \text{m/s}^2$, $\text{Max.}(x_u - x_{us}) \leq 0.127 \, \text{m}$, $a_{max} \leq 4.5 \, \text{m/s}^2$,
$\text{Max.}(x_{us} - x_r) \leq 0.058 \, \text{m}$, $x_{us} \leq 0.07 \, \text{m}$ and $F_{max} \leq 2000 \, \text{N}$

GA Parameters are
Population: 100, Generations: 100, Selection: Tournament.
Search Space of Q and R Matrices:
$10^{10} \leq Q_{11} \leq 10^{12}$, $10^6 \leq Q_{22} \leq 10^7$, $0.01 \leq Q_{33} \leq 10$, $0.01 \leq Q_{44} \leq 10$, $0.001 \leq R_1 \leq 0.1$

4 Result and Discussion

For optimal control and optimization, NLQC is modeled and simulated in Matlab®. Road of class E having $4096 \times 10^{-6} \, \text{m}^2/(\text{cycle/m})$ [19] road roughness is input to NLQC, having speed 80 kmph. Refer Fig. 2.

After simulation and optimization, a trade-off front is obtained of 100 solutions is shown in Fig. 3. In decision making and selecting weight matrices parameters, trade-off front offers flexibility to designer. For analysis, three cases, namely, Case I, II, and III are selected from Fig. 3. Table 1 represents parameters the

Fig. 2 Road surface (Class E, Speed 80 kmph)
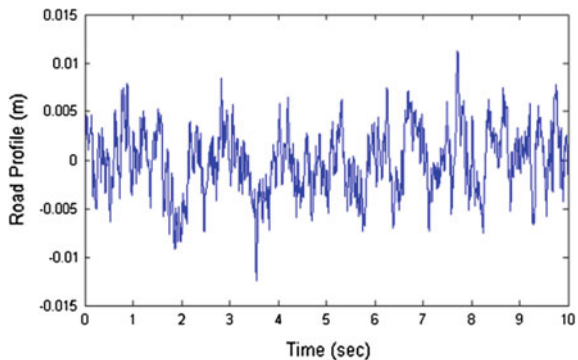
Fig. 3 Trade-off front
(Population 100, Generation
100)
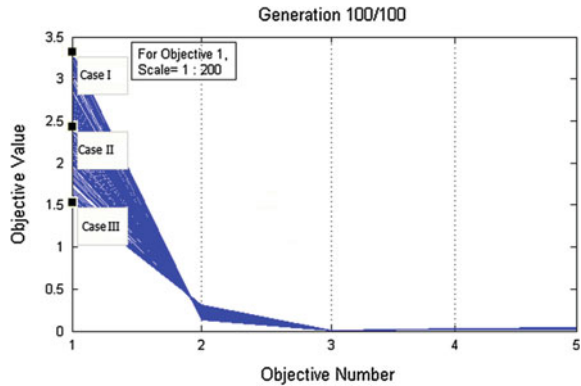
Table 1 Weight matrices—multi-objective optimization

Case	[Q] = Diagonal matrix [Q11, Q22, Q33, Q44]	[R1]
Un-optimized case	[1e + 010, 1e + 006, 0.1, 0.1]	[0.1]
Case I	[8.13947E11, 9.376183E6, 3.5318, 6.9873]	[2.47466E-3]
Case II	[3.68374E11, 8.750031E6, 4.7122, 6.8640]	[4.72202E-3]
Case III	[1E11, 7.426168E6, 3.7001, 6.3031]	[8.35103E-3]

matrices Q and R. From trade-off front, Case I and Case III are chosen from extreme position whereas Case II is from center. These three cases and un-optimized optimal control are simulated and the results are compared.

Simulation results of RMS sprung mass acceleration, RMS control force, RMS suspension/rattle space, tire deflection, unsprung displacement, maximum sprung mass acceleration, and maximum value of controller force are tabulated in Table 2. Time histories of simulation results of control force, sprung mass acceleration, suspension/rattle space, tire deflection, and unsprung displacement are shown in Fig. 4.

RMS sprung mass acceleration is 1.0727 for un-optimized case. Whereas RMS sprung mass acceleration of I, II and III cases is below 0.315 m/s^2 which is not

Table 2 Response of NLQC—LQR control active suspension system

Type	RMS f	Aw	RMS SSD	Max. TD	Max. UMD	VDV	f_{max}	a_{max}	Max. SSD
Un-opt	43.63	1.072	0.005	0.017	0.018	2.466	131.2	3.2662	0.0175
Case I	664.1	0.138	0.011	0.031	0.036	0.315	1999.9	0.4022	0.0361
Case II	484.9	0.208	0.009	0.027	0.030	0.492	1640.7	0.6934	0.0302
Case III	303.6	0.315	0.006	0.022	0.021	0.756	1030.3	1.0815	0.0215

Where, SSD: Suspension Space Deflection, TD: Tire Deflection, UMD: Unsprung Mass Deflection
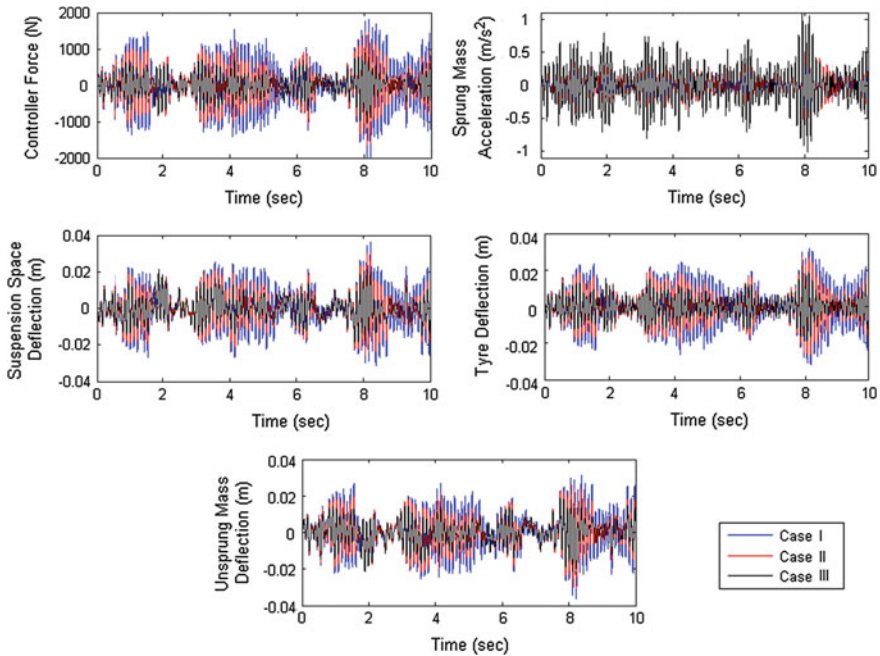
Fig. 4 Response of nonlinear quarter car

uncomfortable to passengers as per ISO 2631. Thus more ride comfort is achieved using optimized optimal control. From Table 2, it is observed that RMS and maximum rattle space increases with decrease in RMS sprung mass acceleration. Thus, to achieve ride comfort, suspension space is compromised. From Table 2, for tire deformation and unsprung mass displacement same trend is observed. Yet constraints are followed.

In an automobile, passengers experiences major portion of vibrations are transferred through seat to the body. With increase in exposure time health risk goes on increasing. Thus, measurement of whole body vibration (WBV) is necessary. According to ISO 2631 [17], WBV measurement is based on VDV which assesses the dose or cumulative effect of vibrations. VDV is the fourth power of acceleration time histories. VDV follows same trend as RMS sprung mass acceleration. Refer Table 2. Lower values of VDV improves health

The vehicle is considered to be traveling at 80 kmph in optimization and simulation. To study the performance, speed is varied from 10 to 120 kmph and NLQC is simulated on class E road. The performance criterion plotted are VDV, RMS sprung mass acceleration, RMS control force and Maximum control force.

From Fig. 5 it is observed that, for Case I RMS sprung acceleration constraint is followed up-to 120 kmph whereas constraint on maximum control force is violated beyond 80 kmph. Whereas Case III violates the RMS sprung acceleration constraint
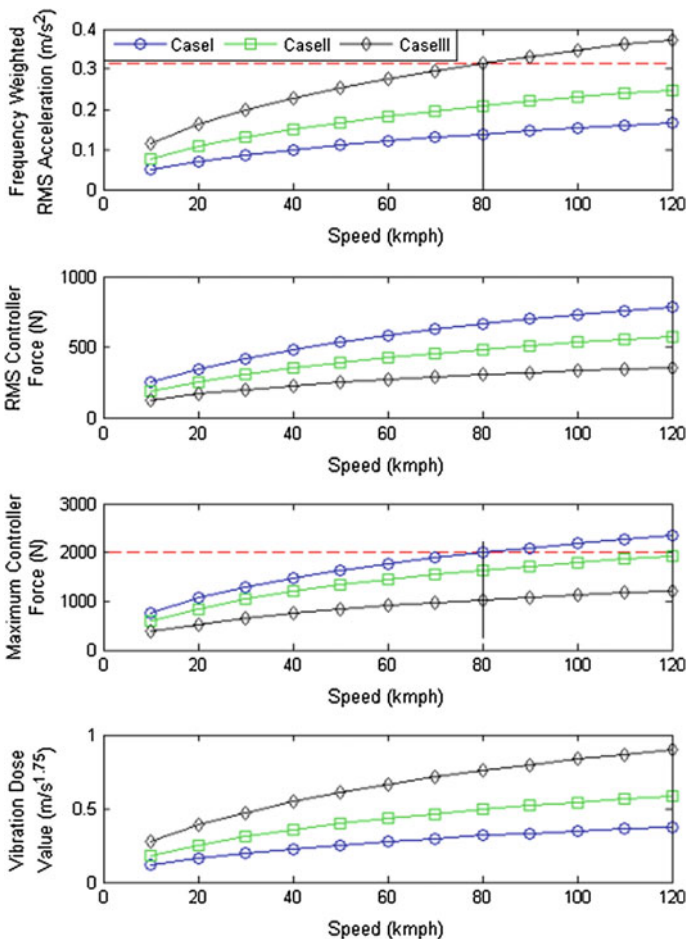
Fig. 5 Response of NLQC to varying speed

beyond 80 kmph. For Case II, it is observed that both constraints are followed well up to 120 kmph. Hence designer may prefer Case II.

5   Conclusion

Multi Objective optimization using GA is implemented to search Q and R parameters. A nonlinear quarter car model, consisting of quadratic stiffness in tire and cubic suspension spring stiffness, in implemented for ride and optimal control study. A GA-based search and optimization technique is presented which avoids selection of parameter and then adjustments or trial and error. Multi-objective

optimization consists of five conflicting objectives hence NASG-II algorithm is implemented for optimization. As per ISO 2631, ride comfort is provided by optimized optimal control by keeping RMS sprung mass acceleration below limit.

Case II follows constraints and gives optimum results up to 120 kmph. Amongst Case I and III, Case I may selected by overriding constraint on control force. Case III can be avoided as it compromises ride comfort beyond 80 kmph. More solutions can be explored from central region of trade-off front following constraints.

References

1. Wong JY. Theory of ground vehicles. 2001, John Wiley & Sons, Inc., NY.
2. Narayanan S, Senthil S. Stochastic optimal active control of a 2-DoF quarter car model with non-linear passive suspension elements. J Sound Vib 1998; 211 (3): 495–506, 1998.
3. McGee CG, Haroon M, Adams DE, Luk YW. A Frequency Domain Technique for Characterizing Nonlinearities in a Tire-Vehicle Suspension System. J Vib Acoust 2005; 127: 61–76.
4. Lixia J, Wanxiang L. Chaotic vibration of a nonlinear quarter -vehicle model. In: Proceedings of IEEE Vehicle Power and Propulsion Conference (VPPC), Harbin, China; 2008: 1–4.
5. Bucak İÖ, Öz HR. Vibration control of a nonlinear quarter-car active suspension system by reinforcement learning. Int J Syst Sci 2012; 43 (6): 1177–1190.
6. Filler CR, Elliott SJ, Nelson PA. Active control of vibrations. 1996, Academic Press, London.
7. Elmadany MM, Al-Majed MI. Quadratic Synthesis of Active Controls for a Quarter-Car Model. J Vib Control 2001; 7: 1237.
8. Yahaya MS, Ruddin M, Ghani A, Ahmad N. LQR Controller for Active Car Suspension. In: Proceedings of TENCON; 2000: 441–444.
9. Zhen L, Luo C, Hu D. Active Suspension Control Design Using a Combination of LQR and Backstepping. In: Proceedings of the 25th Chinese Control Conference; 2006: 123–125.
10. Darus R, Enzai NI. Modeling and Control Active Suspension System for a Quarter Car Model. In: Proceedings of International Conference on Science and Social Research; 2010: 1203–1206.
11. Tusset AM, Rafikov M, Balthazar JM. An intelligent controller design for magneto rheological damper based quarter-car model. J Vib Control 2009; 15 (12): 1907–1920.
12. Oral Ö, Çetin L, Uyar E. A novel method on selection of Q and R matrices in the theory of optimal control. Int J Syst Control 2010; 1 (2): 84–92.
13. Hasbullah F, Waleed F. A comparative Analysis of LQR and Fuzzy Logic Controller for Active Suspension Using Half Car Model. In Proceedings of 11th Int. Conf. Control, Automation, Robotics and Vision Singapore 2010: 2416–2420
14. Anderson B, Moore J. Optimal control – linear quadratic methods. 1990, Prentice Hall, New Jersy.
15. Holland JH. Adaptation in Natural and Artificial Systems. 1975, University of Michigan Press.
16. Song L. NGPM-A NSGA-II Program in Matlab v14. Matlab Code. [cited 2015 Mar 15] Available from http://www.mathworks.com/matlabcentral/fileexchange.
17. ISO: 2631-1. Mechanical vibration and shock - Evaluation of human exposure to whole-body vibration. 1997.

18. Baumal AE, McPhee JJ, Calamai PH. Application of genetic algorithms to the design optimization of an active vehicle suspension system. Comput Meth Appl Mech Eng 1998; 163: 87–94.
19. Zhang Y, Chen W, Chen L, Shangguan W. Non-stationary Random Vibration Analysis of Vehicle with Fractional Damping. In proceedings of 13th National Conference on Mechanisms and Machines (NaCoMM07) 2007: 171–178.

Study of the Influence of the Process Variables on Formability and Strain Distribution in Incremental Sheet Metal Working of AA 1050 Sheets

M. Amala Justus Selvam, R. Velu and T. Dheerankumar

Abstract Incremental sheet metal forming is a novel and quick process suitable for rapid prototyping and production of small batch of sheet metal components. The forming operation is carried out at room temperature employing a CNC machining center. A specially designed spherical tip tool and a simple support to hold the formed sheet are required to undertake the process. In this work, incremental sheet metal forming was carried out on 0.5 mm AA 1050 sheet to study the impact of process and product characteristics. The process parameters involved are rotation of the tool, feed in x, y directions and axial feed in z direction. Two process conditions are used, namely, with lubrication and without lubrication. Frustum of square pyramid has been considered as the shape of the component form the formed component strain distribution was measured. To measure strain distribution, circular grids were etched on the surface. Formability diagram were plotted with the results. The results of forming with lubrication and without lubrication were compared and brought out.

Keywords Spherical tool · Axial feed · Strain distribution · Formability

1 Introduction

Incremental sheet metal forming process (ISMF) is adopted to form metal sheets using a unique forming technique to augment the flexibility of manufacturing processes. ISMF completes a three-dimensional part without using a die. ISMF is a process that is used to make non-symmetrical parts in low cost die and for small

M. Amala Justus Selvam (✉) · R. Velu
Department of Mechanical Engineering, Vel Tech University, Avadi,
Chennai, Tamil Nadu, India
e-mail: amalajustus@veltechuniv.edu.in

T. Dheerankumar
Dhuruva Institute of Engineering & Technology, Hyderabad,
Telangana, India

sized lots of sheet metal parts. A simple hemispherical tool that moves on a controlled tool path is employed in forming the new part. In ISMF, the contact zone between the tool and the processed sheet is limited and also keeps on changing with the progress of the tool. The sheet blank is fixed in a fixture and then the tool deforms the sheet blank in the type of path that is decided by a shape of the part. Using dynamometer, Peteket et al. [1] focused on analysis of force involved in ISMF. When this technique is used for forming, cracks occured on the formed sheets due to tool rotation, in the absence of lubrication. Because of the tool rotation, a large amount of friction force arises in the contact surface between the tool and the sheet. Rauch et al. [2] developed a novel approach for the tool path programming in sheet metal forming and put forth the impact for tool path type. It was also observed that a tough milling software path was not recommended for ISMF. The quality of the final part can be seriously varied by the movement of the tool. The way of adapting the tool path is dedicated to forming applications where a very high forming force results due to the wrong positioning of the forming die. In this study strain distribution influenced by forming parameter like axial feed Z, feed X, Y, rotational investigation is found out. The shape of the part considered for this study is a square pyramid of sides 73 mm and height 32 mm.

1.1 Objectives

The objectives of this work are

1. To find the optimal setup for incremental sheet metal forming and
2. The impact of forming parameters on the sheet metal AA 1050.

2 Analysis of Incremental Sheet Metal Forming Using FEA

Oleksik et al. [3] conducted a comparative study based on the simulation by the FEM techniques of incremental sheet metal forming and classical stretch forming process. Some of the trajectories of tool path that are commonly used are (a) vertical movement of tool followed by movement along border (b) stepped movement of tool and rectangular trajectory (c) vertical movement by tool and covering all formed surface. The thinning of the sheet was the predominant problem noticed during the process. Variation in Von Mises stresses in the section profile of the obtained parts and the forces developed in the processes were also studied in the literature.

Pohlak et al. [4] conducted tests on incremental sheet metal forming process with adequate support and without support. In either case, the deformation mechanism was almost same in which shear deformations dominated. Forming with support

obviously allowed achieving highly accurate geometry, but suffered an extra cost of the need for providing the supports. The maximum positive normal deviation and maximum negative normal deviation are more in the case of forming with support than in the case of forming without support. The accuracy in forming process by providing supports is affected by then existing stretching force. It was found that the stretching force helped to achieve more accurate process. But, if stretching force is too high, it caused additional issues due to sheet necking.

2.1 Tool Path and Force Measurement

Rauch et al. [2] estimated forming forces for incremental sheet metal forming. Here, tool paths were adapted as per the results obtained from the forming force calculations. The main aim was to prevent the sheet metal getting damaged by a large forming force. Two methods were employed to get rid of it. One was to change the speed of the forming tool and the second one was to invoke a subroutine that cleared the tool.

A difficulty arose in this optimization procedure which influenced in its total time consumption. The accuracy of the finished product got influenced by the variations in the tool movements also. Selecting the tool path in this manner is applied to different forming cases, where a high force results due to inaccurate positioning of the die.

A different way to overcome the sheet metal getting damaged during the process is to call a tool clearance procedure as shown in Fig. 1. This solution can be applied for single incremental forming applications also.

In the case of forming without applying lubrication, the crack occurred in the sheet at the forming depth. Because of the rotation of the tool, huge amount of frictional force developed in the contact surface between the tool and the sheet specimen. This increased the tool temperature and the possibility of kneading of the sheet metal.
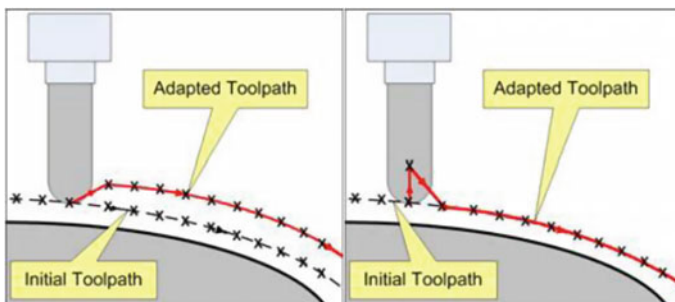
Fig. 1 Tool path adaptations

Jansson et al. [5] had introduced optimization technique to minimize the risk of failure in a sheet metal forming process. In this paper, an optimization technique was employed to minimize the failure of the work piece in the sheet metal forming process. Two different types of finite element solvers were employed. The work was carried out by initially using total plasticity and then using incremental plasticity. It was found that the use of the total plasticity theory reduced the required computing time to a considerable extent. Also, the solution obtained from the SM optimization algorithm was closer to that obtained from the incremental plasticity solver.

2.2   ISMF Using CNC Machine Tool

Kopac and Kampus [6] conducted ISMF using CNC machine where it was performed using a milling tool with suitable CAD/CAM technical support. In this work, in place of a milling tool, a tool with a spherical shape in one end was employed. In the contact zone between the tool and the specimen, the forming took place. It was seen that the surface was having less serrations when the surfaces were applied with a solid lubricant. But, when the operation was carried out without a lubricant, the surface was rough. The sheet did not form into the desired shape at the end of the process. From the above, it may be understood that Finite Element Analysis can be used as an effective tool to determine forming parameter in ISMF and it can be successfully done using a CNC milling machine. In this study, finite element analysis of the ISMF of square frustum was carried out.

3   FEA of Incremental Sheet Metal Forming

For the finite element analysis, pre-processing was done using HYPERMESH, analysis and post-processing was done using LS-DYNA.

HYPERMESH software was used to develop the tool, fixture, base plate, and sheet blank for a sheet metal forming operation. Boundary constraints were specified by defining a tool and a blank. All the four edges of the blank were fixed and the tool was given movement as per the path. The velocity and tool path were defined for the tool and the blank. HYPERMESH includes a quads method for shell elements. In a quads method, the elements are subdivided into smaller elements, whenever an error indicator shows that subdivision of element provided improved accuracy. The user sets the initial mesh and maximum level of separation. In this work, quad element was used.

Simple square sheets of aluminum AA 1050 of 0.5 mm thickness were used as material since it is used frequently in the sheet metal industry. Material definition is one of the most important steps in an analysis. Before defining material property, it is necessary to define true stress versus true strain curve. The curve should be given a unique identification. MAT card is used to define material properties. As the

material we considered for analysis is anisotropically elastic plastic, we numbered it 24 and all the material properties have been provided to it.

Tool path has been assigned using the dialog box of the application in which *X* value is time and *Y* value is displacement of tool. LS-DYNA program manager is the key tool to perform simulation. The '*k*' keyword file that is generated during pre-processing is analyzed with the help of solver.

At the end of the analysis, 'd3plot' file is generated which is used for post-processing. The 'dynain' file has all the properties of the blank that is obtained after first stage drawing. So it is used as the blank for the second stage. Modeling is done again for the new blank with a new press tool set.

4   Experimentation

The selection of materials has been done followed by FEA of ISMF. Fixture design has been carried out followed by experimentation. Measurement of strain was done and then the comparison of results of FEA with that of the experiment was made. Then the comparison of strain results with FLD was made.

ISMF uses a specially designed support which supports the sheet metal. When the support is not employed the quality of the components may be affected. The parts of fixture were machined using milling machine and assembled. The material used for making fixture is mild steel.

In this work, stainless steel is used for making the tool. The shank height is 85 mm, diameter is 12 mm and the ball point diameter is 10 mm. This tool is suitably fitted inside the collet and then the collet is inserted into the tool holder.

The work is undertaken to find out the strain values in the ISMF. To measure the accompanied strain, grid marking on the surface of the forming sheet is done using screen printing. Using this method, 5 mm diameter circular grid was marked. The pattern was directly imprinted on the workpiece using an indelible ink that would not fudge.

For chemical etching, electrolysis process was employed. In this setup, a 12 V battery and sodium hydroxide were used. The job was made as the anode whereas a dummy sheet was made as cathode. In this process, NaOH was mixed with water and was employed as the electrolyte. The anode and cathode plates were dipped into the electrolyte. After a period of 20 min, the plate was taken out and cleaned by turpentine oil.

The work load selected for carrying out this experiment was a CNC vertical milling center, whose specifications are: Control system-FANUC-oi-MATE-MC, *X*-axis 450 mm, *Y*-axis and *Z*-axis 350 mm with a positional accuracy of 0.01 mm. The tool and fixture arrangement is shown in Fig. 2.

Initially, tool was fed axially and was programmed to take a straight line path. After every iteration, the tool was given further movement in the axial direction.

Fig. 2 Tool and fixture arrangement

These displacements are termed as axial feed (Δz), radial feed (Δx), and the feed rate. The procedure was repeated till the required shape of the cone was made.

In the operation, the hemispherical headed tool was fit to the rotating spindle of the machining center. The sheet metal to be worked upon was held by the top blank holder. The top blank holder was moved against the bottom blank holder. The whole support was inserted and fixed onto the worktable of the milling machine. The tool pressed and locally deformed the sheet directly under the tool head with a small value of deformation. During this process, the blank holder and fixture remained fixed. The tool followed to the predetermined tool path and gradually formed the sheet metal in a series of incremental steps till the final depth was achieved. In this work, we considered different parameters like the spindle rotation, axial feed rates, feed in X, Y directions and axial feed in Z direction, rotation of tool, and application of lubrication. The selected parameters are shown in Table 1 and they are shown parametrically in Fig. 3

Using the setup, cups appearing like the frustum of a pyramid were shaped. In addition to the change in the parameters, four conditions were taken up for consideration, namely, tool with lubrication and tool without rotation. The formed cup with circle grids is shown in Fig. 4. Three points are selected from the cup wall and using Mylar tape major and minor strain are measured.

Standard forming limit diagram for AA 1050 obtained from the work of Myoung-Supshim [7] using ISMF. This was considered in this study to compare the deformation zones formed. The strains induced during the process are arrived using the following formulae:

Table 1 ISMF process parameters

Forming depth	Rotational speed	Feed rate (X,Y)	Tool diameter	Tool Path	Axial feed (Z)
31 mm	0 and 60 rpm	100, 150 and 200 mm/min	5 mm	Clockwise	1 and 1.5 mm
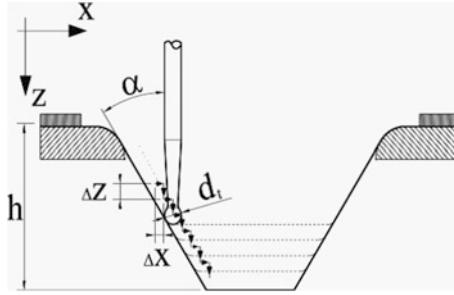
Fig. 3 Steps of SPIF
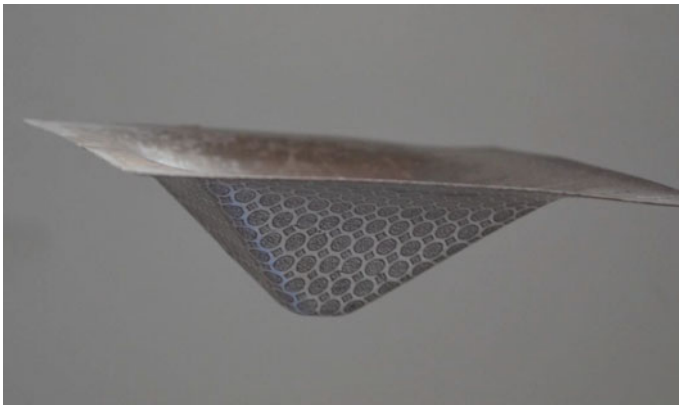
Fig. 4 Formed cup with circle grids

$$\text{Strain}_{\text{major}} = \left(\text{length}_{\text{major axis}} - \text{Initial circle diameter}\right) \times 100/\text{Initial circle diameter}$$

$$\text{Strain}_{\text{Minor}} = \left(\text{length}_{\text{minor axis}} - \text{Initial circle diameter}\right) \times 100/\text{Initial circle diameter}$$

For physical measurement of strain, Mylar tape, which is a transparent scale containing diverging lines scaled to read the strain directly in percent is used. The Mylar tape is positioned on the sheet metal over the formed ellipse over a sharp radius and then moved till the diverging lines coincide with the major axis of the ellipse. The strain value is noted from the scale. The scale is then rotated by 90° to read the value of minor strain. The strain measurements obtained from the simulation are shown in Figs. 5 and 6.
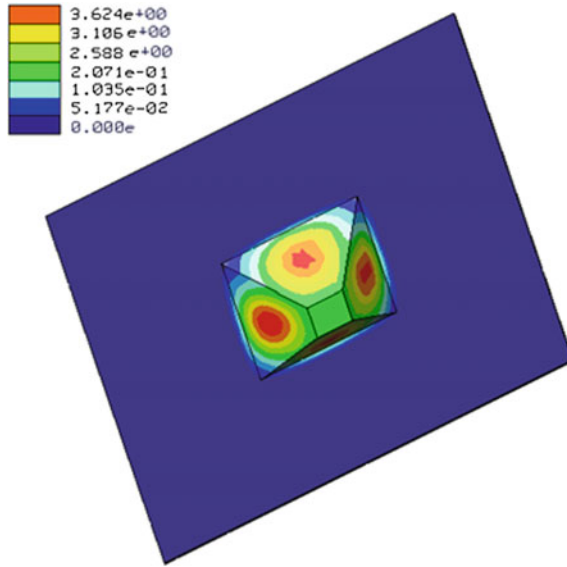
Fig. 5 Major strain distribution on the specimen surface
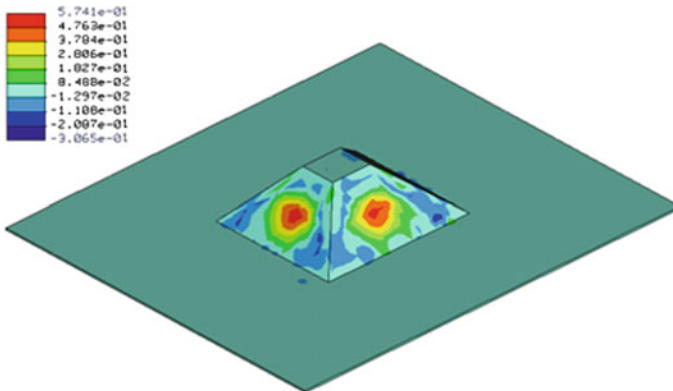
Fig. 6 Minor strain distribution on the specimen surface

5 Results and Discussion

The values of the strains during the process on the sheet metal are vital to carry out various forming processes. It is essential to know in which zones necking and fracture are observed. When the forming limit curve for a particular sheet metal product is known in advance, the shaping process can be successfully carried out

and optimized. By this method, process time can be saved and the costs can be reduced. The quality of the final products can be finally improved.

Specimens were worked in the above chosen conditions in the experimental setup shown in Fig. 2. Three points were chosen on the specimen surface that corresponded to that of the finite element model. Major and minor strains were measured from the surface using Mylar tape. Figures 7 and 8 show the location of strain measurement and the formed frustum. Measured strains were compared with the values of forming limit curve. Test specimens were obtained under four chosen conditions, namely, rotating tool with and without lubrication, non-rotating tool with and without lubrication. Axial feed rate, planar feed rate were varied and cups were formed. Figures 9 and 10 show the comparison of the major and minor strain from the part formed by rotating the tool without the application of the lubricant. It is seen with the axial feed of 1 mm feed rate of 150 and 200 the values of strain are in risk zone (above FLD). For the feed rate value of 200, the strains are below FLD. When the axial feed rate is changed to 1.5 mm, the values of strains moved to acceptable level.

Major and minor strains of some of the elements of the cup are shown in the forming limit diagram (FLD). All these values are below the FLC. The major and minor strains locations included in FLDs are observed to be closely in accordance. The values obtained from FEA match closely to that of the experimental results.

Fig. 7 Locations of strain measurement on the cup with one-fourth of height

Fig. 8 Formed frustum with the locations of strain measurement
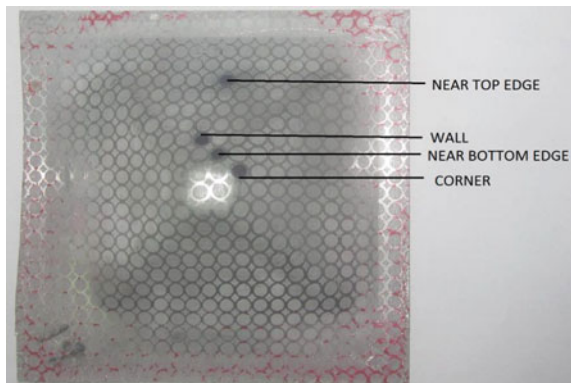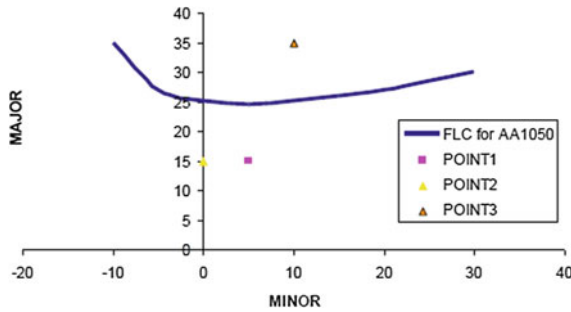
Fig. 9 Comparison of major and minor strains with FLC
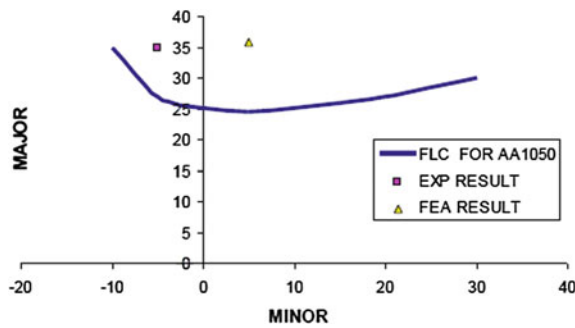
Fig. 10 Comparison of experimental and FEA results of major and minor strains

Figure 10 shows the comparison of experimental values with that of the FEA. Major strain lies on the stretched side whereas the experimental value was on the drawn side. Both the values are found to be in danger zone.

The strain values obtained from the specimen formed with the rotating tool, without lubrication is shown in Fig. 11. It may be seen that with a feed rate of 100 mm/rev, axial feed of 1 mm, the strain values are in the unacceptable zone
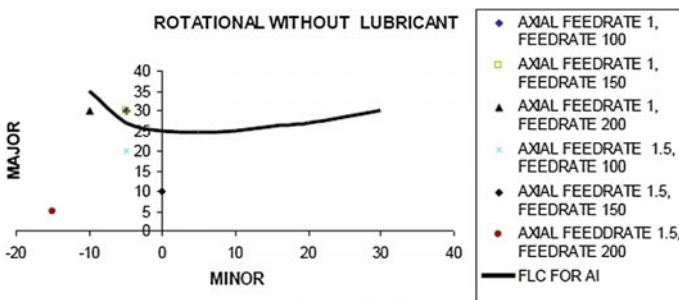
Fig. 11 Comparison of strain-rotational tool without lubrication

(above FLC). For the feed rate 200 mm/rev, the strain values are below the safe values as shown in the FLC. When the axial feed rate is changed to 1.5 mm all the strain values are seen to be in the safe region. For an axial feed rate of 1.5 mm and feed rate of 200 mm/rev, elements suffered larger values of the minor strain.

Comparison of major and minor strain induced in the part formed by the rotating tool with lubricating situation is given in Fig. 12. It may be seen that the strain values are either above the FLC or on the plane strain axis. Strains induced by a feed rate of 200 mm/rev and axial feed rate of 1.5 mm are safe compared to any other conditions. Figure 13 shows the distribution of major and minor strain caused in the part formed by non rotational tool with lubrication condition. All the strain values are in the safe zone. It is observed that an increase in axial feed causes strain values close to plane strain condition.

Figure 14 shows the distribution of major and minor strain caused in the part formed by non-rotational tool without lubrication. Strain is moved to danger zone when axial feed rate is 1 mm and feed rate is 150 mm/rev. Some of the strain is observed in the plane strain condition. Here too, all the strain values are within safe region. It is observed that an increase in axial feed causes strain values close to
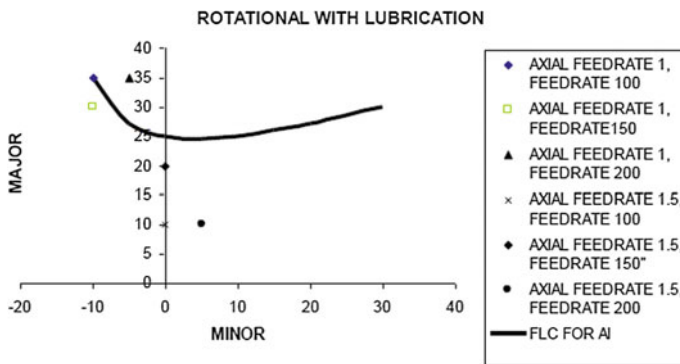
Fig. 12 Comparison of strain-rotational with lubrication

Fig. 13 Comparison of strain-non-rotational with lubrication
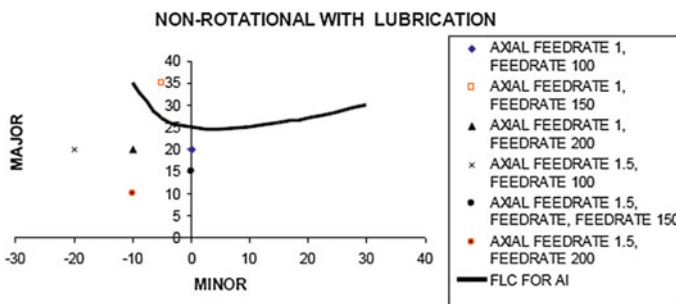
NON-ROTATIONAL WITHOUT LUBRICATION
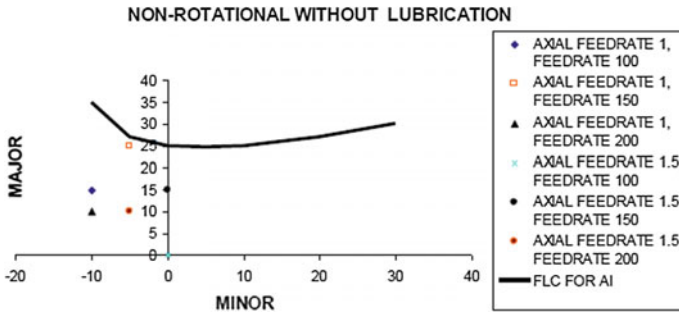
Fig. 14 Comparison of strain-non-rotational without lubrication

plane strain condition. It is observed from the above, that application of lubrication produces negative minor strain, as most of the strain values are in drawing region. Also it is observed that when the tool is not rotating, strains induced are in safe zone. This might also be due to the absence of the localized strains due to rotation.

6   Conclusion

Study of incremental sheet metal forming of AA 1050 to produce the frustum of square pyramid was carried out in a CNC milling machine using suitable setup. When the cup is formed without the lubrication condition, some of the strain values are seen in the danger zone (i.e., over and above the forming limit). Variations in feed in Z, Y, directions cause an increase in minor strain. This shows that all the strain values are placed in the safe drawing zone. Variation in axial feed causes plane strain condition. No significant effect is seen with respect to the rotation of the tool. Application of lubrication changes the mode of deformation from stretching to drawing.

References

1. Peteck, Kuzman K. and Kopae J. "Deformations and forces analysis of single point incremental sheet metal forming", World Academy of Materials and Manuf. Engg., 35, pp. 107–116, 2009.
2. Rauch M., Hascoetn J.Y., Hamann J.C, and Plennel Y., "A new approach for tool path programming in Incremental Sheet Forming", J. of Engg. Manuf., 217, No. 2, pp. 213–225, 2005.
3. Oleksik V., Bologa O., Breaz R. and Racz G., "Comparison between the numerical simulations of incremental sheet forming and conventional stretch forming process", Int. J. Material form, 1, pp. 1187–1190, 2008.

4. Pohlak M., Küttner R., Majak J., Karjust K. and Sutt A. (2004), "Experiment study of incremental forming of sheet metal product", 4th Int. DAAAM Conference, pp. 139–142, 2004.
5. Jansson L. and Nilsson, "Minimizing the risk of failure in a sheet metal forming process", 31, pp. 320–332, 2006.
6. Kopac J. and Kampus Z. "Incremental sheet metal forming on CNC milling machine-tool", J. of materials processing Tech., 162, pp. 622–628, 2005.
7. Myoung-Supshim and Jong-Jin Park, "The formability of aluminium sheet in incremental sheet", J. of materials processing tech., 113, pp. 654–658, 2001.

Operating Characteristics of Multi-cylinder Petrol Engine Using LPG With Methanol

S. Somasundaram, T. Mohanraj, S. Pasupathy Raju and K. Murugu Mohankumar

Abstract Increase in environmental pollution, energy scarcity, depletion of fossil fuels and to secure future fuel supply, the need of non petroleum based alternative fuels becomes essential. These alternative fuels are used to increase the efficiency and reduce adverse effect of green house gases. Owing to high octane rating, liquified petroleum gas (LPG) proves to be more efficient than petrol mixed with methanol up to 2 ml/min which is used as an alternative fuel in this study. This alternative fuel can be used in the SI engine with slight modification in the fuel supply system. The experiments are conducted in 4-cylinder, 4-stroke petrol engine with bi-fuel activated by the solenoid. The actuator diverts LPG through the vaporizer kit to the carburetor. The flow rate of LPG is calculated using suspended weighing scale. Liquid methanol enhances the LPG prior to the vaporizer kit due to gravity. The vaporizer kit is heated by engine hot water which results in temperature raise in LPG vapour thereby methanol gets evaporated. The petrol engine is initiated by LPG and run by a mixture of LPG and methanol by reducing the LPG flow. The operating characteristics of engine are investigated with varying the quantity of methanol and LPG. The thermal and mechanical efficiencies are found to be increasing with the addition of methanol, whereas the specific fuel consumption and the emission characteristics such as CO, CO_2, HC and NO_x are reduced.

Keywords LPG · Methanol · SI engine · Performance · Emission

S. Somasundaram (✉) · T. Mohanraj · S. Pasupathy Raju · K. Murugu Mohankumar
SASTRA University, Thanjavur 613401, Tamilnadu, India
e-mail: somasundaram@mech.sastra.edu

T. Mohanraj
e-mail: tmraj@mech.sastra.edu

S. Pasupathy Raju
e-mail: pasupathyraju@mech.sastra.edu

K. Murugu Mohankumar
e-mail: murugumohan@mech.sastra.edu

Nomenclature

LPG	Liquefied Petroleum Gas
BP	Brake Power
BTH	Brake Thermal Efficiency
SFC	Specific Fuel Consumption
IMEP	Indicated Mean Effective Pressure
CC	Cubic Centimetres
RON	Research Octane Number
SI	Spark Ignition
ml/min	millilitres/minute
NO_x	Nitrogen Oxides
HC	Hydrocarbon
CO	Carbon Monoxide
CO_2	Carbon dioxide
MON	Motor Octane Number

1 Introduction

The fossil oil reserves are going to be exhausted in near future due to increasing utilisation. The engrossment of carbon dioxide and NO_x effects global warming. Crude oil is consumed heavily due to dense transportation. Methanol is considered to be an alternative fuel. Fuel properties of methanol are density of 0.791 kg/l at 20 °C with boiling point of 64.5 °C. Having 470 °C as auto ignition temperature and octane numbers as 110/92 for research/motor, which is greater than petrol. LPG is petroleum and natural gas mixture that exists in a liquid phase at ambient temperatures under moderate pressure (less than 200 psi).

Williams and Lom (1982) have conducted a brief survey on the statistics of the usage of LPG across worldwide conducted up to 1979. They presented a reasonable picture and projections of the LPG usage in 1980s and briefed industrial application of LPG [1]. Heywood (1981) has identified some alternatives for SI engine and claimed that LPG can be used as an alternative fuel [2]. Earl (1984) indicates that methanol had higher octane rating, heat of vaporisation and lean burn limit, produces higher energy efficiency [3]. Gordon and Thomas (1992) conclude that methanol has low vapour pressure that reduces evaporation and running loss emissions. Unburned methanol emissions have low photo chemical reactivity [4]. Celik et al. (2011) experimented that the results for the emissions of CO, CO_2 and NO_x were considerably low than gasoline at increased speeds. At higher compression ratios, the engines acquired ample rise in engine power and brake thermal efficiency [5]. Murillo et al. (2005) stated that the properties of alternative fuels are almost identical with existing types of fuels. Hence, the technology required to

handle them is already well known. LPG fuelled engines show considerable decrease in specific fuel consumption and CO emissions with imperceptible power loss. But HC emissions are slightly affected by fuel substitution. The NO_x emissions might be controlled under the current and future limits though it was higher [6]. Abu-Zaid et al. (2004) appealed that LPG was proved as clean burning than gasoline [7]. Dogu and Varosli (2007) declared that methanol, ethanol, DME, DEE and their blends had desirable clean burning features. They are assumed to be promising fuel alternatives for both gasoline and diesel powered transportation motor vehicles [8]. Lee and Ryu (2005) stated that the octane number could be increased by adding methanol to gasoline, thus engines fuelled with methanol–gasoline blend can be run at higher compression ratios [9]. Bayraktar (2005) concluded that the engine performance parameters like effective power and efficiency increased with increased ethanol amount. Also the blended fuel resulted in improved combustion. ethanol–gasoline mixture leads to leaner combustion. Consequently, cylinder pressure and temperature increased and combustion duration decreased [10]. Ozcan and Jehad (2008) established that the brake specific fuel consumption had deviations of about 6 % decrease to about 3 % increase at low speed, and about 6 % reduction to about 8 % increase at high speed comparatively to the original engine design. The analysis on stroke lengths and engine speeds were done on LPG driven four stroke SI engine under variable stroke length and compression ratio [11]. Syroezhko et al. (2004) found that simultaneous use of different additives was less efficient as compared to their individual introduction. The additives showed high antiknock efficiency, providing higher octane number [12].

Bayraktar and Durgan (2005) determined that in LPG fuelled SI engines, the burning rate of fuel increased with decreased combustion duration. As significance, the cylinder pressures and temperatures projected for LPG were higher than those gained for gasoline [13]. Williamson and Longley (1982) suggested that LPG will be available in abundant quantities, primarily for automotive fuels and feedstock for chemical plant. The automotive sector bid higher prices for secured priority [14]. Ceviz and Yuksel (2006) established that due to decreased cyclic variations and emissions, LPG was more appropriate for lean combustion engines compared with gasoline. It can be deduced that the increase in the relative air–fuel ratio increases the coefficient of dissimilarities in IMEP [15]. Somasundaram et al. (2014) experimented that 0.5 ml/min of methanol addition with LPG showed optimum characteristics in three cylinders, 800 CC SI Engine [16].

Hence the present study attempts alternative fuels with additives which provides an inspiring solution to the complications of oil depletion and increased atmospheric pollution. With this lean mixture of LPG with methanol additive in multi-cylinder gasoline engine, the impact on performance and pollution parameters were analysed.

2   Experimental Setup

The experimental setup is shown in Figs. 1 and 2 contain the following: LPG cylinder with flow regulator, solenoid actuator, vaporizer kit, carburettor, engine, computerised data acquisition system, eddy current dynamometer and exhaust gas analyser.
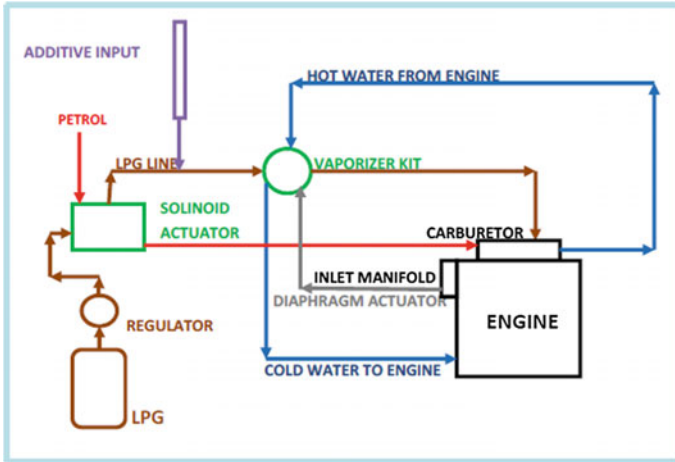
Fig. 1 Layout of experimental setup

Fig. 2 Experimental setup

Table 1 Engine specifications

S.No	Description	Details
1	Engine model	Ambassador
2	Engine type	4 stroke cycle water cooled, Inline
3	Engine displacement	1489 CC
4	Bore and stroke	73.2 × 88.9 mm
5	Fuel type	Petrol
6	No of cylinders	4
7	Valves per cylinder	2
8	Max power	37 kW@4200 rpm

Vaporizer kit has the connections of engine hot water outlet to kit inlet, kit cold water outlet to engine inlet, LPG inlet, LPG outlet and diaphragm actuator connected with inlet manifold. Solenoid actuator directs either petrol to carburettor or LPG to vaporizer kit.

Engine loaded by eddy current dynamometer. Air flow, fuel flow and peak pressure sensors and eddy current dynamometer connected with computerised data acquisition system. The exhaust gas analyses were done with exhaust gas analyser.

Test Procedure

The solenoid actuator switch allows either LPG to vaporizer kit and then to carburetor or petrol directly to the carburetor. LPG is metered by hanging type weighing scale, because of temperature difference between LPG and atmospheric air and to avoid water droplet accumulation on LPG cylinder. Methanol is added from burette separately with LPG due to density difference and is added by gravity by the reduction in LPG flow rate made lean mixture before the vaporizer kit and metered by volume. The vaporizer kit heats up the LPG by using engine hot water as inlet. The LPG flow rate automated through the diaphragm automated by pressure difference which was connected with the inlet manifold. Engine was initiated with LPG and its flow rate adjusted to add methanol. The addition of liquid methanol with gaseous LPG was difficult and complex process. Methanol is added by decreasing the LPG flow rate which made considerable pressure reduction in supply pressure of LPG with suction pressure of engine. It made the fuel mixture lean (Table 1).

Experimental Set Up

Properties of LPG and Methanol

Some important properties of LPG and methanol are compared in the Table 2. These comparisons are done with reference to "Present and Future Automotive Fuels: Performance and Exhaust Clarification", Osamu Hirao & Richard K. Pefley, John Wiley & Sons, 1988.

Table 2 Important properties of LPG and methanol

S.No.	Property	LPG	Methanol
1	Specific gravity	0.570 (at 7 bar pressure)	0.791
2	Boiling point	−6 °C	64.5 °C
3	Ignition point	457 °C	470 °C
4	Calorific value	19.8 MJ/kg	45–46.3 MJ/kg
5	MON/RON	90.5/102	92/110

3 Results and Discussions

The performance and emission characteristics of the petrol engine run by LPG with methanol additive is analysed. The brake thermal efficiency (BTH), specific fuel consumption (SFC), carbon monoxide (CO), carbon dioxide (CO_2), Hydrocarbon (HC) and nitrogen oxides (NO_x) are analysed at different loads and different additive mixtures.

Brake Thermal Efficiency

Figure 3 represents the variations in brake thermal efficiency with brake power. The brake thermal efficiency is the maximum for methanol addition at 0.8 ml/min and is followed by 0.667 ml/min. The other 2.0 and 1.0 ml/min additions lie between 0.8 ml/min and LPG alone (Meth.0 ml/min). The brake thermal efficiency is increased with methanol additions. It is increased with methanol evaporation rate which results in better combustion for fuel mixture. The brake thermal efficiency is achieved at 0.8 ml/min due to methanol addition.

Specific Fuel Consumption

The discrepancy in specific fuel consumption with brake power is shown in Fig. 4. The specific fuel consumption is high at low brake power for all blends of methanol and LPG alone. Specific fuel consumption is more for LPG compared with methanol additions and reduces with further increase in brake power. It was observed low values for both 0.8 and 0.667 ml/min compared with other flow rate of 2.0 and 1.0 ml/min methanol additions. The specific fuel consumption is found to be

Fig. 3 Variation of BTH with BP
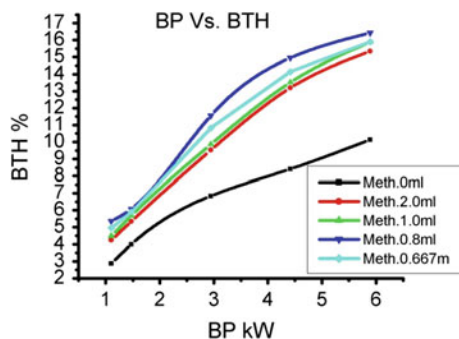
Fig. 4 Variation of SFC with BP
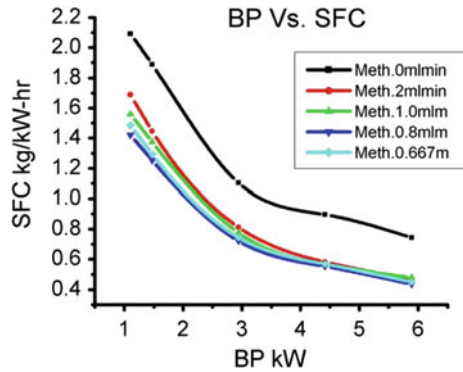
Fig. 5 Variation of CO with BP
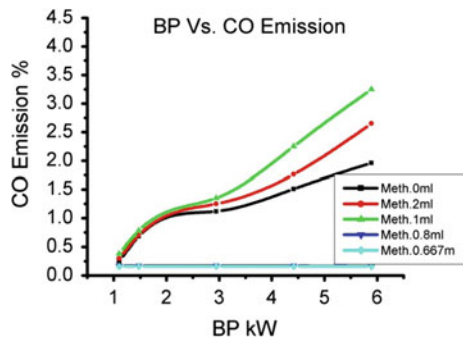
reasonably high for LPG without methanol (Meth.0 ml) and less with addition of methanol. This is due to improved combustion efficiency by adding methanol that increased the diffusion of fuel air mixture. Further decreasing the rate of methanol addition reduces specific fuel consumption. The specific fuel consumption is comparatively lower for 0.8 ml/min methanol addition than other quantity addition.

CO Emission

The variation in carbon monoxide emission with brake power is shown in Fig. 5. The investigation on carbon monoxide emission with various brake power for LPG with different rate of methanol additions was found to be low for 0.667 and 0.8 ml/min, high for 1 ml/min and intermediate value for 2.00 ml/min. It was because of the lean mixture of intake and rate of methanol evaporation. Carbon monoxide emission for LPG alone was observed as intermediate with 2.00 and 0.8 ml/min of methanol additions.

CO$_2$ Emissions

The variation in carbon dioxide emission with brake power is shown in Fig. 6. Carbon dioxide emissions are found to be less for 0.667 ml/min trailed by 0.8 ml/min and high for LPG alone (Meth.0 ml). It showed intermediate results for 2.0 and 1.0 ml/min addition of methanol. For all fuel flow rate in ml/min of methanol indicates carbon dioxide level increased with load. Evaporative losses are

Fig. 6 Variation of CO_2 with BP
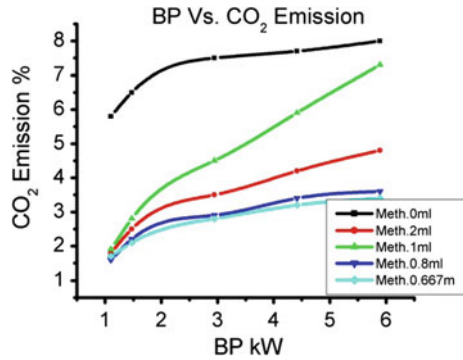
comparatively lower at less addition of methanol and it improved the combustion rate due to leaner mixture.

HC Emission

The variation in Hydrocarbon emission with brake power is shown in Fig. 7. Hydrocarbon emission is at base line values for LPG alone (Meth. 0 ml/min addition). Hydrocarbon emissions are reduced with the increase in brake power for all the rate of methanol addition. For 0.667 and for 0.8 ml/min additions give optimum values compared with remaining rate of additions. For decrease in methanol ml/min additions, the Hydrocarbon emission is decreased with brake power. This dilution of air fuel mixture is due to increase in methanol addition be the cause for the difference in Hydrocarbon emission.

NO_X Emission

The variation in NO_x emission with brake power is shown in Fig. 8. The nitrogen oxide emission is very low for methanol addition of 1, 0.8 and 0.667 ml/min. Up to 1 ml/min addition of methanol at no load condition is almost same. If it is to go for higher flow of methanol addition (2 ml/min), then NO_x will be more at no load condition. This is due to effective combustion and the emission of excessive heat. So the heat released through exhaust gas, the NO_x emission is also high. The emission is increased for LPG (Meth.0 ml) without the addition of methanol but with increased brake power.

Fig. 7 Variation of HC with BP
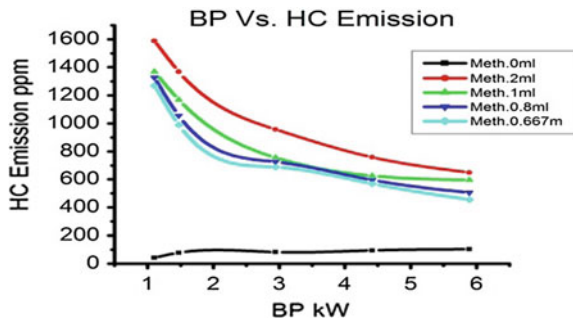
Fig. 8 Variation of NO$_x$ with BP
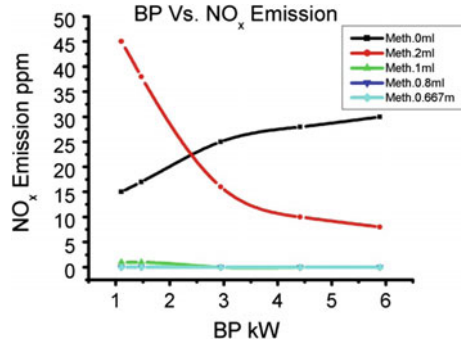
4 Conclusion

To sum up, the operating characteristics of petrol engine operated with LPG and methanol, the brake thermal efficiency is high for methanol addition of 0.8 and 0.667 ml/min. The specific fuel consumption decreases with increase in brake power for all the flow rates of methanol addition and is low for 0.8 and 0.667 ml/min. The observations from the above study delineates the performance and emission parameters for the addition of methanol flow rate with LPG in respect to rise in brake power, increased brake thermal efficiency and decreased the specific fuel consumption. For LPG, with methanol addition of 0.667 and 0.8 ml/min, emission is low compared to other rate of methanol addition and LPG. Methanol addition of 0.8 ml/min with LPG gives optimum characteristics for both in performance and emission parameters. From the investigation, it is confirmed that the LPG can be used as an alternative fuel in petrol engines with methanol additive at constant flow rate.

References

1. Williams A. F.&Lom W.L.(1982). *Liquefied Petroleum Gases*. Ellis Horwood.
2. John B.Heywood. (1981). Automotive Engines and Fuels: A Review of Future Options. *Progress in Energy and Combustion Science*. 7: 155–184.
3. Earl W.B. (1984).Alcohol Use in Engines. *Energy in Agriculture*. 3: 351–362.
4. Gordon A.S. & Thomas C. Austin. (1992). Alternative Fuels for Mobile Transport. *Progress in Energy and Combustion Science*. 8: 493–512.
5. Bahattin Celik M., Bulent Qzdalyan & Faruk Alkan. (2011). The use of pure methanol as fuel at high compression ratio in a single cylinder gasoline engine. *Fuels*. 90: 1591–1598.
6. Murillo S., Miguez J.L., Porteiro J., Lopez Gonzalez L.M., Granada E. & Moran J.C. (2005). LPG: Pollutant emission and performance enhancement for spark-ignition four strokes outboard engines. *Applied Thermal Engineering*. 25: 1882–1893.

7. Abu-Zaid M., Badran O. & Yamin J. (2004). Effect of Methanol Addition on the Performance of Spark Ignition Engines. *Energy & Fuels*. 18: 312–315.

8. Timur DOGU & Dilek VAROSLI. (2007). Alcohols as Alternatives to Petroleum for Environmentally Clean Fuels and Petrochemicals. *Turkish Journal of Chemistry*. 31: 551–567.

9. Kihyung Lee & Jeaduk Ryu. (2005). An experimental study of the flame propagation and combustion characteristics of LPG fuel. *Fuels*. 84: 1116–1127.

10. Hakan Bayraktar. (2005). Experimental and theoretical investigation of using gasoline-ethanol blends in spark-ignition engines. *Renewable Energy*. 30: 1733–1747.

11. Hakan Ozcan & Jehad A.A. Yamin. (2008). Performance and emission characteristics of LPG powered four stroke SI engine under variable stroke length and compression ratio. *Energy Conversion and Management*. 49: 1193–1201.

12. Syroezhko A.M., Yu Begak.O. & Makurnia G. S. (2004). Effect of Various High-Octane Additives on Antiknock Quality of Gasolines. *Russian Journal of Applied Chemistry*. 77 (6): 1002–1006.

13. Hakan Bayraktar & Orhan Durgan. (2005). Investigating the effects of LPG on spark ignition engine combustion and performance. *Energy Conversion and Management*. 46: 2317–2333.

14. Williamson E. I. & Longley R.C.M. (1982). Alternative Fuels for Automobiles the Medium-term Realities. *Long Range Planning*. 15 (2): 32–38.

15. Ceviz M.A. & Yuksel F. (2006). Cyclic variations on LPG and gasoline-fuelled lean burn SI engine. *Renewable Energy*. 31: 1950–1960.

16. Somasundaram S., Mohanraj T. & Pasupathy Raju S. (2014). Effect of methanol additive with LPG in three cylinders four stroke S.I engine. *Applied Mechanics and Materials*. 592: 1503–1509.

Advances in Light Weight Materials for Body-in-White (BIW)

Avinash Arankalle

Abstract Conventional metallic materials are getting replaced by lightweight materials in the last two decades for body-in-white (BiW) structural components for all types of vehicles from two wheelers to heavy commercial trucks and passenger buses. The main driving forces are depleting fuel resources leading to the fuel economy standards, safety and crashworthiness legislations, emission regulations, green environment requirements leading to control CO_2, and other toxic gas emissions, recyclability, etc. The auto industry sees developments of light weight steels to aluminum and magnesium alloy, to fiber-reinforced plastics (FRP) emerging to make lighter vehicles. The other influencing factors for light weight materials technology are customer-driven requirements like styling, aesthetic appearance, reduced NVH (noise, vibration, and harshness) aspects, and comforts. The future vehicle technology is moving ahead with developments of lithium batteries for electric and hybrid cars and buses, Solar cell and hydrogen-driven fuel systems. These technologies also need light weighting vehicles to use these additional gadgets on the vehicle. Variety of options are available in the market, but lightweight materials play a vital role in vehicle design for tomorrow. In India, the light weight materials technology has yet to make a great impact and considering "make in India," the article is focused on challenges and opportunities that need to be addressed soon.

Keywords Light weight materials · Body-in-white · Structural components · Fiber-reinforced plastics · Reduced noise · Vibration and harshness.

A. Arankalle (✉)
Vel Tech Dr. RR & Dr. SR Technical University, Avadi, Chennai, India
e-mail: avinash.arankalle@gmail.com

1   Introduction

Historical perspective of automotive engineering body materials shows that early days' bodies were made of wood by highly skilled workers. However, in 1914 Dodge and Budd produced 5,000 all-steel bodies. They were lighter, easy to make, and most significant advantage was in painting of the body. Since then, the major material for body-in-white (BiW) became iron and steel constituting to about 84 % of gross weight of vehicle (GVW). After the oil crisis in 1973s, the concepts of using light weight technology started penetrating in the market and now iron and steel are on the wane!

2   Driving Forces for Light Weight Technology

2.1   *Fuel Economy*

The basic driving force is the fuel economy which merged as an important issue with—Embargoby Arab Exporting Countries in 1973s, high gasoline prices, shortages with long lines at the pump (Fig. 1). This gave birth to Corporate Average Fuel Economy (CAFÉ) legislations to make fuel efficient vehicle. CAFÉ legislations Increased rapidly from 18 mpg in 1978 to 28 mpg in 1990, where it remained flat until 2010. Since 2010 fuel economy has increased to 33.5 mpg in 2013, and then will rise to 35.5 mpg in 2016 and is expected to continue to climb in response to new regulations and will be 54.5 mpg in 2025. Automobile companies have to pay penalty if they do not meet the fleet average CAFÉ standard. However, these mandates are not yet seen in India. Amongst the various options for fuel economy, the best option is to reduce curb weight (gvw) of the vehicle by using lightweight materials, since each 10 % weight savings could reduce 3–7 % fuel consumption and 13 % CO_2 emissions. Ideally speaking, a 30 % weight reduction, will yield the greatest improvements in fuel economy and associated reductions in emissions.

2.2   *Safety and Crashworthiness*

Automotive design rules are changing due to regulatory requirement of safety and crashworthiness standards, since 1985. Control on energy absorption and intrusion (displacement) are important for crashworthiness vehicles for front and rear zones as well as passenger zones, respectively. Earlier vehicles before 1980s, were designed to meet style, cost and stiffness criteria. But today and tomorrow, with more and more stringent safety standard norms they will require to meet cost, fuel economy (i.e., weight aspect), crash, i.e., lower impulse, high energy absorption,
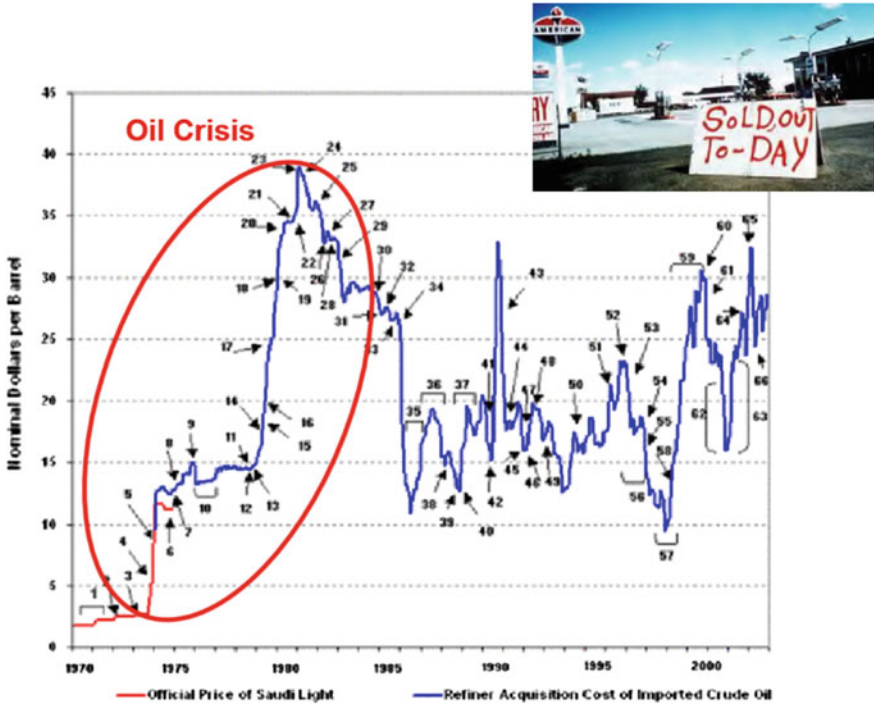
Fig. 1 Oil crisis and rise in fuel prices

intrusion, rollover, side impact, frontal impact, rear impact, etc., in addition to style and corrosion resistance. There is a steep competition in the market to meet requirements of safety of vehicles.

2.3 GHG Emissions

Earth's atmosphere is a thin, gaseous layer of air that envelops the planet known as troposphere. It contains nitrogen (78.09 %), oxygen (20.95 %), argon (0.93 %), CO_2 (0.039 %), and fractions of other gases. The stratosphere, or outer layer, contains ozone (O_3). Ozone layer filters out most of the Sun's harmful ultraviolet radiation, air we breathe, the water we drink, and the places we live, work, and play. Imbalance of these gases leads to "Global warming" and we can say—the Earth has a fever! Auto industry, in life cycle assessment (LCA) contributes a large in Green House Gases (GHG) composing of CO_2, CO, NO_x, and unburned hydrocarbons (HC).

It is the foremost driving force that opens up the path for the lightweight materials for future generation of vehicles. The world has led to control CO_2
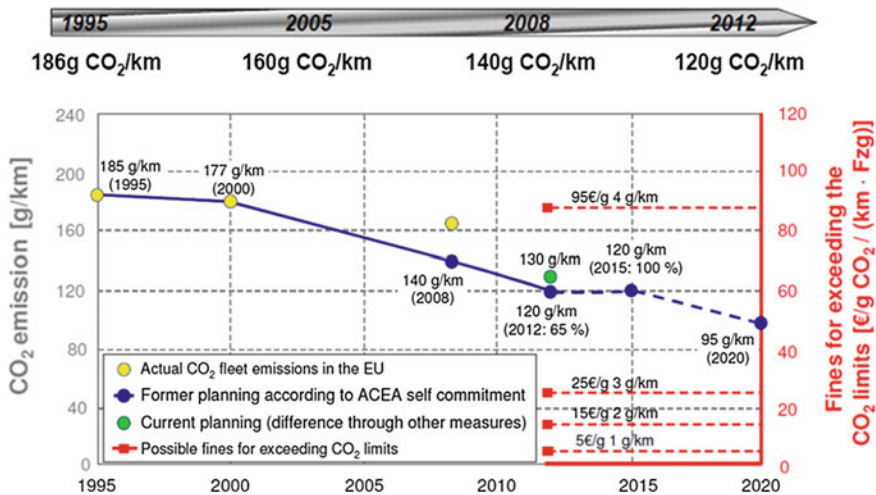
Fig. 2 CO_2 emission legislative norms

evolution with mandatory norms (Fig. 2) for vehicles on the road, which are becoming more and more stringent to balance ecology and reduce effects of global warming. The controls of CO_2 emissions to 185 g/km began way back in 1995 with EU standard and today it is 130 g/km and by 2020 it will be 95 g/km. The auto industry needs to strictly follow, failure to meet, then will have to pay heavy penalties!

One may question—how lightweight materials do contribute significantly in reducing CO_2 levels? Yes, the answer is, reduction in vehicle curb weight by 100 kg achieves in reduction of CO_2 by 10 gm/km and is the highest contributor to meet GHG than any other means like reduction in aerodynamic coefficient, rolling resistance, electric consumption, etc. It is said that 20 % weight savings reduces GHG emissions by 591 million kg (591 kilotons) over the life spans. It is a substantial benefit to improve for "clean environment" much needed in the Indian continents, but so far no legislative measures are introduced in India to control CO_2 emissions from vehicle exhaust.

2.4 End-of-Life of-Vehicle (ELV), Recyclability and RoHS Directives

There is another mandate in the developed countries and it is end-of-life of vehicles (ELV) directives like 2000/53/EC and restrictions on use of hazardous substances (ROHS) (2002/95/EC) which demands for recyclability of materials and control on carcinogenic and mutagenic substances that are harmful to human health, animals, and plants. These directives are also the driving forces to use eco-friendly materials

like natural fiber composites, nanotechnology, surface coatings that do not contain heavy elements (Hexavalent Chromium, Tin, Antimony,Nickel, Cadmium, Lead, mercury, etc.), asbestos, use of additives like PBB, PBDE in plastics, etc.

2.5 Other Driving Forces

Other driving forces which have peripheral importance in the modern era of customers' services are—Passengercomforts, NVH aspects, paintability, good formability and strength, Strength to weight ratio, improved corrosion resistance, style and aesthetic look-out, performance to cost ratio, etc. These needs are required to be met in the steep competitive world market, while meeting the TQM and Six Sigma levels.

2.6 Current Versus Emerging New Generation of Materials

In earlier days before 1980s and oil embargo of 1973s, the main material of construction of automotive vehicle was plain or low alloy steels and cast iron contributing to 82–84 % of gvw of the vehicle. Soon after CAFÉ standards on fuel economy and safety regulations high strength low alloy steels (HSLA) started to emerge in the market. They were:

- Interstitial Free (IF) Steels: Low Strength
- Isotropic (IP) Steels
- Interstitial Free (IF) Steels: Low Strength
- Bake Hardening (BH) Steels
- Carbon–Manganese (C–Mn) Steels
- High Strength Low Alloy (HSLA) Steels.

Aluminum-killed (AK) steels, commercial grades of steels (CS), rephosphorised steels, drawing quality, and extra deep drawn quality steels (DS, EDD) either hot rolled (HR) or cold rolled (CR) form were very commonly used for the body-in-white structural components where criteria of selections were forming characteristics, stiffness, corrosion resistance, etc. Lightweight material was never thought off and achievement of crashworthiness was achieved with use of higher gauge thickness materials and or with heat treatment process. However, with more stringent fuel economy standards, safety and crashworthiness requirement following grades of steels are emerged as second and third generation materials as also light weight non-ferrous metallic materials such as aluminum, magnesium, and titanium-based alloys and non-metallic materials like ceramics, metal matrix composites (MMCs), carbon fiber composites (CFRP) for BiW components. The

recent developments in process are—natural fiber composites and nanocomposites. Many of them are yet to get commercialized for the automotive sector.

2.7   Advanced High Strength and Ultra High Strength Steels (AHSS/UHSS)

In AHSS/UHSS the grades of steel (Fig. 3) that are developed in the last two decades and further getting updated in technology to improve applications in chronology of their development as second and third generation steels are:

- High strength low alloy steels (HSLA)
- Dual phase (DP) steels
- Complex phase (CP) steels
- Martensitic (MART) steels
- Ferrite–bainite (FB) steels
- Hot forming (HF) steels
- Post-forming heat treatable (PFHT) steels
- Transformation-induced plasticity (TRIP) steels
- Plasticity induced by mechanical twining (TWIP) steels
- Nano-acicular duplex steels
- Nanosteels.

Most of these development of steels are governed by the special microalloy additions such as niobium, columbium, titanium, boron to provide grain refinement, strengthening mechanism, controlled transformation of phases which helps in improving drawability/formability characteristics, response to post heat treatment as well as higher strengths with reduced gauge thickness making it a lighter weight structure for BiW components. The penetration and development of these AHSS/UHSS are increasing over past few years as shown in Fig. 4. AHSS/UHSS provide structural optimization to achieve significant weight reduction, while improving safety and fuel economy. The use of mild steels and High strength steels
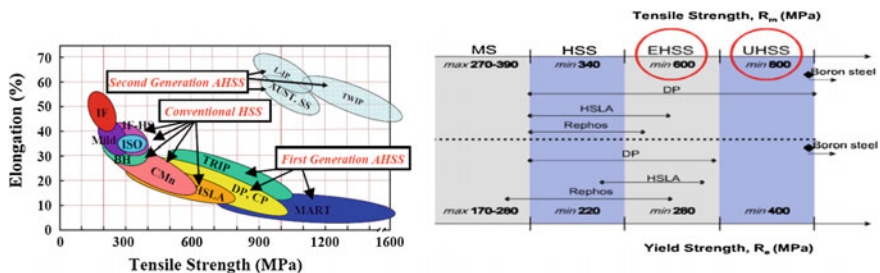
Fig. 3 Second generation of advanced high strength steels (AHSS)
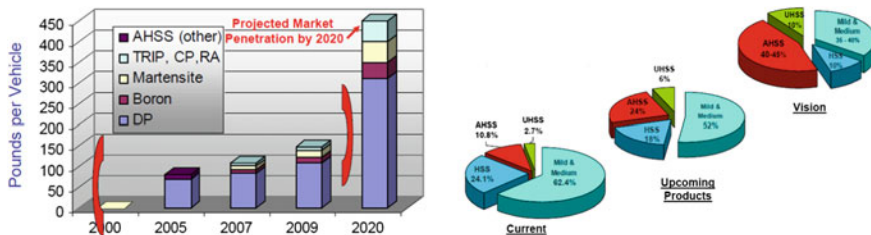
Fig. 4 Growth of AHSS/UHSS for BiW applications

(HSS) is decreasing and is getting replaced by AHSS and in future it will be more replaced by UHSS grades of steels for BiW structural applications.

Indian status shows that it relies more on conventional cold rolled steels, HSS and DP steels that are often used for 700 MPa strength and country relies more on 65 % imports of autograde steels. Ample opportunities do exist if a special program is taken up to create auto cluster of light weighting materials to feel up the technology gap between the developed countries and meet stringent fuel economy, safety, and GHG regulations.

2.8 Aluminum and Magnesium Alloys

Aluminum one-third in weight when compared to steel and magnesium is 36 % lighter than aluminum. Aluminum alloy applications go in power train (engine, fuel system, and liquid lines), chassis and suspension (cradle, axles, and wheels) and BiW (hoods, bonnet and doors, wings, and bumpers) as shown in Fig. 5.

Weight reduction is more with use of magnesium alloys. It finds applications in BiW for—Door inner pane, Radiator support, Front of dashboard structure, Lift gate inner, windshield surround frame, Target roof frame opening, Wiper motor support assembly, Mirror housing, Headlight retainer, etc.
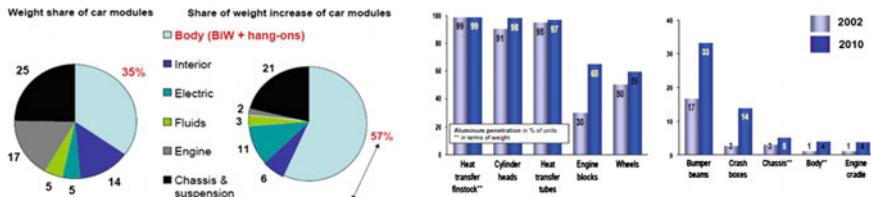
Fig. 5 Use of Aluminum 2002 versus 2010 in an average vehicle

2.9 Fiber-Reinforced Plastics (FRP)

Glass fiber, and carbon fiber-reinforced plastics have great potentials for BiW as they are lighter than aluminum and magnesium alloys (Fig. 6). Industrial analysis shows potential for 60–67 % for CFRP applications for BiW. Specific crash energy absorption of CFRP can be 2–5 times that of steel. It provides greater styling flexibility and reduced assembly steps, finish processes, and tooling through parts consolidation and lay-in-the-mold finish coatings. However, main barrier in market penetration is high cost than steel. Other reasons include low mass production manufacturing techniques, higher skill levels in know-hows and technology to adapt, recyclability, and disposal. The major advantages in using FRPs for BiW include possible part consolidations, primary/secondary weight savings, and increased design flexibility (e.g., aerodynamic design of vehicle body). Due to recyclability and disposal problems, natural fiber composites are finding more applications as they are comparable to glass fiber composites. Some of the vehicles on road do use natural fiber composites such as Flax, Hemp, Sisal, Wool, and other natural fibers Fig. 7. The BiW applications include—glow box, door panels, seat coverings, trunk and floor panels, front-end grill opening, etc.
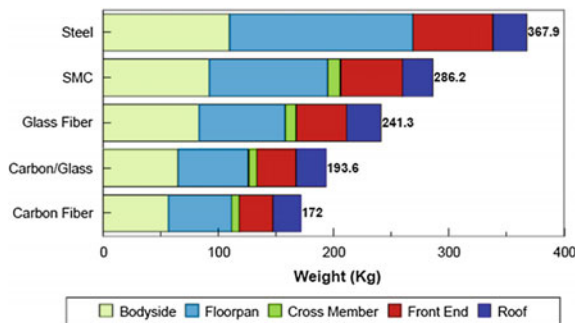
Fig. 6 Part weight comparison for BiW

Fig. 7 Natural fiber composite applications

Nano-composites are futuristic materials for BiW applications. Today one of the vehicle manufacturer is using clay polypropylene composites for the body panels due to benefits of material processing and fuel economy associated with it. Other major benefits that nano-composites will have are—large reduction in CO_2 emissions, low energy required in manufacturing, and much lighter than conventional FRP materials. With these benefits it will find breakthrough applications for auto industry with technology development.

Health Monitoring for Armoured Fighting Vehicles

N. Ponnusamy

Abstract Health Monitoring of Armoured Fighting Vehicles (AFVs) focuses on data collection using various sensors and analysis techniques to ensure availability, reliability and safety of AFVs. There are two types of Health Monitoring system, to be precise Prognostic Health Monitoring System and Diagnostic Health Monitoring System. This paper describes the Diagnostic Health Monitoring system used for the Powerpack of Armoured Fighting Vehicles with a case study on Integrated Automotive Vetronics System.

Keywords Sensors · Health monitoring · Armoured fighting vehicles · Advanced Vetronics System

Abbreviations

AFV	Armoured Fighting Vehicle
BITE	Built In Test Equipment
CAN	Controller Area Network
FCS	Fire Control System
GCS	Gun Control System
HMI	Human Machine Interface
IEEE	Institute of Electrical and Electronics Engineers
LCD	Liquid Crystal Display
MBT	Main Battle Tank
POST	Power On Self Test
RTD	Resistance Temperature Detector
RTOS	Real-Time Operating System

N. Ponnusamy (✉)
Chennai, India
e-mail: ponnuswamy.n@cvrde.drdo.in

527

1 Introduction

1.1 *Armoured Fighting Vehicles and Health Monitoring*

Armoured Fighting Vehicles comprise a large part of any defence forces and they perform as Weapons platform, Personnel carriers and Repair and Recovery vehicles for a wide variety of mission profiles. They are deployed in extreme environmental and terrain conditions. High operational availability of these vehicles is critical to achieve their mission objectives. The amount of Operational Availability depends upon the efficient usage and effective maintenance of the AFV and involves detecting, diagnosing and localising faults. The challenges in achieving this capability are the need for technologies that provide accurate vehicle diagnostic information in real time.

AFVs have many critical systems such as Powerpack, Fire Control System (FCS), Gun Control System (GCS), Suspension System, Communication System, Navigation System and Advance Threat Warning System. To know the health status of critical systems, health of the control system is to be monitored in real time.

With the advancement of semiconductor technology, Health Monitoring has grown significantly. With in-vehicle networking, intelligent sensors, real-time processors and software have changed the health monitoring extensively.

Health Monitoring of AFV encompasses the monitoring of various vehicle parameters using sensors and logging of critical parameters for in depth offline analysis.

Sensors (to name a few) used for monitoring various vehicle parameters include Resistance Temperature Detector (RTD) for measuring the Engine oil temperature and Transmission oil temperature, Magnetic pickup sensor and Hall effect sensor for measuring the Engine rpm and Transmission rpm, Resistance-based pressure sensor for measuring the Engine oil pressure.

2 Components of Health Monitoring System

The main components are network of Sensors, On-board processor and Offline Analyser (Fig. 1).

Fig. 1 Components of health monitoring system
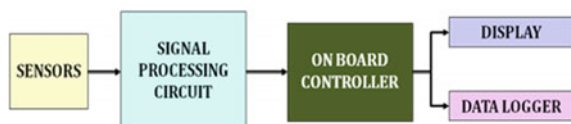
2.1 Sensors

The sensors monitor the various parameters such as speed, oil temperature, oil pressure, coolant temperature, fuel level and battery health on the vehicle and pass this data to the on-board processor.

2.2 On-board Processor

The on-board processor is responsible for displaying the parameters on the Human Machine Interface (HMI). The processor in addition generates warning when the parameters exceed the limit. The critical parameters are logged for offline analysis.

2.3 Offline Analyser

The offline analysis of logged data using an Offline Analyser helps to probe the problem if any abnormalities are noticed.

3 Types of Health Monitoring System

There are two types of Health Monitoring System. They are Prognostic Health Monitoring System and Diagnostic Health Monitoring System.

3.1 Prognostic Health Monitoring System

'Prognostics' is an engineering discipline focused on predicting the time at which a system or a component will no longer perform its intended function. A prognostic Health Monitoring System approach is concerned with predicting the residual life of components and does not require a detectable fault. It uses a quantitative record of the historical load on the vehicle and processes this through an analytical model to determine the cumulative damage on each component.

3.2 Diagnostic Health Monitoring System

The diagnostic Health Monitoring System approach relies on the fundamental principal of damage tolerance. A fault can only be diagnosed once it is present,

therefore, the component must tolerate this fault with sufficient residual life to safely fulfil its mission.

4 Health Monitoring in AFVs—A Case Study on Advanced Vetronics System

Advanced Vetronics System is a state-of-the-art technology development programme envisaged to implement Vetronics in Armoured Fighting Vehicles on par with the contemporary tanks world-wide.

The system consists of two controllers, namely the Powerpack Controller that processes the Engine and Transmission signals and the Display Controller that processes the input signals from the driver's controls which are networked via MIL-STD-1553B, CAN and Ethernet. These Intel Core i7 processor-based systems are designed to be fault tolerant, so that if the processor fails, default handler handles all the processing along with data communication requirements without any degradation in performance. The active matrix LCD multipage touch screen display connected to the Display Controller serves as the Driver's Instrument Panel.

The salient features of Advanced Vetronics System include Embedded System control for the ARJUN MBT Mk-II Powerpack through fault tolerant multibus architecture using MIL-STD-1553B, CAN and Ethernet in RTOS Environment, Automation of Driver's operations, Active Matrix touch screen Dashboard with multipage configuration for the Driver, Data logging and BITE capabilities and Enhanced Vision System for the driver. The software adheres to IEEE 12207 standard for Software Development Lifecycle process and is implemented in VxWorks RTOS environment.

The system has been designed, developed and integrated in the Main Battle Tank ARJUN Mk-II.

Advanced Vetronics System uses Diagnostic Health Monitoring technique for monitoring the various parameters of the Powerpack. The Powerpack is the major part of any AFV. It supplies both electrical and mechanical power to drive the tank and its accessories. It has an Engine which is coupled with a hydro-mechanical Transmission. The Powerpack has to be monitored to track its usage and hence reduce the possibility of failure or malfunction of the system components and thus enhance the dependability of the AFV (Fig. 2).

4.1 Sensors Used to Monitor System Powerpack

The following sensors are used to monitor various parameters of the Powerpack to ensure the proper operation of the AFV.

Fig. 2 Powerpack of AFV
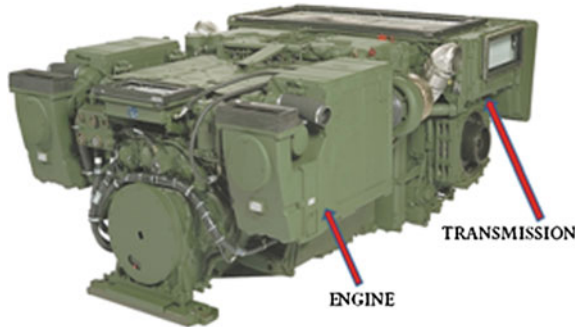
4.1.1 RTD Sensor

Resistance Temperature Detectors (RTD) (E.g. PT1000, PT100) are used to monitor the Transmission oil temperature and Engine coolant temperature. If in case any anomalies are noticed, a warning will be displayed and the crew can take necessary action.

4.1.2 Pressure Sensor

Pressure Sensor is used to monitor the Engine Oil pressure and Clutch pressure. Any anomaly will generate a warning.

4.1.3 Current Sensing Circuit

The current sensing circuits are used to monitor anomalies associated with solenoids. Over current detection, short circuit indication and ON/OFF status of the solenoids can be monitored.

4.1.4 Magnetic Pickup Sensor

Magnetic Pickup sensor is used to measure the speed of the Engine and Transmission in rpm. From the data obtained, the speed of the vehicle can be calculated.

Two Magnetic Pickup sensors with 90° phase shift facilitates to sense the direction of the vehicle, i.e. whether the vehicle is moving forward or reverse.

4.1.5 Limit Switch

Limit Switches are used for indicating the ON/OFF status of various parameters such as selected gear, selected direction, brake pedal status and accelerator pedal status.

4.2 Types of Monitoring in Advanced Vetronics System

4.2.1 Online Monitoring

Online monitoring has limited usage during automotive runs. It does not involve data logging. The crew can view the diagnostic results on the display when the vehicle is running.

Power on Self Test (POST)

POST is done to monitor the health of the modules during power ON. POST ensures that all the modules are in functional state and thus provides assurance for the crew to drive the vehicle (Fig. 3).

Fig. 3 Display with POST results
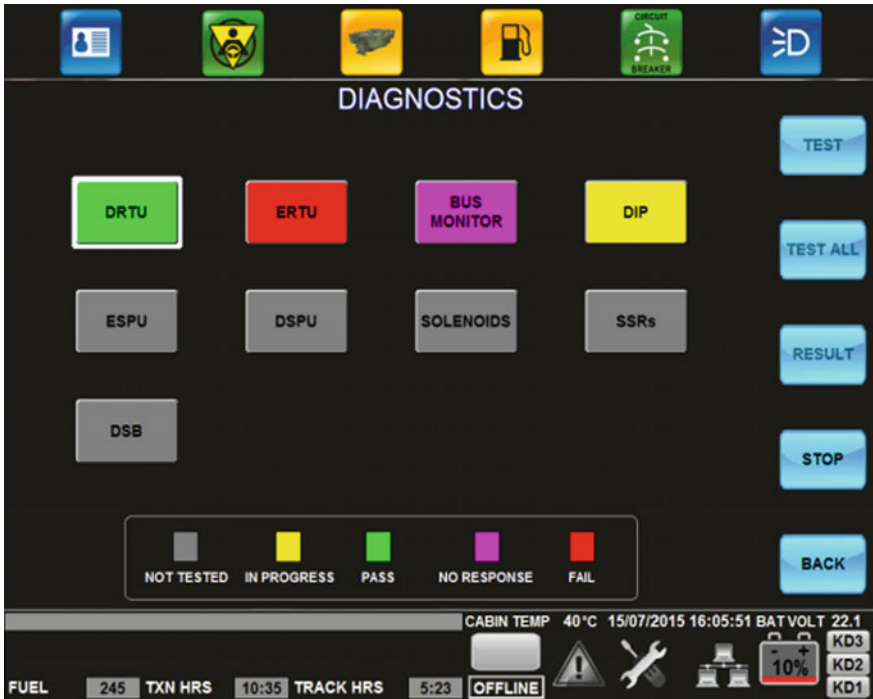
Fig. 4 Display with diagnostics result

Diagnostics

The diagnostics of various modules are done and the results are displayed on the Human–Machine Interface. The HMI is implemented as 10.4 in. Active Matrix touch screen display (Fig. 4).

4.2.2 Offline Monitoring

This type of monitoring plays a major role in the identification of faults in the Powerpack. The data is logged using the data logger and in depth analysis is done using dedicated software application.

Data Logging and Maintenance

The system also features automatic generation of maintenance alert and maintains change history and maintenance history of the modules. The data logging system
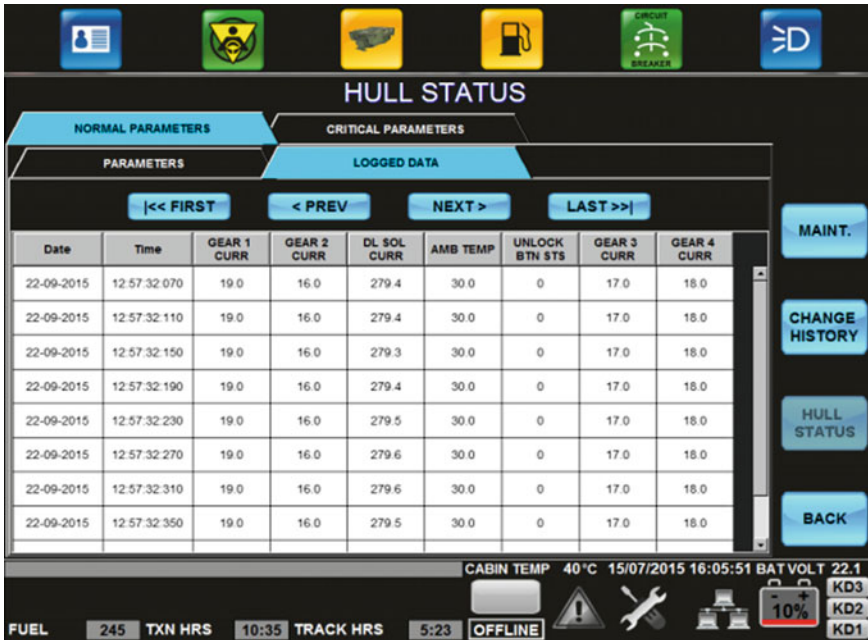
Fig. 5 Display showing the hull status

logs various hull parameters that are monitored by the sensors and stores in the flash memory for offline analysis. The stored information can be retrieved on request and it sends the retrieved data serially to the requester (Fig. 5).

Offline Analyser

The Offline Analyser has been implemented as a stand-alone application. It is used to analyse the data logged during automotive run. The data such as Engine oil pressure, Transmission oil temperature, Engine speed, Transmission speed, Speed of the Vehicle and Gears engaged can be analysed and any anomaly can be identified by comparing it with the normal values. The Offline Analyser has three modes to view data. Chart View, Dash board view and Table view. The chart view displays data as a graph. The table view displays data in the numerical format. The Dash board view has the appearance of driver's dashboard (Fig. 6).
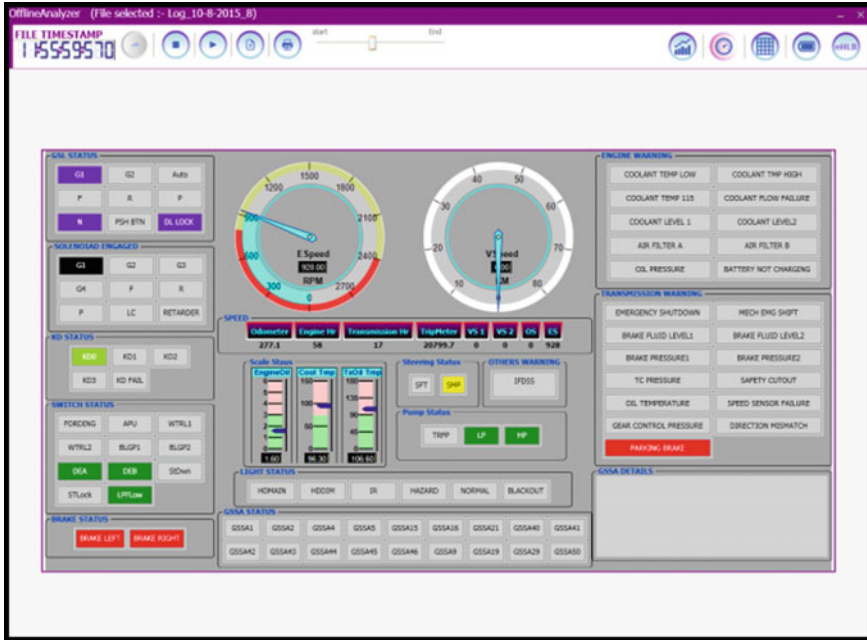
Fig. 6 Dashboard view of offline analyser

5 Conclusion

Health Monitoring provides enhanced safety, improved reliability and effectiveness, decreased maintenance cost, improved performance and in particular increased mission readiness to support the warfighter. Hence Health Monitoring is inevitable to ensure the performance of Armoured Fighting Vehicles and in turn guarantee the availability of the AFVs during vital situations.

Orbital Parameters Variations
of IRNSS Satellites

S. Sivaraj, Umesh Swami, R. Babu and S.C. Rathnakara

Abstract IRNSS is one of the unique constellations first of its type dedicated for providing the satellite-based navigation in Indian subcontinent. The IRNSS constellation consists of seven satellites with three satellites in GEO orbit with inclination of 5° and four satellites in GSO orbits with inclination of 29°. The constellation is designed to get better satellite geometry in terms of Dilution of precision (DOP) over Indian region and its extended area. All satellites in the constellation provide 24 h visibility within and across geographic boundaries of Indian land mass with minimum elevation greater than 15°. This paper presents the variations of Keplerian elements of all four operational satellites of IRNSS Constellation. The satellite state vector, satellite clock and receiver clock parameters are estimated using consolidated orbit determination algorithm of Navigation software installed at ISRO Navigation Center. The estimated state vectors are converted into the Keplerian elements. The variations in the Keplerian elements show the expected behaviour showing the influences of natural perturbations like J2 effect, luni-solar perturbations, etc.

Keywords Orbital elements · Keplerian elements

S. Sivaraj (✉) · U. Swami · R. Babu · S.C. Rathnakara
Space Navigation Group, ISRO Satellite Center, Bangalore, India
e-mail: sivarajs@isac.gov.in

U. Swami
e-mail: urswami@isac.gov.in

R. Babu
e-mail: rbabu@isac.gov.in

S.C. Rathnakara
e-mail: ratnakar@isac.gov.in

1 Introduction

1.1 IRNSS: Indian Regional Navigation Satellite System

Indian Space Research Organization (ISRO) is in process of deploying an independent regional satellite-based navigation system of India compatible with other existing GNSS services. IRNSS is designed to provide navigation services with position accuracy better than 20 m for dual-frequency users over Indian landmass and the region extending about 1500 km around India [1] which is area covered by Latitude −30° to +50° and Longitude 30° to 130°. IRNSS system consists of Space segment, Ground segment and User segment. The IRNSS architecture is shown in Fig. 1. Currently four satellites of IRNSS constellation are operational and supporting the IRNSS mission.

The space segment of IRNSS constellation consists of seven satellites: three satellites in low inclined GEO orbit and four satellites in GSO orbit in two orbital planes with two satellites in each plane. This geometry provides visibility of all the satellites in the Indian region and ensures a Geometric Dilution of Precision (GDOP) of better than 3.0 in the primary service area which is one of the prime requirements for satellite-based navigation system. The ground trace of IRNSS satellites forms loops of figure of eight with longitude crossing as shown in Fig. 1, to provide an optimum coverage in Indian region and its neighbouring countries.

All IRNSS satellites are identical in their hardware and functional specifications. Figure 2, shows the axis definition of IRNSS satellites. The positive Yaw direction

Fig. 1 IRNSS architecture
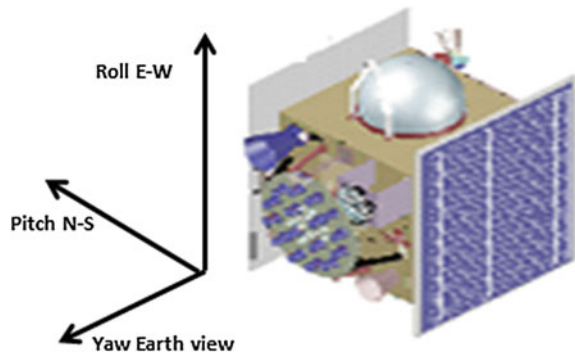
is towards Earth viewing, positive Roll is towards East direction and Pitch direction completes the right-hand system. The atomic clocks are placed along the panel with normal in positive Roll direction. The satellites are maintained in Yaw-Roll plane and attitude is maintained such that the atomic clock never sees the sun.

The Ground segment of IRNSS comprises of IRNSS Navigation Control Centre (INC), IRNSS CDMA Ranging Stations (IRCDR), IRNSS Timing Facility (IRNWT), Satellite LASER Ranging Stations (SLR), IRNSS Spacecraft Control Facility (IRSCF) and IRNSS Range and Integrity Monitoring Stations (IRIMS). Currently, most of the IRIMS are operational and providing the one-way pseudo range measurements for all operational IRNSS satellites. The IRIMS receivers are NOVATEL G-III type receivers with 12 channels to obtain the measurements in two desired frequencies, both in L5 (1776.45 MHz) and S (2492.028 MHz [2]). Also each station is supported with two streams of data chain A and B whose phase centre coordinates are separated by ten to hundreds of metres. The coordinates of all IRIMS stations are known to be precisely surveyed along with calibrated cable delays and hardware delays, which is made available for estimation process. The Bangalore IRIMS station is the Master reference station which is directly fed with IRNSS reference time (IRNWT) (Fig. 3).

The IRNSS user segment comprises of Standard Position Service (SPS) and Restricted Service (RS) users. The navigation payload will have down links in L5 and S bands of the frequency spectrum. Thus, user receiver can be operated in single and or dual-frequency operation mode. S-band signals are used for the first time in the history of satellite-based navigation. The constellation is unique with less number of satellites in GEO and GSO orbits providing independent navigation services over anticipated service area.

Currently four IRNSS satellites are operational and supporting the mission. The first ever dedicated navigation satellite of India, IRNSS-1A was launched on 1° July, 2013. IRNSS-1A is placed in GSO orbit with longitude crossing of 55°, RAAN of 139° and inclination of 27°. The second navigational satellite of IRNSS constellation was launched on 4° April, 2014 which is placed in GSO orbit with longitude crossing of 55°, RAAN of 312° and inclination of 31°. The third navigation satellite, IRNSS-1C of IRNSS constellation was launched on 16° Oct, 2014
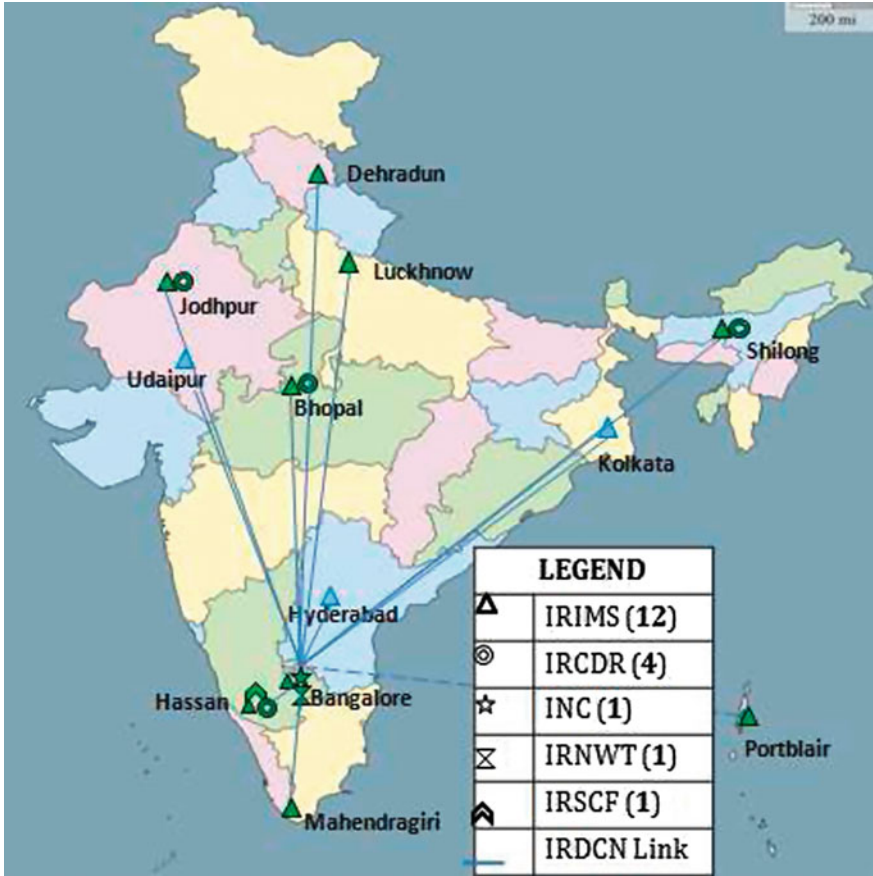
Fig. 3 Operational IRIMS stations

and is placed in GSO orbit with longitude crossing of 83°, RAAN of 271.8° and inclination of 5°. The fourth dedicated navigation satellite, IRNSS-1D of IRNSS constellation was launched on 28° Mar, 2015 and is placed in GSO orbit with longitude crossing of 111.75°, RAAN of 307° and inclination of 30.4°.

2 IRNSS-Measurement System

In order to monitor and process the signals transmitted by IRNSS satellites and to assess the ability of positioning, navigation and timing capability of IRNSS system, ISRO Navigation Centre (INC) has been established in 2012. The prime source of measurement data for IRNSS mission is the one-way pseudorange observables provided by IRIMS reference stations located within and outside the territory of

Indian land mass. Most of the IRIMS stations are operational and supporting the mission and remaining other IRIMS stations will be soon commissioned and play role in improving the IRNSS performances. The measurements are with respect to the on-board primary RAFS. The multi-channel IRIMS G-III reference receivers from Novatel are configured to generate the pseudorange and phase observables. All computations are done with respect to the IRNSS Network time (IRNWT). The reference clock, IRNWT is the paper clock obtained through the ensemble of Active Hydrogen Masers and Caesium atomic clocks. The IRNSS system reference time, IRNWT and IRIMS stations are maintained by ISRO Tracking, Telemetry and Commanding Centre, Bangalore India. All IRNSS Satellite on-board clocks and IRIMS reference station clocks are synchronized with IRNWT. The IRNSS reference clock, IRNWT is continuously monitored and compared with respect to external reference time scales as the Universal Coordinated Time (UTC) realized by the BIPM.

The Orbit and Clock Estimation process solves for satellite state vectors, on-board clock parameters, and the reference station parameters. This algorithm uses dedicated algorithms to deal with different effects (ionosphere, troposphere, relativity, phase centre offsets corrections, tides, site displacements, ocean loading, etc.). Any miss-modelling of the involved deterministic effects will propagate together with other dominant perturbances and noise, which can influence the user position. The apparent clock behaviour estimated as phase offset with respect to IRNWT will not coincide with the real physical onboard clock behaviour since it includes stochastic and deterministic residuals errors introduced by the measurement System. Hence it is very important to separate the errors and provide the correct orbit and satellite clock information to users.

3 Methodology

The parameters, namely satellite state vector, satellite clock parameters and IRIMS receiver clock parameters are estimated using dual-frequency iono-free carrier smoothened observables obtained from active type-A IRIMS stations [3]. Using the appropriate propagation model for orbit and clocks, proper error modelling and measurement modelling, the residuals for each line of sight measurements are obtained. These residuals were subjected to the weighted least square estimation to estimate the desired parameters [4]. The estimation process involves two major methods, namely Single-Difference method, which estimates the receiver clock coefficients and is followed by Zero-Difference method to obtain the satellite state vectors and satellite clock coefficients. In addition to these parameters, dynamic parameters in terms of 9 SRP coefficients are also estimated. The state vector along with the SRP coefficients is estimated using full forced orbit propagation model. The satellite and receiver clocks were estimated using polynomial model [5]. The estimation process starts with an initial guess, and successive differential corrections were applied to obtain the final solution (Fig. 4).
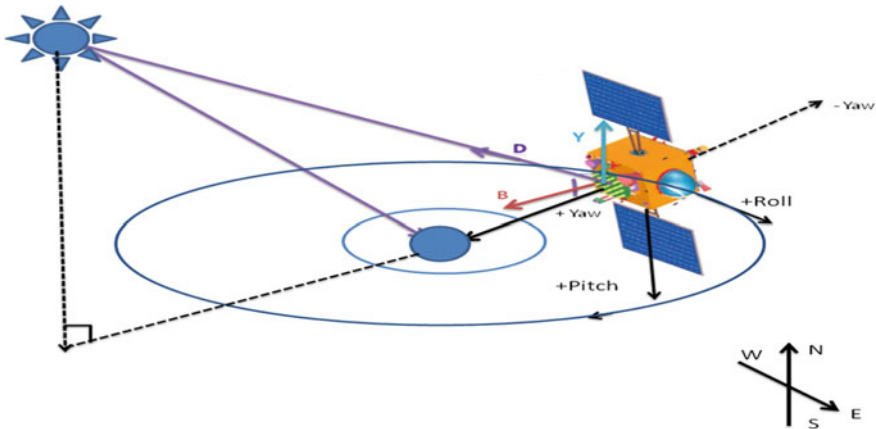
Fig. 4 SRP acceleration direction components

The estimated state vector for all operational IRNSS satellites are converted into the Keplerian elements. The paper presents the variations of the keperian elements of IRNSS1A, IRNSS-1B, IRNSS-1C and IRNSS-1D for the period of year 2015.

4 Results

The keplerian elements variations of IRNSS satellites, namely IRNSS-1A, IRNSS-1B, IRNSS-1C and IRNSS-1D for the period of year 2015 has been presented in this paper. The keplerian elements are derived from the consolidated orbit and clocks estimation using the one-way pseudorange measurements form IRIMS stations.

4.1 *Semi-major Axis Variation*

Figure 5 shows the variation of semi-major axis for four operational IRNSS satellites. The estimated semi-major axis shows the expected secular behaviour with short term and very short term periodic variations. The East–West station keeping (EWSK) operation is performed at regular intervals to maintain the orbital period and longitude crossing for getting the desired satellite geometry in terms of DOP for IRNSS mission.

IRNSS-1A and IRNSS-1B are located at 55° E longitude crossing which lies towards left of the stable point 75° E [6]. These satellites show the eastwards drift towards the stable point and show the decrease in the semi-major axis. The other two IRNSS satellites, IRNSS-1C and IRNSS-1D are located at 83° E and 111.75° E longitude crossing, respectively, which lies towards right of the stable point 75° E.
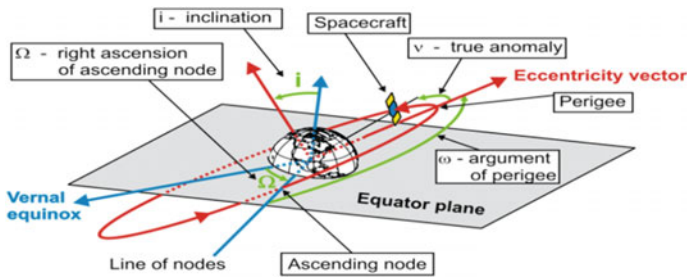
Fig. 5 Orbital elements

These satellites show the westward drift towards the stable point and show increase in the semi-major axis. The jumps at the regular intervals correspond to the EWSK operation to raise or to bring down the orbit to maintain the orbital period and longitude crossing. The average period for EWSK operations for IRNSS-1A and IRNSS-1B is about 32–33 days. IRNSS-1C is relatively close to the stable point as compared to other IRNSS satellites and hence it drifts slowly towards it. So the frequency of EWSK operation is less as compared to other operational IRNSS satellites and is about 45 days. About 8 EWSK operations have been performed for IRNSS-1C in the year 2015. IRNSS-1D is relatively far from the stable point as compared to other IRNSS satellites and hence it drifts with higher rate. So the frequency of EWSK is more as compared to other operational IRNSS satellites and is about 27 days. Since its launch, total 9 EWSK operations are performed for IRNSS-1D.

The IRNSS-1A and IRNSS-1B, the satellites motion is from East to West which is opposite to the longitude drifting direction. Hence it causes the shrinking of semi-major axis due to gravitational pull and additional velocity acting in negative direction of satellite motion and hence orbital period reduces. The other two satellites, namely IRNSS-1C and IRNSS-1D, the satellites motion is from East to West which is in same as longitude drifting direction. This gives an additional velocity in the direction of satellite motion causing the increase in the semi-major axis and hence increases the orbital period. The J2 and other even degree zonal terms also contribute towards the secular behaviour in semi-major axis [7]. Over a period of about one month, the drift of about 3–4 km in semi-major axis is observed for all the satellites. The short and very short periodic variations of about 1–1.5 cycles/month and 2 cycles per day, respectively, are due to the terrestrial coefficients of Earth's gravitational potential.

4.2 Eccentricity Variation

Figure 6 shows the eccentricity variations for all the operational IRNSS satellites. The estimated eccentricity for all operational IRNSS satellites shows the expected
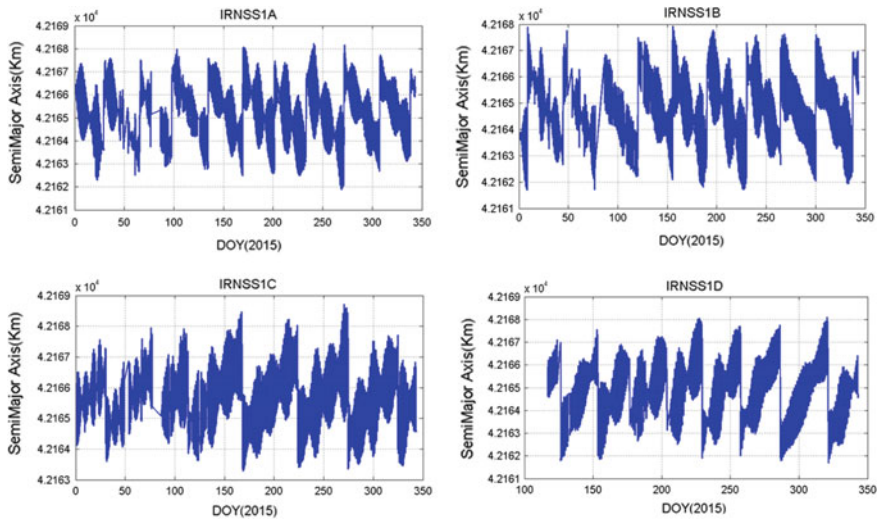
Fig. 6 Semi-major axis variations for IRNSS Satellites

behaviour with long term, short term and very short term periodic variations. The secular behaviour is not observed for the eccentricity parameter for all operational IRNSS satellites. The long term periodic variation of about 1 cycle per year is observed which is due to the odd degree zonal coefficients of Earth's gravitational potential. The luni-solar gravitational attraction also contributes towards the long term periodic variations. The short periodic variation of about 1–2 cycles per month and very short periodic variations of about 1 cycle per day is also observed in the eccentricity parameter. These variations are due to the solar radiation pressure exerted on the satellites and terrestrial coefficients of Earth's gravitational potential.

4.3 Inclination Variation

Figure 7 shows the inclination variations for all four IRNSS satellites. The estimated inclination for all operational IRNSS satellites shows the expected secular behaviour with long term and short term periodic variations. The secular behaviour in inclination parameter is due to the luni-solar gravitational pull and even degree zonal terms of Earth's gravitational potential. Since the launch of IRNSS-1A, the inclination has drifted from 27° to 28° with positive drift of about 0.4° per year; whereas for IRNSS-1B, the inclination has shown drift from 31° to 30° with negative drift of about 0.6° per year. The inclination for IRNSS-1C has shown drift from 5° to 4° since its launch, with negative drift of about 0.8° per year and for IRNSS-1D, the inclination has drifted from 30.4° to 30° with negative drift of about 0.6° per year. The long-term periodic variation of about 2 cycles per year are also
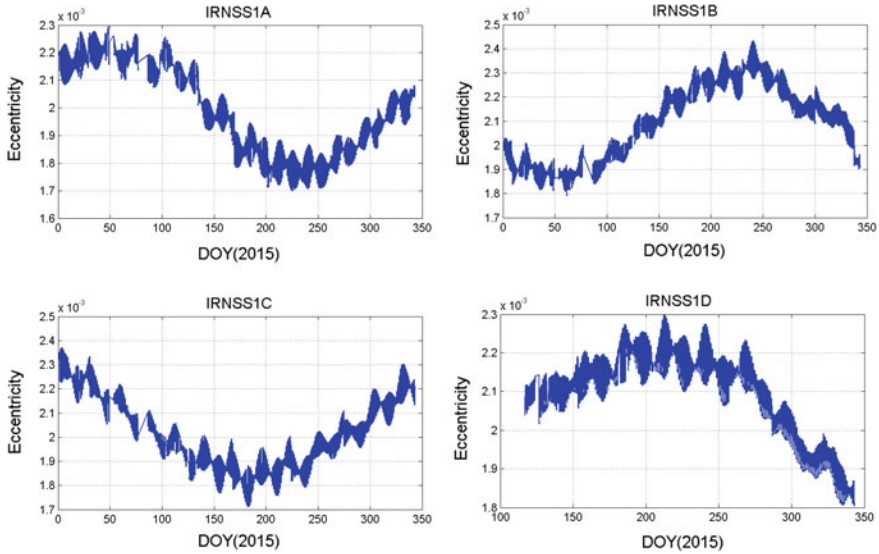
Fig. 7 Eccentricity variations for IRNSS satellites

observed in the inclination parameter of IRNSS satellites, which is due to the odd degree zonal coefficients of Earth's gravitational potential. The short periodic variation of about 2 cycles per month and very short periodic variation of about 1 cycle per day are also observed in the inclination parameter which is due to the terrestrial coefficients of Earth's gravitational potential.

4.4 RAAN Variation

Figure 8 shows the RAAN variations for all IRNSS satellites. The estimated RAAN for all operational IRNSS satellites shows the expected secular behaviour with long term periodic variations. The secular behaviour for RAAN parameter is due to the J2 and other even degree zonal terms of Earth's gravitational potential along with the luni-solar gravitational attraction, Since the launch of IRNSS-1A, the RAAN has drifted from 139° to 124° with negative drift of about 6° per year, whereas for IRNSS-1B, the RAAN has drifted from 312° to 303° with negative drift of about 6° per year since its launch. RAAN variation for IRNSS-1C has shown drift from 272° to 265° with negative drift of about 7° per year and IRNSS-1D has shown drift from 307° to 303.5° since their respective launches. The long term periodic variation of about 1 cycle per year is due to the odd degree zonal terms of Earth's gravitational potential. The RAAN for IRNSS-1C has also shown the short term periodic variation of about 2 cycles per month in addition to secular long term periodic variation.
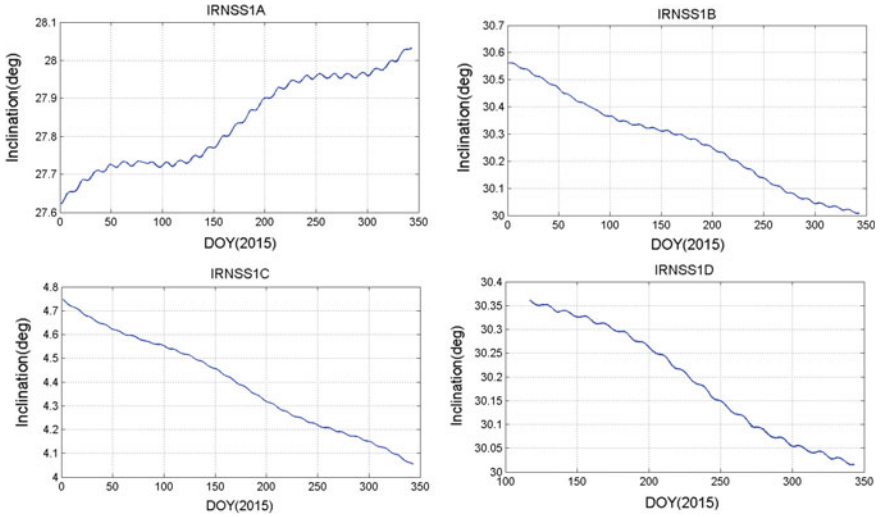
Fig. 8 Inclination variation for IRNSS satellites

4.5 Argument of Perigee Variation

Figure 9 shows the argument of perigee variations for all four IRNSS satellites. The estimated argument of perigee for all operational IRNSS satellites shows the expected behaviour with long term, short term and very short term periodic variations. The long term periodic variation of about 1 cycle per year are observed for
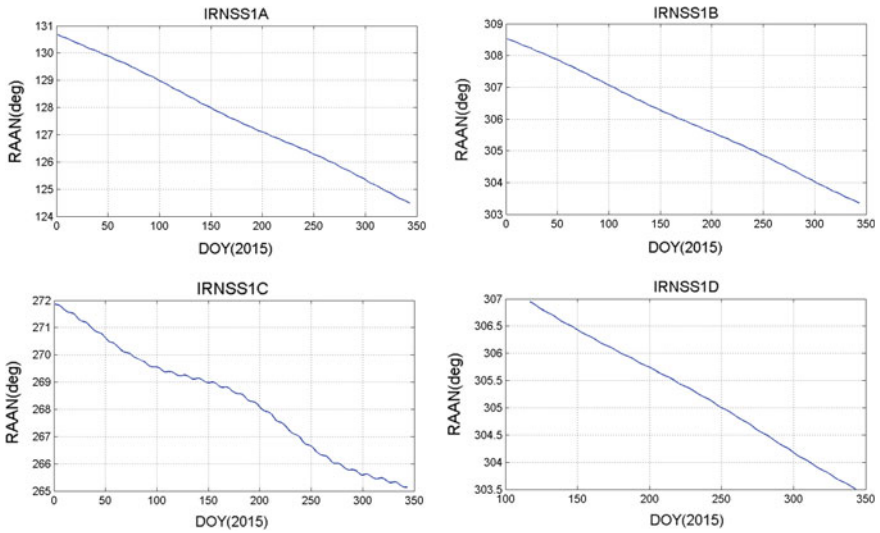
Fig. 9 RAAN variations for IRNSS satellites
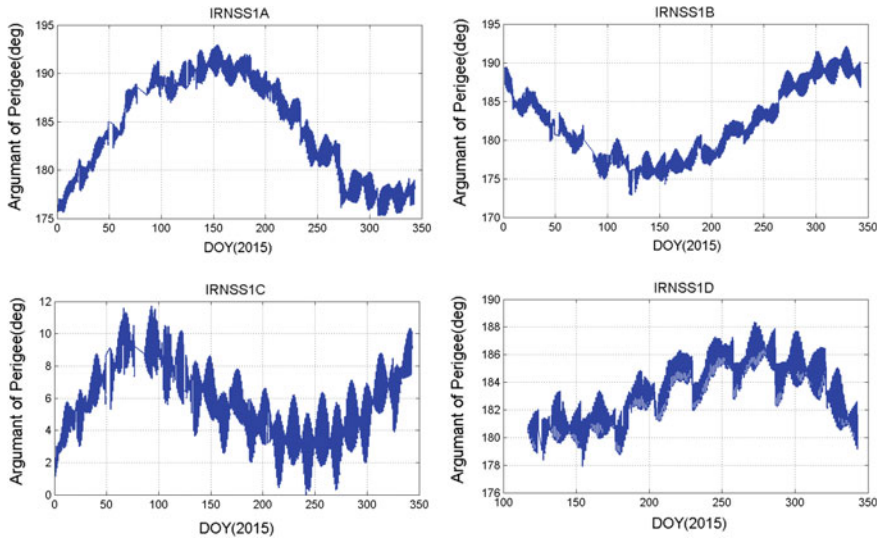
Fig. 10 Argument of perigee variation for IRNSS satellites

all IRNSS satellites which is due to the luni-solar gravitational pull and odd degree zonal coefficients of Earth's gravitational potential. Secular behaviour is not observed in this parameter. The short periodic variation of about 1 cycle per month and very short periodic variations of about 1 cycle per day are observed in the argument of perigee parameter. These variations are due to the terrestrial coefficients of Earth's gravitational potential. The argument of perigee for IRNSS-1A and IRNSS-1B are maintained with phase difference of about 15° (Fig. 10).

5 Summary

The variation of Keplerian elements for all operational IRNSS satellites under influence of major perturbing forces has been discussed in this document. All the Keplerian elements have shown the expected behaviour for GEO/GSO satellites following the nature's laws. The secular long term, short term and very short term periodic variations can be observed in the Keplerian elements. The variations in the Keplerian elements helps in understanding the effect of perturbances due to various effects like J2, planetary effects, etc. The four operational satellites of IRNSS constellation are supporting the mission by providing the position accuracy of about 15 m for about 20 h of time of day.

of IRNSS project. The authors wish to specially thank former Project director of IRNSS, Shri A.S. Ganeshan for the motivation. The authors also wish to acknowledge the vital role of other ISRO centers for this analysis.

References

1. *IRNSS: Functional Specifications*, April 2013, ISRO-ISAC-IRNSS-PR-2256, Space Navigation Group, ISRO Satellite Centre.
2. *IRNSS: Navigation Software Design Document*, Oct 2012, ISRO-ISAC-IRNSS-RR-1000, Space Navigation Group, ISRO Satellite Centre.
3. PratapMisra, Per Enge, Global Positioning System: Signals, Measurements and Performance, Ganga-Jamuna Press.
4. Byron Tapley, Bob Schutz, George H Born, *Statistical Orbit Determination*, Elsevier Academic Press.
5. B.Parkinson, J Spilker Jr., P Axelrad, P.Enge, *Global Positioning System: Theory and Applications,* American Institute of Aeronautics and Astronautics.
6. Oliver Montenbruck, Eberhard Gill, Satellite Orbits: Models, Methods and Application, Springer.
7. D. A. Vallado, Fundamental of Astrodynamics and Application, Springer.

Cabin Control System on Temperature Impact Using Occupant Detection Scheme for M1 Category Vehicles

Surender Dhanasekaran, Andhavarapu Siva, Kevin Nesamani and Patil Pritam

Abstract Temperature influence on parked vehicles in hot climatic conditions is dangerously high and the impact on the occupant is directly felt leading to catastrophic disaster, even loss of lives. Every year hundreds of lives are lost inside the locked vehicle cabin. The cabin safety is ensured by the autonomous door locking system in the vehicle's movement and in parked state depending on the input of the driver and its autonomous nature. The tendency of the occupant within the vehicle depends on the state of vehicle's idling nature and the driver leaving the vehicle in parked state. The automatic door locking system is synchronized with the inputs from the driver control switch, the wheel speed sensor and the engine rpm. The temperature influence in the parked vehicle conditions toward the occupant is tremendous. A maximum of 80 °C can reach within the cabin in parked state of the vehicle. The impact of heat is competitive and the suffocation rate is high. The safety of the occupant within the vehicle is the major concern. The system aims at protecting the safety of the occupant (most supposedly the child occupant) by the detection of weight as the major concern by the testing standards of AIS-008. The system ultimately aims at reducing the casualty rate and protecting the occupant by measuring the weight of the occupant and the cabin temperature and controls the windows to be lowered to reduce the level of suffocation. Fresh air circulation is made to be in the cabin and the occupant safety is ensured.

S. Dhanasekaran (✉)
EEE Department, Vel Tech University, Chennai, India
e-mail: surenderdhanasekaran@gmail.com

A. Siva · K. Nesamani · P. Pritam
Automotive Electronics, Vel Tech University, Chennai, India
e-mail: siva.andh@gmail.com

K. Nesamani
e-mail: kennith.n@gmail.com

P. Pritam
e-mail: pritamp46@gmail.com

1 Introduction

Safety is a primary concern in passenger transportation. Mass vehicle movement happens around the world mostly in passenger cars and the greater proportion of them is comparatively high and so does the safety concerns. Vehicles parked in roofless state, have higher exposure of developing dangerously high temperature within the vehicle. The penetration of IR rays through the window panes and the process is continuous as it is a one-way process, hence the heat is multiplied every minute it takes. A vehicle parked in such condition at 0 min has a temperature of 80 °F outside and after a period of 60 min the temperature reaches to heights of 124 °F, which is equal to 50 °C. The Figs. 1 and 2 explains the state of a vehicle parked in roofless state, exposed to direct sunlight. An average human sustainability for higher temperatures can be up to a maximum of 40 °C [1]. Beyond this defined region, the human body will start to sustain hyperthermia and hence the damage

Fig. 1 Initial vehicle state at 0 min
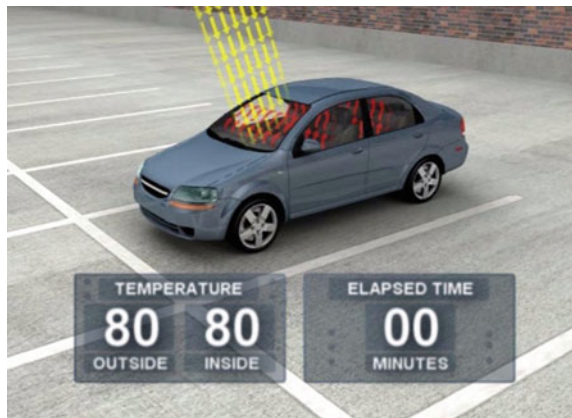
Fig. 2 Final vehicle state at 60 min
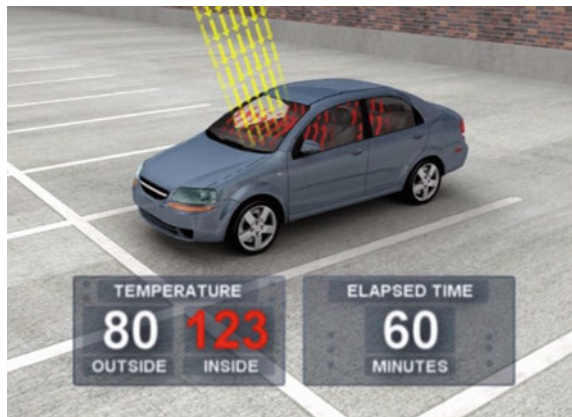
Table 1 Number of causalities by neuro toxic gases from 1998 to 2016 in United States

Sl. No	Cause of death	Percentage value of death	Number of children dead due to suffocation
1	Forgotten by the caregiver	53	356
2	Children playing in unattended vehicle	29	189
3	Intentionally left in the vehicle	17	111
4	Unknown circumstances	1	5

Table 2 Causalities grouped by age group

SI.No	Age group in years	Number of causalities	Percentage of casualty
1	Less than 1	208	32
2	1 year old	146	22
3	2 years' old	131	20
4	3 years' old	84	13
5	4 years' old	41	6
6	5 years' old	23	4
7	6 years' and above	19	3

done to bodily enzymes. Hyperthermia causes the occupant to initially choke for fresh air, developing irritation to skin and develop flu. The final stage which could lead to Hyperthermia is one concern and hence the expulsion of Neuro toxic gases. The materials used to polish the upholsteries in the vehicles comprises of volatile organic compounds (VOC) which has chemical composition of formaldehyde, polybrominated diphenyl ethers (PBDEs), phthalic acid esters(Phthalates), etc., are benzene-based chemicals and the tendency of coated chemicals to evaporate is highly volatile [2]. The exposure of these substances can exacerbate allergy and asthma symptoms and cause eye, nose, and throat irritation. Sometimes it leads to cancer and neural disorders [3]. The Table 1 describes the number of casualties by neurotoxic gases from 1995 to 2016 in the United States as a severity of the situation and Table 2 describes the age group of casualties with the percentage level of casualties described by their age groups in specific.

The parked vehicles are completely enclosed and no circulation of fresh air within the cabin makes the occupant to suffocate for air. The Fig. 3 describes the level of temperature raise within the cabin for a period of 60 min.

The death tolls for the problem encountered is in a constant phase where the death casualty level is a bigger threat for occupants in the closed cabin. The Fig. 4 suggests the severity of the problem faced. The circulation of the free air with the occupant trapped in with a dangerous level of temperature is the case considered.
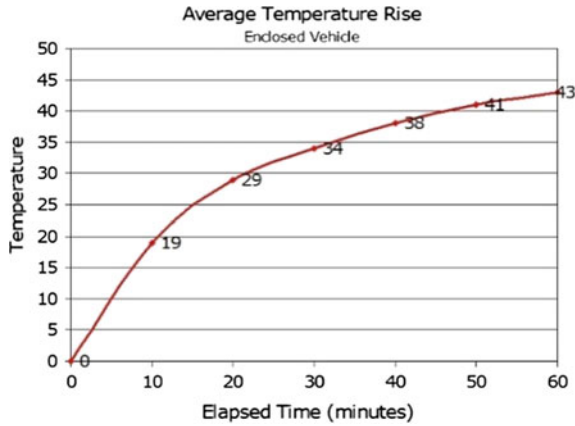
Fig. 3 Graph of temperature raise in a period from 0 to 60 min
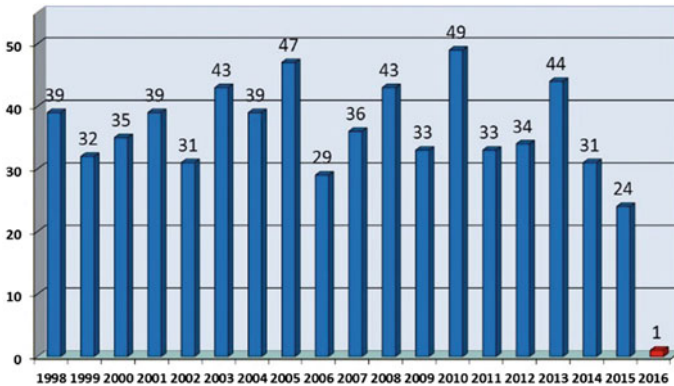
Fig. 4 Bar chart of death toll from 1998 to 2016

Hence, the state of engine ignition is checked and the level of occupant's movement within the vehicle is continuously monitored and the temperature raise are considered as the inputs for the system developed. Depending upon the contingencies of the situation, the system developed has two levels of deployment. The first level as the warning level of letting the driver know about the severity of the situation and the second level is autonomously decided by the system to take control of the door windows to be lowered with a time period of 2 s each to get a free air circulation within the cabin. Hence monitoring the levels of occupants and the cabin temperature depending upon the state of the vehicle parked, the system maintains a safe level of air circulation within the vehicle.

2 System Developed and Control Flow

The central locking system of the considered M1 category of vehicle makes sure that the doors of the vehicle are completely latched and air tight [4, 5]. The system designed aims at controlling the motor for driving the door windows. The driving motor is a 5 V DC motor which is to be alternately driven by the motor driving IC L293D. As described, the inputs for the system are measured by hierarchy of important parameters.

2.1 Occupant Detection Scheme

The occupants within the vehicle are normally considered to be 75 kg according to automotive testing standards AIS-008 [6]. The considered scenario of occupant within the vehicle is from the age group of 0–6 years old and hence, the level of weights within the cabin could be from 3–15 kg on an average. The level of inputs in weight is hence altered to be from this considered range. The presumed level of occupant movement within the vehicle is within the considered existing five seats. Figure 5 describes the top view of the obtained layout and it shows the seats of driver, co-driver, passengers-1, 2, and 3.

The fixed levels of weight are absorbed by the load cells placed in-between the seats and the vehicle frame to support the seats. The CZL-601 load cell is the primary input considered to obtain the input of the occupant from the cabin. The continuous distortion in load cells input due to the movement of the occupant from within makes the microcontroller to receive varied inputs from the different cells and hence the occupant's movement is continuously monitored. The load cell has a maximum capacity of 80 kg and the rated output by it is 2 mV/V and the excitation voltage for the load cell lies in the range of 9–12 V DC. By the rated input from the vehicle as 12 V, the output per kg of weight will be 0.3 mV.

$$1 \text{ Kg} : 80 \text{ kg} = X\text{mV} : 24 \text{ mV}$$

Fig. 5 5 seat layout of the M1 category vehicle
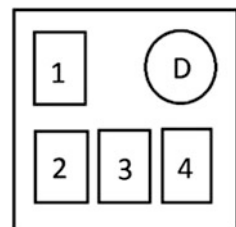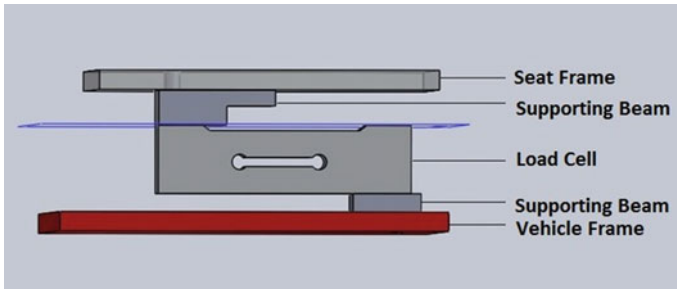
Fig. 6 Load cell mounted fixture

Hence, the output for the desired 3–15 kg input will be ≤1 mV to ≈5 mV. This input is amplified and fed to the microcontroller. The Fig. 6 shows the load cell mounting between the seat and the vehicle frame.

2.2 Block and Flow Process

The system developed has two levels of operation [7]. The primary levels of input are seen to that, the driver locks the doors with the occupants within the vehicle, then the system locks down to the primary initial warning of 10 s Buzzer and LED indication to the driver about the occupant's status [8]. The LM35 temperature sensor simultaneously verifies the level of cabin temperature. With the set point of 40 °C, the maximum sustainable level of the occupant is reached and hence, the window panes are lowered for the circulation of free air within the cabin. The Fig. 7
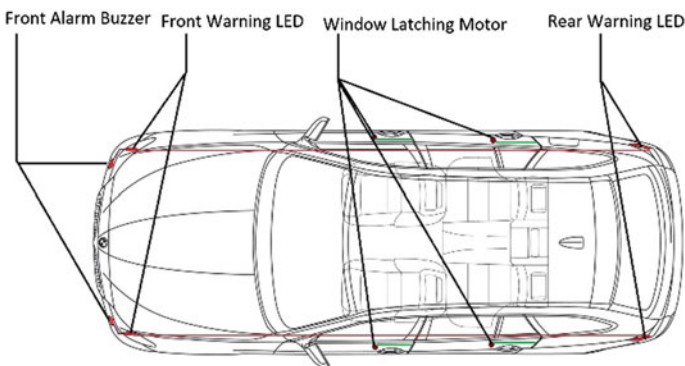
Fig. 7 Proposed system with warning buzzer and LED mountings
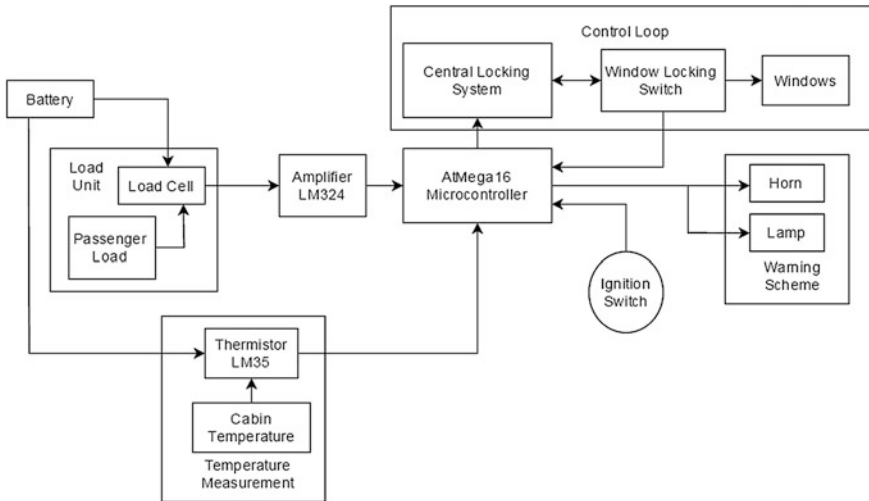
Fig. 8 Block diagram

describes the overall warning and actuation of the system from the top view of a car.

The 12 V battery of the vehicle serves as the unanimous power supply for the system. The load cells initially detects the imbalance between the weight distortions. The input of each load cell is fed to the LM324 amplifier and then to the Atmega16 microcontroller. The ignition switch, temperature input, and input from the central locking system are the important input received by the controller. The horn and lamp are used as the warning trigger and the door windows are the actuation after peer warning. The Fig. 8 explains the complete block architecture of the system.

The process initiates the engine's state of ignition followed by the doors locked state and the occupant's status. If the presence of all these are found, then the direct flow ends at the warning state of the vehicle. After the actuation of the flow process for a programmed 10 s, the system proceeds to check if the other parameters still exist. If the temperature of the cabin is still greater than 40 °C, then the windows are lowered by the controller to let fresh air inside the cabin (Fig. 9).

Fig. 9 Process flow
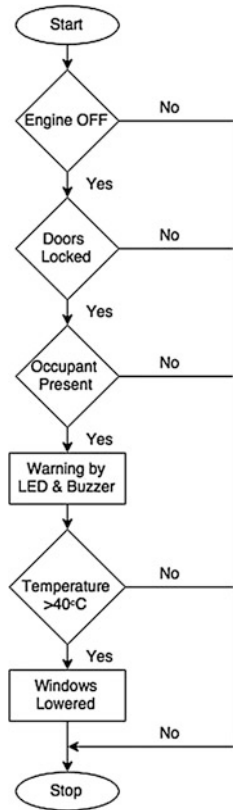
3 System Assembly and Model Developed

The inputs from the occupant are obtained by the load cells and are symbolically represented as the voltage sources here, which is amplified by the consecutive amplifiers LM-234 and fed to the Port-A of AtMega16 microcontroller, where this port is dedicated to the occupant level detection. The Port-B is connected with the LM35 temperature sensor and the input from the ignition switch. Port-C is connected to the LEDs of four extreme ends of the vehicle dedicated for the warning system and to the horn. Port-D is connected with the motor control process through the motor control IC L293D. The pictorial representation of the overall electronic simulated diagram is shown in Fig. 10. The Fig. 11 is the model development did in the laboratory as a part of practical simulation.
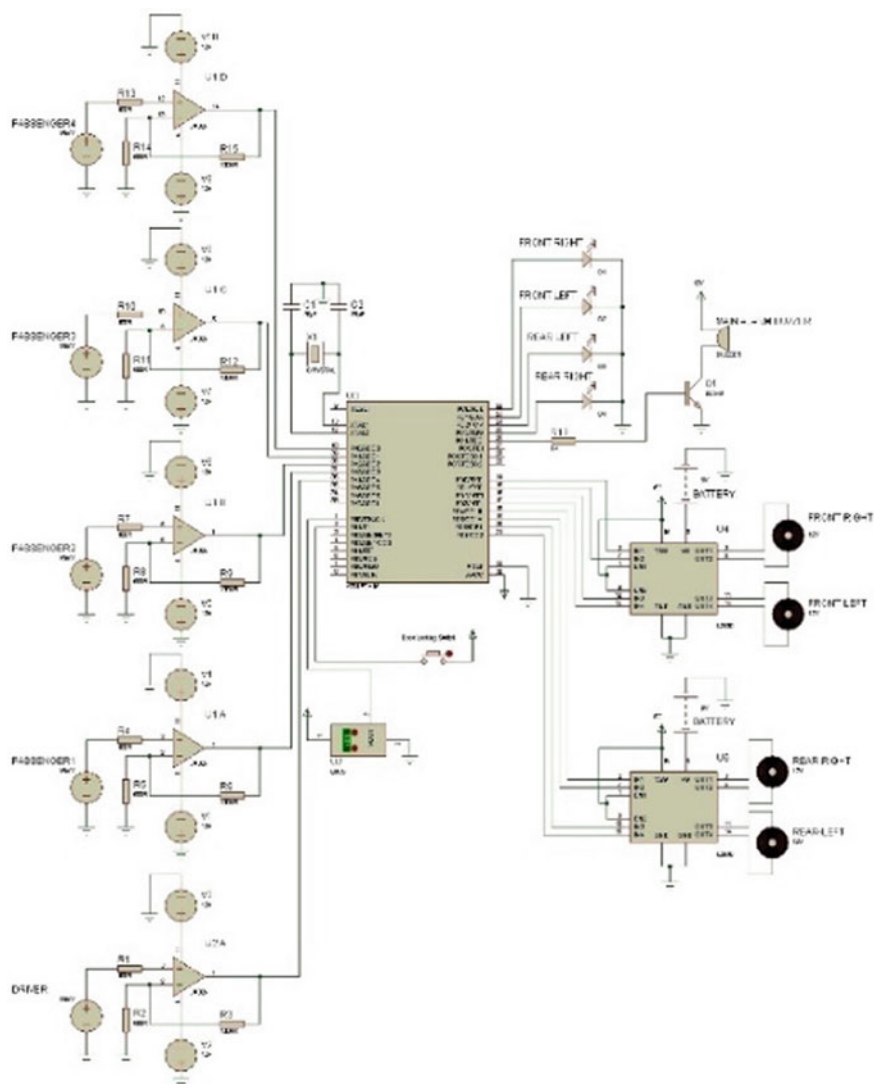
Fig. 10 Electronic system assembly and simulation

Fig. 11 Model developed
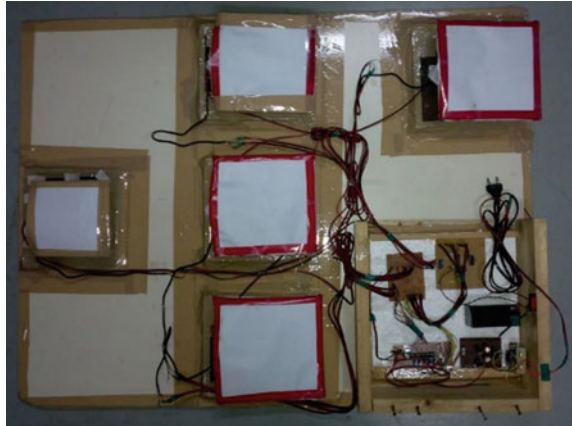
4   Conclusion

The casualties due to the occupant's suffocation within the cabin are constant through years. The system aims at establishing a safer car ride. The system has the robustness and portability to adapt and deploy in a hybrid system development for various purposes. The two level of deployment helps the system occupant to notify and act depending upon the defensive situation.

References

1. Grundstein, Andrew, Vernon Meentemeyer, and John Dowd. "Maximum vehicle cabin temperatures under different meteorological conditions." *International journal of biometeorology* 53.3 (2009): 255–261.
2. Vehicles-Types—Terminology."Faber, Joanna, et al. "Comparison of Air Pollution by VOCs Inside the Cabins of New Vehicles." Environment and Natural Resources Research 4.3 (2014): p 155.
3. AQS. (2006). Indoor air quality hazards of new cars. Air Quality Sciences Inc.
4. Mochida, Haruo, and Ken Miyamoto. "Electronic door locking system for an automotive vehicle." U.S. Patent No. 4,428,024. 24 Jan. 1984.
5. Automotive Industry Standard. "AIS-053: Automotive Vehicles-Types—Terminology
6. Installation Requirements of Lighting and Light-Signaling Devices for Motor Vehicle having more than Three Wheels, Trailer and Semi-Trailer excluding Agricultural Tractor and Special Purpose Vehicle, AIS-008 (Rrevision-1):2010.
7. Surender Dhanasekaran, Siva Kumar, ImmanuelDinesh Paul, ThamaraiKannan, GokulChandrasekaran and VidhyadharanRajendiran. "Automatic Headlamp Leveling System Using occupant Detection Scheme for M1 Category Vehicles: An Alternative Method to

Replace Manual Switching"*International Journal of Applied Engineering Research* ISSN 0973-4562 Volume 9, Number 22 (2014) pp. 16493–16502.

8. Dhanasekaran S, Katekar A, Kumarasamy S, Rao MY. Active cabin safety system for M1 category vehicles. InSmart Technologies and Management for Computing, Communication, Controls, Energy and Materials (ICSTM), 2015 International Conference on 2015 May 6 (pp. 494–498). IEEE.

Viabilities of Replacing Combustion Engine by Electromagnetic Engine

Anirudh Satya Duvvuri and N. Venkatachalapathi

Abstract This manuscript probes about the certainties in having an engine without any fuel by replacing convectional piston and cylinder head with magnet and electromagnet, respectively. Thematic inception of an engine is to produce reciprocating action as an ensue of ignition and fuel consumption in conservative sort of engines, now here in this article we explored and spotted sure possibilities of interchanging polarity of the Electromagnetic head powered by alternating current with controllable frequency which can be done by using Cycloconverter.

Keywords Convectional piston · Conservative engine · Electromagnetic head · Cycloconverter

1 Introduction

Whether it might a classical I.C. heat engine or a highly advanced sport car engine, the basic principle is same. Fuel in the cylinder gets ignited by a sparkplug which makes the piston to make reciprocating action. These will be connected to crankshaft making the vehicle to move [1]. The same action can be produced by using magnets by making changes in the design of the engine. A continuous change in polarity using a cycloconverter [2] makes the magnets attract and repel continuously producing the same action that is produced in a regular engine.

A.S. Duvvuri (✉) · N. Venkatachalapathi
Department of Mechanical Engineering, Vel Tech University, Chennai, India
e-mail: satyaanirudh.duvvuri@gmail.com

N. Venkatachalapathi
e-mail: nvcprincipal@gmail.com
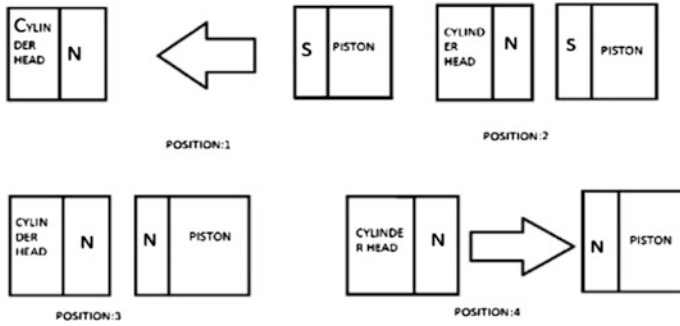
Fig. 1 Cylinder positions with respect to magnetic poles

2   Methodology

The key idea is to replace the piston and cylinder head with a permanent magnet and electromagnet, respectively. The piston side which faces the cylinder head is fixed; for instance let it be North Pole. As the cylinder head is electromagnet, its polarity can be changed continuously. When it is South Pole it attracts piston and the piston moves towards the cylinder head. When it is North Pole, it repels and hence the piston moves away from the cylinder. This causes a reciprocating action similar to a regular automobile engine (Fig. 1).

3   Material Required

To generate bloated magnetic fields neodymium magnets of N52 grade are used. The attraction or repulsion of magnets is very high and we need a material that is non-magnetic and as well as of high strength.

Type 301 is austenitic chromium–nickel stainless steel that provides high strength and ductility when cold worked. In this case it is magnetic. But when annealed it is essentially non-magnetic [3] (Tables 1 and 2).

Table 1 Composition of materials

Composition	Weight (%)
Carbon	0.15
Manganese	2
Phosphorous	0.045
Sulphur	0.030
Silicon	0.75
Chromium	16–18
Nickel	6–8
Nitrogen	0.10
Iron	Balanced

Table 2 Mechanical Properties at Room Temperature

Condition	Annealed
UTS KSI (Mpa)	120 (827)
0.2 % YS KSI (Mpa)	45 (310)
Elongation % in 2″	60
Hardness Rockwell	B86

4 Room Temperature Mechanical Properties

The strength of the material is not just confined to room temperatures alone. Even at elevated temperature of 800 K its tensile strength is 1000 MPa making it perfect for application in designing the components of the engine. The strength comparison ak 301 (austenitic grade) with others is given below [4] (Fig. 2).

4.1 Change of Frequency

The frequency of the AC supply can be changed using AC inductance circuit. When an AC supply is given to electromagnet, the polarity of the magnet changes basing on frequency of the supply. The strength of magnet is directly proportional to the current, whereas the polarity depends on direction of current. As the direction of the AC current varies sinusoidal, the polarity of the magnet varies according to the frequency of the supply. The continuous change in frequency of the piston can be produced by using a cycloconverter.

4.2 Cycloconverter

A cycloconverter is a device that can change the frequency of a given AC supply to the frequency we need [5]. The key idea is to interlink the accelerator of the vehicle and cycloconverter to vary the frequency of the current supplied to the magnet. In

Fig. 2 Ak301 vs other grades
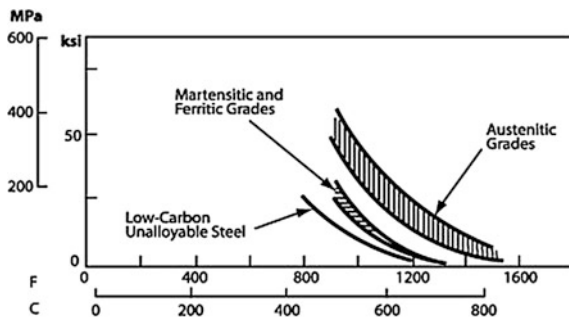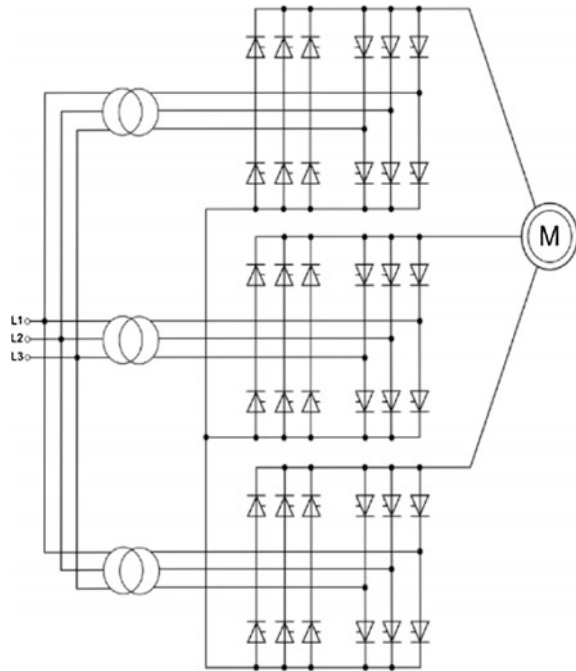
general, the output voltage from a cycloconverter is less than the input voltage but output frequency is selectable (Fig. 3).

5 Calculations and Results

5.1 Magnetic Field

As the engine works completely on the magnetic fields, calculating the power of magnetic field is the key point. Here two forces are calculated. They are pull force and repel force. But both will be same. Now the calculation is as follows basing on the following parameters:

Magnet type: Neodymium N52; Thickness of magnet: 1; Diameter of magnet: 3; Distance between two magnets: 5 (piston and cylinder head).

*All dimensions are in inches.

For the above given parameters, the force of pull or repel is as follows at maximum distance of separation (5 in.) = 8.21 lb = 36.45 N. At minimum distance of separation (0 in.) = 495.24 lb = 2198.86 N the variation of pull force or repel force with respect to distance of separation is shown in Graph 1.

Graph 1 Distance v/s Pull
Force
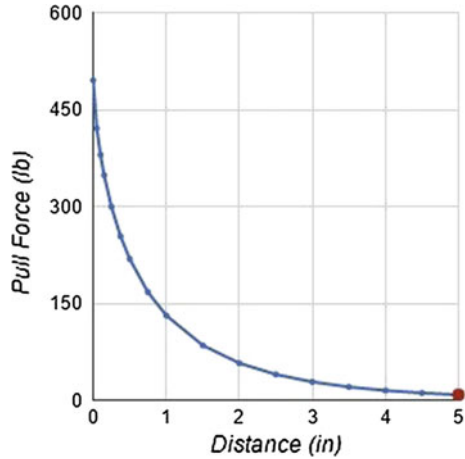
Force that will be produced per unit area:

Radius of magnet = 1.5 in. = 0.038 m, Surface Area = 0.0045 m², Force per unit Area at minimum distance of separation = 488.6 kPa.

5.2 *Required Frequency for Changing Polarity*

Consider the required maximum speed to be 160 kmph and size of tyre to be 25″. Speed = 160 kmph Circumference of tyre = 199.39–200 cm under these conditions the rpm of tyre will be 1333–1350. If the vehicle is in sixth gear the piston needs to reciprocate 225 times per min. Assigning the maximum reciprocations as 250 per minute the required frequency at which the polarity should be changed is 4 times per s. This can be attained using AC supply (Graph 2).

5.3 *Maximum Speed Attained*

As the piston reciprocates 250 times per min, the maximum speed that can be attained in each gear is as follows:

250 (rpm) * 0.002 (radius of tyre in km) * 60 (min per h)* n (gear) = 30 * n

So, the speed (max) will be as follows depending on the gear (Graph 3)

Graph 2 Rotations per second
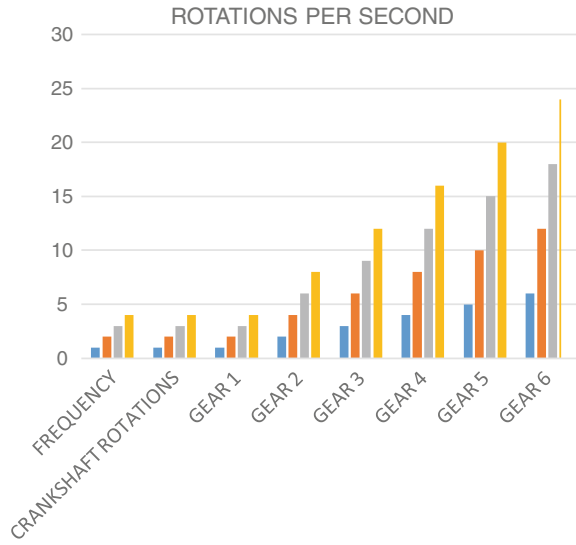
Graph 3 Rotations per second
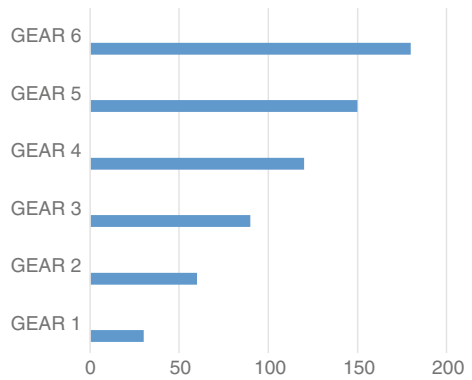
- 1st gear: 30 kmph
- 2nd gear: 60 kmph
- 3rd gear: 90 kmph
- 4th gear: 120 kmph
- 5th gear: 150 kmph
- 6th gear: 180 kmph

6 Conclusion

This script dealt with the sure possibilities of replacing current gasoline fuelled engine with cost effective electromagnetic engine, jeopardize owing to deficit of fuel is the fact to happen in mere future where the world is looking for alternate resolution for combustion engines, tweaking design methodologies for the right amount of magnetic field generation and accordingly hardware modification pays a way for effectual deployment of Electromagnetic engine as a replacement of Combustion engine.

References

 1. M. Priest, C.M. Taylor, "Automobile engine tribology — approaching the surface".
 2. Zahirruddin Idris, siti Zaliha mahammud noor, Mustafar kamal Hamza "Modelling and simulation of Single Phase to single phase Cycloconverter Based on Single phase Matrix Converter Topology with Sinusoidal Pulse Width Modulation Using Matlab/simulink" IEEE PEDS 2005 Conference.
 3. H. Mirzadeh, A. Najafizadeh, "Correlation between processing parameters and strain-induced martensitic transformation in cold worked AISI 301 stainless steel".
 4. M. Azzi, M. Benkahoul, J.A. Szpunar, J.E. Klemberg-Sapieha, L. Martinub, "Tribological properties of CrSiN-coated 301 stainless steel under wet and dry conditions".
 5. H. F. Blanchette, T. Ould-Bachir, and J. P. David, "A state-space modeling approach for the FPGA-based real-time simulation of high switching frequency power converters," Industrial Electronics, IEEE Transactions on, vol. 59, no. 12, pp. 4555–4567, 2012.
 6. P. Syam, P. Nandi, and A. Chattopadhyay, "Improvement in power quality and a simple method of subharmonic suppression for a cycloconverter-fed synchronous motor drive," in *Electric Power Applications, IEE Proceedings*-, vol. 149, pp. 292–303, IET, 2002.
 7. S. Butzmann, J. Melbert, A. Koch, "Sensorless Control of Electromagnetic Actuator for Variable Valve Train", SAE Paper No. 2000-01-1225, 2000.
 8. C. Tai, A. Stubbs, and T.C. Tsao, "Modeling and Controller Design of an Electromagnetic Engine Valve", Proceedings of American Control Conference, pp. 2890-2895, 2001.
 9. Michel Cessenat, "MATHEMATICAL METHODS IN ELECTROMAGNETS Linear Theory and Applications".
10. J. Biela, M. Schweizer, S. Waffler, and J. Kolar, "SiC versus Si—evaluation of potentials for performance improvement of inverter and dc–dc converter systems by SiC power semiconductors," *IEEE Trans. Ind. Electron.*, vol. 58, no. 7, pp. 2872–2882, Jul. 2011.
11. M. Hartmann, S. Round, H. Ertl, and J. Kolar, "Digital current controller for a 1 MHz, 10 kW three-phase VIENNA rectifier," *IEEE Trans. Power Electron.*, vol. 24, no. 11, pp. 2496–2508, Nov. 2009.
12. F. Krismer and J. Kolar, "Accurate power loss model derivation of a high current dual active bridge converter for an automotive application," *IEEE Trans. Ind. Electron.*, vol. 57, no. 3, pp. 881–891, Mar. 2010.
13. H.C. Barshilia, B. Deepthi, K.S. Rajam, Surf. Coat. Technol. 201 (2007) 9468.

Comparative Approach Toward Modified Smith Predictor and Back Calculation design for Conical Tank Level Process Control

Eadala SarathYadav and Thirunavukkarasu Indiran

Abstract The objective of this paper is to show the energy utilization of actuator and its performance in nonlinear process. Objective includes design and comparison of modified Smith predictor, modified back calculation methods, and conventional PI controller for conical tank level process (FOPDT). The design comprises of mathematical modeling of conical tank using two-point method, controller tuning, and architecture of the process. In FOPDT models, integral term influences the actuator to react beyond its limits which results with windup phenomena in the process. This can be controlled by limiting integral term with respect to actuator requirements. Whole experimentation is classified into three operating regions and for all the methods mentioned in the paper. Based on operating region, the methods have their own significance in performance. The design approach has been validated through the real-time results.

Keywords Smith predictor · Nonlinear level process · FOPDT · Skogestad tuning · Reset windup

Nomenclature

FOPDT	First-order plus dead time
K_p	Proportional gain
T_i	Integral time
T_c	Closed loop time constant
T	Time constant
t_d	Dead time
T_t	Tracking time constant
G_m	Process model
G_p	Real-time process
MBC	Modified back calculation
MSP	Modified Smith predictor

E. SarathYadav · T. Indiran (✉)
Department of ICE, MIT, Manipal, India
e-mail: it.arasu@manipal.edu

E. SarathYadav
e-mail: sarath.eadala@gmail.com

1   Introduction

Smith predictor is one of the effective model-based compensator for dead time plant models. Many researchers implemented different modifications to Smith predictor algorithm and succeeded in their domain. Different modified approaches are being designed based on the plant requirement or performance competences. Basic architecture consists of two loop where inner loop copes with reference tracking and outer loop with disturbance rejection. Based on design, Smith predictor can be used for stable [1], unstable, and integrating processes [2–4]. Few researchers produced compensators which suits for all type of processes [5]. In this paper conical tank is considered as plant and control of level has been carried out. Controlling level of conical tank has good significance, because of its nonlinear physical structure with respect to process variable. Mathematical modeling play vital role in control design for such nonlinear processes. Black box method has been followed for modeling of the plant. Usually for linear plants there is less modeling difficulty compared with nonlinear plants. Selection of operating region play very important role on mathematical modeling for such type of nonlinear plants. Model mismatch takes place when the selection of operating region changes. So, far different compensators have been designed for level control of conical tank [6–8]. In this paper Smith predictor is modified with respect to its architecture to eliminate dead time. In FOPDT models, windup is suspected due to integral action which should be limited, modified back calculation method serves to achieve this constraint. Skogestad's controller tuning method [9] with additional modification in the methods and comparison with their performance characteristics has been carried out. The real time experiment is conducted through different operating regions to clearly analyze the response.

2   Methodology

The methodology includes mathematical modeling of conical tank system and controller design. The mathematical modeling is carried out by using two-point method [10] where two points of response to step change will be selected one at 23.8 % and other at 63.2 % of response curve, respectively. Figure 1 represents different variables used to model plant transfer function by two-point method. The standard form of FOPDT model is given by Eq. (1).

$$Q(s) = \frac{k}{\tau s + 1} e^{-t_d s} \tag{1}$$

$$k = \frac{Y_F - Y_I}{U_F - U_I} \tag{2}$$

Fig. 1 Two-point method
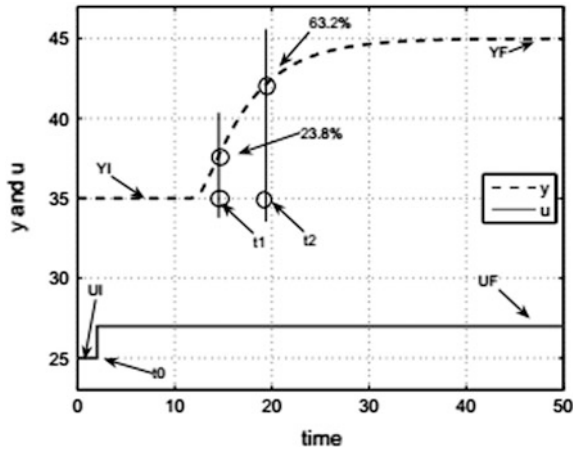
$$\tau = 1.5(t_2 - t_1) \tag{3}$$

$$t_d = 1.5[(t_1 - t_0) - \frac{1}{3}(t_2 - t_0)] \tag{4}$$

By using Eqs. (2)–(4) the mathematical model is obtained as follows:

$$Q(s) = \frac{k}{\tau s + 1} e^{-t_d s} = \frac{0.925}{25.05s + 1} e^{-1.09s} \tag{5}$$

Skogestad's controller tuning method is used for designing manipulated variables. According to Skogestad's, PI controller best suits for the FOPDT models. Controller parameters are designed by using Eqs. (6) and (7)

$$K_p = \frac{\tau}{k(T_c + t_d)} = 12.9 \tag{6}$$

$$T_i = \min[\tau + c(T_c + t_d)] = 3.015 \tag{7}$$

$$T_d = \tau \tag{8}$$

$$C = K_p\left(1 + \frac{1}{T_i}\right) = \frac{38.5669}{3.015s} \tag{9}$$

For this process 'c' and 'T_c' selected as 1.5 and 1, respectively, based on the procedure given in [9]. The value of 'c' is inversely proportional to the disturbance rejection and directly proportional to setpoint tracking. 'T_c' is usually time constant taken as settling time of closed loop response or it can be taken as user defined variable. Skogestad suggested to consider 'T_c' as delay time (t_d), unless user has own specifications to select it. Therefore controller transfer function 'C' is obtained and depicted in Eq. (9).

Fig. 2 Real-time setup for nonlinear level process

Figure 2 shows that real-time experimentation setup consists of nonlinear process tank with 500 mm height, 300 mm, and 20 mm of upper and lower diameter, respectively. Pump acts as an actuator with the driving capacity of 800 LPH and 6500 rpm. Setup includes level transmitter, rotameter and thyristor power driver to control the speed of pump, etc.

3 Different Techniques with Architectural Changes

Modified Smith predictor: It is the method which is used for processes with long time delays. There exist different types of modified Smith predictor controllers based on effectiveness required for the process. Figure 3 represents basic structure of Smith predictor.
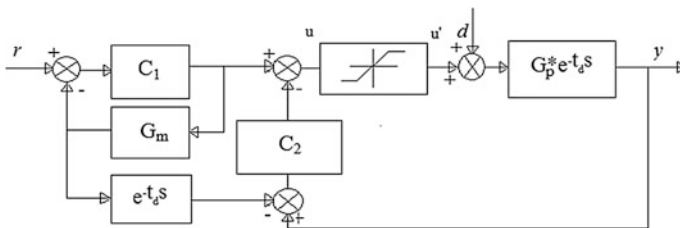
Fig. 3 Modified Smith predictor approach

The controllers are designed as per process requirement but methodology has been followed from [11]. For this architecture controller C_1 is calculated as in the Eq. (10) which acts as reference tracking and controller C_2 is designed using Skogestad's tuning approach and used for load rejection phenomena.

$$C_1 = \frac{Ts + 1}{T_i} = \frac{25.05s + 1}{3.015s} \tag{10}$$

$$C_2 = K_p \left(1 + \frac{1}{T_i} + T_d\right)\left(\frac{1}{T_i + 1}\right) = \left(\frac{312.12s^2 + 12.46s + 4.15}{3.015s^2 + s}\right) \tag{11}$$

Modified back calculation method: Back calculation method consists of a variable called tracking time constant 'T_t' which is factor of integral time constant (T_i) when controller saturates. The difference of saturated and unsaturated control signal is feeded to controller block to optimize integral action by the factor of 'T_t'. In this paper, back calculation approach is modified by introducing controller 'C_2'. The architecture consists of two controller 'C_1' and 'C_2' where 'C_1' is used for servo operation and 'C_2' for load rejection. The block diagram is shown in Fig. 4

Conditions for Saturation is given by

$$u' = +u_{sat} \quad u > +u_{sat} \tag{a}$$

$$u' = u \quad -u_{sat} \leq u \leq +u_{sat} \tag{b}$$

$$u' = -u_{sat} \quad u < +u_{sat} \tag{c}$$

From skogetad's controller tuning C_1 is taken from Eq. (9) and it is used as reference tracking controller. For the process shown in Eq. (5) controller C_2 acts as load rejection. T_t is tracking time constant, as PI controller is used in this paper $T_t = T_i$ [12]

$$C_1 = K_p\left(1 + \frac{1}{T_i}\right) = \frac{38.5669}{3.015s} \tag{12}$$
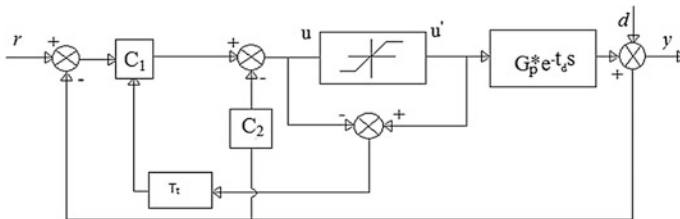
Fig. 4 Modified back calculation approach

$$C_2 = \frac{Ts}{T_i s + 1} = \frac{25.05s}{3.015s + 1} \tag{13}$$

4 Results and Comparison

The real-time experimentation is carried out in three different operating regions with respect to level of conical tank. For all the operating regions, all three control approaches have been applied. The analysis includes the study of controller action and process variable for all operating regions. For each and every operating region three different step changes has been applied. Figure 5 depicts the operating region between (14–21) cm of conical tank. It can be clearly shown that controller action for modified Smith predictor operated between (0–10) % of its whole region, whereas modified back calculation and conventional PI used its whole region, i.e., (0–100) with the band of (90–100) %.

Figure 6 shows the operating region between (21–28) cm of conical tank. Modified Smith predictor maintained its consistent controller response, whereas modified back calculation method improved its controller action with respect to operating region (14–24) cm. Performance characteristics like overshoot and rise time were better in modified back calculation than modified Smith predictor in this operating region (21–28) cm. Conventional PI is neither good in performance characteristics nor in controller action.

Figure 7 shows the response at operating region (28–33) cm. Controller action of modified Smith predictor remained with same consistency but the lags in its performance in terms of over shoot, rise time, and peak time. Whereas Modified back calculation improved action of its manipulated variable and performance
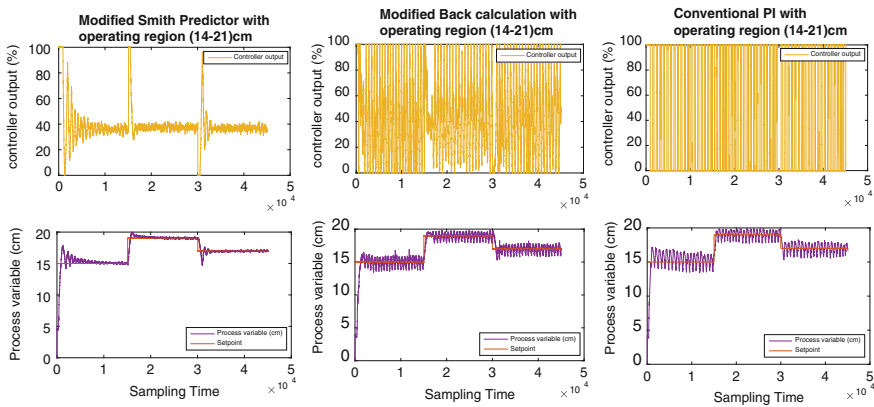
Fig. 5 Response of different methods at operating region (14–21) cm
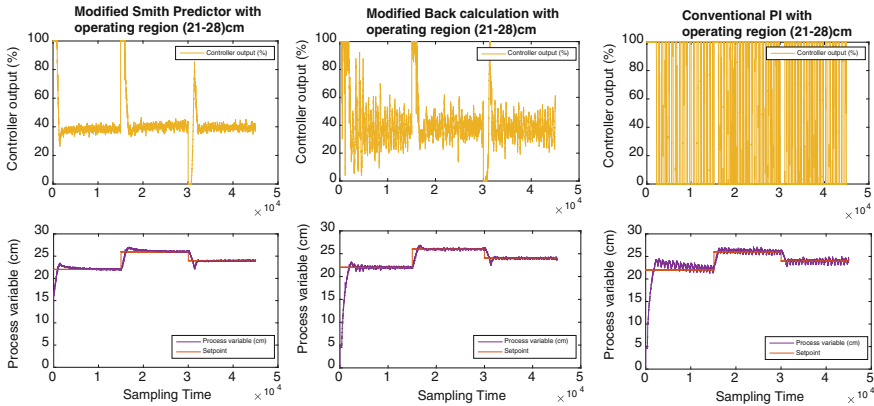
Fig. 6 Response of different methods at operating region (21–28) cm
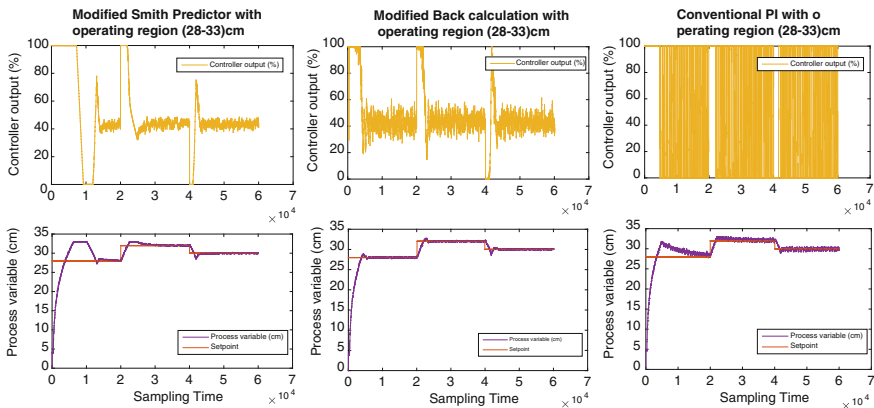
Fig. 7 Response of different methods at operating region (28–33) cm

characteristics compared with other operating regions. Conventional PI is nowhere in the picture in all attributes.

Table 1 depicts brief comparison of performance characteristics of the operating region (14–21) of all methods mentioned in this paper. Even though the model is designed at the operating region (28–33), MSP gave decent performance characteristics at operating region (14–21). Table 2 represents operating region of manipulated variable for all different methods.

The objective of the paper is to show the energy utilization of actuator for different approaches. As the analysis of controller action gives the energy consumption criteria of actuator. Therefore from Figs. 5, 6, and 7, through all operating regions, modified Smith predictor has more energy efficient than other methods in the paper.

Table 1 Performance characteristics for operating region (14–21) cm

Method	Setpoint	Peak time	Rise time	Overshoot	Settling time
Conventional PI	15	19	10	10	–
	19	40	5	3.6	–
	17	10	4	9.4	–
MBC	15	10	10	9.3	–
	19	40	5	3.94	–
	17	10	3	9.4	–
MSP	15	12.5	8	16	45
	19	10	4	4.7	16
	17	10.5	4	7.6	12

Table 2 Controller operating region for different methods

Operating region	Setpoint	Conventional PI Region	MBC Region; band (%)	MSP Region; band (%)
14–21	15	0–100	0–100	30–42
	19	0–100	5–100	32–42
	17	0–100	0–100	32–40
21–28	22	0–100	10–68	33–42
	26	0–100	15–60	34–46
	24	0–100	25–55	35–45
28–33	28	0–100	28–55	37–47
	32	0–100	30–56	38–48
	30	0–100	30–56	38–48

5 Conclusion

The whole paper is concentrated on energy efficiency of actuator through different methodologies. Windup problem is being contrary in performance and stability of FOPDT systems. The control design for such systems is challenging for control engineers. In this paper, design and performance comparison of different algorithms like modified Smith predictor, modified back calculation approach, and conventional PI control are considered at different operating regions. It is observed that modified Smith predictor algorithm operates for longer region with good controller action compared with modified back calculation method. Therefore based on actuator action, it can be justified that energy efficiency is more in modified Smith predictor with little drawback in performance characteristics compared with modified back calculation, whereas conventional PI is nowhere optimal with respect to other two methods. So, the selection of the method should be carried with respect to user requirements.

References

1. Keiji Watanabe; Masami Ito. A Process-Model Control for Linear Systems with Delay. IEEE Transactions on Automatic Control. Vol. Ac-26, No. 6, December 1981.
2. M. R. Matauiek; A. D. Micii.A Modified Smith Predictor for Controlling a Process with an Integrator and Long Dead-Time. IEEE Transactions on Automatic Control. Vol. 41, No 8, August 1996.
3. M. R. Matauiek; A. D. Micii; On the Modified Smith Predictor for Controlling a Process with an Integrator and Long Dead-Time. IEEE Transactions on Automatic Control. Vol. 44, No. 8, August 1999.
4. S. Majhi; Derek P. Atherton. A New Smith Predictor and Controller for Unstable and Integrating Processes with Time Delay. *Proceedings of the 37th IEEE Conference on Decision & Control Tampa*. Florida, USA,WPl0 16:20 December 1998.
5. SomanathMajhi; Derek P. Atherton. Obtaining controller parameters for a new Smith predictor using auto tuning. Automatica. 36, pp. 1651–1658, 2000.
6. Rakesh. M.K; Satheeshbabu. R; I. Thirunavukkarasu. Sliding Mode Control with Dead Time Compensation for a Conical Tank Level Process. International Journal of Electronics and Communication Technology. Vol.5, Issue.2, April–June 2014. P. No: 244–247.
7. Rakesh. M.K; Satheeshbabu. R; I. Thirunavukkarasu. Design and Implementation of a Two Degree of Freedom Nonlinear PID Controller for a Nonlinear Process. IOSR Journal of Electrical and Electronics Engineering. Vol.9, Issue. 3, Ver. III, May–June 2014. P. No: 59–64.
8. Gireesh N; Sreenivasulu G. Comparison of PI Controller Performances for a Conical Tank Process using different tuning methods.*International conference on advances in Electrical Engineering (ICAEE).* pp 1–4, 2014.
9. Finn Haugen. Model-based PID tuning with Skogestad's method. Modeling identification and control journal. PP 1–4. 18th october, 2009.
10. Eadala SarathYadav and Thirunavukkarasu Indiran, "Servo Mechanism Technique based Anti-Reset Windup PI Controller for Pressure Process Station" *Indian Journal of Science and Technology*, Volume 9(8), 2016.
11. K. J. Astrom; C. C. Hang; B. C. Lim. A New Smith Predictor for Controlling a Process with an Integrator and Long Dead-Time. IEEE Transactions. On Automatic Control, Vol. 39, NO. 2. February 1994.
12. Antonio Visioli. *Practical PID Control.* British Library Cataloguing in Publication Data: ISBN-13: 9781846285851 ISBN-10: 1846285852, Springer-Verlag London Limited 2006.

A Study on Effect of Piston Bowl Shape on Engine Performance and Emission Characteristics of a Diesel Engine

K. Sakthisaravanasenthil, S. Senthilkumar and G. Sivakumar

Abstract This paper presents a study on the effect of re-entrant piston bowl configuration on the emissions characteristics and engine performances of a direct injection (DI) diesel engine. In order to meet the emission norms, modern-day diesel engines rely on methods of in-cylinder emission reduction and expensive after treatment device. By using an effective piston bowl shape, one can reduce the in-cylinder emission and the cost increased for the after-treatment device with considerable increase in the engine lifetime. Six piston bowl shapes with various geometric configurations were selected for numerical simulations. Three-dimensional models of the piston bowl shapes and the combustion chamber were created using Pro-E and mesh was generated by using preprocessor ANSYS ICEM CFD. The flow characteristics inside the cylinder with these piston bowls were investigated under steady condition with the RNG k-ε turbulent model using ANSYS Fluent. Numerical simulations under isothermal condition were carried out to select an optimum bowl shape. The mass flow boundary condition was used for inlet manifold and the value of this was measured from the experimental test. The CFD results of mean swirl velocity of the engine at different locations inside the combustion chamber were calculated. From the computational results, it was found that the average swirl number is increased from 0.87 (base shape) to 1.74 (modified bowl shape). It is well known that the swirl number is very important to enhance the homogeneity of air/fuel mixture inside the combustion chamber, which in turn improves the combustion efficiency. The experimental results shows that, as compared to the baseline engine 20 % reduced in hydrocarbons (HC) emissions and 24 % reduced in carbon monoxide (CO) for the engine with modified piston bowl shape. However, there is a small amount of reduction in engine performance. It is observed that the brake specific fuel consumption (BSFC) reduced significantly for all load conditions.

Keywords Piston bowl shape · Numerical simulations · Diesel engine · Swirl number

K. Sakthisaravanasenthil · S. Senthilkumar (✉) · G. Sivakumar
School of Mechanical and Construction Engineering, Vel Tech University,
Chennai 600062, India
e-mail: s.senthilms@gmail.com

1 Introduction

DI diesel engines are used for various automotive and power appliances, because of higher thermal efficiency. In compression ignition engine, the air/fuel charges are in different phases. The air is in gases phase and the fuel in liquid phase, so the atomization of the two different phases without any external force is not possible. So the high injection pressure is required to inject the fuel at the end of compression stroke. Ignition delay period of compression ignition (CI) is shorter, so in the meantime, the air/fuel atomization is not uniform [1]. Because of, exhaust emissions in the CI engines is high as compare to other engines. To obtain a better combustion is to optimizing the piston bowl geometry and the fuel system [2]. Due to stringent emissions norms on diesel engine, it is necessary for further optimization in engine combustion chamber to reduce the emissions as well as increase the overall performance of the engines.

In-cylinder air flow motion in the DI diesel engine is generally the turbulence characteristics. It is used to mix the air/fuel mixture in the combustion chamber. Normally swirl generation techniques in diesel engine is obtained from various intake port design like helical shaped intake port, spiral-shaped intake port. But the difficult in the techniques is, design and optimization of the intake ports are very complicated, and also the swirling motion should be maintained till at the end of the combustion. For sustaining the swirling motion in the combustion chamber until the combustion process, one of best way is to modify the piston bowl shape design to maintain the swirl motion in the combustion chamber till the combustion [2].

For the better engine performance and emission characteristics, swirl plays a vital role [3]. Because of interaction between swirl and fuel, the combustion process is proper/complete. Then it reduces the delay period, to achieve faster combustion. Incomplete combustion of air/fuel charge is mainly responsible for HC and PM emissions; the major part of the fuel impinges on the cavity walls. The combustion chamber wall temperature is the main cause of unburnt HC and soots emissions [4]. Currently, the combustion chambers are re-entrant piston bowl shape which is widely used in high speed diesel engines. The re-entrant combustion chamber shows its affects on the fuel distribution and air/fuel mixing, and also the intensification of a swirl and turbulence are high [5], the effects of re-entrant lip shapes and toroidal radius will leads to better performance [6]. By modifying the piston bowl shape, the engine performance and reduce emission characteristics in DI diesel engine. From the literature review, it was found that, by modifying the piston bowl shape is directly affect the emission characteristic and engine performance [7–10].

The present research is to investigate the effect of different piston bowl geometry on the in-cylinder air flow motion and experimental research on the entire emissions characteristics. The different types of piston bowl geometry were selected for the numerical simulations to perform the air flow motion study. Based on the numerical simulation results, the piston bowl geometry is finalized and it is experimentally tested. The test result showed in the new piston bowl design shows good results in engine exhaust emissions.

2 Numerical Methodology

The numerical simulation methods are the predominated technique to optimizing the DI diesel engine combustion process, and also optimizing various parameters in the engine [10]. In this study, effects of piston bowl shape were tested with different configuration, for the better turbulence reaction in the combustion chamber. The piston bowl shape models are shown in the Table 1 and Fig. 2 shows the parameters which are listed in Table 1. Piston bowls were modelled by using Pro-E and 3D tetrahedral type mesh was generated by using preprocessor ANSYS ICEM CFD as shown in Fig. 1.

Numerical simulations isothermal conditions have been carried out for this engine with different configuration piston bowl shapes. Simulations were performed under full lift inlet valve condition and exhaust valve at closed condition. Mass flow inlet boundary condition at the inlet face of the model. The mass flow rate is calculated experimentally by using U-tube manometer, and no-slip boundary conditions are specified at walls. Pressure velocity coupling was done using SIMPLE pressure correction method. Unsteady computational are performed by an implicit time discretization within the domain using incompressible RNG k-ε turbulence model with swirl enhancement available with ANSYS FLUENT software. The convergence criterion value used is 10^{-6} for all the simulations.

Table 1 Piston bowl shapes
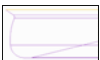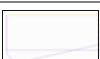
Chamber geometry	Toroidal radius (R_t) (mm)	Maximum bowl diameter (D) (mm)	Volume (mm^3)
Base model	4	62	46229.1
Model-1	4	67.5	51664.6
Model-2	5	63.1	47410.5
Model-3	6	65	48912.4
Model-4	7	67	50922.5
Model-5	4	62	46859.2
Model-6	7	72	67475.7

Fig. 1 Mesh for
computational model
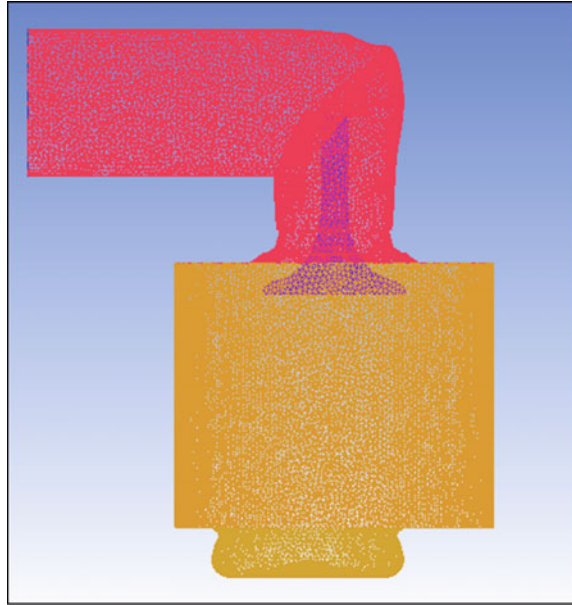
Fig. 2 Schematic diagram of
Piston bowl shape
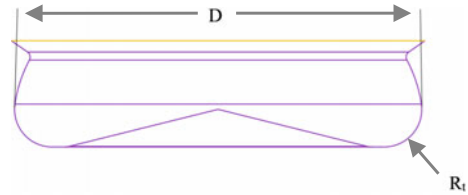
3 Numerical Results

Numerical simulations were performed for the suction stroke with full valve lift
condition for six different piston bowl shapes. Figure 3 shows the variations of
average swirl number with respect to the stroke length for base piston bowl shape
and modified piston bowl shape. From the computational results, the average swirl
numbers are calculated at different stroke lengths (say 10, 20, 30, 40, 50, 60, 70, 80
and 90 mm, from TDC) from the average results the model-5 has the high swirl
number compared to base line and other models. The contours of turbulent intensity
of the base piston bowl and model-5 bowl shapes are presented in Figs. 4 and 5,
respectively. Both figures are cut section view with respect to the piston bowl axis;
the piston bowl axis is offset from the axis of the cylinder.

The turbulent intensity distribution in the model-5 is higher than that of the base
model and also it spreads almost uniformly from the top dead centre (TDC) to

Fig. 3 Variations of averaged swirl number with respect to the stroke length for base piston bowl shape and modified piston bowl shape
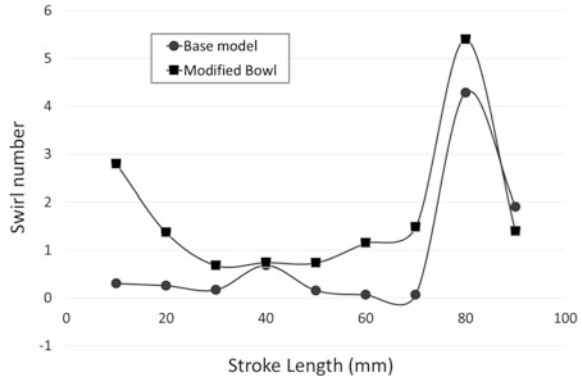
Fig. 4 Contours of turbulent intensity values at centre plane for Base model

Contours of Turbulent Intensity (%) (Time=1.8800e-02)
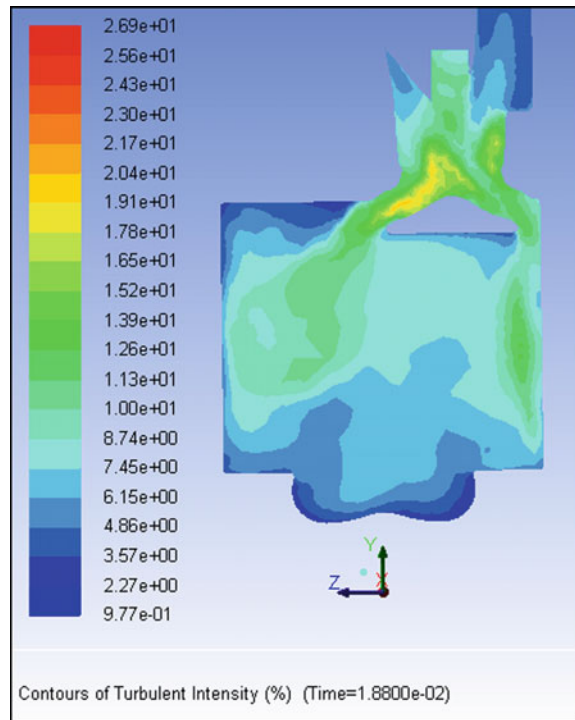
bottom dead centre (BDC) region in the model-5. But in the base model the turbulence intensity is not uniform from TDC to BDC region. It is known that the turbulence will improve the air fuel mixing in the combustion chamber. So it was realized the model-5 geometry will increase the air/fuel mixing in the combustion chamber, which, in turn, will lead to better combustion and consequently improve the emission characteristics.

Fig. 5 Contours of turbulent intensity values at centre plane for piston bowl model-5
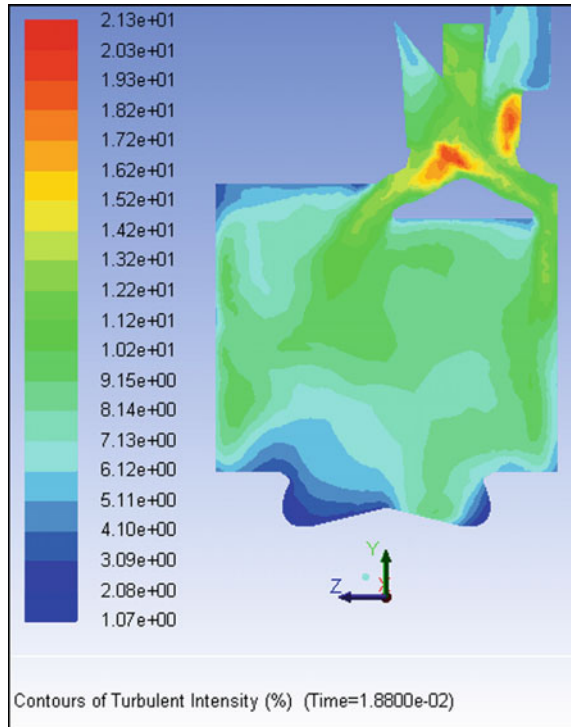
Table 2 Engine specifications

Bore and stroke	108 and 120 mm
Rated power	50 HP @ 2150 rpm
Rated torque	180 Nm @ 1200 rpm
Compression ratio	18.5:1
Connecting rod length	208 mm
Crank radius	60 mm
Capacity	3.3 L
Aspiration	Natural
Type of injection	Direct injection
Type of operation	Four stroke
Maximum inlet valve lift	10.52 mm

4 Experimental Setup and Procedure

The engine has three cylinders DI diesel engines with the specifications are shown in the Table 2. The compression ratio was reduced 5.5 % from the base engine model. From the computational results, the piston bowl shape with an average swirl number of 1.74 is used for study. There is no modification in the fuel injection system, i.e., plunger operated unit injection system with one intake valve and one exhaust valve.

The tests are carried out to study the effect of Piston bowl shape on engine performance and emission characteristics under various load and speed conditions. Schematic of experimental setup is shown in Fig. 6. The experiments were conducted at five load levels, viz. 0, 25, 50, 75 % of full load and full load using Eddy current dynamometer at five different speeds 1200, 1400, 1600, 1800, 2000 RPM. These speeds are set by using Throttle controller which is integrated in data acquisition system. Using manometer setup the air flow was measured, for calculating the fuel consumption SAJ fuel consumption metre was used. For measuring the pressure and temperature, sensors are mounted at different locations in the engine (exhaust pipe, water inlet, water outlet, air intake, lube oil) and those sensors are connected through a Data Acquisition system. Emission characteristics like carbon monoxide (CO), hydro carbon (HC) and carbon dioxide (CO_2) were measured by using AVL Di-gas 444 Gas analyzer based on "ISO 8178-4 "C1" 8 Mode analysis for off road vehicles" all the readings were carried out using ARAI–EDACS controller setup and the readings were stored in a personal computer automatically.

Fig. 6 a Snapshot of experimental setup.*1*. Manometer, *2*. Diesel Engine, *3*. Dynamometer, b layout of experimental system, *1*. Engine, *2*. Dynamometer, *3*. Fuel tank, *4*. Fuel filtre, *5*. Water tank, *6*. Water Filtre, *7*. Manometer setup, *8*. Air filtre, *9*. AVL Di-Gas 444 gas analyzer, *10*. Sensor junction box, *11*. ARAI EDACS Dyno controller, Throttle controller and Monitor setup
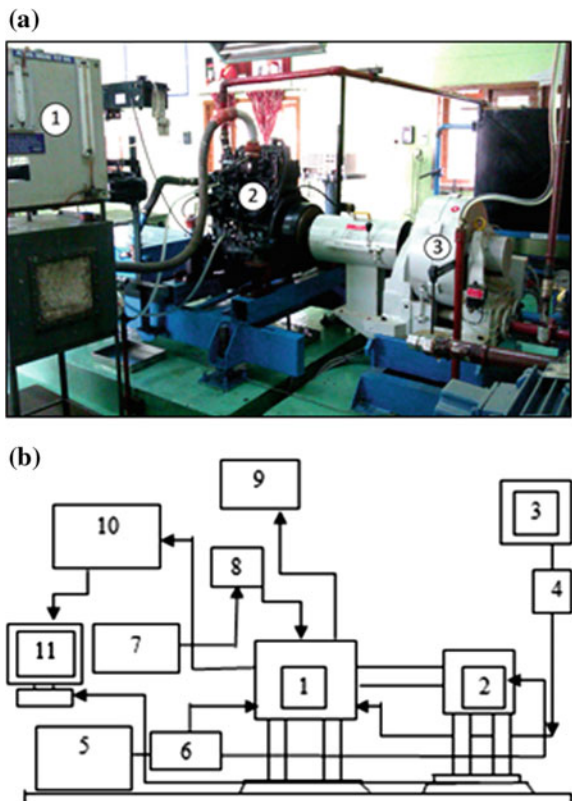
5   Results and Disscusion

The engine performance of the base model and the model-5 are tested in five
different speeds in full load conditions. The Fig. 7a, b shows effect of engine torque
and power with respect to engine speeds. It can be seen that there is no major
different in the engine performance curves like power and torque. Figure 7c shows
BSFC with respect to engine speed. The curve slightly increased in the speeds of
1600, 1800 and 2000 rpm. Hence in those conditions BSFC is increased due to
slight decrease in power.

Figure 7d shows the effect of brake mean effective pressure (BMEP) Versus
brake-specific fuel consumption in full load conditions with base piston bowl and
modified piston bowl shapes. The BSFC is increased in the modified piston bowl
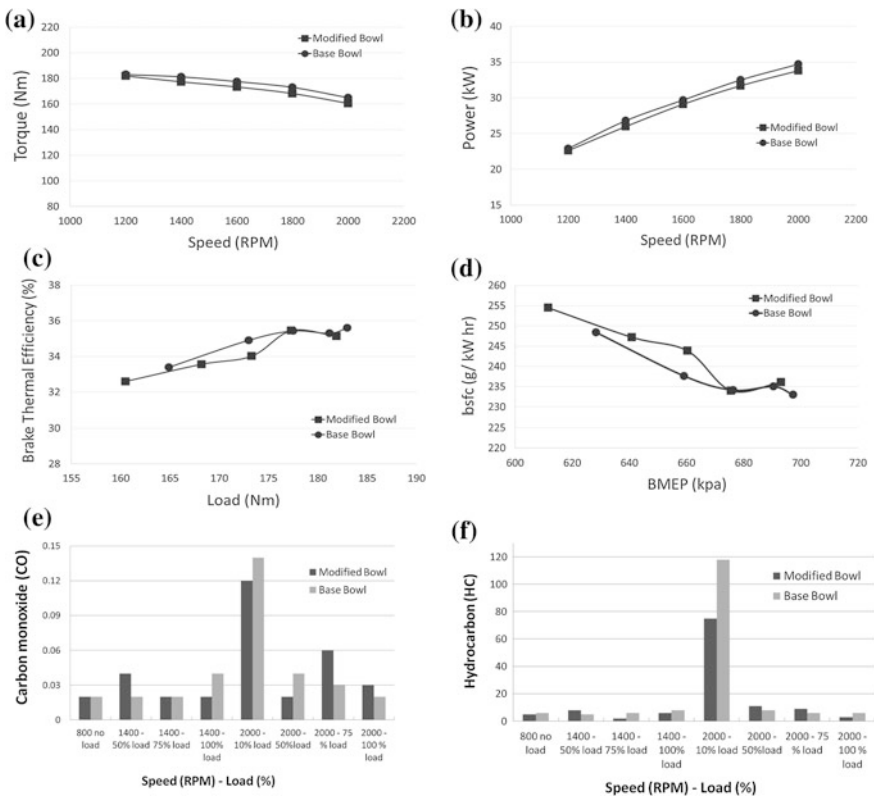
Fig. 7 a Effect of engine torque versus engine speed. **b** Effect of engine power versus engine
speed. **c** Effect of brake thermal efficiency versus engine torque. **d** Effect of brake specific fuel
consumption Versus brake bean effective pressure. **e** Variation in engine carbon monoxide
(CO) emission characteristics of base bowl and modified bowl under ISO 8178-4 "C1" 8 Mode
analysis for off road vehicles. **f** shows the variation in engine hydrocarbon (HC) emission
characteristics of base bowl and modified bowl as per ISO 8178-4 "C1" 8 Mode analysis for off
road vehicles

shape. It is due to the fact that air fuel mixing is completely burn in the time of combustion which results in better combustion so the pressure of the air fuel charge is increased. Hence the amount the useful power generation is improved.

Emission characteristics of the base model and the modified piston bowl are tested as per ISO 8178-4 "C1" 8 Mode analysis for off road vehicles. Figure 7e shows that the carbon monoxide emission level decreases in all the speed levels as compared to base piston bowl model. This may be attributed by the fact that the modified bowl enhances swirl inside the engine cylinder which helps better combustion engine performance [7–10]. For the two combinations of speed and load conditions, as compared to the baseline engine, 1400 rpm and 50 % load, and 2000 rpm and 75 % load, the CO increases slightly.

Figure 7f shows that the unburned hydrocarbon (HC) is plotted with respect to different load in different engine speeds. The HC formations are mainly due to unburned hydrocarbon present in the exhaust gas. These are due to non-uniform mixing of air fuel in the combustion chamber. The modified piston bowl shapes have high turbulence intensity (Fig. 5), in the time of injection it creates proper mixing of air/fuel. The results show that, compared to the baseline engine 20 % reduced in the HC emission.

4 Conclusion

The numerical simulations for different piston bowl shapes are carried out to reduce the emission characteristics, in order to the meet the emissions norms for future trends. It was found that the optimization of piston bowl shapes shows a reduction in emissions levels and slightly reduction in torque, and the BSFC is increased by 5 % compared to baseline engine, the experimental results show that, 20 % reduction in HC and 18 % reduction in CO emissions.

References

1. V. Ganesan, "Internal Combustion Engines" Tata McGraw-Hill publishing, 2012.
2. Lu Lin, DuanShulin, Xiao Jin, Wu Jinxiang and GaoXiaohong "Effects of Combustion Chamber Geometry on In-Cylinder Air Motion and Performance in DI Diesel Engine" Paper no: 2000-01-0510, SAE, 2000.
3. Heywood J.B. "Internal Combustion Engine Fundamental" McGraw-Hill International Editions, New York, 1988.
4. Rahman M. Montajir, H. Tsunemoto and H. Ishitani "Fuel Spray Behaviour in a Small DI Diesel Engine: Effect of Combustion Chamber Geometry" Paper no: 2000-01-0946, SAE, 2000.

5. B.V.V.S.U. Prasad, C.S. Sharma, T.N.C. Anand, R.V. Ravikrishna "High swirl-inducing piston bowls in small diesel engines for emission reduction" Paper no:88 (2011) 2355–2367, Applied Energy, 2011.
6. Y. Zhu, H. Zhao, D. A. Melas and N. Ladommatos "Computational Study of the Effects of the Re-entrant Lip Shape and Toroidal Radii of Piston Bowl on a HSDI Diesel Engine's Performance and Emissions" Paper no: 2004-01-0118, SAE, 2004.
7. Caroline L. Genzale and Rolf D. Reitz "A Computational investigation into the effects of Spary Targeting, Bowl Geometry and Swirl Ratio for Low-Temperature combustion in Heavy-Duty Diesel Engine" Paper No: 2007-01-0119, SAE, 2007.
8. Shabbir Sheikh, Nitin Gokhale and Vishal Thatte "Efficient Approach for Optimization of Piston Bowl Shape, Compression Ratio and EGR for DI Diesel Engine" Paper No: 2011-24-0013, SAE, 2011.
9. Arturo de Risi, Teresa Donateo and Domenico Laforgia "Optimization of the Combustion Chamber of Direct Injection Diesel Engines" Paper No: 2003-01-1064, SAE, 2003.
10. Jaeman Lim and Kyoungdoug Min "The Effects of Spray Angle and Piston Bowl Shape on Diesel Engine Soot Emissions Using 3-D CFD Simulation" Paper no: 2005-01-2117, SAE, 2005.

Investigation of a Novel Turboprop-Driven Aircraft Concept Including Future Technologies

Andreas Johanning and Dieter Scholz

Abstract This paper presents a novel concept for a highly efficient and ecological propeller-driven aircraft. The aircraft has a high wing, T-tail, and two turboprop engines with large propeller diameters decreasing disc loading and therefore increasing propeller efficiency. The aircraft also features a strut-braced wing with natural laminar flow. It is shown that direct operating costs can potentially be reduced by about 17 % while reducing trip fuel mass and therefore CO_2 emissions by about 36 % compared to the reference aircraft Airbus A320.

Keywords Turboprop aircraft · Conceptual aircraft design · Aircraft design optimization · Strut-braced wing · Natural laminar flow

1 Introduction

1.1 Motivation

The protection of the environment gets increased importance in civil aviation (e.g., [1]). Emission reductions can be achieved by reducing fuel consumption because the amount of the major part of emissions is proportional to the amount of burned fuel. Reduced fuel consumption could be achieved by new promising aircraft concepts. The design of these concepts has been one of the tasks of the research project "Airport2030" [2]. This paper presents one of the aircraft concepts designed within the research project. The presented research has been conducted together with the project partner Airbus.

Nowadays, mainly turbofan-driven aircraft is used in the medium range aircraft market. In the future, Turboprop-driven Aircraft (TA) could be an interesting alternative in that market because of their lower fuel consumption. The Thrust

A. Johanning · D. Scholz (✉)
Department of Automotive and Aeronautical Engineering,
Hamburg University of Applied Sciences, Hamburg, Germany
e-mail: info@profscholz.de

Specific Fuel Consumption (TSFC) of TA is 10 … 30 % lower than that of comparable turbojet or turbofan aircraft [3].

However, a disadvantage of TA is that they are usually operated at lower cruise Mach numbers than turbofan aircraft resulting in a lower number of flights in a certain period. Additionally, TA comes along with higher cabin noise levels than turbofan aircraft requiring more soundproofing material and therefore additional mass.

This paper investigates if a novel TA design incorporating the future technologies natural laminar flow (NLF) and strut-braced wing (SBW) could lead to reduced DOC and emissions compared to the medium range aircraft Airbus A320.

1.2 Concept for the Novel Turboprop Aircraft

As already stated, TA usually have lower optimum cruise speeds than turbofan aircraft resulting in longer flight times and possibly a lower number of flights per day. The lower number of flights leads to lower productivity and hereby higher seat mile costs. The proposed TA concept counteracts the disadvantage of the lower optimum Mach number by a lower cruise altitude:

By reducing the cruise altitude of the TA compared to that of the turbofan aircraft, the percentage difference between the cruise speeds will become smaller than the percentage difference of the Mach numbers. This fact is illustrated in Fig. 1 showing that an aircraft flying at an altitude of 6140 m at a feasible turboprop cruise Mach number of 0.71 (the cruise Mach number range of the military transporter
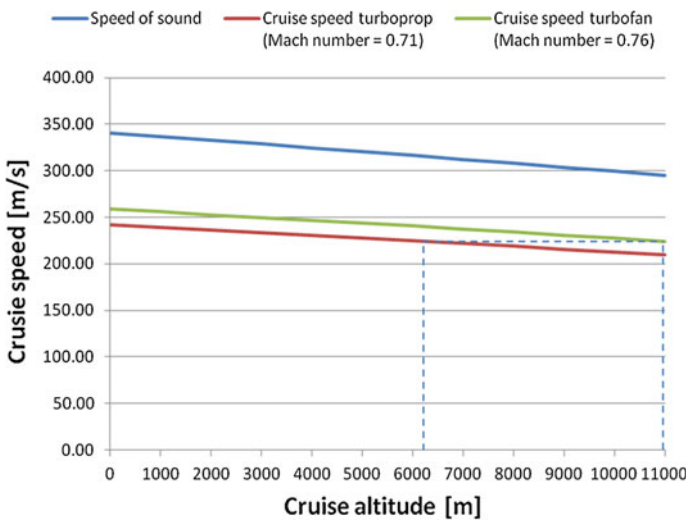
Fig. 1 Reducing the cruise altitude for a given Mach number leads to higher cruise speeds

Airbus A400 M is 0.68 … 0.72 [4]) would have the same cruise speed as an aircraft flying at 11,000 m or above with a cruise Mach number of 0.76.

After optimization for minimum DOC, the cruise Mach number of the proposed TA and the difference in cruise altitude came out lower than in the previous example but the positive effect stays the same. The later described that optimum TA design has an initial cruise altitude of about 7000 m compared to the initial cruise altitude of the redesigned reference aircraft (introduced in Sect. 1.3) which is around 11,800 m. The optimum cruise Mach number of the TA is 0.51 which is around 33 % lower than the cruise Mach number of the reference aircraft. Due to the described positive effect of a lower cruise altitude, the actual cruise speed of the TA is only 29 % lower than that of the reference aircraft.

A drawback of the reduction of cruise altitude is that aircraft are exposed to higher gust speeds and therefore higher gust load factors. An increased wing loading could counteract that effect and keep gust load factors at the same level [5]. However, the dimensioning requirement of the maximum allowable landing field length leads to a wing loading that is not higher than that of the reference aircraft. As a consequence, the load variation due to gusts of the TA is about 36 % higher than that of the reference aircraft.

An investigation of the importance of several aircraft parameters for the evaluation of an aircraft design in [6] shows that the absolute weighting of the variation of gust loads for the evaluation of an aircraft design is 1.1 %. Due to the low weighting leading to a low importance of that parameter for overall aircraft design, the increase in load variation of the TA has been accepted.

Another effect counteracting the disadvantage of the lower optimum Mach number is the limitation of the indicated air speed below FL 100–250 knots. Due to this limitation, TA does not loose time during about 20 min of flight shortly after take-off and before landing under FL 100. During taxiing, there is no time difference between TA and turbofan aircraft anyway. Due to these two reasons, the block time of the TA on a 755 NM trip (which is used for the DOC calculation and optimization) is only 21 % higher than that of the reference aircraft.

In the flight envelope, the concept of the low-flying TA could be placed close to the intersection of the limit defined by maximum operating Mach number and maximum dynamic pressure (in the so called "speed corner") [5].

Indeed, due to the lower cruise speed of the TA, the limit due to dynamic pressure could be reduced to a lower equivalent airspeed so that the operating point of the TA lies close to the speed corner (as illustrated in Fig. 2). In comparison to the reference aircraft, the decrease of the limit due to dynamic pressure could potentially lead to a lighter cabin. However, this effect was outside the scope of this paper.

Development costs for the proposed TA could be kept at an acceptable level, as it is a conventional configuration with only an unconventional set of design parameters. It can be integrated easily into the existing aviation system because existing processes for manufacturing and operation of aircraft would not have to be adapted [5].

Fig. 2 Flight envelope of the TA
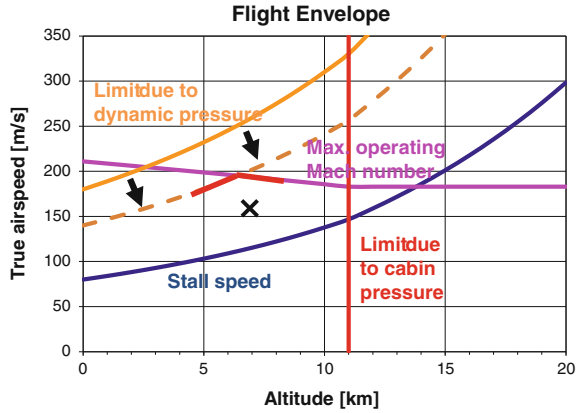
1.3 Reference Aircraft and Reference Mission

The reference aircraft for evaluating the performance of the TA design is the weight variant WV000 of the Airbus A320−200 with CFM56−5A engines [7]. Key parameters of the selected weight variant are listed in Table 1.

The proposed TA has the same requirements as the reference aircraft except for a lower cruise Mach number to take account of the speed limitations of TA.

1.4 Literature Review

There has been a lot of research about TA design. In the scope of the literature review of this paper, only few examples can be mentioned:

Xie researched about conceptual TA design in general. However, the research did not have the objective to design a potential candidate for the next medium-range aircraft generation and future technologies like NLF or SBW have not been integrated into the designs either [8].

The "Citizen Friendly Airplane" is the subject of another research project which is based on a TA concept. However, the requirements for that TA drastically differ from those presented here. For instance, short take-off and landing capabilities are

Table 1 Key parameters of the selected A320−200 weight variant from [7]

Parameter	A320
m_{MTO} (kg)	73,500
m_{OE} (kg)	41,244
m_{MPL} (kg)	19,256
R_{MPL} (NM)	1510
n_{PAX} (1-cl HD) (–)	180
M_{CR} (–)	0.76

required. Additionally, no publication describing the design of the citizen friendly airplane could be identified yet [9].

Geraldo et al. also published about the design of a TA. However, their aircraft is designed for 90 passengers so that the requirements again differ from those in this paper [10].

The "Boeing Subsonic Ultra Green Aircraft Research" team evaluated several future aircraft concepts in a NASA research project. Amongst others, a turboprop-driven aircraft with SBW and NLF has been evaluated. However, research mainly concentrated on turbofan engines with very high bypass ratios and on several other future technologies so that TAs only played a minor role [11].

Summarized, the literature review shows that there is an ongoing interest in TA. However, only [11] could be identified also integrating the future technologies NLF and SBW into the design. Additionally, most of the described research approaches have other design requirements and none of them discusses TA as potential candidate for the next generation of medium-range aircraft which represents the motivation for the research presented here.

The outline of the paper is as follows. Section 2 presents the methodology used for the design of the novel TA concept. Section 3 presents the results of the design process and compares the DOC of the TA with the DOC of the reference aircraft. In Sect. 4, the design results are discussed while Sect. 5 concludes the paper.

2 Methods

For the conceptual design of the proposed TA, the tool "Turboprop Optimization in Preliminary Aircraft Design" (PrOPerA) has been used. PrOPerA is a further development of the tool "Optimization in Preliminary Aircraft Design" (OPerA) developed by Niță [11]. OPerA has been developed for the preliminary design of turbofan aircraft while PrOPerA can additionally be used for the preliminary design of turboprop driven aircraft.

The structure of PrOPerA is illustrated in Fig. 3. In an inner optimization loop, a consistent aircraft is designed based on a set of aircraft parameters and requirements. Thrust-to-weight ratio and wing loading are optimized according to the selected optimization objective.

In an outer optimization loop, all aircraft parameters and requirements can be varied to find an optimum aircraft for the selected optimization objective. The outer optimization is performed using PrOPerA together with the optimization software "Optimus" from "Noesis Solutions."

In PrOPerA, each TA is designed together with an optimum propeller according to the particular requirements of the aircraft using the method proposed by Adkins and Liebeck [12].

Important engine parameters are calculated using empirical equations derived from the turboprop engine database of Roux [13].
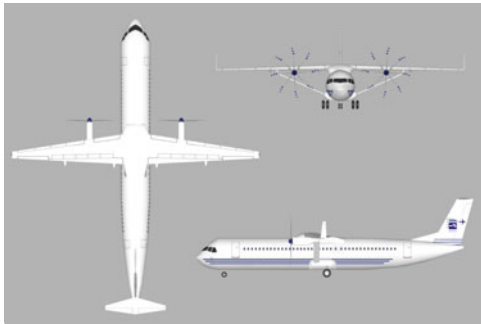
Fig. 3 Structure of PrOPerA
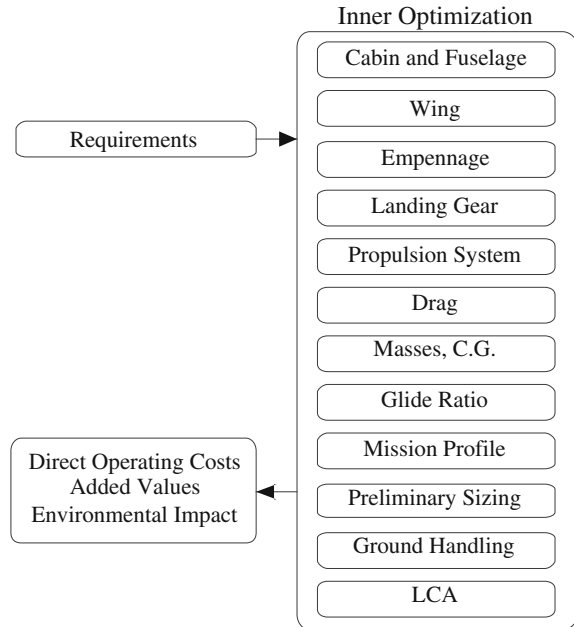
To consider the drawbacks of high propeller diameters with regard to landing gear length and mass, the landing gear is sized according to the requirements from tail strike angle, bank angle clearance, engine ground clearance, and longitudinal, as well as lateral tip stability [5].

The calculation of the power-to-weight ratio and wing loading due to take-off and landing field length requirements and the assumption for the maximum lift coefficients at take-off and landing are based on a statistical analysis of existing TA [5].

The final TA design presented in Sect. 3 is the result of an optimization for minimum DOC. To optimize the aircraft for minimum DOC, an evolutionary algorithm with a population size of 35 and 60 generations is used. For all DOC calculations, the DOC method proposed by the Association of European Airlines [14] is used. The designs have been evaluated for an entry into service in 2030 when the next generation of medium range aircraft might be introduced. For that year, an inflation-adjusted fuel price of 1.44 USD/kg has been assumed based on a forecast presented in [15]. The reference aircraft has been evaluated with the same fuel price to have a fair comparison in the year 2030.

For the integration of the future technology "Natural Laminar Flow" (NLF), a Reynolds number for the transition from laminar to turbulent flow is calculated depending on the sweep angle of the leading edge of the wing to determine the wing fraction with laminar flow. An upper limit of 50 % laminar flow is set. It is assumed that there are no negative side effects from using a laminar flow wing profile.
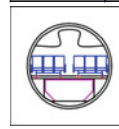
For the integration of the future technology "Strut Braced Wing (SBW)," the strut chord has been set to 30 % of the wing mean aerodynamic chord according to a statistical evaluation of strut-braced wing aircraft. The strut is attached to the wing at 50 % of the wing span (illustrated in Fig. 4). The variation of the wing mass

Parameter	Value	Deviation from A320*
Main aircraft parameters		
m_{MTO}	56000 kg	− 24 %
m_{OE}	28300 kg	− 31 %
m_F	8400 kg	− 35 %
S_W	95 m²	− 22 %
$b_{W,geo}$	36.0 m	+ 6 %
$A_{W,eff}$	14.9	+ 57 %
E_{max}	18.9	≈ + 7 %
P_eq,ssl	5000 kW	—
d_prop	7 m	—
η_prop	89 %	—
PSFC	5.86E-8 kg/W/s	—
h_{ICA}	23000 ft	− 42 %
s_{TOFL}	1770 m	0 %
s_{LFL}	1300 m	− 10 %
t_{TA}	32 min	0 %

Parameter	Value	Deviation from A320*
Requirements		
m_{MPL}	19256 kg	0 %
R_{MPL}	1510 NM	0 %
M_{CR}	0.51	− 33 %
$\max(s_{TOFL}, s_{LFL})$	1770 m	0 %
n_{PAX} (1-cl HD)	180	0 %
m_{PAX}	93 kg	0 %
SP	29 in	+ 0 %

Parameter	Value	Deviation from A320*
DOC mission requirements		
R_{DOC}	755 NM	0 %
$m_{PL,DOC}$	19256 kg	0 %
EIS	2030	—
c_{fuel}	1.44 USD/kg	0 %
Results		
$m_{F,trip}$	3700 kg	− 36 %
$U_{a,f}$	3060 h	0 %
DOC (AEA)	83 %	− 17 %

Operating empty mass breakdown

Wing 13%, Struts 1.4%, Fuselage 25%, Horizontal tail 1.0%, Vertical tail 1.7%, Engines 18%, Landing gear 6%, Systems 26%, Operator's items 7%, Soundpr. material 1.4%

Component drag breakdown

Wing 23%, Struts 9%, Fuselage 48%, Horizontal tail 6%, Vertical tail 8%, Engines 5%

Direct operating cost breakdown

Depreciation 14%, Interest 11%, Insurance 1%, Fuel 27%, Maintenance 6%, Crew 16%, Fees 24%

Fig. 4 TA design results

reduction depending on the position of the strut connection point is derived from [16]. The maximum wing mass reduction is set to 30 % as suggested by Torenbeek [17]. Only high wing configurations have been considered.

3 Results

In this section, the results of the TA design will be described. First, single design parameters have been varied to better understand the design decisions of the optimizer and to analyze their influence on the design. In the following first sub-section, some of these single parameter variations will be presented. In the second subsection, the optimization results of different optimized aircraft configurations will be compared to each other and a configuration will be selected. In the third subsection, the final TA design is presented.

3.1 Single Parameter Variations

For several design parameters, the single parameter variations showed that there was no need to consider them in the following design optimization because minimum DOC was always found at the lower or upper border:

The optimum wing taper ratio λ for minimum DOC has always been at the lower border. The advantage of a lighter wing at lower λ always overcompensated the disadvantage of a sometimes lower glide ratio due to a not optimum lift distribution over the wing. Later, during optimization, λ has therefore been set to 0.2 because this is the suggested minimum allowable λ according to [18].

For minimum DOC, the take-off field length and the maximum lift coefficient at take-off always went to the upper border because this offered minimum power-to-weight ratio P/W which is off course advantageous for the aircraft design. The maximum lift coefficient for landing also always went to the upper border because this offered maximum wing loading which is also advantageous for the design. These parameters have been set to the values of the reference aircraft to enable a fair comparison.

As expected, the cabin parameters seat pitch, seat width and aisle width always went to their lower border so that there was no need to include them in the later optimization either. For this reason, the cabin parameters have also been set to the values of the reference aircraft.

The following seven design parameters did not show such a definite trend and have therefore been included in the design optimization:

Cruise Mach number M_{CR}, propeller diameter d_{prop}, wing sweep at 25 % chord φ_{25}, effective wing aspect ratio $A_{W,eff}$, wing thickness ratio t/c, landing field length s_{LFL}, and ratio of maximum landing mass to maximum take-off mass m_{ML}/m_{MTO}. In the next paragraphs, the main advantages and disadvantages identified during the

single parameter variations will shortly be discussed for a better understanding of the design results

- The higher M_{CR}, the higher the number of flights and therefore transported payload in a certain timeframe lowering the DOC. But a higher M_{CR} also requires a higher P/W and at high M_{CR}, the propeller efficiency starts to decline impairing the DOC. During the common variation of all design parameters, an optimum compromise was found at an M_{CR} of about 0.51.
- The higher d_{prop}, the higher the propeller efficiency decreasing required fuel mass and improving DOC. But high d_{prop} also requires high landing gear length and therefore mass to ensure sufficient propeller ground clearance. An optimum compromise was found at a d_{prop} of about 7 m.
- The lower φ_{25}, the lower the wing mass. For aircraft flying at high Mach numbers, increasing φ_{25} helps to reduce wave drag. However, the optimum M_{CR} of the TA is relatively low so that wave drag does not play an important role. Nevertheless, a certain φ_{25} together with the fixed taper ratio of 0.2 leads to an optimum lift distribution over the wing. An optimum compromise was found at a φ_{25} of about 6°.
- The higher A, the higher the glide ratio leading to lower fuel consumption. But the higher A, the higher the wing mass increasing fuel consumption and impairing the DOC. An optimum compromise was found at an A of about 14.9.
- The higher t/c, the lower the wing mass. But the higher t/c, the lower the critical Mach number of the wing and therefore the higher the wave drag at a certain Mach number. Due to the low optimum Mach number of the TA, the optimum t/c was expected to be a bit higher than that of the reference aircraft. During the common variation of all design parameters, this expectation has been fulfilled because an optimum compromise was found at a t/c of about 0.13.

3.2 Choosing the Optimum TA Configuration

After an isolated variation of these parameters, all parameters have been varied together until a parameter combination with minimum DOC has been found. To be able to compare different design configurations to each other and to identify the best TA configuration, different TA configurations have been optimized separately:

TA with two or four engines, conventional tail or T-tail and low wing or high wing have been designed. Altogether this leads to eight possible TA configurations.

Table 2 contains an overview about the design results. The DOC of different TA configurations are compared to the DOC of the reference aircraft. A TA with a high-wing, T-tail, and two engines offers the highest DOC improvements. The DOC of this aircraft are 13.6 % lower than those of the reference aircraft.

Future technologies have been integrated in the design and their potential has been quantified to further increase the possible DOC savings.

Table 2 Comparison of the DOC of different TA configurations with the DOC of the reference aircraft

Smart turboprop	Number of engines			
	2	4	2	4
	T-tail		Conventional tail	
High wing (%)	−13.6	−11.4	−13.3	−11.1
Low wing (%)	−12.4	−11.5	−12.9	−11.1

In a first step, the future technology "Natural Laminar Flow" (NLF) has been integrated into the design. Table 3 compares the DOC of the TA with NLF to those of the reference aircraft. The results show that the integration of NLF offers additional DOC improvements of 2.6 … 3.5 % points depending on the chosen configuration.

In a second step, a strut-braced wing (SBW) has been integrated into the design. Table 4 presents the DOC improvements compared to the reference aircraft. The results show that the integration of a SBW offers additional DOC improvements of 0.4 … 0.9 % points.

Finally, the technologies NLF and SBW have together been integrated in the TA design. Table 5 shows that together, both technologies lead to an improvement of 2.9 … 3.5 % points compared to the TA without future technologies. Altogether, the optimum TA offers a possible saving of 17.1 % compared to the DOC of the reference aircraft.

Table 3 Comparison of the DOC of different TA configurations (including the technology NLF) with the DOC of the reference aircraft

Smart turboprop + NLF	Number of engines			
	2	4	2	4
	T-tail		Conventional tail	
High wing (%)	−16.2	−14.1	−15.9	−13.7
Low wing (%)	−15.9	−14.2	−15.3	−13.7

Table 4 Comparison of the DOC of different TA configurations (including the technology SBW) with the DOC of the reference aircraft

Smart turboprop + SBW	Number of engines			
	2	4	2	4
	T-tail		Conventional tail	
High wing (%)	−14.3	−11.8	−14.1	−11.7
Low wing	–	–	–	–

Table 5 Comparison of the DOC of different TA configurations (including the technologies NLF and SBW) with the DOC of the reference aircraft

Smart turboprop + NLF + SBW	Number of engines			
	2	4	2	4
	T-tail		Conventional tail	
High wing (%)	−17.1	−14.3	−16.6	−14.1
Low wing	–	–	–	–

3.3 Description of the Optimum TA Design

The final TA configuration with minimum DOC is a strut-braced high-wing with NLF, T-tail, two engines, and a propeller diameter of 7 m. On a mission range of 755 NM, this aircraft could offer fuel mass savings of about 36 % compared to an A320. The CO_2 emissions would therefore also be reduced by about 36 %. DOC could be lowered by about 17 % compared to the reference aircraft.

A simplified analysis of the DOC of the A320neo using OPerA showed that the DOC of the A320neo are about 4 % lower than the DOC of the A320. Comparing the DOC of the previously described TA to the DOC of the A320neo therefore still leads to a potential DOC reduction of about 13 %.

The final aircraft design is illustrated in Fig. 4. The figure shows key parameters of the design and a comparison to the values of the reference aircraft A320. The values for the A320 are taken from a redesign of the reference aircraft in PrOPerA.

Additionally, the figure contains the matching chart, payload range diagram, cabin layout, and pie charts of the operating empty mass, the component drag and the DOC of the TA.

The ground handling and the ability to derive an aircraft family are two important requirements for every new aircraft concept. The conventional design layout of the TA allows to keep the ground handling processes very similar to those of the reference aircraft and allows a conventional derivation of an aircraft family [5].

4 Discussion

Compared to [5], some design parameters changed. These changes will be discussed in the next paragraphs.

Cruise Mach Number
In [5], a cruise Mach number of 0.71 was favored for the TA design. Now, the optimum Mach number went down to 0.51.

This is mainly due to the reason that real aircraft drag polar data in [19] allowed to improve the calibration for the calculation of the drag polar of the TA leading to an increase of the required *P/W* at a certain Mach number which led to a lower optimum Mach number for minimum DOC.

Number of Engines
In [5], a TA configuration with four engines was preferred. Now minimum DOC are reached with two engines. When four engines were preferred, the requirement coming from the second segment was the dimensioning requirement for *P/W*. As the second segment requirement has to be fulfilled with one engine inoperative, four engines are advantageous in comparison with two engines. The main reason for the change of the optimum number of engines again comes from the increase of required *P/W* due to an improved calibration of the drag polar calculation. Now the required cruise Mach number is the dimensioning requirement for *P/W* so that the

advantage of four engines for the second segment requirement has no influence on the design anymore.

Cruise Altitude

The design results confirm that the Cruise Altitude (CA) of the chosen TA configuration is lower (about 40 %) than the CA of the A320.

The cruise altitude for horizontal flight can be found by setting lift equals weight, solving for ρ and after that solving for the cruise altitude:

$$C_L \cdot \frac{\rho}{2} \cdot v^2 \cdot S_W = m \cdot g \tag{1}$$

finally leads to:

$$h_{CA} = \frac{1 - \left(\frac{2 \cdot g}{C_L \cdot \rho_0 \cdot v^2} \cdot \frac{m}{S_W} \right)^{\frac{1}{4.25588}}}{k_a} \tag{2}$$

with

$$K_a = 0.022558 \,\text{km}^{-1}$$

$$\rho_0 = 1.225 \,\frac{\text{kg}}{\text{m}^3}$$

$$g = 9.81 \,\frac{\text{m}}{\text{s}^2}$$

The only variables in this equation influencing the cruise altitude are C_L, v, and m/S_W. v is squared and therefore has a dominating influence on cruise altitude. The lower v, the lower h_{CA}. m/S_W and C_L of TA and reference aircraft are similar and therefore do not lead to a significant change of h_{CA}. The cruise speed v of the TA is 29 % lower than that of the reference aircraft leading to a 40 % reduction of cruise altitude. The parameters C_L, v, and m/S_W have been optimized for minimum DOC. The resulting h_{CA} is therefore also a result of the optimization process and represents the optimum h_{CA} for the TA.

The main reason that the optimizer choses a low M_{CR} (and therefore low v) is the resulting low P/W. The resulting lower h_{CA} leading to a higher v is a positive side effect but not the main reason for the low M_{CR}.

In summary, the proposed TA concept flies at lower altitudes but due to a different reason than initially expected.

In [5], the difference in cruise altitude of TA and reference aircraft was lower. This is simply due to the fact that the optimum M_{CR} and therefore also v were higher leading to a higher cruise altitude of the TA.

5 Summary and Conclusion

In comparison to the reference aircraft Airbus A320, the proposed turboprop-driven aircraft concept potentially reduces fuel consumption and CO_2 emissions by about 36 %. DOC can potentially be reduced by about 17 % on a DOC mission range of 755 NM. The improvements mainly come from the lower fuel consumption of turboprop engines compared to turbofan engines, the increased aspect ratio leading to a high glide ratio and the big propeller diameters leading to high propeller efficiency, all together causing additional positive snowball effects. Drawbacks are the 21 % increase in block time due to the lower cruise speed and additional mass due to the higher landing gear lengths caused by high propeller diameters and additional required soundproofing material due to the engine noise.

Appendix

Notation

A	Aspect ratio
$A_{W,eff}$	Effective aspect ratio of the wing
$b_{W,geo}$	Geometrical span
c_{fuel}	Fuel cost
C_L	Lift coefficient
d_{prop}	Propeller diameter
DOC	Direct Operating Costs
E_{max}	Maximum glide ratio
EIS	Entry into service
G	Standard gravity
h_{CA}	Cruise altitude
h_{ICA}	Initial cruise altitude
k_a	Constant
m_F	Fuel mass
M_{CR}	Cruise Mach number
M	Mass
m_F	Fuel mass
$m_{F,trip}$	Fuel mass for the DOC range
m_{MPL}	Maximum payload mass

m_{MTO}	Maximum take-off mass
m_{OE}	Operating empty mass
m_{PAX}	Passenger mass
$m_{PL,DOC}$	Payload mass for the DOC calculation
n_{PAX}	(1-cl HD) Number of passengers in a one-class high density layout
$P_{eq,ssl}$	Equivalent take-off power at static sea level
PSFC	Power-specific fuel consumption
P/W	Power-to-weight ratio
R_{DOC}	Range for the DOC calculation
R_{MPL}	Maximum range (with maximum payload
s_{TOFL}	Take-off field length
s_{LFL}	Landing field length
SP	Seat pitch
S_W	Wing area
t_{TA}	Turnaround time
t/c	Thickness ratio
$U_{a,f}$	Utilization
V	Speed
η_{prop}	Propeller efficiency
λ	Taper ratio
ρ	Air density
ρ_0	Air density at sea-level of the International Standard Atmosphere
φ_{25}	Sweep angle at 25 % chord

References

1. European Commission. *Flightpath 2050 Europe's Vision for Aviation*. Aerodays, Madrid, 2011 – URL: http://ec.europa.eu/transport/air/doc/flightpath2050.pdf (accessed Feb 10th 2016).
2. Airport2030. Description of the research project, http://www.airport2030.de/Airport2030_de.html (accessed Feb 10th 2016).
3. Babikian, R., Lukacho, S.P. and Waitz, I.A. The historical fuel efficiency characteristics of regional aircraft from technological, operational, and cost perspectives. *Journal of Air Transport Management*, Vol. 8, No. 6, pp 389–400, 2002.
4. Airbus Defence and Space. Specification of A400 M, http://www.airbusmilitary.com/Aircraft/A400M/A400MSpec.aspx (accessed Feb 10th 2016).
5. Johanning, A. and Scholz, D. Novel Low-Flying Propeller-Driven Aircraft Concept For Reduced Direct Operating Costs And Emissions. In: *CD Proceedings : ICAS 2012 - 28th Congress of the International Council of the Aeronautical Sciences* (ICAS, Brisbane, 23-28. September 2012). Edinburgh, UK : Optimage Ltd, 2012. - ISBN: 978-0-9565333-1-9. Paper: ICAS2012-1.10.5 (510.PDF). URL: http://Airport2030. ProfScholz.de (accessed Feb 10th 2016).
6. Niţă, M. F. *Contributions to Aircraft Preliminary Design and Optimization*. München : Verlag Dr. Hut, 2013. - ISBN 978-3-8439-1163-4, Dissertation, Download: http://OPerA.ProfScholz.de (accessed Feb 10th 2016).
7. AIRBUS S.A.S. *A320 AIRPLANE CHARACTERISTICS FOR AIRPORT PLANNING*. Issue: Sep 30/85, Rev: May 2011.

8. Xie, X. *Ein Beitrag zum rechnerunterstützten Konzeptentwurf von Verkehrsflugzeugen mit Propellerantrieb*. Fortschrittsbericht, VDI Reiheihe 12, Nr. 367, Düsseldorf: VDI Verlag, 1998.
9. Citizen Friendly Aircraft. Description of the research project, https://www.tu-braunschweig.de/forschung/zentren/nfl/projekte/buergernahesflugzeug (accessed Feb 10th 2016).
10. Felipe Geraldo, A., Parra, J. E., Soler R. S. et al. Design of an Advanced Turboprop Aircraft for Regional Operations with Ninety Passengers. 51st AIAA Aerospace Sciences Meeting (Grapevine, 07–10. January 2013). AIAA 2013–0024.
11. National Aeronautics and Space Administration. *Subsonic Ultra Green Aircraft Research: Phase I Final Report*. Langley Research Center, Hampton, Virginia, NASA/CR–2011-216847, 2011.
12. Adkins, C. and Liebeck R. Design of optimum propellers. *Journal of Propulsion and Power*, Vol. 10, No. 5, pp 676-682, 1994.
13. Roux É. *Turboshaft, Turboprop & Turbofan Database Handbook*, Éditions Élodie Roux, 2011.
14. Association of European Airlines. *Short-Medium Range Aircraft AEA Requirements*. Brussels, AEA, 1989. (G(T)5656).
15. AIRBUS S.A.S.. *Airbus GMF 2012–2031 Navigating The Future*, Airbus S.A.S, 2012.
16. Carrier, G., Atinault, O., Dequand, S. et al. Investigation of a strut-braced wing configuration for future commercial transport. In: *CD Proceedings : ICAS 2012 - 28th Congress of the International Council of the Aeronautical Sciences* (ICAS, Brisbane, 23.-28. September 2012). Edinburgh, UK : Optimage Ltd, 2012. - ISBN: 978-0-9565333-1-9. Paper: ICAS 2012-1.10.2.
17. Torenbeek, E. *Synthesis of Subsonic Airplane Design*. Delft : Delft University Press, 1982.— ISBN 90-247-2724-3.
18. Scholz, D. *Skript zur Vorlesung Flugzeugentwurf*. Hamburg, Fachhochschule Hamburg, FB Fahrzeugtechnik, Abt. Flugzeugbau, Vorlesungsskript, 1999. - URL: http://FE.ProfScholz.de (accessed Feb 10th 2016).
19. Aviation Safety Council. *GE 791 Occurrence Investigation Report*. Volume I, ASC-AOR-05-04-001, Taipei, Taiwan, 2001.

Correction to: Design and Fabrication of a Quick Dismantlable Remotely Controlled Semirigid Finless Airship

Sohrab R. Mistri and Rajkumar S. Pant

Correction to:
Chapter "Design and Fabrication of a Quick Dismantlable
Remotely Controlled Semirigid Finless Airship"
in: R.P. Bajpai and U. Chandrasekhar (eds.),
Innovative Design and Development Practices
in Aerospace and Automotive Engineering,
Lecture Notes in Mechanical Engineering,
https://doi.org/10.1007/978-981-10-1771-1_16

In the original version of the book, the following belated correction has been incorporated: The author name has been changed from "Mistr S.R." to "Mistri S.R." in the frontmatter and backmatter and in Chapter 16. The erratum chapter has been updated with the changes.

The updated version of this chapter can be found at
https://doi.org/10.1007/978-981-10-1771-1_16

Author Index